MONITORING AND ENGINEERING OF THE STEM CELL MICROENVIRONMENT:

INKJET PRINTING OF GROWTH FACTORS ONTO NOVEL SCAFFOLDS FOR CONTROLLING MUSCULOSKELETAL STEM CELL DIFFERENTIATION AND ALIGNMENT

AND

DEVELOPMENT OF A COMPUTER VISION-BASED SYSTEM TO CHARACTERIZE STEM CELL GROWTH

By:

DAI FEI ELMER, KER

B.Sc. Molecular Biology and Genetics, University of Sydney, 2003

Submitted in Partial Fulfillment of the Requirements for the Degree of

DOCTOR OF PHILOSOPHY

Department of Biological Sciences

Carnegie Mellon University

February 16, 2012

Thesis Advisor: Phil G. Campbell, Ph.D. – Institute for Complex Engineered Systems

Committee Members:
Frederick Lanni, Ph.D. – Department of Biological Sciences
Adam D. Linstedt, Ph.D. – Department of Biological Sciences
Lee E. Weiss, Ph.D. – The Robotics Institute

Department Head: Nathan Urban, Ph. D.

ACKNOWLEDGEMENTS

I am sincerely grateful to my advisor Phil Campbell for giving me the opportunity to work in his lab. Through the varied and multidisciplinary projects he's tasked me to undertake and the numerous students that he's asked me to mentor, I have come into my own as an independent scientist. His easy-going nature has made it a joy to work in his lab. I cannot truly thank you enough for all that you have done for me.

I am greatly indebted to my committee member Lee Weiss for whom all intents and purposes, has served as my unofficial co-advisor. His meticulous attention to detail and emphasis on the engineering aspects of this work has made me a better and more rigorous scientist. I am deeply appreciative of his support and will fondly remember the light jokes and impressions that he often makes during meetings. His impression of a chain-smoking mobster was my favorite.

I am deeply thankful to my other committee members Fred Lanni and Adam Linstedt. Fred Lanni's extensive knowledge and expertise in microscopy has been invaluable in some of this work and made me a better microscopist while Adam Linstedt's emphasis on understanding biological mechanisms has grounded me in the biological aspects of my research.

I am grateful for Larry Schultz, who has been an invaluable member of my research. I am deeply appreciative of his heroic efforts to optimize the inkjet printing process for the many bio-inks used in this research. Many of the experiments presented here would not have been possible without him.

I am deeply indebted to my fellow lab mates (past and present) with whom I have shared many wonderful experiences with. Their willingness to teach me new techniques, involve me in aspects of their research, and dispense both personal and scientific advice has transformed the workplace into a delightful environment to turn up to ever day. In particular, Eric Miller and Jason Smith served as role models whose work ethic and diligence I sought to emulate, Julie Phillippi taught me how to perform quantitative PCR, Elvira Osuna-Highley assisted me with computational efforts in both the inflammation and automated cell tracking aspects of this work and Shuying Kwan-Uchiyama taught me mouse surgery and various cellular techniques in addition to originating the inflammation project. I am especially grateful for the numerous personal and scientific advices that Shuying Kwan-Uchiyama has given me over the years. They have helped me to navigate through the many challenges I faced in my quest for a doctorate. I am also thankful for all the students (Ashley Brienza, Rachel Dzombak, Esther Lee, Robbie Mckinstry, Krystin Meidell, Hirotaka Nakagawa, Kedar Perkins, Elizabeth Ransey, Niya Robinson) who have tolerated my mentoring. They have been instrumental in my success and I can only hope that they have learnt as much from me as I have from them. In particular, Hirotaka Nakagawa was a crucial and indispensable element in the inflammation research presented here.

I am thankful to all members (past and present) of the Molecular Sensor and Bioimaging Center at Carnegie Mellon University. In particular, James Fitzpatrick and Haibing Teng assisted me with microscopy, Sue Andreko and Byron Ballou with mouse surgeries, Yehuda Creeger with fluorescence activated cell analysis and sorting while Lauren Ernst, Michael Patrick, Greg Fisher provided invaluable advice related to my research.

I am thankful to my collaborators at the Computer Vision Cell Tracking Group at Carnegie Mellon University (Kanade Lab), Dai Nippon Printing Co. Ltd., the Stem Cell Research Center at the University of Pittsburgh (Huard lab), the Pediatric Craniofacial Biology Laboratory at the Children's Hospital of Pittsburgh (Cooper lab), the Frisbee Laboratory for Hematopoietic Graft Engineering at Yale University (Krause lab). Through my collaborations with them, I have gained new knowledge and my initial perceptions of the field have been broadened. There are too many people to thank individually but special thanks goes to tireless efforts of Ryoma Bise, Sungeun Eom, Seung-il Huh, Silvina Junkers, Kang Li, Sho Sanami and Zhaozheng Yin who have made invaluable contributions to the automated cell tracking aspect of this work.

I am also grateful to friends who have made my stay in the United States enjoyable. Anmol Groover, Shuying Kwan-Uchiyama, Shiang Yong Looi, Wee Liat Ong, Ee Wah Tan, Allen Tan, Chee Meng Tan, Tomoharu Uchiyama, and Yajuan Wang have each brought a piece of Asia to Pittsburgh.

I am deeply thankful for the love and support my family has given me over the last few years. Words cannot sufficiently convey my gratitude to my parents for their willingness to allow their youngest son to follow his interests halfway around the world, pursuing a doctorate in a field they were unfamiliar with and enduring the many miles and years apart. Yet despite this, my parents have always been my most unwavering supporters. My brother has also been a source of endless encouragement. I am grateful to him for entertaining my phone calls at odd hours despite being sleep-deprived from his work as a medical doctor. His conversations with me offer a badly needed distraction from work and have kept me sane over the last few years. Mom, Dad and Justin, I love you.

This thesis is dedicated to the memory of Lee Yan Xian, my fellow Rafflesian with whom I made a promise to many years ago. It was Yan Xian who embodied and taught me what strength in the face of overwhelming adversity meant.

Auspicium Melioris Aevi.

LIST OF FIGURES

Figure	Title	Page
1.1	The cellular microenvironment is a highly complex system that regulates stem cell behavior.	3
1.2	The structure and composition of muscle at the molecular, cellular, tissue and organ levels.	14
1.3	The structure and composition of tendon at the molecular, cellular and tissue levels.	18
1.4	The structure and composition of bone at the molecular, cellular, tissue and organ levels.	24
2.1	Effect of FGF-2, GDF-7 and BMP-2 on expression of tendon marker Scx in mouse C3H10T1/2 cells after 3.5 days in proliferation media.	47
2.2	Dose-dependent effect of FGF-4 on expression of tendon marker Scx in mouse C3H10T1/2 cells after 72h in proliferation media.	48
2.3	Dose-dependent effect of FGF-2 on expression of tendon marker Scx in mouse C2C12 cells after 72h in proliferation media.	49
2.4	Effect of FGF-2 on expression of tendon marker Scx in mouse C2C12 cells after 72h in myogenic media.	50
2.5	Dose-dependent effect of FGF-2 on expression of tendon marker Scx in mouse MDSCs after 72 h in proliferation media.	51
2.6	Dose-dependent effect of FGF-2 on expression of tendon marker Scx and muscle marker Myogenin in mouse MDSCs after 48h in myogenic media.	52
2.7	Effect of FGF-2 on expression of myofibroblast marker α-Smooth Muscle Actin (α-SMA) in mouse MDSCs after 72h in proliferation media.	53
2.8	Effect of 50 ng/mL FGF-2 on expression of *pea3*, *erm* and *scx* transcription factors in mouse C3H10T1/2 cells at 36 h and 72 h in proliferation media.	54
2.9	Effect of inkjet printed patterns of FGF-2 on expression of tendon marker Scx in mouse C3H10T1/2 cells after 72 h in proliferation media.	56
2.10	Effect of inkjet printed patterns of FGF-2 on expression of tendon marker Scx (red) and muscle marker MF20 (green) in mouse C2C12 cells after 72 h in proliferation and myogenic media.	57
2.11	Effect of inkjet printed patterns of BMP-2 and FGF-2 on expression of osteoblast marker ALP (blue), tendon marker Scx (red) and muscle marker MF20 (green) in mouse C2C12 cells after 72 h in proliferation media.	59
2.12	Effect of FGF-2 on expression of myofibroblast marker α-Smooth Muscle Actin (α-SMA) in mouse C2C12 cells after 72 h in proliferation media.	60
2.13	Dose-dependent effect of IGF-2 on expression of muscle marker MF20 in mouse C2C12 cells after 72h in myogenic media.	61
3.1	Polystyrene Spinneret-based Tunable Engineered Parameter (STEP)	82

	sub-micron fibers.	
3.2	TEM characterization of fibrin-coated polystyrene STEP sub-micron fibers.	83
3.3	Effect of polystyrene STEP fiber organization on myotube alignment.	84
3.4	Effect of polyurethane STEP fiber organization on myotube alignment.	85
3.5	Effect of Printed FGF-2 patterns on Scx expression in C3H10T1/2 cells.	86
3.6	Effect of printed BMP-2 patterns on ALP expression in C2C12 cells (Fibrin-coated polystyrene STEP fibers).	87
3.7	Effect of printed BMP-2 patterns on ALP expression in C2C12 cells (Fibrin-coated polyurethane STEP fibers).	88
3.8	Effect of printed FGF-2 patterns on MF20 and Scx expression in C2C12 cells.	89
3.9	Effect of printed BMP-2 and FGF-2 patterns on ALP, MF20 and Scx expression in C2C12 cells.	91
3.10	Effect of printed BMP-2 and FGF-2 on alignment of C2C12 cells.	92
3.11	Effect of fibrin-coated STEP fibers pre-soaked with BMP-2 and FGF-2 on C2C12 cell alignment.	93
4.1	Printing schematic for DermaMatrix scaffolds.	110
4.2	SEM image of a circular DermaMatrix scaffold (8 mm diameter).	114
4.3	Effect of DermaMatrix scaffold on MF20 expression in C2C12 cells.	114
4.4	Effect of printed BMP-2 patterns on ALP expression in C2C12 cells (DermaMatrix scaffold).	116
4.5	Effect of FGF-2 on expression of the periosteum marker Periostin in rabbit muscle-derived cells after 3 days in proliferation media.	117
4.6	Effect of printed BMP-2, FGF-2, GDF-7, IGF-2 and Noggin patterns on DermaMatrix scaffold *In Vivo*.	118
4.7	Effect of printed BMP-2, FGF-2, PDGF-BB, Noggin and SDF-1β patterns on DermaMatrix scaffold *In Vivo*.	119
5.1	Effect of FSDC conditioned media (t = 48h) on expression of osteoblast marker ALP (blue) in mouse MC3T3-E1 cells after 4 days.	134
5.2	Effect of J774A.1 cell conditioned media (t = 48h) on expression of osteoblast marker ALP (blue) in mouse MC3T3-E1 cells after 4 days.	135
5.3	Effect of J774A.1 cell conditioned media (t = 48h) on expression of osteoblast marker ALP (blue) in mouse MDSCs (Isolate 1, female) after 6 days.	137
5.4	Effect of J774A.1 cell conditioned media (t = 48h) on expression of osteoblast marker ALP (blue) in mouse MDSCs (Isolate 2, male) after 4 days.	139
5.5	Effect of J774A.1 cell conditioned media (t = 48h) on expression of osteoblast marker ALP (blue) in mouse MDSCs (Isolate 3, male) after 4 days.	141
5.6	Effect of J774A.1 cell conditioned media on expression of osteoblast marker ALP (blue) in mouse C2C12 cells grown on printed BMP-2 patterns after 4 days.	143
6.1	Overall Scheme of Real-Time Adaptive Cell Culture System.	160

6.2	Calculation and Evaluation of Confluency.	161
6.3	Modeling C2C12 cell confluency by five methods utilizing every data point/frame: (1) 1st order polynomial (yellow line), (2) 2nd order polynomial (blue line), (3) 3rd order polynomial (green line), (4) logarithmic function (magenta line), (5) Exponential (red line).	162
6.4	Comparison of C2C12 cell confluency predictions utilizing every data point/frame (blue line) versus every 6th data point/frame (red cross).	163
6.5	Remote Monitoring of Confluency and Predictive Modeling via the Internet.	164
6.6	Confluency Prediction.	165
6.7	Email and Text Notification.	165
6.8	Total Theoretical Cell Yield Achieved from Human- and Computer-directed Subcultures.	166
6.9	ALP Staining of Human- and Computer-directed Subcultures.	169
6.10	Myogenin and Pax7 Staining of Human- and Computer-directed Subcultures.	170

LIST OF TABLES

Table	Title	Page
3.1	Characterization of Polystyrene STEP Fibers.	83
4.1	Biochemical Factors for Patterning Ectopic MTB and PBM units.	110
6.1	Confluence Measurements from Computer-Directed Subcultures	167
6.2	Average Cell Yield per 35mm Petri Dish for Human- and Computer-directed Subcultures.	168

LIST OF ABBREVIATIONS

Abbreviation	Term
BFs	Biochemical Factors
BMP-2	Bone Morphogenetic Protein-2
CAM	Cell Adhesion Molecule
CM	Conditioned Media
ECM	Extracellular Matrix
FBS	Fetal Bovine Serum
FSDCs	Fetal Skin Dendritic Cells
GFs	Growth Factors
GDF-7/BMP-12	Growth and Differentiation Factor-7
GUI	Graphical User Interface
FGF-2	Fibroblast Growth Factor-2
HSPG	Heparan Sulfate Proteoglycan
IGF-1	Insulin-like Growth Factor-1
IGF-2	Insulin-like Growth Factor-2
IL-1β	Interleukin-1β
IL-4	Interleukin-4
IL-10	Interleukin-10
IL-12	Interleukin-12
LPS	Lipopolysaccharide
LTA	Lipoteichoic Acid
MAPK	Mitogen Activated Protein Kinase
MDSCs	Muscle-Derived Stem Cells
NO	Nitric Oxide
PBS	Phosphate Buffered Saline
PI3K	Phosphatidylinositol 3-kinase
PLCγ	Phospholipase C γ
PDGF	Platelet-Derived Growth Factor
RPM	Revolutions Per Minute
RT	Room Temperature
scx	Scleraxis
STEP	Spinneret-based Tunable Engineered Parameters
SDF-1/CXCL12	Stromal-Derived Factor-1
3D	Three Dimensional
TGF-β	Transforming Growth Factor-β
TNF- α	Tumor Necrosis Factor-α
VEGF	Vascular Endothelial Growth Factor

TABLE OF CONTENTS

	Page
Title Page	i
Acknowledgements	ii
List of Figures	v
List of Tables	viii
List of Abbreviations	ix
THESIS OVERVIEW	xv
i. Summary	xvi
ii. Motivation	xvii
iii. Objectives	xvii
iv. Rationale for Materials and Methods Employed in Present Study	xxii
v. References	xxiii
CHAPTER ONE: INTRODUCTION	**1**
1.1 Introduction	2
1.1.1 Stem Cell Behavior is Tightly Coupled to its Cellular Microenvironment	2
1.1.2 Wound Healing and Inflammation in the Context of the Cellular Microenvironment	5
1.1.2.1 Wound Healing	5
1.1.2.2 Inflammation	8
1.1.3 Organs and Tissues of the Musculoskeletal System	10
1.1.3.1 Muscle Architecture and Function	10
1.1.3.2 Tendon Architecture and Function	16
1.1.3.3 Bone Architecture and Function	19
1.1.3.4 Architecture of Relevant Musculoskeletal Interfaces	26
1.1.4 GF Signaling Pathways Relevant to Musculoskeletal Tissues	28
1.1.5 Technologies to Mimic Aspects of the Cellular Microenvironment for Tissue Engineering	30
1.2 References	30
CHAPTER TWO: *IN VITRO* PATTERNING OF A PRIMITIVE MUSCLE-TENDON-BONE UNIT: SIMULTANEOUS CONTROL OF MUSCLOSKELETAL CELL DIFFERENTIATION WITH INKJET-BASED PRINTING OF BMP-2 AND FGF-2 PATTERNS ONTO FIBRIN-COATED GLASS COVERSLIPS	**39**
2.1 Abstract	40
2.2 Introduction	40
2.3 Materials and Methods	42
2.3.1 Cell Culture	42
2.3.2 Growth Factor Preparation and Use	43
2.3.3 Preparation of Fibrin Coated Coverslips	43
2.3.4 Growth Factor Printing	44
2.3.5 Quantitative PCR	44
2.3.6 Immunofluorescence staining	45

2.3.7 ALP Stain 46
2.3.8 Statistical Analysis 46
2.4 Results 46
2.4.1 Effect of Liquid-Phase FGF-2 and FGF-4 on Scx Expression in C3H10T1/2 Cells 46
2.4.2 Effect of Liquid-Phase FGF-2 on Scx Expression in C2C12 Cells 48
2.4.3 Effect of Liquid-Phase FGF-2 on Scx Expression in MDSCs 50
2.4.4 Regulation of scx in C3H10T1/2 Cells 53
2.4.5 Effect of Solid-Phase FGF-2 on Scx Expression in C3H10T1/2 Cells 55
2.4.6 Effect of Solid-Phase FGF-2 on MF20 and Scx Expression in C2C12 Cells 56
2.4.7 Effect of Solid-Phase BMP-2 and FGF-2 on ALP, MF20 and Scx Expression in C2C12 Cells 58
2.4.8 Effect of Solid-Phase FGF-2 on α-Smooth Muscle Actin Expression in C2C12 Cells 60
2.4.9 Effect of Liquid-Phase IGF-2 on Sarcomeric Myosin Expression in C2C12 Cells 60
2.5 Discussion 61
2.5.1 Directing Osteoblast Differentiation 61
2.5.2 Directing Myocyte Differentiation 62
2.5.3 Directing Tenocyte Differentiation 63
2.5.4 Simultaneous Control of Multiple Musculoskeletal Cell Fates on Fibrin-Coated Glass Coverslips with Solid-Phase GF Patterns using Inkjet-based Bioprinting 64
2.6 Conclusions 66
2.7 Acknowledgements 66
2.8 References 66

CHAPTER 3: *IN VITRO* PATTERNING OF A PRIMITIVE MUSCLE-TENDON-BONE UNIT: SIMULTANEOUS CONTROL OF MUSCLOSKELETAL CELL ALIGNMENT AND CELL DIFFERENTIATION WITH INKJET-BASED PRINTING OF BMP-2 AND FGF-2 PATTERNS ONTO SPINNERET-BASED TUNABLE ENGINEERED PARAMETERS (STEP) FIBERS **70**

3.1 Abstract 71
3.2 Introduction 71
3.3 Materials and Methods 74
3.3.1 Fabrication of Polystyrene STEP Fibers 74
3.3.2 Fibrin- or Serum-Coating of Polystyrene STEP Fibers 74
3.3.3 Scanning Electron Microscopy 75
3.3.4 Transmission Electron Microscopy 76
3.3.5 Cell Culture 77
3.3.6 Growth Factor Printing 77
3.3.7 Alkaline Phosphatase (ALP) Staining 78
3.3.8 Immunofluorescence Staining 78

3.3.9 Quantification of Immunofluorescence or ALP Staining 79
3.3.10 Actin Staining 79
3.3.11 Statisical Analysis 80
3.4 Results 80
3.4.1 Characterization of Polystyrene STEP Fibers 80
3.4.2 Effect of Polystyrene STEP fibers on Myotube Alignment 83
3.4.3 Effect of Serum-Coated STEP Fibers Patterned with FGF-2 on Tenocyte Differentiation 85
3.4.4 Effect of Fibrin-Coated STEP Fibers Patterned with BMP-2 on Osteoblast Differentiation 87
3.4.5 Effect of Fibrin-Coated STEP Fibers Patterned with FGF-2 on Tenocyte and Myocyte Differentiation and Cell Alignment 88
3.4.6 Effect of Fibrin-Coated STEP Fibers Patterned with BMP-2 and FGF-2 on Osteoblast, Tenocyte and Myocyte Differentiation and Cell Alignment 90
3.5 Discussion 93
3.5.1 Fibrous Scaffolds as ECM Analogs for Musculoskeletal Tissue Engineering 93
3.5.2 Controlling Musculoskeletal Cell Alignment with STEP Fibers 94
3.5.3 Simultaneous Control of Musculoskeletal Cell Alignment and Cell Differentiation on STEP Fibers with Solid-Phase GF Patterns using Inkjet-based Bioprinting 95
3.6 Conclusion 97
3.7 Acknowledgements 98
3.8 References 98

CHAPTER 4: *IN VITRO* AND *IN VIVO* EFFECT OF PRINTED BIOCHEMICAL FACTOR PATTERNS ON DERMAMATRIX SCAFFOLDS **102**

4.1 Abstract 103
4.2 Introduction 104
4.3 Materials and Methods 106
4.3.1 Cell Culture 106
4.3.2 Biochemical Factor Preparation and Use 107
4.3.3 Preparation of Fibrin Coated Coverslips 108
4.3.4 Preparation and Characterization of DermaMatrix Scaffold Structure 108
4.3.5 Biochemical Factor Printing 109
4.3.6 Printed Scaffolds 109
4.3.7 Animal Surgery 111
4.3.8 DermaMatrix Harvesting 111
4.3.9 Sample Preparation for Histology 111
4.3.10 Immunofluorescence Staining 112
4.3.11 Histological Staining 113
4.3.12 Statistical Analysis 113
4.4 Results 113
4.4.1 Characterization of DermaMatrix Scaffolds 113
4.4.2 Effect of DermaMatrix Patterned with BMP-2 on Osteoblast 115

Differentiation
4.4.3 Effect of Fibrin-Coated Glass Coverslips Patterned with FGF-2 on Periostin Expression in Muscle-Derived Cells 116
4.4.4 Effect of DermaMatrix Patterned with BMP-2, FGF-2, GDF-7, IGF-2 and Noggin *In Vivo* 117
4.4.5 Effect of DermaMatrix Patterned with BMP-2, FGF-2, PDGF-BB, Noggin and SDF-1β *In Vivo* 118
4.5 Discussion 119
4.5.1 Characterization of DermaMatrix Scaffold 119
4.5.2 Identification of a Periosteum-Promoting GF 120
4.5.3 Spatial Control of Tissue Formation *In Vivo* 120
4.6 Conclusions 121
4.7 Acknowledgements 121
4.8 References 122

CHAPTER 5: *IN VITRO* EFFECT OF INFLAMMATORY AND ANTI-INFLAMMATORY MICROENVIRONMENTS ON OSTEOBLAST DIFFERENTIATION **124**

5.1 Abstract 125
5.2 Introduction 125
5.3 Materials and Methods 127
5.3.1 Cell Culture 127
5.3.2 Conditioned Media 128
5.3.3 Osteogenic Differentiation 128
5.3.4 ALP Stain 129
5.3.5 Growth Factor Preparation and Use 130
5.3.6 Preparation of Fibrin Coated Coverslips 130
5.3.7 Growth Factor Printing 130
5.3.8 Statistical Analysis 131
5.4 Results 131
5.4.1 Effect of FSDC and J774A.1 Cell Conditioned Media on ALP Expression in MC3T3-E1 Cells 131
5.4.2 Effect of J774A.1 Cell Conditioned Media on ALP Expression in MDSC Cells 136
5.4.3 Effect of J774A.1 Cell Conditioned Media on ALP Expression in C2C12 Cells 142
5.5 Discussion 143
5.5.1 Effect of Immune Cell Conditioned Media on ALP Expression in MC3T3-E1 Cells 143
5.5.2 Effect of Immune Cell Conditioned Media on ALP Expression in MDSCs 144
5.5.3 Effect of Immune Cell Conditioned Media on ALP Expression in C2C12 Cells 146
5.6 Conclusions 146
5.7 Acknowledgements 147
5.8 References 147

CHAPTER 6: REAL TIME ADAPTIVE SUBCULTURE OF PROGENITOR CELLS **149**
6.1 Abstract 150
6.2 Introduction 151
6.3 Materials and Methods 153
6.3.1 Cell Culture 153
6.3.2 Phase-Contrast Time-Lapse Microscopy 154
6.3.3 Confluency Measurement and Evaluation 154
6.3.4 Confluency Prediction and Notification 156
6.3.5 Cell Calculator User Interface Tool 156
6.3.6 Real-time Adaptive Culture 157
6.3.7 Alkaline Phosphatase (ALP) Staining 157
6.3.8 Myogenin and Pax7 Immunofluorescence Staining 158
6.3.9 Statistical Analysis 158
6.4 Results 159
6.4.1 Real-time Adaptive Subculture System 159
6.4.2 Evaluation of Confluency 166
6.4.3 Performance of Real-time Adaptive Subculture System 167
6.5 Discussion 170
6.5.1 Computer-Generated Cell Confluency Measurements for Manual and Adaptive Subculture 170
6.5.2 Accuracy of Computer-Generated Cell Confluency Measurements 172
6.5.3 Computer-Generated Cell Confluency Predictions 173
6.5.4 Adaptive Subculture of C2C12 Cells 174
6.5.5 Adaptive Subculture for Stem Cell Manufacture and QA/QC 175
6.6 Conclusions 176
6.7 Acknowledgements 177
6.8 References 177

CHAPTER 7: CONCLUSIONS AND FUTURE DIRECTIONS **180**
7.1 Growth-Factor Patterning as a Means for Providing Biochemical Cues to Spatially Control Stem Cell Differentiation *In Vitro* 181
7.2 STEP Fibers as a Means for Providing Geometric Cues to Control Stem Cell Alignment *In Vitro* 183
7.3 Growth-Factor Patterning as a Means for Providing Biochemical Cues to Spatially Control Stem Cell Differentiation *In Vivo* 184
7.4 The Role of Inflammation in Stem Cell Differentiation 186
7.5 Automated Cell Tracking as a Tool for Stem Cell Production and Biological Characterization of Stem Cell Behavior 188
7.6 Summary and Conclusions 190
7.7 References 191

APPENDICES **193**
i. Appendix A1: Immune Cell Cross-Talk and *In Vitro* Effect of Inflammatory and Anti-Inflammatory Microenvironments on Osteoblast Mineralization 193
ii. Appendix A2: Development of a Software Package for Manual and Automated 209

In Vitro Stem Cell Tracking Followed by An Analysis of Cell Tracking Errors
iii. Appendix A3: Automated mitosis Detection of Stem Cell Populations in Phase-Contrast Microscopy Images 279
iv. Appendix A4: Data-Driven Prediction on Stem Cell Culture Process 292
v. Appendix A5: Restoring DIC Microscopy Images from Multiple Shear Directions 298
vi. Appendix A6: Role of RHOA Specific Guanine Exchange Factors in Regulation of Endomitosis in Megakaryocytes 312

THESIS OVERVIEW

i. SUMMARY

The primary objective of this study was to develop approaches for controlling and monitoring stem cell behavior *in vitro* and *in vivo* for potential applications in regenerative medicine. To control stem cell behavior *in vitro* and *in vivo*, signaling molecules including growth factors (GFs) were spatially patterned onto novel substrates and scaffolds to instruct stem cells to undergo desired cell behaviors such as musculoskeletal differentiation in register to the biochemical and geometric cues supplied. The premise for this approach is based on the biological phenomenon whereby stem cell behavior can be directed by instructive cues present in its immediate vicinity or microenvironment. Using this methodology, a primitive muscle-tendon-bone (MTB) unit was patterned *in vitro* while ectopic bone tissue was patterned *in vivo*. In addition, the effect of inflammatory and anti-inflammatory microenvironments on osteoblast differentiation was characterized since inflammation is an important component of the wound healing response. In such studies, inflammatory microenvironments were found to inhibit osteoblast differentiation in several musculoskeletal progenitor cells and this inhibition could be reversed with anti-inflammatory IL-10. Primary cells such as muscle-derived stem cells (MDSCs) were also found to display differing levels of sensitivity to such osteoblast inhibition. To monitor stem cell behavior *in vitro*, a computer-vision based system was developed for real-time adaptive subculture of muscle-progenitor cells. This computer-directed subculture system minimizes human labor and subjectivity during progenitor cell expansion and cells cultured with this system were comparable to those grown by a human operator. The work described here illustrates methods for controlling and monitoring stem cell behavior and may have potential applications in regenerative medicine.

ii. MOTIVATION

The musculoskeletal system comprises of organs and tissues such as bone, muscle, tendon, cartilage, ligament as well as various tissue interfaces such as bone-to-tendon entheses or myotendinous junctions. The functions of the musculoskeletal system are diverse owing to its participation in numerous biological processes which include mechanical roles in supporting the body [1-3], maintaining posture [1-3], aiding movement [3-6], protecting internal organs from physical trauma [1-3] and facilitating the mechanics of hearing [3] as well as physiological roles in growth factor (GF) storage [3, 7], fat storage [3], calcium and phosphate homeostasis [3, 8], blood homeostasis [1-3, 9-11], protein and glucose metabolism [3, 8, 12] and thermoregulation [3, 12].

Given its multifaceted roles, disorders of the musculoskeletal system can disrupt these mechanical and physiological processes to dramatically impact the standard of living [13, 14], resulting in significant morbidity or premature death [15]. In the United States alone, the impact of musculoskeletal diseases and trauma has an estimated direct and indirect cost of $849 billion USD annually [15-18]. This problem is likely to be exacerbated as the population of senior citizens increases throughout developed countries, highlighting a need to develop approaches for monitoring and controlling stem cell behavior to advance musculoskeletal stem cell research and therapeutic development.

iii. OBJECTIVES

MTB units occur throughout the musculoskeletal system and act as attachments between muscle and bone, and derivations of these units in the form of ligament-bone attachments and muscle-bone attachments are also physiologically relevant [19, 20]. Presently, the clinical repair of

injuries to MTB represents a significant unmet challenge and presents itself as a potential target for developing novel therapeutics to address diseases and trauma of the musculoskeletal system. As reviewed in Chapter 1, cell behavior is heavily influenced by its surrounding microenvironment. Therefore, the use of highly oriented geometric scaffolds as well as controlling the physical placement of exogenous GFs including dosage modulation were logical considerations for mimicking physical and biochemical cues present in musculoskeletal tissues to study stem cell behaviors including musculoskeletal cell alignment and differentiation. In addition, it was crucial to consider the microenvironment within the context of the inflammatory response since inflammation is an integral component of the wound healing process and can drastically alter the cellular microenvironment [21-24]. To facilitate the application of stem cells in regenerative medicine, it was also important to develop tools to monitor stem cell behavior *in vitro* so that stem cells can be rapidly characterized and used clinically in a predictable fashion.

The goal of this dissertation was to pattern various components of the cellular microenvironment for directing stem cell differentiation and alignment to create a primitive MTB unit and investigate the impact of inflammation on stem cell differentiation. In addition, it was crucial to develop software tools for monitoring and analyzing stem cell behavior *in vitro* to facilitate *ex vivo* stem cell expansion.

The subsequent chapters of this thesis describe the experimental methods developed and the results obtained to fulfill the objectives outlined below. **Chapter 1** is an introductory chapter that reviews the current literature behind the thesis work. **Chapter 2** describes the use of piezoelectric inkjet-based bioprinting to control musculoskeletal stem cell differentiation to pattern a primitive MTB unit *in vitro*. **Chapter 3** builds upon the work described in **Chapter 2** to

pattern a primitive MTB unit while simultaneously controlling cell alignment *in vitro*. **Chapter 4** further builds upon the work of **Chapter 2** and **Chapter 3** to direct ectopic tissue formation *in vivo*. In **Chapter 5** and **Appendix A1**, inflammatory and anti-inflammatory microenvironments are created to examine the immune cell cross-talk as well as the effect of inflammatory and anti-inflammatory microenvironments on osteoblast differentiation and mineralization. In **Chapter 6**, **Appendix A2**, **Appendix A3**, **Appendix A4** and **Appendix A5**, methods for monitoring stem cells via automated cell tracking approaches in time-lapse microscopy image sequences are described to facilitate the biological study of the stem cell microenvironment as well as *ex vivo* stem cell expansion. **Appendix A6** describes the use of fluorescence time-lapse microscopy to investigate the mechanism of endomitosis during megakaryocyte differentiation.

Objective 1: Demonstrate spatially patterning of a primitive MTB unit using solid-phase GFs *in vitro* (Chapter 2).

Since a well-established literature on bone- and muscle-promoting GFs such as BMPs and IGFs already exists, Objective 1 sought to identify tendon-promoting GFs immunofluorescently on the basis of positive staining for the tendon marker Scx and negative staining for other differentiation markers such as Smooth Muscle Actin-α or (SMA- α). Subsequently, quantitative PCR was performed to study the mechanism of tendon cell differentiation. Following this, musculoskeletal progenitor or stem cells were exposed to tendon-promoting GFs in both liquid- and solid-phase experiments to determine if there was a dose dependent effect on tendon cell differentiation. For solid-phase experiments, tendon-promoting GFs were immobilized onto a fibrin-coated glass coverslips using inkjet-based bioprinting. Having identified and characterized the effect of tendon-promoting GFs on musculoskeletal progenitor or stem cells, a primitive MTB unit was patterned *in vitro*.

Objective 2: Demonstrate spatial patterning of a primitive MTB unit concurrently with musculoskeletal cell alignment using solid-phase GFs and highly oriented fibrous scaffolds, respectively, *in vitro* (Chapter 3).

Having established an *in vitro* MTB unit, Objective 2 sought to study the effect of highly oriented polystyrene and polyurethane fibers on musculoskeletal cell alignment by seeding musculoskeletal progenitor or stem cells onto polystyrene and polyurethane STEP fibers. Subsequently, polystyrene and polyurethane STEP fibers were coated with ECM molecules such as fibrin and inkjet-printed with various GFs to pattern various musculoskeletal interfaces such as a primitive MTB unit while simultaneously controlling cell alignment.

Objective 3: Demonstrate spatial patterning of musculoskeletal cell differentiation using solid-phase GFs *in vivo* (Chapter 4).

Having demonstrated spatial control of musculoskeletal progenitor or stem cell differentiation *in vitro*, Objective 3 sought to pattern a MTB unit *in vivo*. First, the suitability of DermaMatrix scaffold for animal studies was determined using SEM and *in vitro* cell differentiation assays to determine if this scaffold could support cellular infiltration and musculoskeletal cell differentiation *in vivo*. In addition, an immunefluorescence screen was performed using the periosteum marker, Periostin to identify periosteum-promoting GFs for patterning a Periosteum-Bone-Bone Marrow (PBM) unit. Subsequently, printed DermaMatrix scaffolds were subcutaneously implanted in mice to attempt to pattern a primitive MTB unit and PBM unit *in vivo*.

Objective 4: To study the influence of macrophage and dendritic cells on osteoblast differentiation under inflammatory and non-inflammatory conditions (Chapter 5).

As inflammation is an integral component of the wound healing process and highly relevant to efficient musculoskeletal repair, Objective 4 sought to characterize the impact of macrophage and dendritic cell secretions on osteoblast differentiation. Various inflammatory (LPS) and anti-inflammatory (IL-10) stimuli were used to activate J774A.1 macrophages and FSDCs towards type 1 pro-inflammatory and type 2 anti-inflammatory phenotypes, respectively. The conditioned media was harvested and used to culture various musculoskeletal progenitor or stem cells such as mouse C2C12 myoblasts, mouse MDSCs and mouse MC3T3-E1 fibroblasts in the presence of an osteogenic stimulus such as BMP-2 to determine the indirect effect of LPS and/or IL-10 on osteoblast differentiation. Similarly, these cells were also be cultured in the presence of LPS and/or IL-10 to determine the direct effect of LPS and/or IL-10 on osteoblast differentiation.

Objective 5: Develop a real-time adaptive subculture system to obtain clinically relevant quantities of cells for cell-based therapy (Chapter 6).

Objective 5 sought to facilitate the use of cell-based therapies in regenerative medicine by developing a real-time adaptive subculture system as a means towards automated stem cell culture. Software tools were developed to analyze phase-contrast time-lapse microscopy images in real time to detect cells and determine the level of cell confluency. Based on the measured level of cell confluency, the software modeled and predicted cell growth, alerting a human operator through email and mobile phone text messaging four hours prior to reaching a pre-determined cell confluency threshold to prepare for cell culture. The software also enabled a human operator to remotely monitor the cell cultures via the Internet. With a target goal of producing 50 million cells, this computer-directed cell culture system was employed to grow

mouse C2C12 myoblasts as a paradigm stem cell population. The performance of this computer vision-based system was determined by assessing the number of serial cultures required to reach the target goal of 50 million cells as well as the capability of cells to differentiate into myocytes and osteoblasts thereafter.

iv. RATIONALE FOR MATERIALS AND METHODS USED IN PRESENT STUDY

In this thesis, various scaffolds and substrates such as ECM-coated glass coverslips, Spinneret-based Tunable Engineered Parameters (STEP) fibers and acellular human skin allograft (DermaMatrix) were used in conjunction with piezoelectric inkjet-based GF bioprinting as well as cells of the musculoskeletal and immune system to achieve this.

Fibrin-coated glass coverslips, fibrin- or serum-coated STEP fibers (polystyrene and polyurethane) and Dermamatrix were utilized as printing substrates due to their inherent cell- and GF-binding capabilities [25-31]. In addition, fibrin has important physiological relevance due to its role as a provisional matrix during wound healing [25]. Spinneret-based Tunable Engineered Parameters (STEP) fibers were employed as they are sub-micron (nano) sized fibers that can be fabricated to approximate the size and morphology natural musculoskeletal ECM fibers [32-34]. DermaMatrix was used as it is a biomaterial that consists primarily of collagen, the most common major constituent in ECM. Furthermore, DermaMatrix has also been approved for clinical use in humans.

To perform solid-phase GF patterning experiments that recreate physiologically-relevant conditions in the body, piezoelectric inkjet-based bioprinting was chosen as it is a non-contact and programmable mode of printing, and as such, would not damage the surface being printed on or require the fabrication of custom stamps. Furthermore, inkjet-based bioprinting is amenable to

a technique known as overprinting, where drops are jetted directly on top of one another, allowing for the dose of GF deposited to an area to be modulated, as long as the binding sites are not completely saturated [26, 29-31, 35]. Although our inkjet-based biopatterning method has much less resolution (approximately 14 pl drops which correspond to 75 μm diameter spots on fibrin-coated glass coverslips) than other protein arraying technologies such as photolithography, it has been demonstrated that this resolution was sufficient for studying the behavior of stem cell populations [26, 29-31, 35]. As such, patterning immobilized solid-phase growth factors coupled with the use of a single multipotent stem cell population will provide the required degree of precision to spatially pattern GFs to control cell behavior.

Mouse C2C12 myoblasts, mouse C3H10T1/2 mesenchymal fibroblasts, mouse MC3T3-E1 fibroblasts and Muscle-Derived Stem Cells (MDSCs) were utilized as they have previously been shown to differentiate into cells of the musculoskeletal system [26, 27, 29-31, 35-38] and may be relevant models of stem cells that participate in wound healing of a musculoskeletal injury while J774A.1 macrophages [39] and Fetal Skin Dendritic Cells (FSDCs) [40] were employed as they could be induced to activate and differentiate into type 1 and type 2 cells when challenged with lipopolysaccharide (LPS; a constituent of gram-negative bacteria cell wall) and IL-10, respectively.

v. REFERENCES

1. Li, X.J. and J. W.S.S., *Integrated Bone Tissue Anatomy and Physiology*, in *Current Topics in Osteoporosis*, H.W. Deng and Y.Z. Liu, Editors. 2005, World Scientific Publishing Co. Pte. Ltd. p. 45.
2. Liebschner, M.A.K. and M.A. Wettergreen, *Optimization of Bone Scaffold Engineering for Load Bearing Applications*, in *Topics In Tissue Engineering*. 2003.
3. Marieb, E.N., *Human Anatomy and Physiology*. 5th ed. 1999: Benjamin Cummings.

4. Banos, C.C., A.H. Thomas, and C.K. Kuo, *Collagen fibrillogenesis in tendon development: current models and regulation of fibril assembly.* Birth Defects Res C Embryo Today, 2008. **84**(3): p. 228-44.
5. Longo, U.G., et al., *Histopathology of rotator cuff tears.* Sports Med Arthrosc, 2011. **19**(3): p. 227-36.
6. Zhang, G., et al., *Development of tendon structure and function: regulation of collagen fibrillogenesis.* J Musculoskelet Neuronal Interact, 2005. **5**(1): p. 5-21.
7. Jadlowiec, J.A., A.B. Celil, and J.O. Hollinger, *Bone tissue engineering: recent advances and promising therapeutic agents.* Expert Opin Biol Ther, 2003. **3**(3): p. 409-23.
8. Fukumoto, S. and T.J. Martin, *Bone as an endocrine organ.* Trends Endocrinol Metab, 2009. **20**(5): p. 230-6.
9. Arnett, T.R., *Acidosis, hypoxia and bone.* Arch Biochem Biophys, 2010. **503**(1): p. 103-9.
10. Hu, H., M. Rabinowitz, and D. Smith, *Bone lead as a biological marker in epidemiologic studies of chronic toxicity: conceptual paradigms.* Environ Health Perspect, 1998. **106**(1): p. 1-8.
11. Li, H., et al., *Adult bone-marrow-derived mesenchymal stem cells contribute to wound healing of skin appendages.* Cell Tissue Res, 2006. **326**(3): p. 725-36.
12. Wolfe, R.R., *The underappreciated role of muscle in health and disease.* Am J Clin Nutr, 2006. **84**(3): p. 475-82.
13. Murray, C.J., *Quantifying the burden of disease: the technical basis for disability-adjusted life years.* Bull World Health Organ, 1994. **72**(3): p. 429-45.
14. Rosser, R. and P. Kind, *A scale of valuations of states of illness: is there a social consensus?* Int J Epidemiol, 1978. **7**(4): p. 347-58.
15. WHO Scientific Group on the Burden of Musculoskeletal Conditions at the Start of the New Millennium, *The burden of musculoskeletal conditions at the start of the new millennium.*, in *World Health Organization Technical Report Series* 2003, World Health Organization. p. 218.
16. American Association of Orthopaedic Surgeons, *Burden of Musculoskeletal Diseases in the United States: Prevalence, Societal and Economic Cost* 2008: AAOS. 247.
17. Connelly, L.B.W., Anthony ; Brooks, Peter *"Cost-Effectiveness of Interventions for Musculoskeletal Conditions." in Disease Control Priorities in Developing Countries* 2nd ed. 2006, New York: Oxford University Press. . 963-980.
18. Lindgren, B., *The economic impact of musculoskeletal disorders.* Acta Orthop Scand Suppl, 1998. **281**: p. 58-60.
19. Clayton, R.A. and C.M. Court-Brown, *The epidemiology of musculoskeletal tendinous and ligamentous injuries.* Injury, 2008. **39**(12): p. 1338-44.
20. Yang, P.J. and J.S. Temenoff, *Engineering Orthopedic Tissue Interfaces.* Tissue Eng Part B Rev, 2009.
21. Colombo, J.S., et al., *Delayed osteoblast differentiation and altered inflammatory response around implants placed in incisor sockets of type 2 diabetic rats.* Clin Oral Implants Res, 2011. **22**(6): p. 578-86.
22. Liu, N., et al., *High levels of beta-catenin signaling reduce osteogenic differentiation of stem cells in inflammatory microenvironments through inhibition of the noncanonical Wnt pathway.* J Bone Miner Res, 2011.

23. Tidball, J.G. and S.A. Villalta, *Regulatory interactions between muscle and the immune system during muscle regeneration.* Am J Physiol Regul Integr Comp Physiol, 2010. **298**(5): p. R1173-87.
24. Zhang, J. and J.H. Wang, *Production of PGE(2) increases in tendons subjected to repetitive mechanical loading and induces differentiation of tendon stem cells into non-tenocytes.* J Orthop Res, 2010. **28**(2): p. 198-203.
25. Breen, A., T. O'Brien, and A. Pandit, *Fibrin as a delivery system for therapeutic drugs and biomolecules.* Tissue Eng Part B Rev, 2009. **15**(2): p. 201-14.
26. Campbell, P.G., et al., *Engineered spatial patterns of FGF-2 immobilized on fibrin direct cell organization.* Biomaterials, 2005. **26**(33): p. 6762-70.
27. Cooper, G.M., et al., *Inkjet-based biopatterning of bone morphogenetic protein-2 to spatially control calvarial bone formation.* Tissue Eng Part A, 2010. **16**(5): p. 1749-59.
28. Miller, E., *Inkjet Printing of Solid-Phase Growth Factor Patterns to Direct Cell Fate*, in *Biomedical Engineering*. 2007, Carnegie Mellon University: Pittsburgh. p. 349.
29. Miller, E.D., et al., *Dose-dependent cell growth in response to concentration modulated patterns of FGF-2 printed on fibrin.* Biomaterials, 2006. **27**(10): p. 2213-21.
30. Miller, E.D., et al., *Spatially directed guidance of stem cell population migration by immobilized patterns of growth factors.* Biomaterials, 2011. **32**(11): p. 2775-85.
31. Phillippi, J.A., et al., *Microenvironments engineered by inkjet bioprinting spatially direct adult stem cells toward muscle- and bone-like subpopulations.* Stem Cells, 2008. **26**(1): p. 127-34.
32. Nain, A.S., et al., *Dry Spinning based Spinneret based Tunable Engineered Parameters (STEP) Technique for Controlled and Aligned Deposition of Polymeric Nanofibers.* Macromol Rapid Commun., 2009. **30**(16): p. 6.
33. Nain, A.S., et al., *Fabrication of Single and Multi-Layer Fibrous Biomaterial Scaffolds for Tissue Engineering*, in *Proceedings of the International Mechanical Engineering Conference and Exposition*. 2008: Boston, Massachusetts, USA.
34. Nain, A.S., et al., *Control of cell behavior by aligned micro/nanofibrous biomaterial scaffolds fabricated by spinneret-based tunable engineered parameters (STEP) technique.* Small, 2008. **4**(8): p. 1153-9.
35. Miller, E.D., et al., *Inkjet printing of growth factor concentration gradients and combinatorial arrays immobilized on biologically-relevant substrates.* Comb Chem High Throughput Screen, 2009. **12**(6): p. 604-18.
36. Matsubara, T., et al., *BMP2 regulates Osterix through Msx2 and Runx2 during osteoblast differentiation.* J Biol Chem, 2008. **283**(43): p. 29119-25.
37. Qu-Petersen, Z., et al., *Identification of a novel population of muscle stem cells in mice: potential for muscle regeneration.* J Cell Biol, 2002. **157**(5): p. 851-64.
38. Reznikoff, C.A., D.W. Brankow, and C. Heidelberger, *Establishment and characterization of a cloned line of C3H mouse embryo cells sensitive to postconfluence inhibition of division.* Cancer Res, 1973. **33**(12): p. 3231-8.
39. Ralph, P., J. Prichard, and M. Cohn, *Reticulum cell sarcoma: an effector cell in antibody-dependent cell-mediated immunity.* J Immunol, 1975. **114**(2 pt 2): p. 898-905.
40. Girolomoni, G., et al., *Establishment of a cell line with features of early dendritic cell precursors from fetal mouse skin.* Eur J Immunol, 1995. **25**(8): p. 2163-9.

CHAPTER 1: INTRODUCTION

1.1 INTRODUCTION

1.1.1 Stem Cell Behavior is Tightly Coupled to its Cellular Microenvironment

Stem cells, which are defined by their ability to self-renew and to give rise to differentiated cell types, reside in highly-regulated microenvironments called stem cell niches [1, 2]. Within these niches, stem cells occur at low frequency and are largely quiescent, in part, to protect the host from over-exuberant stem-cell proliferation that could otherwise lead to tumorigenesis, however, upon tissue injury, these cells migrate towards the injury site and proliferate extensively to participate in tissue repair [2, 3]. The application of multipotent stem cells for regenerative medicine requires a fundamental understanding of how the architecture and biochemical composition of a cell's immediate microenvironment can impact cell behavior and function.

Within the musculoskeletal system, differentiated cells such as myocytes, tenocytes and osteoblasts maintain tissue function primarily by contractile force generation, collagen secretion and collagen mineralization, respectively [4]. During tissue development, homeostasis and wound healing, stem cells integrate various signals from their microenvironment to participate in the generation of these differentiated cells [2] as well as modulate their external microenvironment through secretion of cell signaling molecules, ultimately promoting tissue formation or repair [5-7]. **This highly dynamic and complex process is regulated, in part, by biochemical and physical cues encoded within the cellular microenvironment (Figure 1.1)**. These cues arise as a result of interactions between stem cells with the extracellular matrix (ECM) and neighboring cells as well as secreted local and systemic signaling molecules, including growth factors [2, 8-10]. Together, these microenvironmental cues modulate stem cell

behaviors such as apoptosis [11], cell adhesion [12], cell proliferation [13], cell migration [14], differentiation [15-18] and cell alignment [19-23], ultimately influencing the native organization and function of these tissues.

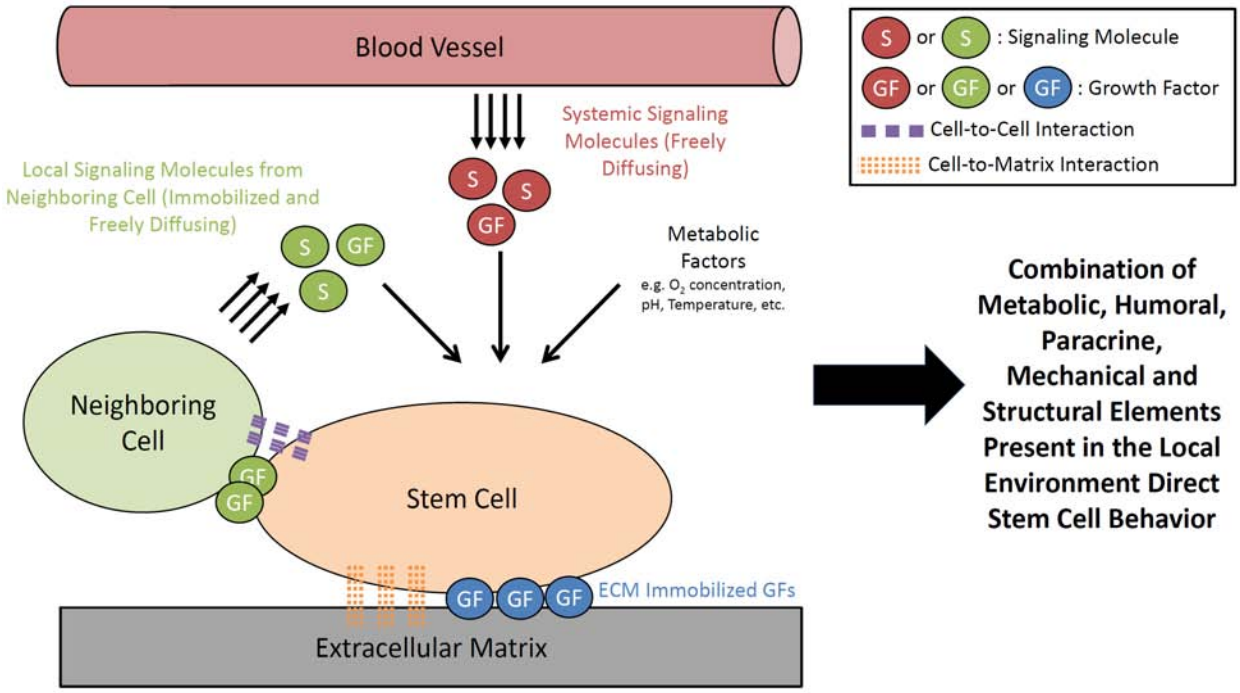

Figure 1.1. The Cellular Microenvironment is a Highly Complex System That Regulates Stem Cell Behavior. Elements of the cellular microenvironment that regulate stem cell behavior include constraint of the architectural space, mechanical forces arising from physical engagement of the stem cell with neighboring cell(s) or the ECM, signaling interactions between stem cells with the ECM, neighboring cells, paracrine or endocrine signals from local or distant sources as well as metabolic products of tissue activity. Adapted from Scadden *et al.*, 2006 [2].

The ECM is a critical component of the cellular microenvironment and is composed of a fibrillar meshwork of secreted proteins that is heterogeneous in nature and specialized for a particular tissue form and function. For example, the controlled deposition of hydroxyapatite in bone-ligament/tendon interfaces has been postulated to minimize injury during the transfer of mechanical loads between rigid and soft tissues [24-27]. Indeed, the unique architecture and biochemical composition of the ECM fulfils both a structural role in facilitating cell attachment

and orientation as well as an instructive role in directing cell behavior through signaling cues derived from mechanical forces, ECM components or ECM-associated GFs [10].

As mentioned, ECM architecture plays an important role by providing the necessary physical cues to control cell adhesion and orientation, which is especially important in the context of musculoskeletal tissue function since myocyte alignment is necessary for efficient force generation along a specific direction during muscle contraction [28-30], while tenocyte and osteoblast alignment are required for building highly oriented unmineralized and mineralized collagen matrices that can withstand mechanical loading during skeletal movement [24, 25, 31-34]. Furthermore, it has recently been shown that aligned fibrous scaffolds promote increased calcium content and mineralization compared to unaligned fibrous scaffolds in a cell proliferation independent manner [34], suggesting that highly aligned fibrous scaffolds may promote more efficient bone differentiation.

The ECM has a unique ability to sequester (immobilize) and release GFs at picogram to nanogram levels [10, 13, 17, 35-38], allowing GFs to reside in both ‘liquid-phase’ (freely diffusing) and ‘solid-phase’ (immobilized) forms in equilibrium between desorption from and adsorption to the ECM and cell surfaces (Figure 1.1) [10, 13, 17, 37, 38]. Immobilization of GFs to the ECM enables large amounts of information that are critical to the maintenance and normal function of a tissue to be stored and utilized for directing cell behavior in a temporal and spatial manner via modification of GF bioavailability and bioactivity [10, 39]. For example, GFs can be rendered with low biological activity by virtue of being bound to the ECM or rendered inert as a result of being buried within the ECM and becoming physically inaccessible for receptor binding

[10]. Under the appropriate conditions, ECM remodeling enzymes degrade the ECM to release these GFs and in certain cases, activate the GFs to increase their biological activity, regulating GF activity in a temporal fashion [10]. In essence, this process enables extracellular signaling to occur in the absence of new protein synthesis and is particularly beneficial during wound healing since GFs may not be rapidly synthesized when cells are injured [10]. Alternatively, the bioactivity of immobilized GFs may be enhanced in a spatially defined manner when compared to their soluble and freely diffusible counterparts since ECM-bound GFs may be protected from degradation and/or the ECM acts as a barrier to slow down diffusion, allowing a signal to persist spatially for a longer duration [10, 35, 39]. In addition, storage of GFs in the ECM further facilitates temporal signaling by allowing cells to transmit signals to other cells that come into contact with the same ECM at a later period [10].

Together, the ECM provides a structural basis for multicellularity with GFs providing a critical regulatory role in the maintenance and function of normal, healthy tissue. Indeed, perturbations to the ECM composition such as elevated levels of ECM remodeling enzymes can affect the bioavailability and bioactivity of signaling molecules such as GFs and have been linked to a wide variety of diseases ranging from chronic wound inflammation to tumor progression [8, 9, 35, 40-43].

1.1.2 Wound Healing and Inflammation in the Context of the Cellular Microenvironment

1.1.2.1 Wound Healing

Wound healing is a series of intricate and well-coordinated events initiated in response to tissue injury. It is characterized by four sequential but overlapping phases – (1) Hemostasis, (2)

Inflammation, (3) Proliferation and (4) Remodeling. This process has been described to exhibit dynamic reciprocity whereby ongoing, bidirectional interactions among cells and their surrounding microenvironment work in concert to direct tissue repair and regeneration [39, 44, 45].

During hemostasis, damaged blood vessels attempt to limit blood loss and isolate pathogens through blood vessel constriction and polymerization of fibrin to form a blood clot while platelet activation and degranulation results in the release of a variety of signaling molecules such as chemokines, cytokines, GFs and other soluble mediators to coordinate tissue repair [39, 44, 45]. Some of these signaling molecules such as platelet-derived growth factor (PDGF) and transforming growth factor-β (TGF-β) act as chemoattractants and/or mitogens for cells involved in the wound healing response including neutrophils, fibroblasts, monocytes, macrophages, and smooth muscle cells [45]. In addition, the polymerization of fibrin forms a provisional ECM that can sequester signaling molecules such as heparin-binding GFs to direct cell behavior [10, 13, 14, 16-19, 46] as well as support cellular attachment to promote tissue in-growth [39, 44, 45].

During the inflammatory phase, immune cells such as neutrophils and monocytes are recruited into the wound microenvironment to remove microbes and damaged tissue [4, 47, 48] as well as synthesize and release signaling molecules to organize the wound microenvironment [39, 44, 47]. For example, neutrophils eliminate invading microbes through the combined action of phagocytosis, release of anti-microbial agents and generation of neutrophil extracellular traps [47, 48] as well as modulate the inflammatory response through juxtacrine and paracrine signaling to activate other immune cells such as macrophages, dendritic cells and T cells [47].

Monocytes can differentiate into macrophages and monocyte-derived dendritic cells that are capable of phagocytosis, acting as antigen presenting cells (APCs) and secreting inflammatory mediators such as Tumor Necrosis Factor-α (TNF- α) [45, 49]. This further aids in the removal of microbes and damaged tissues, activates the acquired immune response and regulates tissue repair, respectively [39, 44, 49]. The net result of this sterilizes the wound and facilitates the eventual infiltration of progenitor cells such pericytes [6, 50, 51] and mesenchymal progenitor cells [7, 52] for the next phase of wound healing.

During the proliferative phase, granulation tissue is formed to cover the wound [45]. This phase is generally characterized by several features [45] including fibroblast infiltration and proliferation, formation of loose connective tissue matrix consisting primarily of type III collagen via fibroblast-mediated ECM deposition, angiogenesis or formation of new blood vessels by vascular endothelial cells and new tissue in-growth from both neighboring cells [6] as well as progenitor cells [6, 7, 50-52]. In addition, myofibroblasts, which are fibroblasts that express smooth muscle characteristics, facilitate wound closure by exerting tractional and contractile forces to pull on the ECM and surrounding cells [53, 54]. Concurrently, immune cells such as neutrophils and macrophages play a key role in this process through maintenance of sterility, removal of the original blood clot or provisional wound matrix and secretion of signaling molecules such as vascular endothelial growth factor (VEGF) that are critical for normal wound healing [4, 47, 49, 55, 56]. Indeed, studies involving the depletion of immune cells such as macrophages in wounds resulted in reduced and abnormal vascularization, leading to impaired healing [57, 58].

During the remodeling phase, tissue development occurs, requiring a delicate balance between elimination of cells and ECM components related to the initial wound healing stages with proliferation and synthesis of native tissue-resident cells and ECM components to restore normal tissue architecture and function [45]. For example, upon clearance of bacteria from the wound site, cells such as neutrophils and myofibroblasts that are no longer needed are removed by apoptosis [45, 47, 49, 53] while originally disorganized collagen fibers are replaced or rearranged, cross-linked and aligned in response to mechanical stimuli present in the wound to increase tissue strength [45, 59, 60]. Depending on the regenerative capability of the tissue as well as the severity of the wound, the remodeling phase can last for up to a year or longer. In tissues that are severely damaged or lack robust regenerative capability, fibrosis or scar tissue formation predominates and substitutes for the lost tissue [45]. Although scar tissue is mechanically strong, it lacks the flexibility and elasticity of most normal tissues and cannot perform native tissue function [4].

1.1.2.2 Inflammation

Given the early presence of neutrophils and monocytes during the initial stages of wound healing as well as the persistence of tissue-resident and monocyte-derived macrophages throughout tissue repair, immune cells play an indispensable role in organizing the cellular microenvironment in response to tissue injury and trauma [45, 47, 61, 62]. Many studies to date have demonstrated that immune cells can be divided in to two broad categories based on their cytokine production profile – (1) Type 1 (Th_1 for T-cells and M_1 for macrophages) immune response associated with secretion of pro-inflammatory cytokines such as TNF-α and Interferon-

Gamma (IFN-γ) and (2) Type 2 (Th_2 for T-cells and M_2 for macrophages, respectively) immune response associated with secretion of anti-inflammatory cytokines such as Interleukin-4 (IL-4) and Interluekin-10 (IL-10) [7, 47, 61-65]. Recent studies have suggested that classification of immune cells maybe more complex than originally envisioned as other subpopulations of T-cells such as T_{reg} [66], Th_3 [67], Th_9 [68] and Th_{17} [69] have been discovered, however, the nomenclature of type 1 and type 2 will be maintained for simplicity.

In general, type 1 and type 2 cytokines possess cross-regulatory properties that coordinate two fundamentally antagonistic immune responses - a pro-inflammatory (type 1) response typically associated with the initial phase of wound healing to remove damaged tissue as well as bacteria and an anti-inflammatory (type 2) response associated with the subsequent attenuation of the initial inflammatory response to facilitate angiogenesis, tissue repair and tissue remodeling [62, 70]. For example, classically-activated or M_1 macrophages, in addition to synthesizing large amounts of Th_1 cytokines such as TNF-α, Interleukin-1β (IL-1β) and Interleukin-12 (IL-12), also express nitric oxide synthase, an enzyme that uses its substrate L-arginine to synthesize large amounts of nitric oxide to kill intracellular pathogens [62, 63]. Alternatively-activated or M_2 macrophages can be divided into at least 3 classes – (1) M_{2a} macrophages which express high levels of arginase to reduce nitric oxide levels and secrete signaling and ECM molecules including insulin-like growth factor-1 (IGF-1) to promote tissue repair, (2) M_{2b} macrophages which are involved in sustaining antibody and high IL-10 production and (3) M_{2c} macrophages which represent deactivated macrophages with increased debris scavenging capability [62, 63]. Both types 1 and 2 responses are required for proper wound healing and an imbalance between the two immune responses can impair musculoskeletal repair. Indeed, it has been demonstrated

that an overly exuberant type 1 response is typically associated with excessive tissue destruction [71] and halting musculoskeletal cell differentiation [63, 72-74] while an excessive type 2 (M_{2b}) response may result in fibrosis [63, 70]. Such an imbalance ultimately affects the healing of bone fractures, tendon ruptures, muscle tears and integration of bone and dental implants, especially under settings of bacterial infection or disorders associated with chronic inflammation such as diabetes and osteoporosis [44, 58, 63, 64, 72-77].

1.1.3 Organs and Tissues of the Musculoskeletal System

The organs and tissues of the musculoskeletal system are highly organized structures designed to shield internal organs from injury, partake in sound transduction during hearing, support and maintain body posture, aid in body movement as well as facilitate homeostasis by virtue of their inherent tissue properties and participation in metabolic processes [4, 78-86]. A brief overview of muscle, tendon and bone is presented here to highlight relationships between their composition and structure with organ or tissue function as well as its response to injury or disease.

1.1.3.1 Muscle Architecture and Function

Muscle function is influenced by its underlying tissue composition and structure. Muscle contractile force is essential for bone movement and joint stabilization to support the body framework, maintain posture and facilitate locomotion [4]. In addition, muscle has an underappreciated metabolic role in homeostasis by generating heat to maintain body temperature and acting as a reservoir of amino acids for protein and glucose synthesis, especially during

starvation [85]. Indeed, perturbations in muscle metabolism have been identified as playing a critical role in the pathogenesis of conditions and diseases such as obesity, osteoporosis and type 2 diabetes [85].

Each skeletal muscle is a discrete organ, composed of several tissues including muscle fibers, blood vessels, nerve fibers and substantial amounts of connective tissue [4]. Figure 1.2 shows the hierarchical composition and structure of muscle at the molecular cellular, tissue and organ levels (Figure 1.2). Muscle fibers, the contractile apparatus of muscle, are surrounded and supported together by three different layers of connective tissue – (1) The epimysium, which is a dense irregular connective tissue that surrounds the entire muscle organ, (2) The perimysium, which is a layer of fibrous connective tissue that groups individual muscle fibers into bundles of sticks called fasicles and (3) The endomysium, a fine sheath of connective tissue that surrounds each muscle fiber [4, 87-89]. The endomysium, perimysium and epimysium are continuous with one another as well as with connective tissue present in nearby muscle and tendon tissues. They contain numerous blood vessels and nerve fibers to supply the muscle, remove metabolic waste and initiate muscle contraction [4]. Together, the architecture of these intramuscular structures provide an efficient mechanism for coordinating and transmitting the propagation of contractile force from individual muscle fibers through the entire muscle organ, protecting muscle against tissue damage arising from friction and facilitating muscle growth [4, 87-89].

Each skeletal muscle fiber is a long cylindrical multinucleated cell produced by the fusion of many progenitor cells, resulting in a large cell with a typical diameter of 10 to 100 μm and a

length that may range up to several hundreds of centimeters long [4]. The obvious banded or striated appearance of skeletal muscle is a reflection of the precise alignment of their myofilaments [4]. The cytoplasm of a muscle fiber, termed a sarcoplasm is similar to those found in other cells, but is adapted for muscle contraction with its large stores of glycosomes (stored glycogen) for energy supply, myoglobin for oxygen supply and specialized organelles and components such as the sarcoplasmic reticulum, transverse (T) tubules and myofibrils for muscle contraction [4].

T tubules are invaginations of the sarcolemma (muscle plasma membrane) that are studded with a large number of calcium channels that regulate the release of calcium ions from the sarcoplasmic reticulum in response to an action potential [4]. Myofibrils are the contractile elements of skeletal muscle and comprise approximately 80% of cellular volume [4]. Each myofibril is about 1-2μm in diameter and is composed of muscle segments called sarcomeres, which in turn is made up of contractile proteins myosin (thick filaments) and actin (thin filaments) as well as their accessory proteins anchored to the Z disk [4]. Myosin-containing thick filaments consist of two globular heads and a long tail with the tail element pointing inwards toward the center of the sarcomere and the head elements pointing towards the ends of the sarcomere [4]. The myosin heads are known as cross-bridges as they have the capability to bind to and move along the actin-containing thin filaments. This actin-myosin interaction subsequently forms the molecular basis for muscular force generation and movement [4].

At rest, most cross-bridges are present in a ‘cocked’ configuration where myosin-containing thick elements are not bound to actin-containing thin filaments but contain adenosine diphosphate (ADP) and an inorganic phosphate (P_i) [4]. The release of calcium ions and its subsequent binding to actin-containing thin filaments of myofibrils results in conformational changes that unmask binding sites for myosin-containing thick filaments [4]. Upon the exposure of these sites, myosin-containing thick filaments bind to actin-containing thin filaments and release ADP and P_i, triggering a ‘power stroke’ where conformational changes to the cross-bridge allow the myosin molecule to ‘walk’ 10-12 nm along the actin filament [4]. The net effect of this pulls the Z-bands towards the M-line and shortens the sarcomere [4]. Subsequently, adenosine triphosphate (ATP) binds myosin-containing thick filaments and causes the release of actin-containing thin filaments [4]. Thereafter, the hydrolysis of ATP releases energy to ADP and P_i ‘cocks’ the cross-bridge in preparation for the next cycle of muscle contraction [4]. The cycle repeats as long as ATP and calcium are present [4]. Muscle contraction stops when calcium has been completely pumped back into the sarcoplasmic reticulum [4]. The sliding interaction between the myosin cross-bridges and actin-containing thin filaments is known as the sliding filament mechanism and is responsible for muscle shortening or contraction [4].

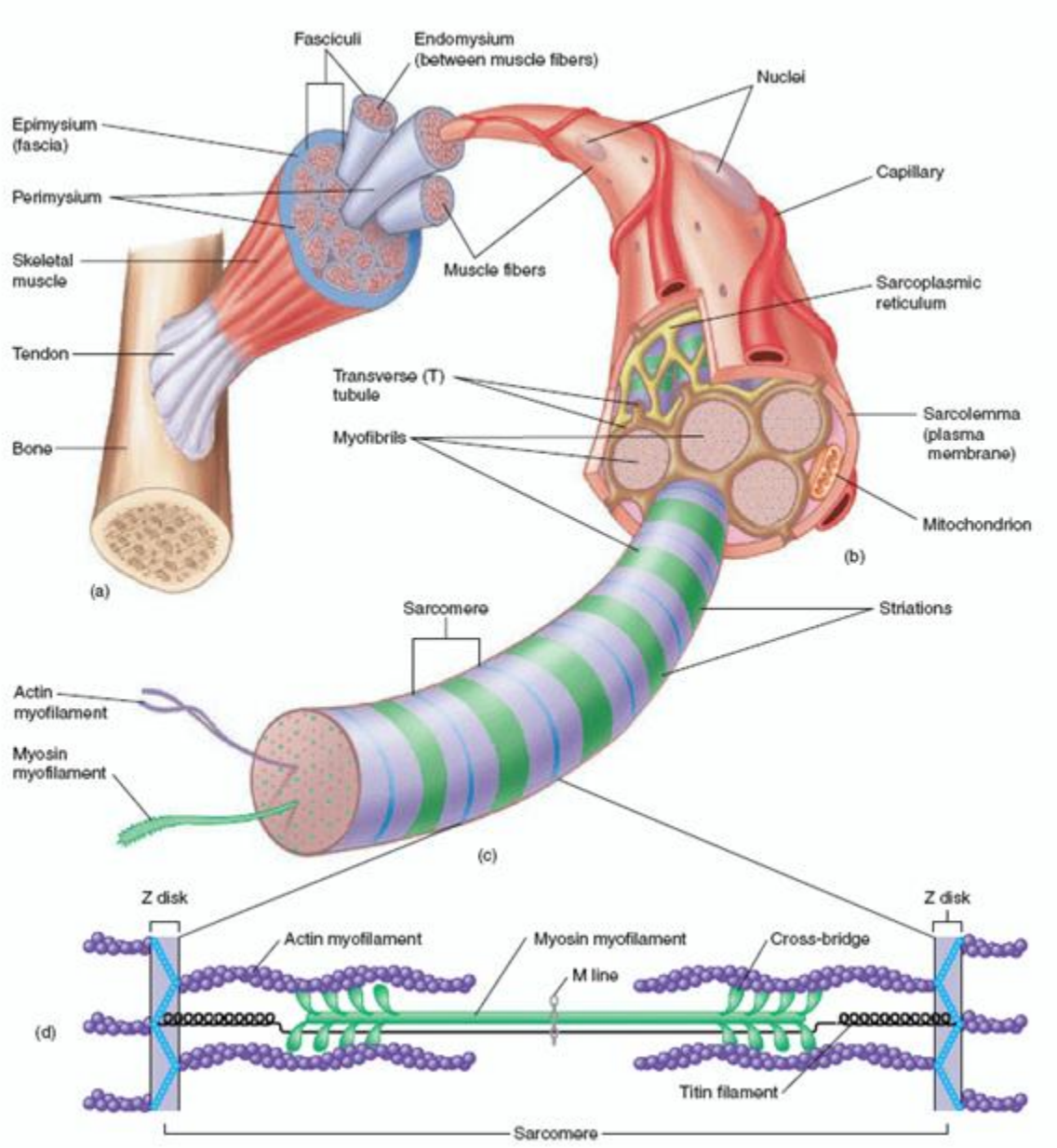

Figure 1.2. The structure and composition of muscle at the molecular, cellular, tissue and organ levels. Taken from Marieb, 1999 [4].

Myosatellite cells or satellite cell**s** are small mononuclear progenitor cells that are capable of self-renewal and are involved in the normal growth of muscle, as well as regeneration following injury or disease [90, 91]. Anatomically, they are found sandwiched between the basement

membrane and sarcolemma of individual muscle fibers, and are identified on the basis of expression of several muscle stem cell markers including the transcription factor Pax7 [91, 92]. Indeed, it has been shown that transplantation of satellite cells, either in the form of whole, intact myofibers [90] or individual cells [91] contributes towards muscle regeneration and can give rise to new satellite cells in the transplanted host muscle. The importance of the cellular microenvironment in muscle regeneration is further highlighted by studies that suggest the transplantation of satellite cells in the form of whole, intact myofibers may be more efficient than implantation of enzymatically isolated, single cell suspensions [90, 91, 93].

In muscle tissue, the repair process following acute tissue injury follows the stereotypical sequence of events displayed during wound healing with inflammatory cells working in concert with tissue-resident stem cells to remove damaged or dead muscle fibers as well as replace lost tissue to restore tissue function [63, 70, 94]. For example, when muscle tissue is damaged as a result of exercise, injury or disease, these normally quiescent cells become activated and proliferate rapidly to produce muscle progenitor cells that eventually fuse with existing myofibers to repair muscle tissue [90, 91]. This proliferation response requires the input of immune cells such as macrophages. During the early stages of wound healing, M_1 macrophages secrete pro-inflammatory TNF-α, which increases NF-κB activation in satellite cells to increase cell proliferation and inhibit muscle differentiation through stabilization of the cell cycle regulator cyclin D1 and decreasing levels of the myogenic transcription factor, MyoD [70], ultimately increasing the number of myoblast progenitors for muscle repair. During the later stages of wound healing, M_2 macrophages secrete anti-inflammatory cytokines such as IL-4 [62] which has been shown to promote muscle growth [70, 94-96]. However, during chronic muscle

damage in diseases such as the muscular dystrophies, a fibrotic microenvironment predominates, while the reparative capacity of satellite cells is diminished. For example, in Duchenne muscular dystrophy, a mutation in the protein Dystrophin causes fragile sarcolemmas which result in an accumulation of damage to myofibers, eventually leading to necrosis [63]. Although satellite cells are able to repair and replace these damaged fibers initially, repeated cycles of muscle damage either exhaust the satellite cell population or result in a loss of its regenerative capability [63, 70, 94, 97]. This ultimately leads to muscle tissue being progressively replaced by adipose and fibrotic tissue [63, 70, 94, 97].

1.1.3.2 Tendon Architecture and Function

Tendons are white, dense regular connective tissues with a fibroelastic texture. Their primary function is to facilitate muscle-to-bone attachments by withstanding the large amount of tensile stress generated as a result of muscle-induced bone displacement during joint movement [4, 84, 86, 98]. Tendons are complex composite materials, composed of 70% water and 30% dry mass. Type I collagen along with much smaller amounts of type III, V, XII and XVI collagen accounts for 65-85% dry mass whereas elastin accounts for 2-3% dry mass and proteoglycans including decorin account for 1-2% dry mass [4, 84, 86, 98]. In addition, tendons are populated by low numbers of cells such as tenocytes, tenoblasts, fibrocartilage cells and the occasional adipocyte. Overall, tenoblasts and tenocytes constitute about 90-95% of the cellular elements of the tendons [4, 84, 86, 98]. Derived from immature and spindle-shaped tenoblasts, tenocytes are located between collagen fibers along the long axis of tendon where they continuously synthesize tightly packed parallel bundles of collagen fibers and other ECM molecules that provide tendon with

tensile strength [4, 84, 86, 98]. Overall, collagen fibers have a crimp or slightly wavy appearance that allows the tissue to stretch in response to strain [4].

To sustain great amounts of tensile stress, the collagen fibers are arranged in several hierarchical levels of increasing complexity (Figure 1.3). The basic unit in the structural hierarchy of tendons is the collagen polypeptide, which is characterized by the presence of a glycine residue at every third amino acid. Three such collagen polypeptides can associate into a triple helical collagen molecule and upon cleavage of their N- and C-terminals, self-assemble into primary bundles known as collagen fibrils, which subsequently group together into secondary bundles known as collagen fibers, which further arrange into tertiary bundles known as fascicles before organizing into tendon (Figure 1.3) [4, 84, 86, 98]. Adult human tendons have a bimodal distribution of collagen fibril diameters that range between 60 and 175 nm [99]. Tendon is surrounded and supported by two different layers of connective tissue – (1) The epitenon, which is a fine, loose connective tissue sheath that surrounds the entire tendon and (2) The endotenon, which is a thin reticular network of connective tissue that envelopes the primary, secondary and tertiary fiber bundles together. Both the epitenon and endotenon are continuous with one another and carry blood vessels, lymphatic vessels and nerve fibers to the tendon [4, 84, 86, 98]. Despite this, tendons are considered to be poorly vascularized and also obtain nutrients from the blood vessels of surrounding tissues including muscle (perimysium) and bone (periosteum) [4, 84, 86, 98]. Between the endotenon and collagen fibers is the hydrophilic proteoglycan-based ECM, which provides structural support for collagen fibers [100], regulates the size of collagen fibers [101, 102] and hydrates the fibers to minimize shear stresses between collagen bundles during tendon gliding [103, 104]. Depending on the type of tendon, additional connective tissues such as

fibrous sheaths or retinaculum, reflection pulleys, synovial sheaths, paratenon and tendon bursa may be present to further supply nutrients as well as facilitate smooth gliding of tendon against surrounding tissues via friction reduction [4, 84, 86, 98].

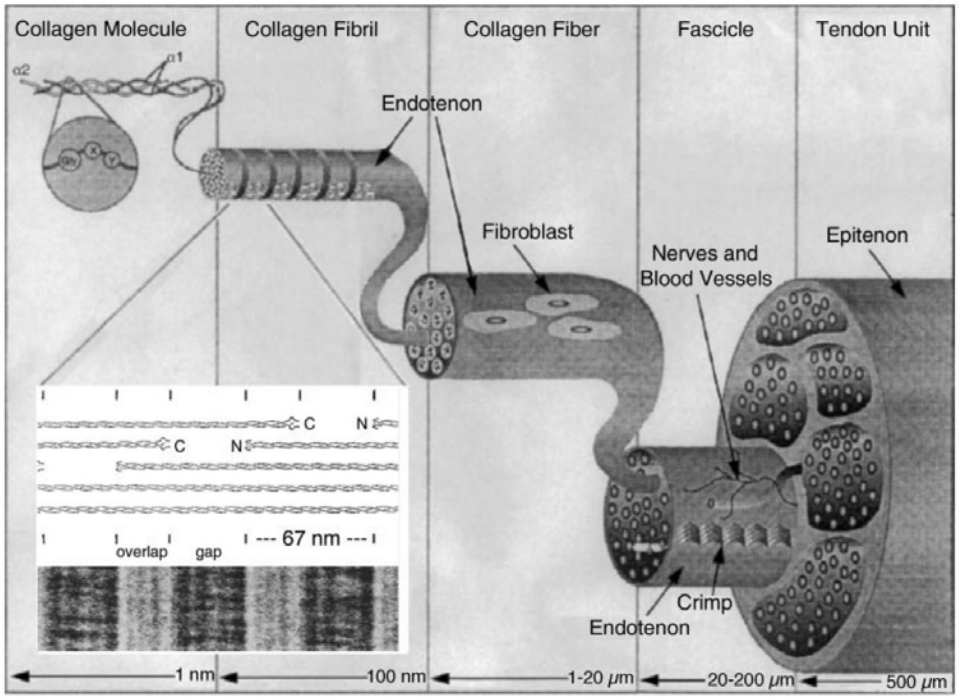

Figure 1.3. The structure and composition of tendon at the molecular, cellular and tissue levels. Taken from Banos *et al*., 2008 [98].

Tendon-derived stem cells have only recently been discovered and represent a population of self-renewing [105], multipotent progenitor cells that are capable of generating cells of bone, fat, cartilage and tendon lineages [105-107] and are involved in the normal growth of tendon as well as regeneration following injury or disease [105, 108, 109]. Anatomically, they are found between parallel collagen fibers along the long axis of tendon within a proteoglycan-rich ECM, which has been shown to be essential for controlling the self-renewal and differentiation of these cells through BMP signaling [105]. Indeed, mice lacking proteoglycans such as fibromodulin and

biglycan show disrupted tendon organization and decreased levels of tendon marker *scleraxis* or *scx* [101, 105, 110].

During tendon healing, the stereotypical events associated with wound healing occur but injured tendon, which is characterized by marked collagen degeneration and disordered fiber arrangement, does not heal completely and ends with mechanically and functionally inferior tissue owing to formation of scar tissue and fibrous adhesions [84, 111-113]. Tendon healing has been described to occur by 2 distinct mechanisms – (1) Intrinsic healing via proliferation of epitenon and endotenon tenocytes, or (2) Extrinsic healing via the invasion of cells from the surrounding sheath and synovium [84]. Tendon tissue that intrinsically heals often has improved biomechanics and fewer complications overall owing to preservation of a normal gliding mechanism within the tendon sheath whereas extrinsic healing may exhibit poorer biomechanics and more complications owing to scar tissue or adhesion formation, which disrupts tendon gliding [84]. At present, the role of inflammation on tendon degeneration remains contentious [114] but recent studies indicate that the amount of inflammatory cell infiltrate correlates with the wound size [115-117], suggesting that the level of inflammatory response mounted in response to injury may ultimately influence tendon healing.

1.1.3.3 Bone Architecture and Function

Bones are organs, comprising predominantly of bone (osseous) tissue along with cartilage tissue at the articulating ends of bone, fibrous connective tissue lining the bone cavities, nervous tissue and vascular tissue [4, 81, 83]. Bone function is influenced by its underlying tissue composition and structure. Bones are involved in several mechanical functions including protecting internal

organs from physical injury [4, 81, 83], supporting the body [4, 81, 83], providing levers for muscles to act on during body movement [4, 81, 83], facilitating sound transduction during hearing [4] as well as several homeostatic functions including housing bone marrow for blood production [4, 81, 83], storing GFs such as bone morphogenetic proteins (BMPs) and minerals such as calcium and phosphorus in bone ECM [4, 118], storing fat in bone marrow [4], buffering blood pH through absorption and release of alkaline calcium phosphate minerals (hydroxyapatite) [78], detoxifying heavy metals from blood [80] and acting as an endocrine organ through secretion of fibroblast growth factor-23 (FGF-23) and osteocalcin to regulate phosphate levels and insulin sensitivity, respectively [79].

The primary tissue of bone is known as osseous tissue and consists primarily of three components – (1) Bone cells, (2) An organic bone ECM consisting primarily of type I collagen along with other proteoglycans and glycoproteins and (3) An inorganic bone ECM consisting of hydroxyapatite crystals that are tightly packed around collagen fibers [4, 81, 83]. Bone ECM comprises about ⅓ mass of the organic bone matrix and ⅔ mass of hydroxyapatite crystals, resulting in a hard but lightweight mineralized matrix that exhibits high compressive strength as well as a significant degree of elasticity [4, 81, 83]. Embedded within this matrix are three main types of bone cells which are osteoblasts, osteocytes and osteoclasts. Osteoblasts are derived from osteoprogenitor cells and function primarily to increase bone formation by secreting organic bone ECM components and increasing the local concentration of calcium and phosphate to form hydroxyapatite crystals while osteoclasts are giant multinucleate cells derived from macrophages and function primarily to increase bone resorption by secreting lysosomal enzymes and acids to digest organic bone ECM and dissolve hydroxyapatite crystals as well as

phagocytize demineralized matrix and dead osteocytes [4, 81, 83]. Osteocytes are derived from osteoblasts that have become trapped within the matrix they secreted and form a network with one another via long cytoplasmic extensions and act to regulate bone turnover through mechanotransduction and paracrine signaling [4, 119-121]. There are two types of osseous tissue – (1) Cortical/compact/lamellar bone, which is dense as well as mechanically strong and (2) Cancellous/trabecular/spongy bone, which is mechanically weaker than compact bone but has a higher surface area and consists of a honeycomb-like lattice that frequently contains red or yellow marrow [4, 81, 83]. The microstructure of compact and spongy bone as it relates to bone organ is further discussed below.

Figure 1.4 shows the macroscopic and microscopic structure of a typical long bone (Figure 1.4). Generally, the overall organization of a long bone consists of a tubular diaphysis or shaft that forms the long axis of bone capped by two epiphyses or bone ends [4, 81, 83]. Both epiphyses and diaphysis have an exterior layer of compact bone and an interior layer of spongy bone [4, 81, 83]. Between the diaphysis and each epiphysis of an adult long bone is an epiphyseal line that is a remnant of the hyaline cartilage disc that participated in bone lengthening during childhood [4, 81, 83]. The diaphysis is comprised of a relatively thick layer of compact bone that surrounds a central medullary or marrow cavity that contains fat or yellow marrow during adulthood [4, 81, 83] The entire external surface of bone is covered by connective tissues. The joint surface of each epiphysis is covered with a thin layer of articular cartilage to act as shock absorbers for opposing bone ends during joint movement while the remainder of the external bone surface is covered by a double-layered membrane called the periosteum, which consists of an outer fibrous layer of dense irregular connective tissue and an inner osteogenic layer of osteoprogenitors,

osteoblasts and osteoclasts [4, 81, 83]. The periosteum provides insertion and anchoring points for tendons/ligaments and is secured to the underlying bone by tufts of collagen fibers termed Sharpey's fibers that extend from the fibrous layer into the bone matrix [4]. In addition, the periosteum contains numerous nerve fibers, lymphatic vessels and blood vessels that supply bone with nutrients and remove waste [4, 81, 83]. The internal surface of bone is covered with a delicate connective tissue membrane known as the endosteum which contains both osteoblasts and osteoclasts [4, 81, 83].

Compact bone has a porous structure and is infiltrated by nerve fibers, blood vessels and lymphatic vessels. The structural unit of compact bone is the osteon or Haversian system [4, 81, 83]. Osteons are approximately 2.5mm elongated cylindrical structures arranged adjacent to one another and oriented parallel to the long axis of bone to function as load-bearing structs that resist compression (Figure 1.4). Each individual osteon consists of numerous lamella, each 3-7 μm thick and arranged concentrically around a Haversian or central canal [4, 81, 83]. The osteon diameter, which is dependent on the number of lamellae present, ranges from 200-250 μm and collagen fibers in a particular lamella, along with their associated hydroxyapatite crystals, are aligned in a single direction with collagen fibers and hydroxyapatite crystals in the adjacent lamellae, often running 90^{o} in the opposing direction, creating an alternating pattern that resists torsion stresses or twisting [4, 83, 122, 123]. The Harversian canal contains small blood vessels and nerve fibers that supply cells and are joined by perforating or Volkmann's canals that lie at right angles to the long axis of the bone [4]. These canals are responsible for connecting the blood and nerve supply of the periosteum to those in the Harversian canals and the medullary cavity [4]. Like all internal bone cavities, both Harversian and Volkmann's canals are lined with

endosteum [4]. Osteocytes occupy small cavities known as lacunae that occur at the junctions of the lamellae. Lacunae are connected to one another and to Harversian canals by hair-like canals called canaliculi, allowing osteocytes to form a network though their cytoplasmic extensions in a manner that mirrors the orientation of bone ECM [4, 33]. As previously mentioned, these osteocyte networks are formed when bone forming osteoblasts become entrapped within the mineralized matrix they secrete and the canaliculi eventually becomes filled with tissue fluid that facilitates exchange of nutrients and waste. This osteocyte network is important as osteocyte death results in resorption of the surrounding bone ECM [4, 124]. The spaces between intact osteons are filled with interstitial or incomplete lamellae and circumferential lamellae [4]. Interstitial lamellae represent new, forming osteons or the remnants of osteons that have been disrupted by bone remodeling while circumferential lamellae extend around the entire circumference of the bone shaft to further resist twisting of the long bone [4].

Spongy bone, contained in the end of long bones, is highly porous and vascularized, being the site for bone marrow synthesis. Spongy bone consists of numerous trabecula, which are characterized as rod- or plate-like structures that are no greater than 200 μm in thickness and about 1000 μm long [4, 81, 83]. Unlike osteons, trabeculae generally do not have a central canal with a blood vessel although it is possible to find unusually thick trabeculae containing a blood vessel and osteon-like structures with concentric lamellae [4, 81, 83]. Similar to compact bone, spongy bone consists of lamellae as well as osteocyte-containing lacunae and canaliculi [4, 81, 83]. However, the lamellae are not arranged in a concentric manner but are arranged longitudinally along the trabeculae [4, 81, 83].

At the molecular level, bone ECM in both compact and spongy consists primarily of mineralized collagen fibrils. Hydroxyapatite crystals are the smallest biogenic crystals known, measuring 2-6 nm thick, 30-50 nm wide, and 60-100 nm long [31]. In mineralized collagen fibrils, hydroxyapatite crystals are organized into parallel arrays that align with the long axes of the collagen fibril [31]. The crystals localize in the approximately 40 nm gaps that occur at the ends of co-linear collagen molecules, as well as between adjacent collagen molecules that overlap with one another, accentuating the well-known D periodicity of collagen when observed under transmission electron microscopy (TEM) [31]. While the precise nature of collagen-mineral interactions is still not well understood, ionic bonds between the carboxyl and carbonyl groups of proteins with calcium ions in the crystals are thought to play a role in such interactions [31].

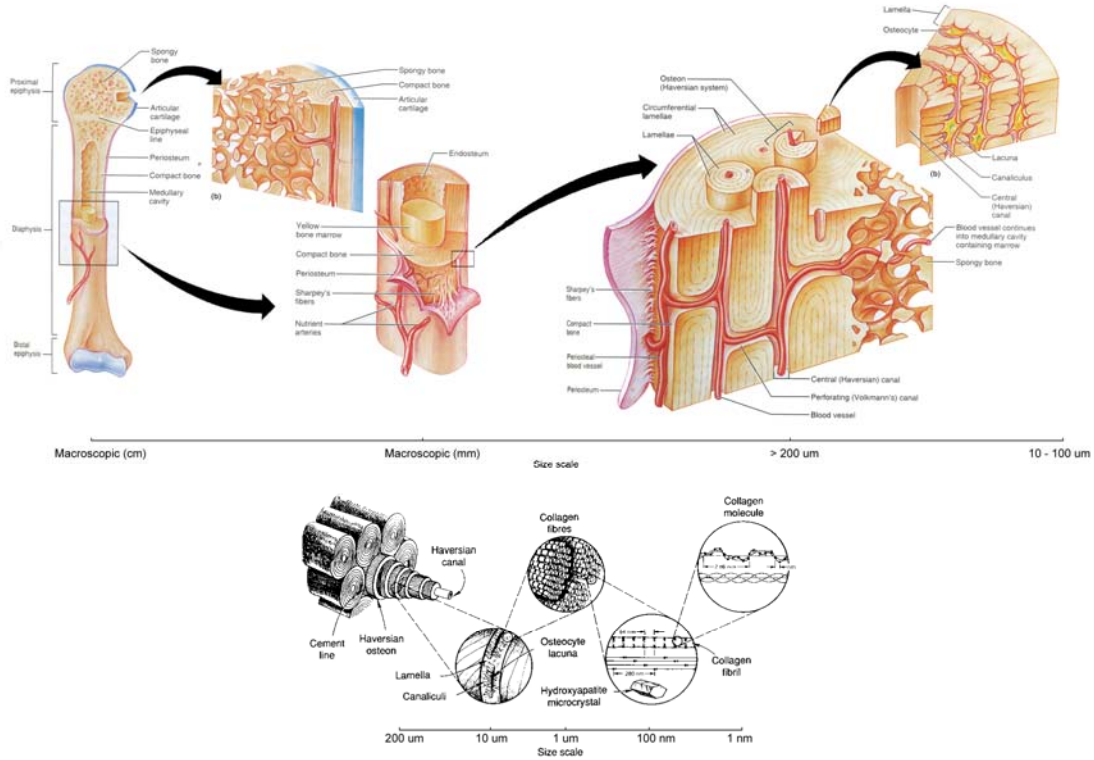

Figure 1.4. The structure and composition of bone at the molecular, cellular, tissue and organ levels. Adapted from Marie, 1999 [4] and Lakes, 1993 [125].

Skeletal stem cells are a population of multipotent cells that have the ability to generate cells of several lineages including osteoblasts, adipocytes, chondrocytes , smooth muscle cells, stromal cells and endothelial cells that participate in bone healing and repair [126-130]. Skeletal stem cells have been purified by flow cytometry using positive selection for multiple markers including STRO-1 [131] as well as negative selection for hematopoietic markers including CD34 [130]. These cells have also been referred to as osteogenic stem cells, marrow stromal fibroblastic cells, bone marrow stem cells, mesenchymal stem cells, stromal precursor cells [130] and are found in the bone marrow in close association with the hematopoietic stem cell niche [126]. Indeed, ectopic studies show that the formation of blood-forming cells is often preceded by bone formation [132] and osteoblast cells have been found to be involved in the regulation of hematopoietic stem cell niche through notch signaling [133]. Recent studies have suggested that skeletal stem cells may possess a pericyte origin and reside in microvascular networks within the bone marrow [50, 51, 130, 134].

During long bone healing, the stereotypical events associated with wound healing occur, requiring an intricate interplay of immune cells as well as bone progenitor cells. Due to the high vascularity of bone and its surrounding tissues, a relatively large hematoma is formed when bone is fractured [4]. Bone cells that are unable to receive nutrients due to disruptions in the vascular network undergo apoptosis and the tissue becomes inflamed [4]. Studies have indicated that a balanced inflammatory reaction is critical in regulating the regenerative healing process [7, 72, 73, 135]. For example, it has been demonstrated that a prolonged pro-inflammatory microenvironment can alter the composition of immune cells that are recruited to the wound site

[73], resulting in an altered microenvironment that suppresses the differentiation of skeletal stem cells and delays bone healing [72, 73, 135]. This effect may be countered by modulating the inflammatory microenvironment to promote wound healing. For example, the systematic infusion of stem cells has been shown to mitigate a pro-inflammatory response by directing macrophages towards an anti-inflammatory or M_2 phenotype to suppress local TNF-α production and increase IL-10 production, resulting in enhanced wound healing [7]. During the proliferation phase, the in-growth of capillaries as well as infiltration of phagocytic cells, fibroblasts and osteoblasts into the hematoma and surrounding area from the periosteum and endosteum forms a soft callus that is comprised fibrocartilage and cartilage [4]. This fibrocartilaginous callus bridges the gap between two fracture fragments and acts to splint the broken bone [4]. Thereafter, the callus is mineralized by osteoblasts and forms a hard bony callus, eventually resulting in bone union [4]. During the remodeling phase, the bony callus is reconstructed in response to mechanical stress in the environment [60] such that excess material on the bone shaft exterior and within the medullary cavity is removed and compact bone is laid down to reconstruct the shaft walls, resulting regenerated tissue that resembles the original tissue composition and architecture [4].

1.1.3.4 Architecture of Relevant Musculoskeletal Interfaces

Musculoskeletal interfaces function to bridge the gap between two dissimilar tissues and facilitate load transfer between bone, cartilage, tendon, ligament and muscle tissue [25-27]. The biochemical composition and architecture of musculoskeletal interfaces is composed such that there is often a gradual transition in mechanical properties when crossing from one distinct tissue

to the other [25-27]. This serves to reduce stress concentrations at the interface and prevent mechanical failure, allowing the interface to undergo repeated and durable load transfer [25-27].

In muscle-bone attachments, the epimysium of the muscle is fused to the periosteum of a bone via the insertion of collagen fiber bundles with other ECM molecules such as tenascin, laminin and fibronectin [4, 136]. The ECM composition at the border of muscle-bone attachments have been found to vary with one another and are likely adapted for the tension and/or stretch applied between a specific muscle-bone pairing [4, 136].

In muscle-tendon attachments, the endomysium, epimysium and perimysium of muscle tissue are interwoven together and eventually become synonymous with proper tendon tissue [4]. At the myotendinous junction, many finger-like processes are formed at the termini of tendons while extensive folding of muscle sarcolemma occurs to increase the surface area available for interdigitation of muscle and tendon tissues, ultimately reducing the tensile stress exerted on tendon during muscle contraction [27, 137, 138]. Specifically, tendon collagen fibrils are inserted into the deep recesses formed by myocyte processes [84, 139], allowing for contractile force to be transmitted from the intracellular proteins of muscle tissue to extracellular collagen fibers of tendon tissue [84].

In bone-tendon attachments, the osteotendinous junction is comprised of four distinct zones that progressively transition from soft tissue to hard tissue – (1) Tendon proper, (2) Fibrocartilage, (3) Mineralized fibrocartilage and (4) Mineralized bone. These four zones have region-specific

mechanical properties and function together to minimize stress concentrations and promote gradual load transfer from soft (tendon) to hard (bone) tissue [25, 27, 84].

1.1.4 GF Signaling Pathways Relevant to Musculoskeletal Tissues

There are numerous GF signaling pathways related to the development and regulation of musculoskeletal tissues. However, only the BMP, FGF and IGF signaling pathways will be reviewed here since they are relevant to the present study.

The BMP gene family is a subfamily of the TGF-β superfamily of GFs [140, 141] that are involved in a variety of cell behaviors such as cell differentiation [16, 18, 19, 142] and apoptosis [142]. BMPs are heparin-binding GFs that consist of two polypeptide chains linked by a single disulfide bond and interact with complexes of type I and type II serine/threonine kinase cell surface receptors [140, 141]. There are essentially two modes of intracellular signaling – (1) The canonical pathway and (2) The non-canonical pathway [141, 143-145]. In the canonical pathway, BMP binding induces phosphorylation of the threosine kinase receptors, which then activate intracellular signaling via the Smad receptors – Smad1, Smad5 and Smad8 [141, 144]. These Smad receptors are phosphorylated at their C-terminus by the activated type I receptor and complex with Smad4 to translocate to the nucleus where they bind to DNA and interact with transcription factors to alter gene expression [141, 144]. In addition, the Smad receptors may also interact with other non-Smad intracellular mediators to transmit signals to other pathways [144]. In the non-canonical pathway, BMP binding results in the direct phosphorylation of non-Smad intracellular mediators such as the Mitogen Activated Protein Kinase (MAPK), eventually resulting in downstream signaling cascades that eventually modify gene transcription [143, 145].

The FGF gene family is composed of 22 members that can be categorized into seven subfamilies based on sequence similarity [146, 147]. FGFs are a family of heparin binding GFs [146, 147] that are involved in a variety of cell behavior including cell proliferation [13] and differentiation [16]. FGF receptors are tyrosine kinase cell surface receptors that consist of an extracellular ligand domain composed of three immunoglobulin-like domains, a single transmembrane helix domain and an intracellular domain with tyrosine kinase activity [142, 146, 147]. There are seven FGF receptor isoforms which are produced as a result of alternative mRNA splicing of four FGF receptor genes – FGFR1, FGFR2, FGFR3 and FGFR4 [142, 146, 147]. When FGF binds to the extracellular domain of its receptor, the receptor dimerizes and rapidly activates the protein's cytoplasmic tyrosine kinase domains, triggering the initiation and subsequent amplification of intracellular signaling cascades such as the MAPK, p38, Phospholipase C γ (PLCγ) and Phosphatidylinositol 3-kinase (PI3K) pathways to modify gene expression [142, 146, 147]. In addition, several members of the FGF family such as FGF-1, FGF-2, FGF-3, FGF-11, FGF-12, FGF-13 and FGF-14 can also localize to the nucleus where it can interact with proteins such as transcription factors to alter gene transcription [147].

The IGF family of GFs comprise of two ligands – IGF-1 and IGF-2 that are structurally similar to insulin [148] and mediate cell behavior such as cell differentiation [143], cell survival [149] and cell proliferation [150]. IGFs are known to interact with three receptors – (1) IGF-1 receptor (a tyrosine kinase cell surface receptor), (2) IGF-2 receptor (a cation-independent mannose-6-phosphate cell surface receptor; regarded as non-functional in the context of IGF signaling) and (3) Insulin receptor (a tyrosine kinase cell surface receptor) [148] as well as six IGF binding

proteins that regulate the bioavailability and bioactivity of the GF [151, 152]. Similar to all tyrosine kinase cell surface receptors, IGF binding causes tyrosine phosphorylation of the intracellular domain of the receptors, resulting in downstream activation of the PI3K/Akt and Ras/MAPK pathways to alter gene transcription [148].

1.1.6 Technologies to Mimic Aspects of the Cellular Microenvironment for Tissue Engineering

Presently, various scaffold and patterning methodologies have been developed for promoting repair and regeneration of damaged tissues and organs. While there exists a large and diverse class of scaffolds such as metal-based implants, glass- and ceramics-based scaffolds, decellularized scaffolds as well as natural and synthetic polymer-based scaffolds whose final form include rigid, porous scaffolds, soft hydrogels and spun nano- or micron-sized fibers [15, 18, 21, 23, 24, 111, 153-159], the general theme of these biomaterials is to recapitulate aspects of the cellular microenvironment such as tissue architecture and biochemical cues. In addition, such scaffolds and substrates may be further functionalized with biochemical cues using a variety of patterning technologies such as precision spraying [160], photolithography [161, 162], photoimmobilization [163], microcontact printing [164, 165], laser-based printing [166], inkjet-based printing [167-169], acoustic droplet ejection [170], adsorption from solution [171], cross-diffusion of alkanethiols [172, 173] to augment their capability.

1.2 REFERENCES

1. Li, L. and T. Xie, *Stem cell niche: structure and function.* Annu Rev Cell Dev Biol, 2005. **21**: p. 605-31.
2. Scadden, D.T., *The stem-cell niche as an entity of action.* Nature, 2006. **441**(7097): p. 1075-9.
3. Mitsiadis, T.A., et al., *Stem cell niches in mammals.* Exp Cell Res, 2007. **313**(16): p. 3377-85.

4. Marieb, E.N., *Human Anatomy and Physiology*. 5th ed. 1999: Benjamin Cummings.
5. Lee, M.J., et al., *Enhancement of wound healing by secretory factors of endothelial precursor cells derived from human embryonic stem cells.* Cytotherapy, 2011. **13**(2): p. 165-78.
6. Paquet-Fifield, S., et al., *A role for pericytes as microenvironmental regulators of human skin tissue regeneration.* J Clin Invest, 2009. **119**(9): p. 2795-806.
7. Zhang, Q.Z., et al., *Human gingiva-derived mesenchymal stem cells elicit polarization of m2 macrophages and enhance cutaneous wound healing.* Stem Cells, 2010. **28**(10): p. 1856-68.
8. Nelson, C.M. and M.J. Bissell, *Of extracellular matrix, scaffolds, and signaling: tissue architecture regulates development, homeostasis, and cancer.* Annu Rev Cell Dev Biol, 2006. **22**: p. 287-309.
9. Nelson, C.M. and J. Tien, *Microstructured extracellular matrices in tissue engineering and development.* Curr Opin Biotechnol, 2006. **17**(5): p. 518-23.
10. Taipale, J. and J. Keski-Oja, *Growth factors in the extracellular matrix.* FASEB J, 1997. **11**(1): p. 51-9.
11. Chen, E.Y., M. Fujinaga, and A.J. Giaccia, *Hypoxic microenvironment within an embryo induces apoptosis and is essential for proper morphological development.* Teratology, 1999. **60**(4): p. 215-25.
12. Houseman, B.T. and M. Mrksich, *The microenvironment of immobilized Arg-Gly-Asp peptides is an important determinant of cell adhesion.* Biomaterials, 2001. **22**(9): p. 943-55.
13. Miller, E.D., et al., *Dose-dependent cell growth in response to concentration modulated patterns of FGF-2 printed on fibrin.* Biomaterials, 2006. **27**(10): p. 2213-21.
14. Miller, E.D., et al., *Spatially directed guidance of stem cell population migration by immobilized patterns of growth factors.* Biomaterials, 2011. **32**(11): p. 2775-85.
15. Cooper, G.M., et al., *Inkjet-based biopatterning of bone morphogenetic protein-2 to spatially control calvarial bone formation.* Tissue Eng Part A, 2010. **16**(5): p. 1749-59.
16. Ker, E.D., et al., *Engineering spatial control of multiple differentiation fates within a stem cell population.* Biomaterials, 2011. **32**(13): p. 3413-22.
17. Miller, E.D., et al., *Inkjet printing of growth factor concentration gradients and combinatorial arrays immobilized on biologically-relevant substrates.* Comb Chem High Throughput Screen, 2009. **12**(6): p. 604-18.
18. Phillippi, J.A., et al., *Microenvironments engineered by inkjet bioprinting spatially direct adult stem cells toward muscle- and bone-like subpopulations.* Stem Cells, 2008. **26**(1): p. 127-34.
19. Ker, E.D., et al., *Bioprinting of growth factors onto aligned sub-micron fibrous scaffolds for simultaneous control of cell differentiation and alignment.* Biomaterials, 2011. **32**(32): p. 8097-107.
20. Nain, A.S., et al., *Dry Spinning based Spinneret based Tunable Engineered Parameters (STEP) Technique for Controlled and Aligned Deposition of Polymeric Nanofibers.* Macromol Rapid Commun., 2009. **30**(16): p. 6.
21. Nain, A.S., et al., *Fabrication of Single and Multi-Layer Fibrous Biomaterial Scaffolds for Tissue Engineering*, in *Proceedings of the International Mechanical Engineering Conference and Exposition*. 2008: Boston, Massachusetts, USA.
22. Nain, A.S., et al., *Control of cell behavior by aligned micro/nanofibrous biomaterial scaffolds fabricated by spinneret-based tunable engineered parameters (STEP) technique.* Small, 2008. **4**(8): p. 1153-9.
23. Sahoo, S., et al., *Growth factor delivery through electrospun nanofibers in scaffolds for tissue engineering applications.* J Biomed Mater Res A, 2010. **93**(4): p. 1539-50.
24. Moffat, K.L., et al., *Novel nanofiber-based scaffold for rotator cuff repair and augmentation.* Tissue Eng Part A, 2009. **15**(1): p. 115-26.

25. Moffat, K.L., et al., *Characterization of the structure-function relationship at the ligament-to-bone interface.* Proc Natl Acad Sci U S A, 2008. **105**(23): p. 7947-52.
26. Moffat, K.L., et al., *Orthopedic interface tissue engineering for the biological fixation of soft tissue grafts.* Clin Sports Med, 2009. **28**(1): p. 157-76.
27. Yang, P.J. and J.S. Temenoff, *Engineering Orthopedic Tissue Interfaces.* Tissue Eng Part B Rev, 2009.
28. Hinds, S., et al., *The role of extracellular matrix composition in structure and function of bioengineered skeletal muscle.* Biomaterials, 2011. **32**(14): p. 3575-83.
29. Shimizu, K., H. Fujita, and E. Nagamori, *Alignment of skeletal muscle myoblasts and myotubes using linear micropatterned surfaces ground with abrasives.* Biotechnol Bioeng, 2009. **103**(3): p. 631-8.
30. Vye, M.V., *The ultrastructure of striated muscle.* Ann Clin Lab Sci, 1976. **6**(2): p. 142-51.
31. Beniash, E., *Biominerals-hierarchical nanocomposites: the example of bone.* Wiley Interdiscip Rev Nanomed Nanobiotechnol, 2010. **3**(1): p. 47-69.
32. Gigante, A., et al., *Collagen I membranes for tendon repair: effect of collagen fiber orientation on cell behavior.* J Orthop Res, 2009. **27**(6): p. 826-32.
33. Kerschnitzki, M., et al., *The organization of the osteocyte network mirrors the extracellular matrix orientation in bone.* J Struct Biol, 2011. **173**(2): p. 303-11.
34. Ma, J., X. He, and E. Jabbari, *Osteogenic differentiation of marrow stromal cells on random and aligned electrospun poly(L-lactide) nanofibers.* Ann Biomed Eng, 2011. **39**(1): p. 14-25.
35. Canalis, E., *Growth factor control of bone mass.* J Cell Biochem, 2009. **108**(4): p. 769-77.
36. Choi, Y.J., et al., *The identification of a heparin binding domain peptide from bone morphogenetic protein-4 and its role on osteogenesis.* Biomaterials, 2010. **31**(28): p. 7226-38.
37. Morin, R., D. Kaplan, and B. Perez-Ramirez, *Bone morphogenetic protein-2 binds as multilayers to a collagen delivery matrix: an equilibrium thermodynamic analysis.* Biomacromolecules, 2006. **7**(1): p. 131-8.
38. Sahni, A., T. Odrljin, and C.W. Francis, *Binding of basic fibroblast growth factor to fibrinogen and fibrin.* J Biol Chem, 1998. **273**(13): p. 7554-9.
39. Schultz, G.S. and A. Wysocki, *Interactions between extracellular matrix and growth factors in wound healing.* Wound Repair Regen, 2009. **17**(2): p. 153-62.
40. Carinci, P., et al., *Extracellular matrix and growth factors in the pathogenesis of some craniofacial malformations.* Eur J Histochem, 2007. **51 Suppl 1**: p. 105-15.
41. Kong, H.J. and D.J. Mooney, *Microenvironmental regulation of biomacromolecular therapies.* Nat Rev Drug Discov, 2007. **6**(6): p. 455-63.
42. Thomson, S.E., et al., *A novel primate model of delayed wound healing in diabetes: dysregulation of connective tissue growth factor.* Diabetologia, 2010. **53**(3): p. 572-83.
43. Wiradjaja, F., T. DiTommaso, and I. Smyth, *Basement membranes in development and disease.* Birth Defects Res C Embryo Today, 2010. **90**(1): p. 8-31.
44. Schultz, G.S., et al., *Dynamic reciprocity in the wound microenvironment.* Wound Repair Regen, 2011. **19**(2): p. 134-48.
45. Velnar, T., T. Bailey, and V. Smrkolj, *The wound healing process: an overview of the cellular and molecular mechanisms.* J Int Med Res, 2009. **37**(5): p. 1528-42.
46. Campbell, P.G., et al., *Engineered spatial patterns of FGF-2 immobilized on fibrin direct cell organization.* Biomaterials, 2005. **26**(33): p. 6762-70.
47. Kumar, V. and A. Sharma, *Neutrophils: Cinderella of innate immune system.* Int Immunopharmacol, 2010. **10**(11): p. 1325-34.

48. Papayannopoulos, V. and A. Zychlinsky, *NETs: a new strategy for using old weapons.* Trends Immunol, 2009. **30**(11): p. 513-21.
49. Brancato, S.K. and J.E. Albina, *Wound macrophages as key regulators of repair: origin, phenotype, and function.* Am J Pathol, 2011. **178**(1): p. 19-25.
50. Crisan, M., et al., *Multilineage stem cells in the adult: a perivascular legacy?* Organogenesis, 2011. **7**(2): p. 101-4.
51. Crisan, M., et al., *A perivascular origin for mesenchymal stem cells in multiple human organs.* Cell Stem Cell, 2008. **3**(3): p. 301-13.
52. Li, H., et al., *Adult bone-marrow-derived mesenchymal stem cells contribute to wound healing of skin appendages.* Cell Tissue Res, 2006. **326**(3): p. 725-36.
53. Desmouliere, A., I.A. Darby, and G. Gabbiani, *Normal and pathologic soft tissue remodeling: role of the myofibroblast, with special emphasis on liver and kidney fibrosis.* Lab Invest, 2003. **83**(12): p. 1689-707.
54. Hinz, B., *Formation and function of the myofibroblast during tissue repair.* J Invest Dermatol, 2007. **127**(3): p. 526-37.
55. Brown, L.F., et al., *Expression of vascular permeability factor (vascular endothelial growth factor) by epidermal keratinocytes during wound healing.* J Exp Med, 1992. **176**(5): p. 1375-9.
56. Werner, S. and R. Grose, *Regulation of wound healing by growth factors and cytokines.* Physiol Rev, 2003. **83**(3): p. 835-70.
57. Goren, I., et al., *A transgenic mouse model of inducible macrophage depletion: effects of diphtheria toxin-driven lysozyme M-specific cell lineage ablation on wound inflammatory, angiogenic, and contractive processes.* Am J Pathol, 2009. **175**(1): p. 132-47.
58. Mirza, R., L.A. DiPietro, and T.J. Koh, *Selective and specific macrophage ablation is detrimental to wound healing in mice.* Am J Pathol, 2009. **175**(6): p. 2454-62.
59. Grenier, G., et al., *Tissue reorganization in response to mechanical load increases functionality.* Tissue Eng, 2005. **11**(1-2): p. 90-100.
60. Wolff, J., *The Law of Bone Remodeling*. 1986: Springer.
61. Geissmann, F., et al., *Blood monocytes: distinct subsets, how they relate to dendritic cells, and their possible roles in the regulation of T-cell responses.* Immunol Cell Biol, 2008. **86**(5): p. 398-408.
62. Martinez, F.O., et al., *Macrophage activation and polarization.* Front Biosci, 2008. **13**: p. 453-61.
63. Mann, C.J., et al., *Aberrant repair and fibrosis development in skeletal muscle.* Skelet Muscle, 2011. **1**(1): p. 21.
64. Marrazzo, G., et al., *The role of neutrophils in corneal wound healing in HO-2 null mice.* PLoS One, 2011. **6**(6): p. e21180.
65. Mosmann, T.R., et al., *Two types of murine helper T cell clone. I. Definition according to profiles of lymphokine activities and secreted proteins.* J Immunol, 1986. **136**(7): p. 2348-57.
66. Sakaguchi, S., *Regulatory T cells: history and perspective.* Methods Mol Biol, 2011. **707**: p. 3-17.
67. Chen, Y., et al., *Regulatory T cell clones induced by oral tolerance: suppression of autoimmune encephalomyelitis.* Science, 1994. **265**(5176): p. 1237-40.
68. Xing, J., Y. Wu, and B. Ni, *Th9: a new player in asthma pathogenesis?* J Asthma, 2011. **48**(2): p. 115-25.
69. Dong, C., *TH17 cells in development: an updated view of their molecular identity and genetic programming.* Nat Rev Immunol, 2008. **8**(5): p. 337-48.
70. Tidball, J.G. and S.A. Villalta, *Regulatory interactions between muscle and the immune system during muscle regeneration.* Am J Physiol Regul Integr Comp Physiol, 2010. **298**(5): p. R1173-87.

71. Suchard, S.J., et al., *An LFA-1 (alphaLbeta2) small-molecule antagonist reduces inflammation and joint destruction in murine models of arthritis.* J Immunol, 2010. **184**(7): p. 3917-26.
72. Liu, N., et al., *High levels of beta-catenin signaling reduce osteogenic differentiation of stem cells in inflammatory microenvironments through inhibition of the noncanonical Wnt pathway.* J Bone Miner Res, 2011.
73. Schmidt-Bleek, K., et al., *Inflammatory phase of bone healing initiates the regenerative healing cascade.* Cell Tissue Res, 2011.
74. Zhang, J. and J.H. Wang, *Production of PGE(2) increases in tendons subjected to repetitive mechanical loading and induces differentiation of tendon stem cells into non-tenocytes.* J Orthop Res, 2010. **28**(2): p. 198-203.
75. Agren, M.S. and M. Werthen, *The extracellular matrix in wound healing: a closer look at therapeutics for chronic wounds.* Int J Low Extrem Wounds, 2007. **6**(2): p. 82-97.
76. Colombo, J.S., et al., *Delayed osteoblast differentiation and altered inflammatory response around implants placed in incisor sockets of type 2 diabetic rats.* Clin Oral Implants Res, 2011. **22**(6): p. 578-86.
77. McNally, E.M. and P. Pytel, *Muscle diseases: the muscular dystrophies.* Annu Rev Pathol, 2007. **2**: p. 87-109.
78. Arnett, T.R., *Acidosis, hypoxia and bone.* Arch Biochem Biophys, 2010. **503**(1): p. 103-9.
79. Fukumoto, S. and T.J. Martin, *Bone as an endocrine organ.* Trends Endocrinol Metab, 2009. **20**(5): p. 230-6.
80. Hu, H., M. Rabinowitz, and D. Smith, *Bone lead as a biological marker in epidemiologic studies of chronic toxicity: conceptual paradigms.* Environ Health Perspect, 1998. **106**(1): p. 1-8.
81. Li, X.J. and J. W.S.S., *Integrated Bone Tissue Anatomy and Physiology*, in *Current Topics in Osteoporosis*, H.W. Deng and Y.Z. Liu, Editors. 2005, World Scientific Publishing Co. Pte. Ltd. p. 45.
82. Lieber, R.L. and S.R. Ward, *Skeletal muscle design to meet functional demands.* Philos Trans R Soc Lond B Biol Sci, 2011. **366**(1570): p. 1466-76.
83. Liebschner, M.A.K. and M.A. Wettergreen, *Optimization of Bone Scaffold Engineering for Load Bearing Applications*, in *Topics In Tissue Engineering*. 2003.
84. Longo, U.G., et al., *Histopathology of rotator cuff tears.* Sports Med Arthrosc, 2011. **19**(3): p. 227-36.
85. Wolfe, R.R., *The underappreciated role of muscle in health and disease.* Am J Clin Nutr, 2006. **84**(3): p. 475-82.
86. Zhang, G., et al., *Development of tendon structure and function: regulation of collagen fibrillogenesis.* J Musculoskelet Neuronal Interact, 2005. **5**(1): p. 5-21.
87. Passerieux, E., et al., *Structural organization of the perimysium in bovine skeletal muscle: Junctional plates and associated intracellular subdomains.* J Struct Biol, 2006. **154**(2): p. 206-16.
88. Passerieux, E., et al., *Physical continuity of the perimysium from myofibers to tendons: involvement in lateral force transmission in skeletal muscle.* J Struct Biol, 2007. **159**(1): p. 19-28.
89. Purslow, P.P., *Muscle fascia and force transmission.* J Bodyw Mov Ther, 2010. **14**(4): p. 411-7.
90. Collins, C.A., et al., *Stem cell function, self-renewal, and behavioral heterogeneity of cells from the adult muscle satellite cell niche.* Cell, 2005. **122**(2): p. 289-301.
91. Sacco, A., et al., *Self-renewal and expansion of single transplanted muscle stem cells.* Nature, 2008. **456**(7221): p. 502-6.
92. Le Grand, F., et al., *Wnt7a activates the planar cell polarity pathway to drive the symmetric expansion of satellite stem cells.* Cell Stem Cell, 2009. **4**(6): p. 535-47.

93. Boonen, K.J., et al., *Essential environmental cues from the satellite cell niche: optimizing proliferation and differentiation.* Am J Physiol Cell Physiol, 2009. **296**(6): p. C1338-45.
94. Tidball, J.G., *Inflammatory processes in muscle injury and repair.* Am J Physiol Regul Integr Comp Physiol, 2005. **288**(2): p. R345-53.
95. Horsley, V., et al., *IL-4 acts as a myoblast recruitment factor during mammalian muscle growth.* Cell, 2003. **113**(4): p. 483-94.
96. Prokopchuk, O., et al., *Skeletal muscle IL-4, IL-4Ralpha, IL-13 and IL-13Ralpha1 expression and response to strength training.* Exerc Immunol Rev, 2007. **13**: p. 67-75.
97. Segawa, M., et al., *Suppression of macrophage functions impairs skeletal muscle regeneration with severe fibrosis.* Exp Cell Res, 2008. **314**(17): p. 3232-44.
98. Banos, C.C., A.H. Thomas, and C.K. Kuo, *Collagen fibrillogenesis in tendon development: current models and regulation of fibril assembly.* Birth Defects Res C Embryo Today, 2008. **84**(3): p. 228-44.
99. Dyer, R.F. and C.D. Enna, *Ultrastructural features of adult human tendon.* Cell Tissue Res, 1976. **168**(2): p. 247-59.
100. Screen, H.R., et al., *The influence of noncollagenous matrix components on the micromechanical environment of tendon fascicles.* Ann Biomed Eng, 2005. **33**(8): p. 1090-9.
101. Svensson, L., et al., *Fibromodulin-null mice have abnormal collagen fibrils, tissue organization, and altered lumican deposition in tendon.* J Biol Chem, 1999. **274**(14): p. 9636-47.
102. Zhang, G., et al., *Decorin regulates assembly of collagen fibrils and acquisition of biomechanical properties during tendon development.* J Cell Biochem, 2006. **98**(6): p. 1436-49.
103. Kohrs, R.T., et al., *Tendon fascicle gliding in wild type, heterozygous, and lubricin knockout mice.* J Orthop Res, 2011. **29**(3): p. 384-9.
104. Tucci, M., et al., *The role of proteoglycans in idiopathic carpal tunnel syndrome.* Biomed Sci Instrum, 2005. **41**: p. 141-6.
105. Bi, Y., et al., *Identification of tendon stem/progenitor cells and the role of the extracellular matrix in their niche.* Nat Med, 2007. **13**(10): p. 1219-27.
106. Rui, Y.F., et al., *Isolation and characterization of multipotent rat tendon-derived stem cells.* Tissue Eng Part A, 2010. **16**(5): p. 1549-58.
107. Zhang, J. and J.H. Wang, *Characterization of differential properties of rabbit tendon stem cells and tenocytes.* BMC Musculoskelet Disord, 2010. **11**: p. 10.
108. Lui, P.P. and K.M. Chan, *Tendon-Derived Stem Cells (TDSCs): From Basic Science to Potential Roles in Tendon Pathology and Tissue Engineering Applications.* Stem Cell Rev, 2011.
109. Ni, M., et al., *Tendon-derived stem cells (TDSCs) promote tendon repair in a rat patellar tendon window defect model.* J Orthop Res, 2011.
110. Cserjesi, P., et al., *Scleraxis: a basic helix-loop-helix protein that prefigures skeletal formation during mouse embryogenesis.* Development, 1995. **121**(4): p. 1099-110.
111. Chen, J., et al., *Scaffolds for tendon and ligament repair: review of the efficacy of commercial products.* Expert Rev Med Devices, 2009. **6**(1): p. 61-73.
112. Gulotta, L.V. and S.A. Rodeo, *Growth factors for rotator cuff repair.* Clin Sports Med, 2009. **28**(1): p. 13-23.
113. Hope, M. and T.S. Saxby, *Tendon healing.* Foot Ankle Clin, 2007. **12**(4): p. 553-67, v.
114. Battery, L. and N. Maffulli, *Inflammation in overuse tendon injuries.* Sports Med Arthrosc, 2011. **19**(3): p. 213-7.
115. Herdrich, B.J., et al., *Fetal tendon wound size modulates wound gene expression and subsequent wound phenotype.* Wound Repair Regen, 2010. **18**(5): p. 543-9.

116. Millar, N.L., et al., *Inflammation is present in early human tendinopathy.* Am J Sports Med, 2010. **38**(10): p. 2085-91.
117. Millar, N.L., et al., *Cytokines and apoptosis in supraspinatus tendinopathy.* J Bone Joint Surg Br, 2009. **91**(3): p. 417-24.
118. Jadlowiec, J.A., A.B. Celil, and J.O. Hollinger, *Bone tissue engineering: recent advances and promising therapeutic agents.* Expert Opin Biol Ther, 2003. **3**(3): p. 409-23.
119. Aarden, E.M., E.H. Burger, and P.J. Nijweide, *Function of osteocytes in bone.* J Cell Biochem, 1994. **55**(3): p. 287-99.
120. Bonewald, L.F., *The amazing osteocyte.* J Bone Miner Res, 2011. **26**(2): p. 229-38.
121. Malone, A.M., et al., *Primary cilia mediate mechanosensing in bone cells by a calcium-independent mechanism.* Proc Natl Acad Sci U S A, 2007. **104**(33): p. 13325-30.
122. Ascenzi, A. and E. Bonucci, *The compressive properties of single osteons.* Anat Rec, 1968. **161**(3): p. 377-91.
123. Giraud-Guille, M.M., L. Besseau, and R. Martin, *Liquid crystalline assemblies of collagen in bone and in vitro systems.* J Biomech, 2003. **36**(10): p. 1571-9.
124. Gu, G., et al., *Death of osteocytes turns off the inhibition of osteoclasts and triggers local bone resorption.* Biochem Biophys Res Commun, 2005. **335**(4): p. 1095-101.
125. Lakes, R., *Materials with structural hierarchy.* Nature, 1993. **361**: p. 511-515.
126. Bianco, P., B. Sacchetti, and M. Riminucci, *Osteoprogenitors and the hematopoietic microenvironment.* Best Pract Res Clin Haematol, 2011. **24**(1): p. 37-47.
127. Friedenstein, A.J., et al., *Heterotopic of bone marrow. Analysis of precursor cells for osteogenic and hematopoietic tissues.* Transplantation, 1968. **6**(2): p. 230-47.
128. Friedenstein, A.J., S. Piatetzky, II, and K.V. Petrakova, *Osteogenesis in transplants of bone marrow cells.* J Embryol Exp Morphol, 1966. **16**(3): p. 381-90.
129. Itoh, S. and J.E. Aubin, *A novel purification method for multipotential skeletal stem cells.* J Cell Biochem, 2009. **108**(2): p. 368-77.
130. Tare, R.S., et al., *Skeletal stem cells: phenotype, biology and environmental niches informing tissue regeneration.* Mol Cell Endocrinol, 2008. **288**(1-2): p. 11-21.
131. Simmons, P.J. and B. Torok-Storb, *Identification of stromal cell precursors in human bone marrow by a novel monoclonal antibody, STRO-1.* Blood, 1991. **78**(1): p. 55-62.
132. Tavassoli, M. and W.H. Crosby, *Transplantation of marrow to extramedullary sites.* Science, 1968. **161**(836): p. 54-6.
133. Calvi, L.M., et al., *Osteoblastic cells regulate the haematopoietic stem cell niche.* Nature, 2003. **425**(6960): p. 841-6.
134. Zhang, X., et al., *The Nell-1 Growth Factor Stimulates Bone Formation by Purified Human Perivascular Cells.* Tissue Eng Part A, 2011.
135. Zhao, L., et al., *TNF Inhibits Mesenchymal Stem Cell Differentiation into Osteoblasts via the Ubiquitin E3 Ligase Wwp1.* Stem Cells, 2011.
136. Kawagoe, T., I. Sato, and T. Sato, *Distribution of macromolecular components in the muscle-bone junction of human masticatory muscles.* Okajimas Folia Anat Jpn, 1997. **74**(1): p. 1-7.
137. Kojima, H., et al., *Ultrastructural changes at the myotendinous junction induced by exercise.* J Orthop Sci, 2008. **13**(3): p. 233-9.
138. Tidball, J.G. and T.L. Daniel, *Myotendinous junctions of tonic muscle cells: structure and loading.* Cell Tissue Res, 1986. **245**(2): p. 315-22.
139. Garau, G., et al., *Traumatic patellar tendinopathy.* Disabil Rehabil, 2008. **30**(20-22): p. 1616-20.
140. Chen, D., M. Zhao, and G.R. Mundy, *Bone morphogenetic proteins.* Growth Factors, 2004. **22**(4): p. 233-41.

141. Wan, M. and X. Cao, *BMP signaling in skeletal development.* Biochem Biophys Res Commun, 2005. **328**(3): p. 651-7.
142. Unsicker, K. and K. Krieglstein, *Cell Signaling and Growth Factors in Development*, ed. K. Unsicker and K. Krieglstein. 2006, Germany: Wiley-VCH 991.
143. Celil, A.B. and P.G. Campbell, *BMP-2 and insulin-like growth factor-I mediate Osterix (Osx) expression in human mesenchymal stem cells via the MAPK and protein kinase D signaling pathways.* J Biol Chem, 2005. **280**(36): p. 31353-9.
144. Moustakas, A. and C.H. Heldin, *Non-Smad TGF-beta signals.* J Cell Sci, 2005. **118**(Pt 16): p. 3573-84.
145. Ulsamer, A., et al., *BMP-2 induces Osterix expression through up-regulation of Dlx5 and its phosphorylation by p38.* J Biol Chem, 2008. **283**(7): p. 3816-26.
146. Chen, G.J. and R. Forough, *Fibroblast growth factors, fibroblast growth factor receptors, diseases, and drugs.* Recent Pat Cardiovasc Drug Discov, 2006. **1**(2): p. 211-24.
147. Sorensen, V., T. Nilsen, and A. Wiedlocha, *Functional diversity of FGF-2 isoforms by intracellular sorting.* Bioessays, 2006. **28**(5): p. 504-14.
148. Siddle, K., *Signalling by insulin and IGF receptors: supporting acts and new players.* J Mol Endocrinol, 2011. **47**(1): p. R1-10.
149. Allen, R.T., et al., *Sustained Akt/PKB activation and transient attenuation of c-jun N-terminal kinase in the inhibition of apoptosis by IGF-1 in vascular smooth muscle cells.* Apoptosis, 2005. **10**(3): p. 525-35.
150. Johnson, S.E. and R.E. Allen, *The effects of bFGF, IGF-I, and TGF-beta on RMo skeletal muscle cell proliferation and differentiation.* Exp Cell Res, 1990. **187**(2): p. 250-4.
151. Baxter, R.C., *Signalling pathways involved in antiproliferative effects of IGFBP-3: a review.* Mol Pathol, 2001. **54**(3): p. 145-8.
152. Drop, S.L., et al., *Structural aspects of the IGFBP family.* Growth Regul, 1992. **2**(2): p. 69-79.
153. Chew, S.Y. and W.C. Low, *Scaffold-based approach to direct stem cell neural and cardiovascular differentiation: an analysis of physical and biochemical effects.* J Biomed Mater Res A, 2011. **97**(3): p. 355-74.
154. Liu, X., et al., *Guidance of neurite outgrowth on aligned electrospun polypyrrole/poly(styrene-beta-isobutylene-beta-styrene) fiber platforms.* J Biomed Mater Res A, 2010. **94**(4): p. 1004-11.
155. Munoz-Pinto, D.J., et al., *Inorganic-organic hybrid scaffolds for osteochondral regeneration.* J Biomed Mater Res A, 2010. **94**(1): p. 112-21.
156. Neumann, T., S.D. Hauschka, and J.E. Sanders, *Tissue engineering of skeletal muscle using polymer fiber arrays.* Tissue Eng, 2003. **9**(5): p. 995-1003.
157. Ott, H.C., et al., *Perfusion-decellularized matrix: using nature's platform to engineer a bioartificial heart.* Nat Med, 2008. **14**(2): p. 213-21.
158. Ratner, B.D., et al., eds. *Biomaterials Science, Second Edition: An Introduction to Materials in Medicine* 2004, Academic Press.
159. Romano, N.H., et al., *Protein-engineered biomaterials: nanoscale mimics of the extracellular matrix.* Biochim Biophys Acta, 2011. **1810**(3): p. 339-49.
160. De Silva, M.N., et al., *Two-step cell patterning on planar and complex curved surfaces by precision spraying of polymers.* Biotechnol Bioeng, 2006. **93**(5): p. 919-27.
161. Chen, G. and Y. Ito, *Gradient micropattern immobilization of EGF to investigate the effect of artificial juxtacrine stimulation.* Biomaterials, 2001. **22**(18): p. 2453-7.
162. Ito, Y., G. Chen, and Y. Imanishi, *Micropatterned immobilization of epidermal growth factor to regulate cell function.* Bioconjug Chem, 1998. **9**(2): p. 277-82.

163. DeLong, S.A., J.J. Moon, and J.L. West, *Covalently immobilized gradients of bFGF on hydrogel scaffolds for directed cell migration.* Biomaterials, 2005. **26**(16): p. 3227-34.
164. Kane, R.S., et al., *Patterning proteins and cells using soft lithography.* Biomaterials, 1999. **20**(23-24): p. 2363-76.
165. Mayer, M., et al., *Micropatterned agarose gels for stamping arrays of proteins and gradients of proteins.* Proteomics, 2004. **4**(8): p. 2366-76.
166. Guillotin, B., et al., *Laser assisted bioprinting of engineered tissue with high cell density and microscale organization.* Biomaterials, 2010. **31**(28): p. 7250-6.
167. Gustavsson, P., et al., *Neurite guidance on protein micropatterns generated by a piezoelectric microdispenser.* Biomaterials, 2007. **28**(6): p. 1141-51.
168. Klebe, R.J., *Cytoscribing: a method for micropositioning cells and the construction of two- and three-dimensional synthetic tissues.* Exp Cell Res, 1988. **179**(2): p. 362-73.
169. Turcu, F., et al., *Ink-jet printing for micropattern generation of laminin for neuronal adhesion.* J Neurosci Methods, 2003. **131**(1-2): p. 141-8.
170. Wong, E.Y. and S.L. Diamond, *Advancing microarray assembly with acoustic dispensing technology.* Anal Chem, 2009. **81**(1): p. 509-14.
171. Jiang, X., et al., *A general method for patterning gradients of biomolecules on surfaces using microfluidic networks.* Anal Chem, 2005. **77**(8): p. 2338-47.
172. Riepl, M., et al., *Molecular gradients: an efficient approach for optimizing the surface properties of biomaterials and biochips.* Langmuir, 2005. **21**(3): p. 1042-50.
173. Smith, J.T., et al., *Measurement of cell migration on surface-bound fibronectin gradients.* Langmuir, 2004. **20**(19): p. 8279-86.

CHAPTER 2: *IN VITRO* PATTERNING OF A PRIMITIVE MUSCLE-TENDON-BONE UNIT: SIMULTANEOUS CONTROL OF MUSCLOSKELETAL CELL DIFFERENTIATION WITH INKJET-BASED PRINTING OF BMP-2 AND FGF-2 PATTERNS ONTO FIBRIN-COATED GLASS COVERSLIPS

Based on published work:

Engineering Spatial Control of Multiple Differentiation Fates within a Stem Cell Population

Dai Fei Elmer Ker, Bur Chu, Julie A. Phillippi, Burhan Gharaibeh, Johnny Huard, Lee E. Weiss and Phil G. Campbell

Biomaterials. 2011 May; **32** (13) 3413-3422.

2.1 ABSTRACT

The capability to engineer microenvironmental cues to direct a stem cell population toward multiple fates, simultaneously, in spatially defined regions is important for understanding the maintenance and repair of multi-tissue units. Our lab has previously developed an inkjet-based bioprinter to create patterns of solid-phase growth factors (GFs) immobilized to an extracellular matrix (ECM) substrate, and applied this approach to drive muscle-derived stem cells toward osteoblasts 'on–pattern' and myocytes 'off–pattern' simultaneously. Here this technology is extended to spatially control osteoblast, tenocyte and myocyte differentiation simultaneously. Utilizing immunofluorescence staining to identify tendon-promoting GFs, fibroblast growth factor-2 (FGF-2) was shown to upregulate the tendon marker Scleraxis (Scx) in C3H10T1/2 mesenchymal fibroblasts, C2C12 myoblasts and primary muscle-derived stem cells, while downregulating the myofibroblast marker α-smooth muscle actin (α-SMA). Quantitative PCR studies indicated that FGF-2 may direct stem cells towards a tendon fate via the *Ets* family members of transcription factors such as *pea3* and *erm*. Neighboring patterns of FGF-2 and bone morphogenetic protein-2 (BMP-2) printed onto a single fibrin-coated coverslip upregulated Scx and the osteoblast marker ALP, respectively, while non-printed regions showed spontaneous myotube differentiation. This work illustrates spatial control of multi-phenotype differentiation and may have potential in the regeneration of multi-tissue units.

2.2 INTRODUCTION

As described in Chapter 1, the musculoskeletal system comprises multiple tissue types including bone, muscle, tendon, ligament and cartilage as well as their respective tissue interfaces such as bone-to-tendon entheses and muscle-to-tendon junctions. The maintenance and repair of these

multi-tissue structures involves the spatial control of stem cell differentiation toward tissue-specific cells, such as osteoblasts, tenocytes and myocytes [1]. This process is regulated by physical and biochemical microenvironmental cues imparted by the interactions of cells with their extracellular matrix (ECM), neighboring cells, and secreted local and systemic signaling molecules, including growth factors (GFs) [1, 2]. Signaling molecules, regulate the pericellular environment where they reside in both the 'liquid-phase' (freely diffusing) form and the 'solid-phase' (immobilized) form that exists in an equilibrium state between desorption from and adsorption to the ECM and cell surfaces [3]. The unique architecture and biochemical composition of the ECM allows it to sequester (immobilize) and release GFs at picogram to nanogram levels [3-7], and can negatively or positively regulate GF bioactivity and bioavailability [3]. As such, GF sequestration by the ECM immobilizes GFs to specific locations, which in turn imparts the temporal and spatial cues required for directing cell behaviors such as cell adhesion, migration, proliferation, differentiation and apoptosis, which are vital for orchestrating complex processes such as development, maintenance and wound healing [3, 7-19]. Therefore, developing toolsets that can be used to selectively control the physical placement and dosage of multiple exogenous GFs in a physiologically-relevant manner in order to spatially direct a stem cell population toward multiple cell fates simultaneously is a logical consideration for studying stem cell behaviors and may also have direct applications in regenerative medicine.

Prior work reported by our group and by others has shown that ECMs patterned with solid-phase GFs can be engineered to control various aspects of stem cell behavior, including proliferation, migration and differentiation *in vitro* [8, 13, 14, 16, 20-23] as well as differentiation *in vivo* [10]. In addition, our lab has previously demonstrated that a GF-patterned fibrin ECM created using an inkjet-based bioprinting technology can drive a single stem cell population toward osteoblast

and myocyte fates simultaneously, in registration to printed patterns *in vitro* [16]. In the work presented here, this approach is extended to spatially drive stem cell differentiation towards a tendon fate simultaneously with osteoblast and myocyte differentiation.

Using solid-phase GFs to direct stem cells to tenocytes *in vitro* has not been previously reported in literature. Therefore, prior to studying multi-lineage patterning, candidate tendon-promoting GFs had to be identified and validated. Candidate GFs were screened against mouse C3H10T1/2 mesenchymal fibroblasts, C2C12 myoblasts and primary muscle-derived stem cells (MDSCs) using both liquid- and solid-phase immunofluorescence staining for the tendon marker Scleraxis (Scx) [24, 25]. Quantitative PCR studies were subsequently performed to elucidate the mechanism by which stem cells differentiated towards a tendon lineage. Following this, solid-phase presentation of FGF-2 and/or BMP-2 on fibrin-coated glass coverslips using either coarse hand-printing or high resolution, low-dose inkjet bioprinting was used to demonstrate spatial control of stem cell differentiation towards multiple cell fates simultaneously.

2.3 MATERIALS AND METHODS

2.3.1 Cell Culture

Multipotent mouse C3H10T1/2 cells (ATTC, Manassas, VA) were grown in Dulbecco's Modified Eagle's Media (DMEM; Invitrogen, Carlsbad, CA), 10% fetal bovine serum (Invitrogen, Carlsbad, CA) and 1% penicillin-streptomycin (PS; Invitrogen, Carlsbad, CA). Mouse C2C12 cells (ATTC, Manassas, VA) were grown in DMEM, 10% bovine serum (Invitrogen, Carlsbad, CA) and 1% PS. Multipotent MDSCs were isolated from primary mouse gastrocnemius muscle biopsies following a modified preplate technique [26] and were grown in DMEM (high glucose), 10% horse serum (HS; Invitrogen, Carlsbad, CA), 10% FBS, 0.5% Chick

Embryo Extract (Accurate Chemical Co, Westbury, NY) as previously described [26, 27]. For myogenic differentiation, cells were grown in low serum containing myogenic differentiation (DMEM, 2% HS, 1% PS) media for 3-5 days. This media is subsequently referred to as myogenic media or myogenic conditions for the remainder of the text. All cells were kept at 37^{o}C, 5% CO_2 in a humidified incubator.

2.3.2 Growth Factor Preparation and Use

Recombinant human BMP-2 (Genetics Institute Inc, Cambridge, MA), FGF-2 (Peprotech, Rockyhill, NJ), FGF-4 (Peprotech, Rockyhill, NJ) and GDF-7 (Prospc Bio, Rehovot, Israel) were reconstituted according to manufacturer's instructions to 1-2 mg/mL, aliquoted and stored at -80^{o}C. Prior to use, GFs were freshly diluted to the desired concentration in 10 mM sodium phosphate, pH 7.4. For liquid-phase GF experiments, cells were seeded at 2.6-3.1 x 10^4 cells/cm^2 in the presence or absence of GF (1-500 ng/mL) under proliferation (High serum) and myogenic (Low serum) media for 3-4 days. For solid-phase GF experiments, cells were seeded at 3.1-3.6 x 10^4 cells/cm^2 over printed fibrin-coated coverslips under proliferation and myogenic media for 3-4 days.

2.3.3 Preparation of Fibrin Coated Coverslips

Homogenous fibrin films were prepared essentially as described by Campbell *et al.*, 2005 [8]. Briefly, 18 x 18 mm epoxy-silanized glass coverslips (Thermo Fisher Scientific, Waltham, MA) were coated with 0.1 mg/mL fibrinogen (Aventis Behring, King of Prussia, PA or American Diagnostica Inc., Stanford, CT) and converted into fibrin by incubating coverslips in 4 U/mL thrombin (Enzyme Research Laboratories, South Bend, IN). Coverslips were then washed with

phosphate buffered saline (PBS) and sterile deionized water before air-drying in a laminar flow hood. The thickness of the fibrin films was previously estimated to be approximately 20 nm [8].

2.3.4 Growth Factor Printing

Prior to printing, GFs were freshly diluted to the desired concentration in 10 mM sodium phosphate, pH 7.4. Prior to filling the inkjet with the GF, the printhead was sterilized by rinsing with 70% ethanol followed by sterile deionized water. The bio-ink, consisting of 100-200 µg/ml GF was loaded into the printhead, and printed onto fibrin-coated glass coverslips as previously described [8, 14]. The concentration of inkjetted GFs can be modulated by overprinting, which is achieved by varying the number of times a GF is deposited in the same (x,y) location. In the case of hand-printed GF patterns, 1-2 µL of a 100 µg/mL GF solution was pipetted onto a fibrin-coated glass coverslip instead and a diamond scribe pen was used to mark the droplet perimeter after it had been allowed to air-dry for 1 h at 37^{o}C. After printing, fibrin-coated coverslips were incubated in PBS for 5 min followed by serum-free DMEM with 1% PS overnight at 37°C, 5% CO_2 to wash off unbound GF prior to cell seeding. The surface concentration of GF present on fibrin-coated coverslips during cell seeding was estimated based on desorption measurements in previous studies [8, 13, 14, 28].

2.3.5 Quantitative PCR

For the experiments investigating *scx* expression during muscle differentiation, C2C12 cells were grown at 1.55 x 10^2 cells/cm^2 under proliferation conditions and at 2.5 x 10^3 cells/cm^2 under myogenic conditions for 4 days to ensure similar number of cells in both conditions prior to RNA extraction. C3H10T1/2 cells were grown in proliferation medium at 1.5-2.0 x 10^4 cells/cm^2 in the presence or absence of FGF-2 (50 µg/mL) for 36 h and 72 h prior to extraction of total

RNA (RNeasy Mini Kit; Qiagen, Valencia, CA). Quantitative polymerase chain reaction analysis for *pea3*, *erm* and *scx* were performed as previously described [29, 30]. Target gene expression was normalized to 18S internal control. Gene expression is displayed as the mean of five independent experiments and represented as mean ± Standard Error Mean (SEM). Statistical analysis was performed as described below.

2.3.6 Immunofluorescence staining

Cells were washed in PBS, fixed in methanol for 5 min, air-dried and blocked with 10% donkey serum (Jackson Immunoresearch, West Gove, PA) for 20 min at RT. For mouse-on-mouse staining, an additional blocking step was performed by incubating cells with 100 µg/mL donkey anti-mouse FAB (Jackson Immunoresearch, West Gove, PA) for 1 h at RT. Cells were then rinsed with wash buffer (PBS, 0.1%BSA) and incubated with primary antibodies: rabbit anti-scx (10 µg/mL; Abcam, Cambridge, MA), mouse anti-myosin MF20 (1 µg/mL; DSHB, Iowa City, Iowa), mouse anti-α-smooth muscle actin (α-SMA; 1 µg/mL; Abcam, Cambridge, MA) or goat anti-myogenin (2 µg/mL; Santa Cruz Biotechnology Inc, Santa Cruz, CA) overnight at 4^{o}C. Cells were then rinsed three times with wash buffer and incubated with secondary antibodies for 1 h at RT – donkey anti-goat FITC (4 µg/mL; Santa Cruz Biotechnology Inc, Santa Cruz, CA), donkey anti-mouse Dylight 488 nm or donkey anti-rabbit Dylight 549 nm (15 µg/mL each; Jackson Immunoresearch, West Gove, PA). Lastly, cells were rinsed five times with wash buffer and imaged using a Zeiss Axiovert 200M microscope (Carl Zeiss Microimaging, Thornwood, NY) equipped with a Colibri LED light source. Quantification of immunofluorescence staining was performed using Adobe Photoshop 7.0 (Adobe Systems, San Jose, CA). Briefly, the rectangular marquee tool was used to draw a bounding box (Approximately 700 pixels by 700

pixels representing an area 0.9 mm by 0.9 mm in size) and the image histogram tool was used to measure average pixel intensity. Statistical analysis was performed as described below.

2.3.7 ALP Stain

Cells were seeded onto GF patterns for 72 h, washed in PBS and fixed for 2 min in 3.7% formaldehyde. Alkaline phosphatase activity (ALP; SIGMAFAST) was detected according to the manufacturer's instructions (Sigma-Aldrich, St. Louis, MO). Where required, alkaline phosphatase-stained images were converted to CMYK format since this color format is representative of reflected light colors as opposed to emitted light colors (RGB). Since cyan and magenta form the color blue, these channels were added together and inverted. The average pixel intensity was determined using the image histogram tool in Adobe Photoshop 7.0 (Adobe Systems, San Jose, CA).

2.3.8 Statistical Analysis

For both quantitative PCR and immunofluorescence analysis, one-way analysis of variance followed by Fisher's least significant difference post hoc test using SYSTAT 9 software (Systat Software Inc., Richmond, CA) was performed to determine significance among treatment groups. A p value ≤ 0.05 was considered statistically significant.

2.4 RESULTS

2.4.1 Effect of Liquid-Phase FGF-2 and FGF-4 on Scx Expression in C3H10T1/2 Cells

By immunostaining for the tendon marker Scx, putative tendon-promoting growth factors (GFs) were identified in C3H10T1/2 cells. Upon addition of 50 ng/mL FGF-2, C3H10T1/2 cells displayed a spindle-like morphology and upregulated the tendon marker Scx (Figure 2.1). Addition of 200 ng/mL BMP-2 alone or 500 ng/mL GDF-7 alone had little to no effect on Scx

levels (Figure 2.1). Unexpectedly, addition of 500 ng/mL GDF-7 to FGF-2-treated cells decreased Scx levels (Figure 2.1). When treated with 50 ng/mL FGF-4, C3H10T1/2 cells exhibited a spindle-like morphology and upregulated the tendon marker Scx, displaying punctate nuclear staining of Scx transcription factor (Figure 2.2).

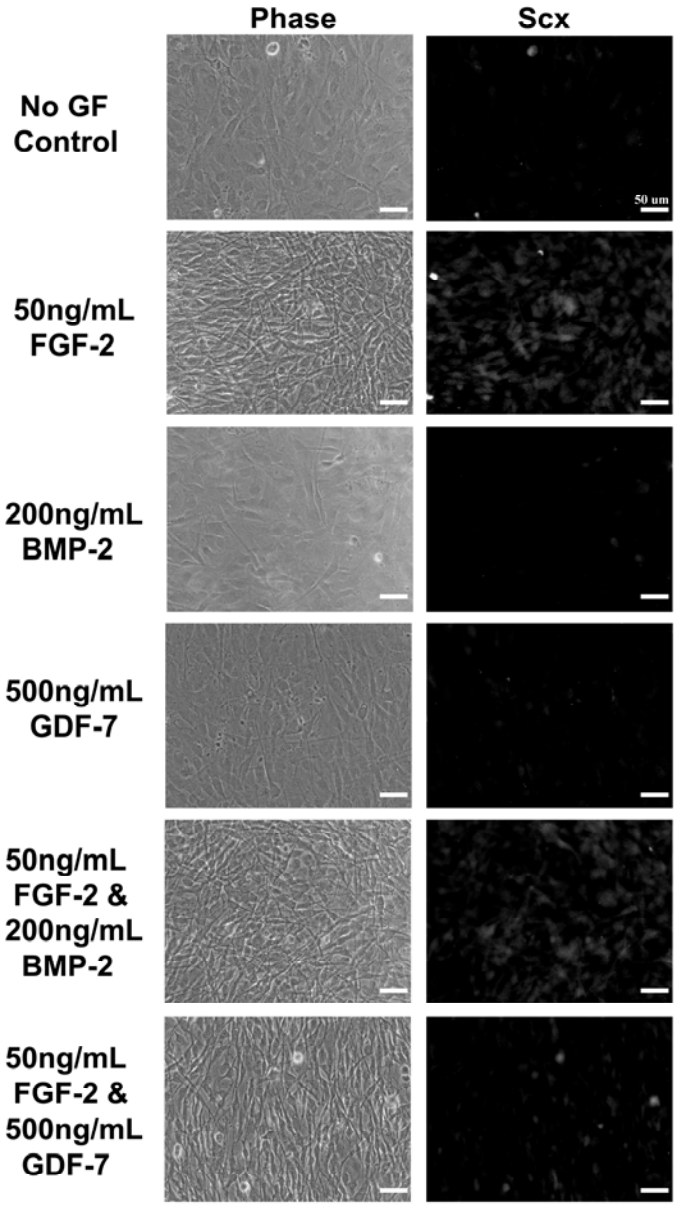

Figure 2.1. Effect of FGF-2, GDF-7 and BMP-2 on expression of tendon marker Scx in mouse C3H10T1/2 cells after 3.5 days in proliferation media. Scx was upregulated in the presence of FGF-2 but not GDF-7 or BMP-2. Cells also adopt an elongated spindle-like morphology when treated with FGF-2. Scale bar is 50 μm.

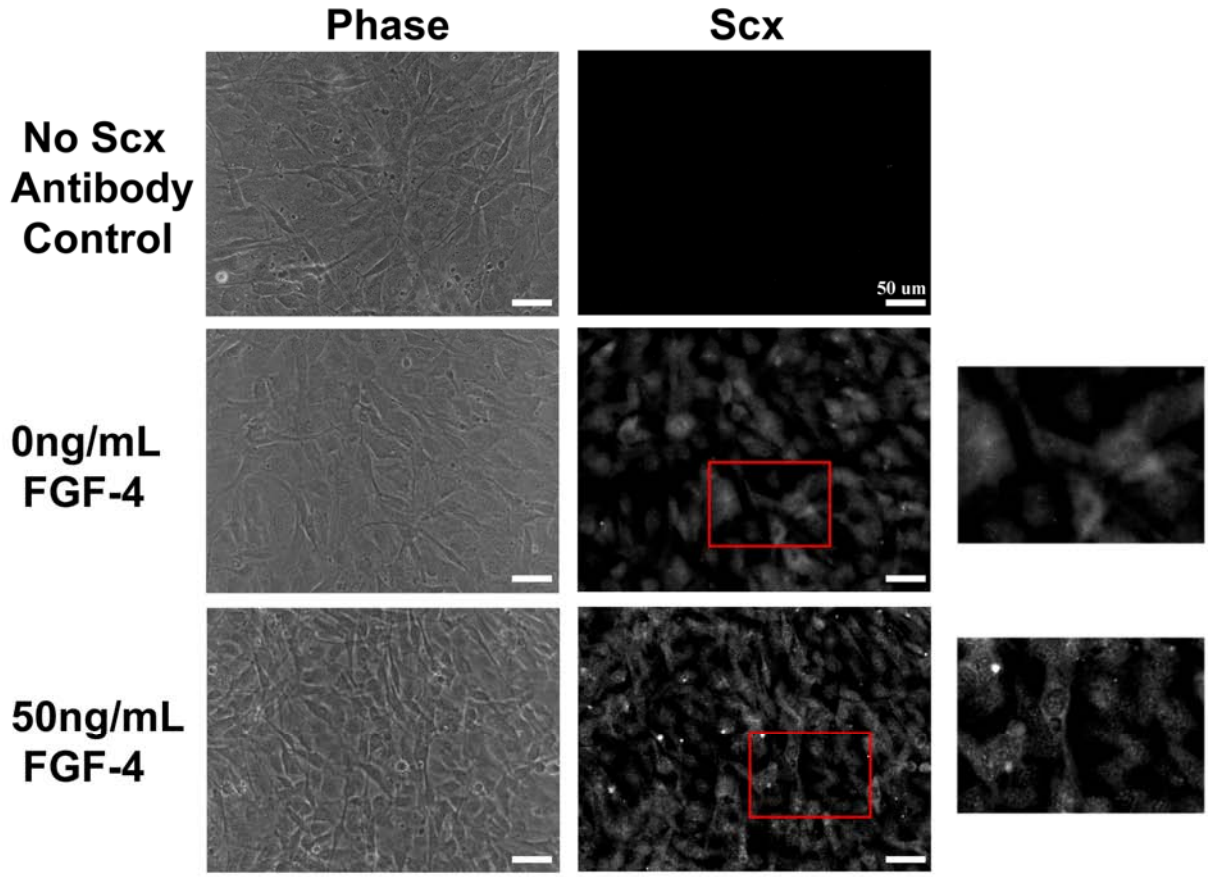

Figure 2.2. Dose-dependent effect of FGF-4 on expression of tendon marker Scx in mouse C3H10T1/2 cells after 72h in proliferation media. The tendon marker Scx was upregulated in the presence of FGF-4. Red box indicates magnified region (right). Note the punctate nuclear staining of Scx transcription factor in 50 ng/ml FGF-4. Scale bar 50 µm.

2.4.2 Effect of Liquid-Phase FGF-2 on Scx Expression in C2C12 Cells

To determine if FGF-2 was indeed a putative tendon-promoting GF, Scx expression in C2C12 cells treated with FGF-2 under proliferation (high serum) as well as myogenic (low serum) conditions. Under proliferation conditions, increasing amounts of FGF-2 resulted in upregulation of the tendon marker Scx in a dose-dependent manner with punctate nuclear staining of Scx observed in cells treated at 25 ng/mL FGF-2 and 50 ng/mL FGF-2 (Figure 2.3). Under myogenic conditions, Scx expression was unexpectedly upregulated in nascent myotubes in the absence of FGF-2 (Figure 2.4). Confocal sectioning studies determined that the thickness of myotubes,

which is observed as a bright halo around cells in phase-contrast images (Figure 2.4), contributed in part to the high levels of Scx (data not shown). Furthermore, quantitative PCR analysis indicated that there was no fold change in *scx* expression between proliferating C2C12 cells (1.003 ± 0.075 fold change) and differentiating myotubes (1.022 ± 0.209 fold change). In the presence of FGF-2, myotube formation was inhibited and cells showed increased Scx expression when compared to non-myocytes in untreated control (Figure 2.4).

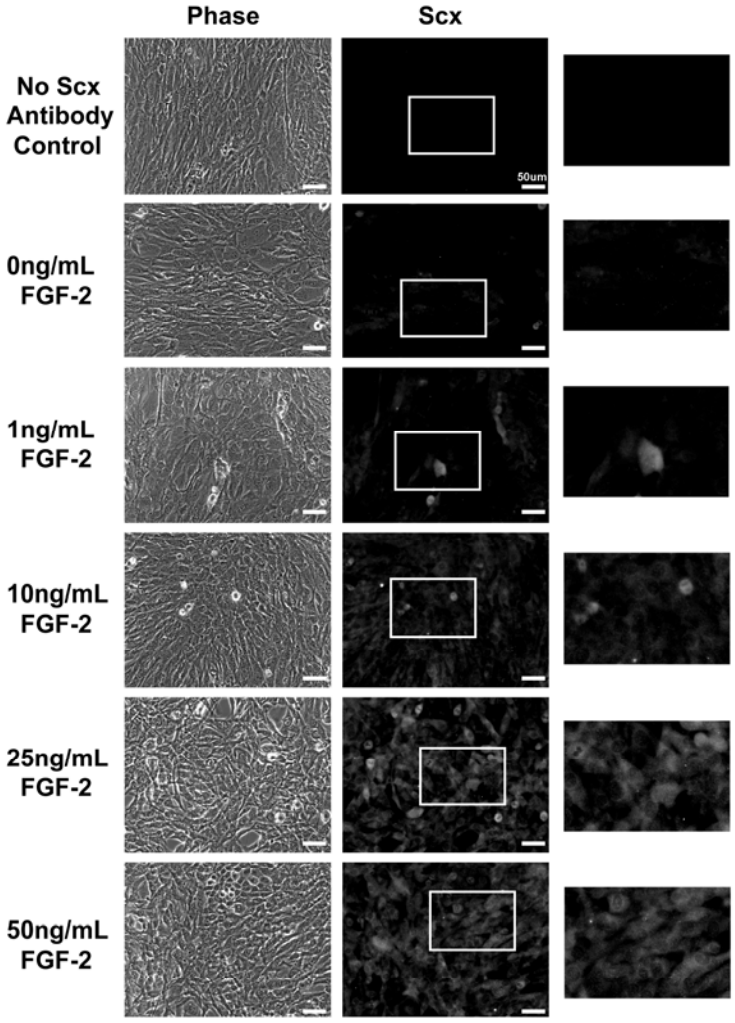

Figure 2.3. Dose-dependent effect of FGF-2 on expression of tendon marker Scx in mouse C2C12 cells after 72h in proliferation media. Increasing amounts of FGF-2 resulted in upregulation of tendon marker Scx. White box indicates magnified region (right). Note the punctate nuclear staining of Scx transcription factor in 25 ng/ml and 50 ng/ml FGF-2. Scale bar 50 µm.

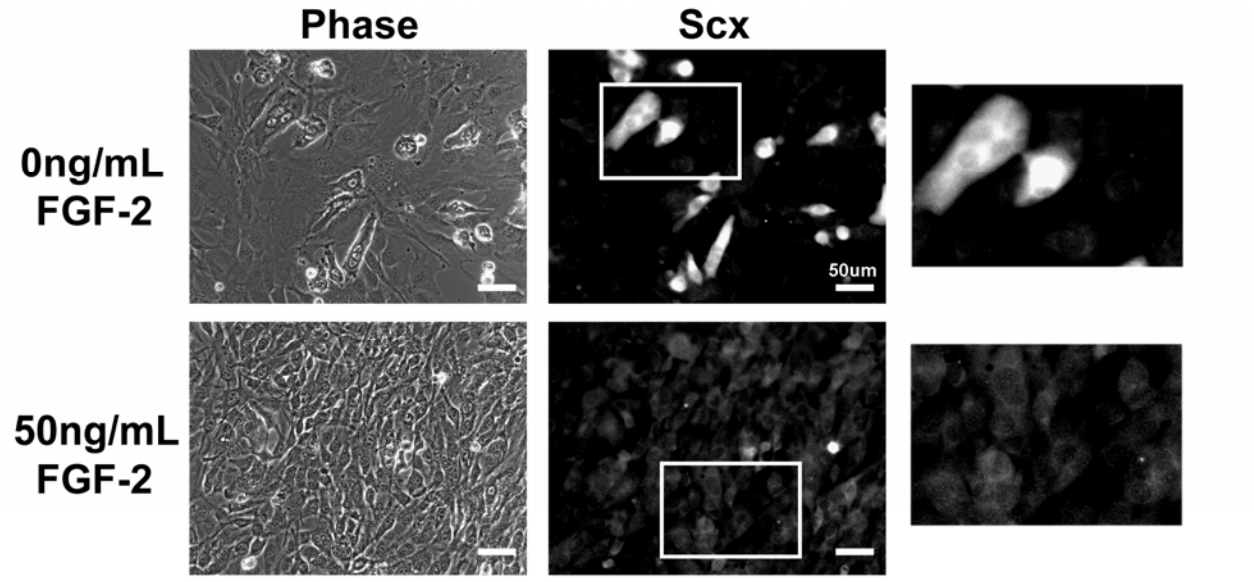

Figure 2.4. Effect of FGF-2 on expression of tendon marker Scx in mouse C2C12 cells after 72h in myogenic media. Scx expression was upregulated in nascent myotubes in the absence of FGF-2. In presence of FGF-2, myotube formation was inhibited and increased Scx expression was observed when compared to non-myotubes. White box indicates magnified region (right). Note the punctate nuclear staining of Scx transcription factor in 50 ng/ml FGF-2 which is absent in 0 ng/ml FGF-2. Scale bar 50 μm.

2.4.3 Effect of Liquid-Phase FGF-2 on Scx Expression in MDSCs

Tendon specification in MDSCs was examined in cells treated with FGF-2 under proliferation and myogenic conditions. Under proliferation conditions, FGF-2 dose-dependently increased expression of the tendon marker Scx with punctate nuclear staining of Scx occasionally observed at 50 ng/mL FGF-2 (Figure 2.5). Similar to C2C12 cells, Scx expression was upregulated in nascent myotubes in the absence of FGF-2 (Figure 2.6). In the presence of FGF-2, myotube formation was inhibited with MDSCs exhibiting lower levels of the myogenic marker myogenin (Figure 2.6). In addition, Scx expression was upregulated when compared to non-myocytes in untreated control (Figure 2.6) and FGF-2-treated cells did not show increased expression for the myofibroblast marker α-smooth muscle actin (α-SMA; Figure 2.7).

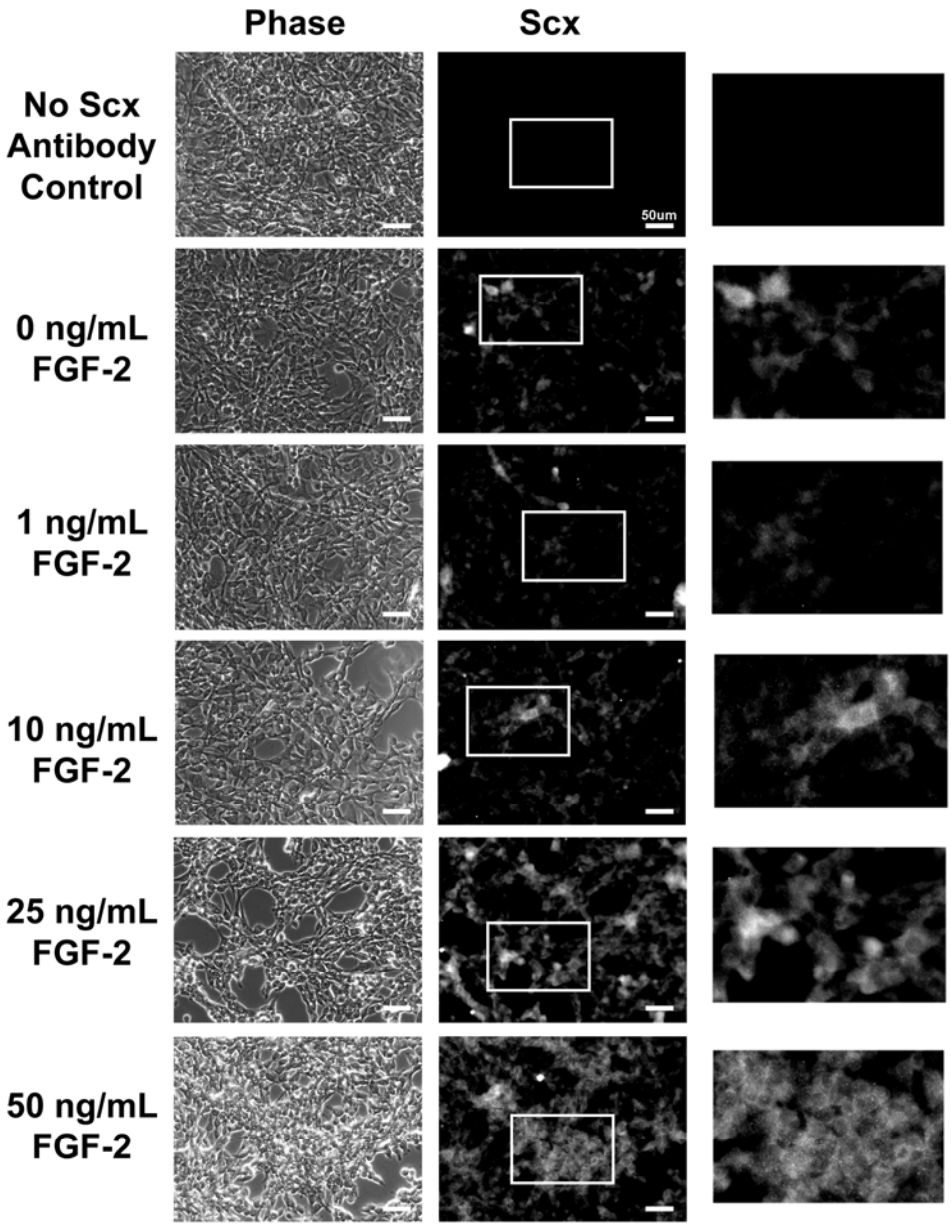

Figure 2.5. Dose-dependent effect of FGF-2 on expression of tendon marker Scx in mouse MDSCs after 72 h in proliferation media. Increasing amounts of FGF-2 resulted in upregulation of tendon marker Scx. White box indicates magnified region (right). Note the punctate nuclear staining of Scx transcription factor in 50 ng/ml FGF-2. Scale bar 50 μm.

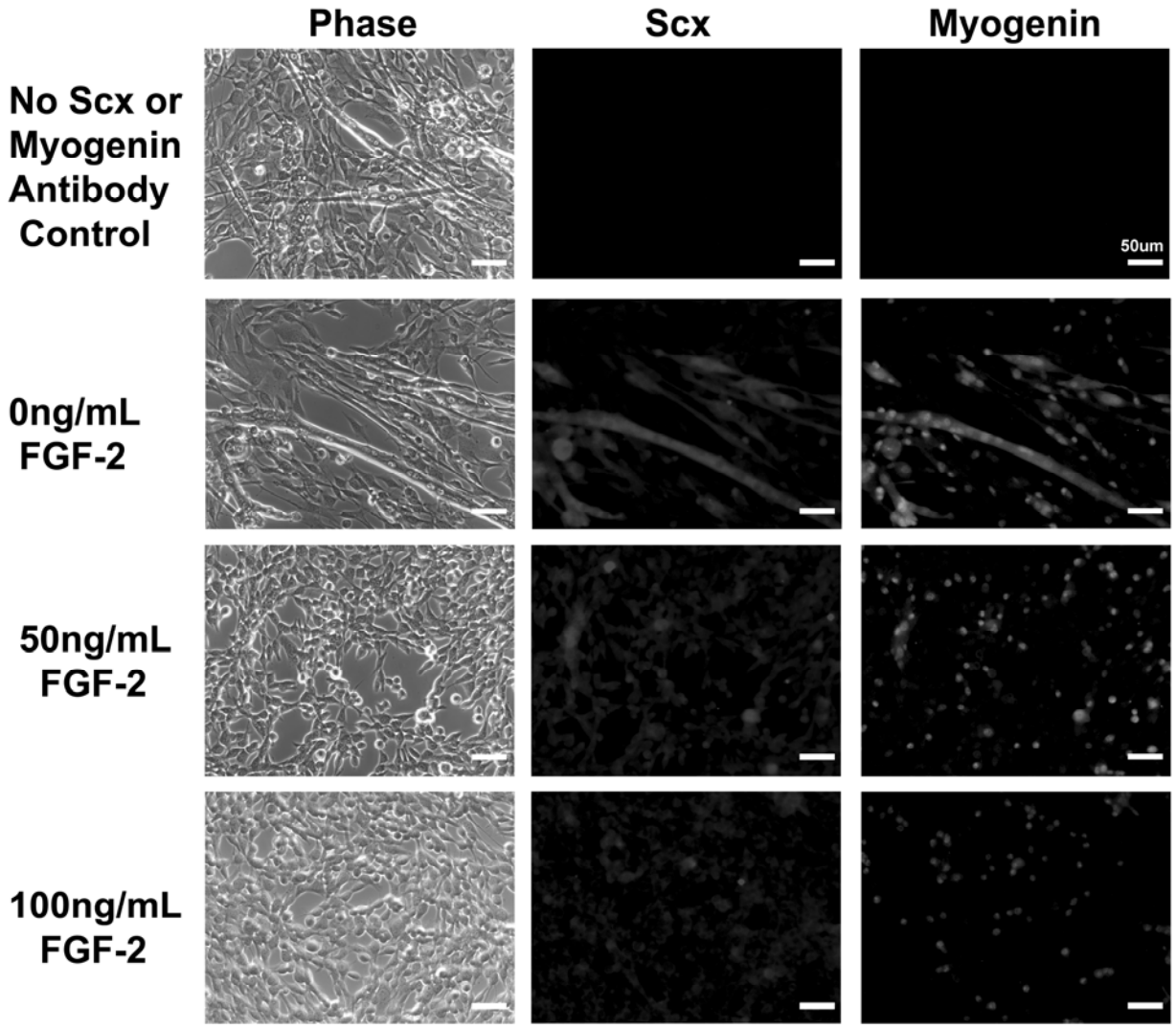

Figure 2.6. Dose-dependent effect of FGF-2 on expression of tendon marker Scx and muscle marker Myogenin in mouse MDSCs after 48h in myogenic media. Scx expression was upregulated in nascent myotubes in the absence of FGF-2. In presence of FGF-2, myotube formation was inhibited with decreased myogenin and increased Scx expression was observed when compared to non-myotubes. Scale bar 50 μm.

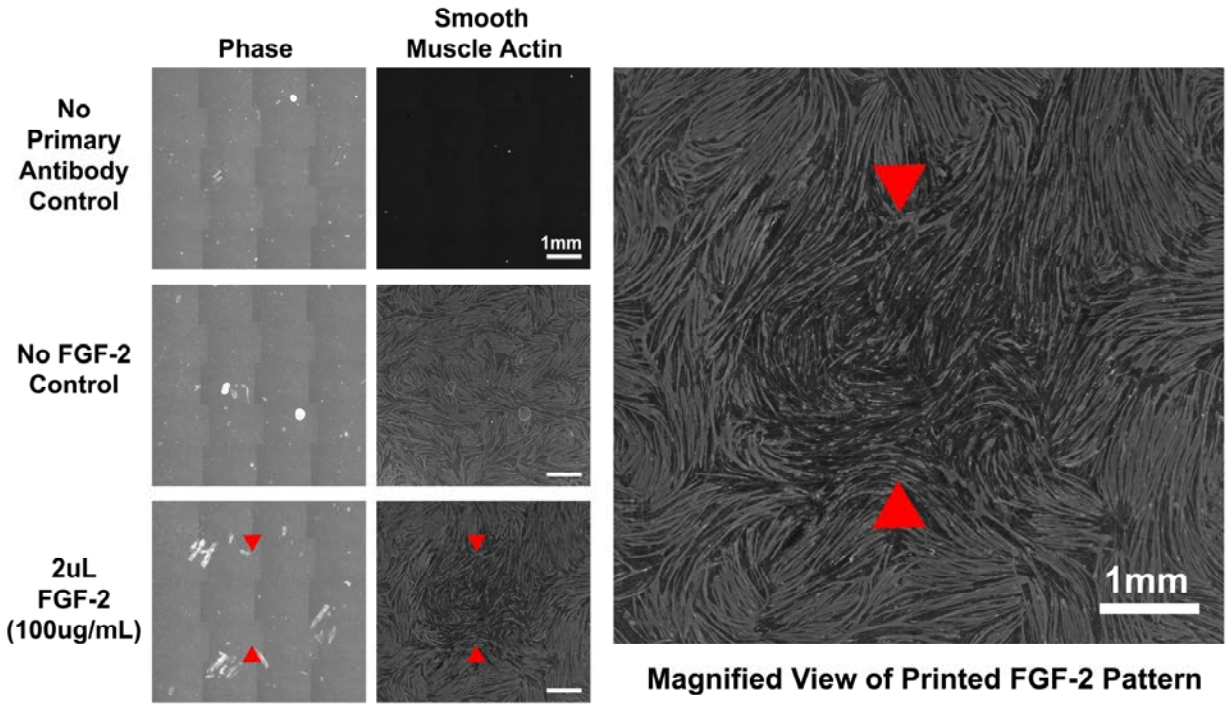

Figure 2.7. Effect of FGF-2 on expression of myofibroblast marker α-Smooth Muscle Actin (α-SMA) in mouse MDSCs after 72h in proliferation media. α-SMA expression was downregulated on printed patterns of FGF-2. Red arrowheads indicate the boundary of the hand-printed FGF-2 pattern. Parallel lines seen in phase-contrast images denote scratch marks used for identifying the location of hand-printed FGF-2 patterns. Scale bar 1000 µm.

2.4.4 Regulation of scx in C3H10T1/2 Cells

As previous studies indicated that members of the *Ets* family of transcription factors such as *pea3* and *erm* were involved in regulation of *scx* during chick tendon development, quantitative PCR analysis of these genes were performed to determine if a similar mechanism was operating in these stem cell populations [31]. 50 ng/mL FGF-2 upregulated *pea3* (43.1 ± 27.5 fold change, $p = 0.005$) and *erm* (16.5 ± 6.5 fold change, $p = 0.178$) at 36 h whereas *scx* levels remained constant. At 72 h, all three genes were upregulated: *pea3* (169.6 ± 45.8 fold change, $p = 0.008$), *erm* (72.5 ± 16.2 fold change, $p = 0.033$) and *scx* (22.8 ± 5.4 fold change, $p = 0.006$). As such, the prior induction of *pea3* and *erm* suggest that these two genes lie upstream of *scx* (Figure 2.8).

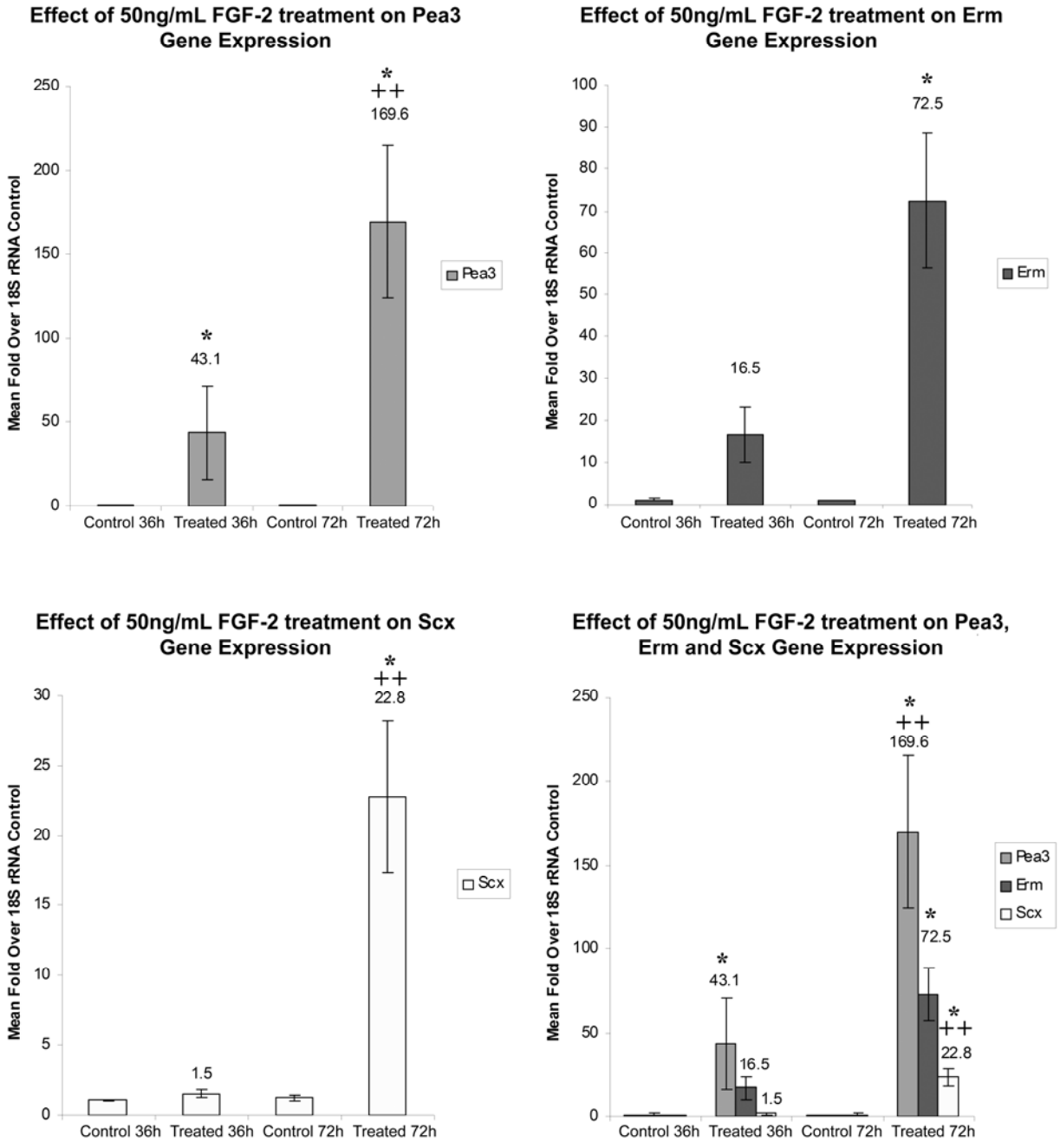

Figure 2.8. Effect of 50 ng/mL FGF-2 on expression of *pea3*, *erm* and *scx* transcription factors in mouse C3H10T1/2 cells at 36 h and 72 h in proliferation media. At 36 h, FGF-2 increased *pea3* and *erm* but not *scx* expression, relative to control. At 72 h, all transcription factors are upregulated, relative to control. Columns indicate fold changes over control ± SEM (n=5). *, Significantly different from control; $p \leq 0.05$. + +, Significantly different from 36 h; $p \leq 0.05$.

2.4.5 Effect of Solid-Phase FGF-2 on Scx Expression in C3H10T1/2 Cells

Having demonstrated that Scx expression was upregulated by liquid-phase FGFs, square patterns of FGF-2 (each measuring 1 by 1 mm) were inkjet printed onto fibrin-coated glass coverslips with 2, 6 and 12 overprints to determine if solid-phase GF patterns can spatially direct tendon specification in a dose-dependent manner. Our previous studies have shown that the surface concentration of GF that is deposited can be modulated by overprinting and that such GF patterns can persist for up to 144 hours under standard cell culture conditions [10, 13, 14, 16]. As shown in Figure 2.9A, the amount of FGF-2 deposited in 2, 6 and 12 overprints after washing and prior to cell seeding was estimated to be 40.8 pg/mm^2, 122.4 pg/mm^2 and 244.8 pg/mm^2 FGF-2 based on previous studies [8, 13, 14, 28]. Under proliferation conditions (High serum), C3H10T1/2 cells showed upregulation of Scx in response to solid-phase patterning of FGF-2 in a dose-dependent manner (Figure 2.9B). Although the lowest dose of solid-phase FGF-2 (40.8 pg/mm^2) was not sufficient to induce an increase in Scx expression relative to negative control/non-printed regions ($p = 0.872$), higher doses of solid-phase FGF-2 resulted in an increase in Scx expression relative to negative control/non-printed regions ($p = 0.009$ for 122.4 pg/mm^2 FGF-2 and $p = 0.001$ for 244.8 pg/mm^2 FGF-2; Figure 2.9) in C3H10T1/2 cells. Thus, solid-phase patterning of FGF-2 can spatially control tendon cell fate (Figure 2.9).

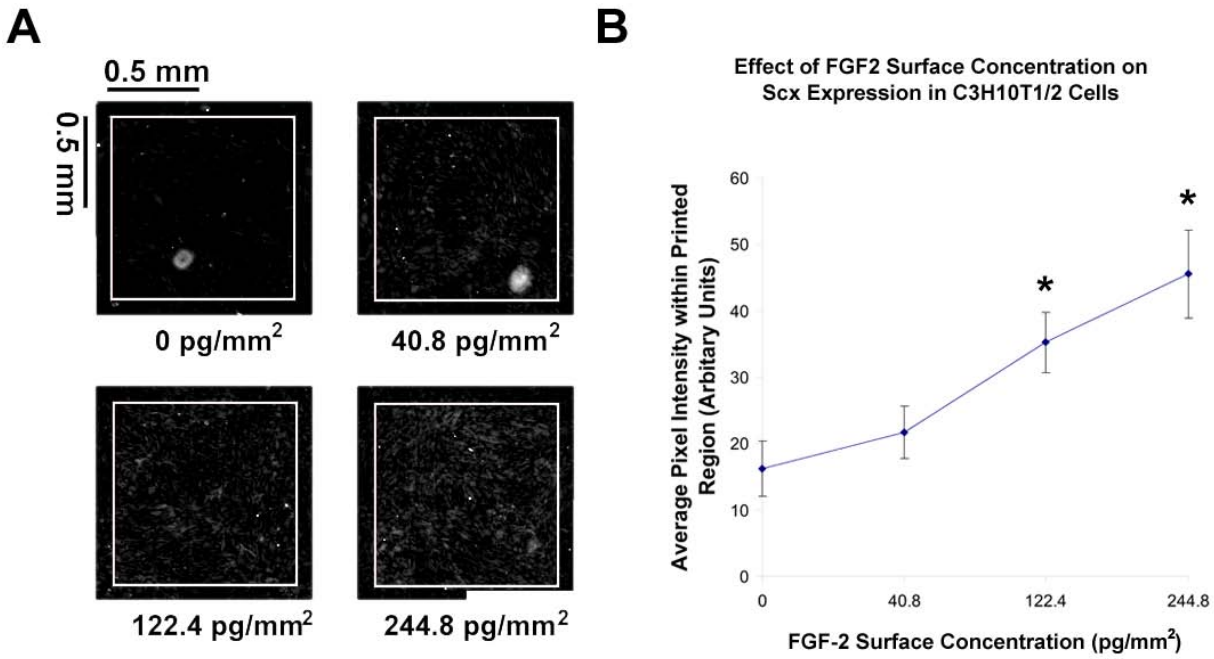

Figure 2.9. Effect of inkjet printed patterns of FGF-2 on expression of tendon marker Scx in mouse C3H10T1/2 cells after 72 h in proliferation media. **A.** Inkjet printed patterns of FGF-2 resulted in upregulation of the tendon marker Scx in a dose-dependent manner. **B.** Quantification of Scx Expression (n = 6). White squares indicates inkjet printed regions. The estimated surface concentration of FGF-2 present during cell seeding (after washing) is shown in terms of picograms/mm^2. Scale bar 500 µm. *, Significantly different from control or non-printed regions; $p \leq 0.05$.

2.4.6 Effect of Solid-Phase FGF-2 on MF20 and Scx Expression in C2C12 Cells

Similarly, square patterns of FGF-2 (each measuring 1 by 1 mm) were inkjet printed onto fibrin-coated glass coverslips with 5, 10 and 30 overprints (corresponding to an estimated amount of 102 pg/mm^2, 203 pg/mm^2 and 612 pg/mm^2 FGF-2) to determine if multiple stem cell fates could be spatially controlled in a dose-dependent manner within the same construct. Under both proliferation and myogenic conditions, inkjet printed patterns of FGF-2 resulted in a dose-dependent increase in Scx expression (Figure 2.10B, C).

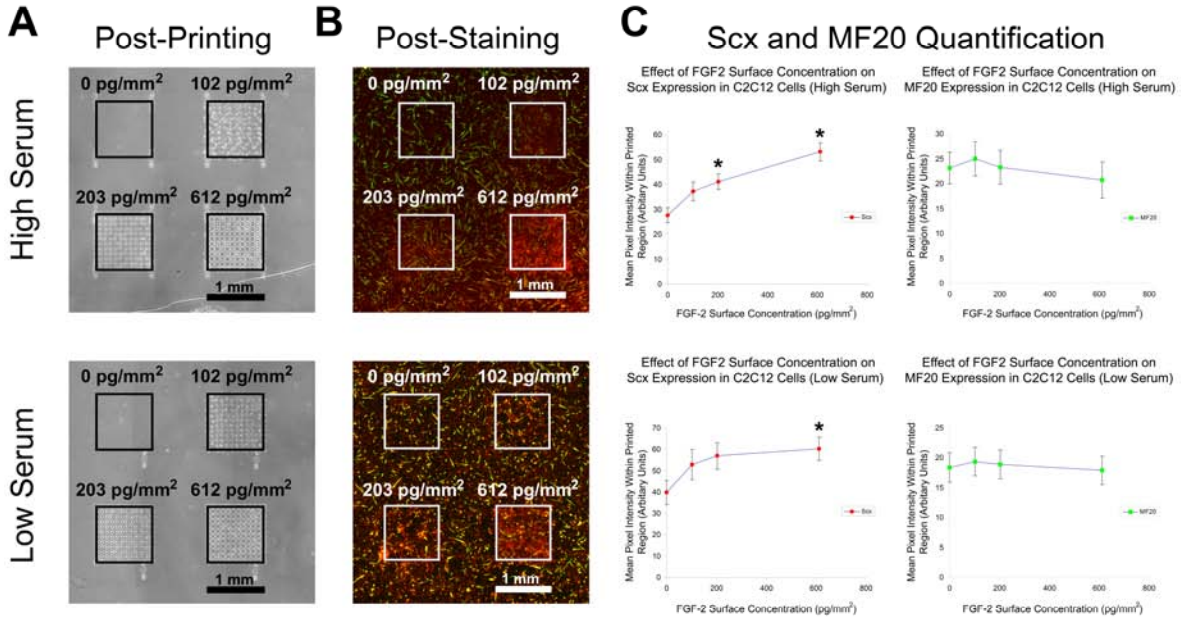

Figure 2.10. Effect of inkjet printed patterns of FGF-2 on expression of tendon marker Scx (red) and muscle marker MF20 (green) in mouse C2C12 cells after 72 h in proliferation and myogenic media. Increasing amounts of FGF-2 dose-dependently upregulated Scx and inhibited myotube formation slightly. Non-printed regions showed spontaneous myotube differentiation due to high confluency levels. **A.** Inkjet printed patterns of FGF-2 (Black squares). **B.** Scx and MF20 staining of printed patterns (White Squares). **C.** Quantification of Scx and MF20 stain. The estimated surface concentration of FGF-2 present during cell seeding (after washing) is shown in terms of picograms/mm^2. Scale bar 1 mm. Error bars indicate Standard Error Mean or SEM (n = 12 for proliferation media, n = 16 for myogenic media). $*$, Significantly different from control or non-printed regions; $p \leq 0.05$.

Under proliferation conditions, although the lowest dose of solid-phase FGF-2 (102 pg/mm^2 FGF-2) was not sufficient to induce an increase in Scx expression relative to negative control/non-printed regions ($p = 0.099$), higher doses of solid-phase FGF-2 resulted in an increase in Scx expression relative to negative control/non-printed regions ($p = 0.01$ for 203 pg/mm^2 FGF-2 and $p = 0.000$ for 612 pg/mm^2 FGF-2) in C2C12 cells (Figure 2.10C). Under myogenic conditions, although lower doses of solid-phase FGF-2 were not sufficient to induce an increase in Scx expression relative to negative control/non-printed regions ($p = 0.139$ for 102 pg/mm^2 FGF-2 and $p = 0.053$ for 203 pg/mm^2 FGF-2), the highest dose of solid-phase FGF-2 resulted in an increase in Scx expression relative to negative control/non-printed regions ($p =$

0.022 for 612 pg/mm^2 FGF-2) in C2C12 cells (Figure 2.10C). Within and outside the printed regions, cells fused to form multinucleated myotubes as a result of high cell density leading to spontaneous cell fusion under proliferation conditions or direct myogenic induction, as evidenced by the presence of muscle myosin or MF20 (Figure 2.10B). No difference in MF20 staining was observed between printed and non-printed regions ($p > 0.05$ for all cases). Taken together, these results demonstrate the simultaneous specification of myocyte and tenocyte fates within the same construct in a spatially defined manner in a dose-dependent fashion.

2.4.7 Effect of Solid-Phase BMP-2 and FGF-2 on ALP, MF20 and Scx Expression in C2C12 Cells

Having demonstrated that multiple stem cell fates could be spatially controlled within the same construct, inkjet bioprinting technology was applied to determine if osteoblast, tenocyte and myocyte fates, representative of a primitive bone-tendon-muscle unit, could be simultaneously specified within the same construct. After 72 h in proliferation media, inkjet printed patterns of BMP-2 and FGF-2 increased ALP and Scx expression, respectively (Figure 2.11). On inkjet printed patterns of BMP-2, ALP expression was increased relative to negative control/non-printed regions ($p = 0.000$) and inkjet printed patterns of FGF-2 ($p = 0.000$) but no increase in Scx expression was observed relative to negative control/non-printed regions ($p = 0.146$). On inkjet printed patterns of FGF-2, Scx expression was increased relative to negative control/non-printed regions ($p = 0.000$) and inkjet printed patterns of BMP-2 ($p = 0.003$) but no increase in ALP expression was observed relative to negative control/non-printed regions ($p = 0.887$). Within and outside the printed regions, myotube formation was promoted due to the high density of cells resulting in spontaneous fusion of cells (Figure 2.11B). No difference in MF20 staining was observed between printed and non-printed regions ($p > 0.05$ for all cases). Taken together,

these results demonstrate the simultaneous specification of osteoblast, tenocyte and myocyte fates within the same construct in a spatially defined manner.

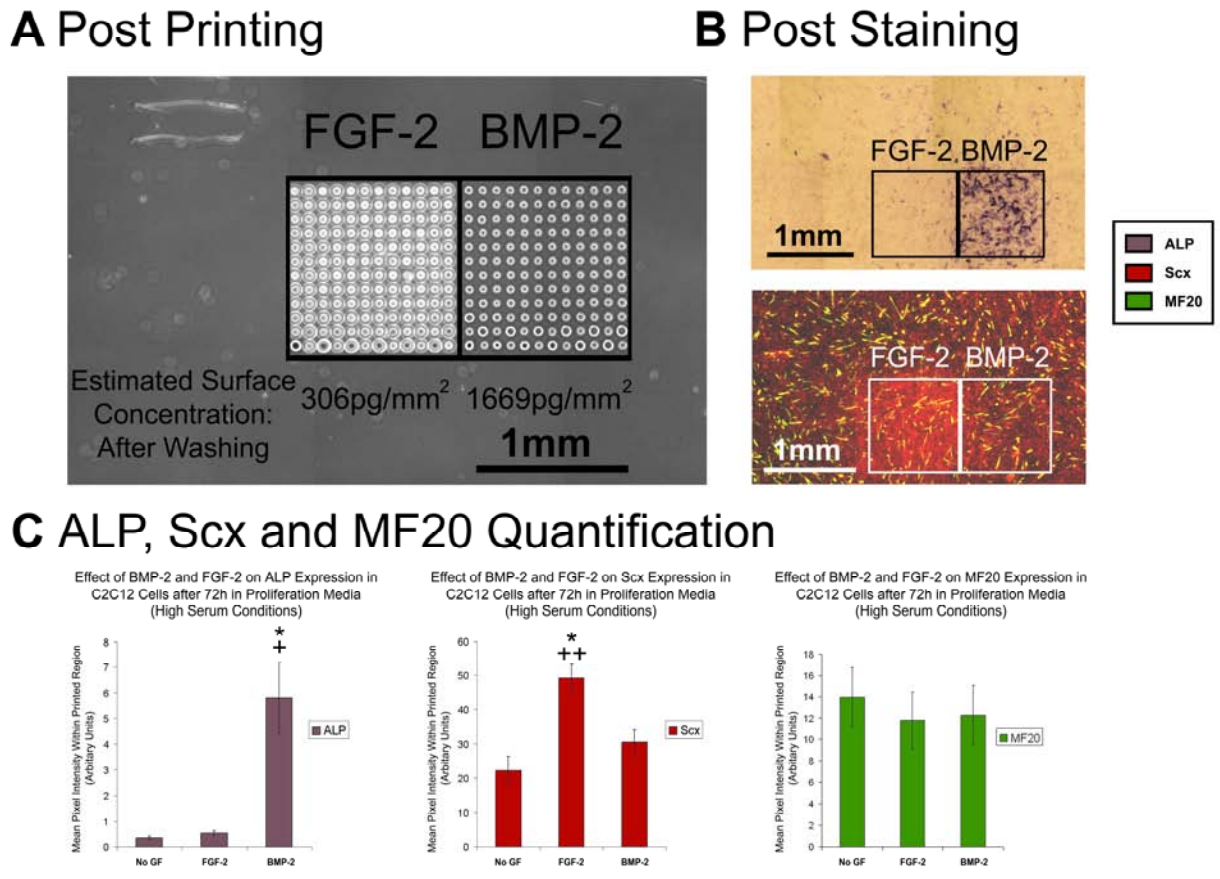

Figure 2.11. Effect of inkjet printed patterns of BMP-2 and FGF-2 on expression of osteoblast marker ALP (blue), tendon marker Scx (red) and muscle marker MF20 (green) in mouse C2C12 cells after 72 h in proliferation media. BMP-2 and FGF-2 patterns induced ALP and Scx expression, respectively, while non-printed regions spontaneously formed myotubes. **A.** Inkjet printed patterns of BMP-2 and FGF-2 (Black squares). **B**. ALP, Scx and MF20 staining of printed patterns (Black and white squares). **C.** Quantification of ALP, Scx and MF20 stain. Squares indicates inkjet printed region post-printing or post-immunofluorescence staining. The estimated surface concentration of GF present during cell seeding (after washing) is shown in terms of picograms/mm^2. Scale bar 1 mm. Error bars indicate Standard Error Mean or SEM (n = 8). $*$, Significantly different from control or non-printed regions; $p \leq 0.05$. +, Significantly different from inkjet printed patterns of FGF-2; $p \leq 0.05$. + +, Significantly different from inkjet printed patterns of BMP-2; $p \leq 0.05$.

2.4.8 Effect of Solid-Phase FGF-2 on α-Smooth Muscle Actin Expression in C2C12 Cells

To rule out the possibility that FGF-2 was directing C2C12 cells towards a myofibroblast fate as opposed to a tenocyte fate, FGF-2 was hand-printed onto a fibrin-coated coverslip and immunostained for the myofibroblast marker α-SMA (Figure 2.12). After 72 h in proliferation media, α-SMA, which is transiently expressed during muscle differentiation [32], was downregulated on hand-printed patterns of FGF-2, indicating that these cells were differentiating towards a tenocyte fate as opposed to a myofibroblast fate.

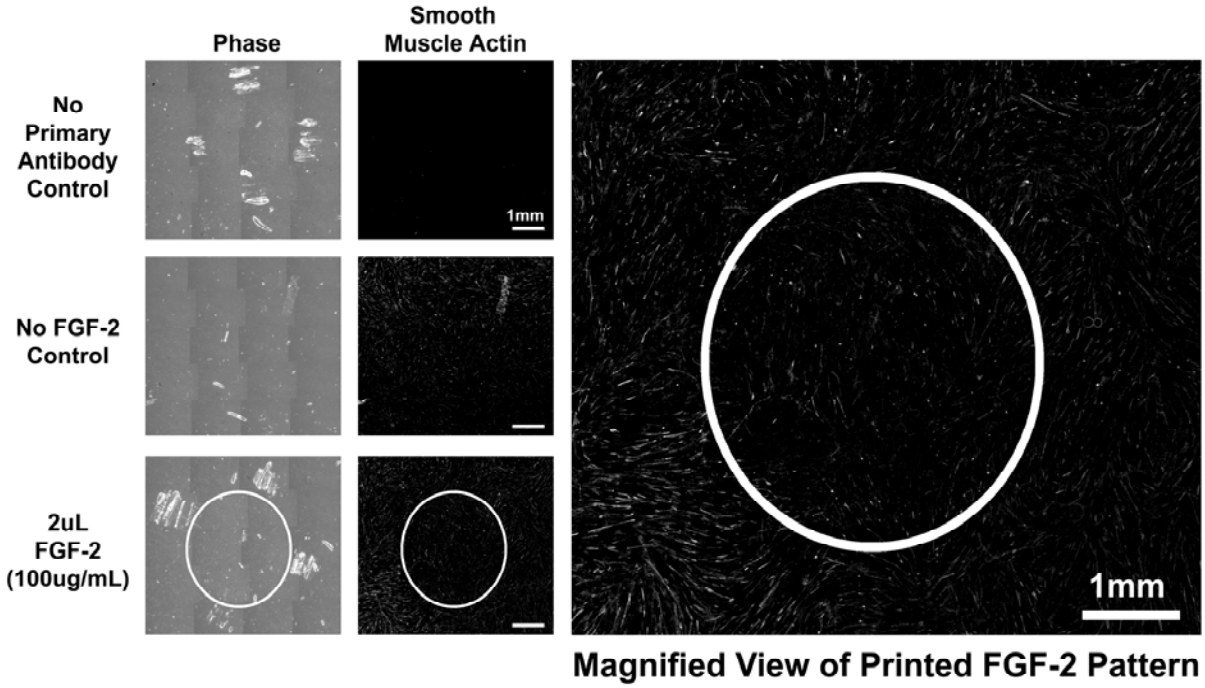

Figure 2.12. Effect of FGF-2 on expression of myofibroblast marker α-Smooth Muscle Actin (α-SMA) in mouse C2C12 cells after 72 h in proliferation media. α-SMA expression was downregulated on hand-printed patterns of FGF-2. Parallel lines observed in phase-contrast images denote scratch marks used for identifying the location of hand-printed FGF-2 patterns. White circle indicates the boundary of the hand-printed FGF-2 pattern. Scale bar 1000 μm.

2.4.9 Effect of Liquid-Phase IGF-2 on Sarcomeric Myosin Expression in C2C12 Cells

To identify potential muscle-promoting GFs, C2C12 cells were treated with numerous GFs and signaling molecules implicated in muscle differentiation, including amphoterin/HMGB1, decorin, follistatin, ghrelin, galectin-1, interleukin-4 (IL-4), insulin-like growth factor-1 (IGF-1),

insulin-like growth factor-2 (IGF-2), neuregulin-1 beta 2, sonic hedgehog and wnt3A and immunostained for upregulation of the muscle marker MF20. However, none of these putative muscle-promoting cues elicited an increased myogenic response relative to control under proliferation conditions in either liquid- or solid-phase experiments (Data not shown). Despite this, C2C12 cells grown under myogenic conditions showed a dose-dependence increase in MF20 staining and myotube size when treated with 0 ng/mL, 100 ng/mL, 500 ng/mL and 1000 ng/mL IGF-2 (Figure 2.13).

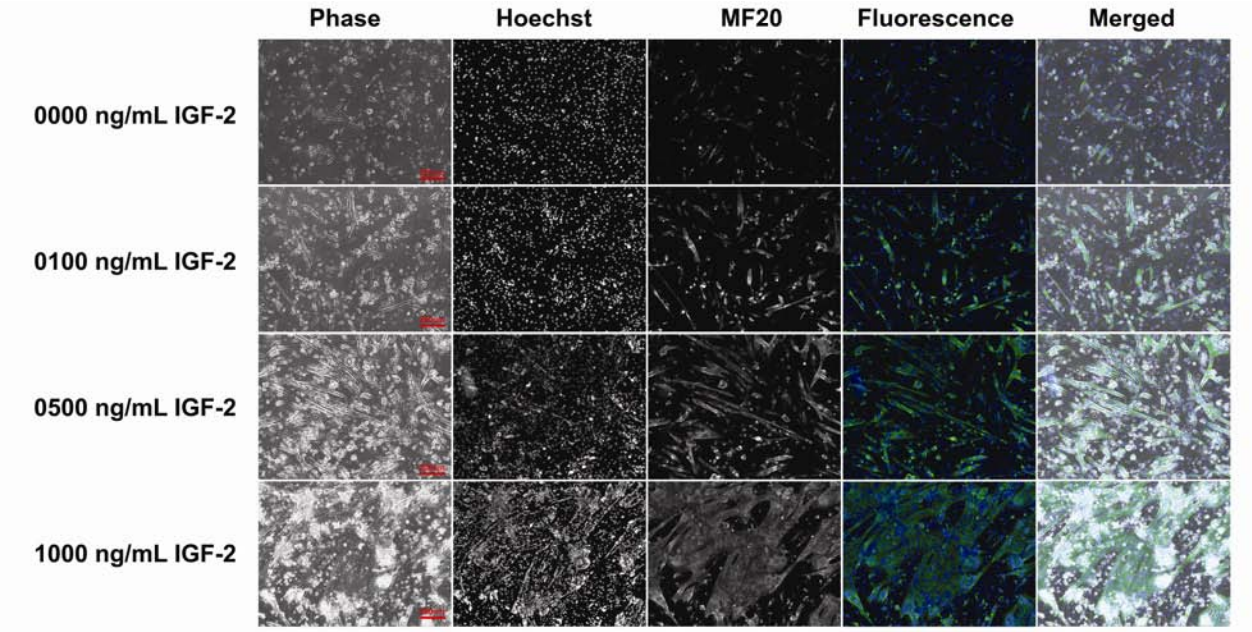

Figure 2.13. Dose-dependent effect of IGF-2 on expression of muscle marker MF20 in mouse C2C12 cells after 72h in myogenic media. Increasing amounts of IGF-2 resulted in upregulation of muscle marker MF20. Note the increase in myotube size in 100 ng/mL, 500 ng/ml and 1000 ng/ml IGF-2. Scale bar 200 µm.

2.5 DISCUSSION

2.5.1 Directing Osteoblast Differentiation

Our inkjet-based bioprinting approach was previously used to demonstrate spatial control of adjacent regions of osteoblast-myocyte differentiation [16]. In particular, when C2C12 cells and

MDSCs were cultured under myogenic conditions on BMP-2 patterns printed on fibrin, cells 'on-pattern' differentiated toward the osteoblast lineage, whereas cells 'off-pattern' differentiated toward the myogenic lineage. The purpose of the research reported here was to extend such prior work to the control of more complex osteoblast-tenocyte-myocyte units, representing primitive but physiologically relevant [33, 34] constructs.

2.5.2 Directing Myocyte Differentiation

As mentioned previously, osteoblast-myocyte patterning experiments performed by Phillippi *et al.* explicitly induced osteoblasts 'on-pattern' with solid-phase BMP-2 and implicitly induced myocytes 'off- pattern' using myogenic media [16]. In an effort to explicitly pattern myocytes for this current study, numerous GFs and signaling molecules implicated in muscle differentiation, including amphoterin/HMGB1, decorin, follistatin, ghrelin, galectin-1, IL-4, IGF-1, IGF-2, neuregulin-1 beta 2, sonic hedgehog and wnt3A were investigated [7, 35-45]. However, these candidate muscle-promoting cues did not elicit an increased myogenic response relative to control under proliferation conditions in either liquid- or solid-phase experiments (Data not shown). These negative results may be attributed to differences in experimental design such as the cell type and manner of myogenic induction used in these studies. Although IGF-2 was able to dose-dependently induce an increased myogenic response (Figure 2.13), it was necessary to perform these experiments under myogenic or low serum conditions, indicating that IGF-2 was involved in muscle growth but not sufficient for initiating myogenesis. Therefore, I continued to rely on implicit patterning of myocytes off-pattern using either myogenic conditions to induce myogenic differentiation through serum starvation or proliferation conditions to increase cell-cell contact via cell receptors such as N-Cadherins, leading to spontaneous cell fusion and myotube formation [46, 47].

2.5.3 Directing Tenocyte Differentiation

There have been no prior reports on the use of solid-phase GFs to direct stem cells toward tenocytes *in vitro*. Furthermore, even liquid-phase protocols for differentiating these cell types to a tendon fate have yet to be firmly established. Since previous studies demonstrated that members of the BMP and FGF family of signaling proteins may be involved in tendon formation [31, 48-50], FGF-2, FGF-4, BMP-2 and BMP-12/GDF-7 were screened in liquid-phase experiments using immunofluorescence staining for the tendon marker Scx [24] to determine if these GFs could direct multipotent stem cells towards a tendon cell fate. Only FGF-2 and FGF-4 in liquid-phase forms were shown to direct C3H10T1/2 cells, C2C12 cells and MDSCs towards a tendon lineage (Figure 2.1-Figure 2.6). To rule out the possibility that FGF-2-treated cells were differentiating towards myofibroblasts as opposed to tenocytes, FGF-2-treated cells were stained for the myofibroblast marker α-SMA. In these studies, FGF-2-treated cells did not induce upregulation of α-SMA in either C2C12 cells or MDSCs, and in fact, reduced expression of α-SMA slightly (Figure 2.7 and Figure 2.12). Quantitative PCR analysis subsequently determined that the mechanism by which these stem cells differentiate towards a tendon fate may involve members of the *Ets* family of transcription factors such as *pea3* and *erm*, which may act upstream of the tendon transcription factor *scx* (Figure 2.8), a finding that parallels tendon development in chick [31].

Unexpectedly, high levels of Scx expression were observed in nascent myotubes (Figure 2.4 and Figure 2.6). This was later shown to be contributed, in part, by the thickness of myotubes, as evidenced by the bright halo around cells in phase-contrast images (Figure 2.4 and Figure 2.6) and confocal sectioning studies (data not shown). In addition, there was no change in *scx* gene

expression during myogenesis although increased levels of Scx protein in myotubes could be accounted for by post-transcriptional processes. Alternatively, myotubes may show increased Scx levels since Scx is a transcription factor that lies upstream of collagen, a major non-contractile component of muscle. However, this is unlikely since nascent myotubes exhibit little to no nuclear staining of Scx when compared to FGF-2-treated cells (Figure 2.4 and Figure 2.6).

2.5.4 Simultaneous Control of Multiple Musculoskeletal Cell Fates on Fibrin-Coated Glass Coverslips with Solid-Phase GF Patterns using Inkjet-based Bioprinting

FGF-2 was used for all subsequent solid-phase tenocyte patterning experiments using high resolution, low-dose inkjet bioprinting because FGF-4 elicted a lower response in hand-printed and qPCR experiments (Data not shown). In these studies, C3H10T1/2 cells were shown to upregulate the tendon marker Scx in a dose-dependent fashion in response to inkjet printed patterns of FGF-2 (Figure 2.9). Similarly, C2C12 cells also dose-dependently upregulated the tendon marker Scx in response to inkjet printed patterns of FGF-2, with spontaneous fusion of myotubes occurring predominantly outside the printed region (Figure 2.10). Having demonstrated that solid-phase patterning of tenocytes and myocytes can be engineered under proliferation and myogenic conditions within the same construct, adjacent printed patterns of FGF-2 and BMP-2 were tested and shown to specify osteoblasts, tenocytes and myocytes within the same construct, representing a primitive muscle-tendon-bone unit (Figure 2.11). Although FGF-2 displays a clear dose-dependence increase on tendon cell differentiation, some variations in cell responses to printed GF patterns were observed. For example, some C2C12 cells that were ‘off-pattern’ but in close proximity to high doses of FGF-2 or BMP-2 patterns exhibited weak Scx (Figure 2.10B, high serum panel) or ALP staining (Figure 2.11B), respectively. These variations may stem from desorption of GF from the printed region followed by its readsorption

outside the printed region prior to cell seeding or by paracrine signaling from cells ‘on-pattern’ to cells ‘off-pattern’ to differentiate. In addition, the differentiation response of cells within a printed GF pattern was not homogenous throughout as shown by non-uniform Scx staining along with sporadic MF20 staining on printed FGF-2 patterns (Figure 2.9, Figure 2.10 and Figure 2.11) and uneven ALP staining on printed BMP-2 patterns (Figure 2.11). This may be a function of several factors, including: non-uniform GF distribution within the printed region following inkjet printing and GF drying [28]; GF desorption followed by readsorption prior to cell seeding [13, 14, 51, 52]; uneven cell density during cell seeding; cell heterogeneity [53]; or, a combination of all these factors. Furthermore, when multiple GFs are utilized, the dosage of individual GFs was found to be critical for simultaneously specifying multiple cell fates. When similar concentrations of FGF-2 and BMP-2 were inkjet bioprinted in close proximity, no positive ALP staining was observed on printed BMP-2 patterns (Data not shown). This may be attributed to desorption of FGF-2 from the fibrin surface followed by binding to the surface of cells seeded on printed BMP-2 patterns, resulting in the inhibition of BMP-2-induced osteoblast differentiation, which is an effect that is well characterized [14, 54]. This problem was eventually resolved by empirically optimizing the amount of BMP-2 and FGF-2 deposited by inkjet bioprinting, resulting in excess surface concentration of BMP-2 to overcome this inhibitory effect (Figure 2.11).

This work has demonstrated that inkjet-based bioprinting technology enables the investigation of spatial control of solid-phase GF-directed differentiation of stem cells toward single or multiple fates in physiologically-relevant engineered microenvironments *in vitro*. Prior work in this lab also provides support for the application of this technology *in vivo* [10]. Together, these *in vitro* and *in vivo* studies suggest that this technology may have practical implications for both basic

scientific research and therapy development and deployment targeting the musculoskeletal system.

2.6 CONCLUSIONS

This chapter identified both liquid- and solid-phase FGF-2 as being capable of upregulating the tendon marker Scx in C3H10T1/2 cells, C2C12 cells and MDSCs. Quantitative PCR analysis suggests that members of the *Ets* family of transcription factors such as *pea3* and *erm* may lie upstream of *scx*. This report also demonstrates how inkjet bioprinting technology can create persistent GF patterns that direct a single stem cell population towards multiple fates, including tenocytes, myocytes or osteoblasts, within the same construct in a spatially defined manner. This capability not only offers an approach to study multi-lineage differentiation *in vitro*, but may also be translatable to new therapies to treat disease and trauma of the musculoskeletal system.

2.7 ACKNOWLEDGEMENTS

I would like to thank James Fitzpatrick for assistance with fluorescence microscopy and Larry Schultz for assistance with GF printing. This work was supported by NIH grants RO1EB004343 and RO1EB007369 as well as funding from the Pennsylvania Infrastructure Technology Alliance (PITA).

2.8 REFERENCES

1. Scadden, D.T., *The stem-cell niche as an entity of action.* Nature, 2006. 441(7097): p. 1075-9.
2. Nelson, C.M. and M.J. Bissell, *Of extracellular matrix, scaffolds, and signaling: tissue architecture regulates development, homeostasis, and cancer.* Annu Rev Cell Dev Biol, 2006. 22: p. 287-309.
3. Taipale, J. and J. Keski-Oja, *Growth factors in the extracellular matrix.* Faseb J, 1997. 11(1): p. 51-9.
4. Canalis, E., *Growth factor control of bone mass.* J Cell Biochem, 2009. 108(4): p. 769-77.

5. Chen, D., M. Zhao, and G.R. Mundy, *Bone morphogenetic proteins.* Growth Factors, 2004. 22(4): p. 233-41.
6. Choi, Y.J., et al., *The identification of a heparin binding domain peptide from bone morphogenetic protein-4 and its role on osteogenesis.* Biomaterials, 2010. 31(28): p. 7226-38.
7. Unsicker, K. and K. Krieglstein, *Cell Signaling and Growth Factors in Development*, ed. K. Unsicker and K. Krieglstein. 2006, Germany: WILEY-VCH. 991.
8. Campbell, P.G., et al., *Engineered spatial patterns of FGF-2 immobilized on fibrin direct cell organization.* Biomaterials, 2005. 26(33): p. 6762-70.
9. Carinci, P., et al., *Extracellular matrix and growth factors in the pathogenesis of some craniofacial malformations.* Eur J Histochem, 2007. 51 Suppl 1: p. 105-15.
10. Cooper, G.M., et al., *Inkjet-based biopatterning of bone morphogenetic protein-2 to spatially control calvarial bone formation.* Tissue Eng Part A, 2010. 16(5): p. 1749-59.
11. Datta, N., et al., *Effect of bone extracellular matrix synthesized in vitro on the osteoblastic differentiation of marrow stromal cells.* Biomaterials, 2005. 26(9): p. 971-7.
12. DeCarlo, A.A. and J.M. Whitelock, *The role of heparan sulfate and perlecan in bone-regenerative procedures.* J Dent Res, 2006. 85(2): p. 122-32.
13. Miller, E.D., et al., *Dose-dependent cell growth in response to concentration modulated patterns of FGF-2 printed on fibrin.* Biomaterials, 2006. 27(10): p. 2213-21.
14. Miller, E.D., et al., *Inkjet printing of growth factor concentration gradients and combinatorial arrays immobilized on biologically-relevant substrates.* Comb Chem High Throughput Screen, 2009. 12(6): p. 604-18.
15. Nelson, C.M. and J. Tien, *Microstructured extracellular matrices in tissue engineering and development.* Curr Opin Biotechnol, 2006. 17(5): p. 518-23.
16. Phillippi, J.A., et al., *Microenvironments engineered by inkjet bioprinting spatially direct adult stem cells toward muscle- and bone-like subpopulations.* Stem Cells, 2008. 26(1): p. 127-34.
17. Ruhrberg, C., et al., *Spatially restricted patterning cues provided by heparin-binding VEGF-A control blood vessel branching morphogenesis.* Genes Dev, 2002. 16(20): p. 2684-98.
18. Schultz, G.S. and A. Wysocki, *Interactions between extracellular matrix and growth factors in wound healing.* Wound Repair Regen, 2009. 17(2): p. 153-62.
19. Wiradjaja, F., T. DiTommaso, and I. Smyth, *Basement membranes in development and disease.* Birth Defects Res C Embryo Today, 2010. 90(1): p. 8-31.
20. de Juan-Pardo, E.M., M.B. Hoang, and I.M. Conboy, *Geometric control of myogenic cell fate.* Int J Nanomedicine, 2006. 1(2): p. 203-12.
21. Flaim, C.J., et al., *Combinatorial signaling microenvironments for studying stem cell fate.* Stem Cells Dev, 2008. 17(1): p. 29-39.
22. Ilkhanizadeh, S., A.I. Teixeira, and O. Hermanson, *Inkjet printing of macromolecules on hydrogels to steer neural stem cell differentiation.* Biomaterials, 2007. 28(27): p. 3936-43.
23. Lee, Y.B., et al., *Bio-printing of collagen and VEGF-releasing fibrin gel scaffolds for neural stem cell culture.* Exp Neurol, 2010. 223(2): p. 645-52.
24. Cserjesi, P., et al., *Scleraxis: a basic helix-loop-helix protein that prefigures skeletal formation during mouse embryogenesis.* Development, 1995. 121(4): p. 1099-110.

25. Scott, A., et al., *Scleraxis expression is coordinately regulated in a murine model of patellar tendon injury.* J Orthop Res, 2011. 29(2): p. 289-296.
26. Gharaibeh, B., et al., *Isolation of a slowly adhering cell fraction containing stem cells from murine skeletal muscle by the preplate technique.* Nat Protoc, 2008. 3(9): p. 1501-9.
27. Qu-Petersen, Z., et al., *Identification of a novel population of muscle stem cells in mice: potential for muscle regeneration.* J Cell Biol, 2002. 157(5): p. 851-64.
28. Miller, E., *Inkjet Printing of Solid-Phase Growth Factor Patterns to Direct Cell Fate*, in *Biomedical Engineering*. 2007, Carnegie Mellon University: Pittsburgh. p. 349.
29. Jadlowiec, J., et al., *Pregnancy-associated plasma protein-a is involved in matrix mineralization of human adult mesenchymal stem cells and angiogenesis in the chick chorioallontoic membrane.* Endocrinology, 2005. 146(9): p. 3765-72.
30. Jadlowiec, J., et al., *Phosphophoryn regulates the gene expression and differentiation of NIH3T3, MC3T3-E1, and human mesenchymal stem cells via the integrin/MAPK signaling pathway.* J Biol Chem, 2004. 279(51): p. 53323-30.
31. Brent, A.E. and C.J. Tabin, *FGF acts directly on the somitic tendon progenitors through the Ets transcription factors Pea3 and Erm to regulate scleraxis expression.* Development, 2004. 131(16): p. 3885-96.
32. Springer, M.L., C.R. Ozawa, and H.M. Blau, *Transient production of alpha-smooth muscle actin by skeletal myoblasts during differentiation in culture and following intramuscular implantation.* Cell Motil Cytoskeleton, 2002. 51(4): p. 177-86.
33. Clayton, R.A. and C.M. Court-Brown, *The epidemiology of musculoskeletal tendinous and ligamentous injuries.* Injury, 2008. 39(12): p. 1338-44.
34. Yang, P.J. and J.S. Temenoff, *Engineering Orthopedic Tissue Interfaces.* Tissue Eng Part B Rev, 2009. 15(2): p. 127-41.
35. Chan, J., et al., *Galectin-1 induces skeletal muscle differentiation in human fetal mesenchymal stem cells and increases muscle regeneration.* Stem Cells, 2006. 24(8): p. 1879-91.
36. Elia, D., et al., *Sonic hedgehog promotes proliferation and differentiation of adult muscle cells: Involvement of MAPK/ERK and PI3K/Akt pathways.* Biochim Biophys Acta, 2007. 1773(9): p. 1438-46.
37. Filigheddu, N., et al., *Ghrelin and des-acyl ghrelin promote differentiation and fusion of C2C12 skeletal muscle cells.* Mol Biol Cell, 2007. 18(3): p. 986-94.
38. Georgiadis, V., et al., *Lack of galectin-1 results in defects in myoblast fusion and muscle regeneration.* Dev Dyn, 2007. 236(4): p. 1014-24.
39. Gros, J., O. Serralbo, and C. Marcelle, *WNT11 acts as a directional cue to organize the elongation of early muscle fibres.* Nature, 2009. 457(7229): p. 589-93.
40. Horsley, V., et al., *IL-4 acts as a myoblast recruitment factor during mammalian muscle growth.* Cell, 2003. 113(4): p. 483-94.
41. Kim, D., et al., *Neuregulin stimulates myogenic differentiation in an autocrine manner.* J Biol Chem, 1999. 274(22): p. 15395-400.
42. Kishioka, Y., et al., *Decorin enhances the proliferation and differentiation of myogenic cells through suppressing myostatin activity.* J Cell Physiol, 2008. 215(3): p. 856-67.
43. Kocamis, H., et al., *Follistatin alters myostatin gene expression in C2C12 muscle cells.* Acta Vet Hung, 2004. 52(2): p. 135-41.

44. Sorci, G., et al., *Amphoterin stimulates myogenesis and counteracts the antimyogenic factors basic fibroblast growth factor and S100B via RAGE binding.* Mol Cell Biol, 2004. 24(11): p. 4880-94.
45. Straface, G., et al., *Sonic hedgehog regulates angiogenesis and myogenesis during post-natal skeletal muscle regeneration.* J Cell Mol Med, 2009. 13(8B): p. 2424-35.
46. Blau, H.M., et al., *Plasticity of the differentiated state.* Science, 1985. 230(4727): p. 758-66.
47. Goichberg, P. and B. Geiger, *Direct involvement of N-cadherin-mediated signaling in muscle differentiation.* Mol Biol Cell, 1998. 9(11): p. 3119-31.
48. Edom-Vovard, F., et al., *Fgf4 positively regulates scleraxis and tenascin expression in chick limb tendons.* Dev Biol, 2002. 247(2): p. 351-66.
49. Hoffmann, A., et al., *Neotendon formation induced by manipulation of the Smad8 signalling pathway in mesenchymal stem cells.* J Clin Invest, 2006. 116(4): p. 940-52.
50. Wolfman, N.M., et al., *Ectopic induction of tendon and ligament in rats by growth and differentiation factors 5, 6, and 7, members of the TGF-beta gene family.* J Clin Invest, 1997. 100(2): p. 321-30.
51. Morin, R., D. Kaplan, and B. Perez-Ramirez, *Bone morphogenetic protein-2 binds as multilayers to a collagen delivery matrix: an equilibrium thermodynamic analysis.* Biomacromolecules, 2006. 7(1): p. 131-8.
52. Sahni, A., T. Odrljin, and C.W. Francis, *Binding of basic fibroblast growth factor to fibrinogen and fibrin.* J Biol Chem, 1998. 273(13): p. 7554-9.
53. Collins, C.A., et al., *Stem cell function, self-renewal, and behavioral heterogeneity of cells from the adult muscle satellite cell niche.* Cell, 2005. 122(2): p. 289-301.
54. Quarto, N., D.C. Wan, and M.T. Longaker, *Molecular mechanisms of FGF-2 inhibitory activity in the osteogenic context of mouse adipose-derived stem cells (mASCs).* Bone, 2008. 42(6): p. 1040-52.

CHAPTER 3: *IN VITRO* PATTERNING OF A PRIMITIVE MUSCLE-TENDON-BONE UNIT: SIMULTANEOUS CONTROL OF MUSCLOSKELETAL CELL ALIGNMENT AND CELL DIFFERENTIATION WITH INKJET-BASED PRINTING OF BMP-2 AND FGF-2 PATTERNS ONTO SPINNERET-BASED TUNABLE ENGINEERED PARAMETERS (STEP) FIBERS

Based on published work:

Bioprinting of Growth Factors onto Aligned Sub-micron Fibrous Scaffolds for Simultaneous Control of Cell Differentiation and Alignment

Dai Fei Elmer Ker, Amrinder S. Nain, Lee E. Weiss, Ji Wang, Joseph Suhan, Cristina Amon and Phil G. Campbell

Biomaterials. 2011 Nov; **32** (32) 8097-8107.

3.1 ABSTRACT

The capability to spatially control stem cell orientation and differentiation simultaneously using a combination of geometric cues that mimic structural aspects of native extracellular matrix (ECM) and biochemical cues such as ECM-bound growth factors (GFs) is important for understanding the organization and function of musculoskeletal tissues. Herein, oriented sub-micron fibers, which are morphologically similar to musculoskeletal ECM, were spatially patterned with GFs using an inkjet-based bioprinter to create geometric and biochemical cues that direct musculoskeletal cell alignment and differentiation *in vitro* in registration with fiber orientation and printed patterns, respectively. Sub-micron polystyrene and polyurethane fibers were fabricated using a Spinneret-based Tunable Engineered Parameters (STEP) technique and coated with serum or fibrin. The fibers were subsequently patterned with tendon-promoting fibroblast growth factor-2 (FGF-2) or bone-promoting bone morphogenetic protein-2 (BMP-2) prior to seeding with mouse C2C12 myoblasts or C3H10T1/2 mesenchymal fibroblasts. Unprinted regions of STEP fibers showed myocyte differentiation while printed FGF-2 and BMP-2 patterns promoted tenocyte and osteoblast fates, respectively, and inhibited myocyte differentiation. Additionally, cells aligned along the fiber length. Functionalizing oriented sub-micron fibers with printed GFs provides instructive cues to spatially control cell fate and alignment to mimic native tissue organization and may have applications in regenerative medicine.

3.2 INTRODUCTION

Musculoskeletal tissues comprise multiple cell types such as osteoblasts, tenocytes and myocytes arrayed within a spatially-graded structural and biochemical

microenvironment. The native organization of these tissues is regulated, in part, by microenvironmental instructive signals such as growth factor (GF) biochemical cues and ECM architectural geometric cues to modulate stem cell behaviors such as differentiation and cell alignment during repair and regeneration [1-5].

Within the pericellular microenvironment, signaling molecules such as GFs, can exist in both ‘liquid-phase’ (freely diffusing in solution) and ‘solid-phase’ (immobilized and bound to the ECM and cell surfaces) forms [4]. When bound to the ECM, GFs are immobilized at picograms to nanogram quantities and impart temporal and spatial cues that regulate cell behaviors such as cell adhesion, migration, proliferation, differentiation and apoptosis [4-12].

In muscle, tendon and bone tissues, differentiated cell types such as myocytes, tenocytes and osteoblasts maintain tissue function by contractile force generation, collagen secretion and collagen mineralization, respectively. In addition, cell orientation plays an integral role since myocyte alignment is necessary for efficient force generation along a specific direction during muscle contraction [13-15], while tenocyte and osteoblast alignment are required for building highly oriented unmineralized and mineralized collagen matrices that can withstand mechanical loading during skeletal movement [1, 16-20]. Furthermore, it has recently been shown that aligned fibrous scaffolds promoted increased calcium content and mineralization compared to unaligned fibrous scaffolds in a manner independent of increased cell proliferation or increased mRNA expression of osteogenic markers [18].

Although there have been numerous investigations using exogenous biochemical cues to control musculoskeletal stem cell differentiation [21-26], and engineered geometric cues to control cell alignment [14, 27-29], such work has yet to address simultaneous control of both cell alignment and differentiation at high spatial resolution.

Our research group has previously developed an inkjet-based bioprinter [6] that spatially patterns low doses (picograms to nanograms) of GFs and other signaling molecules onto and into native ECM-based scaffolds, including fibrin and acellular human skin allografts. The printed GFs subsequently bind to the ECM via native binding affinities to create physiologically-relevant solid-phase GF patterns that can control aspects of stem cell behavior such as differentiation, migration and proliferation *in vitro* [6, 8-12] and *in vivo* [7] in spatial registration with printed patterns. One advantage of using such an approach is that it can provide persistent biochemical cues for directing a single stem cell population towards multiple cell fates such as muscle, tendon and bone cells simultaneously within a single construct [8, 12]. In addition, our research group has also developed a novel pseudo-dry spinning technique that creates highly oriented sub-micron fibers as a means to control cell alignment [30, 31]. In the present study, bioprinted GFs were patterned onto highly oriented sub-micron polystyrene or polyurethane fibers fabricated with our Spinneret-based Tunable Engineered Parameters (STEP) technique [30, 31] to study the interactions of biochemical and geometrical cues on stem cell differentiation and alignment. This study was performed in the context of using the aligned fiber scaffolds patterned with GFs to spatially control stem cell differentiation toward myocyte, tenocyte and osteoblast fates simultaneously *in vitro* while also controlling cell alignment to create a primitive muscle-tendon-bone unit.

3.3 MATERIALS AND METHODS

3.3.1 Fabrication of Polystyrene STEP Fibers

To facilitate comparison of cell alignment between STEP fibers and standard tissue culture vessels, polystyrene STEP fibers were used. In addition, polystyrene is non-resorbable and removes the resorption variable from this study. Sub-micron, oriented polystyrene STEP fibers were fabricated using the STEP pseudo-dry spinning process as previously described [30, 31] (Figure 3.1). Briefly, a glass micropipette was mounted on a manual XYZ stage (562 Ultra-align series, Newport Inc., USA) and oriented perpendicularly to a rotating cover slip substrate mounted on a DC motor. The DC motor was mounted on a motorized XYZ nano-positioner (Newport VP series, Irvine, CA). Polystyrene ($2x10^6$ g/mol, Scientific Polymer Products, USA, dissolved in Xylene 10% by weight) was drawn out and extruded through the pipette and continuously wound around the rotating substrate, becoming fibers as the solvent evaporated. By controlling the speeds of the nanopositioner and rotating motor, scaffolds with defined sub-micron fiber diameters and fiber spacing were fabricated. In addition, subsequent layers can be deposited on top of existing fiber layers and at other orientations to produce, for example, criss-cross fiber patterns that were oriented perpendicular to one another. In addition, aligned fibers wound around a hollowed-out substrate support base can be fabricated to form suspended fibrous structures.

3.3.2 Fibrin- or Serum-Coating of Polystyrene STEP Fibers

Polystyrene STEP fibers were sterilized with 70% ethanol for 5 min, rinsed with Phosphate Buffered Saline (PBS), and subsequently coated with serum by incubation in

100% serum overnight at room temperature (RT). Excess unbound serum proteins were removed by aspiration, rinsed with PBS and air-dried in a laminar flow hood.

For fibrin coating, polystyrene STEP fibers were first coated with fibrinogen by incubation in 0.1 mg/mL fibrinogen (Aventis Behring, King of Prussia, PA or American Diagnostica Inc., Stamford, CT) contained in 10 mM sodium phosphate, pH 7.4 overnight at RT. Excess unbound fibrinogen was removed by aspiration, rinsed with PBS and fibers were blocked with 0.3M glycine (Bio-Rad Laboratories, Hercules, CA), pH 7.4 for 2 h at RT. Immobilized fibrinogen was converted into fibrin by incubating fibers in 4U/mL thrombin (Enzyme Research Laboratories, South Bend, IN) for 2 h at 37^{o}C, rinsed three times with PBS followed by three rinses with sterile deionized water before air-drying in a laminar flow hood. To confirm that the polystyrene STEP fibers were successfully coated with fibrin, Alexa Fluor 647-conjugated fibrinogen (Invitrogen, Carlsbad, CA) was used.

3.3.3 Scanning Electron Microscopy

To characterize the diameter of the polystyrene STEP fibers, samples were gold-coated using a Pelco SC-6 sputter coater (Ted Pella, Inc., Redding, CA) and examined using a Hitachi 2460N Scanning Electron Microscope (Hitachi High Technologies America, Inc., Schaumburg, IL). Images were obtained using Quartz PCI Image software.

For cell-seeded STEP fibers, cells were washed once in PBS and subsequently fixed using 2.5% glutaraldehyde in PBS and prepared for SEM. After three PBS washes, the specimens were fixed for 1 h in 1% osmium tetroxide buffered with PBS. The osmium tetroxide was removed with three washes of DI water for 5 min followed by incubation

for 5 min in 1% thiocarbohydrazide in DI water. The specimens were washed three times in DI water followed by a 5 min exposure to 1% osmium tetroxide in DI water. The specimens were washed with three changes of DI water, and after the exposure to thiocarbohydrazide, the DI water washes, and treatment with osmium tetroxide was repeated. After fixation, the specimens were washed with three changes of DI water followed by dehydration in an ascending series of ethanol (50%, 70%, 80%, 90%, and 3 changes of 100%). The specimens were dried in a Pelco CPD2 critical point dryer (Ted Pella, Inc., Redding, CA) using carbon dioxide at 1200 psi, and 42°C. Dried specimens were attached to SEM stubs using double-sided stick tape and coated with gold using a Pelco SC-6 sputter coater (Ted Pella, Inc., Redding, CA). Specimens were examined using a Hitachi 2460N Scanning Electron Microscope (Hitachi High Technologies America, Inc., Schaumburg, IL). Images were obtained using Quartz PCI Image software.

3.3.4 Transmission Electron Microscopy

To characterize polystyrene STEP fibers, samples were placed in a 35 mm Petri-dish and coated with gold using a Pelco SC-6 sputter coater (Ted Pella, Inc., Redding, CA). Subsequently, the Petri dishes were filled with Epon-Araldite and were infiltrated for at least three days at room temperature and placed in an oven at 30^{o}C for 24 h, at 40^{o}C for 24 h, at 50^{o}C for 24 h and finally at 60^{o}C overnight to allow for slow polymerization of the Epon-Araldite. The samples were cut to fit into an embedding capsule and re-embedded in Epon-Araldite. Thin (100 nm) cross sections of the re-embedded sample were cut using a Reichert-Jung Ultracut E and a DDK Diamond knife. When required, the sections were stained with 1% uranyl acetate and Reynold's lead citrate before

viewing on a Hitachi 7100 transmission electron microscope. Digital images were obtained using an AMT Advantage 10 CCD Camera System and NIH Image software.

3.3.5 Cell Culture

Multipotent C3H10T1/2 cells (ATTC, Manassas, VA) were grown in Dulbecco's Modified Eagle's Media (DMEM; Invitrogen, Carlsbad, CA), 10% fetal bovine serum (Invitrogen, Carlsbad, CA) and 1% penicillin-streptomycin (PS; Invitrogen, Carlsbad, CA). C2C12 cells (ATTC, Manassas, VA) were grown in DMEM, 10% bovine serum (Invitrogen, Carlsbad, CA) and 1% PS. Cells were seeded onto polystyrene STEP fibers in a 50-70 µL droplet containing ~10-15x10^4 cells and allowed to attach for 1.5 h before flooding the dish with complete media. In experiments utilizing fibrin-coated fibers, a final concentration of 1 µg/mL aprotinin was added to complete media to minimize fibrin degradation (Sigma Aldrich, St. Louis, MO). All cells were kept at 37^{o}C, 5% CO_2 in a humidified incubator.

3.3.6 Growth Factor Printing

Prior to printing, GFs were freshly diluted to the desired concentration in 10 mM sodium phosphate, pH 7.4. Prior to filling the inkjet with a GF, the printhead was sterilized by rinsing with 70% ethanol followed by sterile deionized water. The bio-ink, consisting of 50-100 µg/ml GF was loaded into the printhead, and printed as previously described [6, 11]. The deposited concentration of inkjetted GFs was modulated by overprinting, which is achieved by varying the number of times a GF is deposited in the same (x,y) location. After printing, fibrin-coated STEP fibers were incubated in serum-free DMEM with 1% PS overnight at 37°C, 5% CO_2 to wash off unbound GF prior to cell seeding. The surface

concentration of GF present on fibrin-coated STEP fibers prior to cell seeding was estimated based on the desorption measurements from previous studies [6, 9, 11, 32].

3.3.7 Alkaline Phosphatase (ALP) Staining

Staining for the osteoblast marker Alkaline Phosphatase (ALP) was performed using an ALP staining kit (Kit 86C, Sigma Aldrich, St. Louis, MO) according to the manufacturer's instructions.

3.3.8 Immunofluorescence Staining

Cells were washed in PBS, fixed in methanol for 5 min, air-dried and blocked with 10% donkey serum (Jackson Immunoresearch, West Gove, PA) for 20 min at RT. For mouse-on-mouse staining, an additional blocking step was performed by incubating cells with 100 µg/mL donkey anti-mouse FAB (Jackson Immunoresearch, West Gove, PA) for 1 h at RT. Cells were then rinsed with wash buffer (PBS, 0.1% BSA) and incubated with primary antibodies: rabbit anti-scx (10 µg/mL; Abcam, Cambridge, MA) and/or mouse anti-myosin MF20 (1 µg/mL; Developmental Studies Hybridoma Bank, Iowa City, Iowa) overnight at 4^{o}C. Cells were then rinsed three times with wash buffer (5 min each) and incubated with secondary antibodies for 1 h at RT – donkey anti-mouse Dylight 488 nm or donkey anti-rabbit Dylight 549 nm (15 µg/mL each; Jackson Immunoresearch, West Gove, PA). Lastly, cells were rinsed five times with wash buffer (5 min each) and imaged using a Zeiss Axiovert 200M microscope (Carl Zeiss Microimaging, Thornwood, NY) equipped with a Colibri LED light source.

3.3.9 Quantification of Immunofluorescence or ALP Staining

When required, suspended parallel STEP fibers were subsequently transferred to a fresh dish after staining to rule out the possibility that cells below the fibrous layer (either on the support substrate or dish bottom) were aligning or responding to the printed GF patterns. This procedure ensured that any positive signals observed originated only from cells that had attached to the fibers. Quantification of immunofluorescence or ALP staining was performed using Adobe Photoshop 7.0 (Adobe Systems, San Jose, CA). Briefly, the rectangular marquee tool was used to draw a bounding box (depending on the size of the printed pattern and/or magnification) and the image histogram tool was used to measure average pixel intensity. As an alternative to using average pixel intensity, the number of myotubes greater than 250 μm in length was manually counted. Error bars were expressed as standard error of the mean (SEM).

3.3.10 Actin Staining

To determine the cytoskeletal arrangement of cells within GF-printed regions of STEP fibers, fibrin-coated STEP fibers were soaked or hand-printed with BMP-2 or FGF-2. The soaking mimicked the action of GF printing and facilitated these studies because the precise determination of GF-printed boundaries was not required. Briefly, a 50–70 μL of a 100 μg/mL GF solution was pipetted onto fibrin-coated STEP fibers (enough to cover the entire scaffold) and the GF was allowed to air-dry at 37^{o}C. After drying, GF-soaked STEP fibers were stored at 4°C prior to cell seeding. 24 h post cell seeding, the GF-soaked fibrin-coated STEP fibers were washed twice in PBS and fixed in methanol-free 4% paraformaldehyde for 10 min. The fixative was aspirated and cells were washed twice in PBS and permeabilized with 0.1% Triton X-100 (Sigma Aldrich, St. Louis, MO) for 5

min. Cells were washed twice in PBS and blocked with wash buffer (PBS, 0.1% BSA) for 20 min at RT to reduce non-specific staining. Cells were subsequently washed twice in PBS before adding Alexa Fluor 647-conjugated phalloidin (Invitrogen, Carlsbad, CA) according to the manufacturer's instructions (5 µL stock solution for every 200 µL PBS). Lastly, cells were washed twice in PBS and imaged using a Zeiss LSM 510 Meta NLO Confocor 3 inverted spectral confocal microscope (Carl Zeiss Microimaging, Thornwood, NY).

3.3.11 Statisical Analysis

Quantification of immunofluorescence measurements were analyzed using either one-way analysis of variance followed by Fisher's least significant difference post hoc test with SYSTAT 9 software (Systat Software Inc., Richmound, CA) or using a student's t-test with Microsoft Excel (Microsoft Corporation, Redmond, WA) to determine significance among treatment groups. A p value ≤ 0.05 was considered statistically significant.

3.4 RESULTS

3.4.1 Characterization of Polystyrene STEP Fibers

Figure 3.1 illustrates the fabrication and characteristics of polystyrene STEP fibers. Briefly, during the process of pseudo-dry spinning, the solvent is evaporated by the surrounding ambient air as it is extruded from the micropipette (Figure 3.1A). This increases the local concentration of polystyrene and promotes entanglement of polystyrene chains, which reduces chain mobility and starts the process of forming a solidified fiber [30, 31]. By choosing an appropriate DC motor speed to control fiber

deposition as well as controlling the vertical speed of the nanopositioner to affect fiber spacing, scaffolds with parallel fibers are fabricated (Figure 3.1B, left panel). Furthermore, multiple layers can be deposited to produce criss-crossed fibers (Figure 3.1B, middle panel). In addition, these fibers can be spun on a hollowed-out support base to produce suspended fibers (Figure 3.1B, right panel). SEM and TEM analysis of the fibers indicate that polystyrene STEP sub-micron fibers had a diameter of 668 ± 34 nm and 628 ± 63 nm, respectively (Table 3.1 and Figure 3.1C). Fibers were predominantly oriented in parallel arrays and deviated less than 2.54 ± 0.24 degrees with respect to one another (Table 3.1). SEM analysis also showed that polystyrene STEP fibers allowed for cell attachment and promoted cell alignment (Figure 3.1D). Lastly, polystyrene STEP fibers could be coated with various ECM proteins such as fibrin and printed on (Figure 3.1E, F). Fibrin-coating of polystyrene STEP fibers was also confirmed by TEM analysis (Figure 3.2). When stained with Reynold's lead citrate, TEM cross sections of fibrin-coated polystyrene STEP fibers exhibit a dark stain (white arrowhead) around individual fibers which is indicative of an adsorbed protein layer whereas uncoated polystyrene STEP fibers do not (Figure 3.2).

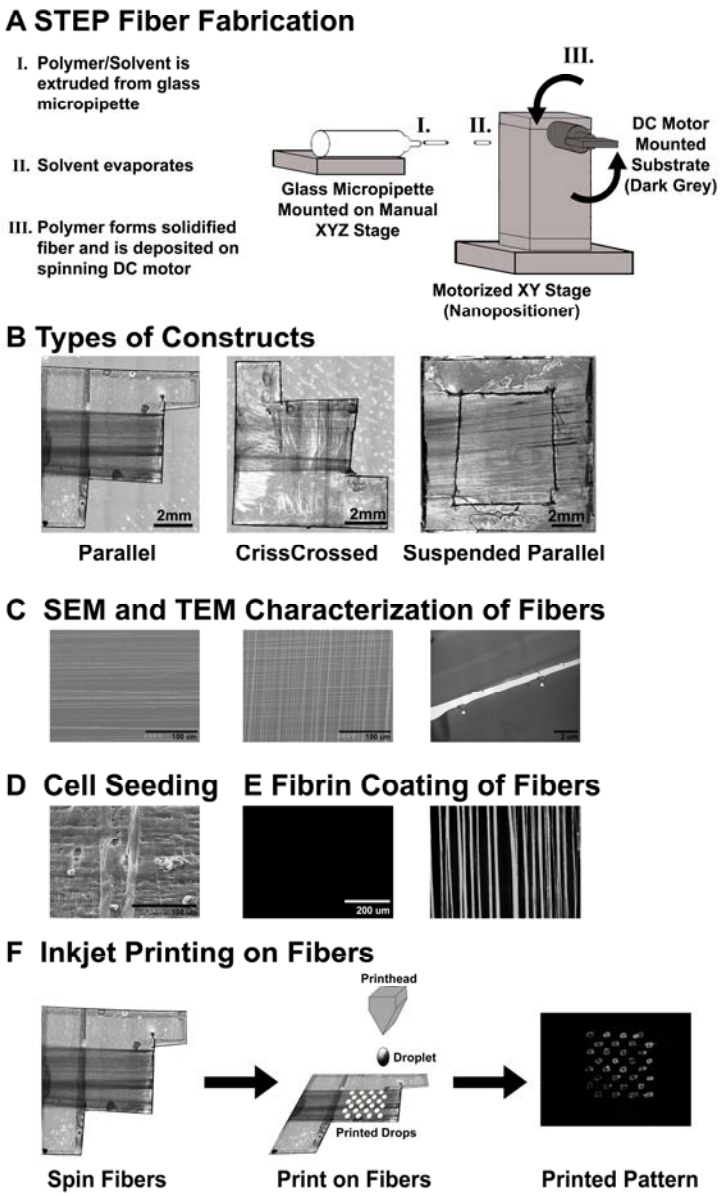

Figure 3.1. Polystyrene Spinneret-based Tunable Engineered Parameter (STEP) sub-micron fibers. **A.** Scheme illustrating STEP fiber fabrication. **B.** Types of STEP fibers that can be fabricated. The left scaffold consists of one set of fibers running in a parallel manner. The middle scaffold consists of two sets of fibers running perpendicular to each other. The right scaffold consists of one set of fibers running in a parallel manner with a hollowed-out support base. **C.** Typical SEM and TEM images of STEP fibers used for quantifying diameter length. **D.** Typical SEM image showing attachment of cells to polystyrene STEP fibers. **E.** Coating of polystyrene STEP fibers with Alexa649-conjugated fibrin. Left image shows uncoated STEP fibers while right image shows fibrin-coated STEP fibers. Some fibers aggregate to form larger fiber bundles after numerous washing steps. **F**. Inkjet printing indicates that polystyrene STEP fibers can be printed on. Scale bars are as indicated.

TABLE. 3.1. Characterization of Polystyrene STEP Fibers.

	Data ± Standard Error Mean
Scanning Electron Microscopy (n = 43)	668 ± 34 nm
Transmission Electron Microscopy (n = 20)	628 ± 63 nm
Linearity of Fibers with respect to one another (n = 45)	2.54 ± 0.24 degrees

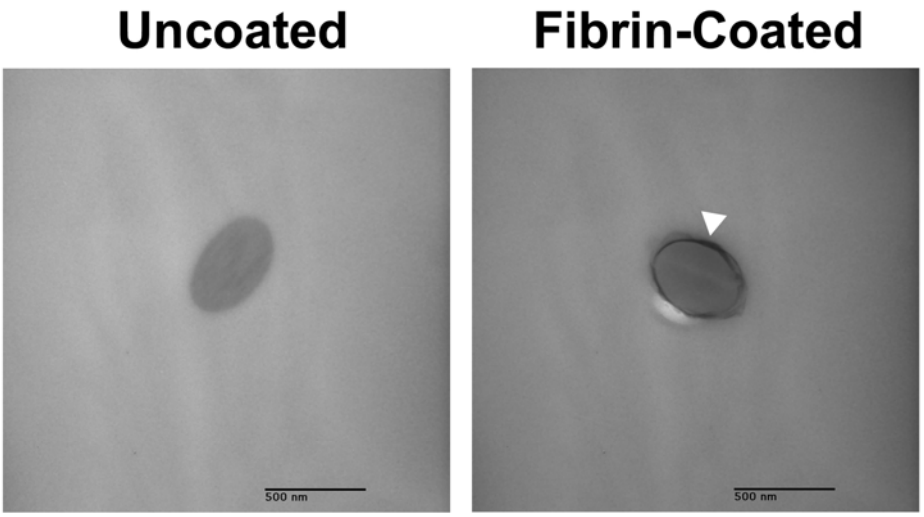

Figure 3.2. TEM characterization of fibrin-coated polystyrene STEP sub-micron fibers. Cross sectional view of a single uncoated and fibrin-coated polystyrene STEP fiber (Dark grey ellipse). A dark stain (white arrowhead) is observed around the fibrin-coated polystyrene STEP fiber, indicative of an adsorbed protein layer. Scale bar 500 nm.

3.4.2 Effect of Polystyrene STEP fibers on Myotube Alignment

Having characterized the structural properties of the polystyrene STEP fibers, Figure 3.3 shows the geometric effect of polystyrene STEP fiber organization on C2C12 cells. Under conditions of high cell density, C2C12 cells spontaneously form elongated myotubes that are randomly oriented in a polystyrene dish. However, when seeded onto criss-crossed and parallel polystyrene STEP fibers, C2C12 cells form elongated myotubes that aligned along the fiber length (Figure 3.3). Similar results were obtained when C2C12 cells are seeded onto criss-crossed and parallel polyurethane STEP fibers under proliferation (High serum conditions for 6 days; Figure 3.4) and myogenic

conditions (Low serum conditions for 4 days; Data not shown). Occasionally, suspended parallel STEP Fibers clumped together (Figure 3.4) after wetting (in the absence of cells) and this phenomenon may be attributed to hydrophobic interactions among fibers in an aqueous environment.

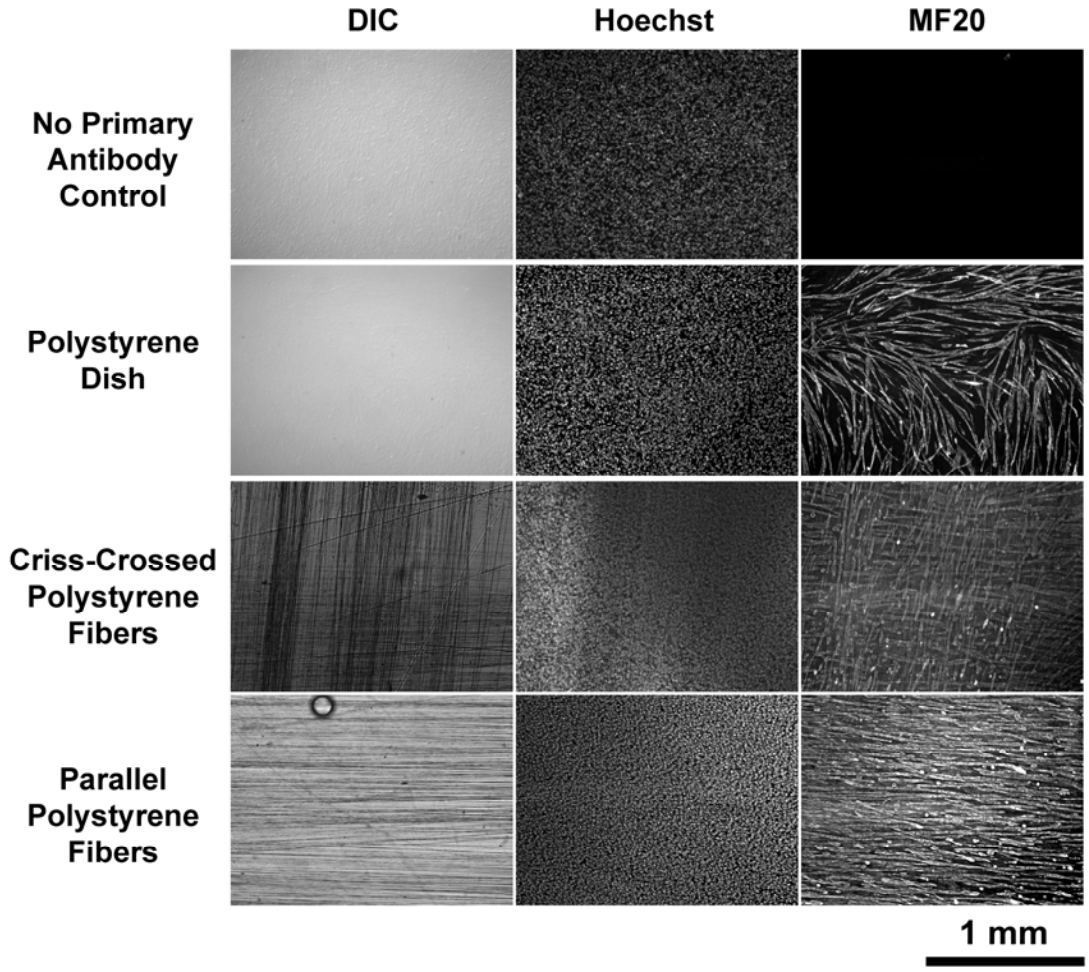

Figure 3.3. Effect of polystyrene STEP fiber organization on myotube alignment. Under conditions of high cell density, C2C12 cells spontaneously form elongated myotubes that are randomly oriented in a polystyrene dish. On criss-crossed and parallel polystyrene STEP fibers, C2C12 cells form elongated myotubes that align along the fiber length. No MF20 signal is observed in the no primary antibody control. Scale bar 1 mm.

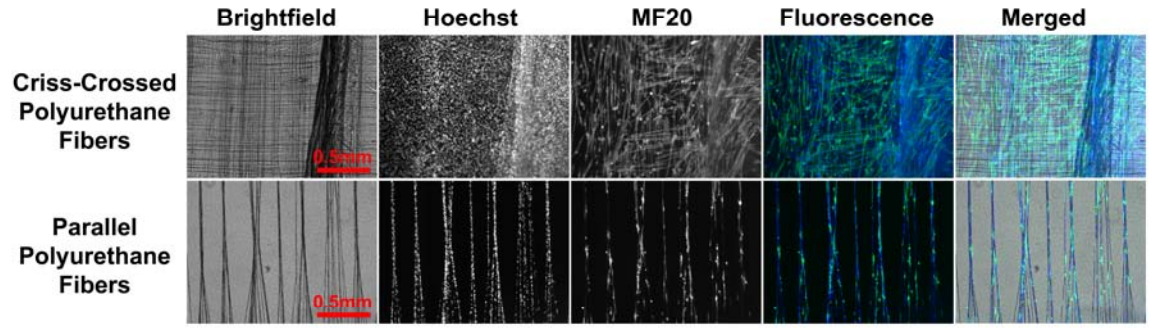

Figure 3.4. Effect of polyurethane STEP fiber organization on myotube alignment. Under conditions of high cell density, C2C12 cells spontaneously form elongated myotubes that align along the fiber length on criss-crossed and parallel polyurethane STEP fibers. Scale bar 0.5 mm.

3.4.3 Effect of Serum-Coated STEP Fibers Patterned with FGF-2 on Tenocyte Differentiation

Given that STEP fibers can induce cell alignment, polystyrene STEP scaffolds were coated with serum and subsequently printed with FGF-2 patterns to determine if these patterns could drive C3H10T1/2 cell differentiation towards a tenocyte fate. As can be seen in Figure 3.5, our bio-inkjet printing technology allows for controlled deposition of varying amounts of GFs such as FGF-2 in a spatially precise manner (Figure 3.5A), which results in a dose-dependent increase in expression of the tendon marker Scleraxis (Scx) in C3H10T1/2 cells (Figure 3.5B, C). Although lower doses of FGF-2 (40 pg/mm^2 and 245 pg/mm^2 FGF-2) immobilized to the scaffold (referred to as 'solid-phase' FGF-2) were not sufficient to induce an increase in the expression of the Scx tenocyte marker relative to non-printed control regions ($p = 0.428$ for 40 pg/mm^2 FGF-2 and $p = 0.052$ for 245 pg/mm^2 FGF-2), higher doses of solid-phase FGF-2 (450 pg/mm^2 and 650 pg/mm^2 FGF-2) resulted in an increase in Scx expression relative to non-printed control regions ($p = 0.048$ for 450 pg/mm^2 FGF-2 and $p = 0.025$ for 650 pg/mm^2 FGF-2; Figure 3.5) in C3H10T1/2 cells. SEM analysis verified that printed FGF-2 remain bound to serum-

coated polystyrene STEP fibers as evidenced by the square bumps which indicate increased cell proliferation on mitogenic FGF-2 patterns (Figure 3.5D).

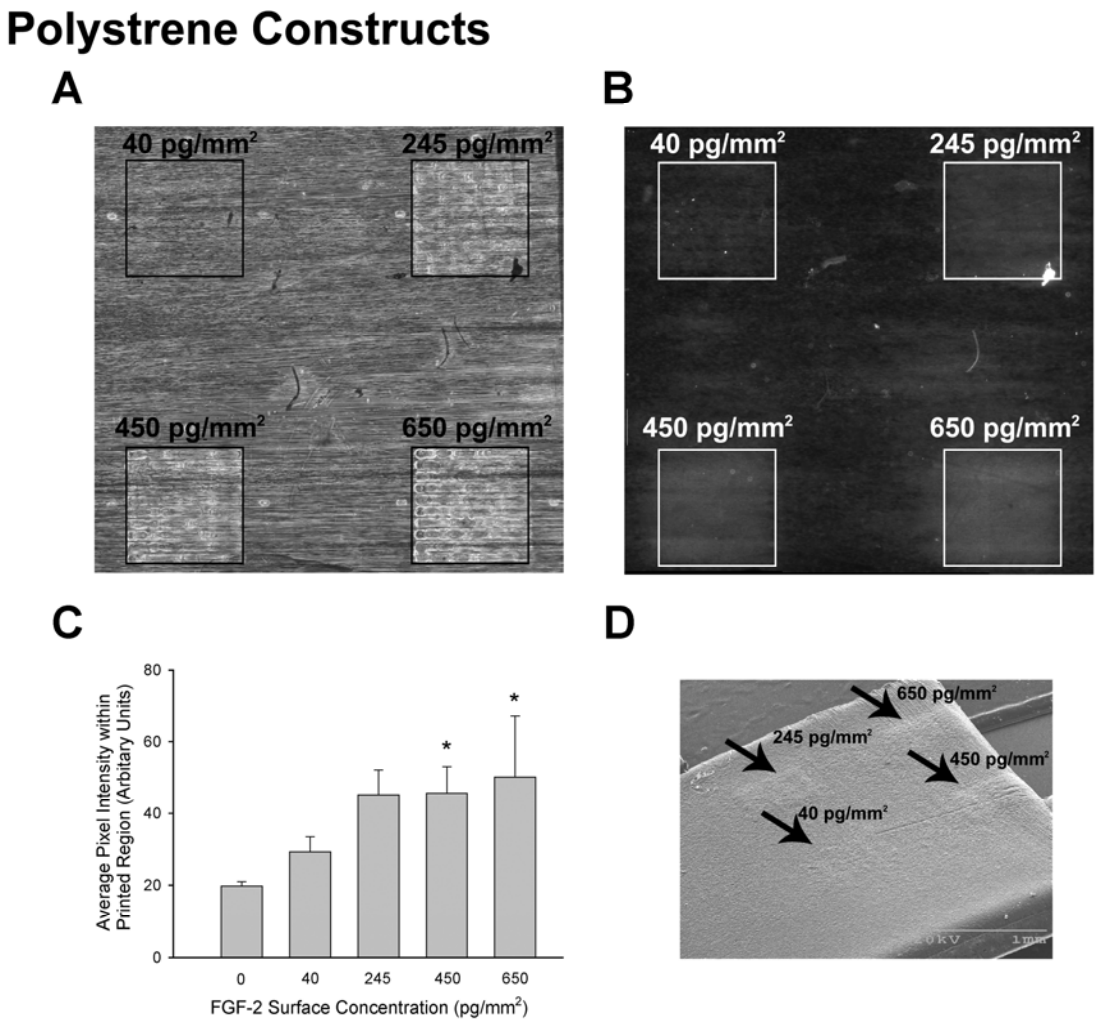

Figure 3.5. Effect of Printed FGF-2 patterns on Scx expression in C3H10T1/2 cells. **A.** Phase-contrast image showing serum-coated STEP fibers post-FGF-2 printing. 2, 12, 22 and 32 Overprints of 100 µg/mL FGF-2 corresponding to 40 pg/mm^2, 245 pg/mm^2, 450 pg/mm^2 and 650 pg/mm^2 FGF-2 were printed. Black boxes indicate 1 x 1 mm printed regions. **B.** On serum-coated STEP fibers, C3H10T1/2 cells show a dose-dependent increase in Scx (tenocyte) staining with increased FGF-2 overprints. White boxes indicate 1 x 1 mm printed regions. **C.** Quantification of Scx signal within printed regions (n = 3). Error bars indicate ± SEM. *, Significantly different from non-printed control regions; $p \leq 0.05$. **D.** SEM image showing serum-coated STEP fibers post-cell seeding. Black arrows and corresponding text indicate printed regions. Scale bar 1 mm.

3.4.4 Effect of Fibrin-Coated STEP Fibers Patterned with BMP-2 on Osteoblast Differentiation

Having demonstrated that printed FGF-2 patterns could induce stem/progenitor cells towards a tendon lineage, polystyrene STEP fibers were coated with fibrin and printed with BMP-2 to determine if osteoblast differentiation could be patterned. As can be seen in Figure 3.6, printed patterns of BMP-2 show increased expression of the osteoblast marker, alkaline phosphatase (ALP) relative to non-printed control regions ($p \leq 0.001$) in C2C12 cells (Figure 3.6). Similar results were obtained when C2C12 cells were seeded onto fibrin-coated polyurethane STEP fibers printed with BMP-2 with printed patterns of BMP-2 showing increased ALP expression relative to non-printed control regions ($p = 0.026$; Figure 3.7).

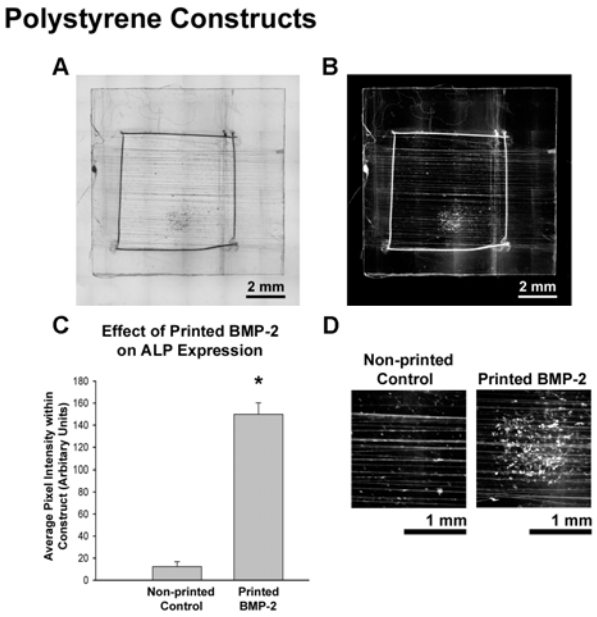

Figure 3.6. Effect of printed BMP-2 patterns on ALP expression in C2C12 cells (Fibrin-coated polystyrene STEP fibers). **A**. Grey-scaled image of ALP staining. 36 Overprints of 200 µg/mL BMP-2 corresponding to 4 ng/mm^2 BMP-2 were printed onto fibrin-coated STEP fibers. Scale bar 2 mm. **B-D.** Quantification of ALP staining within printed regions (n = 5). Error bars indicate ± SEM. *, Significantly different from control or non-printed regions; $p \leq 0.001$. Scale bars as indicated.

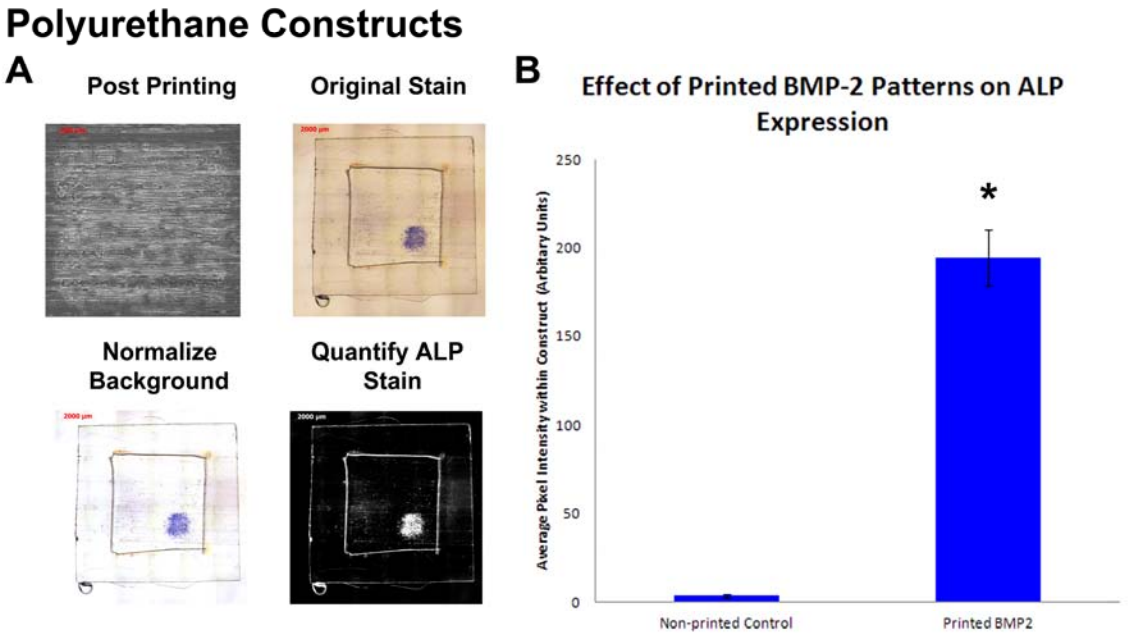

Figure 3.7. Effect of printed BMP-2 patterns on ALP expression in C2C12 cells (Fibrin-coated polyurethane STEP fibers). **A**. Post-printing of 100 µg/mL BMP-2 into a 1x1 mm pattern on fibrin-coated polyurethane STEP fibers (Top left panel). Circular shapes within the printed regions indicate deposited GF droplets (Top left panel). On fibrin-coated STEP fibers, C2C12 cells show increased ALP staining on BMP-2 patterns but little to none on unprinted regions (Top right). Normalization and quantification of ALP stain (Bottom panels). Scale bars as indicated. **B.** Quantification of ALP Signal (n = 2). Error bars indicate ± SEM. *, Significantly different from control or non-printed regions; $p \leq 0.05$.

3.4.5 Effect of Fibrin-Coated STEP Fibers Patterned with FGF-2 on Tenocyte and Myocyte Differentiation and Cell Alignment

To determine if cell alignment and cell differentiation could be controlled simultaneously on oriented fibers printed with a single GF, patterns of FGF-2 were printed onto fibrin-coated STEP fibers and seeded with C2C12 cells. As can be seen in Figure 3.8, printed FGF-2 patterns resulted in increased expression of Scx and decreased expression of the muscle marker MF20 in C2C12 cells (Figure 3.8). Although a low dose of solid-phase FGF-2 (240 pg/mm^2 FGF-2) was not sufficient to induce an increase in Scx expression relative to 120 pg/mm^2 FGF-2 ($p = 0.494$), higher doses of solid-phase FGF-2 (490

pg/mm^2 and 730 pg/mm^2 FGF-2) resulted in an increase in Scx expression relative to 120 pg/mm^2 FGF-2 ($p = 0.04$ for 490 pg/mm^2 FGF-2 and $p = 0.007$ for 730 pg/mm^2 FGF-2) in C2C12 cells. In addition, increasing doses of solid-phase FGF-2 (240 pg/mm^2, 490 pg/mm^2 and 730 pg/mm^2 FGF-2) inhibited myotube formation relative to 120 pg/mm^2 FGF-2 ($p = 0.043$ for 240 pg/mm^2 FGF-2, $p = 0.022$ for 490 pg/mm^2 FGF-2 and $p = 0.019$ for 730 pg/mm^2 FGF-2). Outside of the printed pattern, cells maintained elongated myotube structures that were aligned in a parallel fashion along the fiber length (Figure 3.8A).

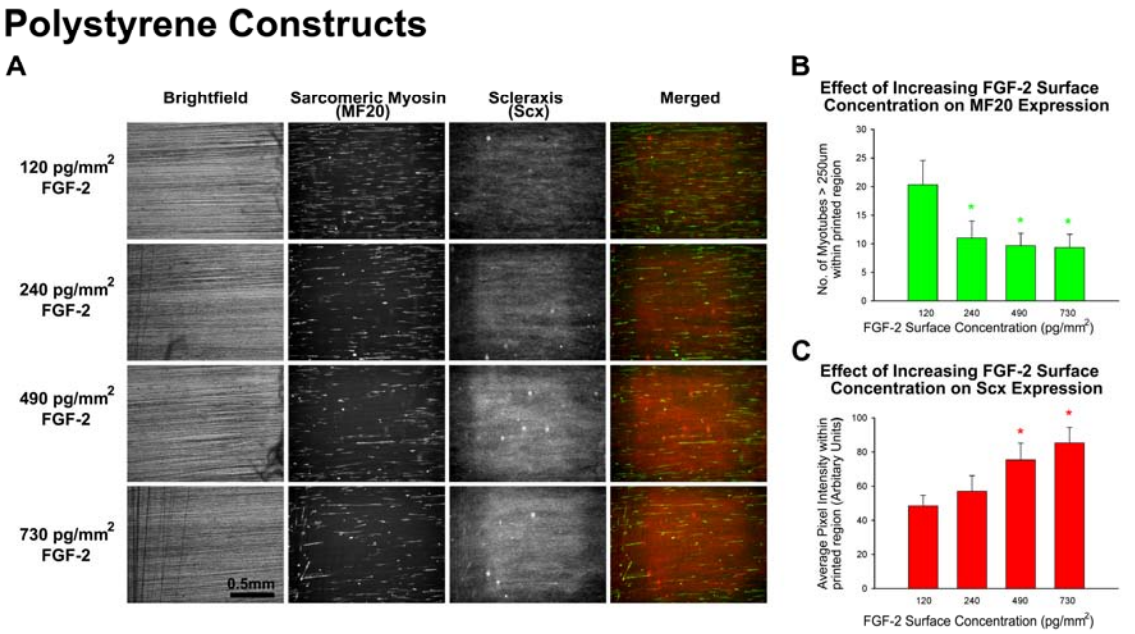

Figure 3.8. Effect of printed FGF-2 patterns on MF20 and Scx expression in C2C12 cells. **A.** 6, 12, 24 and 36 Overprints of 100 µg/mL FGF-2 corresponding to 120 pg/mm^2, 240 pg/mm^2, 490 pg/mm^2 and 730 pg/mm^2 FGF-2 were printed. On fibrin-coated STEP fibers, C2C12 cells show a dose-dependent decrease in MF20 staining and a dose-dependent increase in Scx staining with increasing FGF-2 overprints. Note alignment of myotubes along fiber axis. Scale bar 0.5 mm. **B.** Quantification of MF20 signal within printed FGF-2 regions (n = 6). Error bars indicate ± SEM. *, Significantly different from 6 Overprints (120 pg/mm^2 FGF-2); $p \leq 0.05$. **C.** Quantification of Scx signal within printed FGF-2 regions (n = 6). Error bars indicate ± SEM. *, Significantly different from 6 Overprints (120 pg/mm^2 FGF-2).

3.4.6 Effect of Fibrin-Coated STEP Fibers Patterned with BMP-2 and FGF-2 on Osteoblast, Tenocyte and Myocyte Differentiation and Cell Alignment

To determine if cell alignment and multiple differentiation fates could be controlled simultaneously on the same scaffold, patterns of FGF-2 and BMP-2 were printed onto fibrin-coated STEP fibers and seeded with C2C12 cells (Figure 3.9A). In this experiment, a suspended scaffold comprised of parallel STEP fibers spun over a hollowed-out base was used for cell seeding (Figure 3.1B). This scaffold was subsequently transferred to a fresh dish post-staining to rule out the possibility that cells below the fibrous layer (i.e. cells that had attached onto the support base or dish bottom) were responding to the GF patterns. As can be seen in Figure 3.9, printed BMP-2 and FGF-2 patterns resulted in increased expression of the osteoblast marker ALP and tenocyte marker Scx, respectively, while inhibiting myogenesis in C2C12 cells (Figure 3.9B, C, D). Expression of ALP within the BMP-2 pattern increased relative to both the printed FGF-2 pattern ($p \leq 0.001$) and non-printed control region ($p \leq 0.001$). Expression of Scx within the FGF-2 pattern was increased relative to non-printed control region ($p = 0.033$) but not to the printed BMP-2 pattern ($p = 0.367$). Concurrently, expression of the muscle marker MF20 was decreased on both printed BMP-2 ($p = 0.015$) and FGF-2 ($p = 0.032$) patterns. Outside of the printed patterns, cells stained positive for the myotube marker MF20 and aligned in a parallel fashion along the fiber length (Figure 3.9B, E). To determine the alignment of cells within the printed GF patterns, manual annotation of printed BMP-2 and FGF-2 patterns was performed (Figure 3.10). C2C12 cells adopted a predominantly parallel orientation with respect to the fiber length within and outside of printed regions, indicative of geometric control of cell alignment (Figure 3.10). To determine the

cytoskeletal arrangement of cells within GF-printed regions of STEP fibers, actin staining was performed on C2C12 cells seeded onto fibrin-coated STEP fibers that had been previously pre-soaked in BMP-2 or FGF-2 (Figure 3.11). The pre-soaking step mimicked the action of GF printing and facilitated these studies because the precise determination of GF-printed boundaries was not required. Actin staining demonstrated that actin filaments adopted parallel bundles with respect to fiber orientation (Figure 3.11).

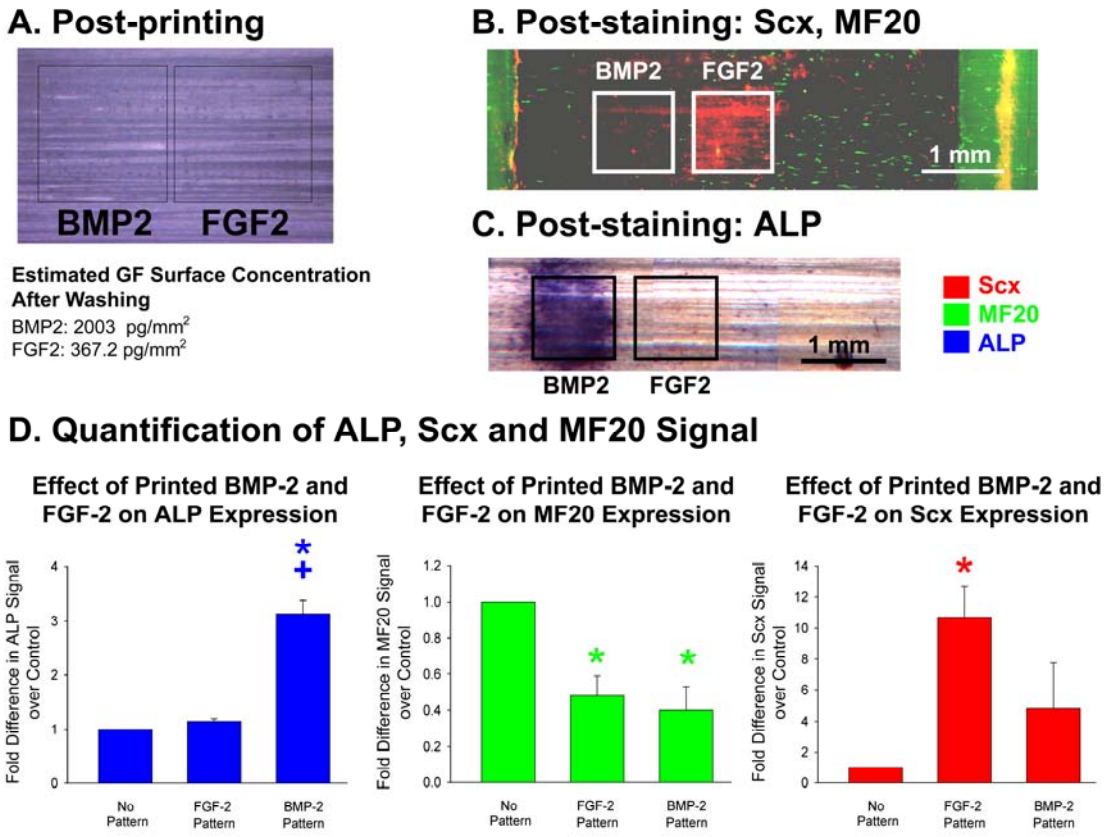

Figure 3.9. Effect of printed BMP-2 and FGF-2 patterns on ALP, MF20 and Scx expression in C2C12 cells. **A.** Post-printing of 100 µg/mL BMP-2 and 50 µg/mL FGF-2 patterns (36 Overprints each) on fibrin-coated STEP fibers. Dark circular shapes within the printed regions (Black boxes) indicate deposited GF droplets. **B.** On fibrin-coated STEP fibers, C2C12 cells show increased Scx staining on FGF-2 patterns but little to none on BMP-2 patterns. Off-pattern, C2C12 cells form myocytes that are aligned along fiber axis. Scale bar 1 mm. **C.** On fibrin-coated STEP fibers, C2C12 cells show increased ALP staining on BMP-2 patterns but little to none on FGF-2 patterns. Scale bar 1 mm. **D.** Quantification of ALP, Scx and MF20 Signal (n = 4). Error bars indicate ± SEM. *, Significantly different from control or non-printed regions; $p \leq 0.05$. +, Significantly different from FGF-2-printed regions; $p \leq 0.05$.

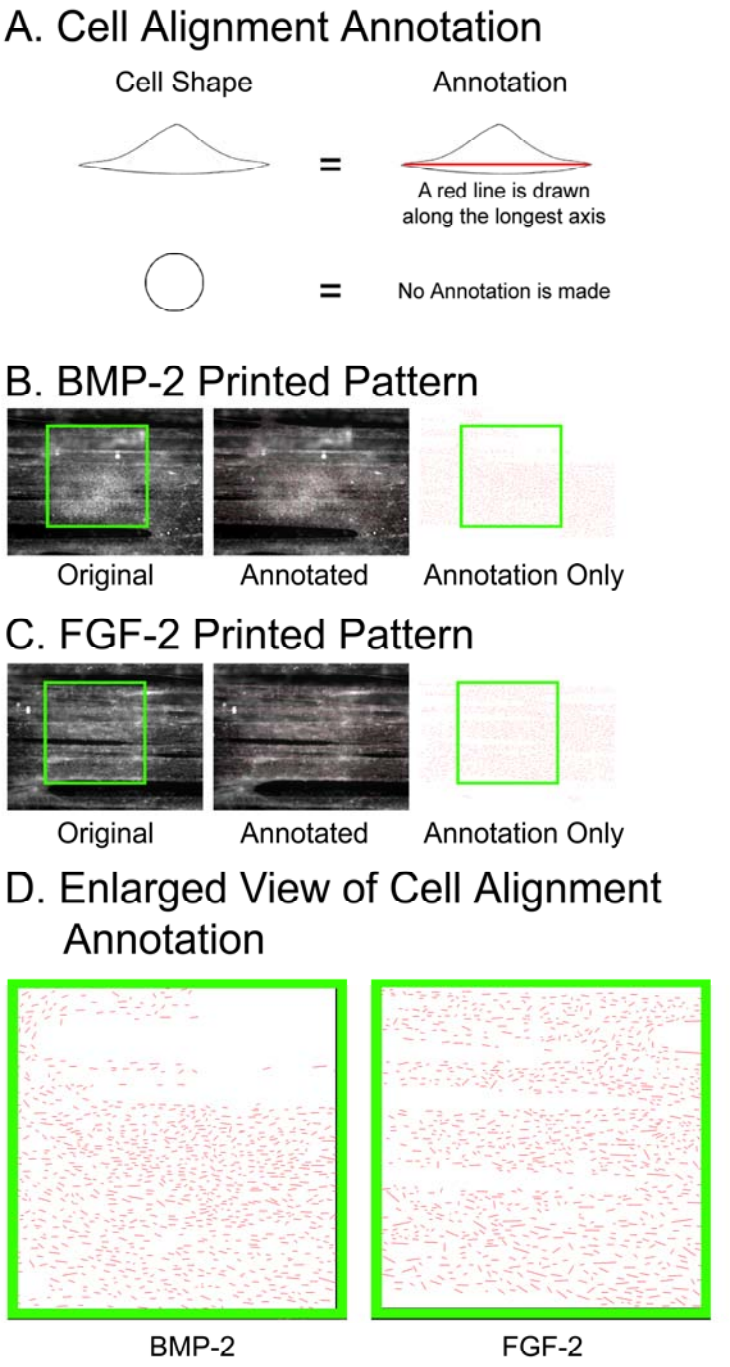

Figure 3.10. Effect of printed BMP-2 and FGF-2 on alignment of C2C12 cells. **A.** Scheme of how manual annotation for cell alignment was performed. **B.** Alignment of cells within printed BMP-2 pattern. Green box indicates approximate region (1 x 1 mm) where printed BMP-2 pattern is. Red lines indicate alignment of C2C12 cells as determined by manual annotation. **C.** Alignment of cells within printed FGF-2 pattern. Green box indicates approximate region (1 x 1 mm) where printed FGF-2 pattern is. Red lines indicate alignment of C2C12 cells as determined by manual annotation. **D.** Enlarged view of cell alignment within printed BMP-2 and FGF-2 patterns.

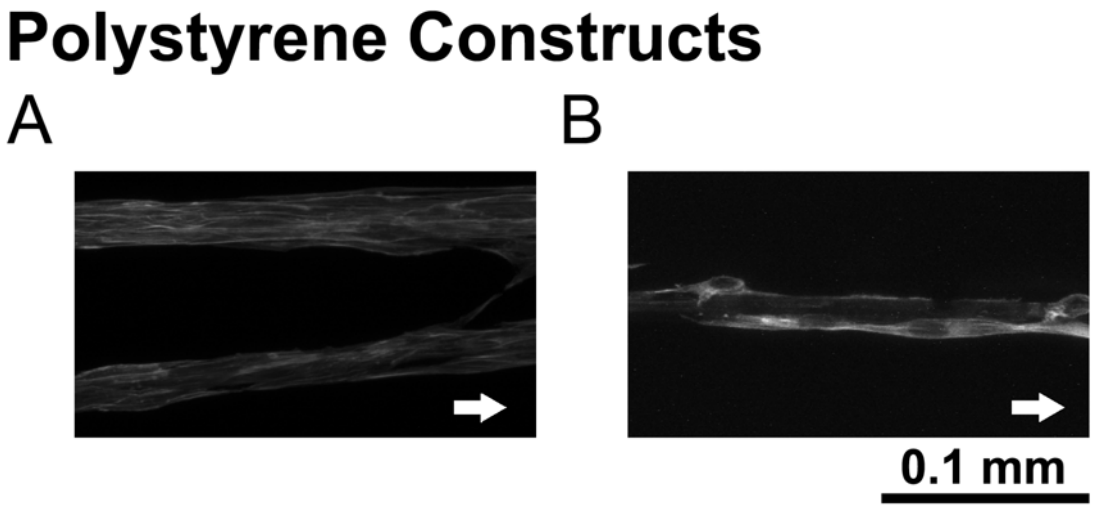

Figure 3.11. Effect of fibrin-coated STEP fibers pre-soaked with BMP-2 and FGF-2 on C2C12 cell alignment. A. BMP-2 soaked fibrin-coated STEP fibers. B. FGF-2 soaked fibrin-coated STEP fibers. White arrow indicates fiber orientation. Scale bar 100 μm.

3.5 DISCUSSION

3.5.1 Fibrous Scaffolds as ECM Analogs for Musculoskeletal Tissue Engineering

Our long-term goal is to engineer biomimetic scaffolds for aiding repair of musculoskeletal tissues. In this report, polystyrene sub-micron fibers, approximately 655 nm in diameter, were fabricated using the STEP technique [30, 31], and then coated with ECM material such as serum or fibrin to make the fibers compatible with GF bioprinting (Figure 3.1 and Figure 3.2). In addition, non-printed and uncoated polystyrene and polyurethane STEP fibers [30, 31] were found to promote myocyte alignment (Figure 3.3 and Figure 3.4). However, for follow-on *in vivo* studies completely biodegradable STEP fibers made with fibrinogen, poly(lactic-co-glycolic acid)-fibrinogen blends [30, 31] or polyurethane are being developed (Figure 3.4).

Polystyrene- and polyurethane-based fibers were fabricated such that the fiber diameter would approximate the diameter of ECM fibers [30, 31]. In particular, polystyrene-based fibers were primarily employed here as an appropriate control since the material used for

tissue culture vessels is based on polystyrene. STEP fiber fabrication is based on a recently discovered pseudo-dry spinning technique, which involves extruding a dissolved polymer solution from a glass micropipette spinneret [30, 31]. Upon extrusion, the polymer solvent is evaporated by ambient air and the solidified fiber is subsequently deposited on the substrate [30, 31]. Similar to electrospinning technique, the STEP technique relies on varying material parameters such as polymer molecular weight and solution polymer concentration to control fiber diameter; however, the fiber distribution and alignment is precisely controlled with the STEP technique by varying the angular and vertical speeds of the rotating substrate [30, 31]. Compared to other fiber fabrication platforms, the STEP technique uniquely allows for fabrication of uniform polymer fibers with diameters ranging from sub-50 nm to submicrometer to several millimeters, with highly defined orientations [30, 31]. Although some clumping was observed between suspended parallel STEP fibers, this could be minimized by spinning multiple fiber layers as observed in criss-crossed STEP fibers (Figure 3.4).

3.5.2 Controlling Musculoskeletal Cell Alignment with STEP Fibers

Although the precise mechanism behind geometry-induced cell alignment is presently unknown, it is likely that the alignment of cells observed on fibers may be attributed to a combination of factors including physical space constraint and relative stiffness of the underlying substrate (fiber), ultimately affecting changes in both cell spreading and cell stiffness [14, 33-37]. Since cell spreading and cell stiffness are not mutually exclusive phenomena and have been reported to interact in a complex fashion to alter cell morphology [36], cells may be predisposed towards a specific orientation through the modulation of mechanotransduction pathways via cytoskeletal rearrangements. This is

evident by the parallel arrangement of actin filaments observed in C2C12 cells grown on GF-soaked fibers (Figure 3.11). In the case of higher-ordered structures such as myotubes, which arise from cell-to cell fusion, this predisposition would promote increased cell-to-cell contact along the fiber length, ultimately biasing the manner in which cell-to-cell fusion occurs to elongate or 'grow' a myotube in a specific direction.

In this study, it should be noted that high levels of cell density (more than 90% confluent on the first day of the experiment) were required before differentiation would occur. Over the course of several days in culture, this results in cells growing on top of one another. As a result, cells that were not in direct contact with fibers may not have exhibited contact guidance. Thus, no attempt was made to quantify the degree of cell alignment because such quantification may not be reliable. However, cells in direct contact with non-printed (Figure 3.3 and Figure 3.4) or GF-soaked STEP fibers (Figure 3.11) exhibited contact guidance by aligning along the fiber length.

3.5.3 Simultaneous Control of Musculoskeletal Cell Alignment and Cell Differentiation on STEP Fibers with Solid-Phase GF Patterns using Inkjet-based Bioprinting

To spatially control stem cell differentiation, polystyrene STEP fibers were coated with ECM molecules such as fibrin and printed with GFs that promoted musculoskeletal cell differentiation. This approach takes advantage of the phenomena that biological spatial patterning occurs, in part, by sequestration of GFs to the ECM and cell surfaces, and it seeks to recreate physiologically-relevant conditions by immobilizing spatially-defined patterns of GFs, in picogram to nanogram levels, to ECM surfaces [4, 6, 8-12]. To create such patterns, GFs that have heparin-binding domains, such as FGF-2, BMP-2 and

heparin-binding EGF-like GF, are employed to immobilize them to appropriate ECM printing substrates via their native binding affinities [4, 6, 8-12]. Fibrin is one appropriate ECM material because of its inherent GF binding capability as well as its physiological relevance as a provisional matrix during the wound healing process [38]. In addition, since serum contains a complex mixture of ECM proteins, it was utilized in this study (Figure 3.5) to demonstrate that different ECM proteins can be used for immobilizing GFs as long as the ECM proteins possess inherent GF-binding capability [4]. BMP-2 and FGF-2 were employed here because previous studies have shown that these GFs can direct stem cells towards osteoblast and tenocyte differentiation, respectively [8, 11, 12, 39, 40]. In addition, these bio-printed GF patterns have been previously shown to persist *in vivo* and can spatially promote or inhibit bone formation [7].

When C3H10T1/2 and C2C12 cells were seeded onto ECM-coated STEP fibers bioprinted with GFs, they differentiated appropriately on printed patterns (Figure 3.5-Figure 3.9). The differentiation markers used for myocytes, tenocytes and osteoblasts were Sarcomeric Myosin [41], Scleraxis [40, 42-45] and Alkaline Phosphatase [46], respectively. Although several other differentiation markers such Eya [47], Six1 [48], Mohawk [49, 50] and tenomodulin [51, 52] are available for tenocytes, Scleraxis was utilized in this study as it is an early marker of tenocytes with highly specific expression in tendon progenitor cells and differentiating tendon cells [39, 44, 45]. In addition, Scleraxis expression is upregulated to coordinate injury response during tendon healing [53]. On serum-coated STEP fibers printed with FGF-2, C3H10T1/2 cells upregulated the tendon marker Scx in a dose-dependent manner, indicative of cells being driven towards a tenocyte fate (Figure 3.5). On fibrin-coated STEP fibers printed with BMP-2, C2C12

cells upregulated the osteoblast marker ALP, indicative of cells being driven towards an osteoblast fate (Figure 3.6 and Figure 3.7). On fibrin-coated STEP fibers printed with FGF-2, C2C12 cells upregulated the tendon marker Scx in a dose-dependent manner, indicative of cells being driven towards a tenocyte fate (Figure 3.8). Outside the printed region, myocytes aligned along the fiber length (Figure 3.8).

To demonstrate that cell alignment and cell differentiation could be controlled simultaneously with oriented sub-micron fibers and multiple GFs, respectively, C2C12 cells were seeded on adjacent patterns of FGF-2 and BMP-2 printed onto fibrin-coated polystyrene STEP fibers. ALP and Scx expression increased on the BMP-2 and FGF-2 patterns, respectively, indicative of cells being driven towards osteoblast and tenocyte fates (Figure 3.9). Outside of the printed region, aligned myocytes were observed (Figure 3.9B). Interestingly, BMP-2 was shown to upregulate expression of the tendon marker Scx although at much lower levels than FGF-2 (Figure 3.9B, D). This upregulation may be attributed to BMP-2 induced activation of the Smad signaling pathway, which has been previously shown to be involved in neotendon formation [54].The results shown here demonstrate that bioprinting of GFs onto aligned configurations of ECM-coated fibers can create a unique microenvironment that simultaneously controls cell differentiation and alignment, respectively.

3.6 CONCLUSIONS

This chapter focused on the characterization and systematic *in vitro* evaluation of a novel biomimetic, sub-micron fiber-based scaffold patterned with GFs to create biochemical and geometric cues that spatially direct a single stem cell population towards multiple

cell fates, including tenocytes, myocytes or osteoblasts, while simultaneously controlling cell alignment within the same construct. The capability to spatially control stem cell orientation and differentiation toward multiple phenotypes simultaneously, allows cells grown *in vitro* to more closely mimic aspects of native tissue organization and structure. This capability offers a systematic approach to study the basic principles involved in tissue formation and function *in vitro* and may lead to bioinspired strategies for improved material design to treat musculoskeletal diseases and trauma.

3.7 ACKNOWLEDGEMENTS

I would like to thank Bur Chu and Larry Schultz for assistance with GF printing. I would also like to thank Dr. Haibing Teng for assistance with confocal microscopy. This work was supported by NIH grants RO1EB004343 and RO1EB007369 as well as funding from the Pennsylvania Infrastructure Technology Alliance (PITA). The MF20 monoclonal antibody developed by Donald A. Fischman was obtained from the Developmental Studies Hybridoma Bank developed under the auspices of the NICHD and maintained by The University of Iowa, Department of Biology, Iowa City, IA 52242. A. N and J. W are also thankful to Institute for Critical Technology and Applied Sciences (ICTAS) along with Nanoscale Characterization and Fabrication Laboratory (NCFL) at VT for SEM work.

3.8 REFERENCES

1. Beniash, E., *Biominerals-hierarchical nanocomposites: the example of bone.* Wiley Interdiscip Rev Nanomed Nanobiotechnol, 2010. 3(1): p. 47-69.
2. Fu, R.H., et al., *Differentiation of Stem Cells: Strategies for Modifying Surface Biomaterials.* Cell Transplant, 2010. 20(1): p. 37-47.

3. Nelson, C.M. and M.J. Bissell, *Of extracellular matrix, scaffolds, and signaling: tissue architecture regulates development, homeostasis, and cancer.* Annu Rev Cell Dev Biol, 2006. 22: p. 287-309.
4. Taipale, J. and J. Keski-Oja, *Growth factors in the extracellular matrix.* FASEB J, 1997. 11(1): p. 51-9.
5. Unsicker, K. and K. Krieglstein, *Cell Signaling and Growth Factors in Development*, ed. K. Unsicker and K. Krieglstein. 2006, Germany: Wiley-VCH 991.
6. Campbell, P.G., et al., *Engineered spatial patterns of FGF-2 immobilized on fibrin direct cell organization.* Biomaterials, 2005. 26(33): p. 6762-70.
7. Cooper, G.M., et al., *Inkjet-Based Biopatterning of BMP-2 to Spatially Control Calvarial Bone Formation.* Tissue Eng Part A, 2010. 16(5): p. 1749-1759.
8. Ker, E.D., et al., *Engineering spatial control of multiple differentiation fates within a stem cell population.* Biomaterials, 2011. 32(13): p. 3413-22.
9. Miller, E.D., et al., *Dose-dependent cell growth in response to concentration modulated patterns of FGF-2 printed on fibrin.* Biomaterials, 2006. 27(10): p. 2213-21.
10. Miller, E.D., et al., *Spatially directed guidance of stem cell population migration by immobilized patterns of growth factors.* Biomaterials, 2011. 32(11): p. 2775-85.
11. Miller, E.D., et al., *Inkjet printing of growth factor concentration gradients and combinatorial arrays immobilized on biologically-relevant substrates.* Comb Chem High Throughput Screen, 2009. 12(6): p. 604-18.
12. Phillippi, J.A., et al., *Microenvironments engineered by inkjet bioprinting spatially direct adult stem cells toward muscle- and bone-like subpopulations.* Stem Cells, 2008. 26(1): p. 127-34.
13. Hinds, S., et al., *The role of extracellular matrix composition in structure and function of bioengineered skeletal muscle.* Biomaterials, 2011. 32(14): p. 3575-83.
14. Shimizu, K., H. Fujita, and E. Nagamori, *Alignment of skeletal muscle myoblasts and myotubes using linear micropatterned surfaces ground with abrasives.* Biotechnol Bioeng, 2009. 103(3): p. 631-8.
15. Vye, M.V., *The ultrastructure of striated muscle.* Ann Clin Lab Sci, 1976. 6(2): p. 142-51.
16. Gigante, A., et al., *Collagen I membranes for tendon repair: effect of collagen fiber orientation on cell behavior.* J Orthop Res, 2009. 27(6): p. 826-32.
17. Kerschnitzki, M., et al., *The organization of the osteocyte network mirrors the extracellular matrix orientation in bone.* J Struct Biol, 2011. 173(2): p. 303-11.
18. Ma, J., X. He, and E. Jabbari, *Osteogenic differentiation of marrow stromal cells on random and aligned electrospun poly(L-lactide) nanofibers.* Ann Biomed Eng, 2011. 39(1): p. 14-25.
19. Moffat, K.L., et al., *Characterization of the structure-function relationship at the ligament-to-bone interface.* Proc Natl Acad Sci U S A, 2008. 105(23): p. 7947-52.
20. Moffat, K.L., et al., *Orthopedic interface tissue engineering for the biological fixation of soft tissue grafts.* Clin Sports Med, 2009. 28(1): p. 157-76.

21. Erisken, C., D.M. Kalyon, and H. Wang, *Functionally graded electrospun polycaprolactone and beta-tricalcium phosphate nanocomposites for tissue engineering applications.* Biomaterials, 2008. 29(30): p. 4065-73.
22. Munoz-Pinto, D.J., et al., *Inorganic-organic hybrid scaffolds for osteochondral regeneration.* J Biomed Mater Res A, 2010. 94(1): p. 112-21.
23. Sahoo, S., et al., *Growth factor delivery through electrospun nanofibers in scaffolds for tissue engineering applications.* J Biomed Mater Res A, 2010. 93(4): p. 1539-50.
24. Sahoo, S., S.L. Toh, and J.C. Goh, *A bFGF-releasing silk/PLGA-based biohybrid scaffold for ligament/tendon tissue engineering using mesenchymal progenitor cells.* Biomaterials, 2010. 31(11): p. 2990-8.
25. Shi, J., et al., *Incorporating protein gradient into electrospun nanofibers as scaffolds for tissue engineering.* ACS Appl Mater Interfaces, 2010. 2(4): p. 1025-30.
26. Wang, F., et al., *Fabrication and characterization of prosurvival growth factor releasing, anisotropic scaffolds for enhanced mesenchymal stem cell survival/growth and orientation.* Biomacromolecules, 2009. 10(9): p. 2609-18.
27. Jose, M.V., et al., *Aligned bioactive multi-component nanofibrous nanocomposite scaffolds for bone tissue engineering.* Macromol Biosci, 2010. 10(4): p. 433-44.
28. Moffat, K.L., et al., *Novel nanofiber-based scaffold for rotator cuff repair and augmentation.* Tissue Eng Part A, 2009. 15(1): p. 115-26.
29. Zhao, Y., et al., *Fabrication of skeletal muscle constructs by topographic activation of cell alignment.* Biotechnol Bioeng, 2009. 102(2): p. 624-31.
30. Nain, A.S., et al., *Dry Spinning based Spinneret based Tunable Engineered Parameters (STEP) Technique for Controlled and Aligned Deposition of Polymeric Nanofibers.* Macromol Rapid Commun., 2009. 30(16): p. 6.
31. Nain, A.S., et al., *Control of cell behavior by aligned micro/nanofibrous biomaterial scaffolds fabricated by spinneret-based tunable engineered parameters (STEP) technique.* Small, 2008. 4(8): p. 1153-9.
32. Miller, E., *Inkjet Printing of Solid-Phase Growth Factor Patterns to Direct Cell Fate*, in *Biomedical Engineering*. 2007, Carnegie Mellon University: Pittsburgh. p. 349.
33. Engler, A.J., et al., *Matrix elasticity directs stem cell lineage specification.* Cell, 2006. 126(4): p. 677-89.
34. Grosberg, A., et al., *Self-organization of muscle cell structure and function.* PLoS Comput Biol, 2011. 7(2): p. e1001088.
35. Liu, X., et al., *Guidance of neurite outgrowth on aligned electrospun polypyrrole/poly(styrene-beta-isobutylene-beta-styrene) fiber platforms.* J Biomed Mater Res A, 2010. 94(4): p. 1004-11.
36. Tee, S.Y., et al., *Cell shape and substrate rigidity both regulate cell stiffness.* Biophys J, 2011. 100(5): p. L25-7.
37. Zemel, A., et al., *Cell shape, spreading symmetry and the polarization of stress-fibers in cells.* J Phys Condens Matter, 2011. 22(19): p. 194110.
38. Breen, A., T. O'Brien, and A. Pandit, *Fibrin as a delivery system for therapeutic drugs and biomolecules.* Tissue Eng Part B Rev, 2009. 15(2): p. 201-14.

39. Brent, A.E. and C.J. Tabin, *FGF acts directly on the somitic tendon progenitors through the Ets transcription factors Pea3 and Erm to regulate scleraxis expression.* Development, 2004. 131(16): p. 3885-96.
40. Cserjesi, P., et al., *Scleraxis: a basic helix-loop-helix protein that prefigures skeletal formation during mouse embryogenesis.* Development, 1995. 121(4): p. 1099-110.
41. Bader, D., T. Masaki, and D.A. Fischman, *Immunochemical analysis of myosin heavy chain during avian myogenesis in vivo and in vitro.* J Cell Biol, 1982. 95(3): p. 763-70.
42. Murchison, N.D., et al., *Regulation of tendon differentiation by scleraxis distinguishes force-transmitting tendons from muscle-anchoring tendons.* Development, 2007. 134(14): p. 2697-708.
43. Perez, A.V., et al., *Scleraxis (Scx) directs lacZ expression in tendon of transgenic mice.* Mech Dev, 2003. 120(10): p. 1153-63.
44. Pryce, B.A., et al., *Recruitment and maintenance of tendon progenitors by TGF{beta} signaling are essential for tendon formation.* Development, 2009. 136(8): p. 1351-61.
45. Schweitzer, R., et al., *Analysis of the tendon cell fate using Scleraxis, a specific marker for tendons and ligaments.* Development, 2001. 128(19): p. 3855-66.
46. Henrichsen, E., *Alkaline phosphatase in osteoblasts and fibroblasts cultivated in vitro.* Exp Cell Res, 1956. 11(1): p. 115-27.
47. Xu, P.X., et al., *Mouse Eya genes are expressed during limb tendon development and encode a transcriptional activation function.* Proc Natl Acad Sci U S A, 1997. 94(22): p. 11974-9.
48. Boucher, C.A., et al., *Cloning of the human SIX1 gene and its assignment to chromosome 14.* Genomics, 1996. 33(1): p. 140-2.
49. Anderson, D.M., et al., *Mohawk is a novel homeobox gene expressed in the developing mouse embryo.* Dev Dyn, 2006. 235(3): p. 792-801.
50. Liu, W., et al., *The atypical homeodomain transcription factor Mohawk controls tendon morphogenesis.* Mol Cell Biol, 2010. 30(20): p. 4797-807.
51. Shukunami, C., et al., *Scleraxis positively regulates the expression of tenomodulin, a differentiation marker of tenocytes.* Dev Biol, 2006. 298(1): p. 234-47.
52. Docheva, D., et al., *Tenomodulin is necessary for tenocyte proliferation and tendon maturation.* Mol Cell Biol, 2005. 25(2): p. 699-705.
53. Scott, A., et al., *Scleraxis expression is coordinately regulated in a murine model of patellar tendon injury.* J Orthop Res, 2011. 29(2): p. 289-96.
54. Hoffmann, A., et al., *Neotendon formation induced by manipulation of the Smad8 signalling pathway in mesenchymal stem cells.* J Clin Invest, 2006. 116(4): p. 940-52.

CHAPTER 4: *IN VITRO* AND *IN VIVO* EFFECT OF PRINTED BIOCHEMICAL FACTOR PATTERNS ON DERMAMATRIX SCAFFOLDS

4.1 ABSTRACT

In previous chapters, the capability to engineer microenvironmental cues such as persistent growth factor (GF) patterns to direct a stem cell population toward multiple fates, simultaneously, in spatially defined regions was demonstrated *in vitro* on fibrin-coated glass coverslips and ECM-coated sub-micron Spinneret-based Tunable Engineered Parameters (STEP) fibers. This chapter serves as a preliminary exploration of cell behavioral responses to inkjet-printed patterns of biochemical factors (BFs; which include GFs and other signaling molecules) immobilized onto an acellularised human dermis scaffold known as DermaMatrix *in vitro* and *in vivo* for the purpose of patterning ectopic muscle-tendon-bone (MTB) units and periosteum-bone-bone marrow (PBM) units. Initial characterization of DermaMatrix indicated that the DermaMatrix scaffold contained a porous internal structure, supported mouse C2C12 myoblast attachment and subsequent differentiation into myotubes. Concentration modulated patterns of BMP-2 were created with our bio-inkjet printer and demonstrated a dose-dependent increase in alkaline phosphatase (ALP) staining in register to printed patterns. Additionally, using rabbit muscle-derived cells, FGF-2 was identified as a periosteum-promoting GF by immunofluorescence staining for the periosteum marker, Periostin. Subsequent *in vivo* experiments were performed using printed DermaMatrix scaffolds containing BMP-2, FGF-2, GDF-7, IGF-2, Noggin, PDGF-BB and SDF-1β to pattern ectopic MTB units and PBM units with and without mouse primary Muscle-Derived Stem Cells (MDSCs). Printed, flat DermaMatrix scaffolds showed spatial control of bone formation but little-to-no tendon or muscle tissue, highlighting the need to identify tendon- and muscle-promoting BFs and the optimal dosage required for ectopic tissue patterning. Printed, rolled DermaMatrix scaffolds showed some cell infiltration and blood vessel formation at the scaffold periphery but little-to-no

cell infiltration in the middle of the scaffold. This work illustrates the potential for bio-printed DermaMatrix to be employed as a suitable scaffold for spatial control of multi-phenotype differentiation *in vivo*.

4.2 INTRODUCTION

As described in Chapter 1, the development and repair of musculoskeletal tissue involves the spatial control of stem cell differentiation toward multiple cell types such as osteoblasts, tenocytes and myocytes [1] and is regulated by physical and biochemical microenvironmental cues imparted by the interactions of cells with their extracellular matrix (ECM), neighboring cells, and secreted local and systemic signaling molecules (Biochemical Factors; BFs), including growth factors (GFs) [1, 2]. The capability to pattern muscle-tendon-bone (MTB) units and periosteum-bone-bone marrow (PBM) units *in vivo* using immobilized BFs is an important and logical consideration for regenerating damaged musculoskeletal tissues.

As mentioned in Chapter 1, MTB units are physiologically relevant tissue units that enable body movement through the generation and subsequent transfer of mechanical force from soft (muscle) tissue to rigid (bone) tissue while minimizing stress damage [3-5]. As such, the capability to engineer a MTB *in vivo* may present an attractive and clinically-relevant option for treating diseases and trauma of the musculoskeletal system such as sports injuries. Similarly, a PBM unit recapitulates the overall architecture and composition of long bone – the outer periosteal layer provides an attachment site for tendon and ligaments, delivers nutrients and removes waste, the middle bone layer consists of mineralized collagen and bone cells, and the inner bone marrow layer houses elements of the hematopoietic system. The capability to engineer a PBM unit *in vivo* may provide a means of accelerating wound healing in severe bone

trauma. Indeed, studies have shown that both periosteum and bone marrow tissues play critical roles in bone healing. For example, it has been shown that transplantation of vascularized periosteum tissue alone is able to promote bone regeneration in bone defects in canines and rabbits [6-8]. In addition, other studies have suggested that skeletal stem cells such as mesenchymal stem cells may have a perivascular origin [9-13]. The intimate relationship between osteoprogenitor cells and hematopoietic progenitor cells in the bone marrow microenvironment has been highlighted by studies which show that osteoblastic cells can regulate the size of the hematopoietic niche through Notch signaling [10] as well as by other studies that demonstrate that bone formation often accompanies bone marrow transplantation and vice versa [9, 10, 13-15].

Previous work in Chapters 2 and 3 demonstrate spatial control of cell differentiation *in vitro* on ECM-based substrates such as fibrin-coated glass coverslips and ECM-coated sub-micron Spinneret-based Tunable Engineered Parameters (STEP) fibers. This chapter seeks to address spatial control of cell differentiation *in vivo* using an acellularised human dermis scaffold known as DermaMatrix. Prior to animal studies, some preliminary Scanning Electron Microscopy (SEM) and *in vitro* studies were performed to characterize DermaMatrix scaffold structure and determine the suitability of using bio-printed DermaMatrix *in vivo*. For animal studies, putative periosteum-promoting GFs such as TGF-β1 and FGF-2 were identified from the literature and screened using immunofluorescence staining for the periosteum marker, Periostin [16] in rabbit muscle-derived cells. Periostin is an extracellular protein that is highly expressed in the periosteum and periodontal ligament as well as collagen-rich connective tissue such as skin and healing wounds [17-20]. To pattern bone tissue, BMP-2 was used as it has been previously demonstrated to induce osteogenesis *in vitro* [21-24] and *in vivo* [25]. To pattern bone marrow

tissue, a combination of SDF-1β, PDGF-BB and Noggin was employed since SDF-1 is a chemotactic GF expressed at high levels in the bone marrow and responsible for the homing and engraftment of hematopoietic stem cells [26] while PDGF has been shown to enhance blood cell production [27]. Noggin was used to suppress bone formation. To pattern muscle tissue, a combination of IGF-2 and Noggin was used as IGF-2 has been demonstrated to enhance myogenesis *in vitro* (Figure 2.13) while Noggin has been shown to inhibit bone formation *in vivo* [25]. To pattern tendon tissue, GDF-7 was used as it has been previously shown that GDF-7 can ectopically induce tendon differentiation *in vivo* [28]. Printed constructs were seeded with or without MDSCs and placed subcutaneously in mice for six weeks.

4.3 MATERIALS AND METHODS

4.3.1 Cell Culture

Multipotent mouse C2C12 cells (ATTC, Manassas, VA) were grown in Dulbecco's Modified Eagle's Media (DMEM; Invitrogen, Carlsbad, CA), 10% fetal bovine serum (Invitrogen, Carlsbad, CA) and 1% penicillin-streptomycin (PS; Invitrogen, Carlsbad, CA). Multipotent MDSCs were isolated from primary mouse gastrocnemius muscle biopsies following a modified preplate technique [29] and were grown in DMEM (high glucose), 10% horse serum (HS; Invitrogen, Carlsbad, CA), 10% FBS, 0.5% Chick Embryo Extract (Accurate Chemical Co, Westbury, NY) as previously described [29, 30]. Muscle-derived cells were isolated from muscle biopsies of 10-day old New Zealand White Rabbits (*Oryctolagus cuniculus*) using an established procedure obtained from our collaborators at the Children's Hospital of Pittsburgh (University of Pittsburgh Medical Center, Pittsburgh, PA). Briefly, approximately 2 mm x 6 mm x 2 mm of muscle tissue was obtained while taking care to avoid bone cartilage, blood vessel and fur. The muscle tissue was dissected into small pieces and placed in ice-cold PBS and kept on ice.

Subsequently, the muscle tissue was centrifuged at 2000 revolutions per min (rpm) for 5 min, aspirated to remove the PBS and incubated in 3 – 5 mL of 0.2% Collagenase XI (Sigma-Aldrich, St. Louis, MO) at 37ºC, 175rpm for 60 min. Following this, the muscle tissue was centrifuged at 2000 rpm for 5 min, aspirated to remove the Collagenase XI and resuspended in 3 – 5 mL of 2.4 U/mL Dispase (Sigma-Aldrich, St. Louis, MO) at 37ºC, 175rpm for 45 min. Next, the muscle tissue was centrifuged at 2000 rpm for 5 min, aspirated to remove the Dispase and resuspended in 3 – 5 mL of 0.1% Trypsin (Invitrogen, Carlsbad, CA) in Hank's Buffered Salt Solution (Invitrogen, Carlsbad, CA) at 37ºC, 175rpm for 30 min. Lastly, the muscle tissue was centrifuged at 2000 rpm for 5 min, aspirated to remove the Trypsin and resuspended in 10 mL of DMEM, 10% fetal bovine serum and 1% PS in a T75cm^2 flask. A total of two isolates from one female and one male rabbit were used in these experiments. All cells were kept at 37^{o}C, 5% CO_2 in a humidified incubator.

Both C2C12 cells and MDSCs were seeded at a density of 30 x 10^4 cells/scaffold in an adequately sufficient volume of media for covering the entire surface of the scaffold. The cells were allowed to attach for 15 – 60 min before flooding the tissue culture vessel with media. Muscle-derived cells were seeded at a density of 30 x 10^4 cells/fibrin-coated coverslip. Cells were grown in normal growth media (Proliferation media) as indicated above. Where necessary, a final concentration of 1 µg/mL Aprotinin (Sigma, St. Louis, MO) was added to the cell cultures to minimize fibrin degradation.

4.3.2 Biochemical Factor Preparation and Use

Recombinant human BMP-2 (Medtronic, Minneapolis, MN), FGF-2 (Peprotech, Rockyhill, NJ), growth and differentiation factor-7 (GDF-7/BMP-12, BioVision Inc., San Francisco, CA),

insulin-like growth factor-2 (IGF-2; Austral Biologicals, San Ramon, CA), noggin (Peprotech, Rockyhill, NJ), platelet-derived growth factor-BB (PDGF-BB, Peprotech, Rockyhill, NJ), stromal derived factor-1β (SDF1β; CXCL12, Peprotech, Rockyhill, NJ) and transforming growth factor-β (TGF-β; R&D Systems, Minneapolis, MN) were reconstituted according to manufacturer's instructions to 1-2 mg/mL, aliquoted and stored at -80^{o}C. Prior to use, BFs were freshly diluted to the desired concentration in 10 mM sodium phosphate, pH 7.4.

4.3.3 Preparation of Fibrin Coated Coverslips

Homogenous fibrin films were prepared essentially as described by Campbell *et al.*, 2005 [31]. Briefly, 18 x 18 mm epoxy-silanized glass coverslips (Thermo Fisher Scientific, Waltham, MA) were coated with 0.1 mg/mL fibrinogen (Aventis Behring, King of Prussia, PA or American Diagnostica Inc., Stanford, CT) and converted into fibrin by incubating coverslips in 4 U/mL thrombin (Enzyme Research Laboratories, South Bend, IN). Coverslips were then washed with phosphate buffered saline (PBS) and sterile deionized water before air-drying in a laminar flow hood. The thickness of the fibrin films was previously estimated to be approximately 20 nm [31].

4.3.4 Preparation and Characterization of DermaMatrix Scaffold Structure

Human Acellular DermaMatrix Dermis scaffolds (Synthes Inc., West Chester, PA) were cut to the required dimensions with a scissors or a biopsy punch (Acuderm Inc., Fort Lauderdale, FL). The structure and porosity of the DermaMatrix scaffold was characterized by SEM. DermaMatrix samples were gold-coated using a Pelco SC-6 sputter coater (Ted Pella, Inc., Redding, CA) and examined using a Hitachi 2460N Scanning Electron Microscope (Hitachi High Technologies America, Inc., Schaumburg, IL). Images were obtained using Quartz PCI Image software.

4.3.5 Biochemical Factor Printing

Prior to printing, BFs were freshly diluted to the desired concentration in 10 mM sodium phosphate, pH 7.4. Prior to filling the inkjet with the BF, the printhead was sterilized by rinsing with 70% ethanol followed by sterile deionized water. The bio-ink, consisting of 100-200 µg/ml BF was loaded into the printhead, and printed onto DermaMatrix in a similar manner as previously described for fibrin-coated glass coverslips [23, 31]. The concentration of inkjetted BFs can be modulated by overprinting, which is achieved by varying the number of times a BF is deposited in the same (x,y) location. In the case of hand-printed BF patterns, 1-2 µL of a 100 µg/mL BF solution was pipetted onto a fibrin-coated glass coverslip instead and a diamond scribe pen was used to mark the droplet perimeter after it had been allowed to air-dry for 1 h at 37^{o}C. After printing, DermaMatrix scaffolds or hand-printed fibrin-coated glass coverslips were incubated in PBS for 5 min followed by serum-free DMEM with 1% PS overnight at 37°C, 5% CO_2 to wash off unbound BF prior to cell seeding or animal surgery.

4.3.6 Printed Scaffolds

DermaMatrix scaffolds were printed with BFs as shown in Figure 4.1 and Table 4.1. For Muscle-Bone and Tendon 1-Tendon 2 patterns, the concentration of BFs and number of overprints (OPs) were adjusted such that a similar mass of BF(s) thought to be responsible for inducing a particular tissue type were deposited between the Muscle and Bone patterns or Tendon 1 and Tendon 2 patterns. Likewise, the concentration of BFs and number of OPs for the Bone Marrow-Bone-Periosteum scaffolds were adjusted such that a similar mass of BF(s) were deposited between the Bone Marrow, Bone and Periosteum patterns.

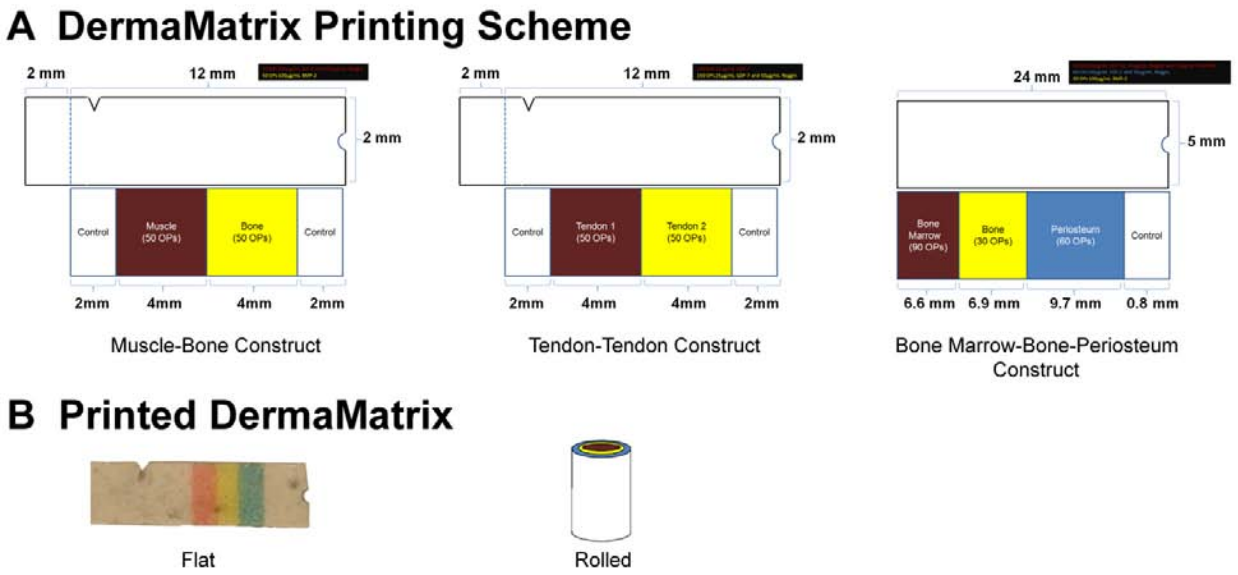

Figure 4.1. Printing schematic for DermaMatrix scaffolds. **A.** Printing scheme for DermaMatrix scaffolds. **B.** Types of DermaMatrix scaffolds used. The size of each individual printed pattern, the concentration of the growth factors and the number of overprints (OPs) used for each construct are indicated as shown.

Table 4.1 Biochemical Factors for Patterning Ectopic MTB and PBM units.

Tissue	Growth Factor(s)	Rationale	References
Muscle	IGF-2	Enhances myogenesis *in vitro*.	Figure 2.13
	Noggin	Prevents bone formation.	Cooper *et al.*, 2010 [25]
Tendon	GDF-7	Induces ectopic tendon in a subcutaneous rat model.	Wolfman *et al.*, 1997 [28]
	Noggin	Prevent bone formation since GDF-7 mice have altered bone structure.	Maloul *et al.*, 2006 [32]
Bone	BMP-2	BMP-2 is a potent osteogenic stimulator *in vitro* and *in vivo*.	Cooper *et al.*, 2010; Ker *et al.*, 2011a, Ker *et al.*, 2011b, Miller *et al.*, 2007, Miller *et al.*, 2009, Phillippi *et al.*, 2008 [21-25, 33]
Periosteum	TGF-β	Induces Periostin expression.	Horiuchi *et al.*, 1999 [16]
	FGF-2	Induces Periostin expression.	Dangaria *et al.*, 2009 [34]
	Noggin	Prevents bone formation.	Cooper *et al.*, 2010 [25]
Bone Marrow	SDF-1β	Chemotactic GF expressed at high levels in the bone marrow and responsible for the homing and engraftment of hematopoietic stem cells.	Sharma *et al.*, 2011 [26]
	PDGF-BB	Enhances blood cell production.	Yang *et al.*, 2001 [27]
	Noggin	Prevents bone formation.	Cooper *et al.*, 2010 [25]

4.3.7 Animal Surgery

6 –18 month old C56BL/6 male and female mice (Jackson, Bar Harbor, ME) were used in this study. The animals were housed in a standard animal facility and all experiments involving animal use were performed in accordance with the Institutional Animal Care and Use Committee. The mice were anesthetized using isoflurane delivered by a gas apparatus (SurgiVet, Dublin, OH) and the fur shaved and cleaned with 70% ethanol prior to surgery. Under sterile conditions, an incision was made in the skin and skin pockets were made on either side of the mouse using a pair of surgical scissors. One scaffold was placed on either side of the mouse onto the muscle layer. Where necessary, scaffolds were sutured in place with 4-0 Ethilon silk and 5-0 Ethilon nylon sutures (Ethicon Inc., Cincinnati, OH). Subsequently, the skin was sutured closed to ensure that no subcutaneous tissue was exposed. Mice were placed to one side to ease breathing and returned to its cage upon waking from anesthesia.

4.3.8 DermaMatrix Harvesting

6 weeks post-surgery, the mice were euthanized and the DermaMatrix scaffolds as well as surrounding tissue were harvested and fixed in 10% neutral buffered formalin overnight. Where necessary, tissue samples were decalcified in 10% EDTA solution prior to paraffin embedding for subsequent histological and immunofluorescence analysis.

4.3.9 Sample Preparation for Histology

The tissue samples were processed by the Thomas E. Starzl Transplantation Institute Histology Core Facility (University of Pittsburgh, Pittsburgh, PA) on an automated tissue processor. Briefly, the samples were first removed from the fixative and placed through a series of graded alchohols, cleared through xylene and subsequently infiltrated with paraffin on the processor

with vacuum. Upon removal from the automated processor, tissues were hand-embedded in paraffin. Once the paraffin blocks solidified, they were faced off, placed on ice and were cut using a microtome to generate 4 µm sections. These tissue sections were floated on a water bath and then collected onto positively charged slides which were baked in a 60 ^{o}C oven for 1 h.

4.3.10 Immunofluorescence staining

For immunofluorescence staining of C2C12-seeded DermaMatrix samples or muscle-derived rabbit cell-seeded fibrin-coated glass co, cells were washed in PBS, fixed in methanol for 5 min, air-dried and blocked with 10% donkey serum (Jackson Immunoresearch, West Gove, PA) for 20 min at RT. For mouse-on-mouse staining an additional blocking step was performed by incubating cells with 100 µg/mL donkey anti-mouse FAB (Jackson Immunoresearch, West Gove, PA) for 1 h at RT. Cells were then rinsed with wash buffer (PBS, 0.1% BSA) and incubated with primary antibody – mouse anti-myosin MF20 (1 µg/mL; Developmental Studies Hybridoma Bank, Iowa City, Iowa) or goat anti-Periostin (4 µg/mL; Santa Cruz Biotechnology Inc, Santa Cruz, CA) overnight at 4^{o}C. Cells were then rinsed three times with wash buffer (5 min each) and incubated with secondary antibodies – donkey anti-mouse Dylight 488 nm or donkey anti-goat Dylight 649 nm for 1 h at RT (15 µg/mL each; Jackson Immunoresearch, West Gove, PA). Lastly, cells were rinsed five times with wash buffer (5 min each) and imaged using a Zeiss Axiovert 200M microscope (Carl Zeiss Microimaging, Thornwood, NY) equipped with a Colibri LED light source.

For immunofluorescence staining of histological sections, this procedure was performed by collaborators at the Stem Cell Research Center (University of Pittsburgh, Pittsburgh, PA). Slides were deparaffinized and antigen retrieval was performed by incubating slides in 10 mM sodium

citrate, 0.05% Tween 20, pH 6.0 at 95 – 98 ^{o}C for 20min. Slides were then air-dried and stained for e-Myosin Heavy Chain. Briefly, slides were blocked with serum and a mouse-on-mouse staining kit, incubated with anti e-Myosin Heavy Chain (1:50 dilution) and subsequently a secondary link antibody (Biotin-Horse Anti-Mouse) followed by Strepavidin-Alexa Fluor 594. In between, slides were rinsed with Phosphate Buffered Saline (PBS). Slides were imaged using a Zeiss Axiovert 200M microscope (Carl Zeiss Microimaging, Thornwood, NY) equipped with a Colibri LED light source.

4.3.11 Histological Staining

Slides were stained for hematoxylin and eosin according to the manufacturer's instructions. Staining for the osteoblast marker Alkaline Phosphatase (ALP) was performed using an ALP staining kit (Kit 86C, Sigma Aldrich, St. Louis, MO) according to the manufacturer's instructions. Where necessary, slides were imaged using a Zeiss Axiovert 200M microscope (Carl Zeiss Microimaging, Thornwood, NY).

4.3.12 Statistical Analysis

For analysis of ALP stained images, one-way analysis of variance followed by Tukey's Honestly Significant–Difference post hoc test using SYSTAT 9 software (Systat Software Inc., Richmond, CA) was performed to determine significance among treatment groups. A p value ≤ 0.05 was considered statistically significant.

4.4 RESULTS

4.4.1 Characterization of DermaMatrix Scaffolds

Figure 4.2 shows an SEM image of an 8 mm diameter circular DermaMatrix scaffold. The top view indicates that the surface of the DermaMatrix scaffold is relatively fibrous with several

pore-like structures and the cross-sectional view indicates that the interior of the DermaMatrix is relatively porous (Figure 4.2). Similar to polystyrene Petri dishes (Figure 3.3), DermaMatrix scaffolds can support the attachment of C2C12 cells and result in the spontaneously formation of elongated myotubes when grown under highly cell confluent conditions (Figure 4.3)

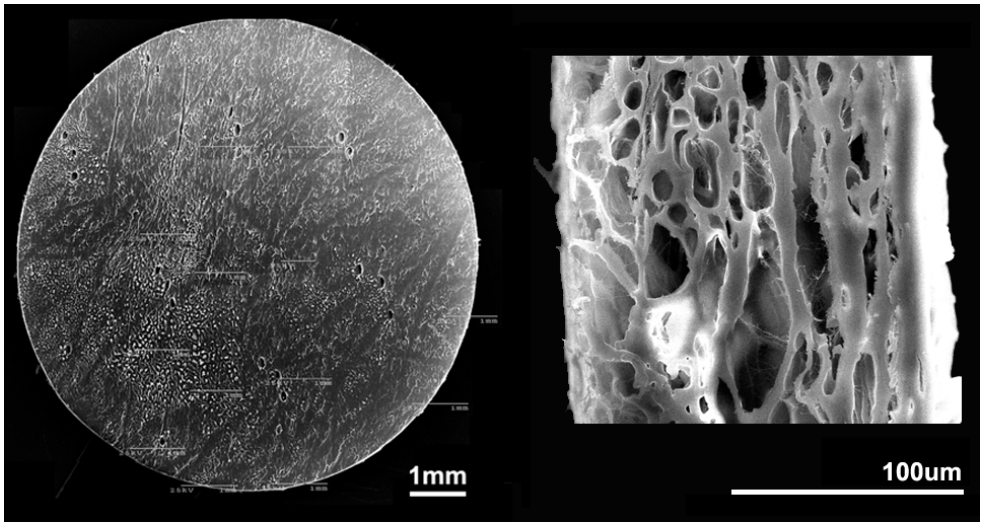

Figure 4.2. SEM image of a circular DermaMatrix scaffold (8 mm diameter). The top view (left) of the side and cross-section (right) of the DermaMatrix are shown. Scale bars as indicated.

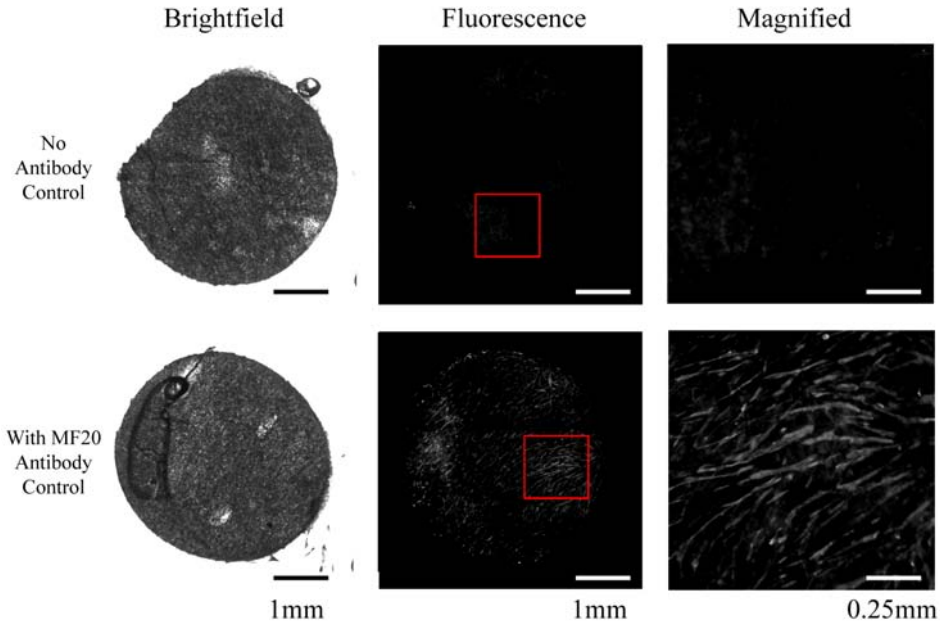

Figure 4.3. Effect of DermaMatrix scaffold on MF20 expression in C2C12 cells. DermaMatrix scaffolds supported C2C12 cell attachment and under confluent conditions, promoted myotube formation. Scale bars as indicated.

4.4.2 Effect of DermaMatrix Patterned with BMP-2 on Osteoblast Differentiation

Having characterized the DermaMatrix scaffold structure and demonstrated that it could support cell attachment, square patterns of BMP-2 (each measuring 0.5 mm x 0.5 mm; 100 µg/mL BMP-2) were inkjet printed onto a 13.5 mm x 13.5 mm Dermamatrix scaffold with 10, 20, 30, 40 and 50 OPs to determine if solid-phase GF-patterned DermaMatrix can spatially direct osteoblast differentiation in a dose-dependent manner (Figure 4.4A). Our previous studies have shown that the surface concentration of GF that is deposited can be modulated by overprinting and that such GF patterns can persist for up to 144 hours under standard cell culture conditions [23-25, 35]. Under proliferation conditions (High serum), C2C12 cells showed upregulation of ALP in response to solid-phase patterning of BMP-2 in a dose-dependent manner (Figure 4.4B, C). Printed BMP-2 patterns with 10, 20, 30, 40 and 50 OPs overprints showed an increase in ALP expression relative to negative control/non-printed regions ($p = 0.015$ for 10 OPs, $p < 0.001$ for 20, 30, 40 and 50 OPs; Figure 4B, C). In addition, printed BMP-2 patterns with 30, 40 and 50 OPs showed an increase in ALP expression relative to 10 OPs ($p = 0.011$ for 30 OPs, $p = 0.001$ for 40 OPs and $p < 0.001$ for 50 OPs; Figure 4B, C). Furthermore, printed BMP-2 patterns with 50 OPs showed an increase in ALP expression relative to 20 OPs ($p = 0.007$; Figure 4B, C). ALP activity did not level off or reach a steady state even at 50 OPs, indicating that BMP-2 binding sites within the DermaMatrix scaffold were not fully saturated (Figure 4.4C). Thus, solid-phase patterning of BMP-2 on DermaMatrix scaffold can spatially control osteoblast differentiation in a dose-dependent manner (Figure 4.4).

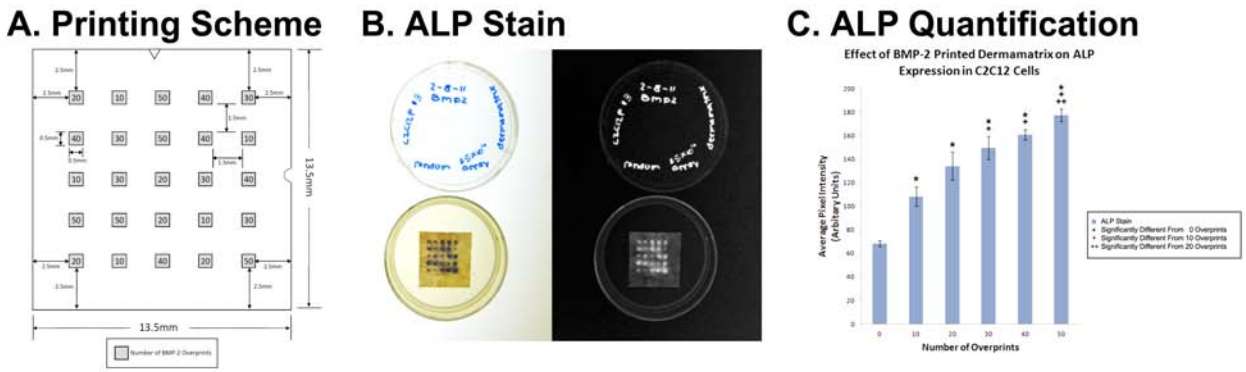

Figure 4.4. Effect of printed BMP-2 patterns on ALP expression in C2C12 cells (DermaMatrix scaffold). **A**. Printing scheme for BMP-2 patterned DermaMatrix scaffold. 10, 20, 30, 40, and 50 Overprints of 100 µg/mL BMP-2 was printed onto a 13.5 mm x 13.5 mm DermaMatrix scaffold. **B-C. I**nkjet printed patterns of BMP-2 resulted in upregulation of the osteoblast marker ALP in a dose-dependent manner. ALP stained images of BMP-2 patterned DermaMatrix scaffold indicate that C2C12 cells show a dose-dependent increase in ALP expression after 4 days in proliferation media $*$, Significantly different from control or non-printed regions; $p \leq 0.05$. +, Significantly different from 10 Overprints; $p \leq 0.05$. ++, Significantly different from 20 Overprints; $p \leq 0.05$.

4.4.3 Effect of Fibrin-Coated Glass Coverslips Patterned with FGF-2 on Periostin Expression in Muscle-Derived Cells

To identify periosteum-promoting GFs, hand-printed patterns of GFs were identified from the literature and screened for their ability to upregulate the periosteum marker, Periostin. TGF-β1 was found not to promote Periostin expression at the concentrations tested (Data not shown) whereas FGF-2 was found to weakly promote Periostin expression in rabbit muscle-derived cells (Figure 4.5).

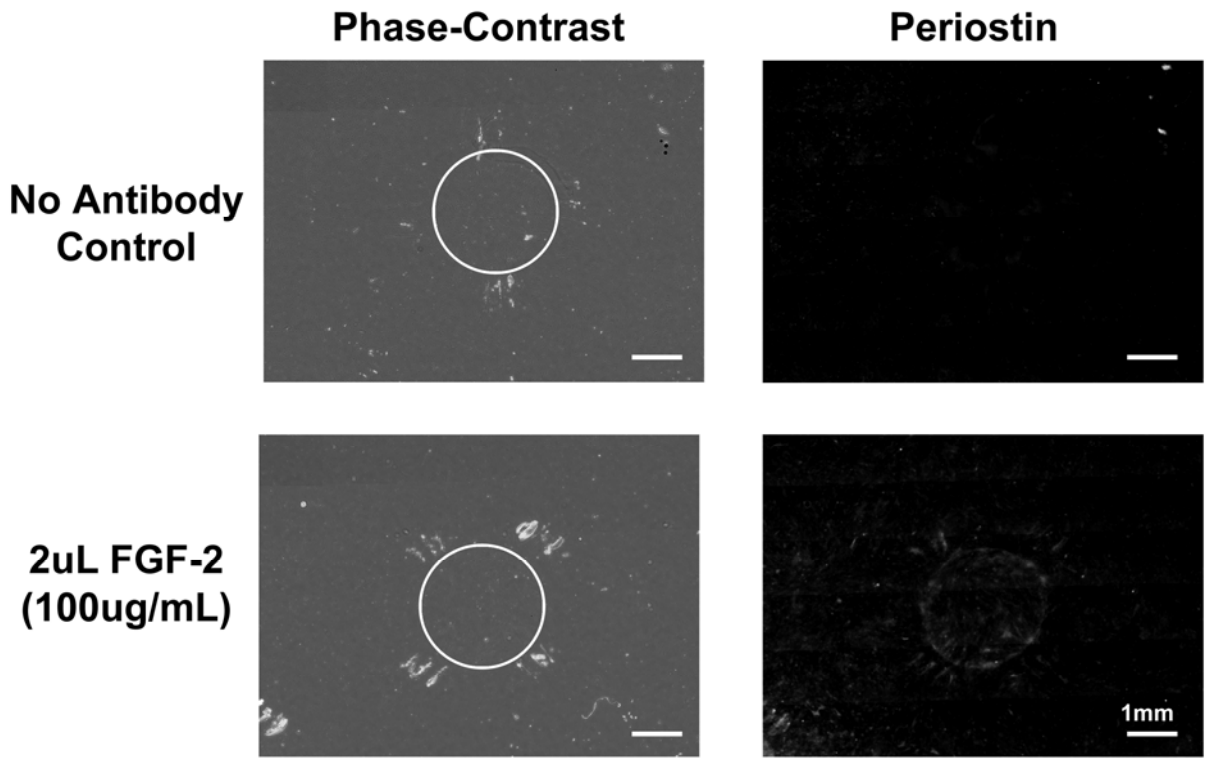

Figure 4.5. Effect of FGF-2 on expression of the periosteum marker Periostin in rabbit muscle-derived cells after 3 days in proliferation media. Periostin was upregulated in the presence of FGF-2. Scale bar is 1000 μm. White circle indicates the boundary of the hand-printed FGF-2 pattern. Parallel lines seen in phase-contrast images denote scratch marks used for identifying the location of hand-printed FGF-2 patterns.

4.4.4 Effect of DermaMatrix Patterned with BMP-2, FGF-2, GDF-7, IGF-2 and Noggin In Vivo

In flat DermaMatrix scaffolds, a high amount of cellular infiltration was observed in scaffolds seeded with and without MDSCs (Figure 4.6B). During surgical implantation of DermaMatrix scaffolds, a silk and nylon suture were each placed on opposing ends of the scaffold, facilitating the fiduciary marking of a particular printed pattern after sample harvesting and histological staining (Figure 4.6A). No ectopic muscle, tendon or bone formation was observed (5/5 DermaMatrix scaffolds) in unprinted DermaMatrix scaffolds (Figure 4.6B, control). Ectopic bone formation was observe in 50% of the printed DermaMatrix scaffolds (5/10 DermaMatrix scaffolds) and these regions correlated with the printed BMP-2 pattern (Figure 4.6B). However, ectopic muscle (0/10 DermaMatrix scaffolds) or tendon (0/5 DermaMatrix scaffolds) tissues

were not observed. Additionally, no differences between MDSC-seeded and non MDSC-seeded scaffolds were observed.

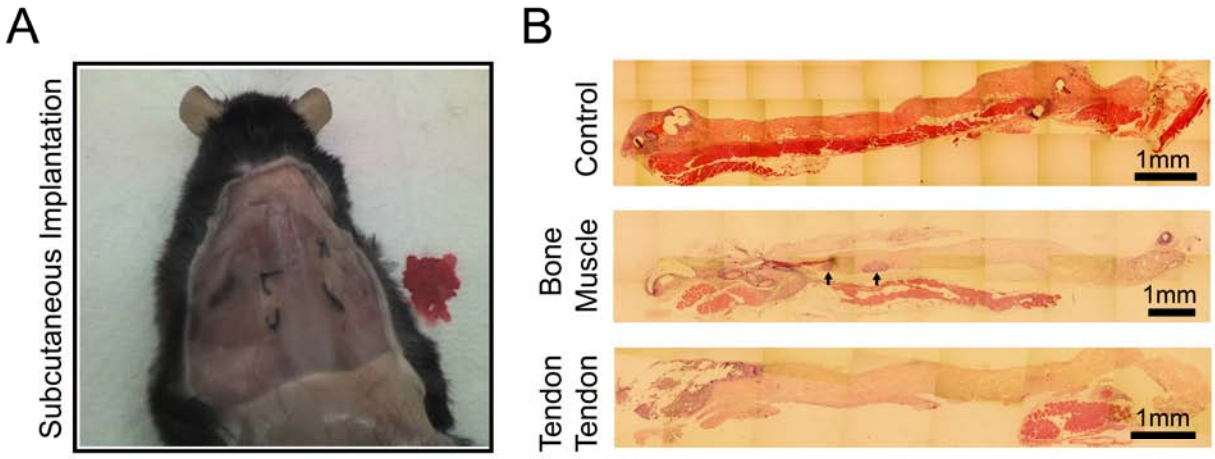

Figure 4.6. Effect of printed BMP-2, FGF-2, GDF-7, IGF-2 and Noggin patterns on DermaMatrix scaffold *In Vivo*. **A.** Subcutaneous implantation of printed DermaMatrix scaffolds. One silk or nylon suture (Black knots) was placed on each end of the DermaMatrix scaffold and anchored onto the superficial back muscles. **B.** Hematoxylin and eosin staining of DermaMatrix scaffold (Longitudinal sections). Ectopic bone formation (Black arrows) was observed within BMP-2 printed regions, indicating spatial control of tissue formation. However, little-to-no ectopic muscle or tendon tissue was observed. Scale bars as indicated.

4.4.5 Effect of DermaMatrix Patterned with BMP-2, FGF-2, PDGF-BB, Noggin and SDF-1β In Vivo

In rolled DermaMatrix scaffolds, three cross-sections corresponding to the top, middle and bottom of the scaffold were obtained (Figure 4.7A). A high amount of cellular infiltration was observed in the top region of the scaffold but little-to-no cellular infiltration was observed in the middle and bottom regions of the scaffold (Figure 4.7B). Little-to-no ectopic periosteum, bone and bone marrow was observed in all constructs (Figure 4.7B, 0/3 DermaMatrix scaffolds).

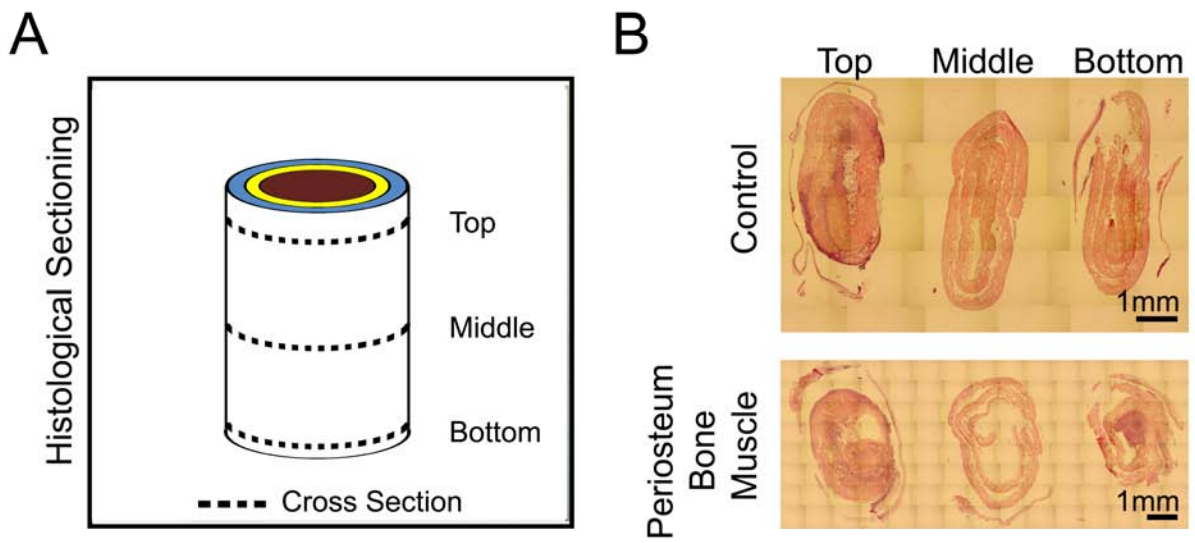

Figure 4.7. Effect of printed BMP-2, FGF-2, PDGF-BB, Noggin and SDF-1β patterns on DermaMatrix scaffold *In Vivo*. **A.** Schematic illustrating histological sectioning of subcutaneously implanted printed DermaMatrix scaffolds. **B.** Hematoxylin and eosin staining of DermaMatrix scaffold cross-sections. High amounts of cell infiltration was observed at the top end of the rolled DermaMatrix scaffold but there was little-to-no cellular infiltration in the middle and bottom ends of the rolled DermaMatrix scaffold. Little-to-no ectopic periosteum, bone or bone-marrow tissue was observed. Scale bar is 1000 μm.

4.5 DISCUSSION

4.5.1 Characterization of DermaMatrix Scaffold

With the long-term goal of engineering biomimetic scaffolds that for musculoskeletal tissue repair, this chapter aims to demonstrate spatial control of MTB units and PBM units *in vivo*. Prior to performing *in vivo* studies, DermaMatrix scaffolds were initially characterized by SEM (Figure 4.2), immunofluorescence staining (Figure 4.3) and ALP staining (Figure 4.4) to determine if scaffolds could support cell attachment and musculoskeletal cell differentiation. DermaMatrix scaffold was determined to be a suitable surrogate material to immobilize BFs onto for *in vivo* studies as its highly internal porous structure supported cell infiltration (Figure 4.2 and Figure 4.5) while the scaffold facilitated both muscle differentiation (Figure 4.3) as well as osteoblast differentiation (Figure 4.4). In addition, DermaMatrix scaffold was capable of

immobilizing BFs at concentrations as high as 50 Ops (Approximately 1.67 μg/cm^2 BMP-2 prior to washing).

4.5.2 Identification of a Periosteum-Promoting GF

To pattern periosteum tissue, an immunofluorescence screen was performed using the periosteum marker, Periostin[16] in rabbit muscle-derived cells. Rabbit muscle-derived cells were chosen as several printed DermaMatrix scaffolds for PBM patterning studies would be surgically implanted in rabbits (Data not shown). Although TGF-β1 did not result in upregulation of Periostin (Data not shown), FGF-2 weakly increased Periostin expression in both male and female muscle-derived rabbit cells (Figure 4.5).

4.5.3 Spatial Control of Tissue Formation In Vivo

To pattern MTB units and PBM units, printed flat and rolled DermaMatrix scaffolds were subcutaneously implanted in mice, respectively (Figure 4.6 and Figure 4.7). Flat DermaMatrix scaffolds supported high amounts of cellular infiltration and printed BMP-2 patterns induced ectopic bone formation (Figure 4.6). However, little-to-no ectopic muscle or tendon was observed, highlighting a need to identify a suitable mixture of BFs (including dosages used) for patterning muscle and tendon tissue (Figure 4.6). Even though ectopic bone formation was patterned, no stark differences were observed at the interface of different printed patterns owing to sporadic and uneven bone formation within printed BMP-2 regions (Figure 4.6). Unlike flat DermaMatrix scaffolds, rolled DermaMatrix scaffolds showed limited amounts of cellular infiltration, indicating that geometry plays an important role (Figure 4.7). Due to limited cellular infiltration, little-to-no ectopic periosteum, bone and bone marrow tissue was observed (Figure 4.7) although other variables such as the choice and dosage of BFs used cannot be ruled out. Due

to the higher dosage of BFs required for ectopic tissue formation, future *in vivo* studies will examine the effect of printed DermaMatrix scaffolds *in situ* (i.e. at non-ectopic sites such as the MTB interface at the Achilles tendon) while rolled DermaMatrix scaffolds will include polyurethane spacers to better facilitate cell infiltration.

4.6 CONCLUSIONS

This chapter characterized the suitability of human acellular dermis (DermaMatrix) as a surrogate material for *in vivo* studies for spatially patterning MTB and PBM units. In addition, FGF-2 was identified as being able to upregulate the periosteum marker Periostin in rabbit muscle-derived cells. *In vivo* studies showed that printed BMP-2 patterns within flat DermaMatrix scaffolds can spatially control ectopic bone formation but further studies are required for patterning muscle and tendon tissue. Rolled DermaMatrix scaffolds showed poor cellular infiltration and little-to-no ectopic periosteum, bone and bone marrow tissue, highlighting a need for scaffold optimization. Future studies will examine the effect of printed BF patterns on DermaMatrix at relevant musculoskeletal interfaces *in situ*.

4.7 ACKNOWLEDGEMENTS

I would like to thank Larry Schultz for assistance with BF printing and Bahar Ahani, Minakshi Poddar, and Burhan Gharaibeh for assistance with immunofluorescence staining. I would also like to thank Dan-Michelle Wang and Adam Kubala for assistance with immunohistochemical staining. This work was supported by NIH grants RO1EB004343 and RO1EB007369 as well as funding from the Pennsylvania Infrastructure Technology Alliance (PITA).

4.8 REFERENCES

1. Scadden, D.T., *The stem-cell niche as an entity of action.* Nature, 2006. 441(7097): p. 1075-9.
2. Nelson, C.M. and M.J. Bissell, *Of extracellular matrix, scaffolds, and signaling: tissue architecture regulates development, homeostasis, and cancer.* Annu Rev Cell Dev Biol, 2006. 22: p. 287-309.
3. Clayton, R.A. and C.M. Court-Brown, *The epidemiology of musculoskeletal tendinous and ligamentous injuries.* Injury, 2008. 39(12): p. 1338-44.
4. Moffat, K.L., et al., *Characterization of the structure-function relationship at the ligament-to-bone interface.* Proc Natl Acad Sci U S A, 2008. 105(23): p. 7947-52.
5. Yang, P.J. and J.S. Temenoff, *Engineering Orthopedic Tissue Interfaces.* Tissue Eng Part B Rev, 2009. 15(2): p. 127-41.
6. Finley, J.M., R.D. Acland, and M.B. Wood, *Revascularized periosteal grafts--a new method to produce functional new bone without bone grafting.* Plast Reconstr Surg, 1978. 61(1): p. 1-6.
7. Liu, J.Y., D. Wang, and H.H. Cheng, *Use of revascularized periosteal allografts for repairing bony defects: an experimental study.* Microsurgery, 1994. 15(2): p. 93-7.
8. Takato, T., K. Harii, and T. Nakatsuka, *Osteogenic capacity of vascularised periosteum: experimental study using rib periosteum in rabbits.* Br J Plast Surg, 1988. 41(5): p. 528-32.
9. Bianco, P., B. Sacchetti, and M. Riminucci, *Osteoprogenitors and the hematopoietic microenvironment.* Best Pract Res Clin Haematol, 2011. 24(1): p. 37-47.
10. Calvi, L.M., et al., *Osteoblastic cells regulate the haematopoietic stem cell niche.* Nature, 2003. 425(6960): p. 841-6.
11. Crisan, M., et al., *Multilineage stem cells in the adult: a perivascular legacy?* Organogenesis, 2011. 7(2): p. 101-4.
12. Crisan, M., et al., *A perivascular origin for mesenchymal stem cells in multiple human organs.* Cell Stem Cell, 2008. 3(3): p. 301-13.
13. Tare, R.S., et al., *Skeletal stem cells: phenotype, biology and environmental niches informing tissue regeneration.* Mol Cell Endocrinol, 2008. 288(1-2): p. 11-21.
14. Friedenstein, A.J., et al., *Heterotopic of bone marrow. Analysis of precursor cells for osteogenic and hematopoietic tissues.* Transplantation, 1968. 6(2): p. 230-47.
15. Friedenstein, A.J., S. Piatetzky, II, and K.V. Petrakova, *Osteogenesis in transplants of bone marrow cells.* J Embryol Exp Morphol, 1966. 16(3): p. 381-90.
16. Horiuchi, K., et al., *Identification and characterization of a novel protein, periostin, with restricted expression to periosteum and periodontal ligament and increased expression by transforming growth factor beta.* J Bone Miner Res, 1999. 14(7): p. 1239-49.
17. Jackson-Boeters, L., W. Wen, and D.W. Hamilton, *Periostin localizes to cells in normal skin, but is associated with the extracellular matrix during wound repair.* J Cell Commun Signal, 2009. 3(2): p. 125-33.
18. Kashima, T.G., et al., *Periostin, a novel marker of intramembranous ossification, is expressed in fibrous dysplasia and in c-Fos-overexpressing bone lesions.* Hum Pathol, 2009. 40(2): p. 226-37.
19. Landis, W.J., et al., *Design and assessment of a tissue-engineered model of human phalanges and a small joint.* Orthod Craniofac Res, 2005. 8(4): p. 303-12.

20. Li, P., et al., *Hypoxia-responsive growth factors upregulate periostin and osteopontin expression via distinct signaling pathways in rat pulmonary arterial smooth muscle cells.* J Appl Physiol, 2004. 97(4): p. 1550-8; discussion 1549.
21. Ker, E.D., et al., *Engineering spatial control of multiple differentiation fates within a stem cell population.* Biomaterials, 2011. 32(13): p. 3413-22.
22. Ker, E.D., et al., *Bioprinting of growth factors onto aligned sub-micron fibrous scaffolds for simultaneous control of cell differentiation and alignment.* Biomaterials, 2011. 32(32): p. 8097-107.
23. Miller, E.D., et al., *Inkjet printing of growth factor concentration gradients and combinatorial arrays immobilized on biologically-relevant substrates.* Comb Chem High Throughput Screen, 2009. 12(6): p. 604-18.
24. Phillippi, J.A., et al., *Microenvironments engineered by inkjet bioprinting spatially direct adult stem cells toward muscle- and bone-like subpopulations.* Stem Cells, 2008. 26(1): p. 127-34.
25. Cooper, G.M., et al., *Inkjet-based biopatterning of bone morphogenetic protein-2 to spatially control calvarial bone formation.* Tissue Eng Part A, 2010. 16(5): p. 1749-59.
26. Sharma, M., et al., *Stromal-derived factor-1/CXCR4 signaling: indispensable role in homing and engraftment of hematopoietic stem cells in bone marrow.* Stem Cells Dev, 2011. 20(6): p. 933-46.
27. Yang, M., et al., *Platelet-derived growth factor enhances granulopoiesis via bone marrow stromal cells.* Int J Hematol, 2001. 73(3): p. 327-34.
28. Wolfman, N.M., et al., *Ectopic induction of tendon and ligament in rats by growth and differentiation factors 5, 6, and 7, members of the TGF-beta gene family.* J Clin Invest, 1997. 100(2): p. 321-30.
29. Gharaibeh, B., et al., *Isolation of a slowly adhering cell fraction containing stem cells from murine skeletal muscle by the preplate technique.* Nat Protoc, 2008. 3(9): p. 1501-9.
30. Qu-Petersen, Z., et al., *Identification of a novel population of muscle stem cells in mice: potential for muscle regeneration.* J Cell Biol, 2002. 157(5): p. 851-64.
31. Campbell, P.G., et al., *Engineered spatial patterns of FGF-2 immobilized on fibrin direct cell organization.* Biomaterials, 2005. 26(33): p. 6762-70.
32. Maloul, A., et al., *Geometric and material contributions to whole bone structural behavior in GDF-7-deficient mice.* Connect Tissue Res, 2006. 47(3): p. 157-62.
33. Miller, E., *Inkjet Printing of Solid-Phase Growth Factor Patterns to Direct Cell Fate*, in *Biomedical Engineering*. 2007, Carnegie Mellon University: Pittsburgh. p. 349.
34. Dangaria, S.J., et al., *Extracellular matrix-mediated differentiation of periodontal progenitor cells.* Differentiation, 2009. 78(2-3): p. 79-90.
35. Miller, E.D., et al., *Dose-dependent cell growth in response to concentration modulated patterns of FGF-2 printed on fibrin.* Biomaterials, 2006. 27(10): p. 2213-21.

CHAPTER 5: *IN VITRO* EFFECT OF INFLAMMATORY AND ANTI-INFLAMMATORY MICROENVIRONMENTS ON OSTEOBLAST DIFFERENTIATION

5.1 ABSTRACT

The capability to control inflammation to create a permissive microenvironment for efficient stem cell differentiation such as osteoblastogenesis is important for understanding the tissue maintenance and repair. Our lab has previously developed a methodology to engineer pro-inflammatory and anti-inflammatory environments by challenging immune cells such as dendritic cells and macrophage cells with lipopolysaccharide (LPS) and IL-10, respectively, and applied this approach to study osteoblast differentiation in mouse C2C12 myoblasts. In this chapter, this approach is extended to study osteoblast differentiation in mouse C2C12 myoblasts, mouse MC3T3-E1 fibroblasts and mouse Muscle-Derived Stem Cells (MDSCs). Utilizing alkaline phosphatase (ALP), inflammatory environments were shown to inhibit osteoblast differentiation and bone mineralization while anti-inflammatory agents such as IL-10 rescued this inhibitory effect. In addition, a specific MDSC isolate was found to be resistant to LPS-mediated inhibition of osteoblast differentiation, highlighting heterogeneity in the stem cell response to inflammatory and anti-inflammatory microenvironments. This work illustrates that inflammatory and anti-inflammatory microenvironments can impact stem cell differentiation and may have potential use in tissue regeneration.

5.2 INTRODUCTION

As described in Chapter 1, inflammation is an integral component of the wound healing process and can drastically alter the cellular microenvironment to affect stem cell behavior. During inflammation, immune cells such as macrophages and dendritic cells respond to tissue injury according to two modes – the type 1 and type 2 pathway [1-5]. In the type 1 or classically activated pathway, a pro-inflammatory response typically associated with bacterial destruction predominates during the early phase of wound healing to eliminate pathogens from the wound

whereas in the type 2 pathway, an anti-inflammatory response typically associated with ECM deposition, angiogenesis and tissue remodeling predominates during the later phase of wound healing to promote wound closure [1, 4, 6, 7]. Both types of response are required for tissue repair and an imbalance between the two pathways can impair musculoskeletal repair by inhibiting stem cell differentiation [1, 3, 4], ultimately affecting the healing of bone fractures, tendon ruptures, muscle tears and integration of bone and dental implants [1, 3, 4, 8-11].

Therefore, developing the capability to selectively control the inflammatory phenotype of immune cells in order to create permissive microenvironments to direct stem cell differentiation is a logical consideration for studying stem cell behaviors and may also have direct applications in regenerative medicine.

Previous work performed in our lab had determined that the introduction of lipopolysaccharide (LPS; a component of gram-negative bacterial cell wall) and IL-10 (An immunomodulatory cytokine) directed immune cells such as dendritic cells and macrophages towards a type 1 (Classically activated; pro-inflammatory) or type 2 (Alternatively activated; anti-inflammatory) pathway, respectively (Kwan *et al.*, 2011 [12]; Chapter 1 and Appendix A1). In addition, prior work has also determined that chemical mediators secreted by type 1-activated immune cells inhibited osteoblast differentiation in mouse C2C12 myoblasts while chemical mediators secreted by type 2-activated immune cells did not have an adverse effect on osteoblast differentiation and could reverse this inhibition. Using conditioned media generated from mouse Fetal Skin Dendritic Cells (FSDCs) and mouse J774A.1 macrophage cells, the effects of type 1- or type 2-activated immune cell conditioned media on BMP-2-induced osteoblast differentiation were characterized using mouse MC3T3-E1 fibroblasts and mouse Muscle-Derived Stem Cells

(MDSCs). In addition, the effects of J774A.1 macrophage cell conditioned media on osteoblast differentiation in C2C12 cells was performed using inkjet-printed (immobilized) BMP-2 to assess the influence of pro-inflammatory and anti-inflammatory microenvironments on spatially-directed stem cell differentiation.

5.3 MATERIALS AND METHODS

5.3.1 Cell Culture

Mouse J774A.1 macrophage cells (ATTC, Manassas, VA) were grown in RPMI media (Invitrogen, Carlsbad, CA), 10% fetal bovine serum (FBS; Atlas Biological, Fort Collins, CO) and 1% penicillin-streptomycin (PS; Invitrogen, Carlsbad, CA). Mouse Fetal Skin Dendritic Cells (FSDCs) were grown in RPMI media, 10% FBS, 1% PS with 8mM Glutamax (Invitrogen, Carlsbad, CA) as previously described [13]. Multipotent Mouse C2C12 cells (ATTC, Manassas, VA) were grown in DMEM (high glucose; Invitrogen, Carlsbad, CA), 10% FBS and 1% PS. Unipotent mouse MC3T3-E1 subclone 4 cells (ATTC, Manassas, VA) were grown in α-Modified Eagle's Media (α-MEM; Invitrogen, Carlsbad, CA), 10% FBS and 1% PS. Multipotent Muscle-Derived Stem Cells (MDSCs) were isolated from primary mouse gastrocnemius muscle biopsies following a modified preplate technique [14] and were grown in DMEM (high glucose), 10% horse serum (HS; Invitrogen, Carlsbad, CA), 10% FBS, 0.5% Chick Embryo Extract (Gemini Bio-Products, West Sacramento, CA) as previously described [14, 15]. Since MDSCs are a primary cell line, 3 different isolates were used to account for isolate-to-isolate variability. Due to heterogeneity in cell growth, different seeding densities were used for different MDSC isolates. Isolate 1 was obtained from female mice while isolate 2 (D15/2) and isolate 3 (MTT PP6) were obtained from male mice. All isolates were obtained from 3 week old C57/BL/6 mice. All cells were kept at 37^{o}C, 5% CO_2 in a humidified incubator.

5.3.2 Conditioned Media

Mouse J774A.1 macrophage cells and FSDCs were seeded at a density of 1 x 10^6 cells per 100 mm Petri dish overnight. The next day, the media was aspirated and 10 mL fresh media was added. Cells were subsequently treated with nothing (Control), 100 ng/mL *Escherichia coli* LPS (Sigma-Aldrich, St Louis, MO; InvivoGen, San Diego, CA), 100 ng/mL IL-10-Fc (A kind gift from Dr. Zheng Xin Xiao, University of Pittsburgh, PA) and 100 ng/mL LPS with 100 ng/mL IL-10-Fc. After 48 h post-treatment, the conditioned media is collected and centrifuged at 110 g, 4^{o}C for 5 min to remove cells and debris. The conditioned media is then aliquoted and stored at -80^{o}C until further use.

5.3.3 Osteogenic Differentiation

To initiate osteogenic differentiation, cells were grown in their RPMI media containing 10% FBS and 1% PS (Unconditioned media) or immune cell-conditioned media in the presence of 100 ng/mL BMP-2 (Medtronic, Minneapolis, MN) for 4-6 days with a media change every 48 h. This media is subsequently referred to as osteogenic media or osteogenic conditions for the remainder of the text. C2C12 cells were seeded at a density of 1.55 x 10^4 cells/cm^2 overnight. MC3T3-E1 cells were seeded at a density of 2.32 x 10^4 cells/cm^2 overnight. Due to heterogeneity in cell growth, different seeding densities were used for different MDSC isolates. MDSC cells (Isolate 1, female) were seeded at a density of 6.19 x 10^4 cells/cm^2 overnight. MDSC cells (Isolate 2, male) were seeded at a density of 4.12 x 10^4 cells/cm^2 overnight. MDSC cells (Isolate 3, male) were seeded at a density of 1.03 x 10^4 cells/cm^2 overnight. For experiments involving use of fibrin-coated coverslips, 1 μg/mL aprotinin (Sigma-Aldrich, St Louis, MO) was added to the media to minimize fibrin degradation.

5.3.4 ALP Stain

Cells were fixed for 1 – 2 min in 3.7% formaldehyde. Alkaline phosphatase activity (ALP; Sigma-Aldrich, St Louis, MO) was detected according to the manufacturer's instructions. For image analysis, regions of ALP activity (blue) were identified using two methods of image analysis which produced comparable results (Data not shown).

In one method, regions of positive ALP activity were selected using the color select tool in Adobe Photoshop 7.0 (Adobe Systems, San Jose, CA). These regions were copied into a new image and converted to a grayscale image. The average pixel intensity was determined using the image histogram tool in Adobe Photoshop 7.0.

Alternatively, images were analyzed using a customized spectral unmixing algorithm written in Matlab R2010 (Mathworks Inc., Natick, MA) by Elvira Osuna-Highley based on prior work by Newberg *et al.* [16]. This customized algorithm quantifies the level of ALP staining by blind spectral unmixing by non-negative matrix factorization. Briefly, simple linear unmixing is defined by: $V = W \times H$, where V is the source image, an $(m \times n)$-by-c matrix (the number of colors, c, is 3 for RGB images), W is the color-bases matrix, a c-by-r matrix (where r is the number of sources to be separated), and H is the unmixed image of the same size as the source image. Because of experimental variation, the spectra of immunocytochemical dyes are often not consistent across every image, making simple 123 linear unmixing inappropriate. Thus, non-negative matrix factorization was used to blindly unmix the images [16]. Briefly, non-negative matrix factorization assumes that each stain contributes non-negatively to the overall image intensity. This method has been shown to be effective in unmixing brightfield images [16]. Blind spectral unmixing by non-negative matrix factorization uses a different color matrix, W, for each

image. H is randomly initialized and non-negative matrix factorization is used to solve for the non-negative matrix factors W and H by iteratively minimizing the distance between V and W × H. The post-processing of H into a new unmixed image was similar to that of linear unmixing, in which each channel was scaled and then remapped into the image data channels. The unmixed image was summed to determine the amount of ALP staining.

5.3.5 Growth Factor Preparation and Use

Recombinant human BMP-2 (Medtronic, Minneapolis, MN)was reconstituted according to manufacturer's instructions to 1-2 mg/mL, aliquoted and stored at -80^{o}C. Prior to use, BMP-2 was freshly diluted to the desired concentration in 10 mM sodium phosphate, pH 7.4.

5.3.6 Preparation of Fibrin Coated Coverslips

Homogenous fibrin films were prepared essentially as described by Campbell *et al.*, 2005 [17]. Briefly, 18 x 18 mm epoxy-silanized glass coverslips (Thermo Fisher Scientific, Waltham, MA) were coated with 0.1 mg/mL fibrinogen (Aventis Behring, King of Prussia, PA or American Diagnostica Inc., Stanford, CT) and converted into fibrin by incubating coverslips in 4 U/mL thrombin (Enzyme Research Laboratories, South Bend, IN). Coverslips were then washed with phosphate buffered saline (PBS) and sterile deionized water before air-drying in a laminar flow hood. The thickness of the fibrin films was previously estimated to be approximately 20 nm [17].

5.3.7 Growth Factor Printing

Prior to printing, GFs were freshly diluted to the desired concentration in 10 mM sodium phosphate, pH 7.4. Prior to filling the inkjet with the GF, the printhead was sterilized by rinsing with 70% ethanol followed by sterile deionized water. The bio-ink, consisting of 100-200 µg/ml GF was loaded into the printhead, and printed onto fibrin-coated glass coverslips as previously

described [17, 18]. The concentration of inkjetted GFs can be modulated by overprinting, which is achieved by varying the number of times a GF is deposited in the same (x,y) location. In the case of hand-printed GF patterns, 1-2 µL of a 100 µg/mL GF solution was pipetted onto a fibrin-coated glass coverslip instead and a diamond scribe pen was used to mark the droplet perimeter after it had been allowed to air-dry for 1h at 37^{o}C. After printing, fibrin-coated coverslips were incubated in PBS for 5 min followed by serum-free DMEM with 1% PS overnight at 37°C, 5% CO_2 to wash off unbound GF prior to cell seeding. The surface concentration of GF present on fibrin-coated coverslips during cell seeding was estimated based on desorption measurements in previous studies [17-21].

5.3.8 Statistical Analysis

For analysis of ALP-stained images, one-way analysis of variance followed by Tukey's honestly significant difference post hoc test using SYSTAT 9 software (Systat Software Inc., Richmond, CA) was performed to determine significance among treatment groups. A p value ≤ 0.05 was considered statistically significant.

5.4 RESULTS

5.4.1 Effect of FSDC and J774A.1 Cell Conditioned Media on ALP Expression in MC3T3-E1 Cells

By staining for the osteoblast marker ALP, the effect of unconditioned media as well as FSDC and J774A.1 cell conditioned media on MC3T3-E1 cells were investigated. In unconditioned media experiments, ALP expression was upregulated in unconditioned media containing BMP-2 with respect to its counterparts that lacked BMP-2 (p = 0.001 for Control vs Control+BMP-2, p = 0.004 for LPS vs LPS+BMP-2, p = 0.001 for IL-10 vs IL-10+BMP-2 and p = 0.002 for LPS with

IL-10 vs LPS with IL-10+BMP-2; Figure 5.1A and C). In addition, ALP expression in LPS unconditioned media containing BMP-2 was not different with respect to Control unconditioned media containing BMP-2 ($p > 0.999$ for Control+BMP-2 vs LPS+BMP-2; Figure 5.1A and C).

In FSDC conditioned media experiments, ALP expression was upregulated in Control, IL-10, and LPS with IL-10 conditioned media containing BMP-2 with respect to its counterparts that lacked BMP-2 ($p = 0.005$ for Control vs Control+BMP-2, $p = 0.002$ for IL-10 vs IL-10+BMP-2 and $p = 0.022$ for LPS with IL-10 vs LPS with IL-10+BMP-2; Figure 5.1B and D). However, ALP expression in LPS conditioned media containing BMP-2 was not different when compared to LPS conditioned media lacking BMP-2 ($p = 0.983$; Figure 5.1D). In addition, ALP expression in LPS conditioned media containing BMP-2 was downregulated with respect to Control conditioned media that contained BMP-2 ($p = 0.056$ for Control+BMP-2 vs LPS+BMP-2; Figure 5.1B and D). These results indicated that LPS media conditioned by FSDCs inhibited MC3T3-E1 osteoblast differentiation whereas unconditioned LPS media did not (Figure 5.1). In addition, this inhibitory effect on osteoblast differentiation was indirectly rescued through IL-10 addition during conditioned media generation.

In J774A.1 cell conditioned media experiments, ALP expression was upregulated in Control, IL-10, and LPS with IL-10 conditioned media containing BMP-2 with respect to its counterparts that lacked BMP-2 ($p < 0.001$ for Control vs Control+BMP-2, $p < 0.001$ for IL-10 vs IL-10+BMP-2 and $p < 0.001$ for LPS with IL-10 vs LPS with IL-10+BMP-2; Figure 5.2B and D). However, ALP expression in LPS conditioned media containing BMP-2 was not different when compared to LPS conditioned media lacking BMP-2 ($p > 0.999$; Figure 5.2D). In addition, ALP expression in LPS conditioned media containing BMP-2 was downregulated with respect to

Control conditioned media that contained BMP-2 ($p < 0.001$ for Control+BMP-2 vs LPS+BMP-2; Figure 5.2B and D). These results indicated that LPS media conditioned by J774A.1 cells inhibited MC3T3-E1 osteoblast differentiation whereas unconditioned LPS media did not (Figure 5.2). In addition, this inhibitory effect on osteoblast differentiation was indirectly rescued through IL-10 addition during conditioned media generation.

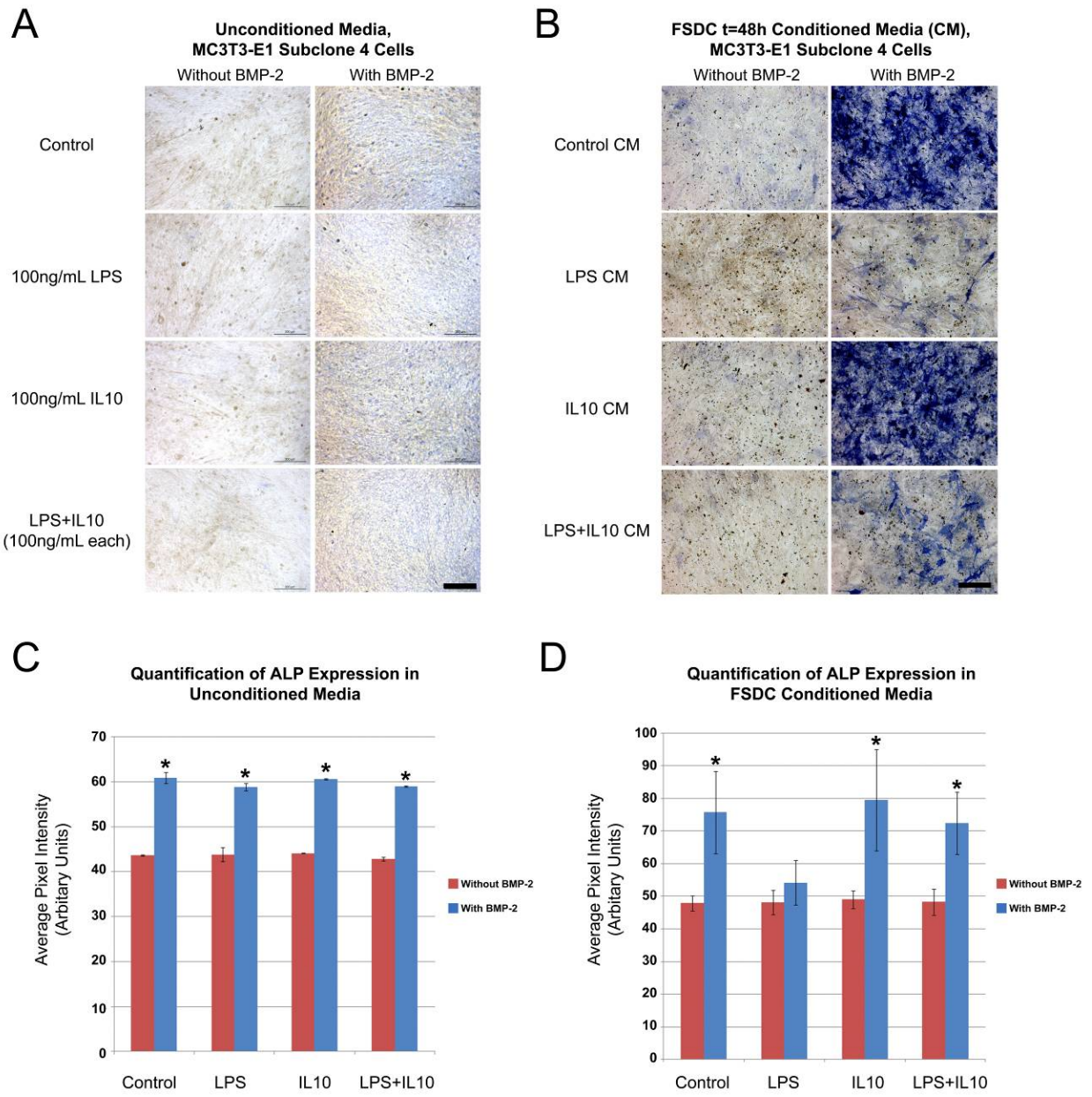

Figure 5.1. Effect of FSDC conditioned media (t = 48h) on expression of osteoblast marker ALP (blue) in mouse MC3T3-E1 cells after 4 days. **A.** For unconditioned media experiments, ALP expression was upregulated in the presence of Control, LPS, IL-10, and LPS with IL-10 conditioned media containing 100 ng/mL BMP-2. **B.** For conditioned media experiments, ALP expression was upregulated in the presence of Control, IL-10, and LPS with IL-10 conditioned media containing 100 ng/mL BMP-2 but not LPS conditioned media. **C.** Quantification of ALP expression in unconditioned media experiments. **D.** Quantification of ALP expression in conditioned media experiments. Scale bar is 200 μm. Error bars indicate Standard Error Mean or SEM (n = 9). *, Significantly different from its respective non-BMP-2 treated counterpart; $p \leq 0.05$. +, Significantly different from Control conditioned media containing 100 ng/mL BMP-2; $p \leq 0.05$.

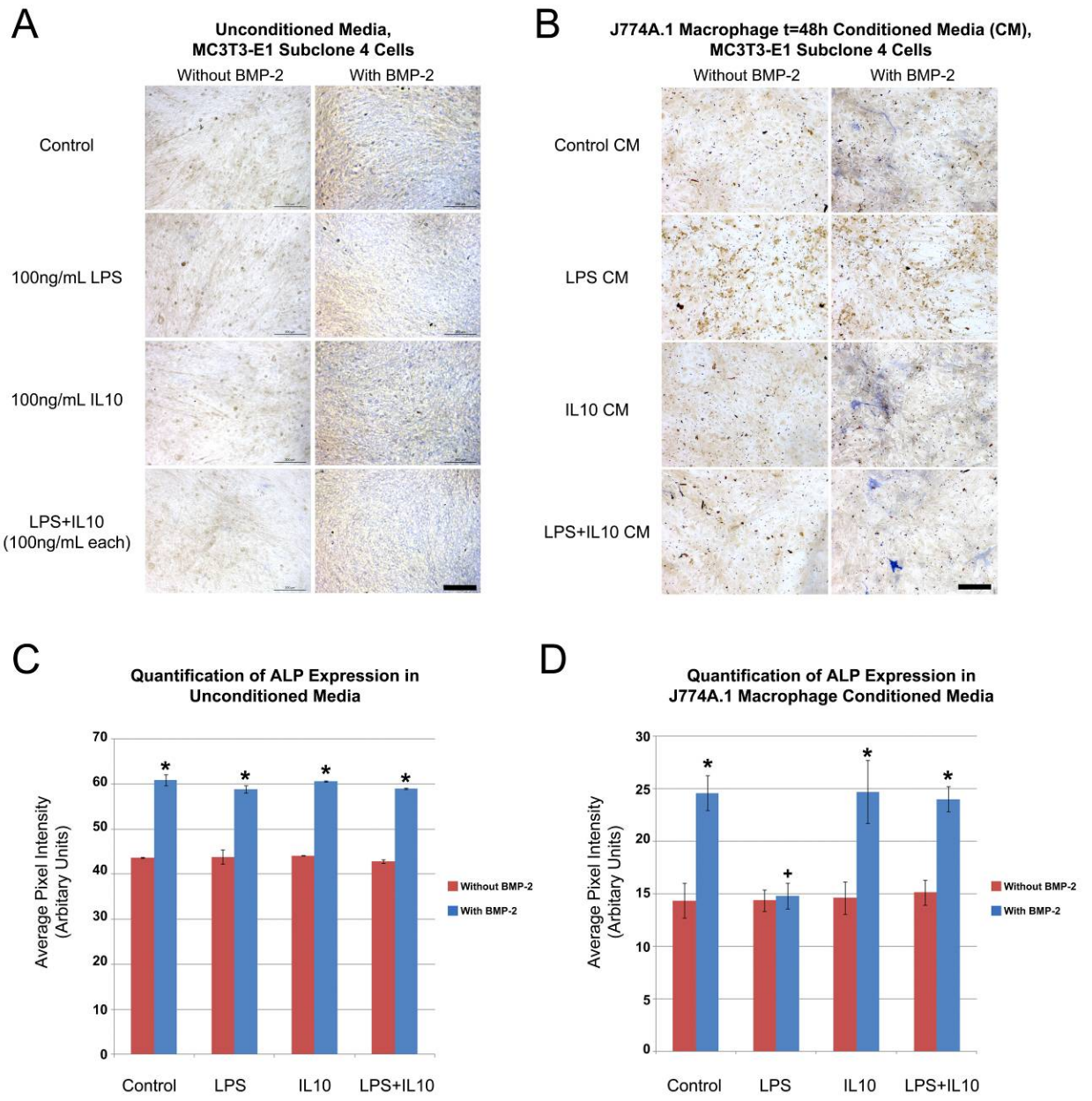

Figure 5.2. Effect of J774A.1 cell conditioned media (t = 48h) on expression of osteoblast marker ALP (blue) in mouse MC3T3-E1 cells after 4 days. **A.** For unconditioned media experiments, ALP expression was upregulated in the presence of Control, LPS, IL-10, and LPS with IL-10 conditioned media containing 100 ng/mL BMP-2. **B.** For conditioned media experiments, ALP expression was upregulated in the presence of Control, IL-10, and LPS with IL-10 conditioned media containing 100 ng/mL BMP-2 but not LPS conditioned media. **C.** Quantification of ALP expression in unconditioned media experiments. **D.** Quantification of ALP expression in conditioned media experiments. Scale bar is 200 µm. Error bars indicate Standard Error Mean or SEM (n = 6). *, Significantly different from its respective non-BMP-2 treated counterpart; $p \leq 0.05$. +, Significantly different from Control conditioned media containing 100 ng/mL BMP-2; $p \leq 0.05$.

5.4.2 Effect of J774A.1 Cell Conditioned Media on ALP Expression in MDSC Cells

To determine that the inhibitory effect of LPS conditioned media on osteoblast differentiation was not restricted only to cell lines but applicable to primary cell isolates, the previous experiments were repeated using unconditioned media as well as J774A.1 cell conditioned media on 3 MDSC isolates (1 female, 2 males).

The effects of unconditioned and J774A.1 cell conditioned media on osteoblast differentiation for the first MSDC isolate (female) are summarized in Figure 5.3. In unconditioned media experiments, ALP expression was upregulated in unconditioned media containing BMP-2 with respect to its counterparts that lacked BMP-2 ($p < 0.001$ for Control vs Control+BMP-2, $p < 0.001$ for LPS vs LPS+BMP-2, $p < 0.001$ for IL-10 vs IL-10+BMP-2 and $p < 0.001$ for LPS with IL-10 vs LPS with IL-10+BMP-2; Figure 5.3A and C). In addition, ALP expression in LPS unconditioned media containing BMP-2 was not different with respect to Control unconditioned media containing BMP-2 ($p = 0.933$ for Control+BMP-2 vs LPS+BMP-2; Figure 5.3A and C). In conditioned media experiments, ALP expression was upregulated in Control, LPS, IL-10, and LPS with IL-10 conditioned media containing BMP-2 with respect to its counterparts that lacked BMP-2 ($p < 0.001$ for Control vs Control+BMP-2, $p < 0.001$ for LPS vs LPS+BMP-2, $p < 0.001$ for IL-10 vs IL-10+BMP-2 and $p < 0.001$ for LPS with IL-10 vs LPS with IL-10+BMP-2; Figure 5.3B and D). In addition, ALP expression in LPS conditioned media containing BMP-2 was not different with respect to Control conditioned media that contained BMP-2 ($p > 0.999$ for Control+BMP-2 vs LPS+BMP-2; Figure 5.3B and D). These results indicated that both unconditioned and conditioned LPS media generated by J774A.1 cells did not inhibit MDSC osteoblast differentiation in this particular isolate (Figure 5.3).

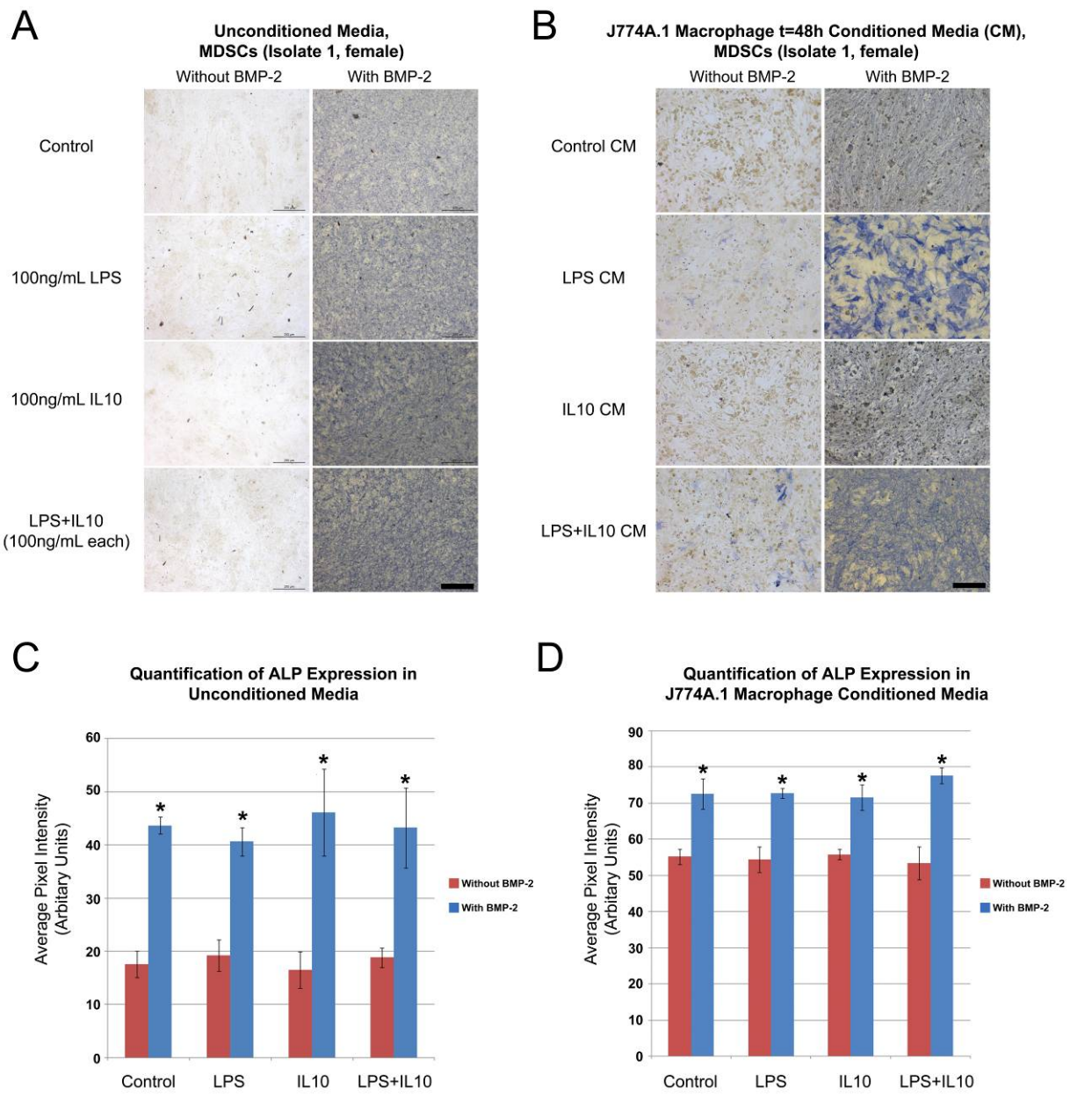

Figure 5.3. Effect of J774A.1 cell conditioned media (t = 48h) on expression of osteoblast marker ALP (blue) in mouse MDSCs (Isolate 1, female) after 6 days. **A.** For unconditioned media experiments, ALP expression was upregulated in the presence of Control, LPS, IL-10, and LPS with IL-10 conditioned media containing 100 ng/mL BMP-2. **B.** For conditioned media experiments, ALP expression was upregulated in the presence of Control, LPS, IL-10, and LPS with IL-10 conditioned media containing 100 ng/mL BMP-2. **C.** Quantification of ALP expression in unconditioned media experiments. **D.** Quantification of ALP expression in conditioned media experiments. Scale bar is 200 μm. Error bars indicate Standard Error Mean or SEM (n = 9). *, Significantly different from its respective non-BMP-2 treated counterpart; $p \leq 0.05$. +, Significantly different from Control conditioned media containing 100 ng/mL BMP-2; $p \leq 0.05$.

The effects of unconditioned media and J774A.1 cell conditioned media on osteoblast differentiation in the second MSDC isolate (male) are summarized in Figure 5.4. In unconditioned media experiments, ALP expression was upregulated in unconditioned media containing BMP-2 with respect to its counterparts that lacked BMP-2 ($p < 0.001$ for Control vs Control+BMP-2, $p < 0.001$ for LPS vs LPS+BMP-2, $p < 0.001$ for IL-10 vs IL-10+BMP-2 and $p < 0.001$ for LPS with IL-10 vs LPS with IL-10+BMP-2; Figure 5.4A and C). In addition, ALP expression in LPS unconditioned media containing BMP-2 was not different with respect to Control unconditioned media that contained BMP-2 ($p = 0.660$ for Control+BMP-2 vs LPS+BMP-2; Figure 5.4A and C). In conditioned media experiments, ALP expression was upregulated in Control, IL-10, and LPS with IL-10 conditioned media containing BMP-2 with respect to its counterparts that lacked BMP-2 ($p < 0.001$ for Control vs Control+BMP-2, $p < 0.001$ for IL-10 vs IL-10+BMP-2 and $p < 0.001$ for LPS with IL-10 vs LPS with IL-10+BMP-2; Figure 5.4B and D). However, ALP expression in LPS conditioned media containing BMP-2 was not different when compared to LPS conditioned media lacking BMP-2 ($p = 0.427$; Figure 5.4D). In addition, ALP expression in LPS conditioned media containing BMP-2 was downregulated with respect to Control conditioned media that contained BMP-2 ($p < 0.001$ for Control+BMP-2 vs LPS+BMP-2; Figure 5.4B and D). These results indicated that in this particular isolate, LPS media conditioned by J774A.1 cells inhibited MDSC osteoblast differentiation whereas unconditioned LPS media did not (Figure 5.4). In addition, this inhibitory effect on osteoblast differentiation was indirectly rescued through IL-10 addition during conditioned media generation.

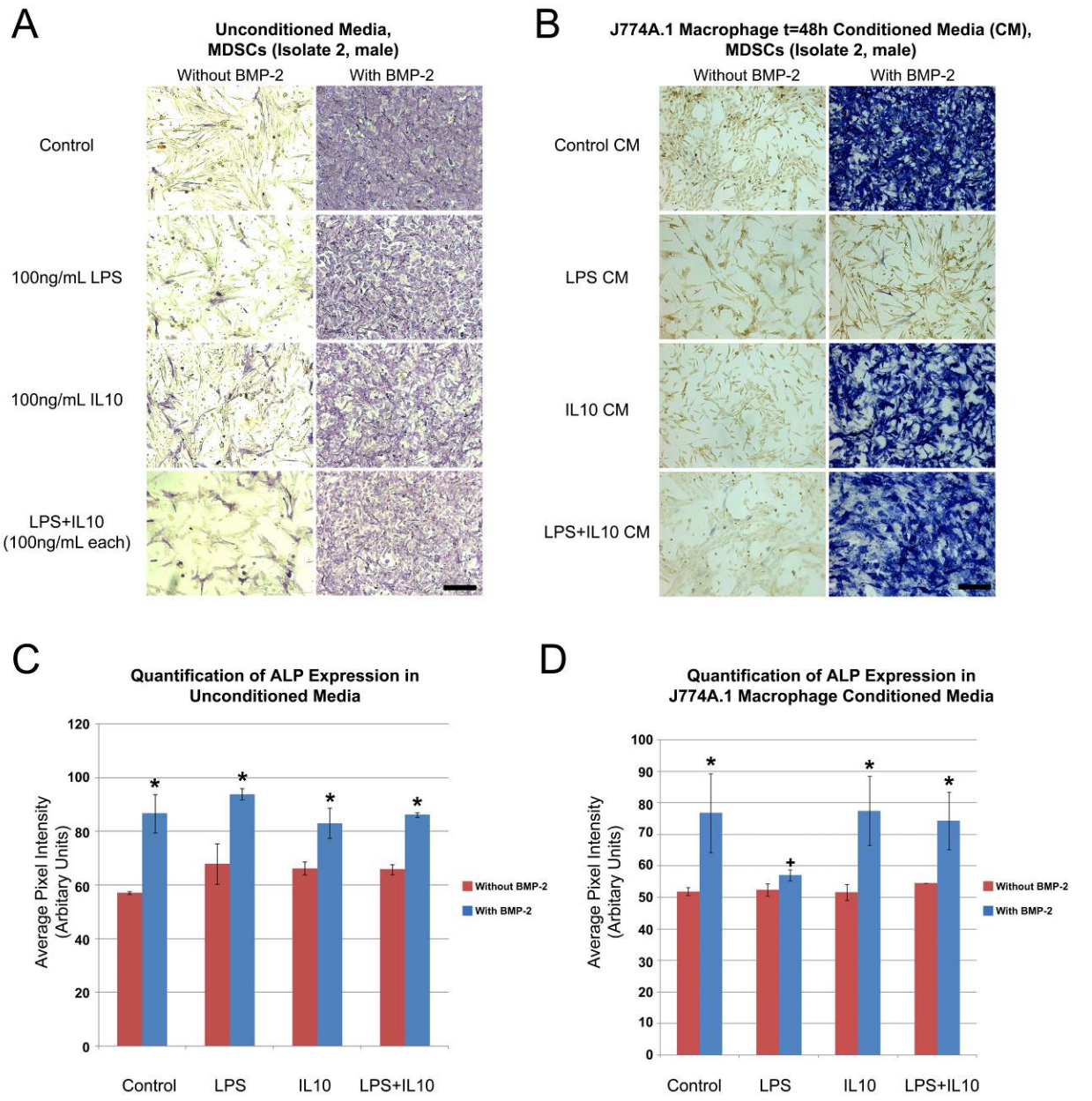

Figure 5.4. Effect of J774A.1 cell conditioned media (t = 48h) on expression of osteoblast marker ALP (blue) in mouse MDSCs (Isolate 2, male) after 4 days. **A.** For unconditioned media experiments, ALP expression was upregulated in the presence of Control, LPS, IL-10, and LPS with IL-10 conditioned media containing 100 ng/mL BMP-2. **B.** For conditioned media experiments, ALP expression was upregulated in the presence of Control, IL-10, and LPS with IL-10 conditioned media containing 100 ng/mL BMP-2 but not LPS conditioned media. **C.** Quantification of ALP expression in unconditioned media experiments. **D.** Quantification of ALP expression in conditioned media experiments. Scale bar is 200 µm. Error bars indicate Standard Error Mean or SEM (n = 6). *, Significantly different from its respective non-BMP-2 treated counterpart; $p \leq 0.05$. +, Significantly different from Control conditioned media containing 100 ng/mL BMP-2; $p \leq 0.05$.

The effects of unconditioned media and J774A.1 cell conditioned media on osteoblast differentiation in the third MSDC isolate (male) are summarized in Figure 5.5. In unconditioned media experiments, ALP expression was upregulated in unconditioned media containing BMP-2 with respect to its counterparts that lacked BMP-2 ($p < 0.001$ for Control vs Control+BMP-2, $p < 0.001$ for LPS vs LPS+BMP-2, $p < 0.001$ for IL-10 vs IL-10+BMP-2 and $p < 0.001$ for LPS with IL-10 vs LPS with IL-10+BMP-2; Figure 5.5A and C). In addition, ALP expression in LPS unconditioned media containing BMP-2 was not different with respect to Control unconditioned media that contained BMP-2 ($p = 0.641$ for Control+BMP-2 vs LPS+BMP-2; Figure 5.5A and C). In conditioned media experiments, ALP expression was upregulated in Control, IL-10, and LPS with IL-10 conditioned media containing BMP-2 with respect to its counterparts that lacked BMP-2 ($p < 0.001$ for Control vs Control+BMP-2, $p < 0.001$ for IL-10 vs IL-10+BMP-2 and $p < 0.001$ for LPS with IL-10 vs LPS with IL-10+BMP-2; Figure 5.5B and D). However, ALP expression in LPS conditioned media containing BMP-2 was not different when compared to LPS conditioned media lacking BMP-2 ($p = 0.964$; Figure 5.5D). In addition, ALP expression in LPS conditioned media containing BMP-2 was downregulated with respect to Control conditioned media that contained BMP-2 ($p < 0.001$ for Control+BMP-2 vs LPS+BMP-2; Figure 5.5B and D). These results indicated that in this particular isolate, LPS media conditioned by J774A.1 cells inhibited MDSC osteoblast differentiation whereas unconditioned LPS media did not (Figure 5.5). In addition, this inhibitory effect on osteoblast differentiation was indirectly rescued through IL-10 addition during conditioned media generation.

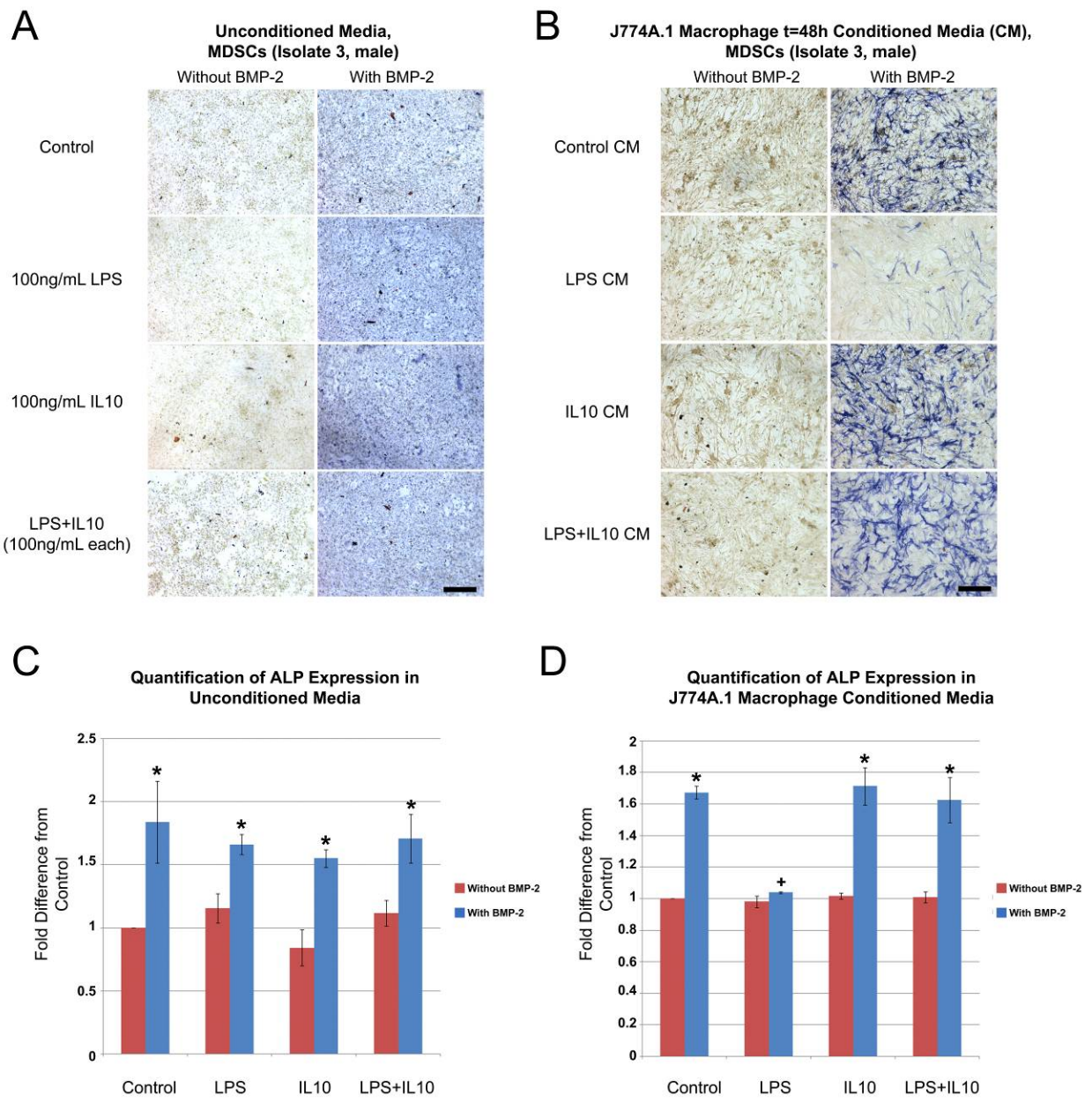

Figure 5.5. Effect of J774A.1 cell conditioned media (t = 48h) on expression of osteoblast marker ALP (blue) in mouse MDSCs (Isolate 3, male) after 4 days. **A.** For unconditioned media experiments, ALP expression was upregulated in the presence of Control, LPS, IL-10, and LPS with IL-10 conditioned media containing 100 ng/mL BMP-2. **B.** For conditioned media experiments, ALP expression was upregulated in the presence of Control, IL-10, and LPS with IL-10 conditioned media containing 100 ng/mL BMP-2 but not LPS conditioned media. **C.** Quantification of ALP expression in unconditioned media experiments. **D.** Quantification of ALP expression in conditioned media experiments. Scale bar is 200 µm. Error bars indicate Standard Error Mean or SEM (n = 6). *, Significantly different from its respective non-BMP-2 treated counterpart; $p \leq 0.05$. +, Significantly different from Control conditioned media containing 100 ng/mL BMP-2; $p \leq 0.05$.

5.4.3 Effect of J774A.1 Cell Conditioned Media on ALP Expression in C2C12 Cells

Since GFs are capable of binding to the ECM *in vitro* and *in vivo*, the effect of J774A.1 cell conditioned media on ALP expression in C2C12 cells was assessed using immobilized patterns of BMP-2 created by inkjet printing (Figure 5.6). In such conditioned media experiments, C2C12 cells grown on printed patterns of BMP-2 showed increased ALP expression for Control, IL-10, and LPS with IL-10 conditioned media when compared to Non-Printed Control ($p < 0.001$ for Control vs Non-Printed Control, $p < 0.001$ for IL-10 vs Non-Printed Control and $p = 0.036$ for LPS with IL-10 vs Non-Printed Control; Figure 5.6) as well as LPS conditioned media ($p < 0.001$ for Control vs LPS, $p < 0.001$ for IL-10 vs LPS and $p = 0.032$ for LPS with IL-10 vs LPS; Figure 5.5). In addition, C2C12 cells grown on printed patterns of BMP-2 in LPS with IL-10 conditioned media showed an ALP staining intensity intermediate between Control conditioned media and LPS conditioned media ($p < 0.001$ for Control vs LPS with IL-10 and $p = 0.032$ for LPS vs LPS with IL-10; Figure 5.5). Together, these results indicate that similar to liquid-phase experiments (where the BMP-2 is diffusing freely in solution; Figure 5.1, Figure 5.2, Figure 5.3 and Figure 5.4), solid-phase or immobilized patterns of BMP-2 were inhibited from directing C2C12 osteoblast differentiation in LPS media conditioned by J774A.1 cells. In addition, this inhibitory effect on osteoblast differentiation was indirectly rescued through IL-10 addition during conditioned media generation.

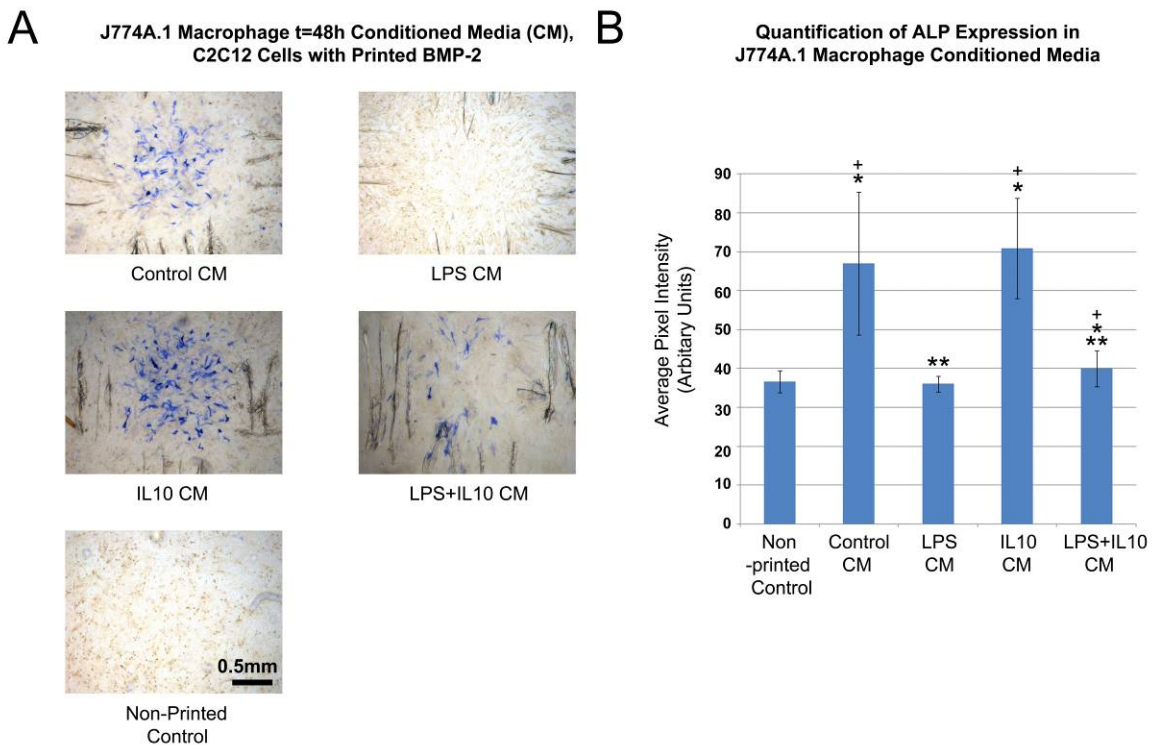

Figure 5.6. Effect of J774A.1 cell conditioned media on expression of osteoblast marker ALP (blue) in mouse C2C12 cells grown on printed BMP-2 patterns after 4 days. **A.** ALP staining of C2C12 cells. ALP expression was upregulated within printed BMP-2 patterns in the presence of Control, IL-10, and LPS with IL-10 conditioned media compared to Non-Printed Control. No difference in ALP expression was observed between LPS conditioned media compared to Non-Printed Control. Scale bar is 500 µm. **B.** Quantification of ALP expression within printed BMP-2 regions. Error bars indicate Standard Error Mean or SEM (n = 8). $*$, Significantly different from Non-Printed Control; $p \leq 0.05$. $**$, Significantly different from Control conditioned media; $p \leq 0.05$. +, Significantly different from LPS conditioned media; $p \leq 0.05$.

5.5 DISCUSSION

5.5.1 Effect of Immune Cell Conditioned Media on ALP Expression in MC3T3-E1 Cells

Prior work had previously determined that addition of LPS and IL-10 to immune cell cultures activated dendritic cells and macrophages towards a type 1 pro-inflammatory and type 2 anti-inflammatory response, respectively [12]. The goal of this chapter was to characterize the effect of pro-inflammatory and anti-inflammatory microenvironments on osteoblast differentiation (Figure 5.1, Figure 5.2, Figure 5.3, Figure 5.4 and Figure 5.5).

In MC3T3-E1 cells, the presence of LPS and IL-10 in unconditioned media did not perturb BMP-2-induced ALP expression when compared to Control unconditioned media (Figure 5.1A and C). In addition, IL-10 media and LPS with IL-10 media conditioned by FSDCs did not perturb BMP-2-induced ALP expression when compared to Control conditioned media (Figure 5.1B and D). However, LPS media conditioned by FSDCs inhibited BMP-2-induced ALP expression (Figure 5.1B and D). This inhibitory effect on BMP-2-induced ALP expression was rescued in LPS with IL-10 media conditioned by FSDCs (Figure 5.1B and D). Similarly, IL-10 media and LPS with IL-10 media conditioned by J774A.1 cells did not perturb BMP-2-induced ALP expression when compared to Control conditioned media (Figure 5.2B and D). However, LPS media conditioned by J774A.1 cells inhibited BMP-2-induced ALP expression (Figure 5.2B and D). This inhibitory effect on BMP-2-induced ALP expression was rescued in LPS with IL-10 media conditioned by J774A.1 cells (Figure 5.2B and D). Together, these results illustrate that although LPS and IL-10 do not have a direct effect on MC3T3-E1 osteoblast differentiation, LPS conditioned media inhibited osteoblast differentiation and this inhibitory effect was rescued using LPS with IL-10 conditioned media (Figure 5.1 and Figure 5.2).

5.5.2 Effect of Immune Cell Conditioned Media on ALP Expression in MDSCs

To ensure that the inhibitory effect of LPS conditioned media on osteoblast differentiation was not only restricted to cell lines but applicable to primary cells, these experiments were repeated using primary MDSCs. To rule out isolate-to-isolate variability, a total of 3 isolates (1 female, 2 male) were used (Figure 5.3, Figure 5.4 and Figure 5.5).

In all three isolates, the presence of LPS and IL-10 in unconditioned media did not perturb BMP-2-induced ALP expression when compared to Control unconditioned media (Figure 5.3A and C, Figure 5.4A and C, and Figure 5.5A and C).

In the first isolate (female), LPS media conditioned by J774A.1 cells did not inhibit BMP-2-induced ALP expression (Figure 5.3B and D). This indicated that LPS conditioned media did not have an inhibitory effect on BMP-2-induced ALP expression in this particular isolate. However, in the second and third isolate (both males), LPS media conditioned by J774A.1 cells inhibited BMP-2-induced ALP expression (Figure 5.4B and D, and Figure 5.5B and D). This inhibitory effect on BMP-2-induced ALP expression was rescued in LPS with IL-10 media conditioned by J774A.1 cells (Figure 5.4B and D, and Figure 5.5B and D). This indicated that LPS conditioned media had an inhibitory effect on BMP-2-induced ALP expression in these two particular isolates. These contrasting results demonstrate the heterogeneous nature of MDSCs and may be attributed to a variety of factors including sex difference, variability in the cell isolation technique and differences in initial cell seeding density.

Together, these results illustrate that although LPS and IL-10 did not have a direct effect on MDSC osteoblast differentiation, LPS conditioned media inhibited osteoblast differentiation (in two of three isolates) and this inhibitory effect was rescued using LPS with IL-10 conditioned media (Figure 5.3, Figure 5.4 and Figure 5.5).

5.5.3 Effect of Immune Cell Conditioned Media on ALP Expression in C2C12 Cells

As described in Chapter 1, growth factors (GFs) occur naturally both in the liquid-phase (freely-diffusing in solution) as well as in the solid-phase (immobilized or bound to the ECM) [22]. In addition, sequestration of GFs by the ECM can alter the bioavailability and bioactivity of a particular GF [22]. Since the preceding experiments involved osteoblast differentiation using liquid-phase BMP-2, inkjet printed patterns of BMP-2 were used to assess the impact of type 1 pro-inflammatory and type 2 anti-inflammatory microenvironments on osteoblast differentiation (Figure 5.6). In these experiments utilizing J774A.1 cell conditioned media, C2C12 cells grown on printed patterns of BMP-2 in Control, IL-10, and LPS with IL-10 conditioned media showed increased ALP expression when compared to Non-Printed Control and LPS conditioned media, indicating that LPS conditioned media inhibited osteoblast differentiation (Figure 5.6). In addition, C2C12 cells grown on printed patterns of BMP-2 in LPS with IL10 showed levels of ALP expression intermediate between Control conditioned media and LPS conditioned media, indicating that the inhibitory effect of LPS conditioned media could be rescued (Figure 5.6). Together, these data suggest that similar to liquid-phase experiments, type 1 pro-inflammatory microenvironments inhibit BMP-2-induced osteoblast differentiation whereas type 2 anti-inflammatory microenvironments can rescue this inhibitory effect.

5.6 CONCLUSIONS

This chapter identified LPS and IL-10 as being capable of directing the activation of immune cells such as dendritic cells and macrophages towards type 1 pro-inflammatory and type 2 anti-inflammatory pathways to create inhibitory or permissive microenvironments for osteoblast differentiation in several musculoskeletal progenitor/stem cells, respectively. This chapter also highlights the heterogeneous nature of primary cells in regards to their response under pro-

inflammatory and anti-inflammatory microenvironments. The capability to modulate the inflammatory response to create pro-inflammatory and anti-inflammatory microenvironments not only offers an approach to study the physiological role of stem cells during wound healing *in vitro*, but may also be translatable to new therapies to treat disease and trauma of the musculoskeletal system.

5.7 ACKNOWLEDGEMENTS

I would like to thank Larry Schultz for assistance with GF printing. I would also like to thank Shuying Kwan, Eun Hwa Esther Lee, Krystin Meidell, Elizabeth Ramsey, Niya Robinson and Hirotaka Nakagawa for assistance with performing conditioned media experiments. In addition, I would like to thank Zheng Xin Xiao for providing IL-10-Fc and Elvira Osuna-Highley for assistance with quantification of ALP signal in microscopy images. This work was supported by NIH grants RO1EB004343 and RO1EB007369 as well as funding from the Pennsylvania Infrastructure Technology Alliance (PITA).

5.8 REFERENCES

1. Martinez, F.O., et al., *Macrophage activation and polarization.* Front Biosci, 2008. **13**: p. 453-61.
2. Segawa, M., et al., *Suppression of macrophage functions impairs skeletal muscle regeneration with severe fibrosis.* Exp Cell Res, 2008. **314**(17): p. 3232-44.
3. Tidball, J.G., *Inflammatory processes in muscle injury and repair.* Am J Physiol Regul Integr Comp Physiol, 2005. **288**(2): p. R345-53.
4. Tidball, J.G. and S.A. Villalta, *Regulatory interactions between muscle and the immune system during muscle regeneration.* Am J Physiol Regul Integr Comp Physiol, 2010. **298**(5): p. R1173-87.
5. Valencia, J., et al., *Wnt5a skews dendritic cell differentiation to an unconventional phenotype with tolerogenic features.* J Immunol, 2011. **187**(8): p. 4129-39.
6. Brancato, S.K. and J.E. Albina, *Wound macrophages as key regulators of repair: origin, phenotype, and function.* Am J Pathol, 2011. **178**(1): p. 19-25.
7. Kumar, V. and A. Sharma, *Neutrophils: Cinderella of innate immune system.* Int Immunopharmacol, 2010. **10**(11): p. 1325-34.

8. Colombo, J.S., et al., *Delayed osteoblast differentiation and altered inflammatory response around implants placed in incisor sockets of type 2 diabetic rats.* Clin Oral Implants Res, 2011. **22**(6): p. 578-86.
9. Liu, N., et al., *High levels of beta-catenin signaling reduce osteogenic differentiation of stem cells in inflammatory microenvironments through inhibition of the noncanonical Wnt pathway*. J Bone Miner Res, 2011.
10. Longo, U.G., et al., *Histopathology of rotator cuff tears.* Sports Med Arthrosc, 2011. **19**(3): p. 227-36.
11. Zhang, J. and J.H. Wang, *Production of PGE(2) increases in tendons subjected to repetitive mechanical loading and induces differentiation of tendon stem cells into non-tenocytes.* J Orthop Res, 2010. **28**(2): p. 198-203.
12. Kwan, S., *The Flip Side of Osteoimmunity: Crosstalk Among Stem Cells, BMP-2 and Innate Immune Cells, and the Control of Osteoblastogenesis,* in *Biological Sciences.* 2011, Carnegie Mellon University: Pittsburgh. p. 158.
13. Girolomoni, G., et al., *Establishment of a cell line with features of early dendritic cell precursors from fetal mouse skin.* Eur J Immunol, 1995. **25**(8): p. 2163-9.
14. Gharaibeh, B., et al., *Isolation of a slowly adhering cell fraction containing stem cells from murine skeletal muscle by the preplate technique.* Nat Protoc, 2008. **3**(9): p. 1501-9.
15. Qu-Petersen, Z., et al., *Identification of a novel population of muscle stem cells in mice: potential for muscle regeneration.* J Cell Biol, 2002. **157**(5): p. 851-64.
16. Newberg, J.Y., et al., *Automated Analysis of Human Protein Atlas Immunofluorescence Images.* Proc IEEE Int Symp Biomed Imaging, 2009. **5193229**: p. 1023-1026.
17. Campbell, P.G., et al., *Engineered spatial patterns of FGF-2 immobilized on fibrin direct cell organization.* Biomaterials, 2005. **26**(33): p. 6762-70.
18. Miller, E.D., et al., *Inkjet printing of growth factor concentration gradients and combinatorial arrays immobilized on biologically-relevant substrates.* Comb Chem High Throughput Screen, 2009. **12**(6): p. 604-18.
19. Miller, E., *Inkjet Printing of Solid-Phase Growth Factor Patterns to Direct Cell Fate*, in *Biomedical Engineering*. 2007, Carnegie Mellon University: Pittsburgh. p. 349.
20. Miller, E.D., et al., *Dose-dependent cell growth in response to concentration modulated patterns of FGF-2 printed on fibrin.* Biomaterials, 2006. **27**(10): p. 2213-21.
21. Miller, E.D., et al., *Spatially directed guidance of stem cell population migration by immobilized patterns of growth factors.* Biomaterials, 2011. **32**(11): p. 2775-85.
22. Taipale, J. and J. Keski-Oja, *Growth factors in the extracellular matrix.* FASEB J, 1997. **11**(1): p. 51-9.

CHAPTER 6: REAL TIME ADAPTIVE SUBCULTURE OF PROGENITOR CELLS

Based on published work:

An Engineered Approach to Stem Cell Culture: Automating the Decision Process for Real-Time Adaptive Subculture of Stem Cells

Dai Fei Elmer Ker, Lee E. Weiss, Silvina N. Junkers, Mei Chen, Zhaozheng Yin, Michael F. Sandbothe, Seung-il Huh, Sungeun Eom, Ryoma Bise, Elvira Osuna-Highley, Takeo Kanade, Phil G. Campbell

PLoS ONE. 2011 Nov; **6** (11) e27672.

6.1 ABSTRACT

Current cell culture practices are dependent upon human operators and remain laborious and highly subjective, resulting in large variations and inconsistent outcomes, especially when using visual assessments of cell confluency to determine the appropriate time to subculture cells. Although efforts to automate cell culture with robotic systems are underway, the majority of such systems still require human intervention to determine when to subculture. Thus, it is necessary to accurately and objectively determine the appropriate time for cell passaging. Optimal stem cell culturing that maintains cell pluripotency while maximizing cell yields will be especially important for efficient, cost-effective stem cell-based therapies. Toward this goal a real-time computer vision-based system that monitors the degree of cell confluency with a precision of 0.791 ± 0.031 and recall of 0.559 ± 0.043 was developed. The system consists of an automated phase-contrast time-lapse microscope and a server. Multiple dishes are sequentially imaged and the data is uploaded to the server that performs computer vision processing, predicts when cells will exceed a pre-defined threshold for optimal cell confluency, and provides a Web-based interface for remote cell culture monitoring. Human operators are also notified via text messaging and e-mail 4 hours prior to reaching this threshold and immediately upon reaching this threshold. This system was successfully used to direct the expansion of a paradigm stem cell population, C2C12 cells. Computer-directed and human-directed control subcultures required 3 serial cultures to achieve the theoretical target cell yield of 50 million C2C12 cells and showed no difference for myogenic and osteogenic differentiation. This automated vision-based system has potential as a tool toward adaptive real-time control of subculturing, cell culture optimization and quality assurance/quality control, and it could be integrated with current and developing robotic cell cultures systems to achieve complete automation.

6.2 INTRODUCTION

The use of stem cells for *in vitro* models of biological processes or for *in vivo* cell-based therapies typically requires total initial cell numbers that exceed those normally available from a single isolate of primary cells [1-6]. To produce sufficient numbers of cells requires first inducing proliferation *in vitro* utilizing standard subculturing processes whereby cells undergoing proliferation in each culture vessel are periodically subdivided and re-plated into multiple vessels through several passages [1]. The decision on when to passage cells is currently based on a human operator's visual assessment of cell confluency, which refers to the amount of space in a tissue culture vessel that is occupied by cells and reflects cell population density. Predetermined schedules of time-points for subculturing might be sufficient for growing well characterized, established cell lines [7-10]. However, in general, unpredictable changes or disturbances in culture conditions [11] or large variations in isolate-to-isolate applications of primary cells [12, 13] dictate that subculture be adaptively determined on-the-fly by direct observation of confluence over time [14]. Traditionally, human operators manually estimate confluence by microscopic observations and subsequently decide on the appropriate time for performing subculture. Presently, the majority of automated or semi-automated cell culture systems that are commercially available or in development still rely on either human oversight or a pre-determined schedule to monitor cell cultures [7-10, 14]. While there are systems that use electrical impedance measurements of the cell-substrate as an indirect but automatic measure of confluence [15], some human oversight will still likely be required to monitor the process, including observing cell density and morphology to ensure optimal culture quality. The use of human operators to make decisions on subculturing is highly subjective and prone to intra- and inter-operator variability [7]. And, in the production of clinical-grade cells, the high cost of

skilled labor substantially increases the costs of quality control (QC) and quality assurance (QA) operations [16]. Furthermore, it is not practical or cost-effective for human operators to manually observe and monitor cell cultures continuously, and therefore key events such as the optimal times to perform subculture or identify problems might be missed. Delayed subculturing can result in cell overgrowth, which leads to loss of stem cell differentiative potential or stemness [11, 17], whereas premature subculturing can lead to longer production times to achieve targeted cell yields, with associated added costs. The overall lack of reproducibility and control of clinical-grade cell expansion processes is a major concern of government regulatory bodies since this has a direct impact on product performance and product reproducibility [18-20]. In addition, the lack of subculture standardization and reproducibility hampers scaled, robust and cost-effective manufacture of cells and has been cited as a major hurdle in the development of stem cell engineered products [7, 16].

Therefore, whether using a manual or robotic cell culture system, there is a need to automate monitoring of and decision-making for the subculturing process [16]. To begin to address this need, machine vision technology has been applied to detect cells and measure confluence to determine the appropriate time to culture cells [17, 21]; however, the images derived from this system are similar to that of a brightfield microscope and as such, of low-contrast [21], making it difficult to verify cell detection performance. Additionally, this system did not incorporate real-time predictive modeling of cell growth, and lacks the capability to function as part of a QA/QC system by raising warning alarms if growth was not progressing as expected and, in manually operated systems, as a tool to alert human operators in a timely manner to make preparations for subculture.

Herein a new technology platform for continuous, fully automated monitoring, analysis, and predictive growth modeling of phase-contrast time-lapse microscopy imaging of the subculturing process has been developed. This platform is based on a previously developed real-time, computer vision-based cell tracking system [22], which is capable of tracking all cells and their lineages in an image sequence at high levels of confluence with high levels of accuracy and is amenable to analysis with population growth modeling tools [23]. These components are combined within the framework of a Web-based human-computer interface whereby images are acquired at 5 minute-intervals and uploaded to a server for image processing and analysis to predict future confluency. These results can be viewed over the Web, allowing human operators to conveniently monitor the process remotely. Furthermore, the system alerts the operators by email and text messaging 4 hours prior to reaching a pre-defined confluency threshold so that preparations for cell culture can be made, and an additional reminder is sent when the predefined threshold for confluency is reached. This system was validated by directing the expansion of mouse C2C12 cells as a paradigm stem cell population with the criterion that confluency must not exceed 0.5 (50%) in order to minimize the incidence of myoblast fusion that would otherwise deplete the stem cell population. Subsequently, C2C12 cells were differentiated towards myogenic and osteogenic fates to confirm that cells retained their capacity to differentiate into multiple cell types following cell expansion.

6.3 MATERIALS AND METHODS

6.3.1 Cell Culture

Mouse C2C12 cells (ATTC, Manassas, VA) were grown in Dulbecco's Modified Eagle's Media (DMEM; Invitrogen, Carlsbad, CA), 10% fetal bovine serum (Invitrogen, Carlsbad, CA) and 1% penicillin-streptomycin (PS; Invitrogen, Carlsbad, CA). For myogenic differentiation, cells were

grown in low serum containing myogenic differentiation media (DMEM, 2% Heat-inactivated horse serum, 1% PS) for 4 days with media renewal every 48 hours. For osteogenic differentiation, cells were grown in complete serum containing 100 ng/mL BMP-2 (Genetics Institute, Cambridge, MA) for 4 days with media renewal every 48 hours. Cells were kept at 37^{o}C, 5% CO_2 in a humidified incubator.

6.3.2 Phase-Contrast Time-Lapse Microscopy

Time-lapse phase-contrast microscopy was performed using a Zeiss Axiovert T135V microscope (Carl Zeiss Microimaging, Thornwood, NY) equipped with a 5X, 0.15 N.A. phase-contrast objective, a custom-stage incubator capable of housing up to four 35mm Petri dishes, and InVitro software 3.2 (Media Cybernetics Inc., Bethesda, MD). Three fields of view representative of the cell density from each dish were selected, resulting in a total of 12 fields of view per culture experiment for both human- and computer-directed subculture experiments. Microscope images contained 1392 x 1040 pixels with a resolution of 1.3μm/pixel. Images were acquired at a frequency of every 5 minutes over a course of 1.5 – 3 days as determined by either the human operator or computer-generated confluency measurements.

6.3.3 Confluency Measurement and Evaluation

Every 5 minutes, a set of phase-contrast microscope images was acquired (12 different fields of view from 4 Petri dishes) and the images were automatically uploaded from the local microscope computer to a server (Open Cirrus™, a HP/Intel/Yahoo! Open Cloud Computing Research Testbed, https://opencirrus.org/) via a fast and versatile file copying tool known as rsync [24], which is available at http://www.samba.org/ftp/rsync/rsync.html. The server also contained the

computer vision-based cell tracking software, which segmented each image to identify and label cell and non-cell regions [25].

Confluency for each image was calculated by dividing the number of pixels labeled as ‘cells’ over the total number of pixels in the image. The overall confluency was then calculated by averaging the confluency values from an entire image set (12 images) acquired at a single time point. To evaluate the accuracy of the algorithm, 3 phase-contrast images containing cells at different levels of confluency (low, medium and high) were printed onto a piece of paper and manually segmented using a red marker pen to trace the outline of cells. These cell tracings were then digitized using a Hewlett Packard Scanjet 5550c flatbed scanner (Hewlett Packard, Palo Alto, CA). Then, the cell tracings were selected using the ‘Color Range’ tool in Adobe Photoshop 7.0 (Adobe Systems, San Jose, CA) and manually filled in with color using the ‘Paintbrush’ tool to generate a binary image consisting of cell and non-cell regions. Where necessary, a combination of the ‘Paintbrush’ and ‘Eraser’ tools was used to touch up the images because the scanner did not accurately capture the cell tracings. Pixels that contained cells in both the manually segmented and computer segmented images were considered true positives. Pixels that contained cells in the computer segmented images but did not overlap with cell positive regions in the manually segmented images were considered false positives. Pixels that contained cells in the manually segmented images but did not overlap with cell positive regions in the computer segmented images were considered false negatives. Pixels in the manually segmented images that did not contain any cells were considered true negatives. ‘Precision’ was defined as true positives divided by the sum of true positives and false positives. ‘Recall' was defined as true positives divided by the sum of true positives and false negatives.

6.3.4 Confluency Prediction and Notification

The algorithm for confluency prediction was written in Matlab® (Mathworks, Natick, MA) and ran on a server, which is part of the HP/Intel/Yahoo!'s Open Cirrus™ Project. For the server, a virtual machine running a dual core processor and 2 GB Ram was created. For each set of images, the average confluency for the previous 300 frames was fitted to a 2nd order polynomial curve using the Matlab® polyfit() function and the estimated confluency in the next 4 hours was determined using the Matlab® polyval() function. If the value of the estimated confluency within the next 4 hours was greater than or equal to the threshold for confluency (0.5), the Matlab® sendmail() function was used in conjunction with Matlab® TxtMsgCreate to send an email and text message via a Gmail (Google Inc., Mountain View, CA) simple mail transfer protocol (SMTP) server. Similarly, a reminder email and text message was also sent when the threshold for confluency had been reached.

6.3.5 Cell Calculator User Interface Tool

The web calculator interface was developed using HTML and Javascript to facilitate calculation of the theoretical cell yield. At the beginning of the experiment, the target number of cells and the initial number of dishes were entered into the calculator by the user. Subsequently, during cell passaging, the average number of cells obtained per dish was obtained using a hemocytometer and this number was entered into the web calculator. If the total number of cells harvested was more than or equal to the target number of cells, a 'Stop experiment' message was displayed and broadcast to signal that the experiment should be terminated. Otherwise, a 'Continue experiment' message was issued and the user replated the cells at low density into additional Petri dishes for further cell expansion until the target cell number was achieved. For these experiments, a subculture ratio of 1:8 was assumed.

6.3.6 Real-time Adaptive Culture

C2C12 cells were seeded at a density of 1.5 x 10^4 cells/35mm dish (~ 0.156 x 10^4 cells/cm^2) and allowed to attach for 3-6 hours prior to initiating phase-contrast time-lapse microscopy. Cells were cultured until an average confluency of 0.5 was reached in 4 dishes as determined by either the human operator or computer-generated confluency measurements. Both human- and computer-directed subculture observations were limited to 12 fields of view per culture experiment. At ~ 0.5 confluency, the cells were trypsinized and the total number of cells were manually determined with the aid of a hemocytometer. This number was entered into the web-based cell calculator. If the total number of cells was less than the target number of cells, the experiment was continued and a serial culture of cells was plated for a subsequent round of cell expansion with monitoring of cultures via phase-contrast time-lapse microscopy. For each serial culture, a subculture ratio of 1:8 was assumed. The experiment was terminated when the total cell number was equal to or more than the target number of cells. Following this, the differentiation capability of this expanded population of cells were tested by growing these under osteogenic and myogenic conditions and subsequently performing staining for osteogenic (Alkaline phosphatase; ALP), myogenic (Myogenin) and pluripotency (Pax7) markers.

6.3.7 Alkaline Phosphatase (ALP) Staining

Cells were seeded into 12 well plates at a density of 12 x 10^4 cells/well or 3.16 x 10^4 cells/cm^2 under osteogenic and control conditions for 4 days. Cells were washed in PBS and fixed for 2 min in 3.7% formaldehyde. ALP activity was detected according to the manufacturer's instructions (Kit 86C, Sigma-Aldrich, St. Louis, MO). Where required, ALP-stained images were converted to CMYK format since this color format is representative of reflected light colors as opposed to emitted light colors (RGB). Since cyan and magenta form the color blue, these

channels were added together and inverted. The 'levels' tool and the 'histogram' tool in Adobe Photoshop 7.0 were used to normalize the background and determine the average pixel intensity, respectively. Statistical analysis was performed as described below.

6.3.8 Myogenin and Pax7 Immunofluorescence Staining

Cells were seeded into 35mm glass-bottom Petri dishes at a density of 30 x 10^4 cells/dish or 3.16 x 10^4 cells/cm^2 under myogenic conditions for 4 days. Cells were washed in PBS, fixed in methanol for 5 min, air-dried and blocked with 10% donkey serum (Jackson Immunoresearch, West Gove, PA) for 20 min at room temperature (RT). For mouse-on-mouse staining, an additional blocking step was performed by incubating cells with 100 µg/mL donkey anti-mouse FAB (Jackson Immunoresearch, West Gove, PA) for 1 h at RT. Cells were then rinsed with wash buffer (PBS, 0.1% BSA) and incubated with primary antibodies: rabbit anti-myogenin (2 µg/mL; Santa Cruz Biotechnology Inc, Santa Cruz, CA) and mouse anti-Pax7 (2 µg/mL; Santa Cruz Biotechnology Inc, Santa Cruz, CA) overnight at 4^{o}C. Cells were then rinsed three times with wash buffer and incubated with secondary antibodies for 1 h at RT – donkey anti-mouse Dylight 488 nm and donkey anti-rabbit Dylight 649 (15 µg/mL each; Jackson Immunoresearch, West Gove, PA). Lastly, cells were rinsed 5 times with wash buffer and imaged using a Zeiss Axiovert 200M microscope (Carl Zeiss Microimaging, Thornwood, NY) equipped with a LED light source.

6.3.9 Statistical Analysis

A student's t-test was performed using Microsoft Excel software (Microsoft Corporation, Redmond, WA) to determine significance among treatment groups. A *p-value* ≤ 0.05 was considered statistically significant.

6.4 RESULTS

6.4.1 Real-time Adaptive Subculture System

The overall scheme of the real-time adaptive subculture system is summarized in Figure 6.1. The automated computer vision system comprised of an automated phase-contrast time-lapse microscope that acquired images every 5 minutes from multiple dishes housed in a heated-stage incubation chamber. These phase-contrast images were subsequently uploaded with Rsync to a server, where computer vision processing was used to identify cells within each image to determine the degree of confluency (Figure 6.1 and Figure 6.2). Predictive modeling employing a 2^{nd} order polynomial fit was empirically found to be most suitable for predicting C2C12 growth (Figure 6.3 and Figure 6.4) and was used to determine when the level of confluency would reach a user-defined threshold of 0.5 confluency (Figure 6.1, Figure 6.5 and Figure 6.6). 4 hours prior to reaching this threshold, the predictive modeling subroutine alerted the human operator, via text messaging and email to make preparations for cell culture (Figure 6.1 and Figure 6.8). In addition, the web-based application facilitated remote monitoring of confluency in individual dishes as well as confluency measurements and predictions via the Internet (Figure 6.5). When cells reached the threshold for confluency, another email and text message was sent to remind the user (Figure 6.1, Figure 6.7). The cells were then subcultured and the total number of cells was determined (Figure 6.1 and Figure 6.8). If the target cell number was achieved, the experiment was terminated (Figure 6.1). Otherwise, the cells were re-plated at low density for further cell expansion and the process was repeated until the target cell number was reached (Figure 6.1).

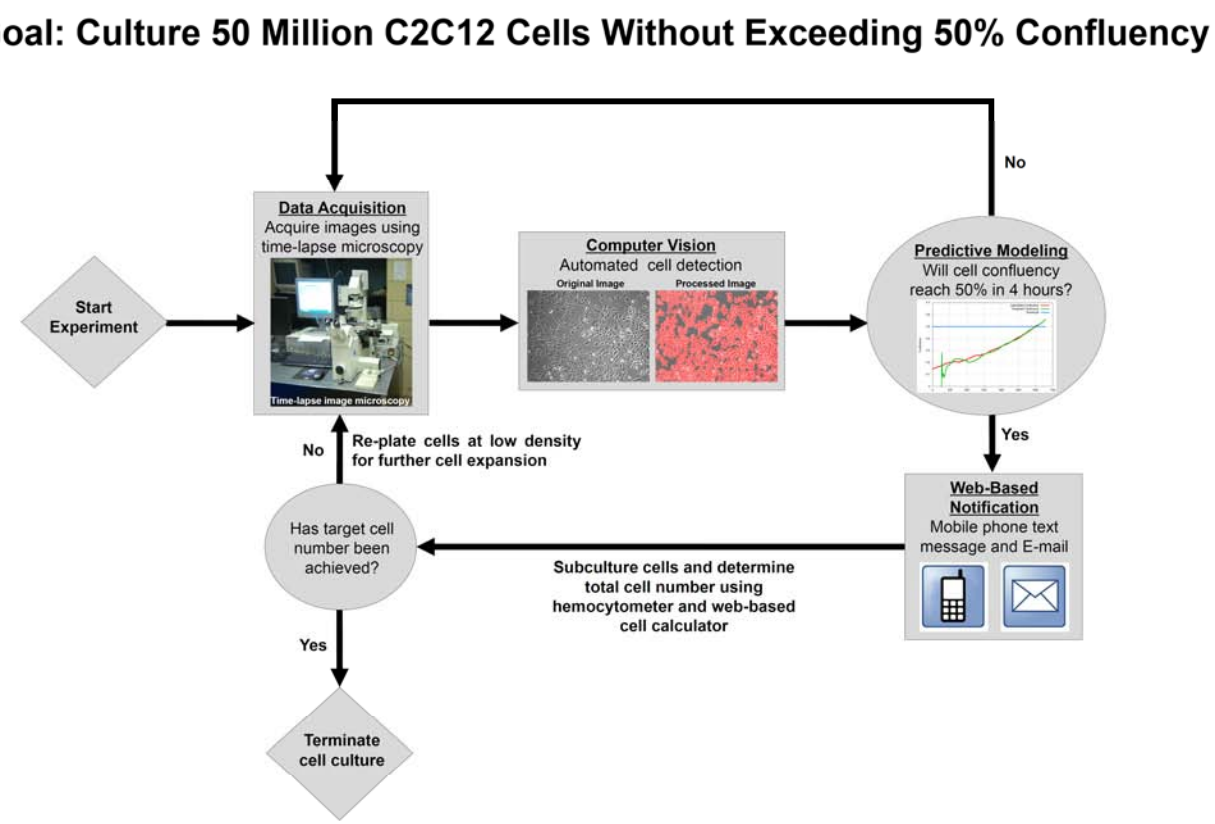

Figure 6.1. Overall Scheme of Real-Time Adaptive Cell Culture System. Data are acquired using phase-contrast time-lapse microscopy and sent to a server for image processing where the confluency is calculated and predicted. 4 hours prior to reaching a predefined threshold for confluency (0.5 confluence), an email and text message is sent to alert the user to prepare for subculture. When the cells have achieved the threshold for confluency, another email and text message is sent to remind the user. The cells are subcultured and the total cell number is counted. If the target cell number has been achieved, the experiment is terminated. Otherwise, the cells are replated at low density for further cell expansion and the process is repeated until the target cell number is achieved.

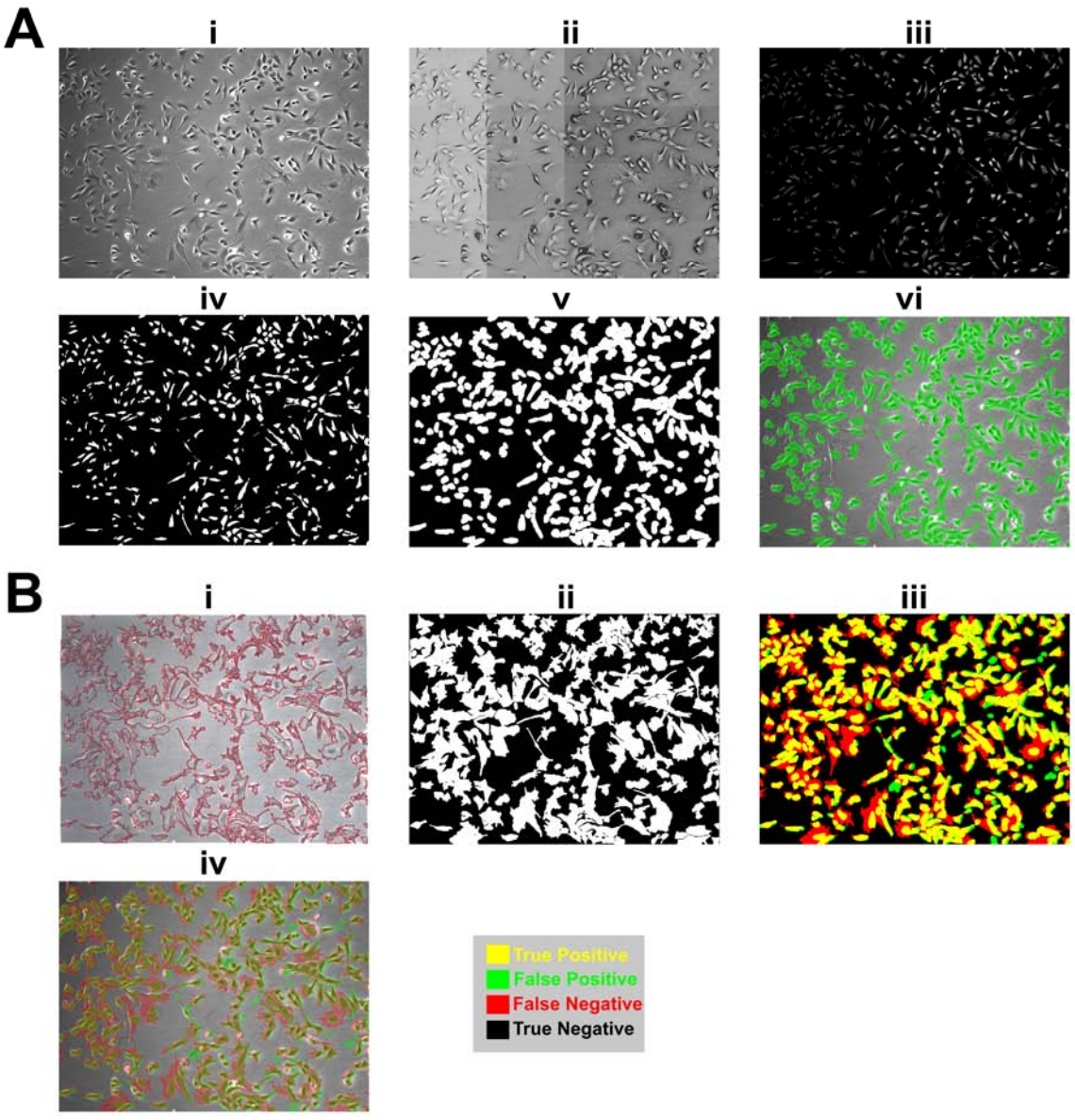

Figure 6.2. Calculation and Evaluation of Confluency. **A.** Process of computer-generated confluency. (i) Original image. (ii) Image is inverted during the initial part of the restoration process to remove halo and shade-off artifacts. (iii) After restoration. (iv) Basic thresholding is applied to obtain a confluency mask. (v) The confluency mask is dilated to capture cellular processes that are hard to discern from background. (vi) The computer-generated confluency mask (green) is overlaid on top of the original image. **B.** Evaluation of computer-generated confluency versus human-generated confluency. (i) Human-generated cell tracing. (ii) The cell tracing is digitized and filled in to generate a confluency mask. (iii) The computer-generated confluency mask (green) is overlaid on top of the human-generated confluency mask (red) with overlapping regions (yellow, true positive) against the background (black, true negative). Green-only regions (false positive). Red-only regions (false negative). (iv) The computer- (green) and human-generated (red) confluency masks are overlaid on top of the original image with overlapping regions highlighted (yellow).

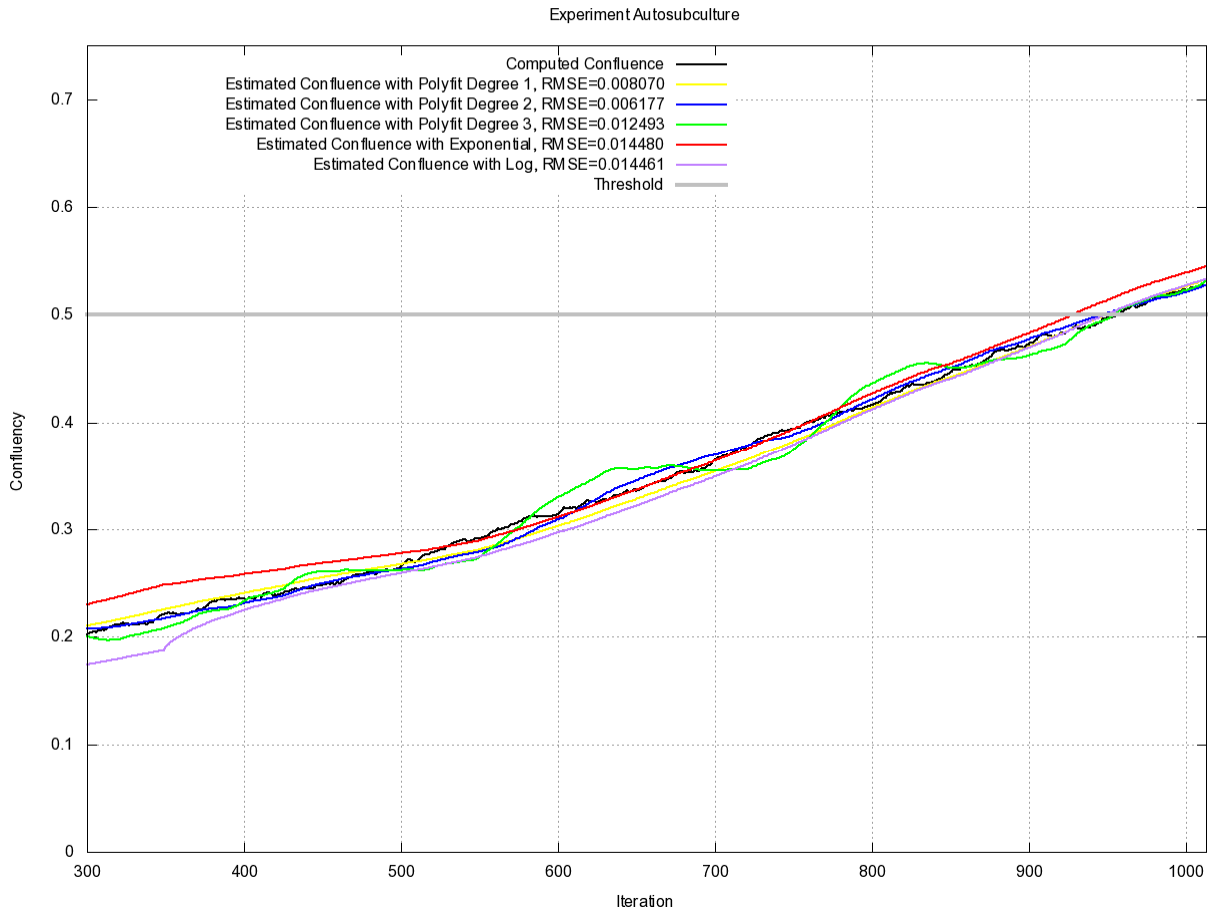

Figure 6.3. Modeling C2C12 cell confluency by five methods utilizing every data point/frame: (1) 1st order polynomial (yellow line), (2) 2nd order polynomial (blue line), (3) 3rd order polynomial (green line), (4) logarithmic function (magenta line), (5) Exponential (red line). The computer-generated confluency measurement (black line) and the confluency threshold (grey line) are indicated. The 2nd order polynomial model fits the observed data (actual computed confluence) with the least root mean square error (RMSE). 1 data point/frame is equivalent to 5 min. The data shown were derived from image sequences of C2C12 cells from 3 independent experiments, each with at least 4 replicates (n = 12).

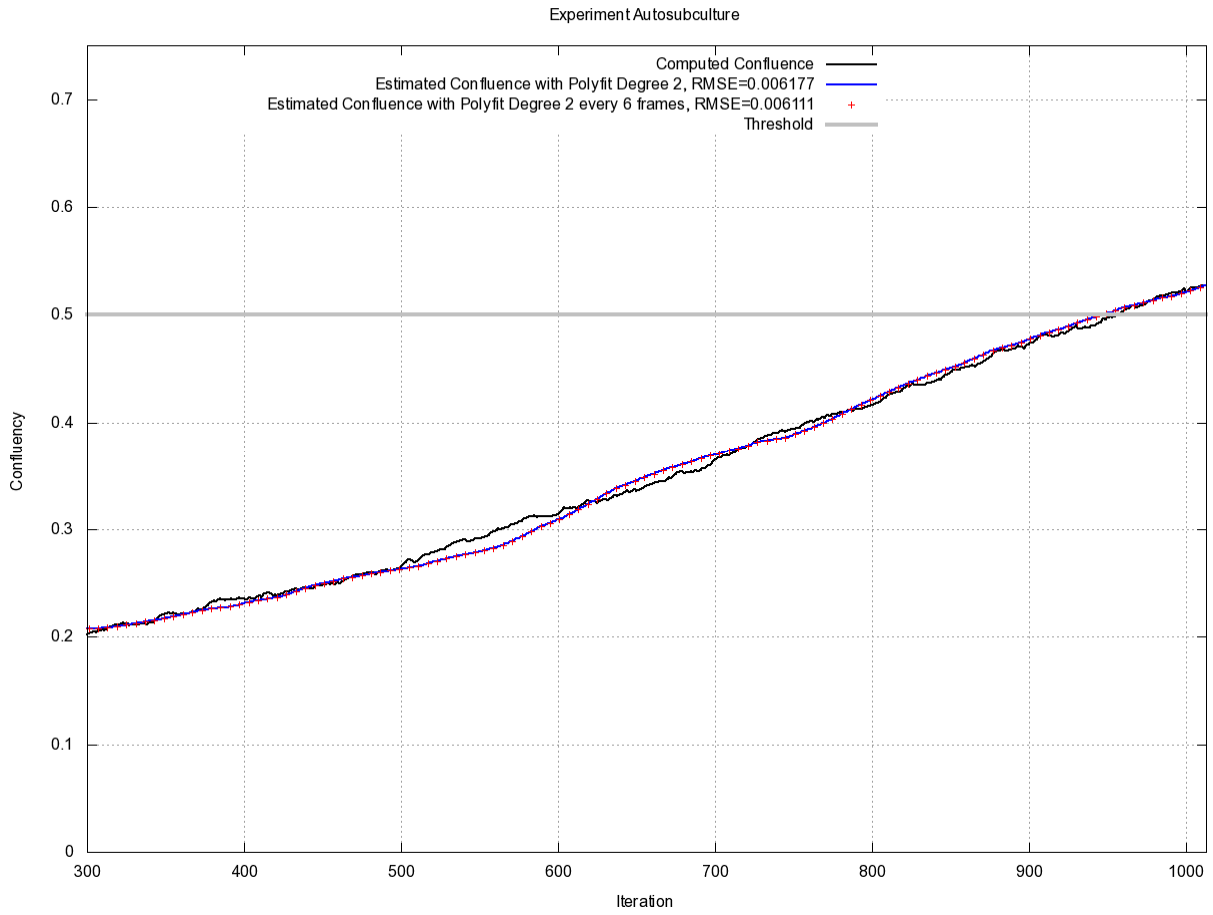

Figure 6.4. Comparison of C2C12 cell confluency predictions utilizing every data point/frame (blue line) versus every 6th data point/frame (red cross). The computer-generated confluency measurement (black line) and the confluency threshold (grey line) are indicated. Both 2nd order polynomial models fit the observed data (actual computed confluence) with little-to-no difference in root mean square error (RMSE), indicating that every 6th data point/frame is sufficient to make accurate cell confluency predictions. 1 data point/frame is equivalent to 5 min. The data shown were derived from image sequences of C2C12 cells from 3 independent experiments, each with at least 4 replicates (n = 12).

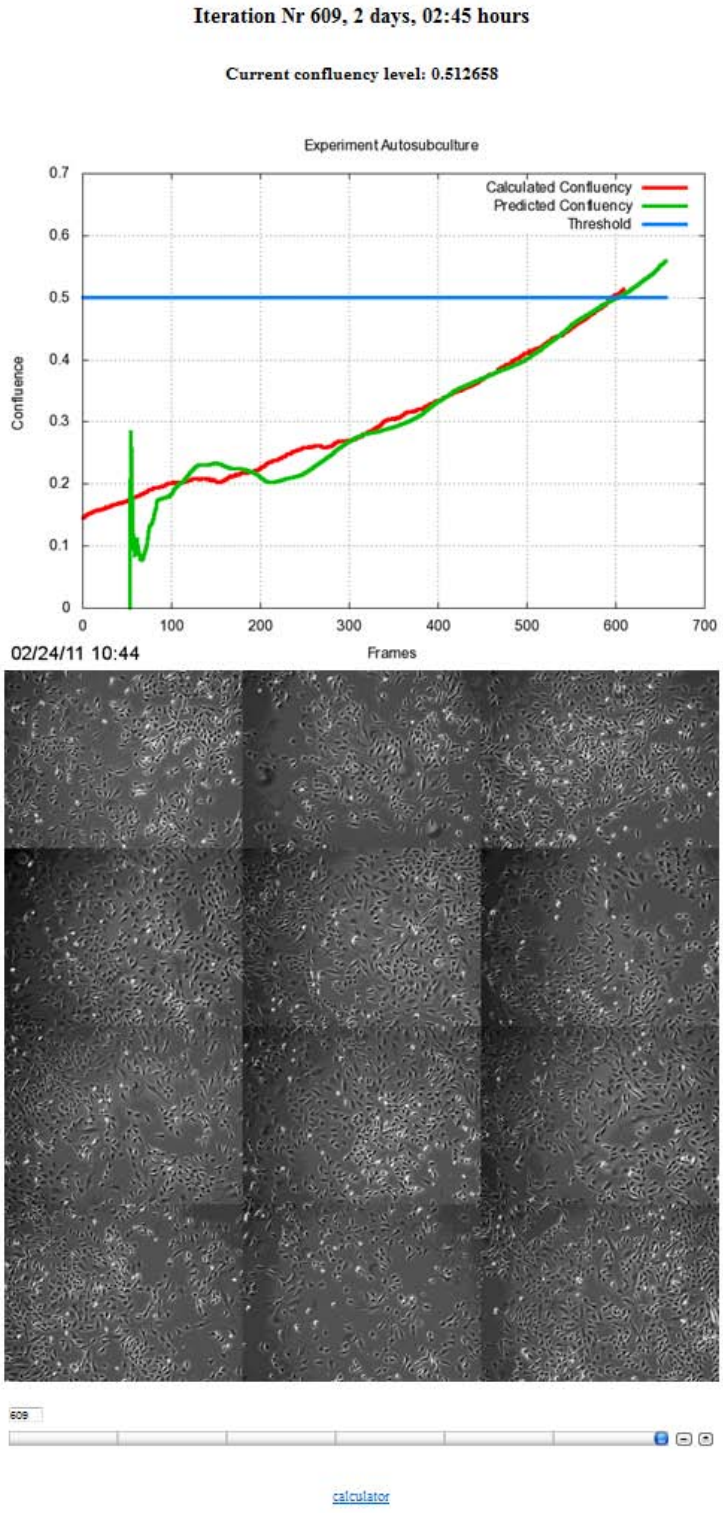

Figure 6.5. Remote Monitoring of Confluency and Predictive Modeling via the Internet. A screen capture of the graphic user interface from the real-time adaptive cell culture system illustrating the calculated confluency level and predictions (top) and individual fields of view (bottom).

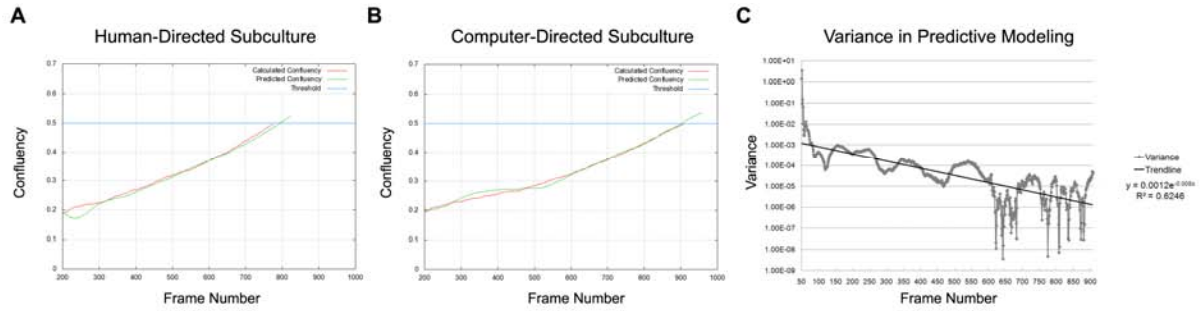

Figure 6.6. Confluency Prediction. **A.** Human-directed subculture. Confluency prediction was based on the human operator's previous cell culture experience. The graphs show archived time-lapse image data from the human-directed subculture that was processed with the confluency prediction model for the purpose of comparison with the computer-directed subculture. **B.** Computer-directed subculture. The predefined threshold for confluency (blue line). The calculated confluency (red line). The predicted confluency (green line). 1 frame is equivalent to 5 minutes. **C.** Variance in confluency prediction and actual confluency measurement in computer-directed subculture. Variance (grey line) and trendline (black line) are as indicated.

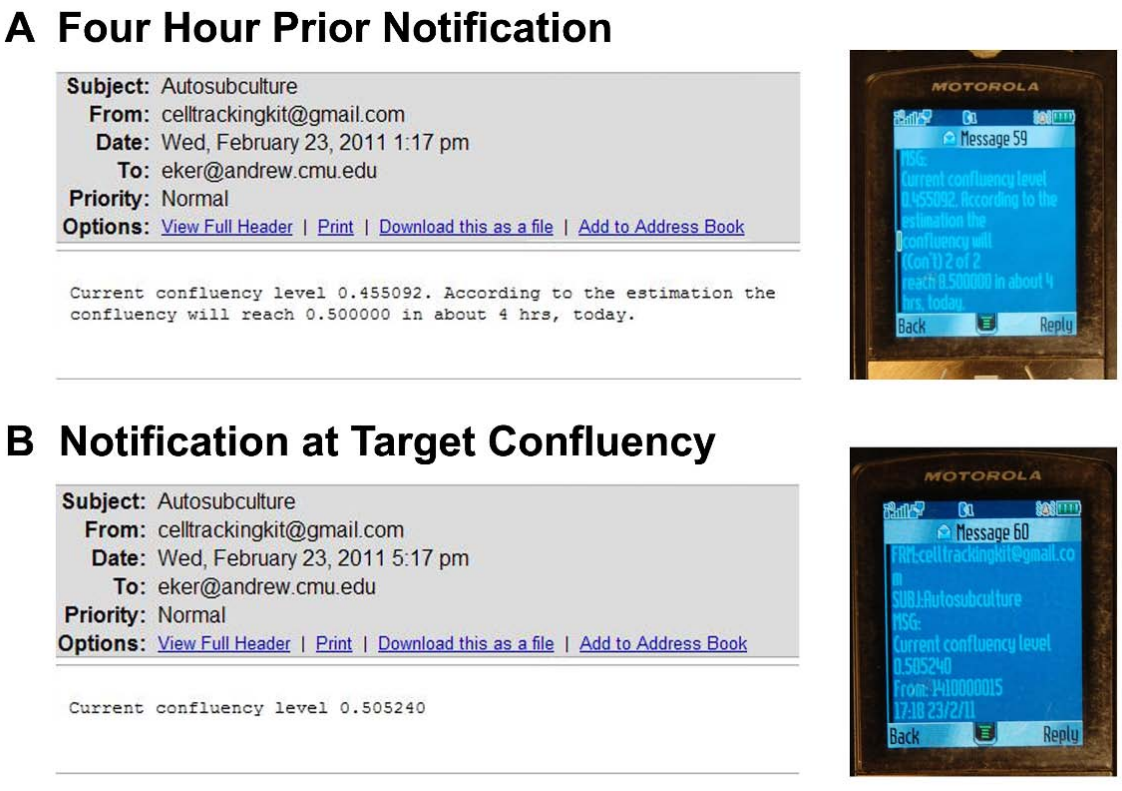

Figure 6.7. Email and Text Notification. **A.** 4 hours prior to reaching the predefined threshold for confluency, an email and text message is sent to alert the human user to prepare for subculture. **B.** Once the threshold for confluency is reached, a reminder email is sent.

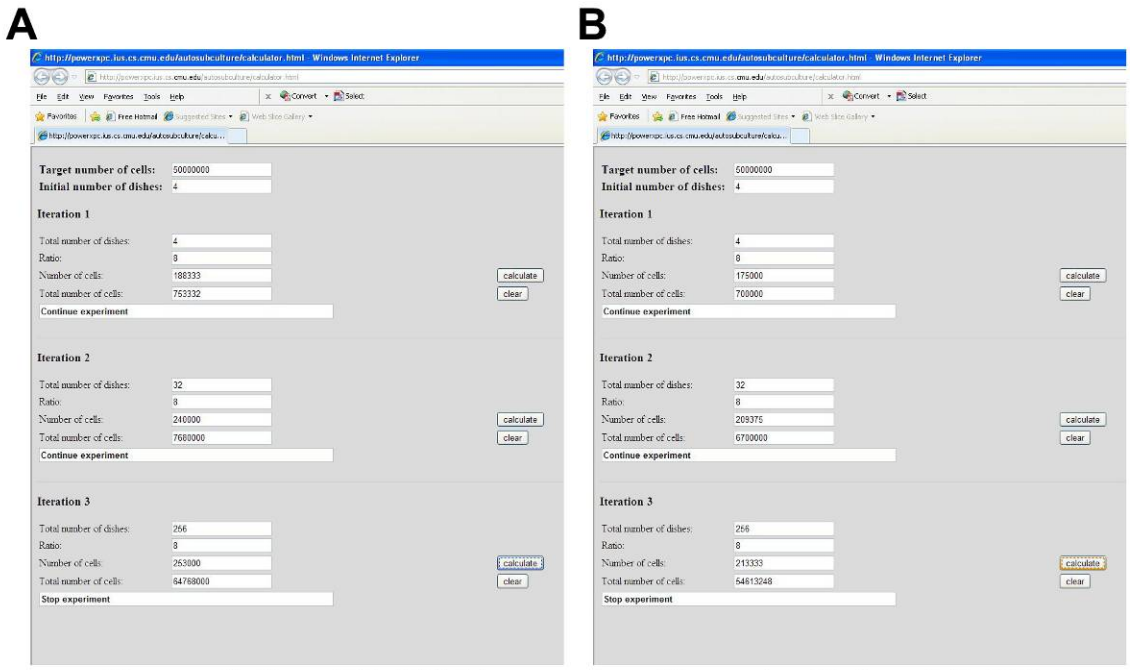

Figure 6.8. Total Theoretical Cell Yield Achieved from Human- and Computer-directed Subcultures. **A.** Human-directed subculture. **B.** Computer-directed subculture. Both human- and computer-directed subcultures required 3 serial passages to achieve a theoretical cell yield of 50 million C2C12 cells without exceeding 0.5 confluency.

6.4.2 Evaluation of Confluency

To determine the confluency in a given phase-contrast image (Figure 6.2Ai), a process known as restoration was applied (Figure 6.2Aii, Aiii) to generate an artifact-free image (Figure 6.2Aiii). Basic thresholding was subsequently used to obtain a binary image (Figure 6.2Aiv) consisting of cell (white) and non-cell regions (black), which was termed as a 'confluency mask'. Taking into account that several cellular structures such as filopodia and lamellipodia were difficult to distinguish against the image background, this confluency mask was further dilated by a factor of 8 (Figure 6.2Av). The resultant confluency mask (Figure 6.2Avi, green) was overlaid on top of the original image and showed good correspondence with regions containing cells. To quantify this correspondence, phase-contrast images at different levels of cell density were manually segmented using a red marker pen to trace the outline of cells (Figure 6.2Bi). The cell tracings

were digitized and filled in to generate confluency masks (Figure 6.2Bii). The human-generated confluency mask (Figure 6.2Biii, red and yellow regions) shows good correspondence with the computer-generated confluency mask (Figure 6.2Biii, green and yellow regions) with overlapping regions highlighted in yellow (Figure 6.2Biii, true positive) against the background (Figure 6.2Biii, black regions, true negative). Regions highlighted only in green and red were considered false positives and false negatives, respectively (Figure 6.2Biii). Some discrepancies between the human- and computer-generated confluency masks were observed, particularly for large, well-spread out cells (Figure 6.2Biv). The precision of the computer-generated confluency measurement was determined to be 0.791 ± 0.031 with a recall of 0.559 ± 0.043 (Table 6.1).

Table 6.1. Confluence Measurements from Computer-Directed Subcultures.

	± SEM
Difference between Time-to-Estimated Threshold for Confluency and Actual Threshold for Confluency[a] (hours)	4 ± 0
Average Confluency at Time of Notification[a]	0.499 ± 0.003
Precision[b] (TP/TP+FP)[c]	0.791 ± 0.031
Recall[b] (TP/TP+FN)[c]	0.559 ± 0.043

[a] n = 3 independent experiments, [b] n = 3 phase-contrast images, [c] TP = true positive; FP = false positive; FN = false negative

6.4.3 Performance of Real-time Adaptive Subculture System

To determine if the performance of the real-time adaptive subculture system was similar to that of an experienced human operator, a set of human- and computer-directed cell expansions were performed. To facilitate such a comparison, time-lapse images from the human-directed cell

expansions were processed similarly as the computer-directed cell expansions *a posteriori* to determine confluency in human-directed cell expansions. Both human- and computer-directed subculture data showed similar performance in estimating and predicting when actual confluency (Figure 6.6A, B, red line) was close to the threshold for confluency (Figure 6.6, blue line). The predictive modeling performed poorly in the initial 200 frames (Data not shown) but progressively became more accurate as more data points were acquired and achieved a variance of close to zero (Figure 6.6A, B, green and red line, Figure 6.6C and Table 6.1). This enabled an accurate 4 hour prior notification (4 hours ± 0, $\sigma^2 = 0$) of when the confluency threshold (0.499 ± 0.003) would be exceeded (Figure 6.7 and Table 6.1). Using the criteria that C2C12 cells should not exceed a confluency of 0.5, both human- and computer-directed cell expansions required 3 serial cultures to reach a theoretical yield of 50 million C2C12 cells (Figure 6.8) with an average cell yield of 22.71 ± 1.97 x 10^4 cells/dish and 19.92 ± 1.22 x 10^4 cells/dish, respectively (Table 6.2). No significant difference was observed between the average cell yield obtained from human- and computer-directed cell expansions ($p = 0.308$).

Table 6.2. Average Cell Yield per 35mm Petri Dish for Human- and Computer-directed Subcultures.

	Number of Cells (x 10^4 cells per 35mm Petri dish) ± SEM
Human-directed Subculture	22.71 ± 1.97
Computer-directed Subculture	19.92 ± 1.22

In addition, human- and computer-expanded C2C12 cells showed increased ALP expression compared to control ($p = 0.021$ for human-directed cell expansion and $p = 0.002$ for computer-directed cell expansion) in response to BMP-2 treatment, indicating that BMP-2-treated cells were differentiating towards an osteoblast fate (Figure 6.9). Furthermore, when grown under low-serum conditions to induce myogenesis, both human- and computer-expanded C2C12 cells stained positive for the myogenic marker, Myogenin in multi-nucleated and elongated myotubes (Myogenin, Figure 6.10) whereas undifferentiated mononuclear cells stained positive for the stem cell marker, Pax7 in the cell nucleus (Figure 6.10). Together, these results confirmed that both human- and computer-directed expanded cells maintained their stem cell capacity and were capable of undergoing osteogenic and myogenic differentiation under the appropriate conditions (Figure 6.9 and Figure 6.10).

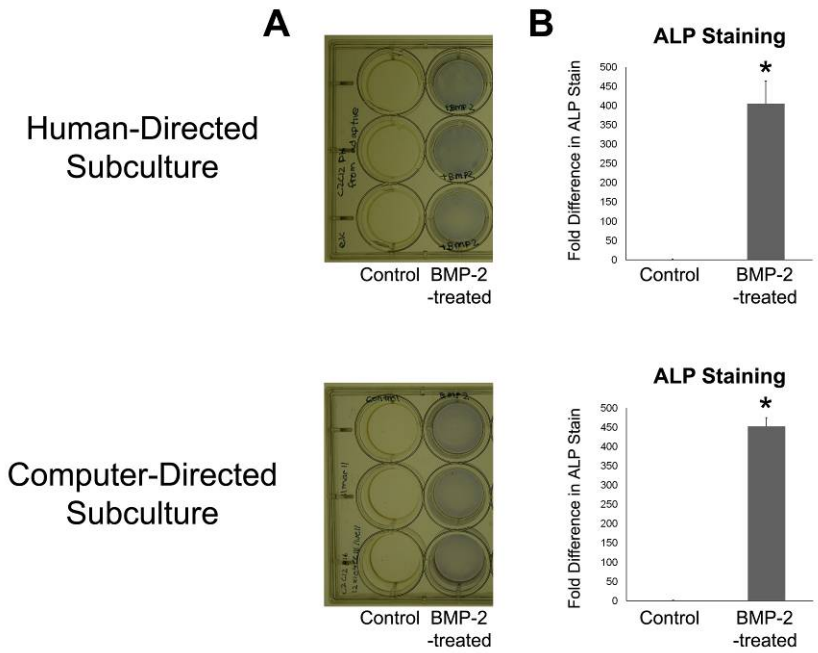

Figure 6.9. ALP Staining of Human- and Computer-directed Subcultures. **A.** ALP-stained plates. BMP-2-treated cells stain positive (blue) for the osteogenic marker, ALP. **B.** Quantification of ALP intensity (fold difference compared to control). This shows that cells expanded from both human- and computer-directed subcultures were still responsive to BMP-2-induced ALP expression, indicating that cells were differentiating towards an osteoblast fate.

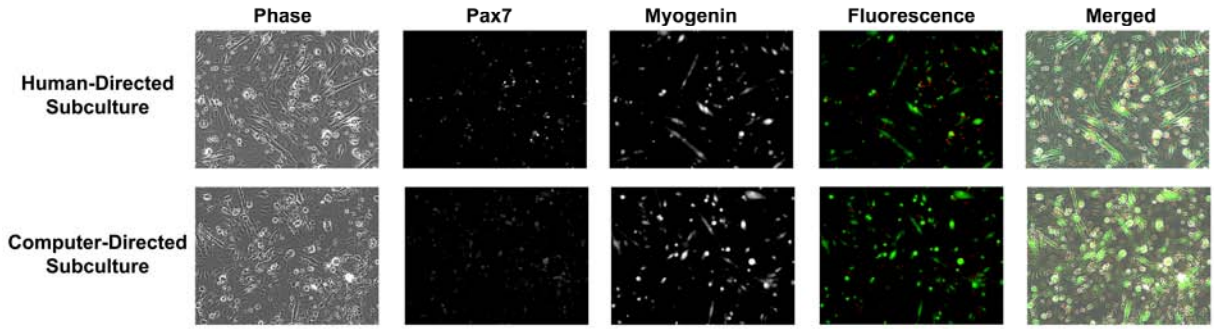

Figure 6.10. Myogenin and Pax7 Staining of Human- and Computer-directed Subcultures. After 96h in myogenic conditions, cells that have fused and differentiated towards a myocyte fate (elongated cells containing multiple nuclei) stain positive for the myogenic marker Myogenin (green). Undifferentiated cells stain positive for the stemness marker, Pax7 (red). This shows that cells expanded from both human- and computer-directed subcultures were capable of myocyte differentiation while undifferentiated cells retained their stemness marker.

6.5 DISCUSSION

6.5.1 Computer-Generated Cell Confluency Measurements for Manual and Adaptive Subculture

Toward the goal of achieving complete automation and consistency for stem cell culture expansions, an automated computer vision-based system was developed for continuous monitoring and analysis of *in vitro* cell cultures to objectively determine the appropriate time to subculture cells based on confluency measurements (Figure 6.1). The main impetus for this work is that in the current state-of-art automated cell culture machines are capable of executing the cell passing procedure with high precision and minimal variability [7], however, they lack the ability to make adaptive decisions based on how fast or slow a culture of cells are growing. Furthermore, in manually-operated systems, estimation of confluency by human operators is highly subjective and dependent on the experience of the operator. The confluency measurement algorithm developed here may additionally serve as a useful training aid for new tissue culture users and help to reduce the subjective nature of confluency estimation.

This system employs phase-contrast microscopy as it is a non-destructive imaging modality that is capable of generating high-contrast images of transparent specimens such as cells [26]. Thus,

cells can be easily visualized and imaged at high frequency, allowing the user to continuously monitor live cultures without affecting cell viability. Although an image acquisition period of 5 minutes was utilized in these experiments, cells can be imaged at a higher or lower frequency in accordance to experimental requirements, with computer hard disk space and computer algorithm run-time being the only limitations. After image acquisition, the archived data is sent to a server for processing (Figure 6.2) and 2^{nd} order polynomial curve fitting is used to predict future confluency (Figure 6.1, Figure 6.5 and Figure 6.6). Although the system is designed to be eventually autonomous when combined with a robotic-handling cell system, a human operator can remotely monitor the current and predicted levels of confluency as well as individual fields of view over the Internet (Figure 6.5). 4 hours prior to reaching a predefined threshold for confluency of 0.5, the human operator is alerted by the computer vision system via email and text messaging (Figure 6.7) to facilitate preparations such as warming media and various other reagents for cell culture. An additional reminder is sent when the predefined threshold for confluency is reached (Figure 6.7).

Although a standard computer with a dual core processor and 2 GB Ram is sufficient for implementing the confluency measurement and predictions on a local machine, a server (cloud computing cluster) was utilized so that multiple experiments can be conducted in parallel from different microscope computers or locations. This capability was recently demonstrated for single-cell tracking experiments using image data acquired simultaneously from Tokyo, Japan and Pittsburgh, USA (Intel Developer Forum 2010, California, USA; data not shown). Rsync was chosen for facilitating file transfers because it utilizes a delta-transfer algorithm, which reduces the amount of data sent over the network by sending only the differences between the source files and the existing files in the destination [24]. The algorithms employed in this

automated computer vision-based system are efficient and can process one set of images (12 phase-contrast images) prior to acquisition of the next set (within 5 minutes), enabling real-time monitoring and analysis of cell cultures. Although a high image acquisition rate is unnecessary for predicting confluency 4 hours ahead of time (Figure 6.4), it was used to demonstrate that accumulated photonic energy from a high image rate is non-detrimental to cell growth and that it would be feasible to eventually incorporate it into a real-time cell tracking software to monitor actively migrating and proliferating cells (Intel Developer Forum 2010, California, USA; data not shown), a process requiring high image rates. Furthermore, although less frequent data acquisition is adequate under normally progressing culture conditions (Figure 6.4), more frequent acquisition times would enable earlier identification of problems in a given culture, which may facilitate earlier interventions to mediate against possible loss of expensive or unique stem cell culture populations.

6.5.2 Accuracy of Computer-Generated Cell Confluency Measurements

Confluency, which is the percentage of the surface area in the cell culture vessel covered by cells, is traditionally used by cell biologists as a convenient indirect way to estimate the number of cells in a cell culture vessel. Thus, measuring confluency of an image area occupied by cells is an appropriate measure for estimating cell growth rates. The confluency algorithm utilized here segments cells on the basis of thresholding on the local intensity value of image pixels, a frequently applied methodology used in image segmentation. However, phase-contrast microscopy images have several characteristic halo and shade-off artifacts that arise as a result of technical limitations in the optical assembly of a phase-contrast microscope [26]. To improve segmentation results, a restoration process was applied to remove the halo and shade-off patterns to reconstruct an artifact-free image [25]. The output of the confluency algorithm has good

correspondence with manually annotated confluency (Figure 6.2B) with a precision of 0.791 ± 0.031 and recall of 0.559 ± 0.043 (Table 6.1). Precision and recall were used to assess the performance of the computer-generated confluency measurements because they are widely employed performance metrics used for pattern recognition algorithms. In general, a precision and recall close to 1.0 indicates good recognition performance. Although some discrepancies between the human- and computer-generated confluency masks were observed, these errors stemmed largely from large, well-spread out cells whose cellular processes were difficult to discern from the image background (Figure 6.2Biv), resulting in low recall (0.559 ± 0.043) owing to higher false negatives (Figure 6.2Biv and Table 6.1). However, the precision (0.791 ± 0.031) of the computer-generated confluency measurements is fairly high and these discrepancies in confluency measurement ultimately did not adversely impact C2C12 cell growth and differentiation (Figure 6.8, Figure 6.9 and Figure 6.10). Given that it is possible to segment cells with ease using computer vision technology, future improvements to the algorithm will incorporate additional measures such as cell density and assessment of cell shape, which may further inform cell culture decisions such as determining the percentage of differentiated cells in culture.

6.5.3 Computer-Generated Cell Confluency Predictions

To make confluency predictions, several data fitting models were empirically tested using previously acquired time-lapse phase contrast microscopy images of C2C12 cells and it was determined that that a 2^{nd} order polynomial model produced the best curve fit (Figure 6.3) and that approximately 200 frames were required before prediction becomes reliable and the variance becomes lower than 0.001 (Figure 6.6). A 4 hour advance notification was used in conjunction with the prediction model because this was a sufficient time window to allow for planning if

personnel were on site, or for a reasonable transport timeframe back to the laboratory, and/or preparation for subculture. Although a 2nd order polynomial was empirically found to be most suitable for predicting C2C12 cell confluency (Figure 6.3) and adequate for expanding C2C12 cells (Figure 6.9, Figure 6.10 and Table 6.2), this growth model may prove inadequate when culture conditions are altered or when different cell types are used. This is due to the sensitive nature of cells to their environments, which can be severely impacted by variability arising from cell handling, cell passage number, undefined media components such as fetal bovine serum as well as differences in growth and cell spreading rates when considering different cell types. For example, a population of cells that has been recently thawed from liquid nitrogen storage will display a slower rate of growth when compared to the same population after several passages. Mathematical models such as a 2nd order polynomial do not take perturbations in cell culture conditions into account and will exhibit poor performance when used under such scenarios. To overcome such limitations, a data-driven prediction model specific for C2C12 cells was developed by Yin *et al.* [23] using previously acquired time-lapse data. As long as cell culture conditions are constant, this model is able to predict confluency at least 8 hours in advance with a low error rate [23] and this will be incorporated into subsequent work.

6.5.4 Adaptive Subculture of C2C12 Cells

This system was successfully used to direct the expansion of C2C12 cells with the confluency threshold set at 0.5 (Figure 6.5, Figure 6.8, Figure 6.9, Figure 6.10, Table 6.1 and Table 6.2). C2C12 cells are utilized as a paradigm stem cell population because they are a multipotent cell line that has been previously shown to differentiate into cells of the musculoskeletal system [27-31]. In addition, C2C12 cells are sensitive to the level of confluency and must not be allowed to become confluent, otherwise, cells will spontaneously fuse and deplete the progenitor or stem

cell population. Thus, such a cell line serves an excellent model for testing this real-time adaptive subculture system. Both human- and computer-directed subculture experiments each required 3 serial passages to theoretically reach a target number of 50 million cells (Figure 6.8) and showed no significant difference ($p = 0.308$) in average cell yields per dish (Table 6.2).

Following cell expansion, C2C12 cells were differentiated towards osteogenic and myogenic fates to confirm that cells retained their capacity to differentiate into multiple cell types such as osteoblasts and myocytes (Figure 6.9 and Figure 6.10). In addition, undifferentiated mononuclear cells were shown to retain their stem cell identity as evidenced by positive staining for the stemness marker, Pax7 (Figure 6.10).

It is interesting to note that although the computer-directed cell expansion had lower variability in terms of cell yield compared to the human-directed cell expansion (Table 6.1), it is not drastically different. This result may stem from the limitation that only 12 fields of view were utilized in this experiment. Although attempts were made to ensure that the 12 fields of view were representative of culture conditions in each of the 4 dishes, it is possible that sampling a larger number of fields of view may lower the variability observed from cell yield. In addition, the use of a hemocytometer for manual cell counting may have also contributed to an increase in cell yield variability due to sampling error.

6.5.5 Adaptive Subculture for Stem Cell Manufacture and QA/QC

Given that stem cell manufacture for different applications, including large-scale production for multiple patient use and small-scale production for autologous use, requires extensive *ex vivo* handling and expansion of cells from various tissue sources [32], a QA/QC system is vital to ensure robust production of cells that are of consistent quality. Although this system currently

does not incorporate warning alarms to alert users of potential problems associated with cell growth, such problems are easily noticed when overall cell confluency decreases. In such scenarios, individual fields of view can be observed remotely to identify problems (Figure 6.5). Future work will incorporate additional algorithms that detect and measure cell behaviors such as mitosis [33], apoptosis and cell fusion to provide a more comprehensive view of cell population behavior for maximizing stem cell growth while minimizing stem cell differentiation. Although the use of a microscope stage incubation chamber limited the number of petri dishes that can be observed at a particular given moment, it provided a representative overview of cell growth and confluency to facilitate manual stem cell production with little to no obvious loss in myogenic and ostegenic potential (Figure 6.9, Figure 6.10 and Table 6.2). In addition, this system can be integrated with existing commercially available robotic technology for handling cell culture flasks, allowing for the confluency of every individual flask or dish to be monitored provided that the time required for imaging the desired number of cell culture flasks does not exceed the image acquisition rate. In scenarios where a large numbers of cell culture vessels must be monitored, multiple instruments and computers may be employed in parallel to decrease the time required for image acquisition and image processing.

6.6 CONCLUSIONS

In summary, an automated computer vision-based system for adaptive subculture of stem cells based on confluency has been developed. Using mouse C2C12 cells as a paradigm stem cell population, this study demonstrated that both human- and computer-directed cell expansions had similar performance in terms of the number of serial passages required to reach a target cell yield. Furthermore, both human- and computer-expanded cell populations were capable of differentiating towards osteoblast and myocyte fates, indicating that stem cell capacity was not

lost during cell expansion. This capability offers an approach to reproducibly expand cell populations and may have applications in the manufacture of clinically-relevant cells and/or their cell-derived products. Future work on this system will move towards complete automation of cell culture and QA/QC along with improved algorithm accuracy.

6.7 ACKNOWLEDGEMENTS

I would like to thank Silvina N. Junkers for coding assistance and execution of the server application. I would also like to thank Mei Chen, Elvira Osuna-Highley, Ryoma Bise, Sungeun Eom, Seung-il Huh, Michael F. Sandbothe and Zhaozheng Yin for helpful discussions related to these experiments. This work was supported by NIH grants RO1EB004343 and RO1EB007369 as well as funding from the Pennsylvania Infrastructure Technology Alliance (PITA).

6.8 REFERENCES

1. Koc, O.N., et al., *Rapid hematopoietic recovery after coinfusion of autologous-blood stem cells and culture-expanded marrow mesenchymal stem cells in advanced breast cancer patients receiving high-dose chemotherapy.* J Clin Oncol, 2000. **18**(2): p. 307-16.
2. Lindgren, K., et al., *Automation of cell line development.* Cytotechnology, 2009. **59**(1): p. 1-10.
3. Mason, C. and M. Hoare, *Regenerative medicine bioprocessing: building a conceptual framework based on early studies.* Tissue Eng, 2007. **13**(2): p. 301-11.
4. Qin, J., et al., *A stem cell-based tool for small molecule screening in adipogenesis.* PLoS One, 2010. **5**(9): p. e13014.
5. Saha, K. and J.B. Hurlbut, *Disease modeling using pluripotent stem cells: making sense of disease from bench to bedside.* Swiss Med Wkly, 2011. **141**: p. w13144.
6. Xu, Y., Y. Shi, and S. Ding, *A chemical approach to stem-cell biology and regenerative medicine.* Nature, 2008. **453**(7193): p. 338-44.
7. Liu, Y., et al., *Human cell culture process capability: a comparison of manual and automated production.* J Tissue Eng Regen Med, 2010. **4**(1): p. 45-54.
8. Terstegge, S., et al., *Automated maintenance of embryonic stem cell cultures.* Biotechnol Bioeng, 2007. **96**(1): p. 195-201.
9. Thomas, R.J., et al., *Automated, scalable culture of human embryonic stem cells in feeder-free conditions.* Biotechnol Bioeng, 2009. **102**(6): p. 1636-44.
10. Thomas, R.J., et al., *Manufacture of a human mesenchymal stem cell population using an automated cell culture platform.* Cytotechnology, 2007. **55**(1): p. 31-9.

11. Veraitch, F.S., et al., *The impact of manual processing on the expansion and directed differentiation of embryonic stem cells.* Biotechnol Bioeng, 2008. **99**(5): p. 1216-29.
12. Ivanovic, Z., *Hematopoietic stem cells in research and clinical applications: The "CD34 issue".* World J Stem Cells, 2010. **2**(2): p. 18-23.
13. Narsinh, K.H., et al., *Single cell transcriptional profiling reveals heterogeneity of human induced pluripotent stem cells.* J Clin Invest, 2011. **121**(3): p. 1217-21.
14. Kato, R., et al., *A compact, automated cell culture system for clinical scale cell expansion from primary tissues.* Tissue Eng Part C Methods, 2010. **16**(5): p. 947-56.
15. Solly, K., et al., *Application of real-time cell electronic sensing (RT-CES) technology to cell-based assays.* Assay Drug Dev Technol, 2004. **2**(4): p. 363-72.
16. Archer, R. and D.J. Williams, *Why tissue engineering needs process engineering.* Nat Biotechnol, 2005. **23**(11): p. 1353-5.
17. Kino-Oka, M., et al., *Automating the expansion process of human skeletal muscle myoblasts with suppression of myotube formation.* Tissue Eng Part C Methods, 2009. **15**(4): p. 717-28.
18. BSI, B.S.I., *Publicly available specification 83 - Guidance on codes of practice, standardised methods and regulations for cell-based therapies*. 2006.
19. FDA, F.D.A., *Proposed approach to regulation of cellular and tissue based products*. 1997.
20. FDA, F.D.A., *Guidance for Industry: Regulation of Human Cells, Tissues, and Cellular and Tissue-Based Products (HCT/Ps)Small Entity Compliance Guide*. 2007.
21. Kino-Oka, M. and J.E. Prenosil, *Development of an on-line monitoring system of human keratinocyte growth by image analysis and its application to bioreactor culture.* Biotechnol Bioeng, 2000. **67**(2): p. 234-9.
22. Li, K., et al., *Cell population tracking and lineage construction with spatiotemporal context.* Med Image Anal, 2008. **12**(5): p. 546-66.
23. Yin, Z., et al., *Data-driven Prediction on Stem Cell Culture Process* in *33rd Annual International Conference of IEEE Engineering in Medicine and Biology Society*. 2011: Boston, USA.
24. Tridgell, A., *Efficient Algorithms for Sorting and Synchronization*, in *Computer Science*. 1999, Australian National University: Canberra. p. 106.
25. Yin, Z., et al., *Understanding the optics to aid microscopy image segmentation.* Med Image Comput Comput Assist Interv, 2010. **13**(Pt 1): p. 209-17.
26. Murphy, D.B., *Fundamentals of Light Microscopy and Electronic Imaging*. 2001: Wiley-Liss Inc. 374.
27. Blau, H.M., et al., *Plasticity of the differentiated state.* Science, 1985. **230**(4727): p. 758-66.
28. Ker, E.D., et al., *Engineering spatial control of multiple differentiation fates within a stem cell population.* Biomaterials, 2011. **32**(13): p. 3413-22.
29. Matsubara, T., et al., *BMP2 regulates Osterix through Msx2 and Runx2 during osteoblast differentiation.* J Biol Chem, 2008. **283**(43): p. 29119-25.
30. Miller, E.D., et al., *Inkjet printing of growth factor concentration gradients and combinatorial arrays immobilized on biologically-relevant substrates.* Comb Chem High Throughput Screen, 2009. **12**(6): p. 604-18.

31. Phillippi, J.A., et al., *Microenvironments engineered by inkjet bioprinting spatially direct adult stem cells toward muscle- and bone-like subpopulations.* Stem Cells, 2008. **26**(1): p. 127-34.
32. Sharma, S., et al., *Stem cell culture engineering - process scale up and beyond.* Biotechnol J, 2011.
33. Huh, S., et al., *Automated mitosis detection of stem cell populations in phase-contrast microscopy images.* IEEE Trans Med Imaging, 2011. **30**(3): p. 586-96.

CHAPTER 7: CONCLUSIONS AND FUTURE DIRECTIONS

7.1 GROWTH-FACTOR PATTERNING AS A MEANS FOR PROVIDING BIOCHEMICAL CUES TO SPATIALLY CONTROL STEM CELL DIFFERENTIATION *IN VITRO*

Although protocols for bone and muscle cell differentiation are well-established, this was not the case for tendon cell differentiation. The objective of Chapter 2 was to identify tendon-promoting GFs and employ them in conjunction with inkjet-based bioprinting of muscle- and bone-promoting GFs to pattern a primitive MTB unit *in vitro*. Using immunofluorescence staining, members of the FGF family such as FGF-2 and FGF-4 were identified as tendon-promoting GFs on the basis of its ability to upregulate the tendon marker, Scx and downregulate the myofibroblast marker, SMA-α [1]. Quantitative PCR studies further indicated that FGF-2 may upregulate *scx* expression via members of the Ets family of transcription factors, Pea3 and Erm, indicating that tendon cell differentiation shares a similar mechanism to tendon development in chick [1, 2]. To definitively establish that Pea3 and Erm were involved in Scx upregulation, it would be necessary to repeat the quantitative PCR studies with a siRNA against *pea3* or *erm*. If Pea3 and Erm regulated *scx* expression, knockdown of *pea3* and *erm* should correlate with little-to-no change in Scx expression relative to control. However, if Pea3 and Erm were not involved in Scx regulation, knockdown of these 2 transcription factors should have no effect on FGF-2-induced upregulation of *scx*.

In inkjet-based bioprinting studies, immobilized patterns of FGF-2 were shown to upregulate Scx expression in C3H10T1/2 mesenchymal fibroblasts and C2C12 myoblasts in a dose-dependent manner [1]. To pattern a primitive MTB unit, FGF-2 was to be printed in conjunction with bone-

and muscle-promoting GFs. BMP-2 was employed as bone-promoting GF as it had been previously shown to induce osteoblast differentiation [3-5]. However, although IGF-2 was shown to promote muscle differentiation in a dose-depedent manner under low serum conditions (Chapter 2), it did not enhance muscle differentiation under high serum conditions (Data not shown). As such, MTB patterning studies relied only on FGF-2 and BMP-2 to spatially direct tendon and osteoblast differentiation in C2C12 muscle-progenitor cells, respectively, with spontaneous muscle cell differentiation occurring within regions of high cell density. Future work will seek to identify and screen for GFs and other signaling molecules that initiate muscle differentiation in stem cells. Potential candidates include members of the Wnt family [6-8] but technical limitations in expressing these highly insoluble recombinant proteins must be overcome. Alternatively, molecules such as N-cadherin which are known to induce myogenesis [9] but do not bind to the ECM may be engineered with ECM-binding domains to bind to ECM as well as direct muscle cell differentiation.

During inkjet-based bioprinting studies, heterogeneity in cell responses (Chapter 2 and Chapter 3) was observed. This may be a function of several factors, including: non-uniform GF distribution within the printed region following inkjet printing and GF drying [10]; GF desorption followed by readsorption prior to cell seeding [4, 11-13]; uneven cell density during cell seeding; cell heterogeneity [14]; cross-talk between cells located in adjacent patterns or, a combination of all these factors. Some of these limitations may be overcome by modifying the ECM-based substrate composition to augment GF-binding capability or engineering the GF to have enhanced ECM-binding capability. By increasing the affinities of the ECM and GF for each

other, the likelihood of GF desorption may be decreased. Alternatively, GFs may be covalently linked to the substrate after inkjet-based bioprinting to reduce GF desorption.

The results from the studies described in Chapter 2 demonstrate that multiple GFs may be patterned simultaneously to direct multiple cell fates to produce a primitive MTB unit *in vitro*. Identifying GFs that promote myogenesis under high serum conditions as well as reducing the heterogeneity of printed pattern cell responses will improve and facilitate the patterning of more complex tissues.

7.2 STEP FIBERS AS A MEANS FOR PROVIDING GEOMETRIC CUES TO CONTROL STEM CELL ALIGNMENT *IN VITRO*

Although Chapter 2 demonstrated that inkjet-based bioprinting could pattern a MTB unit *in vitro*, it was necessary to demonstrate that cell alignment could also be controlled since cell orientation plays a critical role in the functioning of musculoskeletal tissues. Such examples include efficient force generation by parallel configurations of myofibers during muscle contraction [15-17] and fabrication of highly aligned and mechanically robust collagen matrices by tendon and bone cells for skeletal movement [18-23]. Using polystyrene and polyurethane-based STEP fibers, musculoskeletal stem cells were shown to exhibit contact guidance and align along the fiber length (Chapter 3). Upon coating with ECM proteins such as serum or fibrin, STEP fibers were patterned with GFs and seeded with C3H10T1/2 cells and C2C12 cells. These cells differentiated in register to the printed pattern(s) while simultaneously aligning along the fiber length (Chapter 3). Actin staining of cells grown on fibers indicated that cells may be predisposed towards a

specific orientation through the modulation of mechanotransduction pathways via cytoskeletal rearrangements (Chapter 3). Perturbation of mechanotransduction pathways such as inhibtion of myosin II with blebbistatin [24] or inhibition of RhoGTPase [25] with Y-27632 or C3 transferase may yield insights into the mechanism of STEP fiber-induced cell alignment. Presently, efforts are underway to adapt the STEP fiber fabrication apparatus for *in vivo* studies.

The results from the studies described in Chapter 3 demonstrate that multiple GFs may be patterned simultaneously onto highly oriented scaffolds (STEP fibers) to direct multiple cell fates as well as cell alignment to produce a primitive MTB unit *in vitro*. Future work will focus on elucidating the mechanism of STEP-fiber-induced cell alignment and characterizing the effect of STEP fibers on cell alignment *in vivo*.

7.3 GROWTH-FACTOR PATTERNING AS A MEANS FOR PROVIDING BIOCHEMICAL CUES TO SPATIALLY CONTROL STEM CELL DIFFERENTIATION *IN VIVO*

While Chapter 2 and Chapter 3 focused on the patterning of a primitive MTB unit *in vitro,* Chapter 4 sought to pattern MTB and PBM units *in vivo*. Prior to *in vivo* studies, several preliminary *in vitro* studies were performed to assess the suitability of an FDA-approved product called DermaMatrix (human acellular dermis) as a printing substrate and scaffold for supporting osteoblast and myocyte differentiation (Chapter 4). These preliminary studies indicated that DermaMatrix scaffold had a highly internal porous structure and could support C2C12 myoblast attachment as well as subsequent differentiation into myotubes (Chapter 4). In addition, *in vitro*

GF patterning experiments indicated that DermaMatrix scaffolds were amenable to GF printing and dose-dependently increased ALP expression in C2C12 cells when patterned with BMP-2 (Chapter 4). In addition, using a similar methodology as in Chapter 2, FGF-2 was identified as being capable of upregulating the periosteum marker, Periostin in Rabbit muscle-derived cells (Chapter 4). Following this, DermaMatrix scaffolds were patterned with either muscle-, tendon- and bone-promoting GFs or periosteum-, bone- and bone marrow-promoting GFs and implanted in mice subcutaneously for 4-6 weeks to pattern MTB and PBM units *in vivo*. However, only ectopic bone tissue was spatially patterned in MTB patterning experiments while none of the desired tissues were spatially patterned in PBM patterning experiments (Chapter 4). This highlights a need to identify suitable BFs and the correct dosage required for *in vivo* experiments. In addition, PBM constructs had poor tissue formation owing to low cell infiltration. Increasing the porosity of the constructs by including polyurethane spacers may improve cell infiltration and tissue formation. Furthermore, it may be more challenging to pattern ectopic tissue as opposed to patterning a tissue within an orthotopic site. Presently, experiments are underway to pattern a MTB unit in an injured Achilles tendon mouse model.

The results from the studies described in Chapter 4 demonstrate that GF patterning can spatially direct the formation of ectopic bone tissue *in vivo* but further GF and scaffold optimization is required for patterning a primitive MTB or PBM unit. Future work will focus on optimizing GF dosage as well as scaffold in an orthotopic model.

7.4 THE ROLE OF INFLAMMATION IN STEM CELL DIFFERENTIATION

In Chapter 5 and Appendix A1, the effect of immune cell cross-talk between dendritic cells and macrophages was studied and the effect of inflammatory and anti-inflammatory microenvironments on osteoblast differentiation and mineralization were characterized. Using LPS and IL-10, immune cells were stimulated towards an inflammatory and anti-inflammatory phenotype, respectively (Kwan *et al*. [26], [27], Chapter 5 and Appendix A1).

In immune cross-talk studies, LPS dose-dependently increased CD86 expression and the amount of NO production in J774A.1 cells, which are indicative of a type 1 phenotype (Appendix A1). Using griess reaction [26-28], FSDC conditioned media generated with LPS-conjugated beads activated J774A.1 cells towards a type 1 phenotype while FSDC conditioned media generated with IL-10-conjugated beads did not (Appendix A1). Similar results were obtained with the reciprocal experiment (Appendix A1). However, FSDC conditioned media generated with LPS- and IL-10-conjugated did not show decreased NO production relative to FSDC conditioned LPS-conjugated beads (Appendix A1). This may be due to steric hinderance of LPS- and IL-10-conjugated beads, resulting in activation of type 1 and type 2 phenotypes in subpopulations of J774A.1 cells (Appendix A1). Future work may employ beads that are smaller in size relative to FSDCs and J774A.1 cells.

In studies characterizing the effect of inflammatory and anti-inflammatory microenvironments on osteoblast differentiation, conditioned media was harvested from type 1- and type 2-activated J774A.1 cells and FSDCs (Chapter 5). Inflammatory microenvironments (consisting of

conditioned media generated using LPS) were found to inhibit BMP-2-induced ALP expression in MC3T3-E1 cells, C2C12 cells and MDSCs while anti-inflammatory microenvironments (consisting of conditioned media generated using IL-10) did not (Kwan *et al*. [26] and Chapter 5). In addition, this inhibition could be overcome by culturing cells in conditioned media generated using a combination of LPS and IL-10 (Kwan *et al*. [26] and Chapter 5). Furthermore, primary cells such as MDSCs demonstrated differing levels of sensitivity to LPS conditioned media with one isolate showing osteoblast differentiation that was not significantly inhibited relative to Control (Chapter 5). Although Chapter 5 was primarily devoted to studying the impact of inflammation on osteoblast differentiation, it would also be interesting to determine if inflammatory microenvironments had any detrimental effects on muscle and tendon differentiation. These would be relevant in diseases such as the muscular dystrophies as well as tedinopathy.

To characterize the effect of LPS and IL-10 on osteoblast mineralization, MC3T3-E1 cells were grown in mineralization media in the presence of LPS, IL-10 or LPS with IL-10. MC3T3-E1 cells cultured in the presence of LPS, IL-10 and LPS with IL-10 show decreased levels of mineralization relative to Control (Appendix A1). This inhibition in mineralization occurred in a manner independent of ALP expression. (Appendix A1). Presently, the effect of LPS and IL-10 on bone healing is being studied in a mouse calvarial defect model. Furthermore, the effect of lipoteichoic acid (LTA), a component of gram-positive bacterial cell wall on osteoblast differentiation is presently being studied *in vitro*.

Together, these results demonstrate that during immune cell cross-talk, signaling molecules secreted by type 1-activated immune cells can activate neighboring cells to a type 1 phenotype and this activation can be reversed with IL-10. Also, inflammatory microenvironments were shown to inhibit BMP-2-induced osteoblast differentiation in several cell types and this inhibition can be reversed with anti-inflammatory microenvironments. Furthermore, the effect of LPS and IL-10 on osteoprogenitor cells is highly complex as direct treatment of MC3T3-E1 cells with these factors inhibit BMP-2-induced osteoblast mineralization in an ALP-independent manner. Future work will characterize the effect of LPS and IL-10 *in vivo* as well as the effects of other inflammatory molecules such as LTA *in vitro*. In addition, these experiments may also be repeated in the context of muscle and tendon cell differentiation.

7.5 AUTOMATED CELL TRACKING AS A TOOL FOR STEM CELL PRODUCTION AND BIOLOGICAL CHARACTERIZATION OF STEM CELL BEHAVIOR

In Chapter 6, Appendix A2, Appendix A3, Appendix A4 and Appendix A5, different software tools were developed to facilitate the *in vitro* monitoring of stem cells for *ex vivo* cell expansion and biological discovery.

In Chapter 6 and Appendix A4, a computer vision-based system was developed for real-time adaptive subculture of stem cells. This system automatically measures cell confluency at frequent time-intervals, predicts future cell confluency and alerts a human operator several hours ahead of reaching a pre-defined confluency threshold so that cell culture preparations can be made in advance (Chapter 6 and Appendix A4). The system also permits a human operator to

monitor cell growth remotely via the Internet (Chapter 6). C2C12 cells grown using this computer-directed cell culture system required the same number of serial passages as those grown by a human operator to reach the target goal of 50 million cells (Chapter 6). In addition, *in vitro* differentiation assays indicated that cells grown by the computer-directed cell culture system were no different to cells grown by a human operator (Chapter 6). Future work will integrate this software system into a robotic cell culture system to fully automate the cell culture process.

In Appendix A2 and Appendix A3, a software known as CTK was developed to facilitate both manual and automated cell tracking in phase-contrast time-lapse microscopy images as well as exporting of biologically relevant measurements such as various growth indices and indicators, the time taken for cell division, cell cycle length, cell speed, cell perimeter, cell area, cell confluence as well as a cell lineage tree. The software algorithms for automated cell tracking were robustly assessed with a single fully annotated image sequence (Target effectiveness = 82.7% and Track purity = 68.3%) and 48 partially annotated image sequences (Appendix A2). The results indicated that although automated cell tracking can robustly detect and track cells in image sequences containing Control (Target effectiveness = 70.5%) and BMP-2-treated cells (Target effectiveness = 76.6%), changes in cell morphology for FGF-2-treated cells (Target effectiveness = 47.2%) and FGF-2 with BMP-2-treated cells (Target effectiveness = 58.6%) can dramatically reduce cell tracking capabilities (Appendix A2). An analysis of tracking errors was conducted by substituting human-based annotations for cell detection and cell division into the automated tracking system, resulting in a target effectiveness of 99.5% and a track purity of 96.8%, indicating that further improvements need to be made with respect to cell detection and

cell division (Appendix A2). In addition, since biological interpretation of automated cell tracking results is entirely dependent on the construction of accurate cell lineages, it is vital that tracking errors are kept to a minimum, especially at the beginning of each image sequence as these errors may be further compounded with time. In Appendix A5, a new algorithm was developed for detecting cells using multiple DIC images. Presently, efforts are underway to improve cell detection algorithms by employing multi-modal (DIC and phase-contrast) imaging. In addition, a web-based version of the CTK software is being developed to facilitate real-time automated cell tracking.

These results describe the development of computer vision-based tools for monitoring and characterizing stem cells *in vitro*. Future work will integrate the real-time adaptive subculture system into a robotic subculture system while further improvements will be made to automated cell tracking algorithms, especially with regards to cell detection and cell division.

7.6 SUMMARY AND CONCLUSIONS

This thesis utilized inkjet-based bioprinting to spatially pattern biochemical cues such as GFs to direct stem cell differentiation *in vitro* and *in vivo*. In addition, novel substrates and scaffolds such as fibrin-coated glass coverslips, STEP Fiber sand DermaMatrix were employed. In particular, the use of highly oriented STEP fibers in conjunction with GF patterning facilitated the simultaneous patterning of musculoskeletal stem cell alignment and differentiation, respectively. The biological principles utilized in these methods are applicable to biomaterial development and may prove useful in tissue engineering applications. In addition, the impact of inflammation on osteoblast differentiation was characterized while software tools for monitoring

stem cells were employed to facilitate stem cell expansion and biological discovery. The methods and principles developed here will be useful for controlling and monitoring stem cell behavior and may have potential applications in regenerative medicine.

7.7 REFERENCES

1. Ker, E.D., et al., *Engineering spatial control of multiple differentiation fates within a stem cell population.* Biomaterials, 2011. **32**(13): p. 3413-22.
2. Brent, A.E. and C.J. Tabin, *FGF acts directly on the somitic tendon progenitors through the Ets transcription factors Pea3 and Erm to regulate scleraxis expression.* Development, 2004. **131**(16): p. 3885-96.
3. Cooper, G.M., et al., *Inkjet-based biopatterning of bone morphogenetic protein-2 to spatially control calvarial bone formation.* Tissue Eng Part A, 2010. **16**(5): p. 1749-59.
4. Miller, E.D., et al., *Inkjet printing of growth factor concentration gradients and combinatorial arrays immobilized on biologically-relevant substrates.* Comb Chem High Throughput Screen, 2009. **12**(6): p. 604-18.
5. Phillippi, J.A., et al., *Microenvironments engineered by inkjet bioprinting spatially direct adult stem cells toward muscle- and bone-like subpopulations.* Stem Cells, 2008. **26**(1): p. 127-34.
6. Gros, J., O. Serralbo, and C. Marcelle, *WNT11 acts as a directional cue to organize the elongation of early muscle fibres.* Nature, 2009. **457**(7229): p. 589-93.
7. Naito, A.T., et al., *Developmental stage-specific biphasic roles of Wnt/beta-catenin signaling in cardiomyogenesis and hematopoiesis.* Proc Natl Acad Sci U S A, 2006. **103**(52): p. 19812-7.
8. Toyofuku, T., et al., *Wnt/frizzled-2 signaling induces aggregation and adhesion among cardiac myocytes by increased cadherin-beta-catenin complex.* J Cell Biol, 2000. **150**(1): p. 225-41.
9. Gavard, J., et al., *N-cadherin activation substitutes for the cell contact control in cell cycle arrest and myogenic differentiation: involvement of p120 and beta-catenin.* J Biol Chem, 2004. **279**(35): p. 36795-802.
10. Miller, E., *Inkjet Printing of Solid-Phase Growth Factor Patterns to Direct Cell Fate*, in *Biomedical Engineering*. 2007, Carnegie Mellon University: Pittsburgh. p. 349.
11. Miller, E.D., et al., *Dose-dependent cell growth in response to concentration modulated patterns of FGF-2 printed on fibrin.* Biomaterials, 2006. **27**(10): p. 2213-21.
12. Morin, R., D. Kaplan, and B. Perez-Ramirez, *Bone morphogenetic protein-2 binds as multilayers to a collagen delivery matrix: an equilibrium thermodynamic analysis.* Biomacromolecules, 2006. **7**(1): p. 131-8.
13. Sahni, A., T. Odrljin, and C.W. Francis, *Binding of basic fibroblast growth factor to fibrinogen and fibrin.* J Biol Chem, 1998. **273**(13): p. 7554-9.

14. Collins, C.A., et al., *Stem cell function, self-renewal, and behavioral heterogeneity of cells from the adult muscle satellite cell niche.* Cell, 2005. **122**(2): p. 289-301.
15. Hinds, S., et al., *The role of extracellular matrix composition in structure and function of bioengineered skeletal muscle.* Biomaterials, 2011. **32**(14): p. 3575-83.
16. Shimizu, K., H. Fujita, and E. Nagamori, *Alignment of skeletal muscle myoblasts and myotubes using linear micropatterned surfaces ground with abrasives.* Biotechnol Bioeng, 2009. **103**(3): p. 631-8.
17. Vye, M.V., *The ultrastructure of striated muscle.* Ann Clin Lab Sci, 1976. **6**(2): p. 142-51.
18. Beniash, E., *Biominerals-hierarchical nanocomposites: the example of bone.* Wiley Interdiscip Rev Nanomed Nanobiotechnol, 2010. **3**(1): p. 47-69.
19. Gigante, A., et al., *Collagen I membranes for tendon repair: effect of collagen fiber orientation on cell behavior.* J Orthop Res, 2009. **27**(6): p. 826-32.
20. Kerschnitzki, M., et al., *The organization of the osteocyte network mirrors the extracellular matrix orientation in bone.* J Struct Biol, 2011. **173**(2): p. 303-11.
21. Ma, J., X. He, and E. Jabbari, *Osteogenic differentiation of marrow stromal cells on random and aligned electrospun poly(L-lactide) nanofibers.* Ann Biomed Eng, 2011. **39**(1): p. 14-25.
22. Moffat, K.L., et al., *Characterization of the structure-function relationship at the ligament-to-bone interface.* Proc Natl Acad Sci U S A, 2008. **105**(23): p. 7947-52.
23. Moffat, K.L., et al., *Orthopedic interface tissue engineering for the biological fixation of soft tissue grafts.* Clin Sports Med, 2009. **28**(1): p. 157-76.
24. Engler, A.J., et al., *Matrix elasticity directs stem cell lineage specification.* Cell, 2006. **126**(4): p. 677-89.
25. Provenzano, P.P., et al., *Contact guidance mediated three-dimensional cell migration is regulated by Rho/ROCK-dependent matrix reorganization.* Biophys J, 2008. **95**(11): p. 5374-84.
26. Kwan, S., *The Flip Side of Osteoimmunity: Crosstalk Among Stem Cells, BMP-2 and Innate Immune Cells, and the Control of Osteoblastogenesis*, in *Biological Sciences*. 2011, Carnegie Mellon University: Pittsburgh. p. 158.
27. Martinez, F.O., et al., *Macrophage activation and polarization.* Front Biosci, 2008. **13**: p. 453-61.
28. Griess, P., *Bemerkungen zu der Abhandlung der HH. Weselky und Benedikt Ueber einige Azoverbindungen.* Berichte der Deutschen chemischen Gesellschaft, 1879. **12**(1): p. 3.

APPENDIX A1: IMMUNE CELL CROSS-TALK AND *IN VITRO* EFFECT OF INFLAMMATORY AND ANTI-INFLAMMATORY MICROENVIRONMENTS ON OSTEOBLAST MINERALIZATION

A1.1 ABSTRACT AND RELEVANCE TO THESIS

As described in Chapter 1 and Chapter 5, the capability to control inflammation to create a permissive microenvironment for efficient stem cell differentiation is crucial for understanding the tissue maintenance and repair. The work described here primarily reflects the efforts of Hirotaka Nakagawa, an undergraduate researcher in our lab who studied how immune cell activation was affected by crosstalk between dendritic cells and macrophages as well the direct effect of lipopolysaccharide (LPS) and Interleukin-10 (IL-10) on osteoblast mineralization. Using Griess assay and fluorescence activated cell analysis, LPS- and IL-10-free conditioned media demonstrated that immune cells such as Fetal Skin Dendritic Cells (FSDCs) and J774A.1 macrophages can signal to one another to induce immune cell activation. Using alizarin red staining, LPS and IL-10 were shown to have a direct inhibitory effect on MC3T3-E1 fibroblast mineralization. Together, these results demonstrate that the cellular microenvironment is important in cell behaviors such as immune cell activation as well as osteoblast mineralization and may have potential use in tissue regeneration.

A1.2 INTRODUCTION

As described in Chapter 1 and Chapter 5, inflammation is an integral component of the wound healing process and can drastically alter cellular behavior. In addition, prior work performed in our lab (Kwan *et al.*, 2011 [1]; Chapter 1 and Chapter 5) as well as by others in the field [2] have determined that the introduction of lipopolysaccharide (LPS; a component of gram-negative bacterial cell wall) and IL-10 (An immunomodulatory cytokine) directs immune cells such as dendritic cells and macrophages towards a type 1 (Classically activated; pro-inflammatory) or type 2 (Alternatively activated; anti-inflammatory) pathway, respectively. The studies described

herein seeks to characterize the effect of LPS- and IL-10-free conditioned media on FSDC and J774A.1 cell activation as well as the effect of LPS and IL-10 on MC3T3-E1 cell mineralization.

To characterize the effect of immune cell crosstalk on immune cell activation, conditioned media from FSDCs were used to culture J774A.1 cells and vice versa. However, the procedure used in Chapter 5 for generating conditioned media cannot be applied as there may be residual LPS and IL-10 left in the media. Thus, LPS and IL-10 were conjugated to sepharose beads for inducing immune cell activation whilst facilitating ease of separation of beads and media via centrifugation to generate LPS- and IL-10-free conditioned media. This step enables the culturing of FSDCs in J774A.1 cell conditioned media and vice versa without any residual LPS and IL-10 in the conditioned media. Both Griess reaction [3-5] and flow cytometry were used to monitor nitric oxide (NO) production and upregulation of the type 1 marker CD 86 [6], respectively, to assess type 1 immune cell activation.

To characterize the effect of LPS and IL-10 on MC3T3-E1 cell mineralization, alizarin red staining was used to assess the extent of calcium deposition in LPS- and IL-10 treated cultures [7-9].

A1.3 MATERIALS AND METHODS

A1.3.1 Cell Culture

Mouse J774A.1 macrophage cells (ATTC, Manassas, VA) were grown in RPMI media (Invitrogen, Carlsbad, CA), 10% fetal bovine serum (FBS; Atlas Biological, Fort Collins, CO) and 1% penicillin-streptomycin (PS; Invitrogen, Carlsbad, CA). Mouse Fetal Skin Dendritic Cells (FSDCs) were grown in RPMI media, 10% FBS, 1% PS with 8mM Glutamax (Invitrogen, Carlsbad, CA) as previously described [10]. Unipotent mouse MC3T3-E1 subclone 4 cells

(ATTC, Manassas, VA) were grown in α-Modified Eagle's Media (α-MEM; Invitrogen, Carlsbad, CA), 10% FBS and 1% PS. All cells were kept at 37^{o}C, 5% CO_2 in a humidified incubator.

A1.3.2 Conjugation of LPS and IL-10 to Sepharose Beads

Epoxy activated, Sepharose CL-4B beads (Insight Genomics, Falls Church, VA) were conjugated to LPS (Sigma-Aldrich, St Louis, MO; InvivoGen, San Diego, CA) and IL-10-Fc (A kind gift from Dr. Zheng Xin Xiao, University of Pittsburgh, PA) according to manufacturer's instructions. Conjugation of LPS to epoxy-activated Sepharose beads was confirmed by performing Griess Assay (Biotium Inc., Hayward, CA) on LPS-treated immune cells (Figure 1). Efficiency of IL-10 conjugation to epoxy-activated Sepharaose beads was estimated at 65 – 75% (Data not shown) using Pierce BCA assay (Thermo Fisher Scientific Inc., Rockford, IL).

A1.3.3 Conditioned Media

Mouse J774A.1 macrophage cells or FSDCs were seeded at a density of 20 x 10^4 cells per well (10.5 x 10^4 cells/cm^2) in a 24 well plate overnight. The next day, the media was aspirated and 0.5 mL fresh media was added. For experiments utilizing LPS- and IL-10 conjugated beads, cells were treated with 30 – 60 µL unconjugated beads (Control), 15 – 25 µL LPS-conjugated beads, 15 – 35 µL IL-10-Fc-conjugated beads and 15 – 25 µL LPS-conjugated beads with 15 – 35 µL IL-10-Fc-conjugated beads. For experiments utilizing LPS-conjugated beads and 100 ng/mL IL-10, cells were treated with nothing (Control), 15 – 25 µL LPS-conjugated beads, 100 ng/mL IL-10 and LPS with IL-10 (15 – 25 µL LPS-conjugated beads and 100 ng/mL IL-10). After 48 h post-treatment, the conditioned media was collected and centrifuged at 110 g, 4^{o}C for 5 min to remove beads and debris to generate LPS- and IL-10-free conditioned media. The conditioned

media was then used immediately or aliquoted and stored at -80^{o}C until further use. Conditioned media generated using unconjugated beads, LPS beads, IL-10 beads and LPS with IL-10 beads were referred to as Control-stimulated conditioned media, LPS-stimulated conditioned media, IL-10-stimulated conditioned media and LPS with IL-10-stimulated conditioned media, respectively. Conditioned media generated using unconjugated beads, LPS-conjugated beads, 100 ng/mL IL-10 and LPS-conjugated beads with 100 ng/mL IL-10 was referred to as control conditioned media, solid-phase LPS conditioned media, liquid phase IL-10 conditioned media and solid phase LPS with liquid-phase IL-10 conditioned media.

To characterize the effect of immune cell crosstalk on immune cell activation, mouse J774A.1 macrophage cells or FSDCs were seeded at a density of 20 x 10^4 cells per well (10.5 x 10^4 cells/cm^2) in a 24 well plate overnight. The next day, the media was aspirated and 0.5 mL of LPS-, IL-10- or LPS with IL-10-stimulated conditioned media was added. After 48 h post-treatment, Griess assay was performed on the cell media. Where necessary, the immune cells on the well plate were detached using a cell scraper (for J774A.1 cells) or 0.05% trypsin (Invitrogen, Carlsbad, CA; for FSDCs) for flow cytometry analysis. If fixation was required, cells were fixed in 4% paraformaldehyde (Electron Microscopy Sciences, Hatfield, PA) for 15 mins, washed once with PBS and stored in PBS at 4^{o}C until flow cytometry analysis.

A1.3.4 Griess Assay

NO detection (Biotium Inc., Hayward, CA) was performed according to the manufacturer's instructions.

A1.3.5 Flow Cytometry

Cell surface marker analysis on J774A.1 cells was performed using a flow cytometer (Becton Dickinson FACS DIVA, Becton, Dickinson and Company, Franklin Lakes, NJ). J774A.1 cells were washed with phosphate buffered saline (PBS; Fisher Scientific, Pittsburgh, PA), blocked with 1% BSA in PBS for 1 hour at 4 ^{o}C and subsequently washed in PBS prior to incubation with an antibody for the type I marker, FITC-conjugated rat anti-mouse CD86 (1:250 dilution, BD Biosciences, San Jose, CA) for 1 hour at 4 ^{o}C. Subsequently, cells were washed and analyzed on the flow cytometer.

A1.3.6 Osteogenic Differentiation

For mineralization experiments, MC3T3-E1 cells were grown in their respective growth media in the presence of 50 µg/mL ascorbic acid (Sigma-Aldrich, St Louis, MO), 10mM β-glycerophosphate (Santa Cruz Biotechnology, Santa Cruz, CA) and 100 ng/mL BMP-2 (Medtronic, Minneapolis, MN) for 18 – 21 days with a media change every 72 h. MC3T3-E1 cells were seeded at a density of 10 x 10^4 cells per well (5.15 x 10^4 cells/cm^2) in a 24-well plate overnight.

A1.3.7 ALP Stain

Cells were fixed for 1 – 2 min in 3.7% formaldehyde. Alkaline phosphatase activity (ALP; Sigma-Aldrich, St Louis, MO) was detected according to the manufacturer's instructions. For image analysis, positive regions of ALP activity (blue) were identified using the color select tool in Adobe Photoshop 7.0 (Adobe Systems, San Jose, CA). These regions were copied into a new image and converted to a grayscale image. The average pixel intensity was determined using the image histogram tool. Alternatively, images were analyzed using a customized spectral unmixing

algorithm written by Elvira Osuna-Highley (Manscript in preparation) in Matlab R2010a (Mathworks, Natick, MA). Both methods of image analysis produced comparable results.

A1.3.8 Alizarin Red Stain

Cells were fixed for 15 min in 10% formalin at room temperature (RT). An osteogenesis assay kit (Millipore, Billerica, MA) was used according to the manufacturer's instructions.

A1.3.9 Statistical Analysis

For quantification of ALP signal, alizarin red stain and FITC fluorescence, one-way analysis of variance followed by Tukey's honestly significant difference post hoc test using SYSTAT 9 software (Systat Software Inc., Richmond, CA) or STATPLUS2009 (AnalystSoft Inc., Alexandria, VA) to determine significance among treatment groups. A p value ≤ 0.05 was considered statistically significant.

A1.4 RESULTS

A1.4.1 Effect of LPS on J774A.1 Cell Activation

The effects of LPS on J774A.1 cell activation are summarized in Figure A1.1. When J774A.1 cells were treated with LPS, a dose-dependent increase in NO production was observed ($p = 0.03$ for Control vs 50 ng/mL LPS, $p < 0.001$ for Control vs 100 ng/mL LPS and $p < 0.001$ for Control vs 200 ng/mL LPS; Figure A1.1A). In addition, LPS dose-dependently increased expression of the type 1 marker CD86 relative to Control (Figure A1.1B). Together, these results show that LPS can dose-dependently activate J774A.1 macrophages towards a pro-inflammatory type 1 phenotype.

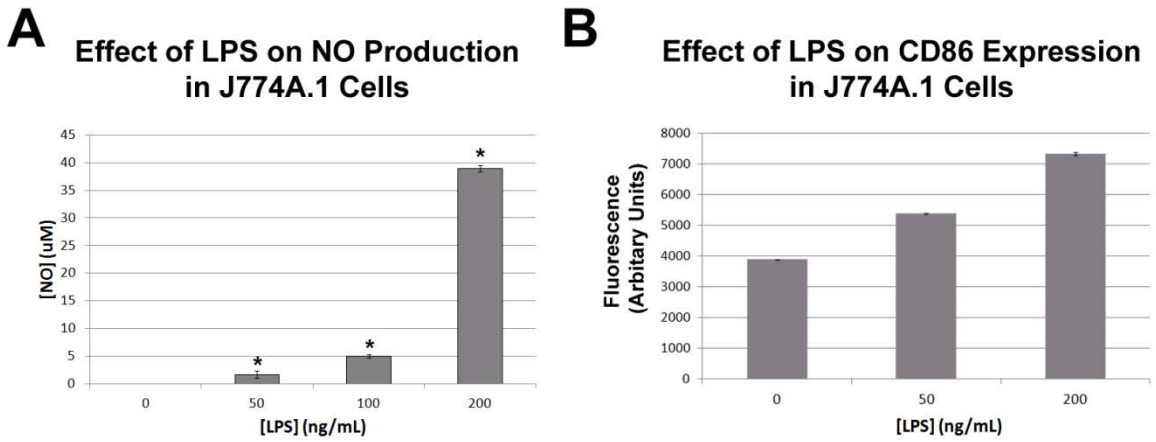

Figure A1.1. Effect of LPS on J774A.1 cell activation. **A.** Effect of LPS on NO Production in J774A.1 cells. LPS dose-dependently increased NO production in J774A.1 cells. **B.** Effect of LPS on CD86 expression (Type 1 marker) in J774A.1 cells. LPS dose-dependently increased expression of type 1 marker CD86 in J774A.1 cells. Error bars indicate Standard Error Mean or SEM. *, Significantly different from Control; $p \leq 0.05$.

A1.4.2 Effect of LPS- and IL-10-free FSDC Conditioned Media on J774A.1 Cell Activation

The effects of LPS-stimulated and IL-10-stimulated FSDC conditioned media on J774A.1 cell activation are summarized in Figure A1.2. When J774A.1 cells were treated with LPS-stimulated conditioned media, an increase in NO production was observed relative to Control while IL-10-stimulated conditioned media did not ($p < 0.001$ for Control vs LPS, $p > 0.99$ for Control vs IL-10 and $p < 0.001$ for Control vs LPS with IL-10; Figure A1.2A). However, LPS with IL-10-stimulated conditioned media did not dramatically decrease NO production relative to LPS-stimulated conditioned media ($p = 0.57$ for LPS vs LPS with IL-10; Figure A1.2A). Similarly, LPS-stimulated conditioned media increased expression of the type 1 marker CD86 relative to Control-stimulated conditioned media while IL-10-stimulated conditioned media did not (Figure A1.2B). However, LPS with IL-10-stimulated conditioned media did not dramatically decrease CD86 expression relative to LPS-stimulated conditioned media (Figure A1.2B). Together, these results show that LPS can dose-dependently activate J774A.1 macrophages towards a pro-inflammatory type 1 phenotype.

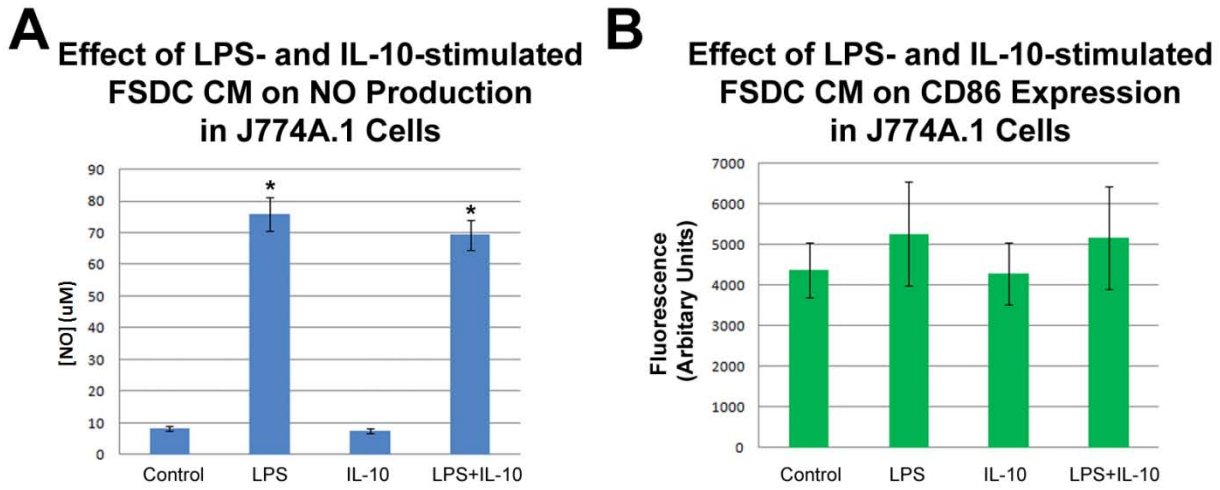

Figure A1.2. Effect of LPS- and IL-10-free FSDC conditioned media on J774A.1 cell activation. **A.** Effect of LPS- and IL-10-free FSDC conditioned media on NO Production in J774A.1 cells. LPS-stimulated conditioned media increased NO production compared to control-stimulated conditioned media while IL-10-stimulated conditioned media did not increase NO production compared to control-stimulated conditioned media in J774A.1 cells. LPS and IL-10-stimulated conditioned media resulted in NO production intermediate between control- and LPS-stimulated conditioned media. **B.** Effect of LPS- and IL-10-free FSDC conditioned media on CD86 expression (Type 1 marker) in J774A.1 cells. LPS-stimulated conditioned media increased CD86 expression compared to control while IL-10-stimulated conditioned media did not increase CD86 expression compared to control in J774A.1 cells. LPS and IL-10-stimulated conditioned media resulted in CD86 expression intermediate between control and LPS-stimulated conditioned media. Error bars indicate Standard Error Mean or SEM (n = 9). $*$, Significantly different from Control; $p \leq 0.05$.

A1.4.3 Effect of Solid-phase LPS and Liquid-Phase IL-10 J774A.1 Cell Conditioned Media on FSDC Activation

The effects of solid-phase LPS and liquid-phase IL-10 FSDC conditioned media on J774A.1 cell activation are summarized in Figure A1.3. When J774A.1 cells were treated with solid-phase LPS or solid-phase LPS, NO production was increased relative to Control, respectively whereas liquid-phase IL-10 decreased NO production relative to control ($p < 0.001$ for Control vs LPS, $p = 0.002$ for Control vs IL-10 and $p < 0.001$ for Control vs LPS with IL-10; Figure A1.3). In addition, solid-phase LPS with liquid-phase IL-10 conditioned media decreased NO production relative to LPS-stimulated conditioned media ($p < 0.001$ for LPS vs LPS with IL-10; Figure

A1.3). Together, these results show that LPS can dose-dependently activate J774A.1 macrophages towards a pro-inflammatory type 1 phenotype and this can activation can be attenuated with liquid-phase IL-10.

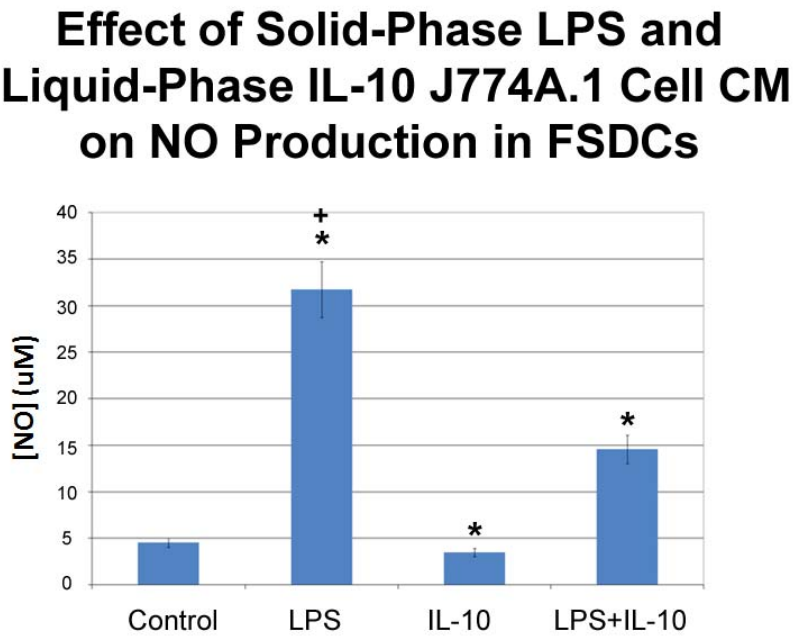

Figure A1.3. Effect of solid-phase LPS and liquid-phase IL-10 J774A.1 cell conditioned media on FSDC activation. **A.** Effect of solid-phase LPS and liquid-phase IL-10 J774A.1 cell conditioned media on NO Production in FSDCs. Solid-phase LPS and solid-phase LPS with liquid-phase IL-10 conditioned media increased NO production compared to control while liquid-phase IL-10 conditioned media decreased NO production compared to control in FSDCs. Conditioned media generated using solid-phase LPS with liquid-phase IL-10 resulted in NO production intermediate between control and solid-phase LPS conditioned media. Error bars indicate Standard Error Mean or SEM (n = 12). *, Significantly different from Control; $p \leq 0.05$.

A1.4.4 Effect of LPS and IL-10 on MC3T3-E1 Cell Mineralization

The effects of LPS and IL-10 on MC3T3-E1 cell mineralization are summarized in Figure A1.4 and Figure A1.5. When MC3T3-E1 cells were grown in mineralization media, increased calcium deposition was observed in BMP-2-treated samples relative to non-BMP-2-treated counterparts ($p < 0.001$ for Control vs Control+BMP-2, $p < 0.001$ for LPS vs LPS+BMP-2, $p < 0.001$ for IL-10 vs IL-10+BMP-2 and $p < 0.001$ for LPS with IL-10 vs LPS with IL-10+BMP-2). When MC3T3-E1 cells were treated with 100 ng/mL LPS, 100 ng/mL IL-10 or 100 ng/mL LPS with

100 ng/mL IL-10, alizarin red staining was decreased relative to Control ($p < 0.001$ for Control vs LPS, $p = 0.002$ for Control vs IL-10 and $p < 0.001$ for Control vs LPS with IL-10; Figure A1.4). This inhibition was independent of ALP staining (Figure A1.5). Together, these results indicate that LPS and IL-10 can inhibit BMP-2-induced osteoblast mineralization.

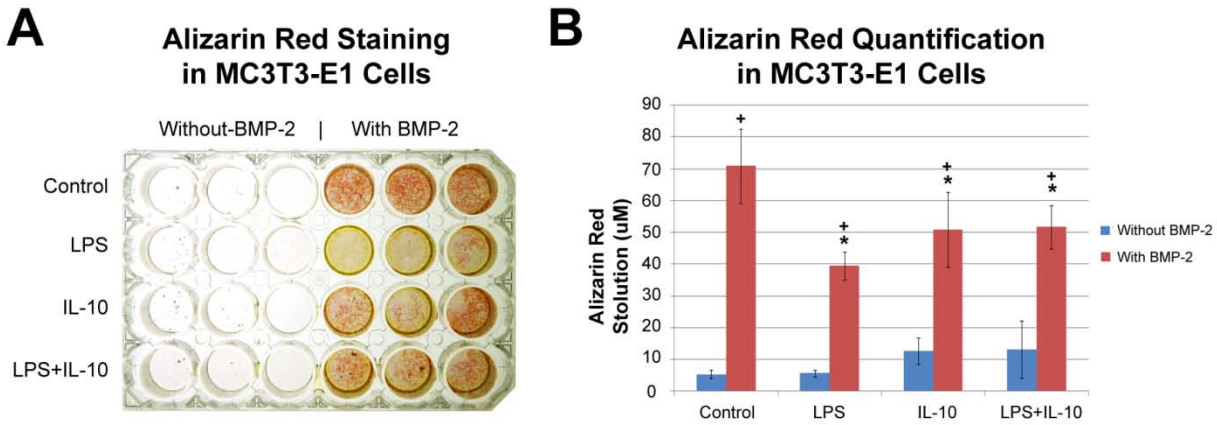

Figure A1.4. Effect of LPS and IL-10 on MC3T3-E1 cell mineralization (Alizarin red staining) after 18 - 21 days. **A.** Alizarin red staining of LPS- and IL-10-treated MC3T3-E1 cells grown in the presence or absence of 100 ng/mL BMP-2. Alizarin red staining was not present in non-BMP-2 treated cells. Alizarin red staining was present in Control, IL-10- and LPS with IL-10-treated MC3T3-E1 cells, indicating that LPS and IL-10 directly inhibits MC3T3-E1 cell mineralization. **B.** Quantification of alizarin red staining in Control, LPS, IL-10 and LPS with IL-10-treated MC3T3-E1 cells. Error bars indicate Standard Error Mean or SEM (n = 9). +, Significantly different from its respective non-BMP-2 treated counterpart; $p \leq 0.05$. *, Significantly different from Control conditioned media containing 100 ng/mL BMP-2; $p \leq 0.05$.

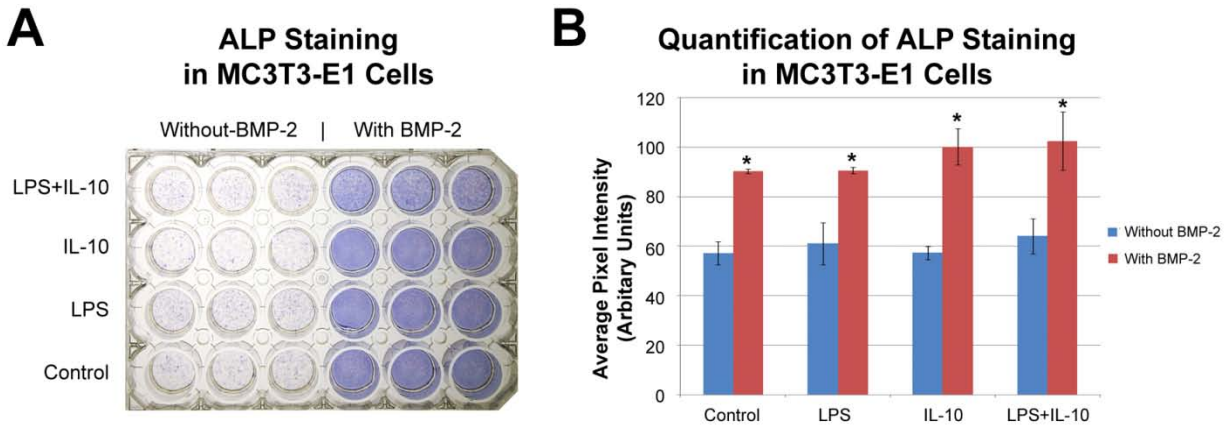

Figure A1.5. Effect of LPS and IL-10 on Alkaline phosphatase (ALP; blue) expression in MC3T3-E1 cells after 18 - 21 days. **A.** ALP expression of Control-, LPS-, IL-10 and LPS with IL-10-treated MC3T3-E1 cells grown in the presence or absence of 100 ng/mL BMP-2 in mineralization media. Basal levels of ALP staining was present in non-BMP-2 treated cells. ALP expression was upregulated in BMP-2-treated MC3T3-E1 cells compared to non-BMP-2-treated counterparts. No differences in ALP expression were detected among Control-, LPS-, IL-10- and LPS with IL-10-treated MC3T3-E1 cells. **B.** Quantification of ALP staining in Control, LPS-, IL-10 and LPS with IL-10-treated MC3T3-E1 cells. Error bars indicate Standard Error Mean or SEM. *, Significantly different from its respective non-BMP-2 treated counterpart.

A1.5 DISCUSSION

A1.5.1 Effect of LPS- and IL-10-free Immune Cell Conditioned Media on Immune Cell Activation

Prior work in our lab [1] and Chapter 5 had shown that addition of LPS and IL-10 to immune cell cultures activated dendritic cells and macrophages towards a type 1 pro-inflammatory and type 2 anti-inflammatory response, respectively. In addition, conditioned media obtained from type 1 activated cells were shown to inhibit osteoblast differentiation whereas conditioned media obtained from type 2 activated cells could rescue this inhibitory effect as determined by ALP staining (Kwan *et al.* [1] and Chapter 5). The goal of this chapter was to further characterize the effect of macrophage conditioned media on dendritic cell activation and vice versa (Figure A1.1, Figure A1.2 and Figure A1.3). In addition, the effect of LPS and IL-10 on osteoblast mineralization was also assessed (Figure A1.4 and Figure A1.5).

Type 1 activated cells show upregulation of type 1 surface markers such as CD86 as well as increased NO levels due to increased inducible NO synthase activity [2]. As such, the Griess reaction and flow cytometry were appropriate tools for determining type 1 activation of immune cells. When immune cells such as macrophages were treated with LPS, a dose-dependent increase in type 1 immune cell activation was observed as indicated by increased NO production and expression of type 1 marker CD86 (Figure A1.1).

To assess the effect of J774A.1 cell conditioned media on FSDCs and vice versa, it was necessary to generate conditioned media that did not contain LPS or IL-10 since LPS and IL-10 can directly activate immune cells. Using LPS- and IL-10-conjugated beads provided a simple means of generating LPS- and IL-10-free conditioned media. J774A.1 cells cultured in type 1-activated FSDC conditioned media (LPS-stimulated conditioned media) showed increased NO levels and CD86 expression relative to Control-stimulated conditioned media (Figure A1.2). Similarly, FSDCs cultured in type 1-activated J774A.1 cell conditioned media (solid-phase LPS conditioned media) showed increased NO levels relative to Control conditioned media (Figure A1.3). Together, these results indicate that type 1-activated conditioned media contains molecules other than LPS which can a type 1 response (Figure A1.3). Cytokine analysis of immune cell conditioned media indicates that pro-inflammatory molecules such as Tumor Necrosis Factor-α (TNF-α) may be responsible [1, 2]. Although type 2-activated FSDC conditioned media (IL-10-stimulated conditioned media) did not increase J774A.1 cell type 1 activation relative to Control-stimulated conditioned media, there was little-to-no downregulation of the type 1 response for J774A.1 cells cultured in LPS with IL-10-stimulated conditioned media (Figure A1.2) in stark contrast to previous experiments utilizing unconjugated LPS and IL-10 (Kwan *et al.* [1] and Chapter 5). This may be due to steric hindrance from the

beads (45 – 165 μm in diameter), which may prevent both LPS and IL-10 beads from contacting the same cell to exert an effect. When liquid-phase IL-10 was substituted in place of IL-10 beads during J774A.1 cell conditioned media generation, there was a pronounced attenuation of the type 1 response in FSDCs (Figure A1.3). Together, these studies show that crosstalk between immune cells such as dendritic cells and macrophages can result in activation of type 1 or type 2 inflammatory phenotypes, highlighting the importance of the cellular microenvironment.

A1.5.2 Effect of LPS and IL-10 on MC3T3-E1 Cell Mineralization

As described in Chapter 5, prior experiments showed that LPS and IL-10 had little-to-no effect on osteoblast differentiation as determined by ALP staining. To assess the effect of LPS and IL-10 on osteoblast mineralization, MC3T3-E1 cells were cultured in mineralization media containing LPS, IL-10 or LPS with IL-10 in the presence or absence of BMP-2 for about 3 weeks (Figure A1.4 and Figure A1.5). Alizarin red staining indicated that BMP-2-treated MC3T3-E1 cells showed increased mineralization over their non-BMP-2-treated counterparts (Figure A1.4). However, BMP-2-treated MC3T3-E1 cells cultured in the presence of LPS, IL-10 and LPS with IL-10 showed decreased levels of mineralization relative to Control (Figure A1.4). A parallel experiment indicated that this inhibition occurred in a manner independent of ALP expression (Figure A1.5). Together, these results show that the interaction between LPS and IL-10 with progenitor and stem cells is highly complex and warrants further study.

A1.6 CONCLUSIONS

This chapter identified LPS and IL-10 as being capable of directing the activation of immune cells such as dendritic cells and macrophages towards and away from type 1 pro-inflammatory pathways, respectively. In addition, LPS- and IL-10-free conditioned media from type 1

activated J774A.1 macrophages could induce FSDCs towards a type 1 pathway as well as vice versa. This chapter also shows that LPS and IL-10 has a direct inhibitory effect on MC3T3-E1 cell mineralization. The study of immune cell crosstalk between dendritic cells and macrophages as well as the characterization of the impact of LPS and IL-10 on osteoblast mineralization offers an approach to study the physiological roles of immune cells during wound healing and may be translatable to new therapies to treat disease and trauma of the musculoskeletal system.

A1.7 ACKNOWLEDGEMENTS

This research is primarily the work of Hirotaka Nakagawa. I would also like to thank Yehuda Creeger for assistance with flow cytometry and William Clafshenkel for assistance with alizarin red staining. In addition, I would like to thank Zheng Xin Xiao for providing IL-10-Fc and Elvira Osuna-Highley for assistance with quantification of ALP signal in microscopy images. This work was supported by NIH grants RO1EB004343 and RO1EB007369 as well as funding from the Pennsylvania Infrastructure Technology Alliance (PITA).

A1.8 REFERENCES

1. Kwan, S., *The Flip Side of Osteoimmunity: Crosstalk Among Stem Cells, BMP-2 and Innate Immune Cells, and the Control of Osteoblastogenesis*, in *Biological Sciences*. 2011, Carnegie Mellon University: Pittsburgh. p. 158.
2. Martinez, F.O., et al., *Macrophage activation and polarization.* Front Biosci, 2008. **13**: p. 453-61.
3. Green, L.C., et al., *Analysis of nitrate, nitrite, and [15N]nitrate in biological fluids.* Anal Biochem, 1982. **126**(1): p. 131-8.
4. Griess, P., *Bemerkungen zu der Abhandlung der HH. Weselky und Benedikt Ueber einige Azoverbindungen.* Berichte der Deutschen chemischen Gesellschaft, 1879. **12**(1): p. 3.
5. O'Farrell, A.M., et al., *IL-10 inhibits macrophage activation and proliferation by distinct signaling mechanisms: evidence for Stat3-dependent and -independent pathways.* Embo J, 1998. **17**(4): p. 1006-18.
6. Tang, Y., C. Han, and X. Wang, *Role of nitric oxide and prostaglandins in the potentiating effects of calcitonin gene-related peptide on lipopolysaccharide-induced interleukin-6 release from mouse peritoneal macrophages.* Immunology, 1999. **96**(2): p. 171-5.

7. Hood, R.C. and W.M. Neill, *A modification of alizarin red S technic for demonstrating bone formation.* Stain Technol, 1948. **23**(4): p. 209-18.
8. Landoff, G.A., *On the influence of the bone salts on the radiograph of so-called acute atrophy of bone; roentgen-experimental and histological examinations as well as a new alizarin staining technique.* Acta Orthop Scand, 1948. **17**(3-4): p. 270-302.
9. Williams, T.W., Jr., *The differentiation of placoid, ctenoid and cycloid scales by means of alizarin red S.* Stain Technol, 1946. **21**: p. 55-8.
10. Girolomoni, G., et al., *Establishment of a cell line with features of early dendritic cell precursors from fetal mouse skin.* Eur J Immunol, 1995. **25**(8): p. 2163-9.

APPENDIX A2: DEVELOPMENT OF A SOFTWARE PACKAGE FOR MANUAL AND AUTOMATED *IN VITRO* STEM CELL TRACKING FOLLOWED BY AN ANALYSIS OF CELL TRACKING ERRORS

Based on unpublished work (Manuscript in preparation):

Cell Tracking Kit (CTK) Software for Manual and Automated *In Vitro* Stem Cell Tracking including an Analysis of Tracking Errors

Dai Fei Elmer Ker, Sungeun Eom, Sho Sanami, Ryoma Bise, Karen Lujie Chen, Corinne Pascale, Zhaozheng Yin, Seung-il Huh, Elvira Osuna-Highley, Silvina N. Junkers, Lee E. Weiss, Casey J. Helfrich, Peter Yongwen Liang, Jiyan Pan, Soojin Jeong, Steven S. Kang, Jinyu Liu, Ritchie Nicholson, Michael F. Sandbothe, Phu T. Van, Anan Liu, Artur W. Dubrawski, Jeff Schneider, Mei Chen, Takeo Kanade, Phil G. Campbell

A2.1 ABSTRACT AND RELEVANCE TO THESIS

Live cell microscopy imaging is a useful tool for assessing and characterizing both individual and population behaviors of progenitor and stem cells such as cell division, cell morphology and cell motility simultaneously. Although a variety of software have been developed to facilitate individual cell tracking, the majority of these efforts have been focused on fluorescence time-lapse microscopy images due to its ease of cell detection and relatively short image sequences owing to fluorescence-induced phototoxicity and photobleaching. In contrast, phase-constrast time-lapse microscopy is a non-destructive imaging modality that allows for cells to be imaged at high frequency over a period of several days. Presently, the availability of cell tracking software for manual as well as automated cell tracking to provide biologically-relevant measurements for analyzing cell growth kinetics is limited. In addition, there are no validation reports of various cell tracking software under multiple culture conditions due to the extremely time-consuming nature of manual cell annotation. In this section, a highly versatile software known as Cell Tracking Kit (CTK) was developed. This software contains features that are dedicated for both manual and automated cell tracking in phase-contrast time-lapse microscopy images. In addition, an evaluation of its automated cell tracking capabilities using C2C12 cells as a paradigm stem cell population under a variety of culture conditions was performed along with a detailed analysis of tracking errors to identify potential areas for further algorithm improvement. Furthermore, the CTK software exports a variety of biologically-relevant measurements at both individual and cell population level including mitotic index, cell cycle length, cell motility, cell morphology and a cell lineage tree that are amenable to further data transformation and subsequent statistical analysis. This work demonstrates the use of cell tracking software for

biologically-relevant analysis of cell cultures and may have potential applications in stem cell characterization and expansion for regenerative medicine.

A2.2 INTRODUCTION

The study and characterization of cells generally requires a variety of molecular and cytological techniques to be employed including genomic, proteomic, immunocytochemical, histological and microscopy approaches. In particular, the use of cell tracking methodologies for stem cell characterization provides rapid assessment of primary cell growth kinetics for biological discovery as well as potential applications in regenerative medicine.

Presently, the expansion and application of primary cells for tissue engineering is often hampered by a lack of knowledge on cell growth kinetics owing to confounding factors such as cell heterogeneity as well as isolate-to-isolate variability [1-7]. Indeed, studying cell growth kinetics is vital for understanding biological processes including animal development [3, 8], tissue growth and repair [9], cell proliferation [10, 11], cell migration [12, 13], cell differentiation [14-18] as well as pursuing biotechnological applications such as stem cell reprogramming [19], optimal stem cell expansion [20-29], drug screening [30, 31] and disease modeling [32, 33].

Traditionally, characterization of cell growth kinetics often employs various techniques such as immunofluorescence staining to label a particular marker of interest. For example, fluorescently-conjugated antibodies that react with Ki67 protein or the thymidine analog bromodeoxyuridine are used as cell proliferation markers. However, such experiments are often one-dimensional as they only provide a single data point with regards to a particular cell behavior of interest at a single time-point. As a result, multiple reagents and/or experiments may need to be used to

obtain a comprehensive view of cell growth kinetics, requiring high expenditure on reagents, time and human labor. In contrast, live cell tracking methodologies encompass a wide variety of optical and non-optical approaches that can be used to characterize multiple cell behaviors *in vitro* and *in vivo* with high spatiotemporal resolution simultaneously, which is important for biological discovery [2-7, 19, 34, 35] as well as *ex vivo* stem cell expansion [6, 20-24, 26-28, 35-39].

Cell tracking methodologies can be broadly categorized into optical and non-optical techniques although such techniques need not be mutually exclusive. Common optical approaches include fluorescence [40, 41], bioluminescence [42], brightfield [43, 44], differential interference contrast (DIC) [45] and phase-contrast time-lapse microscopy [46-50] while non-optical approaches also include fluorescence [51, 52] and bioluminescence [42, 51, 53] as well as magnetic resonance imaging [54], positron emission tomography [41, 52], and single photon emission computed tomography [52]. However, non-optical approaches such as magnetic resonance imaging are often used for *in vivo* cell tracking and presently do not offer sensitivity at the resolution of a single cell [55] and as such, not considered further.

Recent advancements in optical microscopy such as improved microscope cameras, microscope stage incubation systems, computer processor speeds and computer disk storage have facilitated the automation and widespread adoption of time-lapse microscopy systems [5, 10, 11, 13, 40, 56]. Automated tracking of cell populations *in vitro* using time-lapse microscopy images enable high-throughput spatiotemporal measurements of a range of cell behaviors, including mitosis (cell division), apoptosis (cell death), cell migration (cell movement), cell differentiation (cell fate), cell morphology (cell area and shape) and the reconstruction of cell lineages (mother-

daughter relations) simultaneously [3, 5, 6, 8, 10, 11, 13, 34, 46-48, 50, 56-64]. As such, time-lapse microscopy is a vital tool for studying the dynamic nature of stem cells given that such cell populations are often heterogeneous in nature and can exhibit a wide range of cell behaviors that occur within a time-span of several seconds to hours or even days [5, 6].

Given the utility of time-lapse microscopy for cell tracking, a brief review of the advantages and disadvantages of each optical approach is presented. Both fluorescence and bioluminescence are popular modes of time-lapse microscopy as they provide data that facilitate simple cell detection methods owing to a high signal to noise ratio [52], resulting in higher cell tracking performance [48]. However, these modes of imaging may require genetic manipulation, which can introduce unknown perturbations on cell growth kinetics and cell fate [19, 65-67]. In addition, data interpretation may be challenging especially in situations where quantification of fluorescence or bioluminescence signal is desired owing to complex gene interactions such as non-steady-state promoter activity [68, 69]. In scenarios where exogenous fluorescence labels such as dyes and quantum dots are used instead of genetically expressed proteins, these exogenous labels are diluted over time due to cell division and are not conducive for long-term cell tracking studies as a result of decreased fluorescence signal over time [55]. Furthermore, fluorescence time-lapse microscopy imaging is often limited to short and infrequent time exposures owing to fluorescence-induced phototoxicity and photobleaching [40]. In contrast, brightfield, DIC and phase-contrast time-lapse microscopy are label-free and non-destructive methods of cell imaging [40]. As such, cells do not require genetic modification or exogenous labels and can be imaged with high frequency (every min) over long periods (several days) with little-to-no phototoxicity [40]. Of these three imaging modes, phase-contrast microscopy is the most advantageous due to high specimen contrast and relative cost-effectiveness [40] since brightfield microscopy offers

low image contrast while DIC microscopy requires the use of expensive optics and glass substrates for culturing cells [40].

With the advent of highly automated time-lapse microscopy systems, generating time-lapse microscopy image sequences has become a relatively simple affair. However, analysis of cell behavior is a highly time-consuming and labor intensive task. For example, analyzing cell morphology would require a biologist to spend several weeks tracing the cell boundaries for each individual cell in every image frame of a give time-lapse microscopy image sequence. Such tasks would benefit from a software program that has robust manual annotation tools and/or automated cell tracking capabilities. A comprehensive review of biological tracking software is challenging since tracking in cell and developmental biology encompasses several size scales ranging from single molecules to individual cells to entire organisms [56]. Here, an attempt has been made to review major and relevant cell tracking systems and programs. These include – (1) commercial software such as Volocity [70], Imaris [71] and Simi BioCell [60, 62], (2) academic software such as the MTrack2 plugin for ImageJ [72], CellProfiler [73], Cell Tracker [63, 64, 74], Timelapse Analyzer [75], the Large Scale Digital Cell Analysis System [57], Timm's Tracking Tool [58, 61], and (3) several in-house cell tracking systems [46-50, 59, 76].

Although a diverse range of these toolsets are available, each of them has its own inherent advantages as well as limitations with regards to its specialization for a particular type of dataset, lack of robust validation and lack of a graphical user interface (GUI). For example, programs that offer a GUI such as Volocity [70], Imaris [71], Timm's Tracking Tool [58, 61], CellTrack [77], ImageJ [72], CellProfiler [73] and Cell Tracker [63, 64, 74] have historically been used for tracking fluorescence datasets and may lack the versatility required for cell tracking in phase-

contrast time-lapse microscopy images [48] whereas Simi Biocell [60, 62] despite possessing the capability to construct cell lineages is specialized for developmental studies (especially for *Caenorhabditis elegans*) [62]. In addition, there are little-to-no reports of validation results for Timm's Tracking System [58, 61], ImageJ [72], CellTrack [77], CellTracker [63, 64, 74], the Large Scale Digital Cell Analysis System [57], Timelapse Analyzer [75], Volocity [70], Imaris [71], Cell Profiler [73] and Simi BioCell [60, 62] with regards to phase-contrast time-lapse microscopy images. Despite this, there are several in-house cell tracking systems built that are specialized for phase-contrast microscopy with reported validation results [46-50, 59]. These systems perform cell tracking based on an image registration algorithm [48], an extension to the Chan-Vese Level Set segmentation algorithm [47], algorithmic information theoretic prediction [46], topological alignments [59], a novel algorithm that systemically searches for tracking errors and discards incorrect cell tracks [50] and a modified level set method [49, 76]. However, many in-house systems are built with a specific biological question in mind and may not offer the capability to track and export biologically relevant measurements that may be of interest in other studies. For example, the tracking system based on algorithmic information theoretic prediction [46] was built specifically for retinal progenitor cell tracking and predicting cell differentiation. In addition, none of these systems performed robust validation [46-48, 50, 59] since they verified their tracking results within a single cell culture condition. In some cases, validation was performed on small data sets comprising of 40 cells [46]. In addition, several of these in-house built systems have no GUI available for public use [47, 48, 50, 59]. In summary, none of these commercial and academic software as well as in-house developed systems [46-50, 57-64, 70-77] have versatile annotation tools for manual cell tracking, dedicated automated cell tracking capabilities for phase-contrast microscopy, robust validation across multiple culture conditions

and a user-friendly GUI that exports biologically relevant measurements that may serve the broader interest of the biological research community.

To address some of these issues, a GUI program called Cell Tracking Kit (CTK) has been developed to enable both manual and automated cell tracking in time-lapse phase-contrast microscopy images. This software incorporates active detection of cell behaviors such as cell division, is robustly validated on large multiple datasets with different culture conditions and generates a variety of biologically-relevant measurements at both individual and cell population level including mitotic index, cell cycle length, cell motility, cell morphology and a cell lineage tree for further data transformation and subsequent statistical analysis. In addition, a detailed analysis of cell tracking errors was conducted to highlight areas for further algorithm improvement.

A2.3 MATERIALS AND METHODS

A2.3.1 Cell Culture

Mouse C2C12 cells (ATTC, Manassas, VA) were grown in Dulbecco's Modified Eagle's Media (DMEM; Invitrogen, Carlsbad, CA), 10% fetal bovine serum (Invitrogen, Carlsbad, CA) and 1% penicillin-streptomycin (PS; Invitrogen, Carlsbad, CA). Cells were kept at 37^{o}C, 5% CO_2 in a humidified incubator.

In this study, C2C12 cells were seeded at a density of 2×10^4 cells per 35mm Petri dish overnight. The media was changed the next day and cells were grown under 4 different conditions – (1) Control (Untreated), (2) 100 ng/mL fibroblast growth factor-2 (FGF-2; Peptrotech Inc., Rocky Hill, NJ), (3) 100 ng/mL bone morphogenetic protein-2 (BMP-2;

Medtronic, Minneapolis, MN) and (4) 100 ng/mL FGF-2 and 100 ng/mL BMP-2 in complete media over the course of 3 – 4 days.

A2.3.2 Phase-Contrast Timelapse Microscopy

Time-lapse phase-contrast microscopy was performed using a Zeiss Axiovert T135V microscope (Carl Zeiss Microimaging, Thornwood, NY) equipped with a 5X, 0.15 N.A. phase-contrast objective, a custom-stage incubator capable of housing up to four 35mm Petri dishes, and InVitro software 3.2 (Media Cybernetics Inc., Bethesda, MD). Four fields of view representative of the cell density from each of the four dishes (Control, FGF-2 treated, BMP-2 treated, and FGF-2 and BMP-2 treated) were selected, resulting in a total of 16 fields of view per culture experiment. Each experiment was repeated a total of three times, resulting in a total of 48 image sequences (12 per treatment group). Images were acquired at a frequency of every 5 minutes over a course of 3.5 days and each image sequence contained approximately 1013-1062 frames. Microscope images were 1392 x 1040 pixels with a resolution of 1.3μm/pixel.

A2.3.3 Development of Cell Tracking Kit (CTK) Software

The CTK software was written in C++ [78] and Qt (Qt Development Frameworks, Oslo, Norway) and can be installed on a personal computer with a 32-bit or 64-bit Microsoft Windows (Microsoft, Redmond, WA) operating system.

A2.3.4 Human-Aided Cell Annotation

The data obtained were manually annotated using cell tracking software known as Cell Tracking Kit (CTK), which was developed in-house (Kang Li, 2007). Cells were individually tagged by placing a marker at the center of the cell (Cell centroid) at approximately every 1-8 frames with the CTK software applying interpolation to determine the cell centroid between these frames.

Within each frame, individual cells were also assigned a label to highlight the status of the cell. These include ‘Normal’, ‘Apoptosis’, ‘Dead’, ‘Mitotic’, ‘Newborn’, ‘Apoptotic/Mitotic’, ‘Fused’, ‘Lost’, ‘Entered’ and ‘Departed’. Due to the time consuming process of manual annotation, a minimum of 3 cells per image sequence representing approximately 10% of the initial number of cells in the field of view was manually annotated from the beginning of the image sequence through to the end, resulting in 48 partially-annotated image sequences. A single image sequence (100 ng/mL BMP2, 3rd March 2009 Dataset) was manually annotated for all cells for 780 frames, representing 65 h. The manually annotated datasets are summarized as cell lineage trees, which illustrate the relationship between mother and daughter cells over time.

A2.3.5 Computer-Based Cell Annotation

Computer-based cell tracking was performed based on a tracking-by-detection approach, which first segments cells and then associates those cells over consecutive frames. The tracking algorithm consists of three modules – (1) Segmentation, (2) Mitosis detection, and (3) Association.

During segmentation, cells are segmented from background using a microscope image restoration process [79]. Rather than utilizing traditional image segmentation methods such as intensity thresholding, gradient detection, and morphological operations, the microscope images were processed to remove phase-contrast microscopy artifacts such as the halo and shading effects, resulting in ‘restored’ microscope images. Using a recently discovered microscopy imaging model, a regularized quadratic objective function was formulated and minimized to restore the artifact-free images where background pixels had uniform zero values and foreground

pixels had positive values. On the restored high-contrast images, a simple thresholding method was sufficient to separate cell pixels from background pixels [79].

During mitosis detection, images were processed using a three-step approach to identify the end of cytokinesis [80], facilitating improved tracking performance by establishing accurate parent-daughter relationships. The three-step approach consisted of – (1) Candidate patch sequence construction, (2) Feature extraction, and (3) Identification of mitosis occurrence and localization of birth event. Briefly, during the first step, potential regions that may contain mitotic events were located in the image sequence based on their level of their pixel intensity and these areas were subsequently cropped to construct small-size candidate patch sequences. This step narrowed down the available search space required for locating mitotic cells to facilitate efficient mitosis detection and spatially locate the birth event. In the second step, visual features (a set of numbers that describe the characteristics of an image patch) were extracted from each candidate patch. Since cell size does not vary significantly during cell division and each cell can freely rotate when dividing, these visual features were extracted with a unique scale and a rotation invariance scheme was applied. In the third step, the visual features were examined by a probabilistic model constructed using machine learning approaches [80] to determine whether each candidate patch sequence contained a birth event and if so, detect the temporal locations of the birth event in the sequence.

During the association step, results obtained from the segmentation and mitosis modules were used to correlate or link cell identities across successive images to facilitate cell tracking. Briefly, the segmentation algorithm identified cell-positive regions termed ‘blobs’ from the original input images that contained either individual cells or cells clustered together while the mitosis

detection algorithm determined when and where a cell completed cytokinesis and divided into two cells. Based on the outputs of these two algorithms, a hypothesis was constructed using data association methods that compared cells segmented at a particular time point (frame t = n) and cells segmented in the next time point (frame t = n + 1), generating a link or correspondence between the identities of individual cells or 'blobs' between the two images, which are termed 'cell tracks' [76]. The association algorithm also considered for scenarios that include cell migration within the field of view, cell migration into and out of the field of view, mitosis, and cell clustering. The most possible links from the entire hypothesis set were founded by solving a linear programming problem [76], thus the cell identities with their characteristics (e.g. cell position, cell shape etc.) were identified between consecutive images.

Both human- and computer-aided cell annotation data can be computed into biologically-relevant data and subsequently exported by CTK software into text-delimited files for further analysis. Presently, three types of data files can be exported – (1) an event-centric file which lists the time (frame) in which a particular cell underwent a particular process (event) as determined by its annotated cell status, (2) a population-centric file which lists the total number or fraction of cells involved in various particular biological processes as a function of time (frame), and (3) a cell-centric file which lists individual cell data such as the length of its cell cycle. Data were graphed using Microsoft Excel (Microsoft, Redmond, WA) and Tableau Desktop (Tableau Software, Seattle, WA).

A2.3.6 Evaluation of Human-Aided Cell Annotation versus Computer-Based Cell Annotation

To evaluate the performance of computer-based cell tracking, four measures were used – (1) Precision, (2) Recall, (3) Target Effectivenss and (4) Track Purity. In the field of information

retrieval, Precision and Recall are widely employed evaluation metrics [81] and were used to evaluate individual components of the computer-based cell tracking system such as cell detection and cell division. Target Effectiveness and Track Purity [76, 82, 83] are modified versions of Recall and Precision for evaluating the computer-based cell tracking. Each of these is described in further detail below.

A2.3.7 Statistical Analysis

One-way analysis of variance followed by Tukey's honestly significant difference post hoc test using SYSTAT 9 software (Systat Software Inc., Richmond, CA) was performed to determine significance among treatment groups. A $p\text{-}value \leq 0.05$ was considered statistically significant.

A2.4 RESULTS

A2.4.1 Overview of Cell Tracking Kit (CTK) Software

An overview of the CTK software capabilities and the software's GUI is presented in Figure A2.1. The primary aim of this software is to provide a user friendly interface for performing versatile manual cell tracking of time-lapse microscopy images, automated cell tracking of phase-contrast time-lapse microscopy images and export of biologically relevant measurements for subsequent analysis (Figure A2.1). The CTK software displays time-lapse microscopy image sequences in the 'Image Window' and images can be manipulated using the 'Image Adjustments', 'Image Frame', 'Solution Explorer' and 'Zoom' tools. Multiple annotations can be added to a single time-lapse microscopy image sequence using the 'Annotation Explorer' to allow for comparison between different human annotators or different computer-based cell tracking algorithms. Manual cell tracking can be performed with the 'Manual Annotation Toolbar' and 'Manual Annotation Explorer' windows while automated cell tracking can be

performed using the 'Process' and 'Track' menubars. Cell annotations are displayed in a collapsible tree structure in the 'Manual Annotation Explorer' window and parent cells can be expanded or collapsed to show or hide daughter cells. Lastly, biologically-relevant measurements can be exported via the 'Analyze' and 'File' menubars (Figure A2.1).

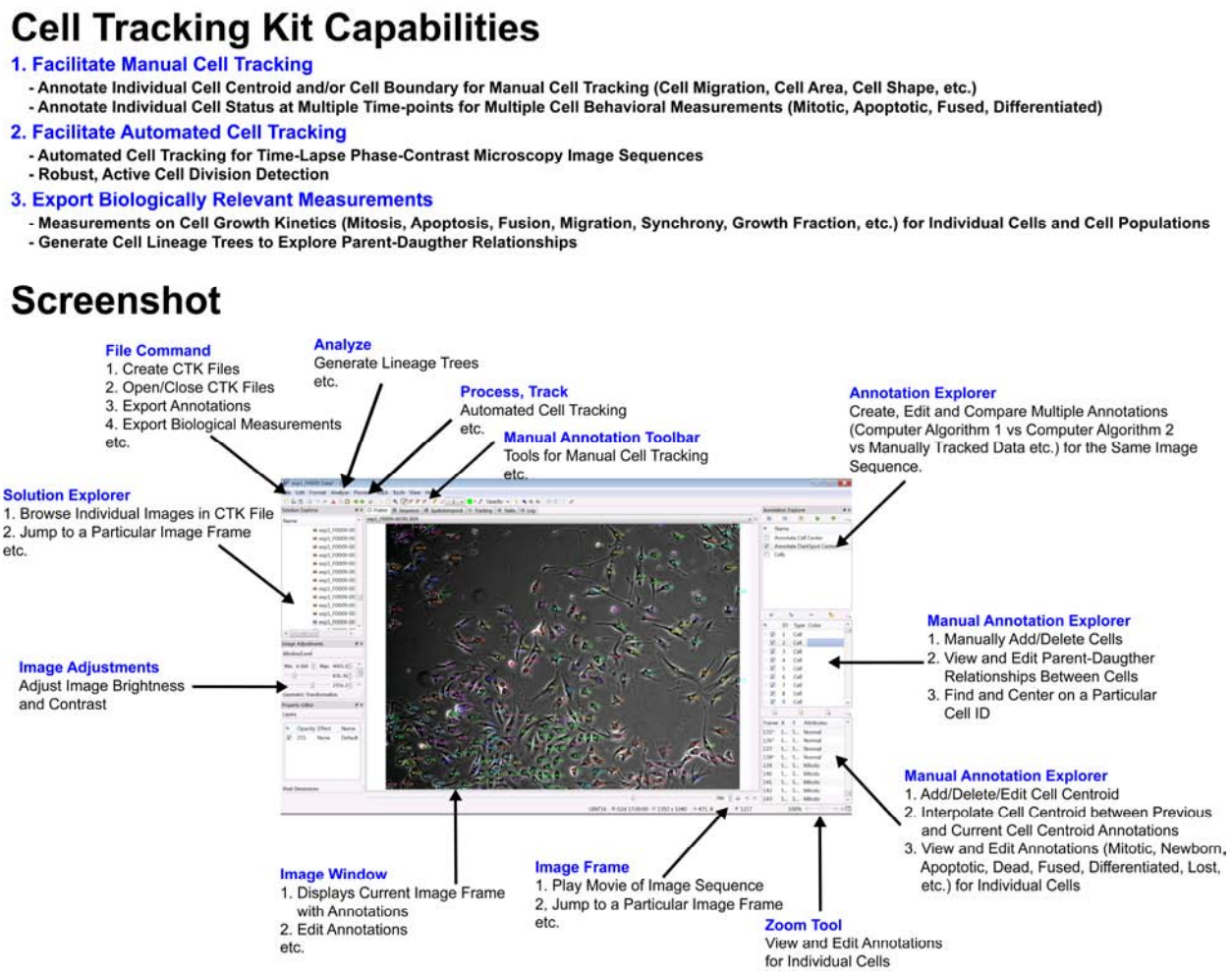

Figure A2.1. Overview of the CTK software. The CTK software allows for manual and automated cell annotation as well as export of biologically-relevant measurements.

The process of manual cell tracking is shown in Figure A2.2. After importing a time-lapse microscopy image sequence, cells are added using the 'Manual Annotation Explorer' windows and subsequently marked with a cell centroid and/or cell boundary. The CTK software interpolates the location of the cell centroid between successive annotations such that annotation

of the cell centroid in every image frame is not required. Subsequently, a cell may be additionally labeled with various cell statuses at multiple time-points to mark changes in cell behavior (Figure A2.2).

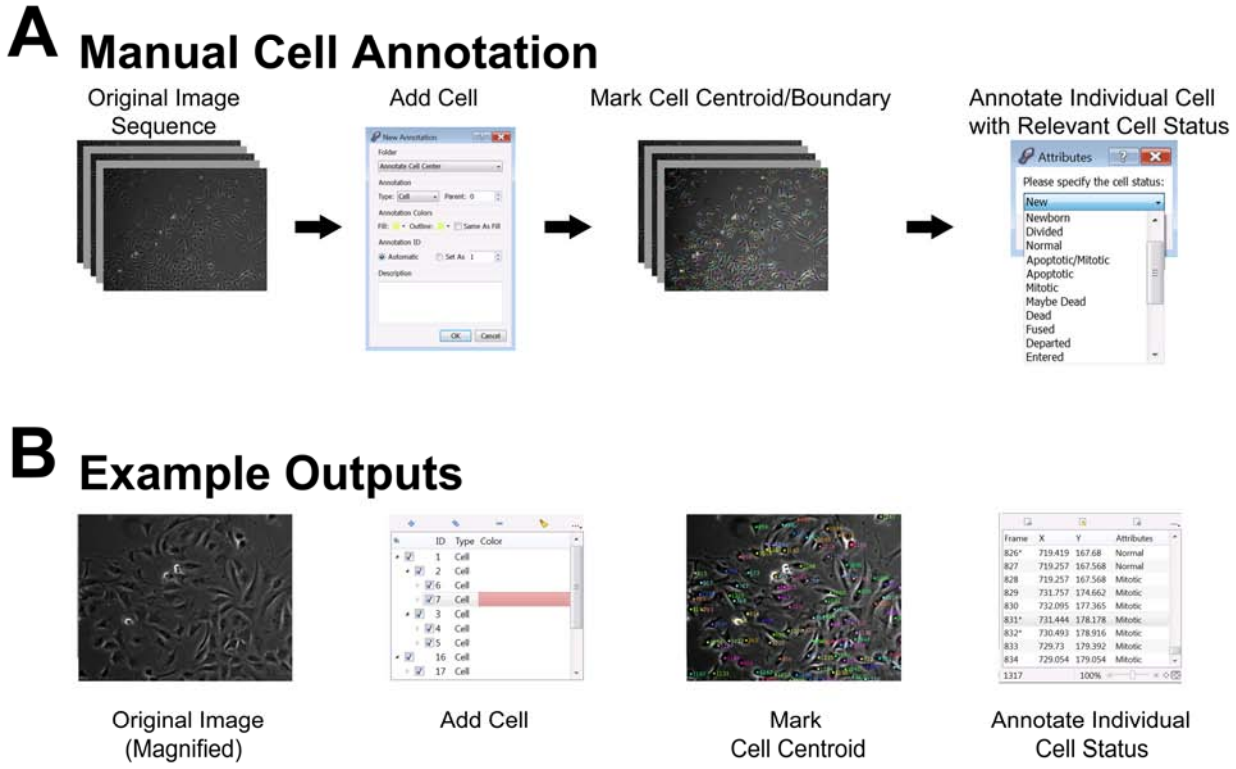

Figure A2.2. Manual cell annotation. **A.** Steps for performing manual cell annotation. **B.** Example outputs of each step during manual cell annotation.

The process of automated cell tracking is shown in Figure A2.3. During automated cell tracking, an image segmentation algorithm is applied to detect individual cells in each image. In addition, a cell division algorithm is used to detect the end-point of cytokinesis. These two outputs are used by the computer-based cell tracking system to generate hypotheses to link individual cells across successive image frames to produce computer-aided cell annotations (Figure A2.3).

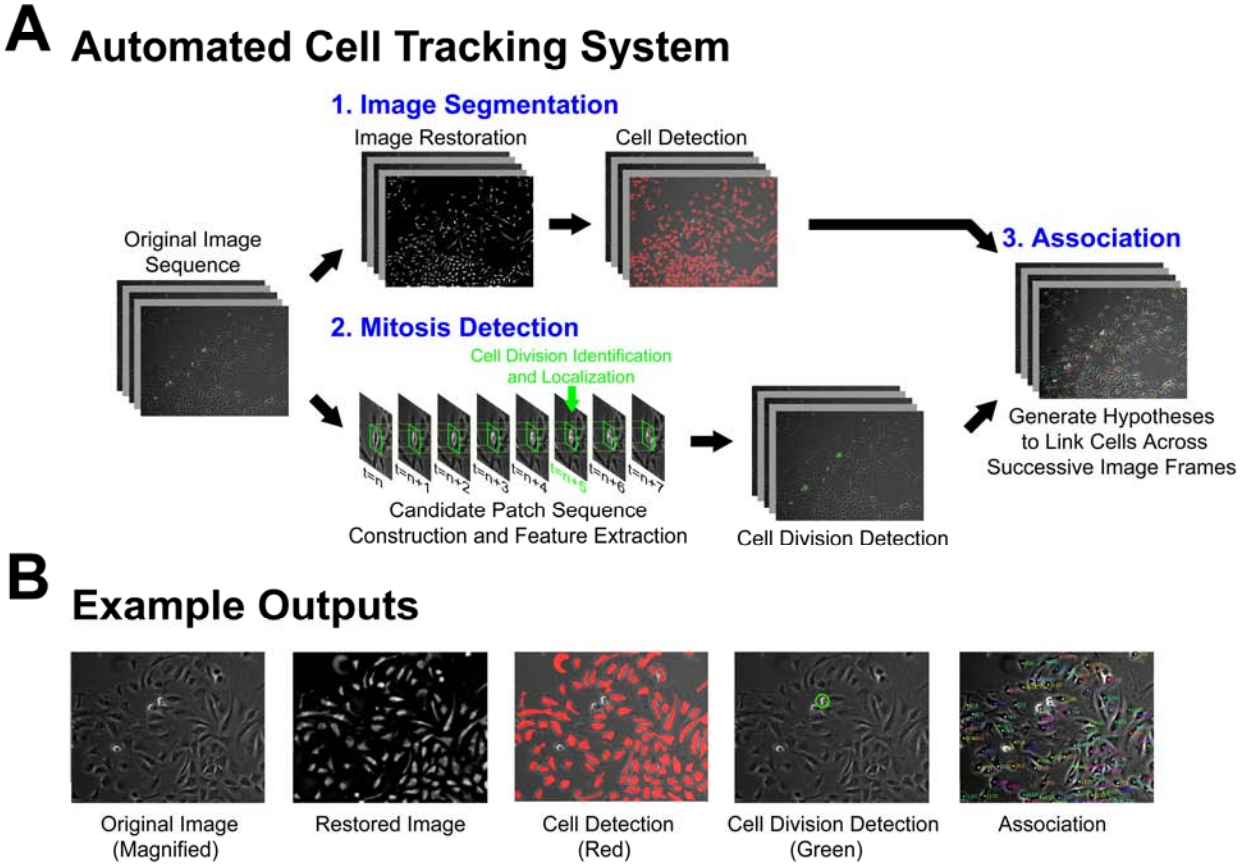

Figure A2.3. Automated cell annotation. **A.** Steps for performing automated cell annotation. **B.** Example outputs of each step during automated cell annotation.

A2.4.2 Analysis of Automated Cell Tracking Errors

To evaluate the performance of the automated cell tracking system, an image sequence comprising initially of 31 cells at the beginning of time-lapse was manually annotated for 780 frames (65 hours) for all cells and their subsequent progeny as well as cells that migrated into the field of view. In addition another 48 image sequences where at least three initial cells and their subsequent progeny were manually tracked. In these 48 image sequences, C2C12 cells were cultured under multiple conditions including Control (untreated), FGF-2 (100 ng/mL FGF-2), BMP-2 (100 ng/mL BMP-2) and FGF-2 with BMP-2 (100 ng/mL growth-factor each). This fully annotated image sequence and 48 partially annotated image sequences were used to evaluate cell detection, cell division detection and cell tracking performance.

To compare cell detection performance, it was necessary to match human- and computer-annotations together (Figure A2.4A). Within each image frame, matching was performed based on the nearest neighbor rule with a limit of 15 pixels. In addition, the matching must be bi-directional in that a human annotated cell must be matched to its closest computer annotated neighbor and vice versa. Otherwise, the cell would be considered a false positive. For example, in Figure A2.4A, Human Annotated Cell 1 is the closest neighbor for Computer Detected Cell A while Computer Detected Cell A is the closest neighbor of Human Annotated Cell 1. Since the criterion of bi-directional matching is fulfilled, Human Annotated Cell 1 is matched to Computer Detected Cell A. In the case of Computer Detected Cell C, its nearest neighbor is Human Annotated Cell 1 but since there is no bi-directional matching, Computer Detected Cell C is considered a false positive (Figure A2.4A). In addition, Human Detected Cell 3 is considered a false negative since no matching partner can be found (Figure A2.4A). Using this criterion, precision was computed as the number of true positives divided by the sum of true and false positives while recall was computed as the number of true positives divided by the sum of true positives and false negatives (Figure A2.4B). Figure A2.4C shows a plot of precision and recall for each individual frame number as well as the overall precision and recall for the fully annotated sequence (Figure A2.4C). Although cell detection initially had an average precision of 0.78 and recall of 0.61 for the first 50 frames (250 min), these subsequently increase in the next 50 frames (Average precision of 0.88 and recall of 0.89) where it remains high, giving an overall precision of 0.89 and recall of 0.89 (Figure A2.4C). Further analysis indicated that the low precision and recall in the first 50 frames was caused by the round morphology of C2C12 cells as they had yet to fully adhere to the tissue culture substrate, resulting in a bright halo effect that interfered with the cell detection algorithm (Data not shown).

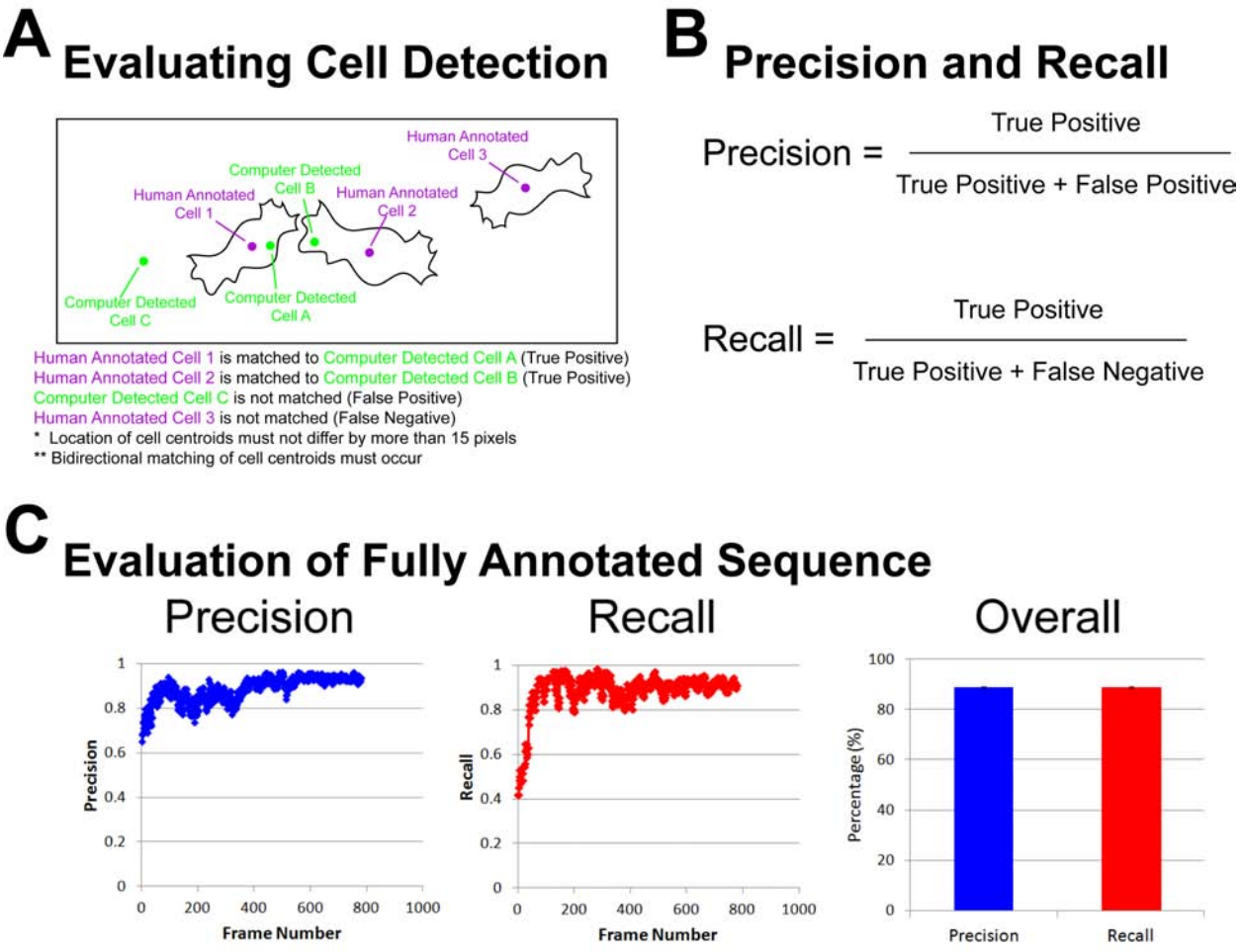

Figure A2.4. Evaluation of automated cell detection. **A.** Schematic for matching a detected cell to its human annotated counterpart. **B.** Calculation of precision and recall. **C.** Evaluation of fully annotated sequence. The overall as well as individual precision and recall for each frame is shown.

To compare cell division detection performance, it was necessary to match human- and computer-annotations together (Figure A2.5A). Similar to cell detection evaluation, matching was performed based on the nearest neighbor rule with a limit of 25 pixels. In addition, since cell division is a spatiotemporal event, an additional tolerance of 10 frames (50 min) was used. Detected cell division events must satisfy both criteria to be matched to a human-annotated mitosis event otherwise it would be considered a false positive (Figure A2.5A). For example, in Figure A2.5A, Human Annotated Cell Division 1 is the closest neighbor for Computer Detected

Cell Division A and these events occur within 10 frames of each other. Since both spatial and temporal criteria are fulfilled, Human Annotated Cell Division 1 is matched to Computer Detected Cell Division A. In the case of Computer Detected Cell Division B and Human Detected Cell Division 2, if no match is found, they are considered a false positive and a false negative, respectively (Figure A2.5A). Using these criteria, precision was computed as the number of true positives divided by the sum of true and false positives while recall was computed as the number of true positives divided by the sum of true positives and false negatives (Figure A2.5B). In addition, a moving average of 50 frames was used for plotting precision and recall as a function of time. Figure A2.5C shows a plot of precision and recall for each individual frame number as well as the overall precision and recall for the fully annotated sequence (Figure A2.5C). Although cell division detection initially had an average precision of 0.43 and recall of 0.75 for the first 50 frames (250 min), these subsequently increase in the next 50 frames (Average precision of 0.75 and recall of 1.00) where it remains high, giving an overall precision of 0.89 and recall of 0.88 (Figure A2.5C). Further analysis indicated that the low precision and recall in the first 50 frames was also caused by the round morphology of C2C12 cells as they had yet to fully adhere to the tissue culture substrate, resulting in a bright halo effect that the cell division detection algorithm misinterpreted as cell division (Data not shown).

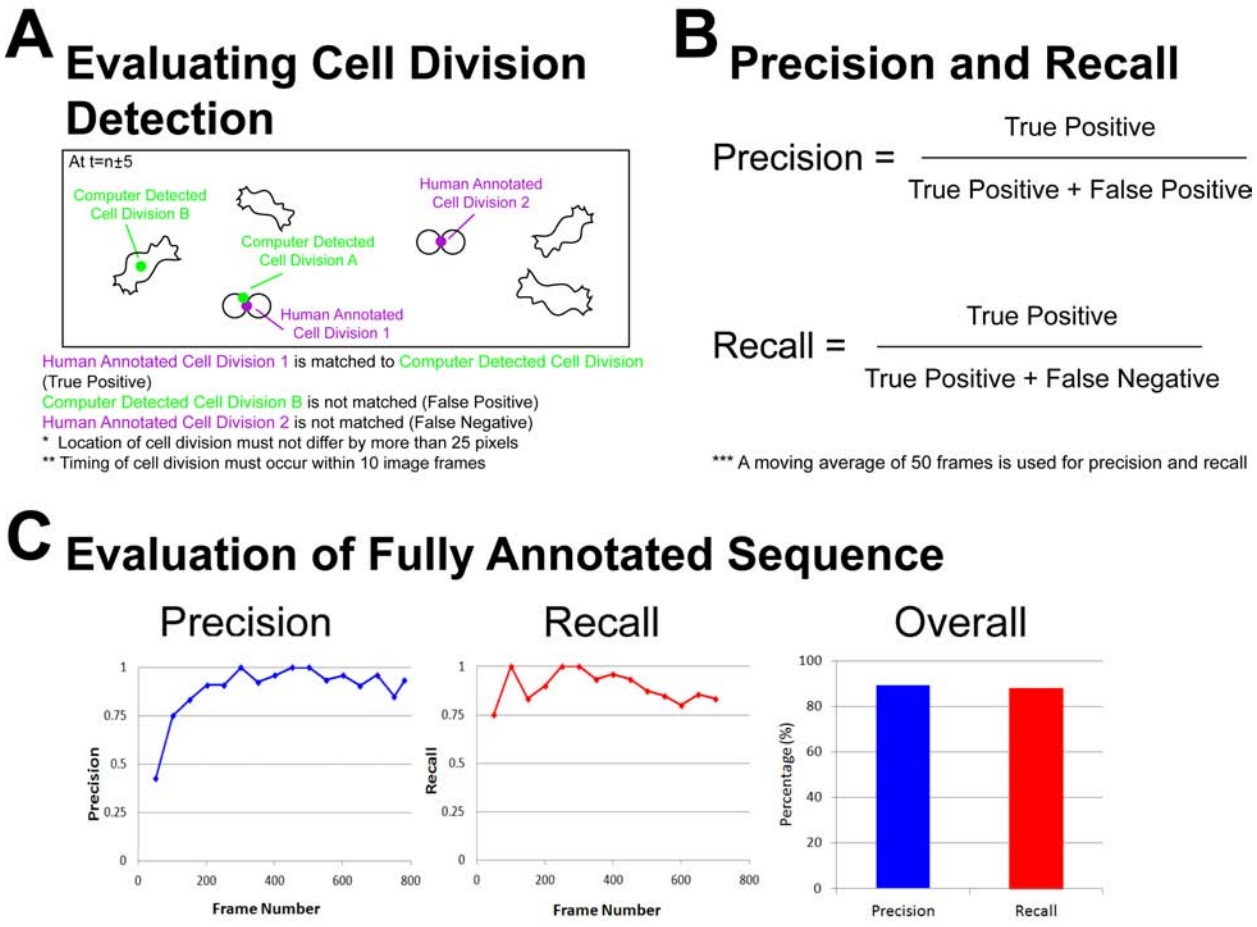

Figure A2.5. Evaluation of automated cell division detection. **A.** Schematic for matching a detected cell division event to its human annotated counterpart. **B.** Calculation of precision and recall. **C.** Evaluation of fully annotated sequence. The overall as well as individual precision and recall for a sliding window (10 frames) is shown.

To evaluate automated cell tracking, it was necessary to match human- and computer-annotations together (Figure A2.6A). Due to inherent errors in computer-based cell tracking, multiple cell tracks from computer-based cell annotations may be assigned to a single human-aided cell annotation at different time points, particularly when cell identity swaps occur (Figure A2.6A and Figure A2.6B). As such, both human- and computer-based annotations were paired together using the following criterion – if multiple computer-annotated cell tracks overlapped with a human-annotated cell track, the longest matching computer-annotated cell track was assigned to that particular human annotated cell track (Figure A2.6A). For example, Computer

Cell Track 1 overlaps with both Actual Cell Track 1 and Actual Cell Track 2. However, since Computer Cell Track 1 overlaps with Actual Cell Track 2 more, it is assigned to Actual Cell Track 2. Likewise, Computer Cell Track 2 is assigned to Actual Cell Track 1 (Figure A2.6A). Using these criteria, target effectiveness is computed as the number of correctly assigned frames divided by the total number of frames in a particular actual cell track (Figure A2.6C) while track purity is computed as the number of correctly assigned frames divided by the total number of frames in a particular computer track (Figure A2.6D). Although target effectiveness can be calculated using a partially annotated image sequence, track purity cannot since the number of correctly assigned frames in a computer track cannot be computed. Using these evaluation metrics, automated cell tracking of the fully annotated sequence was shown to have a target effectiveness of 0.83 and a track purity of 0.68 (Figure A2.7A). To robustly evaluate automated cell tracking under multiple culture conditions, automated cell tracking results were compared to the partially annotated 48 image sequences, achieving a target effectiveness of 0.71, 0.47, 0.77 and 0.59 for Control, FGF-2-, BMP-2- and FGF-2 with BMP-2-treated C2C12 cells, respectively (Figure A2.7B). A preliminary analysis of the image sequences indicated that FGF-2- and FGF-2 with BMP-2 treated cells exhibit a drastic morphological change (Figure A2.10A and Figure A2.10B) that interfered with the cell detection and cell division detection algorithms. At 17h, C2C12 cells show relative little-to-no difference in cell shape and appearance relative to control (Figure A2.10A). However, at 84h, FGF-2-treated cells adopt an elongated morphology and appear bright while BMP-2-treated cells adopt a well-spread morphology and appear larger relative to Control (Figure A2.10B). Also, FGF-2 with BMP-2-treated cells adopted a morphology intermediate between FGF-2- and BMP-2-treated cells (Figure A2.10B). Since both cell detection [79] and cell division detection [80] algorithms were dependent on such image

features for reliable cell and mitosis detection, low tracking performance was associated with FGF-2- and FGF-2 with BMP-2-treated C2C12 cells. Indeed, human annotators also experienced great difficulty in tracking FGF-2 and FGF-2 with BMP-2 time-lapse image sequences and at times could not track cells beyond 600 frames or 50 h (personal communications). To determine the effectiveness of the tracking module independent of cell detection and cell division detection results, human annotations of cell centroids and mitosis locations were used in conjunction with the automated tracking system and achieved a target effectiveness of 0.995 and track purity of 0.968, respectively (Figure A2.8A and Figure A2.8B). Together, these results indicate that automated cell tracking systems could benefit from improvements in individual cell tracking components.

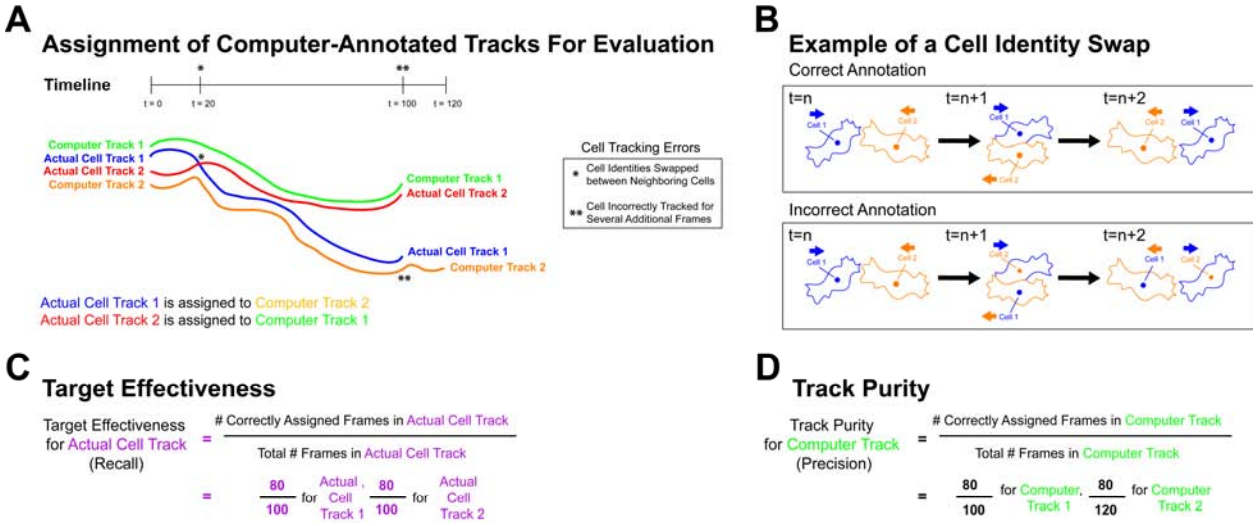

Figure A2.6. Evaluation of automated cell tracking. **A.** Schematic for matching a detected cell track to its human annotated counterpart. **B.** Schematic example of a cell identity swap. **C.** Calculation of target effectiveness. **D.** Calculation of track purity.

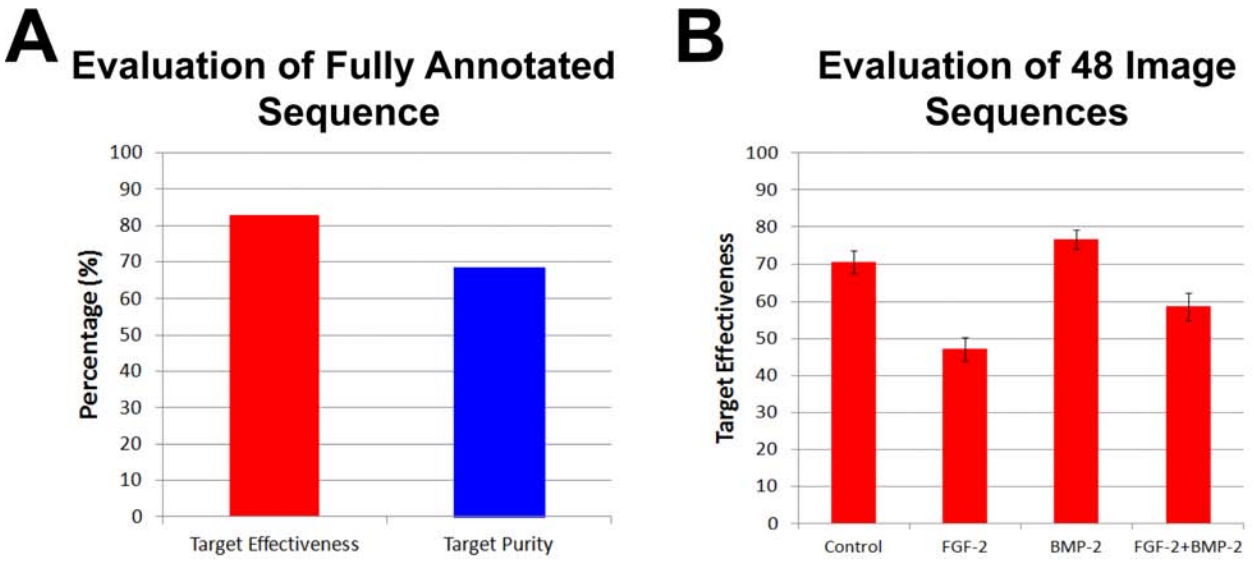

Figure A2.7. Evaluation of automated cell tracking. **A.** Overall target effectiveness and track purity of fully annotated sequence. **B.** Overall target effectiveness of Control, FGF-2-treated, BMP-2-treated and FGF-2 with BMP-2-treated C2C12 cells (n = 48 image sequences). At least 3 cells from the first frame of the image sequence and all their subsequent progeny were manually tracked for each sequence.

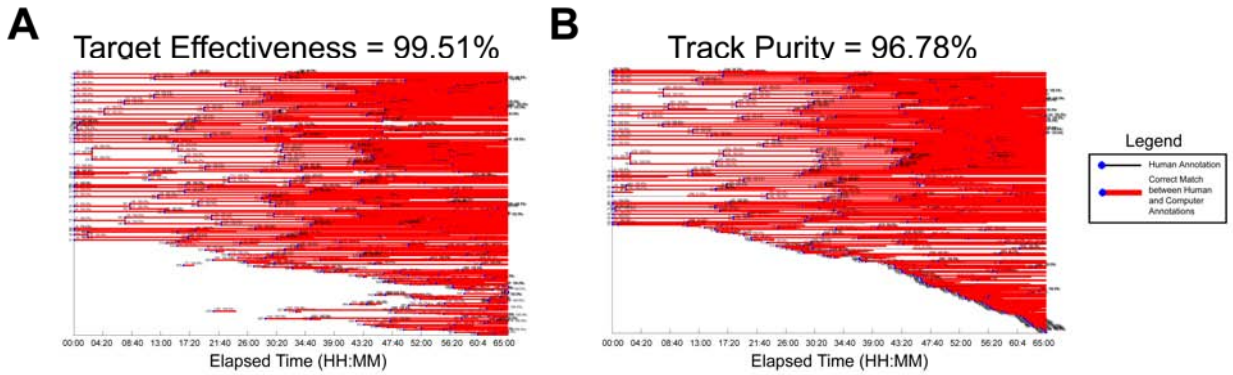

Figure A2.8. Evaluation of automated cell tracking when human-annotated segmentation and mitosis results are used. **A.** Overall target effectiveness of fully annotated sequence is presented in a cell lineage tree format. **B.** Overall track purity of fully annotated sequence is presented in a cell lineage tree format. Both human (black line) and correctly matched computer (red line) annotations are indicated.

A2.4.3 Generating Biologically-Relevant Measurements

To facilitate characterization of cell growth kinetics, the CTK software allows for several biological measurements to be computed and exported including cell number, various growth indices and indicators, the time taken for cell division and cytokinesis, cell cycle length, cell

speed, cell perimeter, cell area, cell confluence as well as a cell lineage tree (Figure A2.9). Using the partially annotated 48 Sequences, it was shown that although growth factor treatment did not perturb the amount of time required for cell division and cytokinesis, BMP-2 was shown to increase the cell cycle length ($p < 0.05$; Figure A2.10).

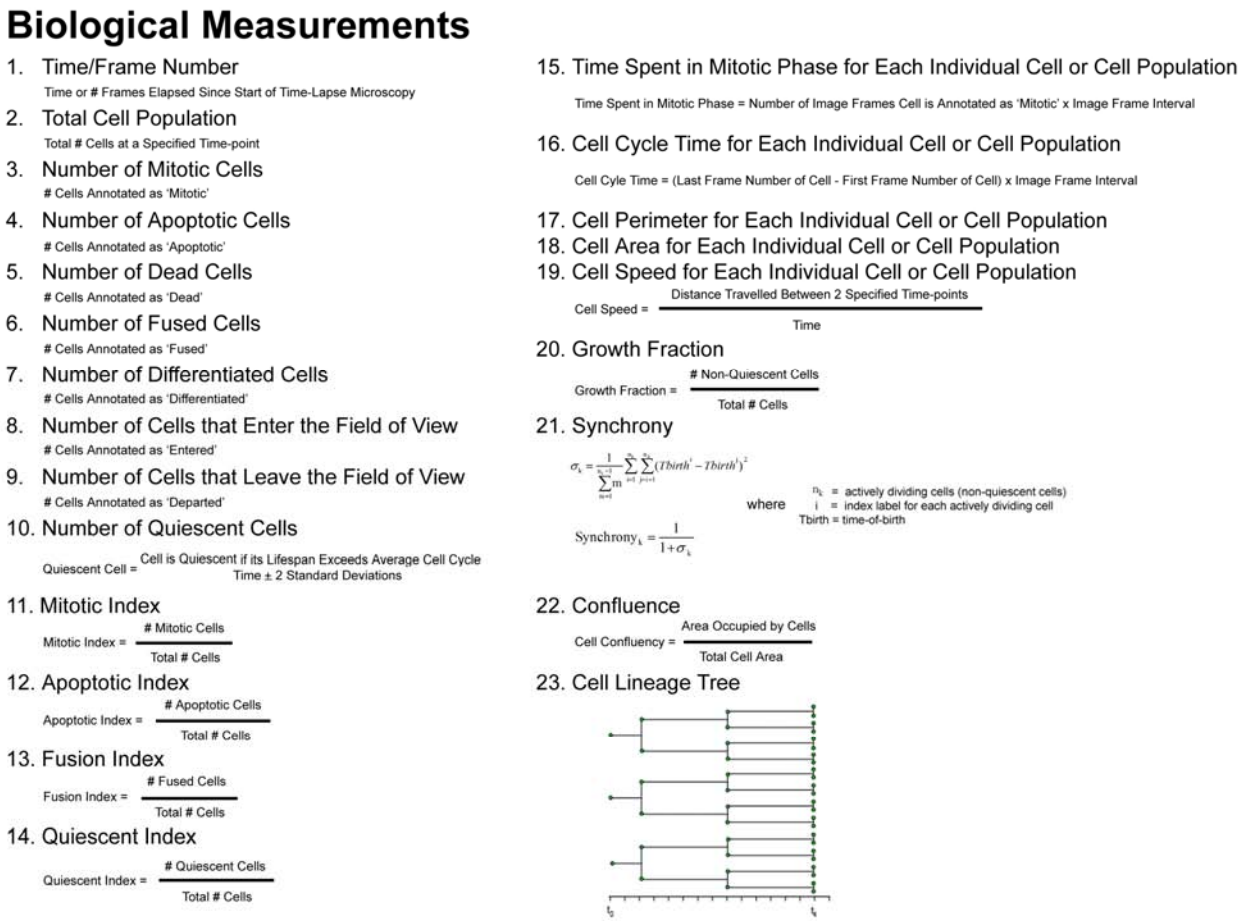

Figure A2.9. Biological measurements that can be derived from CTK software. The definition of each biological measurement is as indicated.

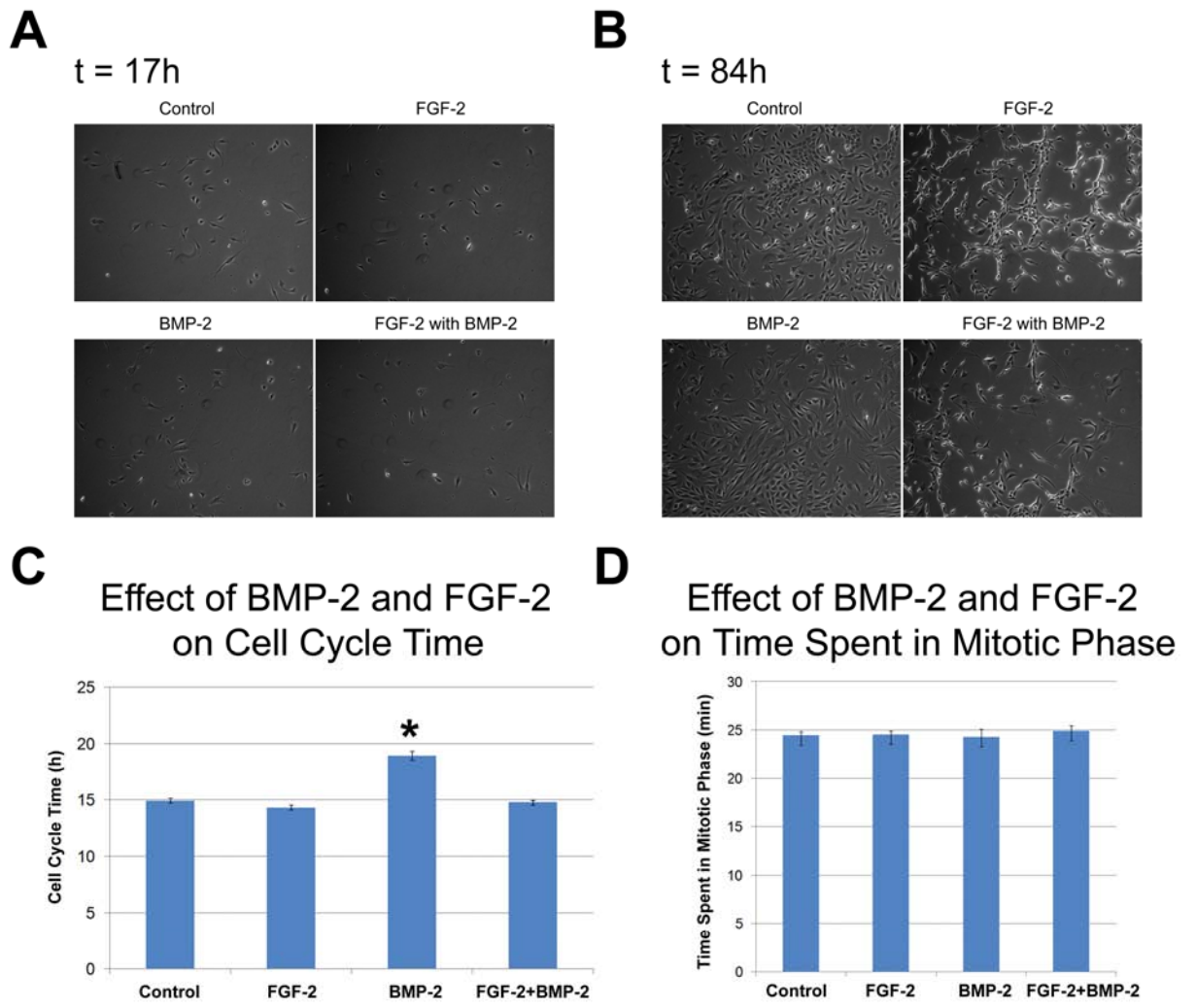

Figure A2.10. Effect of BMP-2 and FGF-2 on C2C12 cell cycle length and division time. **A.** C2C12 cells show little-to-no morphological changes 17 h after growth-factor treatment. **B.** C2C12 cells show dramatic morphological changes 84 h after growth-factor treatment. FGF-2-treated cells adopt an elongated morphology and appear bright while BMP-2-treated cells adopt a well-spread morphology and appear larger relative to Control. FGF-2 with BMP-2-treated cells adopt a morphology intermediate between FGF-2- and BMP-2-treated cells. **C.** FGF-2 had no effect on C2C12 cell cycle length relative to control whereas BMP-2 increased C2C12 cell cycle length. **D.** Both BMP-2 and FGF-2 have no effect on the amount of time taken for C2C12 cells to undergo mitosis and cytokinesis. $*$, Significantly different from Control; $p \leq 0.05$.

A2.5 DISCUSSION

A2.5.1 Development of CTK Software

With the aim of achieving rapid cell characterization, a software package dedicated for both manual and automated analysis of time-lapse microscopy image sequences was developed

(Figure A2.1, Figure A2.2 and Figure A2.3). The CTK software provides a user-friendly GUI for performing manual annotation of the cell centroid or cell boundary in any type of optical time-lapse microcopy image sequence (Fluorescence, bioluminescence, brightfield, DIC or phase-contrast). The software reduces the tedious burden of manual annotation by interpolating the cell centroid between successive frames. As a result, the user is not required to annotate every single image frame in a sequence. In addition, the CTK software also allows for a variety of cell labels such as 'mitotic', 'differentiated', 'fused', etc. to be applied to the same cell at various time-points to facilitate analysis of multiple cell behavior (Figure A2.2). Although the automated cell tracking system is presently specialized for cell tracking in phase-contrast time-lapse microscopy image sequences (Figure A2.3), future work will incorporate cell tracking algorithms for other imaging modalities as well as new modules for detecting other cell behaviors such as apoptosis and cell differentiation. Since it is likely that no single cell detection algorithm will be universally applicable to all cell types, the program has been modularly designed such that new algorithms can be added in subsequent work. To serve the broader interests of the biological research community, the CTK software can export biological measurements related to cell growth kinetics for subsequent data transformation and analysis (Figure A2.9). In addition, the CTK software can allow users to visualize parent-daughter relationships quickly and simply by generating a cell lineage tree (Figure A2.9). Using this software, manual annotation of 48 image sequences indicated that BMP-2-treated cells show increased cell cycle length (Figure A2.10C), which is in agreement with a reduction in cell proliferation during bone cell differentiation [84].

A2.5.2 Analysis of Automated Cell Tracking Errors

To evaluate the automated cell tracking system and its individual components, precision, recall, target effectiveness and track purity were utilized [76, 81-83].

Precision and recall are widely used metrics for evaluating information retrieval [81] and thus are appropriate for evaluating cell detection (Figure A2.4) and cell division detection (Figure A2.5). In this context, precision refers to the fraction of correctly detected cell centroids or mitosis locations out of all computer-detected events while recall refers to the fraction of correctly detected cell centroids or mitosis locations out of all actual (human-detected) events. As such, a precision and recall value close to 1.0 is indicative of good algorithm performance. Using a fully annotated image sequence, cell detection had a precision of 0.89 and a recall of 0.89 (Figure A2.4) while cell division detection had a precision of 0.89 and a recall of 0.88 (Figure A2.5).

Both target effectiveness (Figure A2.6C) and track purity (Figure A2.6D) are based on the concept of precision and recall, respectively, and are used in radar tracking where multiple objects of an unknown quantity must be tracked [76, 82, 83]. In this scenario, target effectiveness refers to the fraction of correctly-annotated computer cell tracks out of all actual (human-annotated) cell tracks while track purity refers to the fraction of correctly-annotated computer cell tracks out of all computer-constructed cell tracks. [76, 82, 83]. Using a fully annotated sequence, cell tracking was shown to have a target effectiveness of 0.83 and a track purity of 0.68 (Figure A2.7A). Using 48 partially annotated image sequences, the automated cell tracking system was robustly evaluated under multiple culture conditions where different growth factors such as FGF-2 and BMP-2 were present. FGF-2 and BMP-2 were used as they have been shown to promote C2C12 differentiation towards a tendon and osteoblast fate, respectively [15, 16]. FGF-2-treated cells showed elongated morphology and appeared brighter (indicative of increased cell height) while BMP-2-treated cells showed a well-spread morphology and appeared larger than Control cells (Figure A2.10). Control, FGF-2-, BMP-2- and FGF-2 with BMP-2-treated

C2C12 cells had a target effectiveness of 0.71, 0.47, 0.77 and 0.59, respectively (Figure A2.7B). A preliminary analysis of the image sequences indicated that different growth factor treatments, particularly the addition of FGF-2 lead to dramatic changes to the overall image and cell appearance (Figure A2.10A and Figure A2.10B), resulting in lowered cell detection (increased false negatives) and more cell division artifacts (increased false positives), ultimately causing a low target effectiveness (Figure A2.7B). These results highlight the need for automated cell tracking systems to be robustly validated under multiple conditions to ensure that these systems can be applied for biological experimentation since such studies often employ the use of multiple treatment conditions while most cell tracking studies only employ a single culture condition. When cell detection and cell division results were substituted with human annotations, a target effectiveness of 0.995 and a track purity of 0.968 is achieved (Figure A2.8A and Figure A2.8B), indicating that the tracking system can achieve good cell tracking performance independent of its individual cell tracking components. Subsequent work on automated cell tracking systems will emphasize on improving in individual cell tracking components.

A major challenge in the development of automated cell tracking systems is that for any analysis to be relevant, it is critical that cell annotations are as complete and error-free as possible. This is particularly difficult as any error in cell tracking such as a cell identity swap can potentially obscure true parent-daughter relationships as well as other cell measurements such as cell cycle length to produce misleading biological results and interpretations. In addition, any errors that occur early in the sequence may potentially generate incorrect tracking hypotheses that further compound tracking errors. As such, a plot of precision or recall against time (image frame) is a useful indicator of the confidence level that can be assigned during interpretation of computer-tracked time-lapse sequences as well as aiding in error analysis (Figure A2.4 and Figure A2.5).

In this scenario, it was observed that initiating time-lapse microscopy when cells had not fully spread-out after cell seeding resulted in brighter images, which caused cell detection and cell division detection artifacts that lowered precision and recall (Figure A2.4 and Figure A2.5). Such artifacts could be simply resolved by omitting the initial affected frames from automated cell tracking analysis or cells could be seeded overnight in future time-lapse experiments. Alternatively, the algorithms could be further improved to handle such exceptions as well. In the case of cell division detection, this may involve using a larger data set containing human annotated mitosis for improved supervised machine learning.

In summary, a software package for manual and automated cell tracking was developed to serve as a standardized tool for biologically relevant cell culture analysis. Analysis of automated cell tracking performance indicated that automated cell tracking systems must be validated under multiple culture conditions for such systems to be used for biological experimentation. Future work on this system will seek to implement additional algorithms for more accurate automated cell tracking. This work demonstrates the use of cell tracking software for biologically-relevant analysis of cell cultures and may have potential applications in stem cell characterization and expansion for regenerative medicine.

A2.6 HUMAN- AND COMPUTER-ANNOTATED CELL LINEAGE TREES

A2.6.1 Human-Aided Cell Annotations

A2.6.1.1 3rd March 2009 Dataset

Control

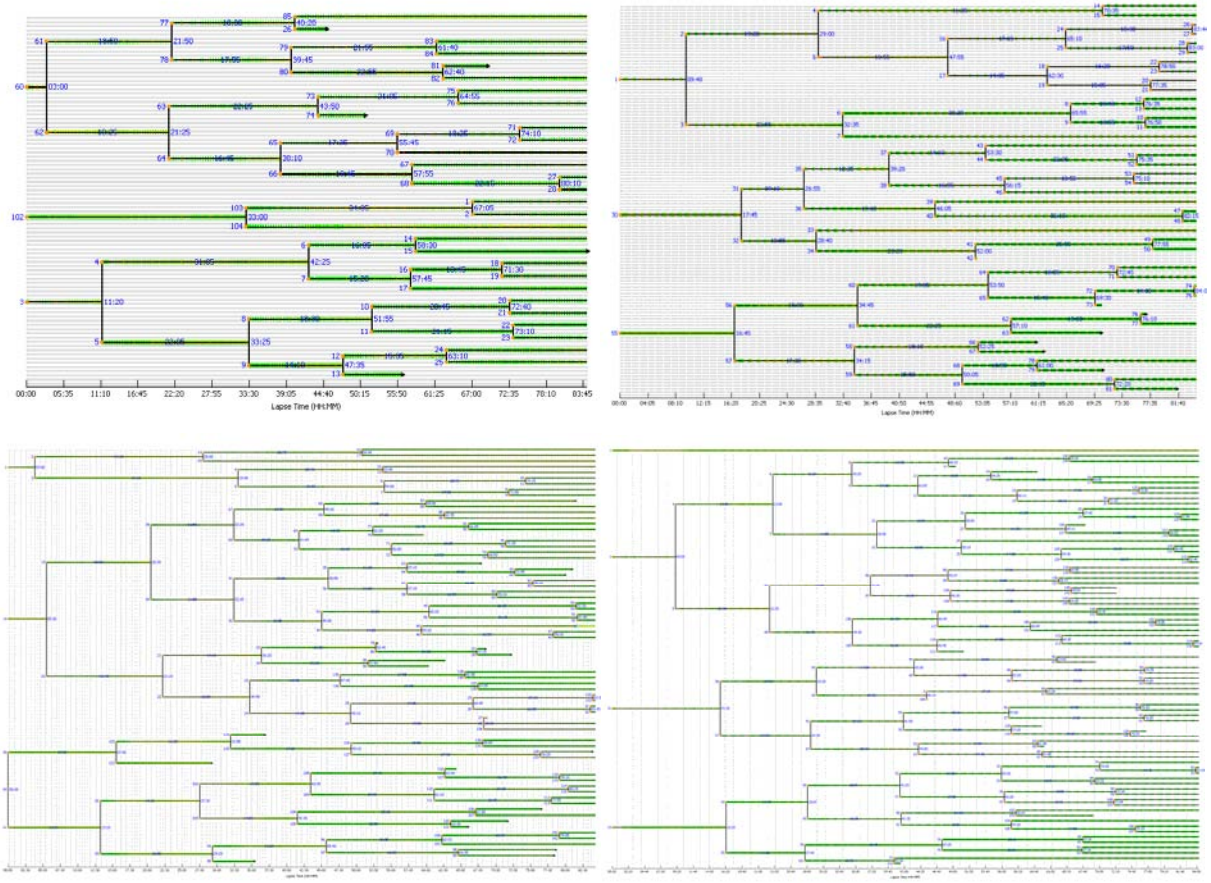

100 ng/mL FGF-2

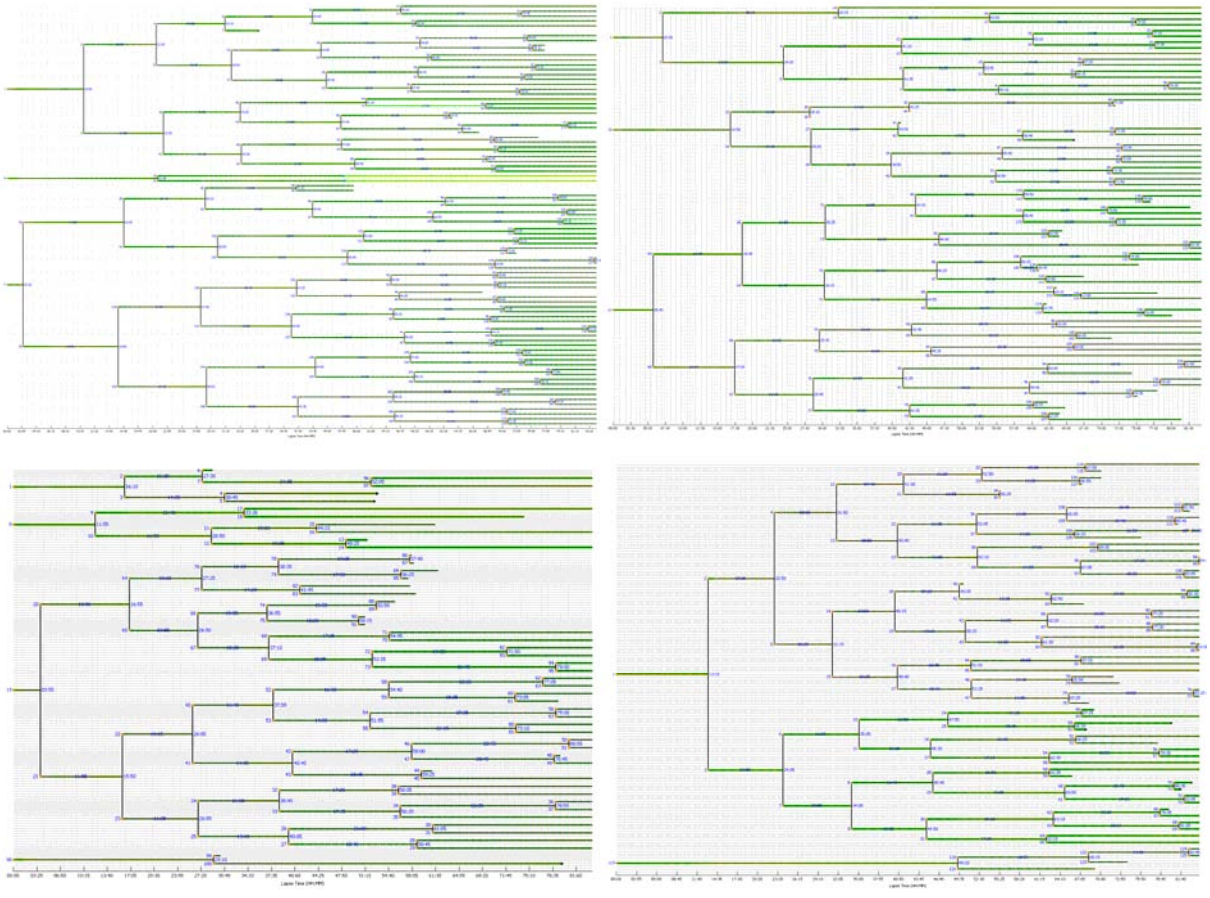

100 ng/mL BMP-2

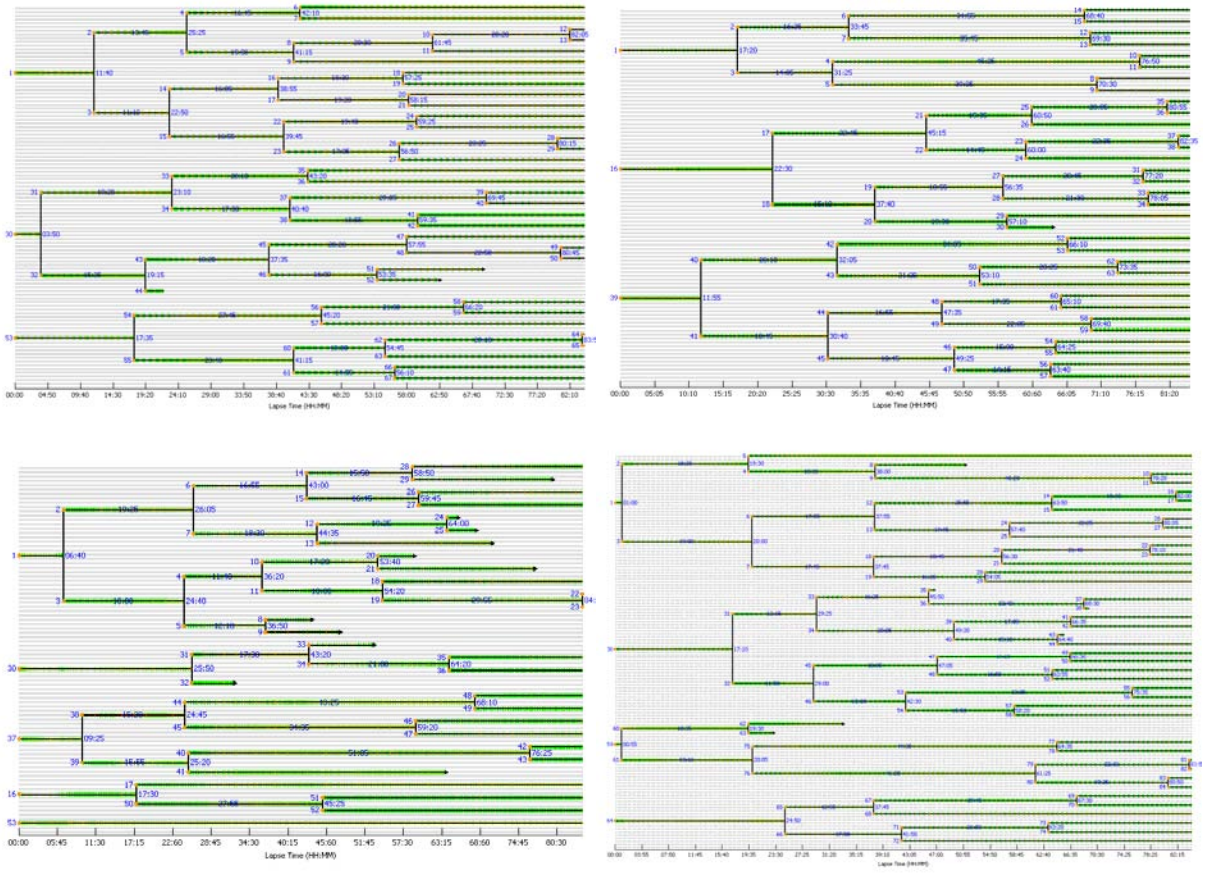

100 ng/mL BMP-2 (Fully annotated up to frame 780)

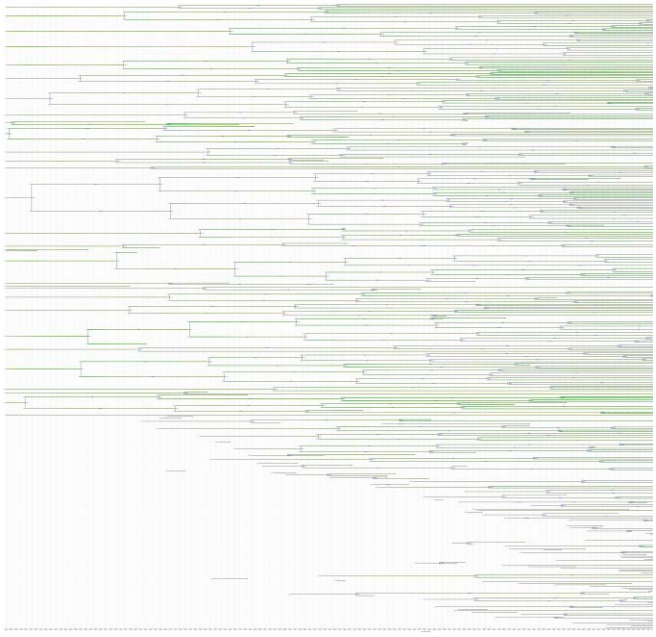

100 ng/mL BMP-2 and 100 ng/mL FGF-2

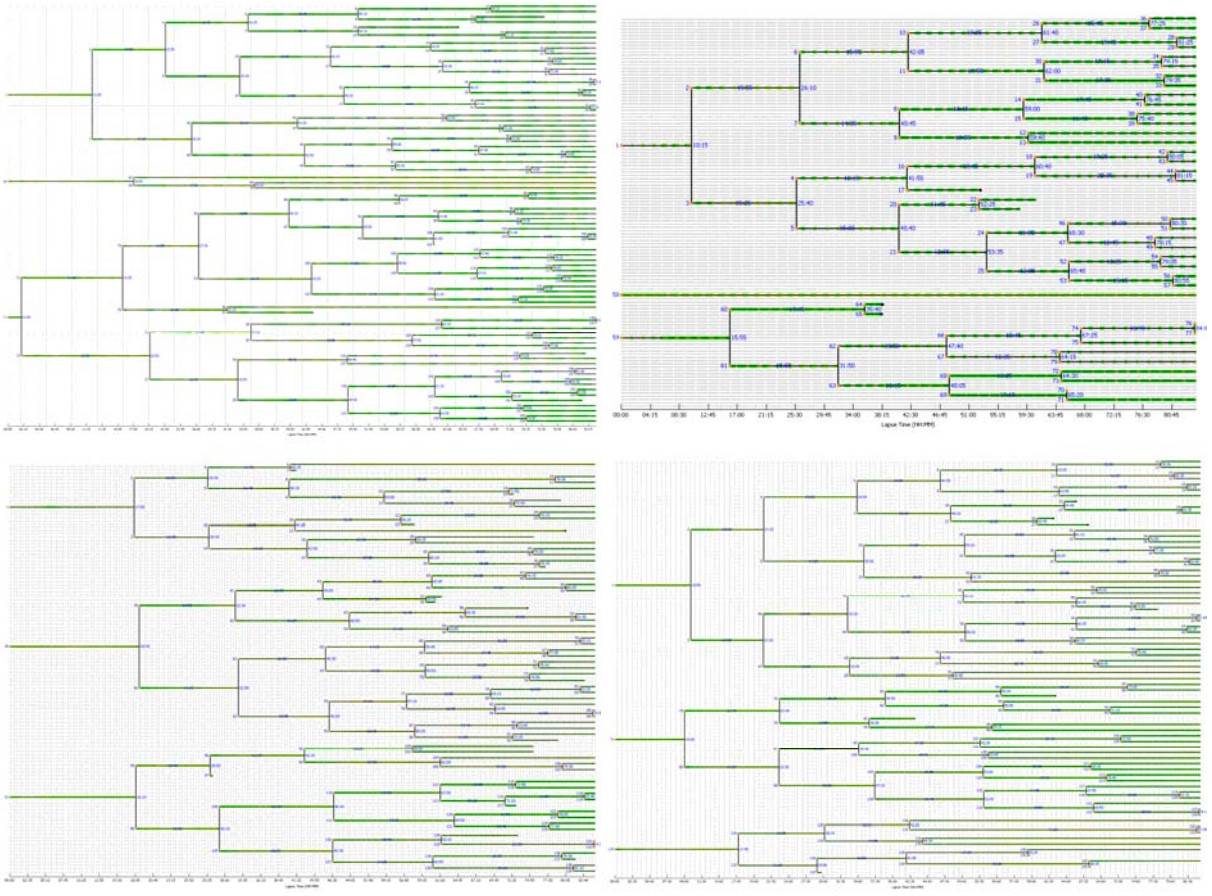

A2.6.1.2 18th March 2009 Dataset

Control

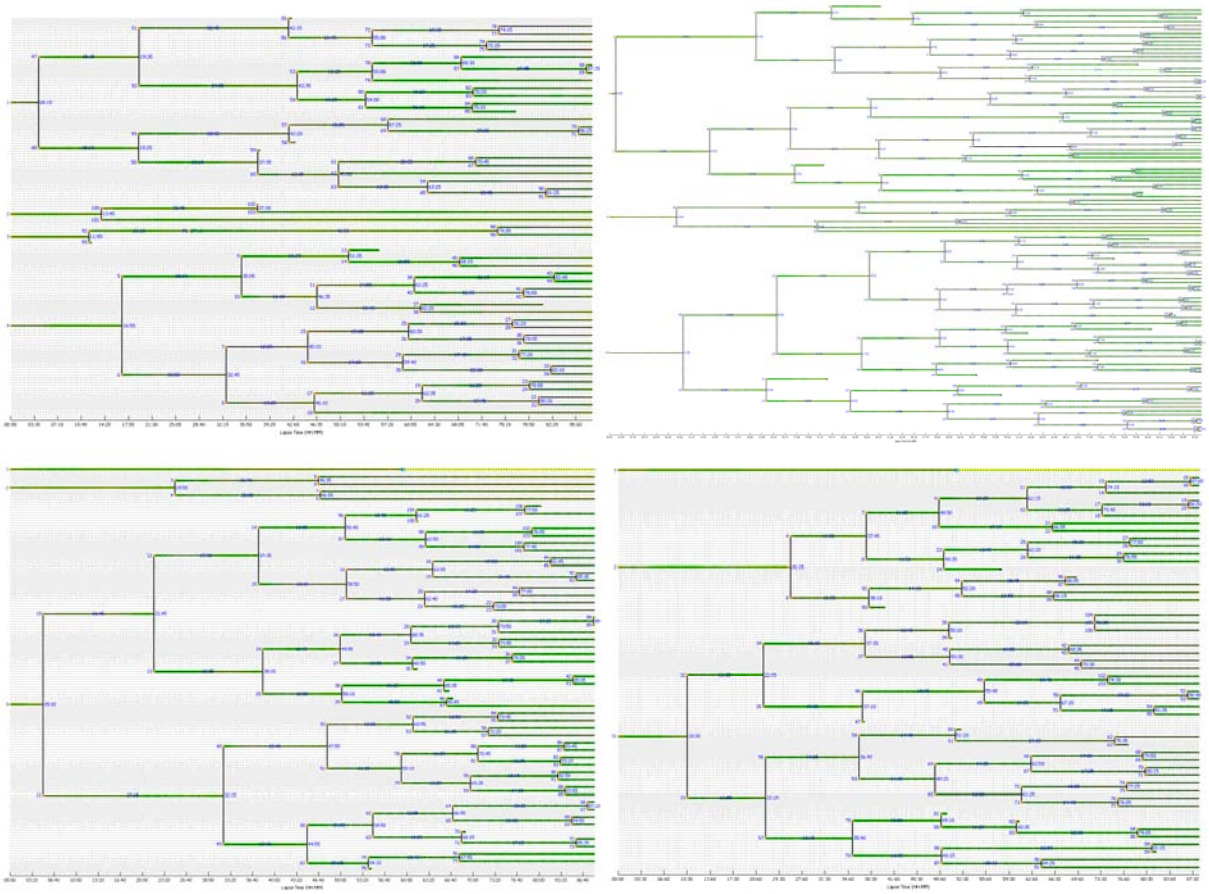

100 ng/mL FGF-2

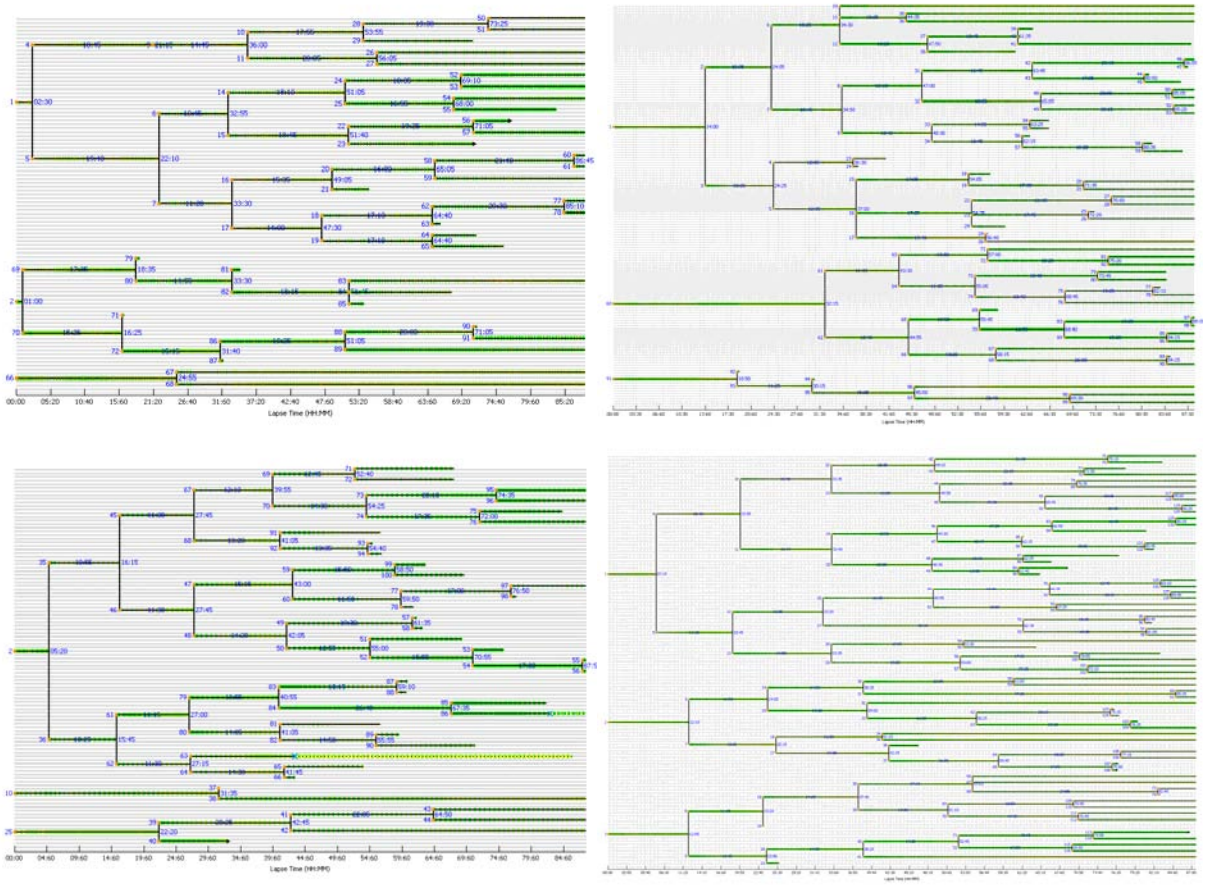

100 ng/mL BMP-2

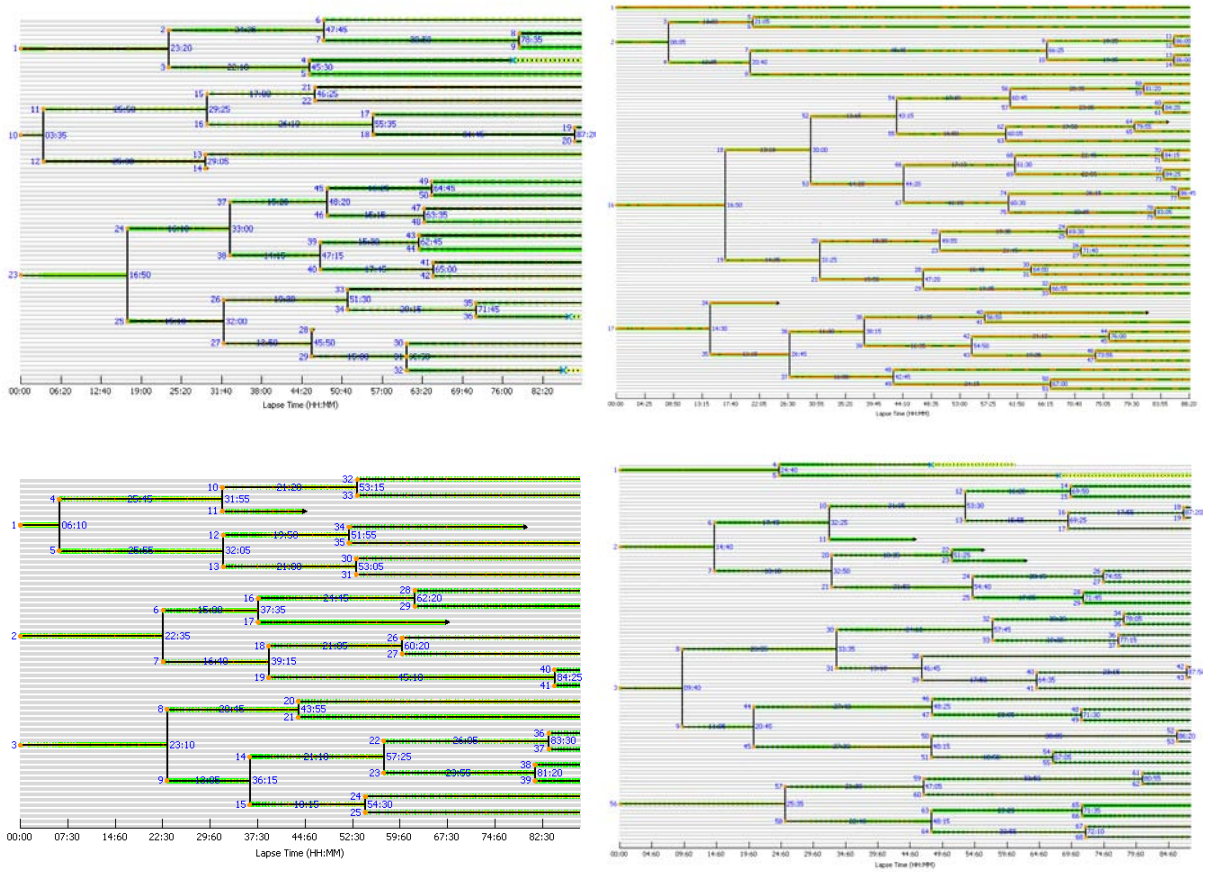

100 ng/mL BMP-2 and 100 ng/mL FGF-2

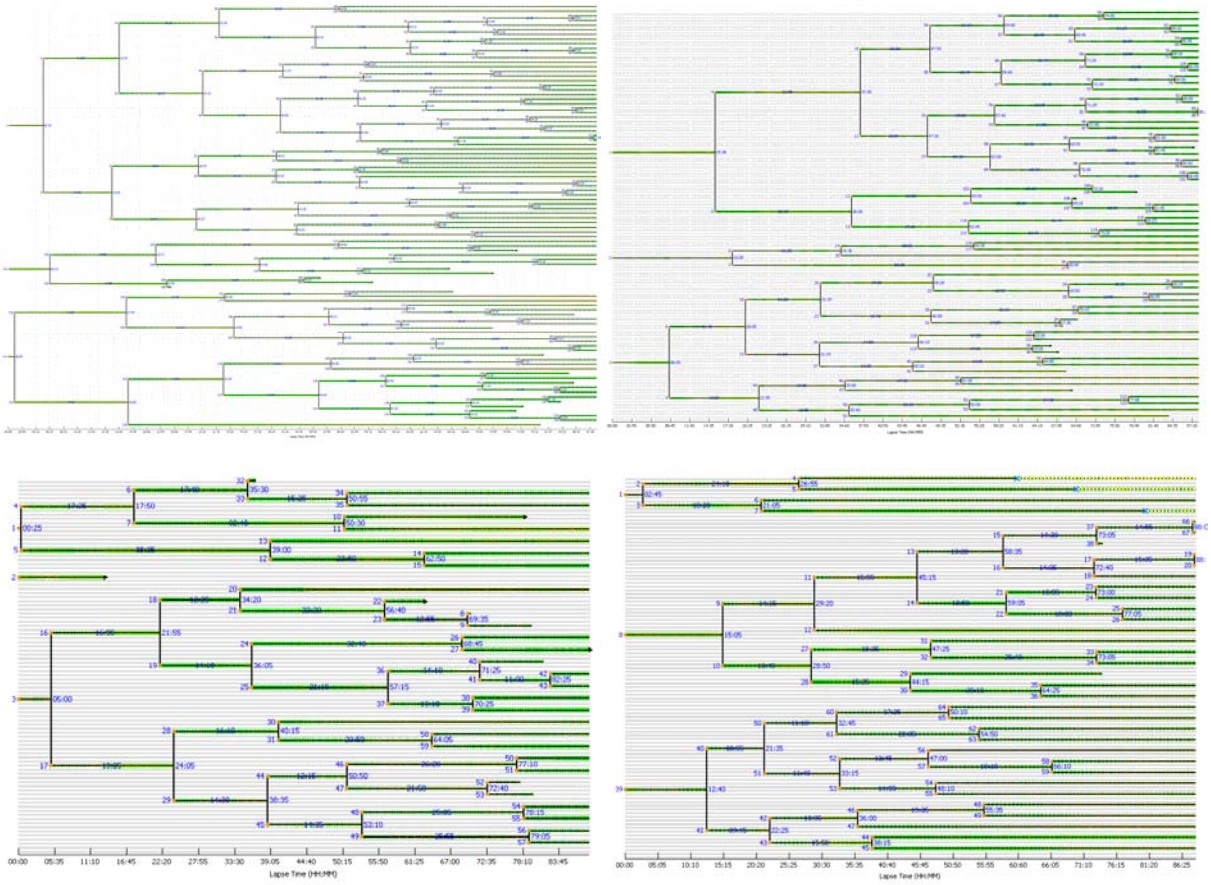

A2.6.1.3 25th March 2009 Dataset

Control

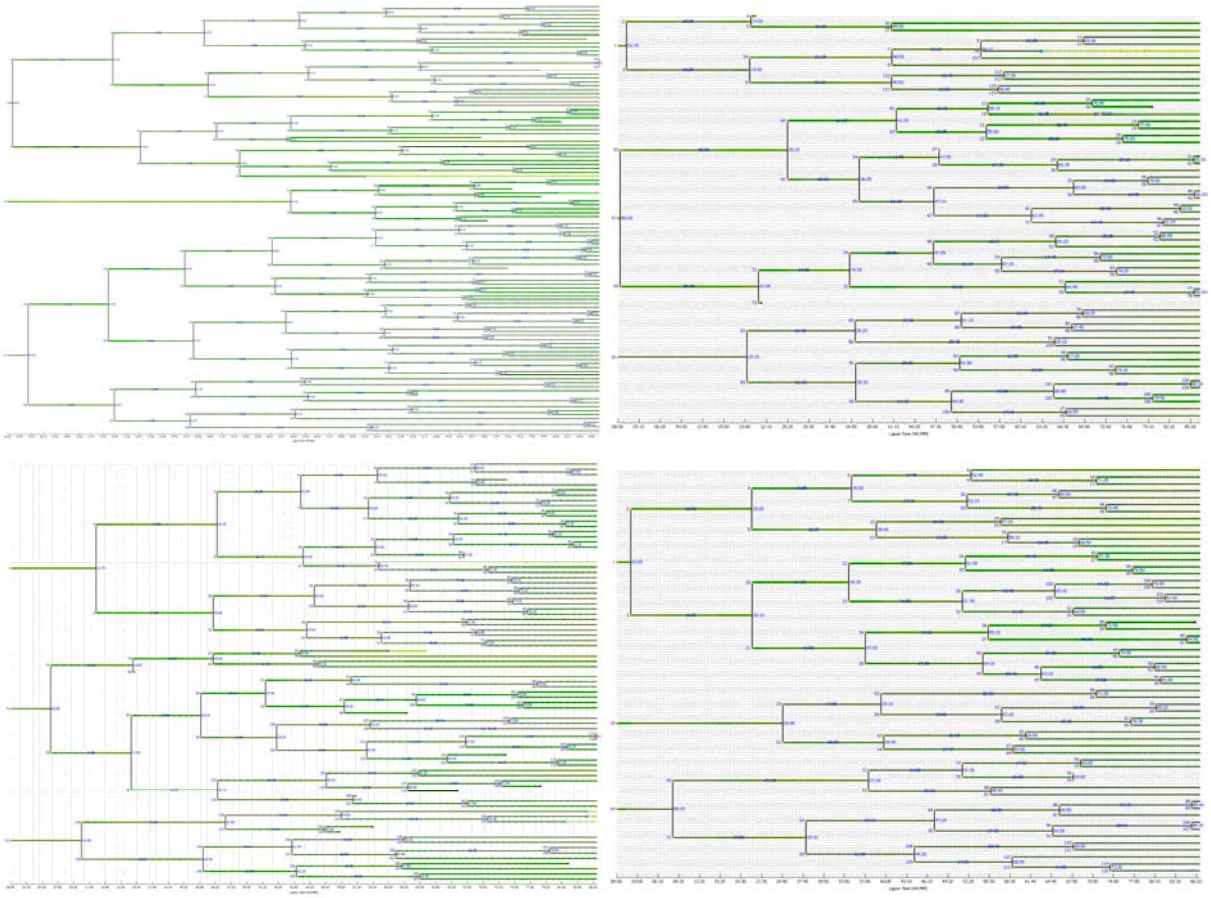

100 ng/mL FGF-2

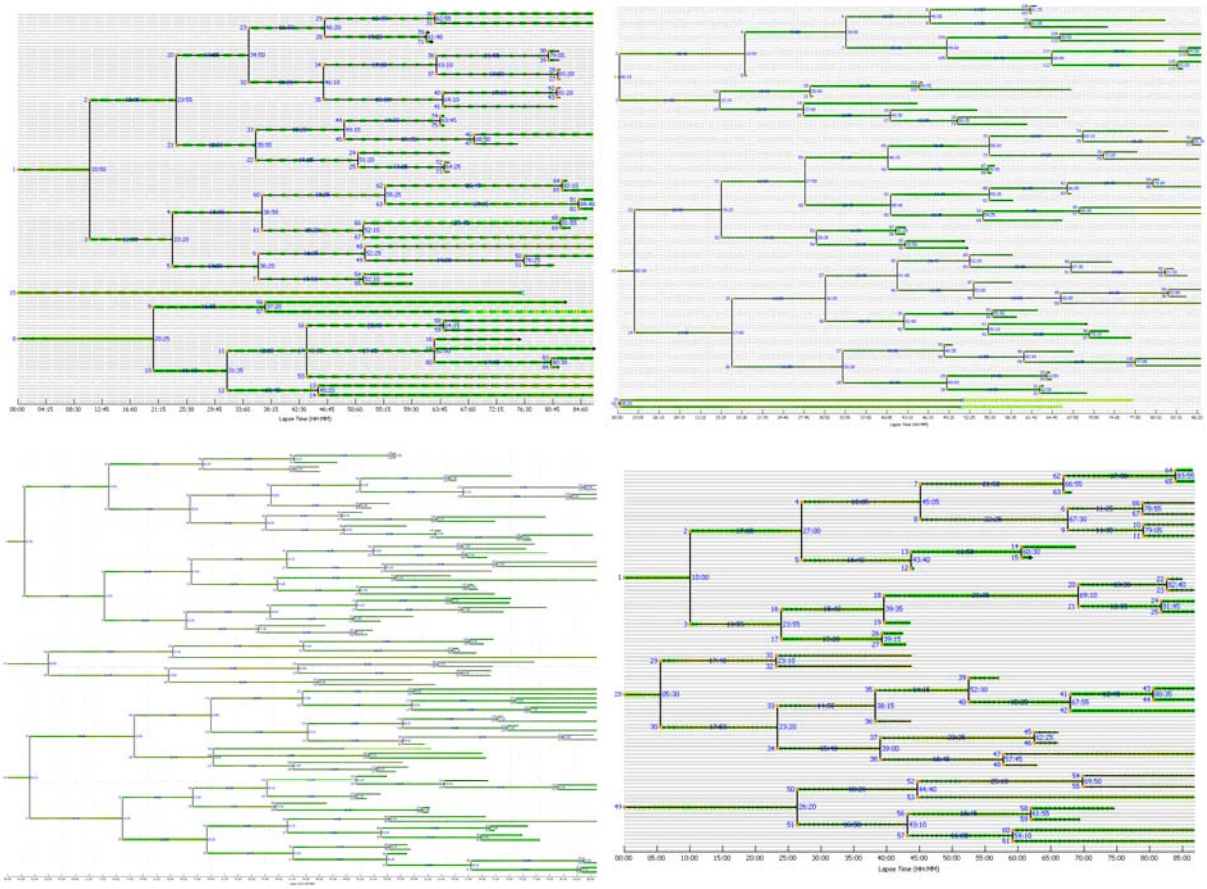

100 ng/mL BMP-2

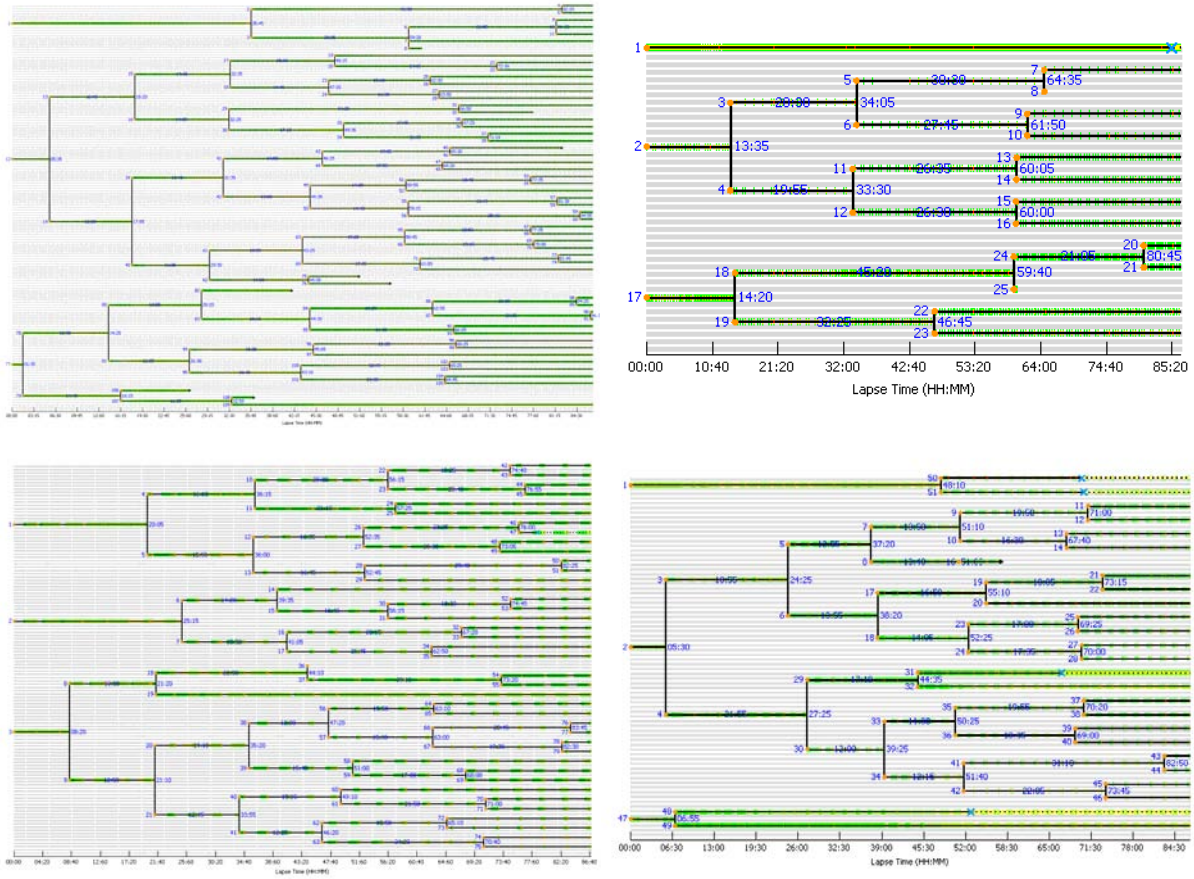

100 ng/mL BMP-2 and 100 ng/mL FGF-2

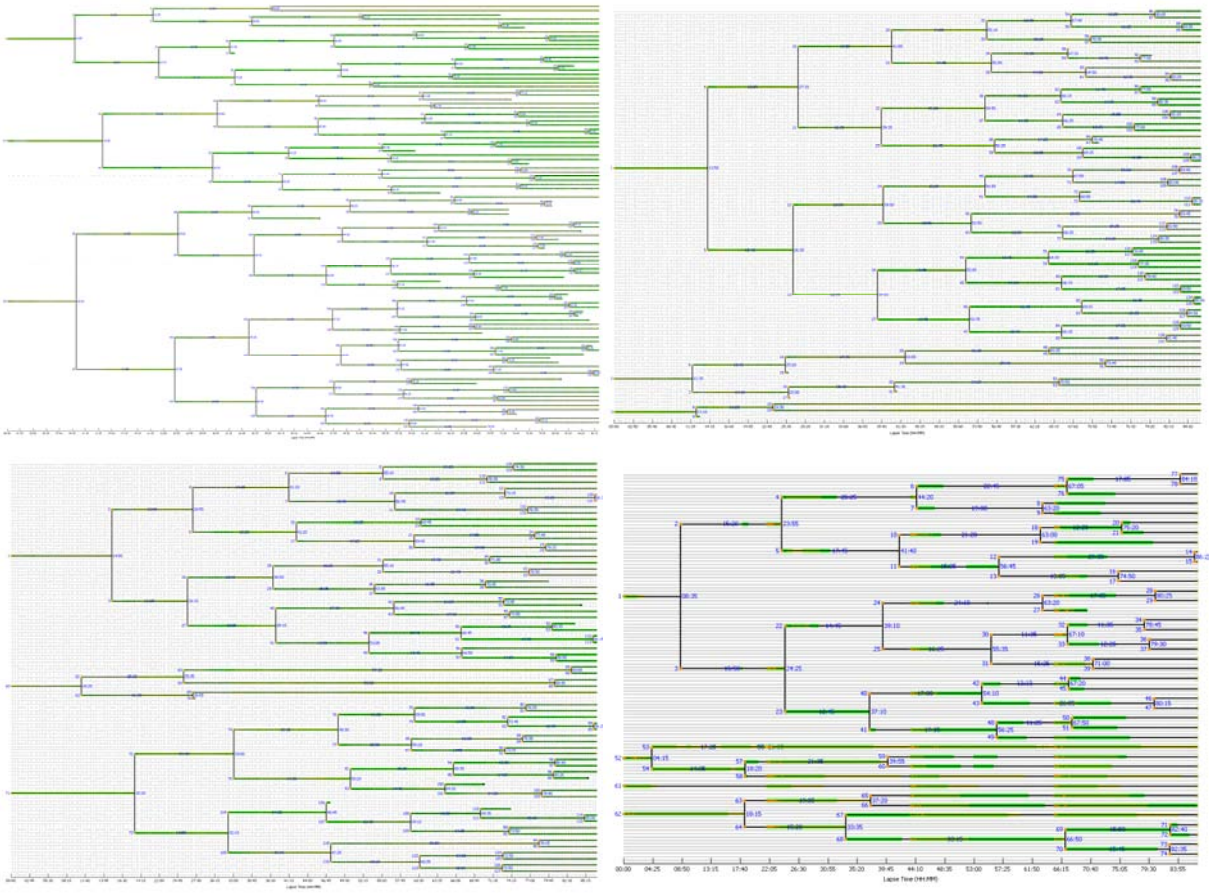

A2.6.2 Computer-Aided Cell Annotations

A2.6.2.1 3rd March 2009 Dataset

Control

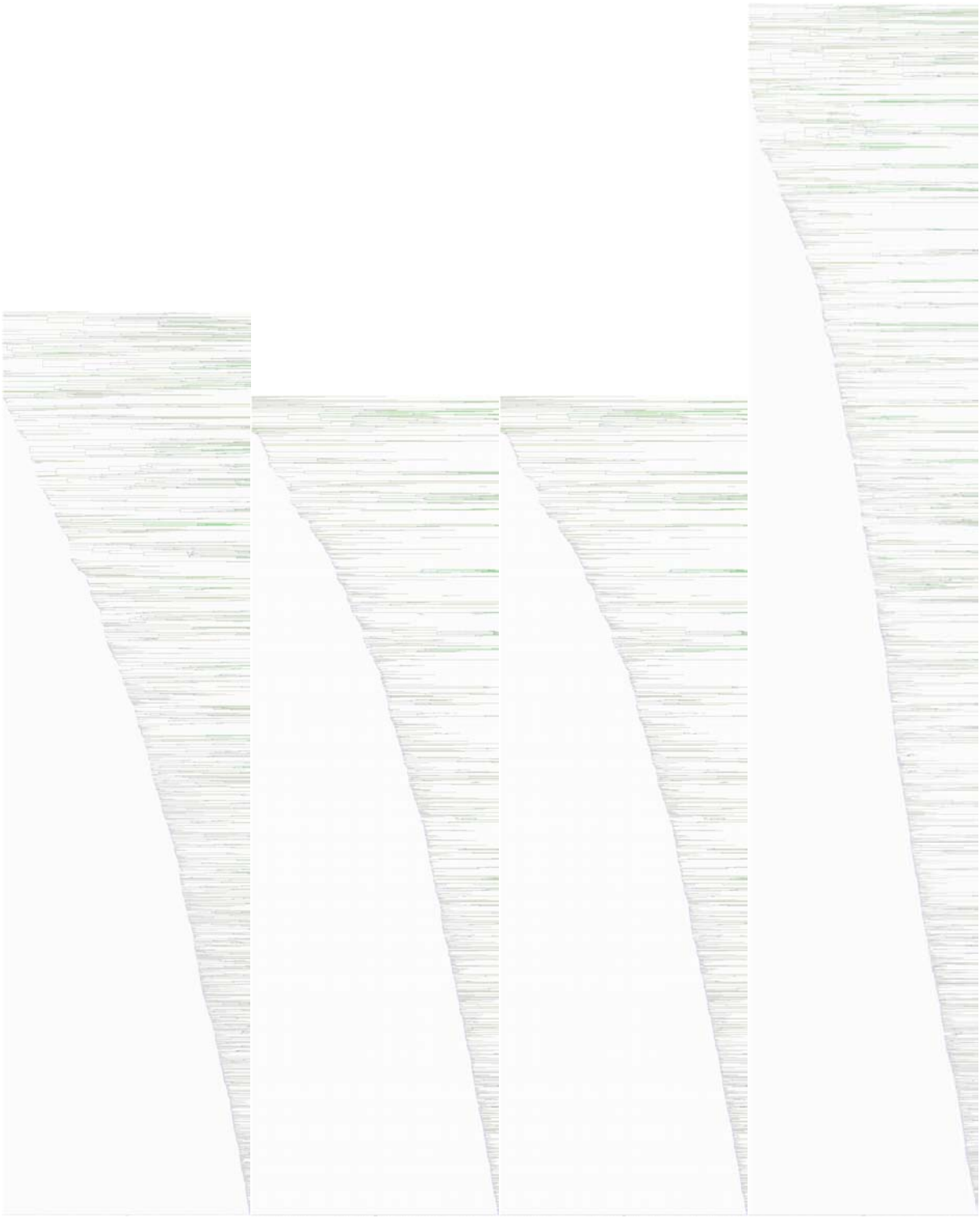

100 ng/mL FGF-2

100 ng/mL BMP-2

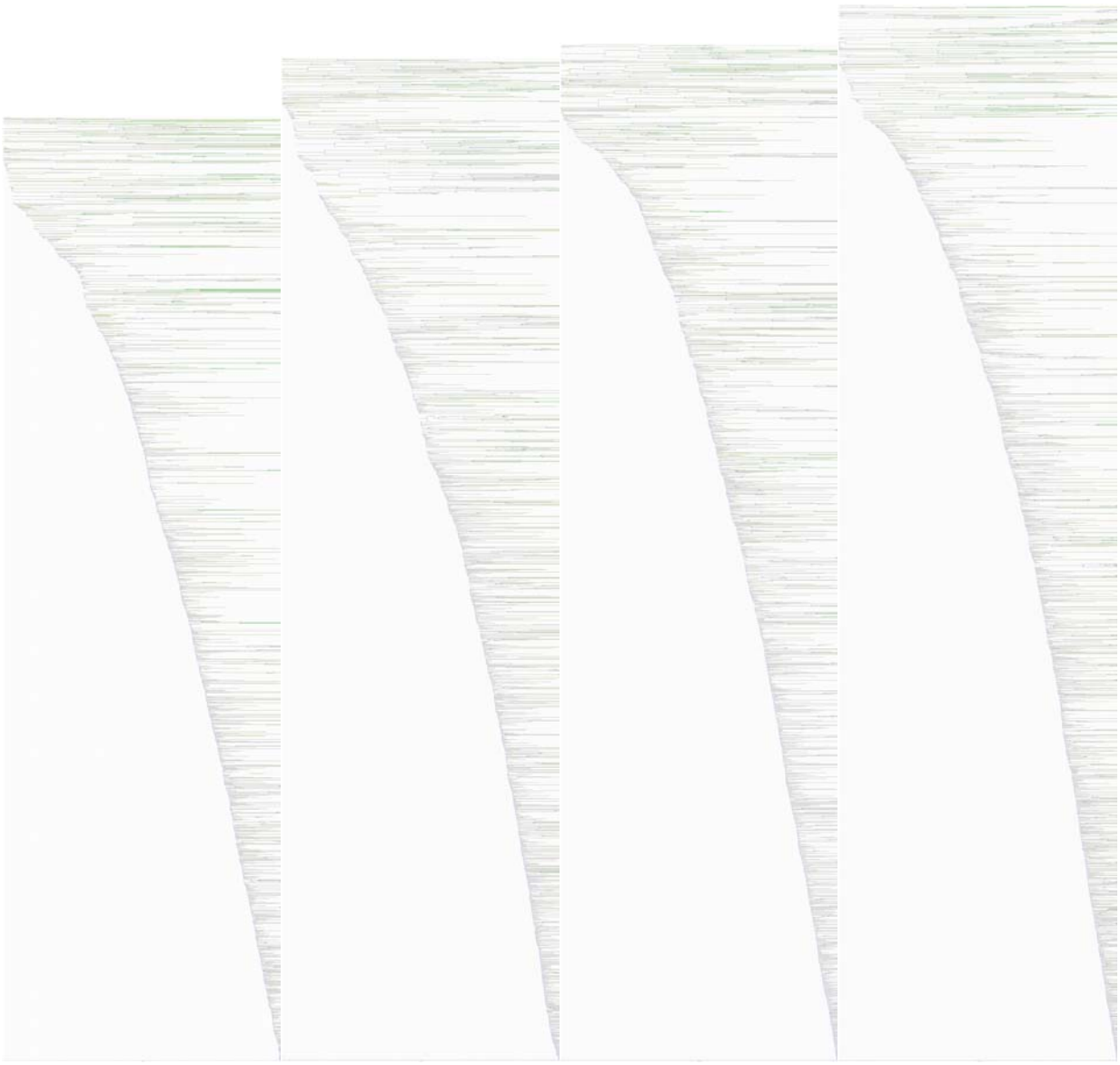

100 ng/mL BMP-2 and 100 ng/mL FGF-2

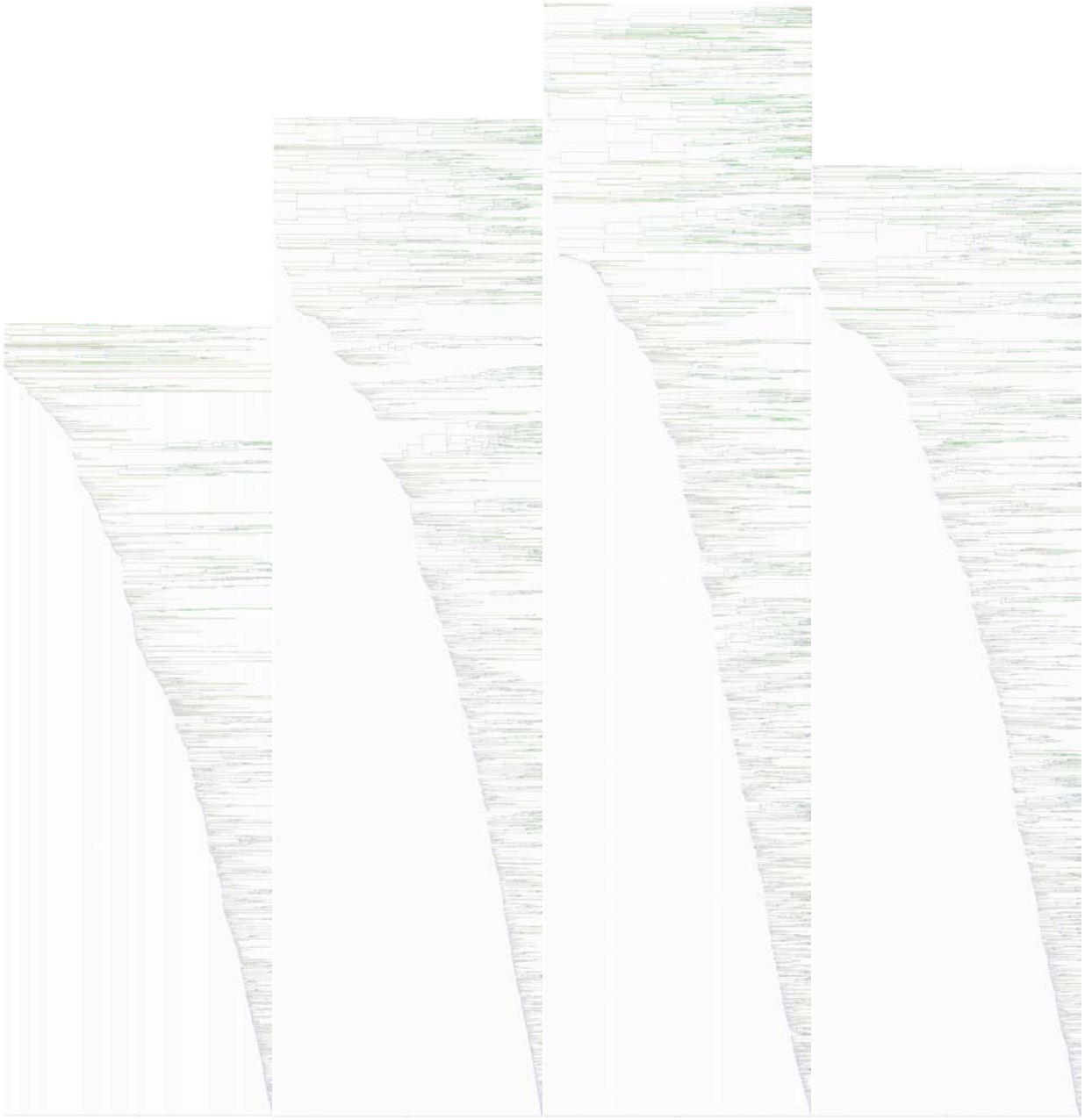

A2.6.2.2 18th March 2009 Dataset

Control

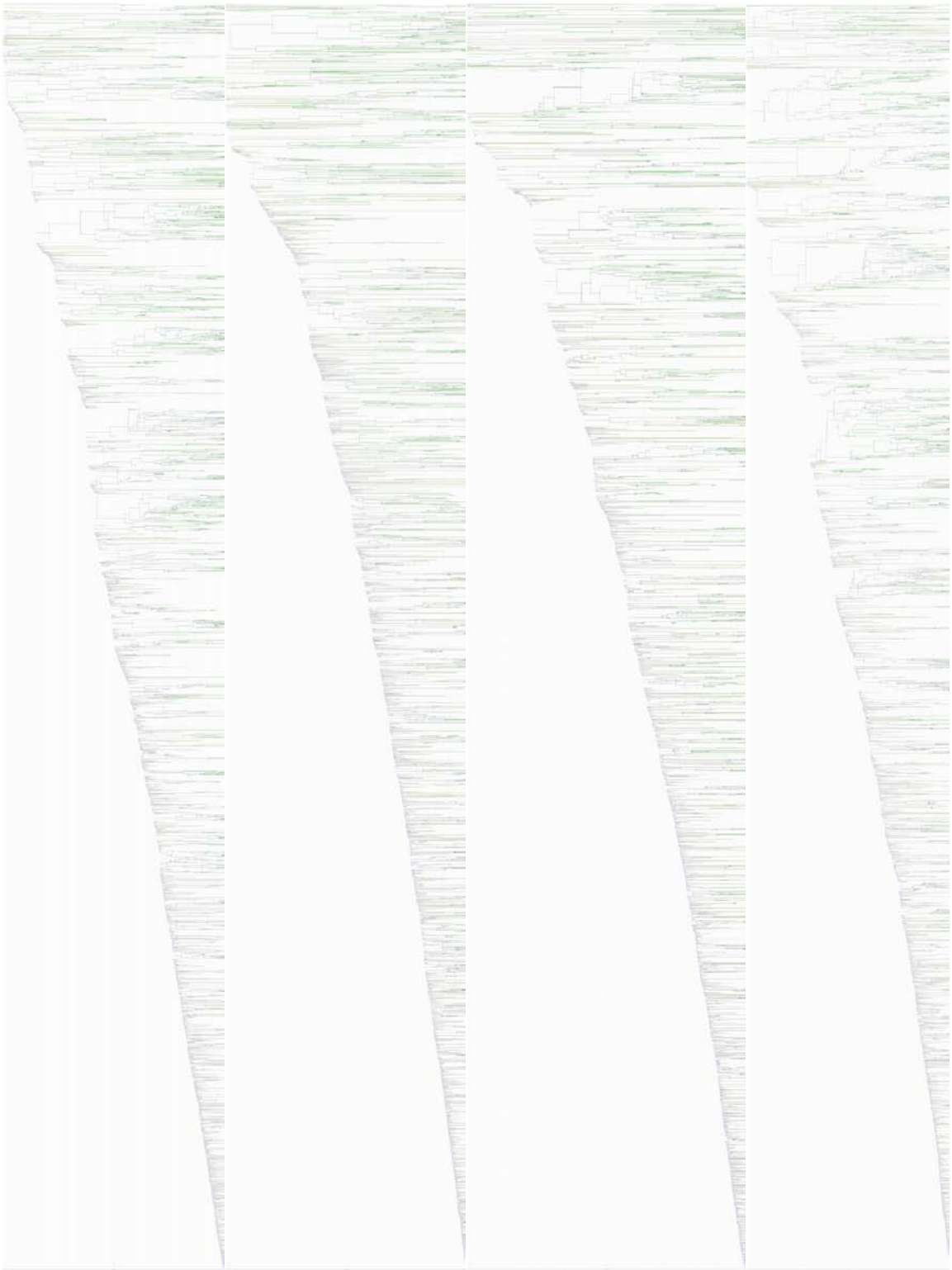

100 ng/mL FGF-2

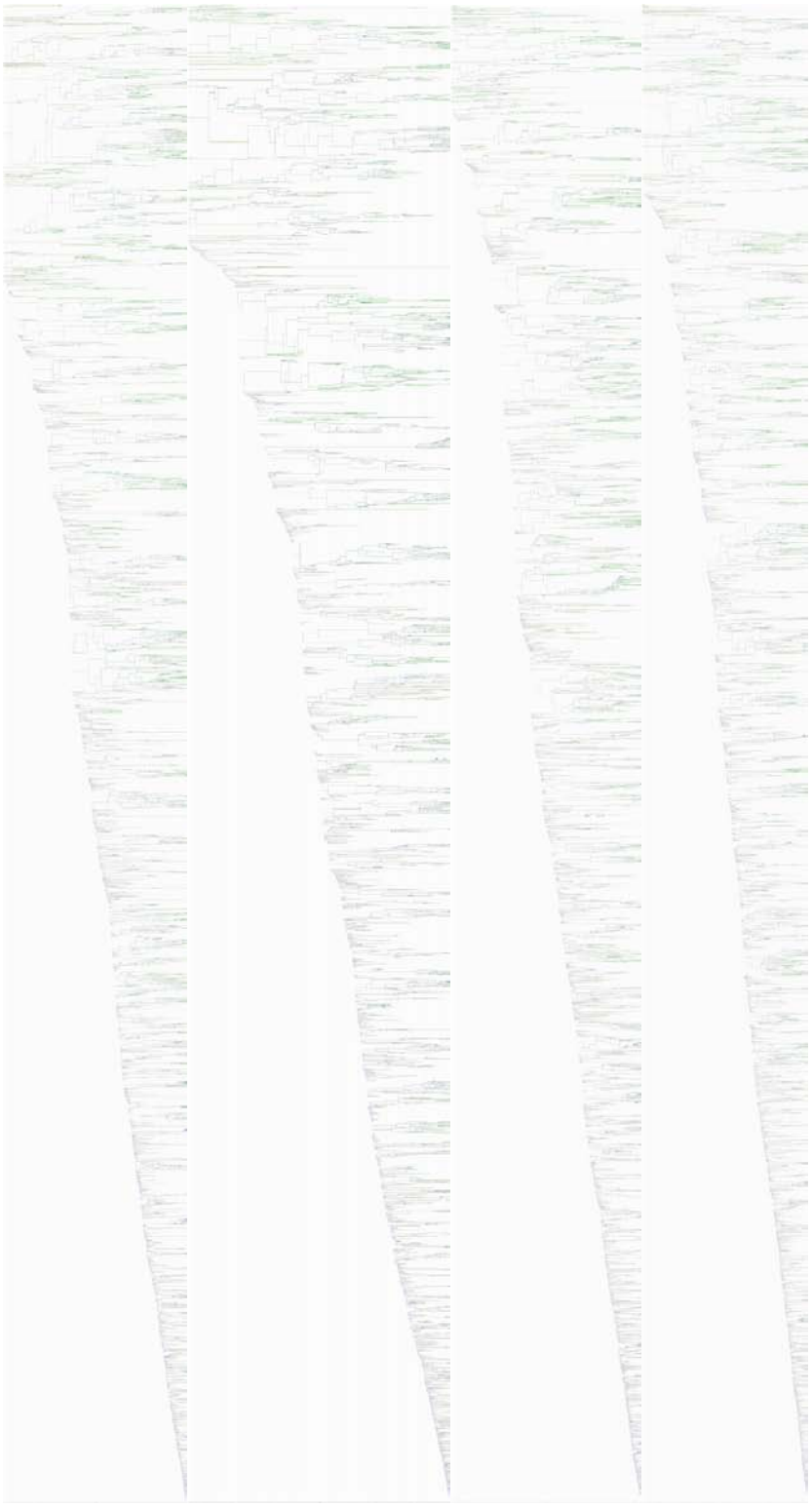

100 ng/mL BMP-2

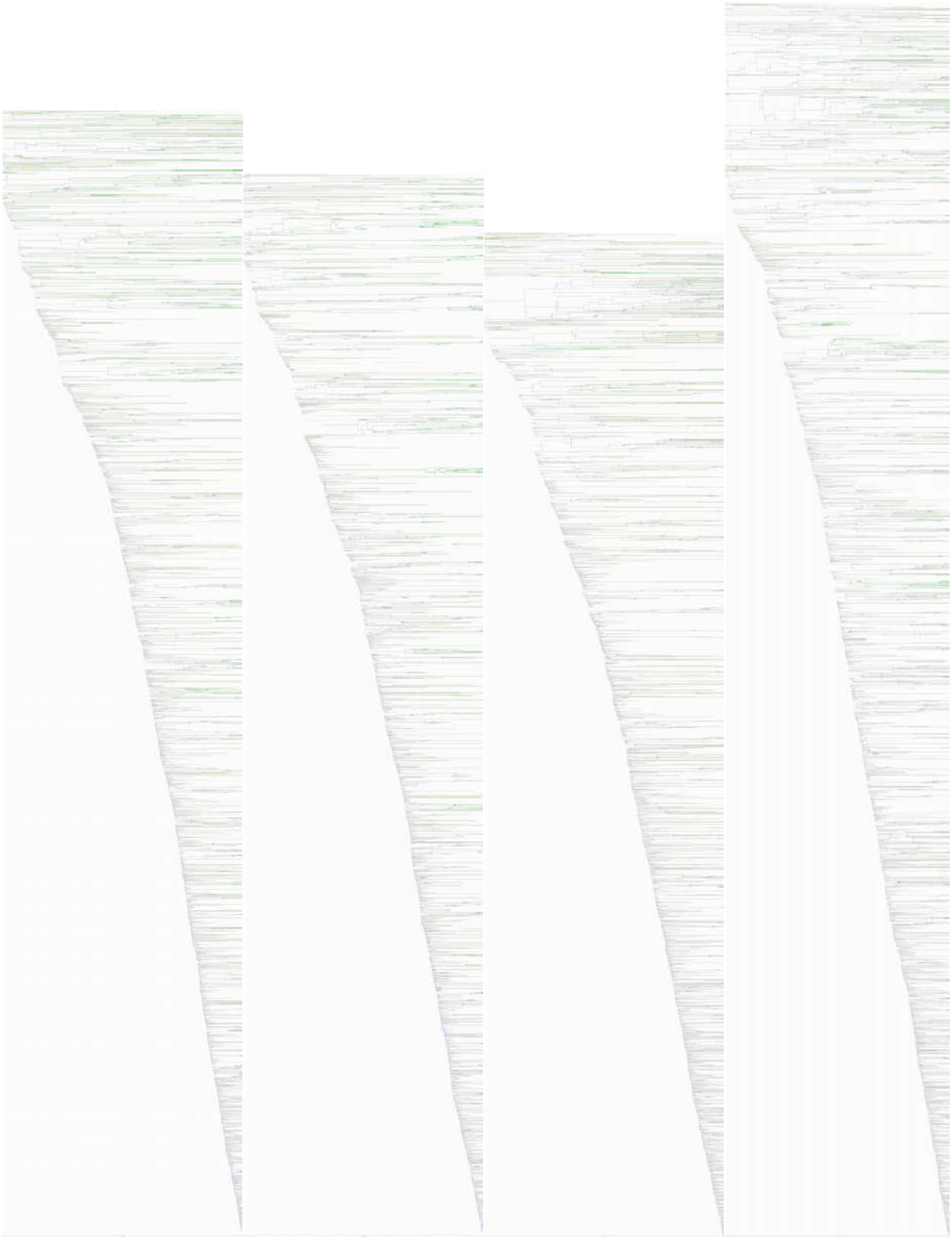

100 ng/mL BMP-2 and 100 ng/mL FGF-2

A2.6.2.3 25th March 2009 Dataset

Control

100 ng/mL FGF-2

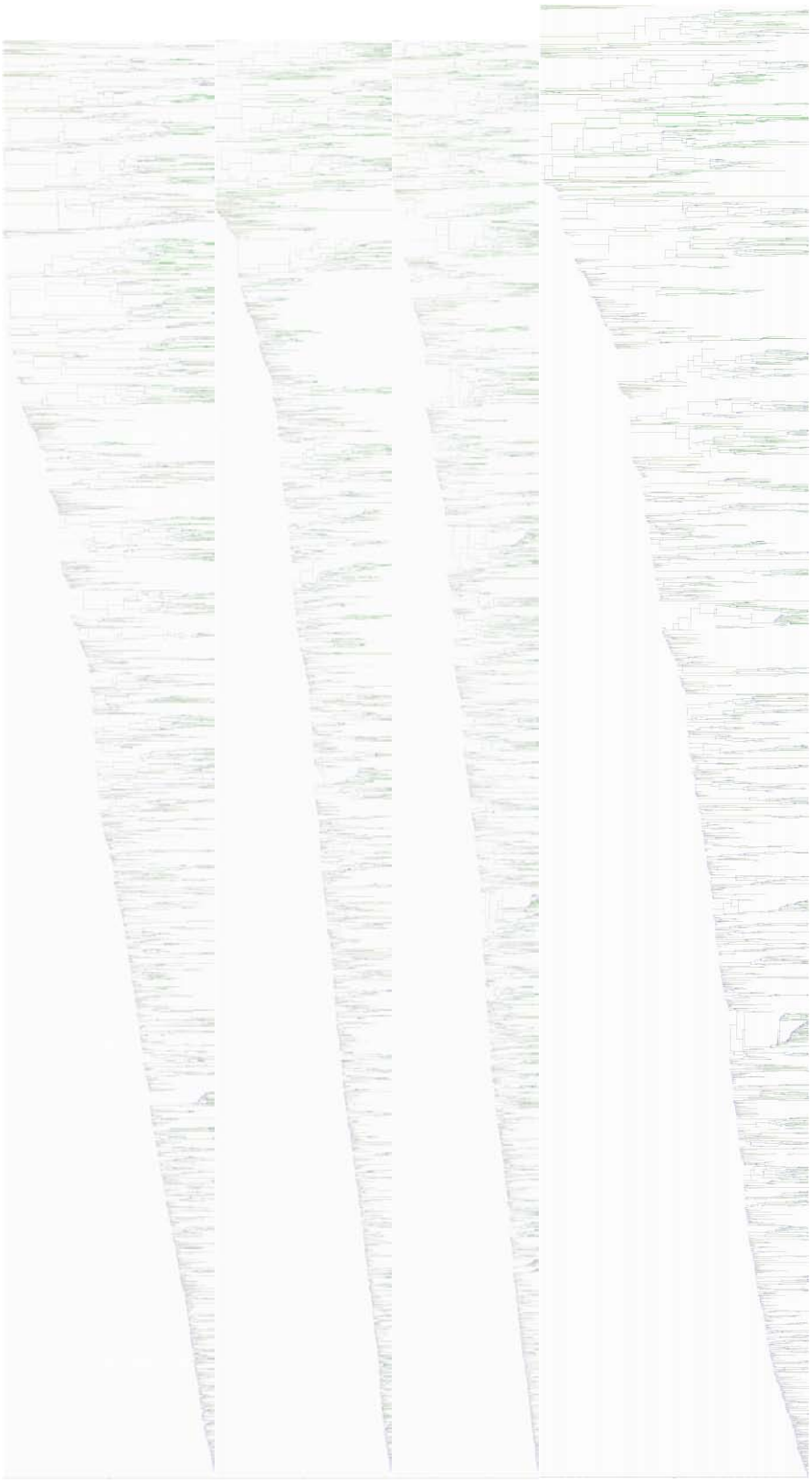

100 ng/mL BMP-2

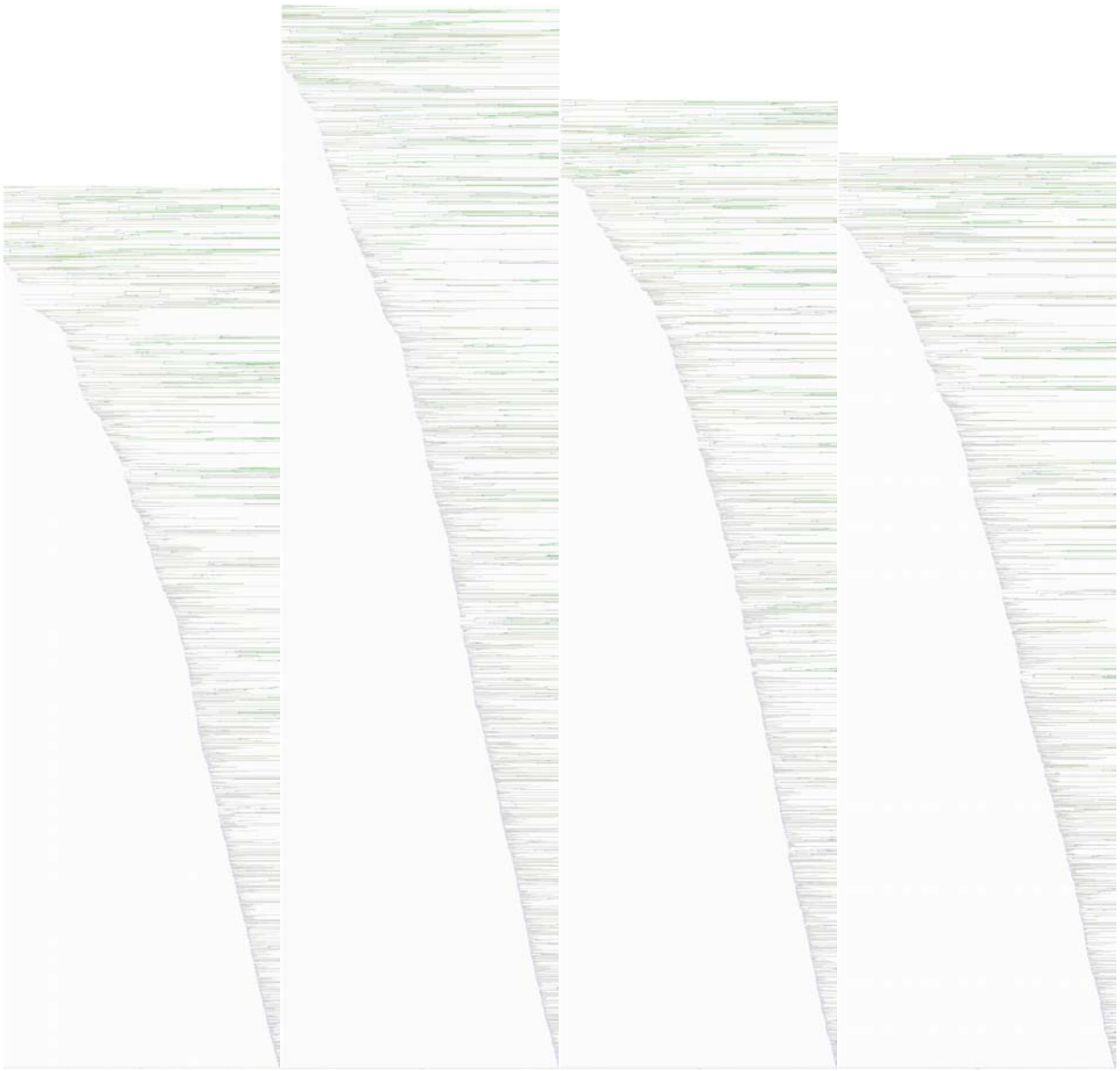

100 ng/mL BMP-2 and 100 ng/mL FGF-2

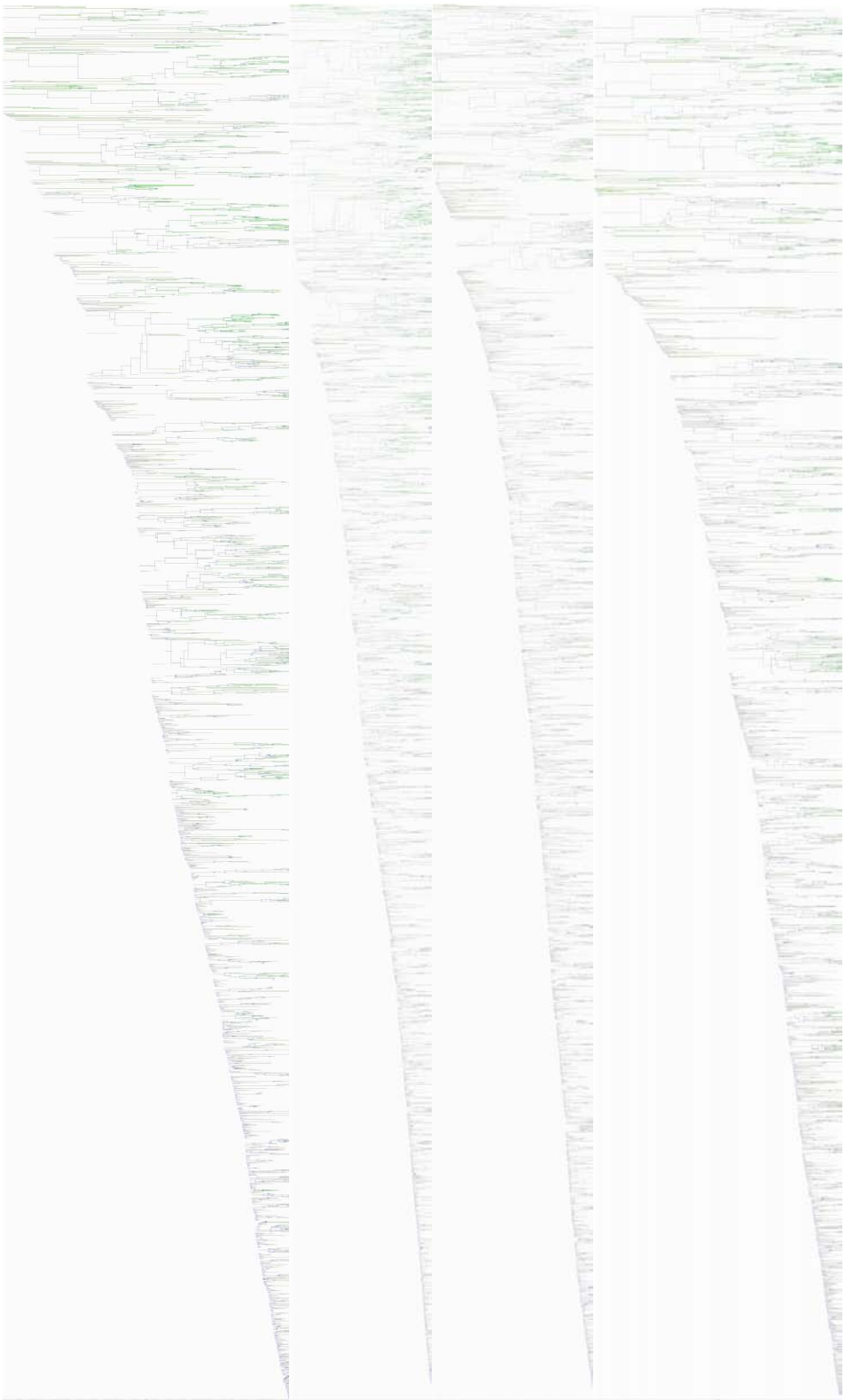

A2.6.3 Computer-Aided Cell Annotations (Red) versus Human-Aided Cell Annotations (Black)

A2.6.3.1 3rd March 2009 Dataset

Control

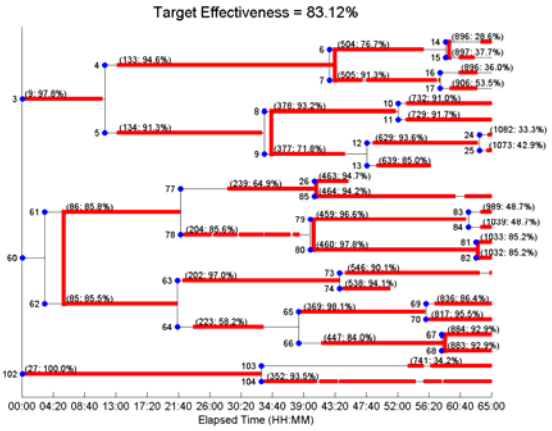

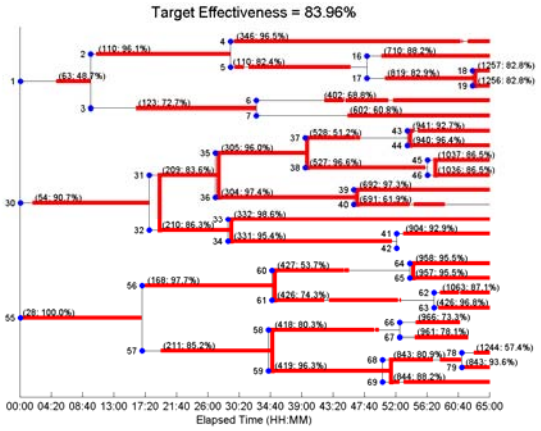

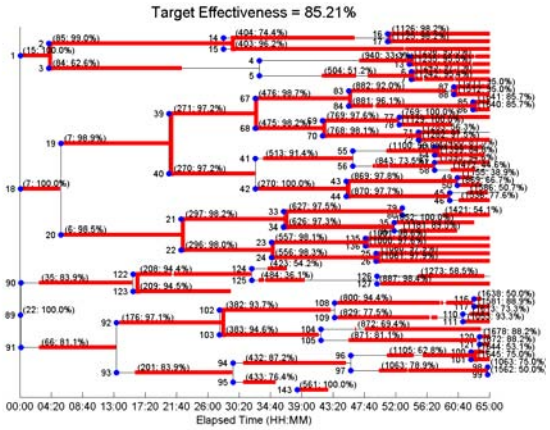

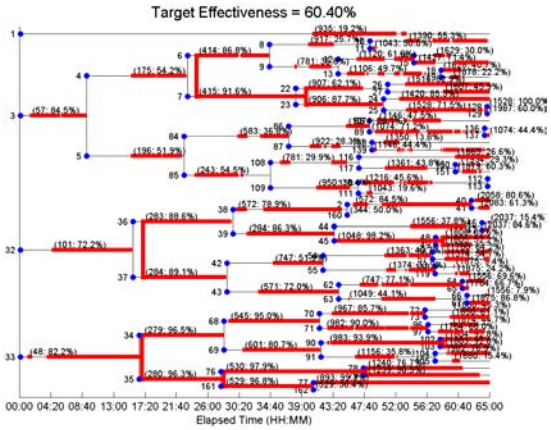

100 ng/mL FGF-2

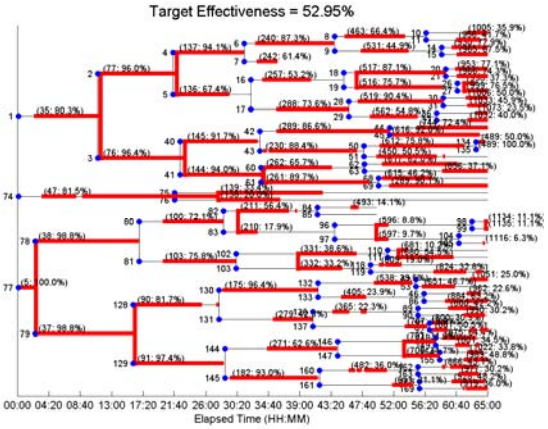

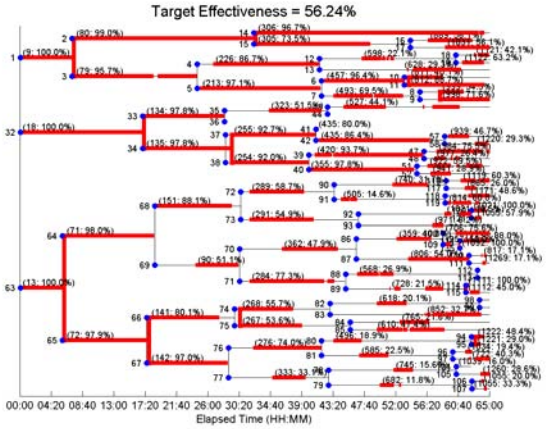

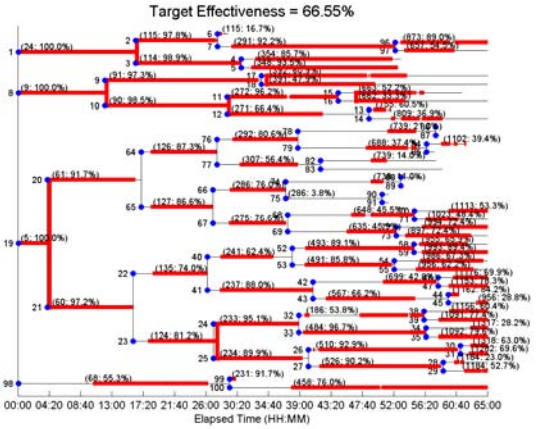

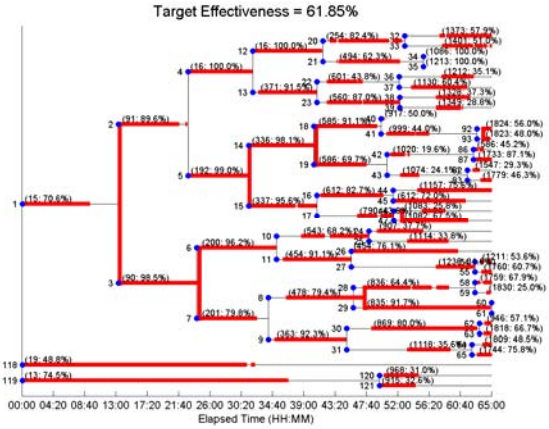

100 ng/mL BMP-2

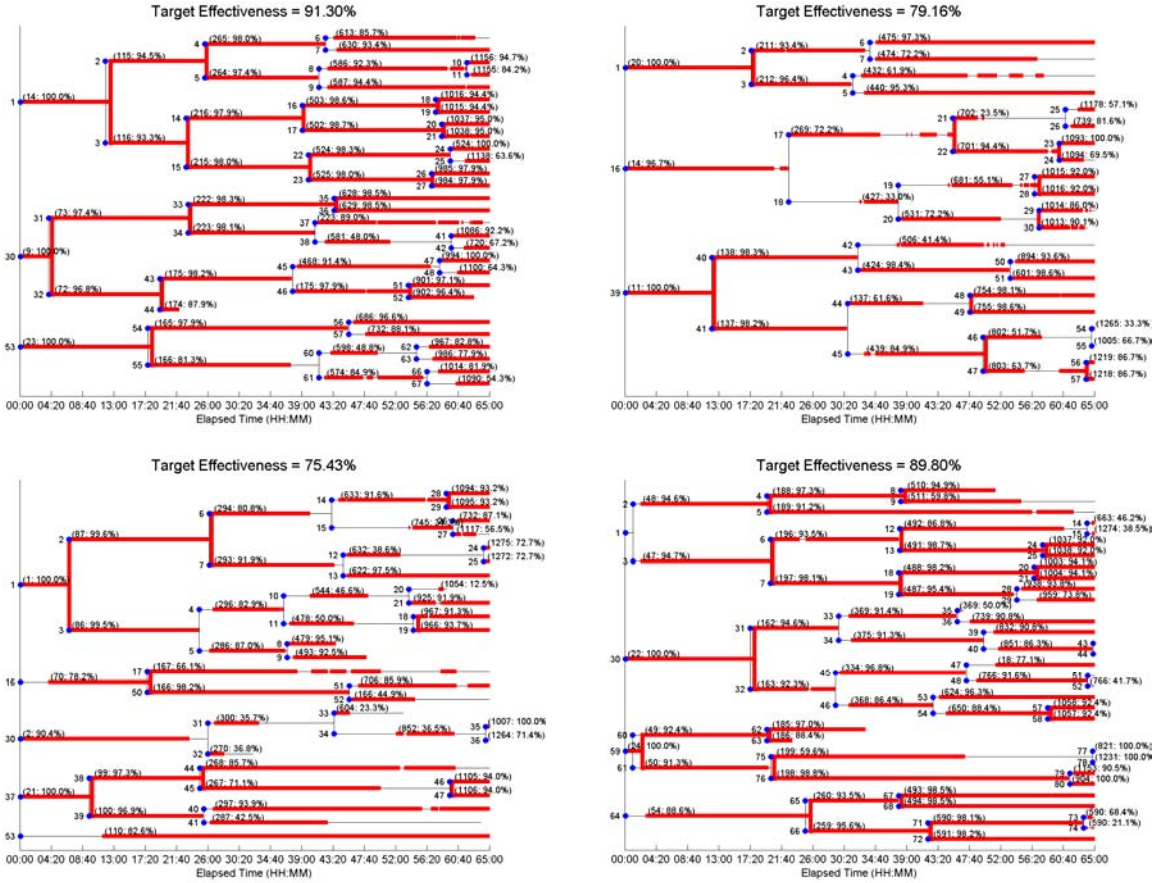

100 ng/mL BMP-2 (Fully annotated up to frame 780)

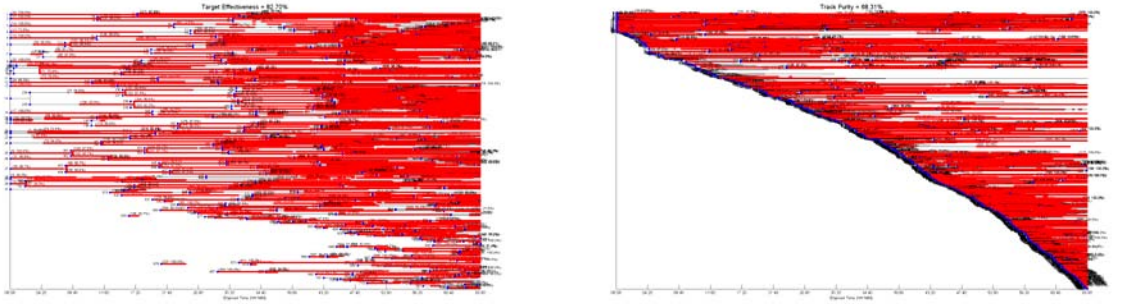

100 ng/mL BMP-2 and 100 ng/mL FGF-2

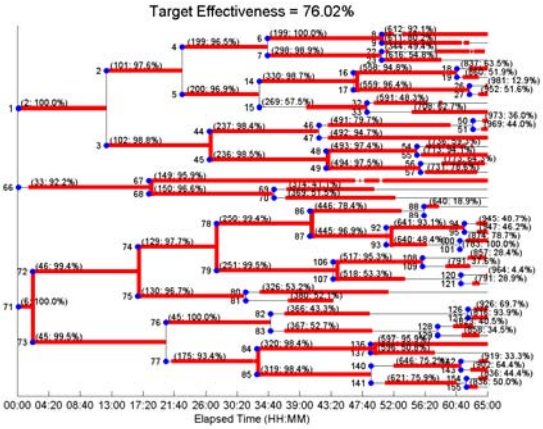

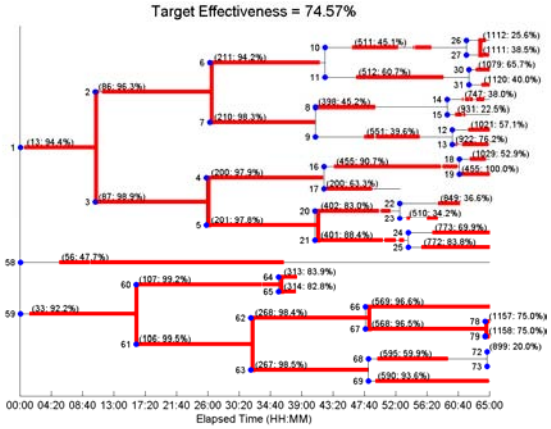

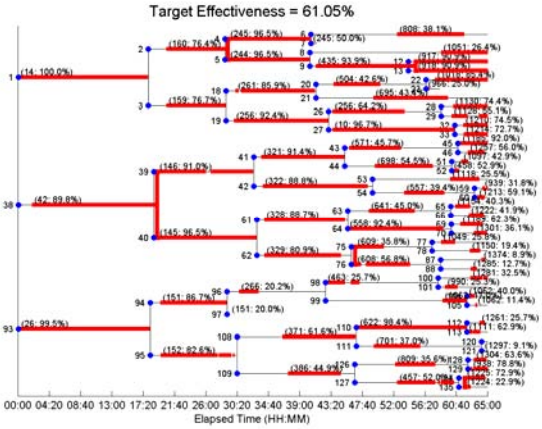

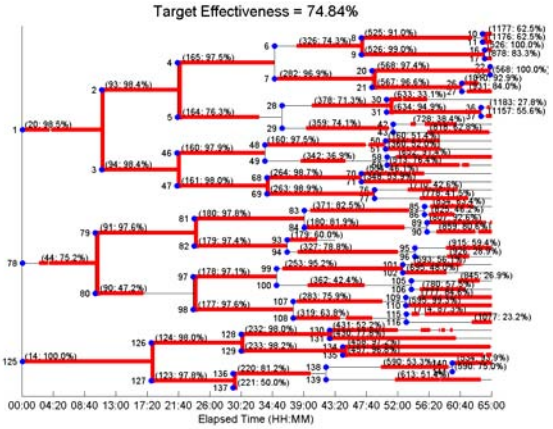

A2.6.3.2 18th March 2009 Dataset

Control

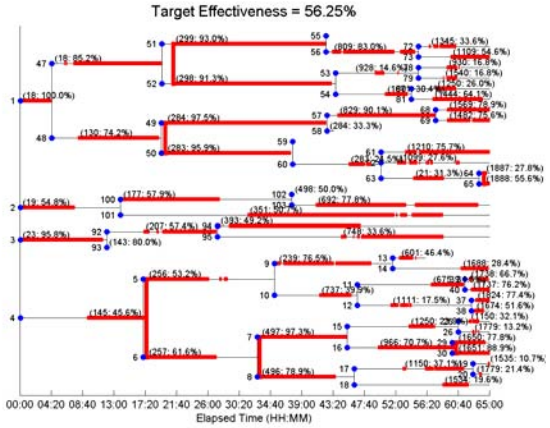

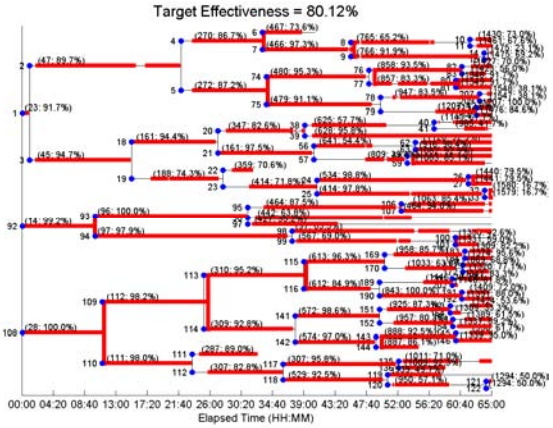

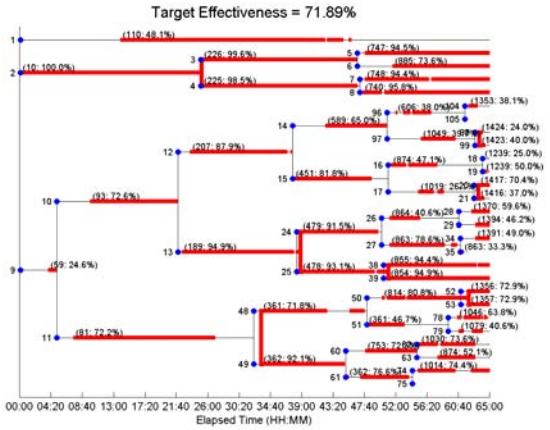

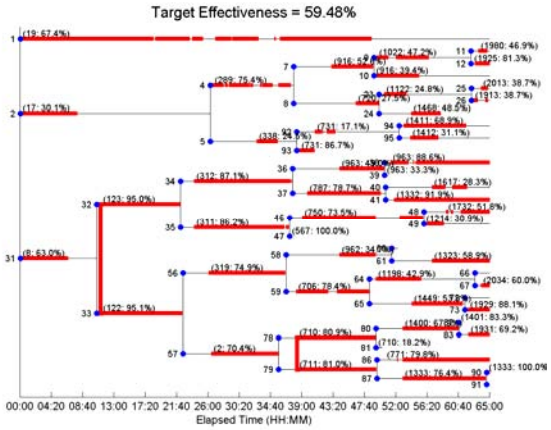

100 ng/mL FGF-2

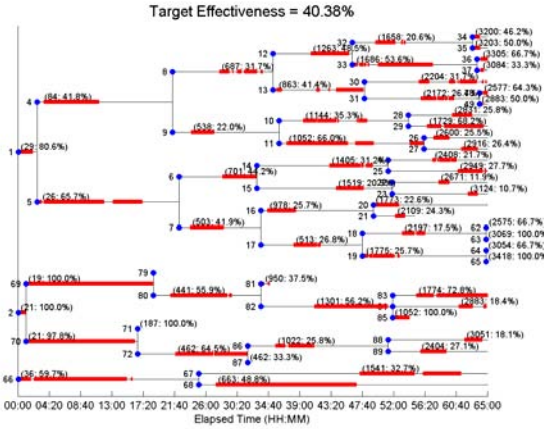

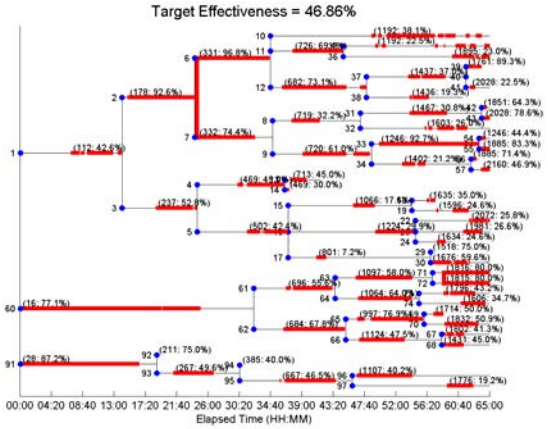

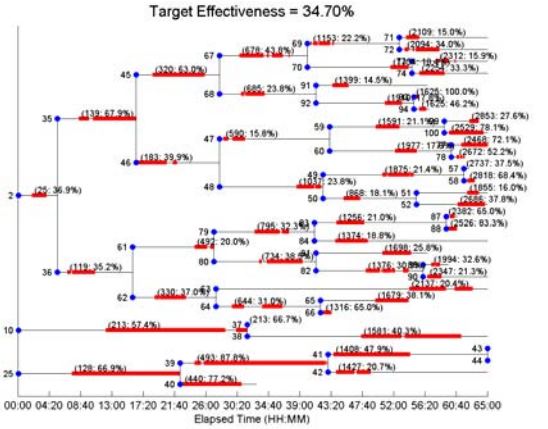

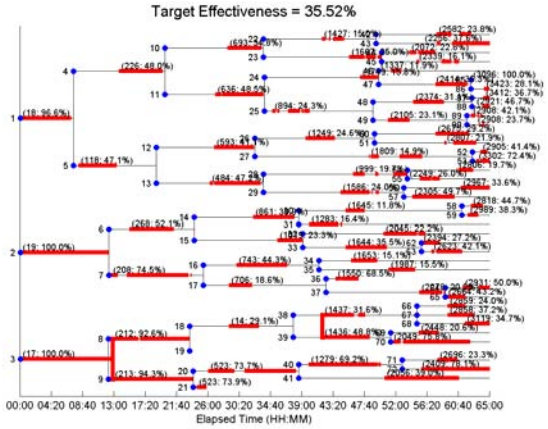

100 ng/mL BMP-2

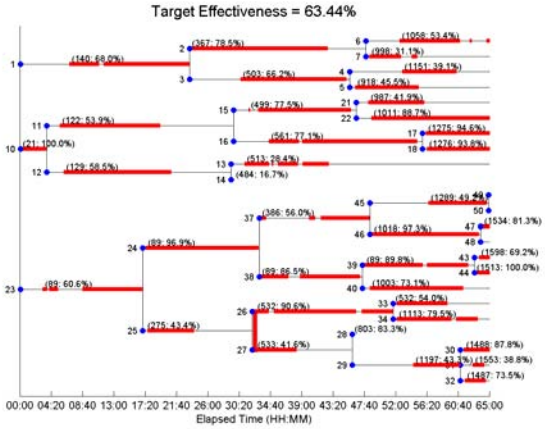

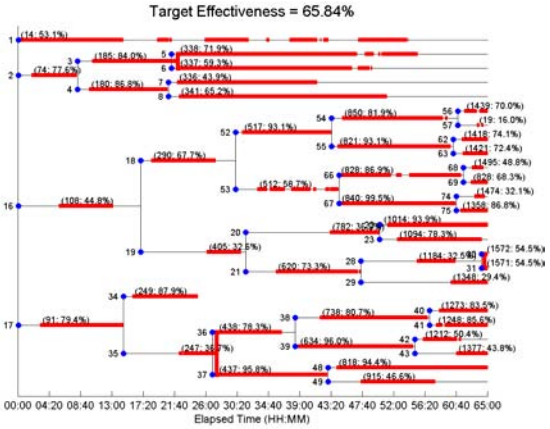

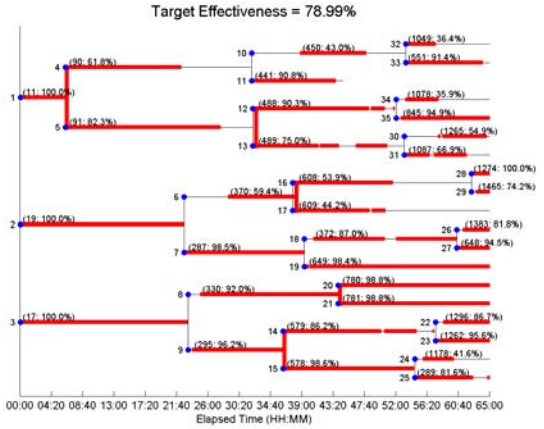

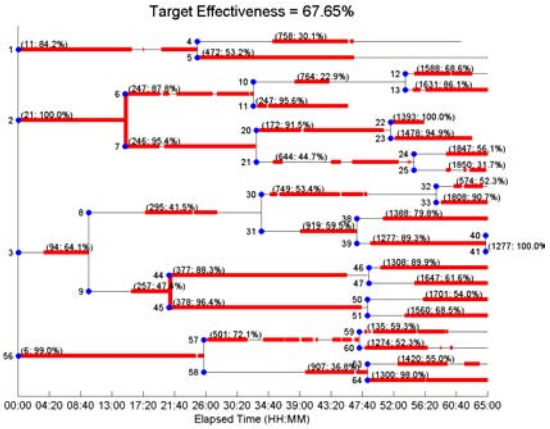

100 ng/mL BMP-2 and 100 ng/mL FGF-2

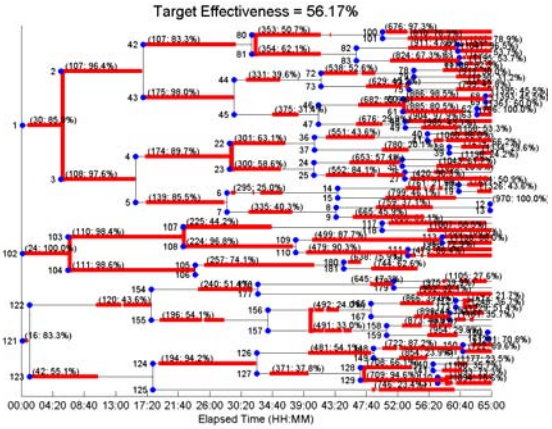

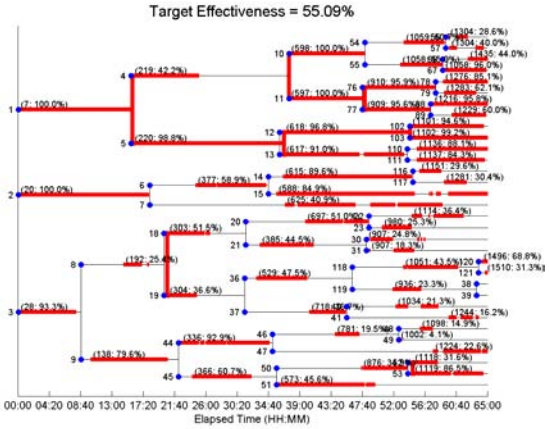

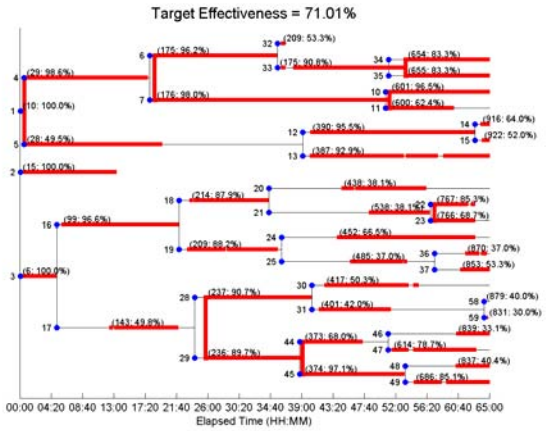

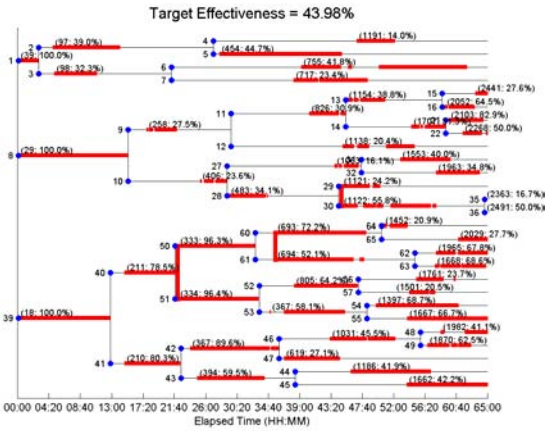

A2.6.3.3 25th March 2009 Dataset

Control

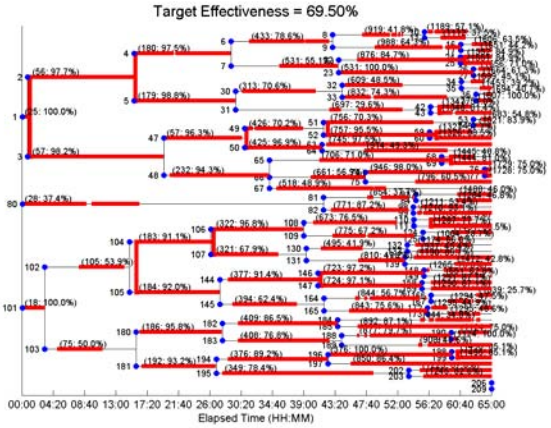

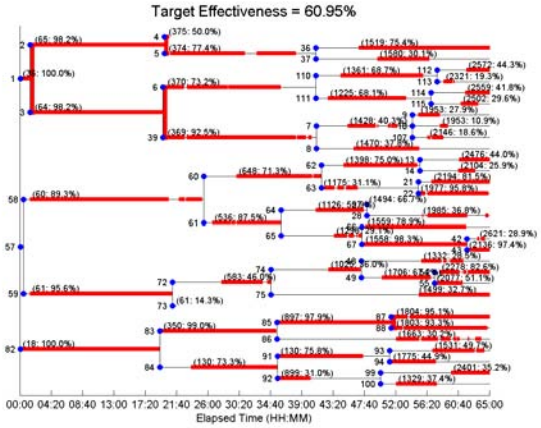

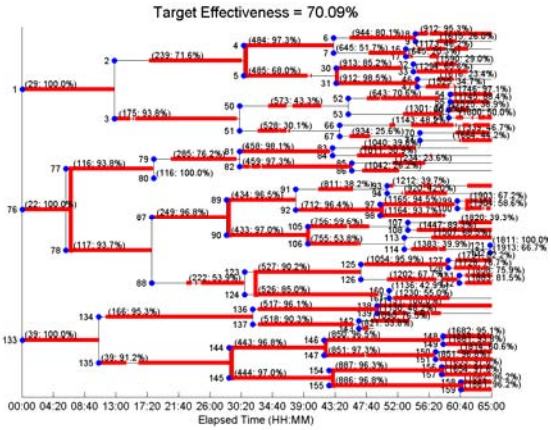

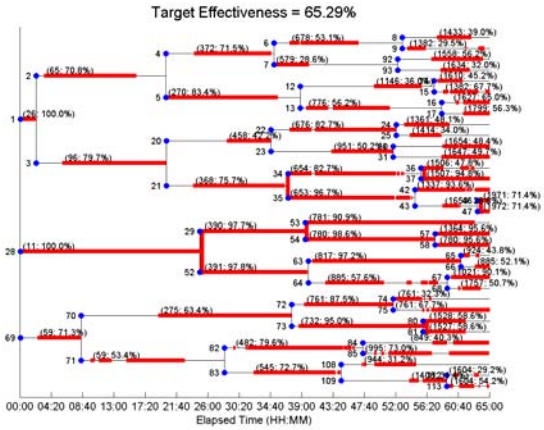

100 ng/mL FGF-2

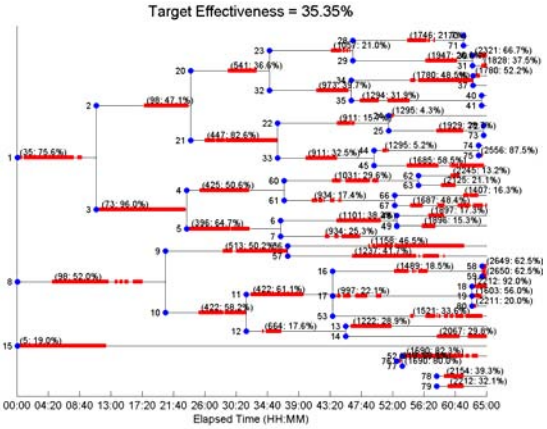

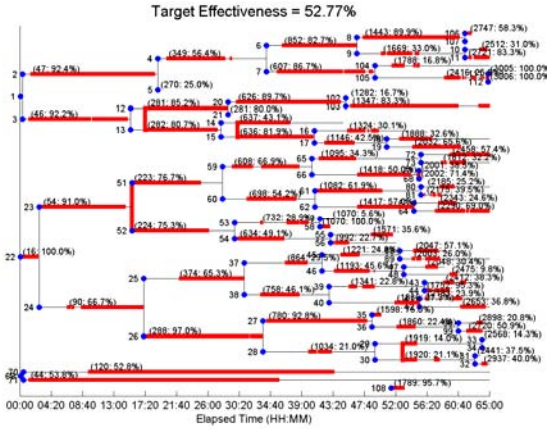

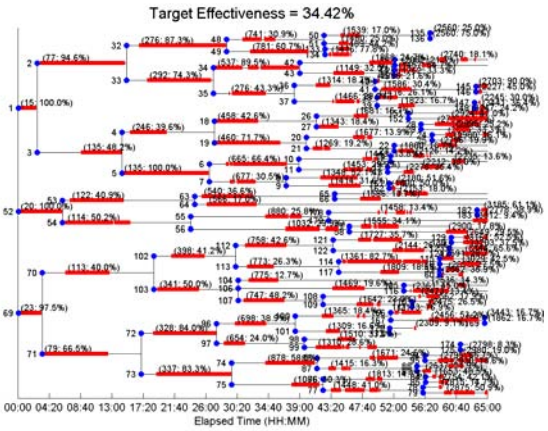

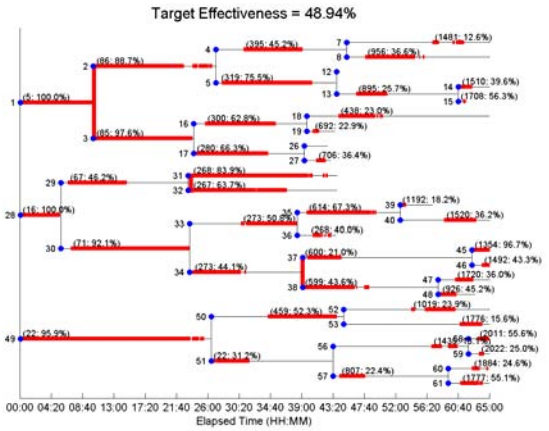

100 ng/mL BMP-2

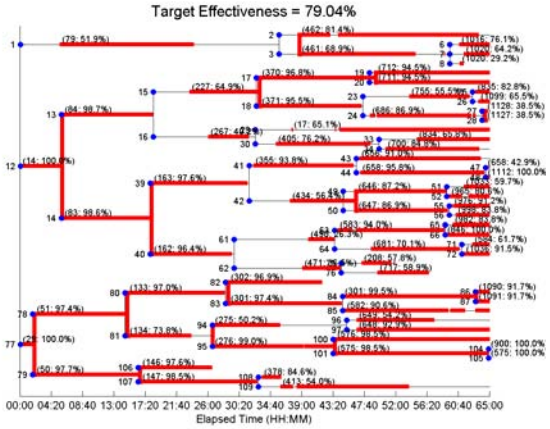

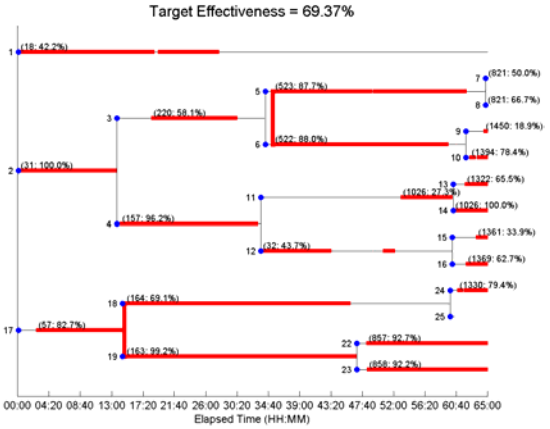

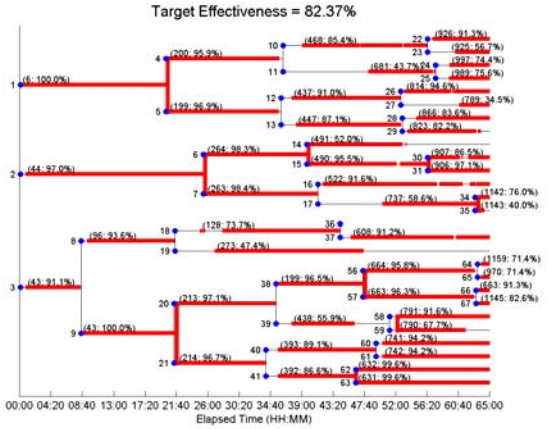

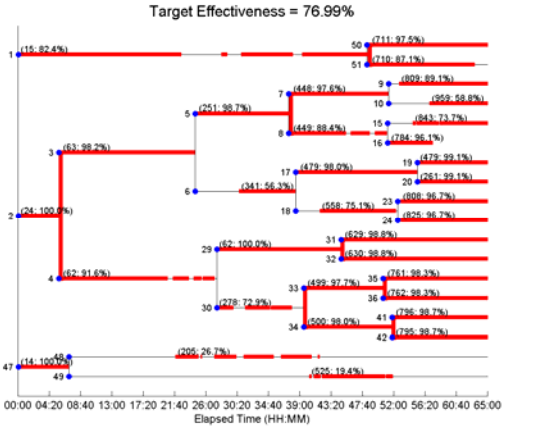

100 ng/mL BMP-2 and 100 ng/mL FGF-2

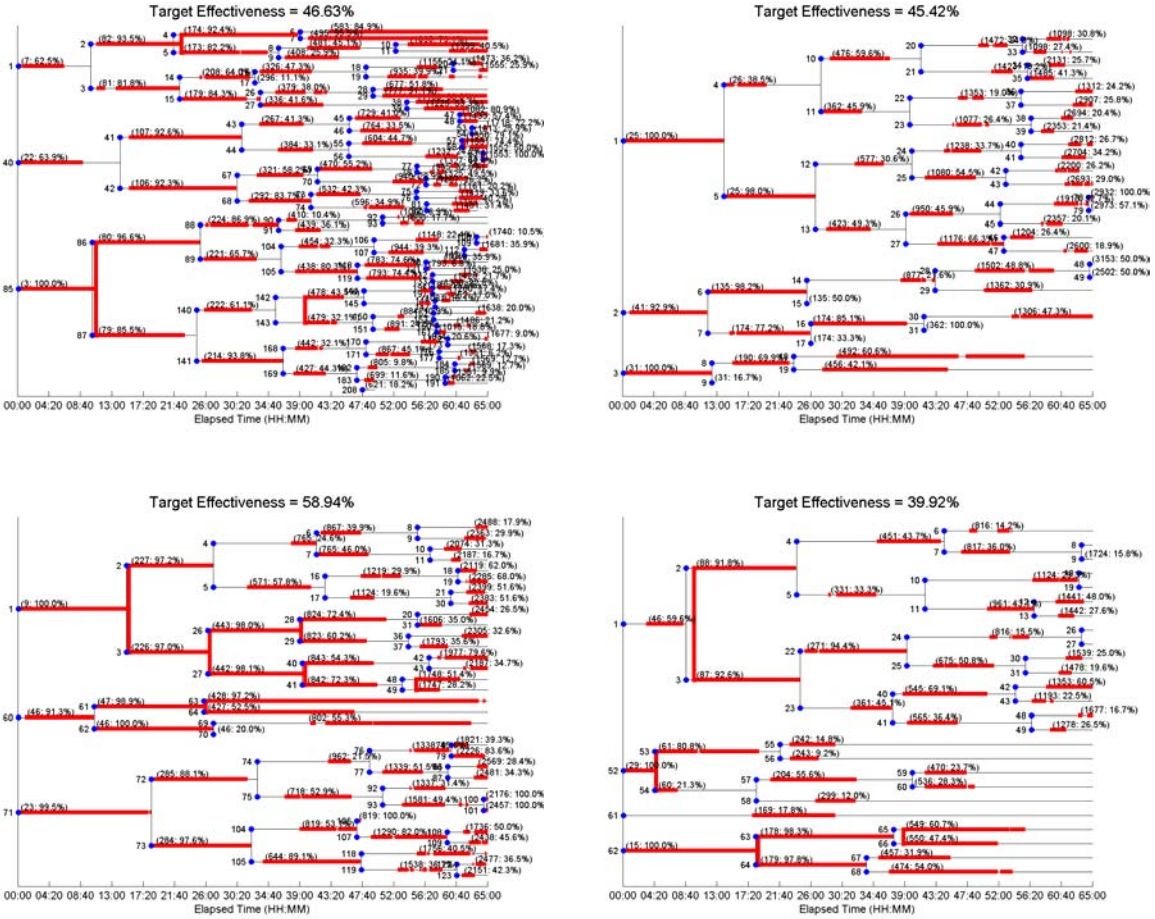

A2.7 ACKNOWLEDGEMENTS

This work was supported by NIH grants RO1EB004343 and RO1EB007369 as well as funding from the Pennsylvania Infrastructure Technology Alliance (PITA). I would like to thank Ryoma Bise, Phil G. Campbell, Karen Lujie Chen, Mei Chen, Artur W. Dubrawski, Sungeun Eom, Casey J. Helfrich, Elvira Osuna-Highley, Seung-il Huh, Soojin Jeong, Takeo Kanade, Steven S. Kang, Peter Yongwen Liang, Anan Liu, Jinyu Liu, Ritchie Nicholson, Jiyan Pan, Corinne Pascale, Sho Sanami, Michael F. Sandbothe, Jeff Schneider, Phu T. Van, Lee E. Weiss, Zhaozheng Yin for helpful discussions and assistance with experiments.

A2.8 REFERENCES

1. Corsi, K.A., et al., *Osteogenic potential of postnatal skeletal muscle-derived stem cells is influenced by donor sex.* J Bone Miner Res, 2007. 22(10): p. 1592-602.
2. Gundry, R.L., P.W. Burridge, and K.R. Boheler, *Pluripotent stem cell heterogeneity and the evolving role of proteomic technologies in stem cell biology.* Proteomics, 2011. 11(20): p. 3947-61.
3. Huang, S., *Non-genetic heterogeneity of cells in development: more than just noise.* Development, 2009. 136(23): p. 3853-62.
4. Lemischka, I.R., D.H. Raulet, and R.C. Mulligan, *Developmental potential and dynamic behavior of hematopoietic stem cells.* Cell, 1986. 45(6): p. 917-27.
5. Schroeder, T., *Long-term single-cell imaging of mammalian stem cells.* Nat Methods, 2011. 8(4 Suppl): p. S30-5.
6. Spiller, D.G., et al., *Measurement of single-cell dynamics.* Nature, 2010. 465(7299): p. 736-45.
7. Yazid, M.D., et al., *Stem cell heterogeneity of mononucleated cells from murine peripheral blood: molecular analysis.* ScientificWorldJournal, 2011. 11: p. 2150-9.
8. Chattwood, A. and C.R. Thompson, *Non-genetic heterogeneity and cell fate choice in Dictyostelium discoideum.* Dev Growth Differ, 2011. 53(4): p. 558-66.
9. Spath, S.S., et al., *Local regulation of growth plate cartilage.* Endocr Dev, 2011. 21: p. 12-22.
10. Campbell, P.G., et al., *Engineered spatial patterns of FGF-2 immobilized on fibrin direct cell organization.* Biomaterials, 2005. 26(33): p. 6762-70.
11. Miller, E.D., et al., *Dose-dependent cell growth in response to concentration modulated patterns of FGF-2 printed on fibrin.* Biomaterials, 2006. 27(10): p. 2213-21.
12. Fuseler, J.W. and M.T. Valarmathi, *Modulation of the migration and differentiation potential of adult bone marrow stromal stem cells by nitric oxide.* Biomaterials, 2012. 33(4): p. 1032-43.
13. Miller, E.D., et al., *Spatially directed guidance of stem cell population migration by immobilized patterns of growth factors.* Biomaterials, 2011. 32(11): p. 2775-85.
14. Cooper, G.M., et al., *Inkjet-Based Biopatterning of BMP-2 to Spatially Control Calvarial Bone Formation.* Tissue Eng Part A, 2010.
15. Ker, E.D., et al., *Engineering spatial control of multiple differentiation fates within a stem cell population.* Biomaterials, 2011. 32(13): p. 3413-22.
16. Ker, E.D., et al., *Bioprinting of growth factors onto aligned sub-micron fibrous scaffolds for simultaneous control of cell differentiation and alignment.* Biomaterials, 2011. 32(32): p. 8097-107.
17. Miller, E.D., et al., *Inkjet printing of growth factor concentration gradients and combinatorial arrays immobilized on biologically-relevant substrates.* Comb Chem High Throughput Screen, 2009. 12(6): p. 604-18.
18. Phillippi, J.A., et al., *Microenvironments engineered by inkjet bioprinting spatially direct adult stem cells toward muscle- and bone-like subpopulations.* Stem Cells, 2008. 26(1): p. 127-34.
19. Hanna, J., et al., *Direct cell reprogramming is a stochastic process amenable to acceleration.* Nature, 2009. 462(7273): p. 595-601.

20. Ker, D.F., et al., *An engineered approach to stem cell culture: automating the decision process for real-time adaptive subculture of stem cells.* PLoS One, 2011. 6(11): p. e27672.
21. Kino-Oka, M., et al., *Automating the expansion process of human skeletal muscle myoblasts with suppression of myotube formation.* Tissue Eng Part C Methods, 2009. 15(4): p. 717-28.
22. Kino-Oka, M. and J.E. Prenosil, *Development of an on-line monitoring system of human keratinocyte growth by image analysis and its application to bioreactor culture.* Biotechnol Bioeng, 2000. 67(2): p. 234-9.
23. Lindgren, K., et al., *Automation of cell line development.* Cytotechnology, 2009. 59(1): p. 1-10.
24. Liu, Y., et al., *Human cell culture process capability: a comparison of manual and automated production.* J Tissue Eng Regen Med, 2010. 4(1): p. 45-54.
25. Narkilahti, S., et al., *Monitoring and analysis of dynamic growth of human embryonic stem cells: comparison of automated instrumentation and conventional culturing methods.* Biomed Eng Online, 2007. 6: p. 11.
26. Sharma, S., et al., *Stem cell culture engineering - process scale up and beyond.* Biotechnol J, 2011.
27. Thomas, R.J., et al., *Automated, scalable culture of human embryonic stem cells in feeder-free conditions.* Biotechnol Bioeng, 2009. 102(6): p. 1636-44.
28. Thomas, R.J., et al., *Manufacture of a human mesenchymal stem cell population using an automated cell culture platform.* Cytotechnology, 2007. 55(1): p. 31-9.
29. Zhao, Y., S.D. Waldman, and L.E. Flynn, *The Effect of Serial Passaging on the Proliferation and Differentiation of Bovine Adipose-Derived Stem Cells.* Cells Tissues Organs, 2011.
30. Qin, J., et al., *A stem cell-based tool for small molecule screening in adipogenesis.* PLoS One, 2010. 5(9): p. e13014.
31. Xu, Y., Y. Shi, and S. Ding, *A chemical approach to stem-cell biology and regenerative medicine.* Nature, 2008. 453(7193): p. 338-44.
32. Barrett, D.M., et al., *Noninvasive bioluminescent imaging of primary patient acute lymphoblastic leukemia: a strategy for preclinical modeling.* Blood, 2011. 118(15): p. e112-7.
33. Saha, K. and J.B. Hurlbut, *Disease modeling using pluripotent stem cells: making sense of disease from bench to bedside.* Swiss Med Wkly, 2011. 141: p. w13144.
34. Parsa, H., R. Upadhyay, and S.K. Sia, *Uncovering the behaviors of individual cells within a multicellular microvascular community.* Proc Natl Acad Sci U S A, 2011. 108(12): p. 5133-8.
35. Smith, Z.D., et al., *Dynamic single-cell imaging of direct reprogramming reveals an early specifying event.* Nat Biotechnol, 2010. 28(5): p. 521-6.
36. Kato, R., et al., *A compact, automated cell culture system for clinical scale cell expansion from primary tissues.* Tissue Eng Part C Methods, 2010. 16(5): p. 947-56.
37. Mason, C. and M. Hoare, *Regenerative medicine bioprocessing: building a conceptual framework based on early studies.* Tissue Eng, 2007. 13(2): p. 301-11.
38. Terstegge, S., et al., *Automated maintenance of embryonic stem cell cultures.* Biotechnol Bioeng, 2007. 96(1): p. 195-201.

39. Veraitch, F.S., et al., *The impact of manual processing on the expansion and directed differentiation of embryonic stem cells.* Biotechnol Bioeng, 2008. 99(5): p. 1216-29.
40. Murphy, D.B., *Fundamentals of Light Microscopy and Electronic Imaging*. 2001: Wiley-Liss Inc. 374.
41. Serganova, I., et al., *Molecular imaging: reporter gene imaging.* Handb Exp Pharmacol, 2008(185 Pt 2): p. 167-223.
42. Wilson, K., et al., *In vitro and in vivo bioluminescence reporter gene imaging of human embryonic stem cells.* J Vis Exp, 2008(14).
43. Sullivan, J.A. and G.L. Mandell, *Motility of human polymorphonuclear neutrophils: microscopic analysis of substrate adhesion and distribution of F-actin.* Cell Motil, 1983. 3(1): p. 31-46.
44. Zaritsky, A., et al., *Cell motility dynamics: a novel segmentation algorithm to quantify multi-cellular bright field microscopy images.* PLoS One, 2011. 6(11): p. e27593.
45. Jiang, R.M., et al., *Live-cell tracking using SIFT features in DIC microscopic videos.* IEEE Trans Biomed Eng, 2010. 57(9): p. 2219-28.
46. Cohen, A.R., et al., *Computational prediction of neural progenitor cell fates.* Nat Methods, 2010. 7(3): p. 213-8.
47. Degerman, J., et al., *An automatic system for in vitro cell migration studies.* J Microsc, 2009. 233(1): p. 178-91.
48. Hand, A.J., et al., *Automated tracking of migrating cells in phase-contrast video microscopy sequences using image registration.* J Microsc, 2009. 234(1): p. 62-79.
49. Li, K., et al., *Cell population tracking and lineage construction with spatiotemporal context.* Med Image Anal, 2008. 12(5): p. 546-66.
50. Rapoport, D.H., et al., *A novel validation algorithm allows for automated cell tracking and the extraction of biologically meaningful parameters.* PLoS One, 2011. 6(11): p. e27315.
51. Cai, W., Y. Zhang, and T.J. Kamp, *Imaging of Induced Pluripotent Stem Cells: From Cellular Reprogramming to Transplantation.* Am J Nucl Med Mol Imaging, 2011. 1(1): p. 18-28.
52. Reagan, M.R. and D.L. Kaplan, *Concise review: Mesenchymal stem cell tumor-homing: detection methods in disease model systems.* Stem Cells, 2011. 29(6): p. 920-7.
53. de Almeida, P.E., J.R. van Rappard, and J.C. Wu, *In vivo bioluminescence for tracking cell fate and function.* Am J Physiol Heart Circ Physiol, 2011. 301(3): p. H663-71.
54. Berman, S.C., et al., *Long-term MR cell tracking of neural stem cells grafted in immunocompetent versus immunodeficient mice reveals distinct differences in contrast between live and dead cells.* Magn Reson Med, 2011. 65(2): p. 564-74.
55. Sutton, E.J., et al., *Cell tracking with optical imaging.* Eur Radiol, 2008. 18(10): p. 2021-32.
56. Meijering, E., et al., *Tracking in Cell and Developmental Biology.* Seminars in Cell and Dev Bio, 2009. 20(8): p. 9.
57. Davis, P.J., et al., *The large-scale digital cell analysis system: an open system for nonperturbing live cell imaging.* J Microsc, 2007. 228(Pt 3): p. 296-308.
58. Eilken, H.M., S. Nishikawa, and T. Schroeder, *Continuous single-cell imaging of blood generation from haemogenic endothelium.* Nature, 2009. 457(7231): p. 896-900.
59. Mosig, A., et al., *Tracking cells in Life Cell Imaging videos using topological alignments.* Algorithms Mol Biol, 2009. 4: p. 10.

60. Ravin, R., et al., *Potency and fate specification in CNS stem cell populations in vitro.* Cell Stem Cell, 2008. 3(6): p. 670-80.
61. Rieger, M.A., et al., *Hematopoietic cytokines can instruct lineage choice.* Science, 2009. 325(5937): p. 217-8.
62. Schnabel, R., et al., *Assessing normal embryogenesis in Caenorhabditis elegans using a 4D microscope: variability of development and regional specification.* Dev Biol, 1997. 184(2): p. 234-65.
63. Shen, H., et al., *Automatic tracking of biological cells and compartments using particle filters and active contours.* Chemometrics and Intelligent Laboratory Systems, 2006. 82(1-2): p. 276-82.
64. Shen, H., et al., *Automated tracking of gene expression in individual cells and cell compartments.* J R Soc Interface, 2006. 3(11): p. 787-94.
65. Bar-Nur, O., et al., *Epigenetic memory and preferential lineage-specific differentiation in induced pluripotent stem cells derived from human pancreatic islet Beta cells.* Cell Stem Cell, 2011. 9(1): p. 17-23.
66. Kim, K., et al., *Epigenetic memory in induced pluripotent stem cells.* Nature, 2010. 467(7313): p. 285-90.
67. Wissing, S., et al., *Reprogramming somatic cells into iPS cells activates LINE-1 retroelement mobility.* Hum Mol Genet, 2012. 21(1): p. 208-18.
68. Bagchi, B., M. Kumar, and S. Mani, *CMV promotor activity during ES cell differentiation: potential insight into embryonic stem cell differentiation.* Cell Biol Int, 2006. 30(6): p. 505-13.
69. Cara, A., E. Lucarelli, and P. Cornaglia-Ferraris, *Engineering viral promoters for gene transfer to human neuroblasts.* Cell Mol Neurobiol, 2000. 20(3): p. 409-15.
70. PerkinElmer, *Volocity*. 2011.
71. BitPlane, *Imaris*. 2011.
72. Collins, T.J., *ImageJ for microscopy.* Biotechniques, 2007. 43(1 Suppl): p. 25-30.
73. Lamprecht, M.R., D.M. Sabatini, and A.E. Carpenter, *CellProfiler: free, versatile software for automated biological image analysis.* Biotechniques, 2007. 42(1): p. 71-5.
74. Shen, H., et al., *CellTracker*. 2006.
75. Huth, J., J.M. Kraus, and H.A. Kestler, *Timelapse Analyzer*. 2010.
76. Kanade, T., et al. *Cell Image Analysis: Algorithms, Systems and Applications*. in *IEEE Workshop on Applications of Computer Vision*. 2011. Kona, Hawaii.
77. Sacan, A., H. Ferhatosmanoglu, and H. Coskun, *CellTrack: an open-source software for cell tracking and motility analysis.* Bioinformatics, 2008. 24(14): p. 1647-9.
78. Stroustrup, B., *The C++ Programming Language*. 3rd ed. 1997.
79. Yin, Z., et al., *Understanding the optics to aid microscopy image segmentation.* Med Image Comput Comput Assist Interv, 2010. 13(Pt 1): p. 209-17.
80. Huh, S., et al., *Automated mitosis detection of stem cell populations in phase-contrast microscopy images.* IEEE Trans Med Imaging, 2011. 30(3): p. 586-96.
81. Manning, C.D., P. Raghavan, and H. Schutze, *Introduction to Information Retrieval*. 2008: Cambridge University Press.
82. Bise, R., Z. Yin, and T. Kanade, *Reliable Cell Tracking By Global Data Association*, in *IEEE International Symposium on Biomedical Imaging*. 2011: Chicaogo, USA.
83. Blackman, S., *Multiple-Target Tracking with Radar Applications*. 1986: Artech House Publishers.

84. Zhang, J. and J.H. Wang, *BMP-2 mediates PGE(2) -induced reduction of proliferation and osteogenic differentiation of human tendon stem cells.* J Orthop Res, 2012. 30(1): p. 47-52.

APPENDIX A3: AUTOMATED MITOSIS DETECTION OF STEM CELL POPULATIONS IN PHASE-CONTRAST MICROSCOPY IMAGES

Based on published work:

Automated Mitosis Detection of Stem Cell Populations in Phase-Contrast Microscopy Images

Seung-il Huh, Dai Fei Elmer Ker, Ryoma Bise, Mei Chen, Takeo Kanade

IEEE Transactions on Medical Imaging. 2011 March; **30** (3) 586-596.

A3.1 RELEVANCE TO THESIS

Automated tracking of cells in phase-contrast time-lapse microscopy imaging offers a powerful and versatile tool for studying the cellular microenvironment via *in vitro* characterization of cell behavior. In this section, Seung-il Huh, a graduate student at the Robotics Institute devised a method for detecting cell division in phase-contrast time-lapse microscopy images independent of cell detection and cell tracking performance. This algorithm was based on machine learning methodologies and mitosis events were detected on the basis of image features such as local regions of high image intensity (brightness), which are often correlated with mitosis events. This algorithm precisely detects the spatial and temporal occurrence of cytokinesis and contributes towards accurate cell tracking by determining when a single cell has divided into two daughter cells.

Automated Mitosis Detection of Stem Cell Populations in Phase-Contrast Microscopy Images

Seungil Huh*, Dai Fei Elmer Ker, Ryoma Bise, Mei Chen, and Takeo Kanade

***Abstract*—Due to the enormous potential and impact that stem cells may have on regenerative medicine, there has been a rapidly growing interest for tools to analyze and characterize the behaviors of these cells *in vitro* in an automated and high throughput fashion. Among these behaviors, mitosis, or cell division, is important since stem cells proliferate and renew themselves through mitosis. However, current automated systems for measuring cell proliferation often require destructive or sacrificial methods of cell manipulation such as cell lysis or *in vitro* staining. In this paper, we propose an effective approach for automated mitosis detection using phase-contrast time-lapse microscopy, which is a nondestructive imaging modality, thereby allowing continuous monitoring of cells in culture. In our approach, we present a probabilistic model for event detection, which can simultaneously 1) identify spatio-temporal patch sequences that contain a mitotic event and 2) localize a birth event, defined as the time and location at which cell division is completed and two daughter cells are born. Our approach significantly outperforms previous approaches in terms of both detection accuracy and computational efficiency, when applied to multipotent C3H10T1/2 mesenchymal and C2C12 myoblastic stem cell populations.**

***Index Terms*—Event detection modeling, mitosis detection, phase-contrast microscopy image analysis, sequential image analysis.**

I. Introduction

STEM cell research has attracted increasing attention due to its enormous potential in regenerative medicine for replacing damaged or diseased tissues or organs. Methods for assessing the proliferative activity of stem cells grown *in vitro* are critical tools for monitoring the health and growth rate of a cell population. Such methods have historically relied on detecting mitosis [1], which is the process whereby the genetic material of a eukaryotic cell is equally distributed between its descendants through nuclear division, resulting in the birth of daughter cells. Presently, many cell proliferation assays that are compatible with automated sample handling and high-throughput screening have been developed to measure cell proliferation [2]. However, the majority of these procedures utilize fluorescent, luminescent or colorimetric assays which may require destructive methods of cell manipulation, such as cell lysis and *in vitro* staining, and do not allow for continuous monitoring of cells in culture.

Since phase-contrast microscopy is a form of nondestructive imaging, automated time-lapse systems employing this imaging modality for monitoring and analyzing cell populations *in vitro* have enormous potential for cell biology and stem cell engineering [3]–[6]. Such systems not only enable high-throughput analysis of time-lapse microscopy images, but also facilitate continuous monitoring of live and intact cells for studying biological phenomena and quantifying various cell responses. Moreover, since samples are continuously monitored, sampling at various time points is abrogated, resulting in reduced human labor and eliminating the costs of expensive reagents required for cell lysis or *in vitro* staining. Within the context of such microscopy systems, automated detection of mitosis can provide quantitative information regarding cell proliferation on a continuous basis. This functionality is also expected to improve automated cell tracking systems, a comprehensive tool for the analysis of cell behavior [5], [7], [8].

In order to achieve these benefits, automated mitosis detection systems are required to localize *birth events*; we define a birth event in each mitotic event as the time and location at which the two daughter cells first appear and the boundary between the two is clearly observed. Accurate detection of birth events facilitate the quantification of biological metrics, such as the mitotic index and synchrony, allowing biologists to experimentally assess how altering the conditions under which cells are cultured can impact population growth. In addition, birth event information is helpful in determining when and where a trajectory of a mother cell branches into two trajectories of its daughter cells in cell tracking. Furthermore, precise localization of birth events may aid in the discovery and characterization of novel biological phenomenon that occur at rare frequencies such as a single cell division event giving rise to more than two daughter cells.

Several mitosis detection methods for phase-contrast time-lapse microscopy images have been proposed based on cell tracking. Yang *et al.* [7] obtained blob regions along each cell's trajectory produced by a tracking method. Each blob region is then examined to determine if it contains a mitotic event based on several blob properties, including area, perimeter, circularity, and average intensity. Debeir *et al.* [9] adopted a combination of several mean-shift-processes to track

Manuscript received September 09, 2010; revised October 13, 2010; accepted October 14, 2010. Date of publication October 21, 2010; date of current version March 02, 2011. This work was supported in part by the National Institutes of Health under Grant RO1EB004343 and Grant RO1EB007369, and in part by the Pennsylvania Infrastructure Technology Alliance (PITA). The work of S. Huh was supported by a Samsung Fellowship. *Asterisk indicates corresponding author.*

*S. Huh is with Robotics Institute, Carnegie Mellon University, Pittsburgh, PA 15213 USA (e-mail: seungilh@cs.cmu.edu).

R. Bise and T. Kanade are with Robotics Institute, Carnegie Mellon University, Pittsburgh, PA 15213 USA.

D. F. E. Ker is with the Department of Biological Sciences and Biomedical Engineering, Carnegie Mellon University, Pittsburgh, PA 15213 USA.

M. Chen is with Intel Labs Pittsburgh, Pittsburgh, PA 15213 USA.

Color versions of one or more of the figures in this paper are available online at http://ieeexplore.ieee.org.

Digital Object Identifier 10.1109/TMI.2010.2089384

cells using an ensemble of nested kernels. One of the kernels was designed to model cells in the mitotic state by taking into account their morphological changes. Al-Kofahi *et al.* [10] presented a multiple-object matching method that can handle cell divisions in the typical frame-by-frame segmentation tracking method. Padfield *et al.* [11] investigated cell cycle phases through tracking each nucleus over time. Mitotic events were then identified by linking nonmitotic phases using both the Euclidean distance metric and the fast marching method. These approaches are intuitive but limited in that mitosis detection is dependent on tracking performance, which is generally more challenging to achieve than mitosis detection performance itself. Several mitosis detection algorithms that do not involve cell tracking have recently been proposed. Li *et al.* [5] applied a fast cascade learning framework [13] adopting AdaBoost classifiers [14] to volumetric Haar-like features extracted from spatio-temporal patches covering the whole image region. This approach requires a large number of training samples and searches through the entire space due to the lack of explicit candidate detection. Debeir *et al.* [12] proposed a method to detect mitotic cell regions based on brightness change and link the regions in consecutive frames into a cell division candidate linkage. Each candidate was then validated based on its length (the number of frames). This approach is efficient due to the reduced search space by the candidate detection, but the validation scheme is too simple to effectively distinguish actual mitotic events from the other candidates.

More recently, Liu *et al.* [15] proposed an approach to compensate for the drawbacks of the previous methods. After mitosis candidate patch sequences are constructed through 3-D seeded region growing, Hidden Conditional Random Fields (HCRF) [16] are trained to examine each of the candidates. This approach does not resort to tracking and adopts explicit candidate detection as well as model-based validation, achieving good performance on C3H10T1/2 stem cell populations. However, this work does not detect birth events and is as such limited in that its mitosis detection results may not be sufficient for accurate quantitative analysis of cell proliferation or cell tracking. In fact, the HCRF model is intrinsically not capable of modeling birth events. In addition to inadequate modeling power, this approach is computationally expensive due to the preconditioning step [17], which was originally devised to segment nonmitotic cell regions from background rather than mitotic cell regions.

In this paper, we propose an effective mitosis detection approach that explicitly detects birth events. We developed a probabilistic model that not only determines whether a mitotic event occurs, but also provides the time at which the mitosis is completed and daughter cells are born. By additionally handling the information of cell birth, EDCRF achieves higher discriminating power than HCRF in the identification of mitosis occurrence. In addition, EDCRF is superior to possible alternatives based on HCRF in the temporal localization of birth events as well. We conducted experiments on multipotent C3H10T1/2 mesenchymal and C2C12 myoblastic stem cell populations, and achieved good performance on the population with high confluency. Furthermore, we bypassed the time-consuming preconditioning without sacrificing performance; as a result, computational efficiency is significantly improved compared to the previous work [15].

The remainder of this paper is organized as follows. We introduce the overall process of our approach and describe the details of the image processing part in Section II. We then formulate a probabilistic model to determine mitosis occurrence and birth event timing in Section III. The experimental setup and results with discussions are presented in Sections IV and V, followed by conclusions in Section VI.

II. Approach

Given a sequence of phase-contrast microscopy images, our goal is to detect mitosis in the sequence and localize a birth event during mitosis. To achieve this goal, we adopt the idea of candidate patch sequence construction from the previous work [12] and form a process comprising three steps: candidate patch sequence construction, visual feature extraction, and identification of mitosis occurrence/temporal localization of birth event. We sketch each step to provide an overall view of our approach. The detailed methods will be subsequently described in this and the following sections.

- *Candidate patch sequence construction*: The goal of this step is to detect all spatio-temporal patch sequences that contain mitosis, while detecting as small a number of sequences not containing mitosis as possible. Through this step, mitotic events are spatially localized and the search space is significantly reduced from entire image sequences to candidate patch sequences. As a result, the subsequent steps can be more efficiently conducted, while maintaining mitosis detection accuracy. Fig. 1 shows some examples of candidate patch sequences our method automatically extracted.
- *Visual feature extraction*: Visual features are extracted from each patch of candidate patch sequences based on the characteristics of phase-contrast microscopy images.
- *Identification of mitosis occurrence/Temporal localization of birth event*: For each candidate patch sequence, we perform two decision tasks regarding mitosis occurrence and birth event. The identification of mitosis occurrence determines whether each candidate patch sequence contains a mitosis, specifically, a birth event. For each patch sequence determined to contain a birth event, the temporal localization of the birth event decides which patch contains the birth event in the patch sequence.

A. Candidate Patch Sequence Construction

For preprocessing, we compute the average image of all images in a given sequence; the average image is then subtracted from each image. By this simple procedure, stationary bright artifacts which may be misrecognized as mitosis cell candidates are removed. In addition, intrinsic illumination variation in phase-contrast microscopy images can be corrected.

For each image, candidate patches are first extracted based on brightness (pixel intensity); it is known that the process of mitosis typically exhibits a series of distinctive cell features including increased brightness, increased circularity, and decreased size [5] (see Fig. 2). Each preprocessed image is convolved with a small-sized $d \times d$ rectangular average filter and

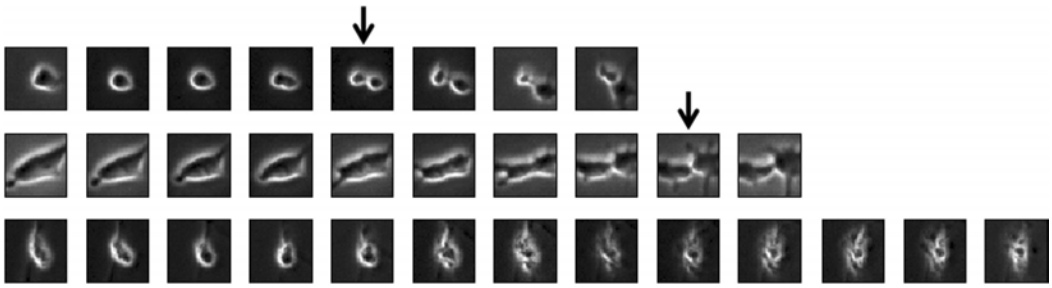

Fig. 1. Positive (top two) and negative (bottom) candidate patch sequences extracted from a multipotent C3H10T1/2 mesenchymal stem cell population. The numbers of patches in candidate patch sequences are varied. The arrows indicate the frames containing manually annotated birth events, the location and time in which daughter cells are born. The end of the mitotic phase involves cytokinesis, which is the pinching of the cell membrane to split a cell into two, typically shown as a figure eight shape as in the first sequence; however, a figure eight shape is often not clearly observed as in the second sequence. The last sequence contains apoptosis, or cell death, which exhibits similar visual characteristics to mitosis in the beginning of the process. Due to the increased brightness, apoptotic events are mostly captured in candidate patch sequences. These sequences are extracted from frames 86 through 93 (top), 350 through 359 (center), and 819 through 831 (bottom) among the entire sequence consisting of 1436 frames.

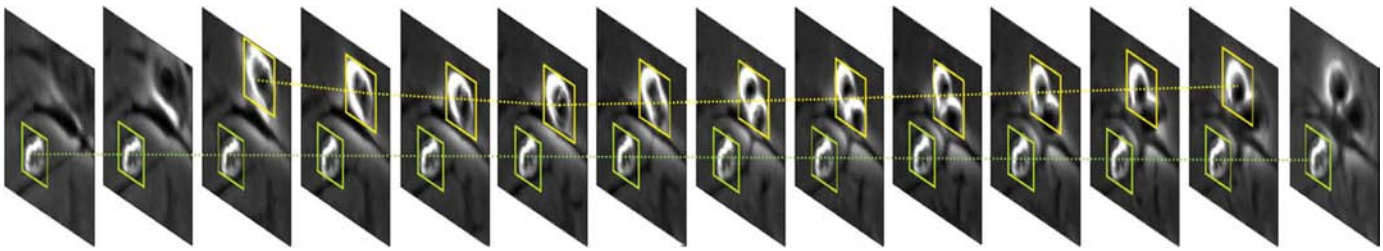

Fig. 2. An example of candidate patch sequences located in consecutive phase-contrast microscopy images. After candidate patch extraction based on brightness, spatially overlapped patches in consecutive frames are linked into a candidate patch sequence.

the result is thresholded with th, producing a binary image. For each connected component in the binary image, a bounding box is obtained and overlapping bounding boxes are then combined into one bounding box that encloses all the overlapping boxes. We then extract fixed-sized $s \times s$ rectangular patches from the image at the center position of each bounding box. The parameters d and s are closely related to the average cell size[1]. In our experiments, we set parameters d, th, and s to be 10, 1000, and 50 using a typical cross validation scheme.

Following this, candidate patch sequences are constructed by associating spatially overlapped patches in consecutive frames as shown in Fig. 2. In the case that a patch in frame t can be linked with two or more patches in the following frame $t+1$, the patch in frame t is associated with the one of the patches in frame $t+1$, whereas each of the other patches in frame $t+1$ initiates a new candidate patch sequence. In our experiments, multiple possible associations seldom occur except right after a birth event; a patch containing two new born cells that stick to each other can be linked with two patches each of which contains one of the daughter cells. In such a case, a birth event appears in the patch sequence before multiple possible associations; thus, association with either of the possibilities does not affect birth event detection performance.

B. Visual Feature Extraction

Unique scale gradient histogram features are extracted from each patch in candidate patch sequences. The unique scale gradient histogram features reflect the characteristics of phase-contrast microscopy images.

- *Relativity*: The pixel values in phase contrast microscopy images are influenced by many factors, such as artifacts and neighboring cells. Thus, relative features which reflect the change of pixel values, e.g., intensity gradient, are more reliable than absolute features.
- *Unique scale*: The variation of cell scales is minimal since the distances between the microscope lens and cells are almost uniform. Although cell sizes can differ within a certain range even during mitosis, the variation is limited and can thus be statistically modeled by training samples.
- *Rotation invariance*: Cells in a given field show various orientations. Regardless of the orientations, rotation invariance generally allows similar features to be extracted from cells with similar appearances.

The process computing unique scale gradient histograms follows scale invariance feature transform (SIFT) [19]. After dividing each patch into 4×4 subregions, we accumulate gradient magnitudes weighted by a Gaussian function into 4 bins along the orientations at each subregion as shown in Fig. 3. After $4 \times 4 \times 4 = 64$ features are computed for each patch, L2 normalization is applied to the feature vectors.

To achieve rotation invariance, each training candidate patch sequence is duplicated by rotating all patches in the sequence along several different orientations. This scheme results in performance improvement when training samples are insufficient. In our experiments, we applied three different orientations: 90°, 180°, and 270° as shown in Fig. 3. Other rotation schemes are not as effective as this simple duplication scheme because the

[1]Our experiments show that the best performance is achieved when parameters d and s are set to be approximately half and twice of the length of the square enclosing the average size of mitotic cells.

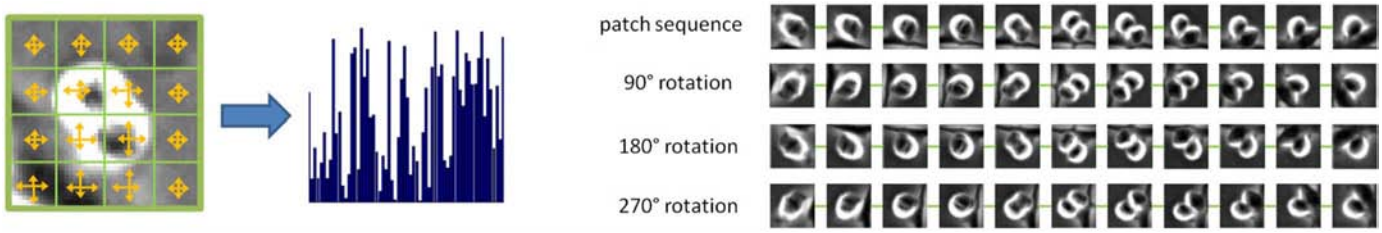

Fig. 3. Schematic of unique scale gradient histogram computation. At each of 4×4 subregions in a patch, a gradient histogram with four bins along the orientations are computed. To achieve rotation invariance, each candidate patch sequence in the training set is duplicated by rotating all patches in the sequence along three different orientations: 90°, 180°, and 270°.

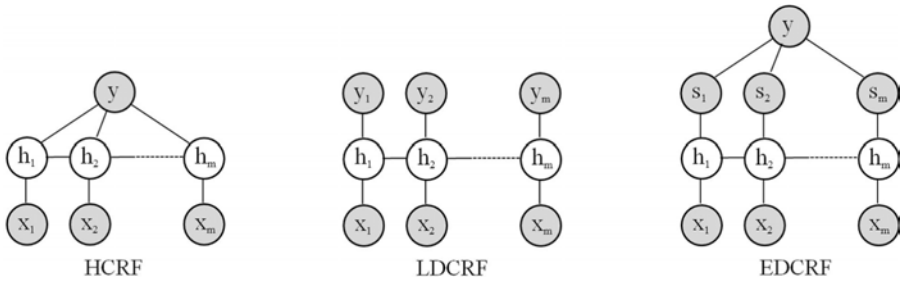

Fig. 4. Graphical representations of two previous models (HCRF and LDCRF) and our EDCRF model. x_i and h_i represent the ith observation (the ith patch in a given candidate sequence in our work) and the hidden state assigned on x_i, respectively. y represents a class label; one class label is assigned on the entire sequence in HCRF, while a class label is assigned for each of observations in LDCRF. In EDCRF, y is the label indicating the timing of the birth event and s_i is the ith sub-label determined by y. Gray circles denote observed variables for training. For testing, y and s are not observed.

major axis is not reliably found in phase-contrast microscopy images [19] or the relative spatial information is generally lost [20].

III. Mitosis Decision Using Event Detection Conditional Random Field

After candidate patch sequence construction and visual feature extraction, the problem reduces to determining whether each candidate contains a birth event and which frame the birth event is located in. For these two decision tasks, we present event detection conditional random field (EDCRF), a probabilistic model for birth event detection and localization. After introducing related probabilistic models, we formulate the EDCRF model and describe its learning and inference process.

A. Related Models

We review two previous probabilistic models: hidden conditional random fields (HCRFs) [16] and latent-dynamic conditional random fields (LDCRFs) [18]. The graphical representations of these two models are shown in Fig. 4.

HCRF was devised to analyze temporal sequences, such as vision and speech applications [21], [22]. Particularly, it has been applied to gesture recognition tasks and demonstrates its superiority to hidden Markov models (HMM) and conditional random fields (CRF) [23]. HCRF also excels in mitosis occurrence detection [15]. However, since HCRF handles sequences on each of which only one label is imposed, it cannot capture the timing of particular events, such as birth events, in candidate patch sequences.

LDCRF was proposed to additionally capture extrinsic class dynamics based on the idea of HCRF [18]. Hidden variables in LDCRF not only model substructure of a class sequence, but also learn dynamics between class labels; thus, the model can be directly applied to unsegmented sequences. Efficient training and inference schemes can be achieved by constraining each class label to have a disjoint set of associated hidden states. LDCRF has the potential to be modified into a model for event detection in that an event can be expressed as a class dynamic change when different labels are assigned on observations before and after the event.

B. EDCRF Formulation

EDCRF has one more variable containing event timing on the top of LDCRF as shown in Fig. 4. Given the event timing information, the sub-label variables in the subsequent layer are set to show an explicit label transition between before and after the event, which implies dynamic changes of observations. The formulation of EDCRF is as follows.

Suppose that n candidate patch sequence and label pairs $\{(\mathbf{x_1}, y_1), (\mathbf{x_2}, y_2), \ldots, (\mathbf{x_n}, y_n)\}$ are given. Each label y_i is defined as

$$y_i = \begin{cases} p, & \text{if the } p\text{th patch of } \mathbf{x_i} \text{ contains a birth event} \\ 0, & \text{if there exists no birth event in } \mathbf{x_i} \end{cases}. \tag{1}$$

Each sequence $\mathbf{x} = (x_1, x_2, \ldots, x_m)$ consists of m candidate patches where x_j denotes the jth patch (m can be varied for different sequences). We assume hidden variables $\mathbf{h} = (h_1, h_2, \ldots, h_m)$ and sub-labels $\mathbf{s} = (s_1, s_2, \ldots, s_m)$ where h_j and s_j correspond to x_j. When a sequence label y is given, the sub-labels $s_1, s_2, \ldots$, and s_m are defined as

$$s_j = \begin{cases} N, & \text{if } y = 0 \\ B, & \text{if } y > 0 \text{ and } j < y \\ A, & \text{if } y > 0 \text{ and } j \geq y \end{cases} \tag{2}$$

where label N, B, and A represent *no event*, *before the event*, and *after the event (including the event)*, respectively. In other words,

if there exists a birth event in a given candidate sequence, the sub-labels before the event are set to be B and the other sub-labels set to be A. Otherwise, all the sub-labels are set to be N.

Under these definitions, we define a latent conditional model for each sequence

$$P(y|\mathbf{x},\theta) = P(\mathbf{s}|\mathbf{x},\theta) = \sum_{\mathbf{h}} P(\mathbf{s}|\mathbf{h},\mathbf{x},\theta)P(\mathbf{h}|\mathbf{x},\theta) \quad (3)$$

where θ is a set of parameters of the model.

In order to make the modeling efficient, we adopt the same scheme as LDCRF [18], which restricts that each sub-class label s is associated only with hidden states in a disjoint set $\mathcal{H}_s$. Then

$$P(\mathbf{s}|\mathbf{h},\mathbf{x},\theta) = \begin{cases} 1, & \text{if } \forall h_j \in \mathcal{H}_{s_j} \\ 0, & \text{otherwise} \end{cases}. \quad (4)$$

The proposed model is thus simplified as

$$P(y|\mathbf{x},\theta) = \sum_{\mathbf{h}:\forall h_j \in \mathcal{H}_{s_j}} P(\mathbf{h}|\mathbf{x},\theta). \quad (5)$$

We define $P(\mathbf{h}|\mathbf{x},\theta)$ using the typical conditional random field (CRF) formulation

$$P(\mathbf{h}|\mathbf{x},\theta) = \frac{1}{Z}\exp\left(\sum_{j=1}^{m} f^{(s)}(h_j,\mathbf{x},j)\cdot\theta^{(s)}(h_j) + \sum_{j=2}^{m} f^{(t)}(h_{j-1},h_j,\mathbf{x},j)\cdot\theta^{(t)}(h_{j-1},h_j)\right) \quad (6)$$

where Z is a partition function. $f^{(s)}(h_j,\mathbf{x},j)$ and $f^{(t)}(h_{j-1},h_j,\mathbf{x},j)$ are a state and a transition function, respectively. $\theta^{(s)}$ and $\theta^{(t)}$ are the parameters of state and transition functions, respectively. Also, $\theta = \{\theta^{(s)},\theta^{(t)}\}$.

We define state functions as

$$f^{(s)}(h_j,\mathbf{x},j) = \phi(x_j) \quad (7)$$

where $\phi(x_j)$ is a visual feature vector of x_j. The inner product of $\phi(x_j)\cdot\theta^{(s)}(h_j)$ can be interpreted as a compatibility measure between observation x_j and hidden state h_j [16]. We define transition functions as

$$f^{(t)}(h_{j-1},h_j,\mathbf{x},j) = \begin{cases} 1, & \text{if } (h_j-1,h_j)\in\mathcal{U} \\ 0, & \text{otherwise} \end{cases} \quad (8)$$

where $\mathcal{U} = \mathcal{H}_N\times\mathcal{H}_N \cup \mathcal{H}_B\times\mathcal{H}_B \cup \mathcal{H}_B\times\mathcal{H}_A \cup \mathcal{H}_A\times\mathcal{H}_A$. We restrict sub-level transitions among $(N,N),(B,B),(B,A)$, and (A,A), which respectively represent *no event*, *before the event*, *during the event*, and *after the event*. Aside from these four transitions, there exists no other transition in our setting.

C. Learning Model Parameters

For learning parameters, we maximize the following regularized log-likelihood function as conventionally [24], [25]

$$L(\theta) = \sum_{i=1}^{n} \log P(y_i|\mathbf{x_i},\theta) - \frac{1}{2\sigma^2}||\theta||^2 \quad (9)$$

where σ is the variance of a Gaussian prior.

This optimization problem can be solved by gradient ascent methods. The derivative of $L(\theta)$ with respect to $\theta_k^{(s)}(h')$, which is the kth element of $\theta^{(s)}(h')$, is computed as

$$\begin{aligned}\frac{\partial L(\theta)}{\partial\theta_k^{(s)}(h')} &= \sum_{i=1}^{n}\sum_{j=1}^{m} P(h_j = h'|y_i,\mathbf{x}_i,\theta) f_k^{(s)}(h',\mathbf{x}_i,j) \\ &\quad - \sum_{i=1}^{n}\sum_{y'=0}^{m}\sum_{j=1}^{m} P(h_j = h', y'|\mathbf{x}_i,\theta) \\ &\quad \times f_k^{(s)}(h',\mathbf{x}_i,j) - \frac{\theta_k^{(s)}(h')}{\sigma^2} \end{aligned} \quad (10)$$

where $f_k^{(s)}(h,\mathbf{x}_i,j)$ is the kth element of $f^{(s)}(h,\mathbf{x}_i,j)$. $P(h_j = h'|y_i,\mathbf{x}_i,\theta)$ can be computed by belief propagation [26] in $O(m)$ [18].

Similarly, the derivative of $L(\theta)$ with respect to $\theta^{(t)}(h',h'')$ is computed as

$$\begin{aligned}\frac{\partial L(\theta)}{\partial\theta^{(t)}(h',h'')} &= \sum_{i=1}^{n}\sum_{j=2}^{m} P(h_{j-1} = h', h_j = h''|y_i,\mathbf{x}_i,\theta) \\ &\quad \times f^{(t)}(h',h'',\mathbf{x}_i,j) \\ &\quad - \sum_{i=1}^{n}\sum_{y'=0}^{m}\sum_{j=2}^{m} P(h_{j-1} = h', h_j = h'', y'|\mathbf{x}_i,\theta) \\ &\quad \times f^{(t)}(h',h'',\mathbf{x}_i,j) \\ &\quad - \frac{\theta^{(t)}(h',h'')}{\sigma^2}. \end{aligned} \quad (11)$$

For valid transition $(h_{j-1} = h', h_j = h'')$, since $f^{(t)} = 1$, the derivative can be simplified as

$$\begin{aligned}\frac{\partial L(\theta)}{\partial\theta^{(t)}(h',h'')} &= \sum_{i=1}^{n}\sum_{j=2}^{m} P(h_{j-1} = h', h_j = h''|y_i,\mathbf{x}_i,\theta) \\ &\quad - \sum_{i=1}^{n}\sum_{y'=0}^{m}\sum_{j=2}^{m} P(h_{j-1} = h', h_j = h'', y'|\mathbf{x}_i,\theta) \\ &\quad - \frac{\theta^{(t)}(h',h'')}{\sigma^2}. \end{aligned} \quad (12)$$

$P(h_{j-1} = h', h_j = h''|y_i,\mathbf{x}_i,\theta)$ can also be efficiently computed by belief propagation.

D. Inferences

For testing of a new sequence $\mathbf{x}$, we first compute the probabilities of our conditional model with all possible y and the optimal parameter θ^* obtained in the training step

$P(y = 0|\mathbf{x},\theta^*)$ can be computed as

$$\begin{aligned} P(y = 0|\mathbf{x},\theta^*) &= P(s_1 = N,\ldots,s_m = N|\mathbf{x},\theta^*) \\ &= P(s_1 = N|\mathbf{x},\theta^*) = \sum_{h_1\in H_N} P(h_1|\mathbf{x},\theta^*) \end{aligned} \quad (13)$$

TABLE 1
COMPARISON OF MITOSIS DETECTION PERFORMANCE BETWEEN EDCRF AND HCRF MODELS WHEN THE TIMING OF BIRTH EVENTS IS NOT CONSIDERED. COMPARISON IS CONDUCTED IN TERMS OF PRECISION, RECALL, F-MEASURE, AND THE AUC OF THE PR-CURVE ON FOUR C3H10T1/2 AND ONE C2C12 STEM CELL POPULATIONS. EDCRF OUTPERFORMS HCRF IN TERMS OF ALL THE METRICS

	C3H10T1/2				C2C12			
Model	Precision	Recall	F-measure	AUC	Precision	Recall	F-measure	AUC
EDCRF	0.913 ± 0.040	0.870 ± 0.048	0.889 ± 0.007	0.958 ± 0.006	0.950	0.893	0.921	0.930
HCRF	0.890 ± 0.019	0.863 ± 0.033	0.876 ± 0.010	0.952 ± 0.005	0.924	0.875	0.899	0.866

because $s_1 = N$ leads to $s_2, \ldots, s_m = N$ under our restricted transition rule. Similarly

$$\begin{aligned} &P(y = 1|\mathbf{x}, \theta^*) \\ &\quad = P(s_1 = A, \ldots, s_m = A|\mathbf{x}, \theta^*) \\ &\quad = P(s_1 = A|\mathbf{x}, \theta^*) = \sum_{h_1 \in H_A} P(h_1|\mathbf{x}, \theta^*). \end{aligned} \tag{14}$$

The other conditional probabilities can be computed as

$$\begin{aligned} &P(y = j|\mathbf{x}, \theta^*) \\ &\quad = P(s_1 = B, \ldots, s_{j-1} = B, s_j = A, \ldots, s_m = A|\mathbf{x}, \theta^*) \\ &\quad = P(s_{j-1} = B, s_j = A|\mathbf{x}, \theta^*) \\ &\quad = P(s_{j-1} = B|\mathbf{x}, \theta^*) - P(s_{j-1} = B, s_j = B|\mathbf{x}, \theta^*) \\ &\quad = P(s_{j-1} = B|\mathbf{x}, \theta^*) - P(s_j = B|\mathbf{x}, \theta^*) \\ &\quad = \sum_{h_{j-1} \in H_B} P(h_{j-1}|\mathbf{x}, \theta^*) - \sum_{h_j \in H_B} P(h_j|\mathbf{x}, \theta^*) \\ &\qquad\qquad \text{for } j = 2, \ldots, m. \end{aligned} \tag{15}$$

For mitosis occurrence decision on each candidate sequence, we compare $P(y = 0|\mathbf{x}, \theta^*)$ and $1 - P(y = 0|\mathbf{x}, \theta^*)$. If the former is greater, EDCRF determines that there is no mitotic event in the given sequence. Otherwise, the temporal localization of the birth event follows by comparing $P(y = 1|\mathbf{x}, \theta^*), \ldots$, and $P(y = m|\mathbf{x}, \theta^*)$. More formally,

$$y^* = \begin{cases} 0, & \text{if } P(y = 0|\mathbf{x}, \theta^*) > 0.5 \\ \arg\max_{y=1,\ldots,m} P(y|\mathbf{x}, \theta^*), & \text{otherwise} \end{cases} \tag{16}$$

IV. EXPERIMENTAL SETUP

A. Data and Ground Truth

Multipotent C3H10T1/2 mesenchymal stem cells (ATTC, Manassas, VA) serve as a model for the adult human mesenchymal stem cell and were grown in Dulbecco's Modified Eagle's Media (DMEM; Invitrogen, Carlsbad, CA), 10% fetal bovine serum (Invitrogen, Carlsbad, CA) and 1% penicillin-streptomycin (PS; Invitrogen, Carlsbad, CA). C2C12 myoblastic stem cells (ATTC, Manassas, VA) have the capacity to differentiate into osteoblasts and myocytes and were grown in DMEM, 10% bovine serum (Invitrogen, Carlsbad, CA) and 1% PS. All cells were kept at 37 °C, 5% CO_2 in a humidified incubator.

Phase-contrast microscopy images of the two types of stem cell populations (C3H10T1/2 and C2C12) were generated as follows. During the growth of stem cells, microscopy cell images were acquired every 5 min using a Zeiss Axiovert T135V microscope (Carl Zeiss Microimaging, Thornwood, NY) equipped with a 5X, 0.15 N.A. phase-contrast objective, a custom-stage incubator, and the InVitro software (Media Cybernetics Inc., Bethesda, MD). Each of the images contains 1392×1040 pixels with a resolution of 1.3 μm/pixel. C3H10T1/2 and C2C12 microscopy image sequences consist of 1436 and 1013 images, respectively.

After acquiring the image sequences, manual annotation of birth events was performed on one C2C12 and five C3H10T1/2 image sequences. For each birth event, the center of the boundary between two daughter cells was marked when the boundary is clearly observed. Since C2C12 myoblasts were cultured to a much higher level of confluence than C3H10T1/2 mesenchymal stem cells in our data, each of the C3H10T1/2 sequences contain 41–128 mitotic events, while the C2C12 sequence contains 673 mitotic events.

B. Experiments

For mitosis detection without considering the timing of birth events, we compare EDCRF with HCRF [16], which was previously used for mitosis occurrence detection. HCRF is known to outperform hidden Markov models (HMM) and conditional random fields (CRF) [15], [23].

To the best of our knowledge, there exists no probabilistic model which has been used for automated temporal localization of birth events given candidate patch sequences; in this respect, our EDCRF model is original. In order to compare EDCRF with possible alternatives, we additionally use either support vector machines (SVM) or conditional random fields (CRF) for the temporal localization of the birth event after the identification of mitosis occurrence using HCRF. In these alternative approaches, the identification of mitosis occurrence and the temporal localization of birth event are sequentially performed.

In the model incorporating HCRF and SVM (HCRF + SVM), a version of SVM that outputs probabilities is applied to the sequences determined by HCRF to have a mitosis occurrence. More specifically, for training, candidate patches containing manual annotation of birth events are used as positive samples and all patches in the candidate patch sequences that do not contain mitosis as negative samples. For testing, the SVM produces the probabilities that each patch contains a birth event; the patch with the highest probability in the sequence is then decided to contain a birth event.

In the model combining HCRF and CRF (HCRF + CRF), the same labeling scheme as EDCRF is applied to temporally localize birth events. More specifically, for training, one label is assigned to the label variables before the birth event and another label is assigned after the event. If there exists no birth event, a third label is assigned to all the label variables. For testing,

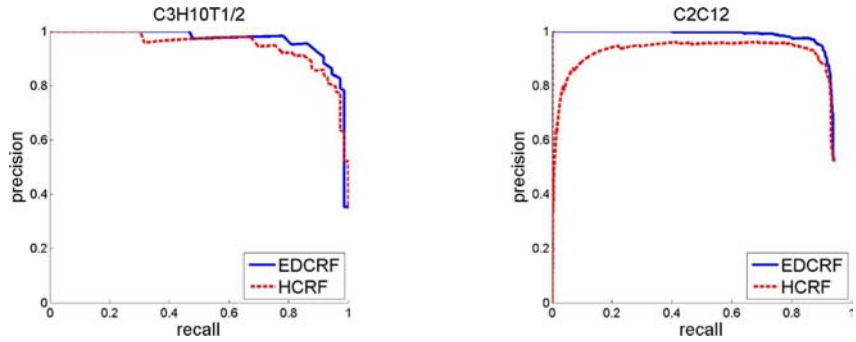

Fig. 5. The PR-curves of mitosis detection on the first C3H10T1/2 and the C2C12 image sequences when the timing of birth events is not considered. In terms of AUC, the EDCRF model outperforms the HCRF model in both cell types.

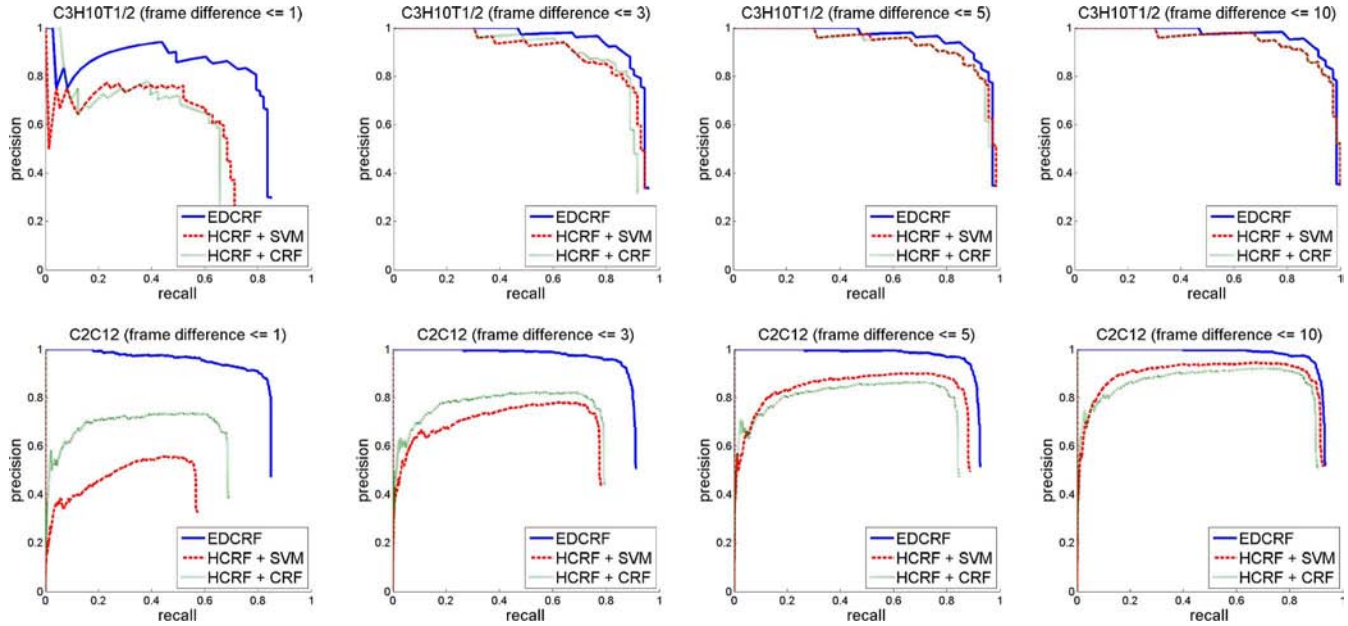

Fig. 6. The PR-curves of EDCRF and two alternative models ($\mathrm{HCRF} + \mathrm{SVM}$ and $\mathrm{HCRF} + \mathrm{CRF}$) showing mitosis detection accuracy on the first C3H10T1/2 (top) and the C2C12 (bottom) image sequences. Detection results are considered true positive when the timing error of the birth event is not greater than a given threshold (one of 1, 3, 5, and 10). In terms of AUC, our approach consistently outperforms the alternative approaches regardless of the threshold. The superiority of our approach is more evident when the threshold is small, i.e., the evaluation on birth event timing is strict.

the same inference scheme as the EDCRF model is utilized to determine a birth event's temporal location.

For C3H10T1/2 image data, one sequence is used for training and the other four sequences for testing whereas for C2C12 image data, half of all mitotic cells are used for training in turn, and the other half are used for testing.

C. Evaluation

After constructing candidate patch sequences, the number of undetected mitosis is counted. Each mitotic event, specifically the birth event, is expected to be captured by one of the candidate patch sequences. However, if there are birth events which are not contained in any candidate patch sequence, such cases are considered undetected. If one candidate patch sequence contains more than one birth event, all of the birth events except the first one are considered undetected as well. All of the undetected mitosis are counted as false negatives when precision and recall are computed.

After applying the probabilistic models, we first evaluated the identification of mitosis occurrence in terms of precision and recall without examining the timing of birth events. In this case, true positive is defined as the case that a candidate patch sequence containing a birth event is correctly identified no matter how great the timing error of the birth event is. If one birth event is located in more than one candidate patches, the birth event is considered to exclusively belong to the patch whose center is the closest to the birth event among the candidate patches.

We then evaluate the identification of mitosis occurrence with the constraint of birth event timing. In this case, among the aforementioned true positive cases, only the cases in which the timing error of the birth event is equal to or less than a certain threshold are considered true positive. In other words, although a candidate sequence including an actual birth event is correctly identified, if the timing error of the birth event is greater than the threshold, the birth event is considered undetected as well as the detection is regarded false. More specifically, the timing error is measured as the frame difference between the patch containing the ground truth and the patch containing the detected birth event in the sequence. We use four different thresholds (1, 3, 5, and 10) and report precision and recall for each

TABLE II
MITOSIS DETECTION PERFORMANCE COMPARISON WHEN THE TIMING OF BIRTH EVENTS IS EXAMINED IN ADDITION TO MITOSIS OCCURRENCE. OUR APPROACH IS COMPARED WITH THE ALTERNATIVE APPROACHES BASED ON HCRF ($\mathrm{HCRF} + \mathrm{SVM}$ AND $\mathrm{HCRF} + \mathrm{CRF}$) IN TERMS OF PRECISION, RECALL, F-MEASURE, AND THE AUC OF THE PR-CURVE ON C3H10T1/2 AND C2C12 STEM CELL POPULATIONS. DETECTION RESULTS ARE CONSIDERED TRUE POSITIVE WHEN THE TIMING ERROR OF THE BIRTH EVENT IS NOT GREATER THAN A GIVEN THRESHOLD (ONE OF 1, 3, 5, AND 10). WHEN A THRESHOLD IS SMALL (THE EVALUATION IS STRICT), OUR APPROACH MORE CLEARLY OUTPERFORMS THE ALTERNATIVES

EDCRF								
Threshold of frame difference	C3H10T1/2				C2C12			
	Precision	Recall	F-measure	AUC	Precision	Recall	F-measure	AUC
1	0.740 ± 0.067	0.703 ± 0.035	0.720 ± 0.041	0.660 ± 0.047	0.880	0.828	0.853	0.819
3	0.863 ± 0.044	0.822 ± 0.043	0.840 ± 0.015	0.882 ± 0.026	0.925	0.870	0.897	0.895
5	0.899 ± 0.037	0.857 ± 0.052	0.876 ± 0.014	0.934 ± 0.017	0.940	0.884	0.911	0.913
10	0.910 ± 0.042	0.867 ± 0.047	0.886 ± 0.009	0.952 ± 0.013	0.947	0.890	0.918	0.923

HCRF + SVM								
Threshold of frame difference	C3H10T1/2				C2C12			
	Precision	Recall	F-measure	AUC	Precision	Recall	F-measure	AUC
1	0.604 ± 0.052	0.585 ± 0.051	0.594 ± 0.049	0.466 ± 0.055	0.550	0.520	0.535	0.270
3	0.795 ± 0.045	0.773 ± 0.064	0.783 ± 0.052	0.785 ± 0.090	0.765	0.724	0.744	0.552
5	0.872 ± 0.010	0.847 ± 0.043	0.859 ± 0.019	0.920 ± 0.022	0.873	0.826	0.849	0.745
10	0.887 ± 0.019	0.860 ± 0.033	0.873 ± 0.010	0.946 ± 0.007	0.909	0.861	0.884	0.828

HCRF + CRF								
Threshold of frame difference	C3H10T1/2				C2C12			
	Precision	Recall	F-measure	AUC	Precision	Recall	F-measure	AUC
1	0.583 ± 0.044	0.565 ± 0.036	0.574 ± 0.037	0.463 ± 0.031	0.687	0.650	0.668	0.473
3	0.771 ± 0.055	0.749 ± 0.071	0.759 ± 0.060	0.744 ± 0.099	0.788	0.746	0.767	0.612
5	0.853 ± 0.036	0.827 ± 0.039	0.839 ± 0.028	0.890 ± 0.043	0.838	0.793	0.815	0.685
10	0.884 ± 0.020	0.857 ± 0.034	0.870 ± 0.012	0.943 ± 0.018	0.892	0.845	0.868	0.787

case. The smaller a threshold is, the stricter the evaluation is. To compare the detection results, we also compute F-measure, which is the harmonic mean of precision and recall, and the area under the curve (AUC) of the precision-recall curve (PR-curve). PR-curves are obtained by varying the decision probability in (16).

V. RESULTS AND DISCUSSIONS

During candidate patch sequence extraction, one birth event is not captured in four C3H10T1/2 sequences which are used for testing. There is no case that one candidate patch sequence contains more than one birth event in the C3H10T1/2 sequences. In the case of the C2C12 sequence, one birth event is missed and 36 birth events are detected following another birth event in the same sequence; as a result, a total of 37 false negative cases are reported before the decision tasks. Multiple mitosis in a candidate patch sequence occur due to the adhesion of mitotic cells at high confluency present in the C2C12 sequence. Under such circumstances, it is difficult to identify attached cells as separate entities.

As shown in Table I, the proposed mitosis detection method achieves 0.913/0.870 and 0.950/0.893 in terms of precision/recall on C3H10T1/2 and C2C12 stem cell populations, respectively, when only mitosis occurrence is considered. In terms of F-measure and AUC, the accuracy on C2C12 is comparable to that of C3H10T1/2, although the C2C12 cell population is more challenging due to its higher level of confluence and deformability. Having more training samples for C2C12 might be the reason.

Compared with the HCRF model, the EDCRF model is superior in mitosis occurrence detection in terms of precision, recall, F-measure, and the AUC of the PR-curve as shown in Table I and Fig. 5. A Student's paired t-test on the F-measures shows that the performance improvement is statistically significant at the significance level 0.01 ($p = 0.0008$). These results indicate that the information of birth event timing is actually helpful for identifying the occurrence of mitosis. HCRF cannot utilize such additional information due to its limited expression power. On the other hand, EDCRF simultaneously models both mitosis occurrence and birth event timing, resulting in higher discriminating power than HCRF in mitosis occurrence identification.

When we additionally consider the timing errors of birth events and threshold them to obtain true positive cases, the superiority of EDCRF is more obvious. Compared to the alternative models, $\mathrm{HCRF} + \mathrm{SVM}$ and $\mathrm{HCRF} + \mathrm{CRF}$, EDCRF consistently outperforms them in terms of precision, recall, F-measure, and AUC regardless of the cell type and the threshold for the timing error of birth events as shown in Table II. Student's paired t-tests on the F-measures show that the performance improvements are statistically significant at the significance level 0.01 regardless of the threshold of the timing error (EDCRF versus $\mathrm{HCRF} + \mathrm{SVM}$: $p = 0.0024$, 0.0038, 0.0092, and 0.0028; EDCRF versus $\mathrm{HCRF} + \mathrm{CRF}$: $p = 0.0001$, 0.0013, 0.0055, and 0.0037 for the threshold $= 1$, 3, 5, and 10, respectively). When a smaller threshold corresponding to a stricter evaluation of temporal localization is applied, our approach significantly outperforms the alternative approaches as seen in Fig. 6. In the alternative models, the identification of mitosis occurrence and the temporal localization of birth events are separately performed so the localization step may not be meaningful if mitosis occurrence is incorrectly identified. In this sense, the preceding mitosis occurrence decision may undermine the full potential of the localization step that follows. It is worth mentioning that recalls do not reach one in the PR-curves because some of existing mitosis are not detected regardless of the decision probability of mitosis occurrence. The undetected

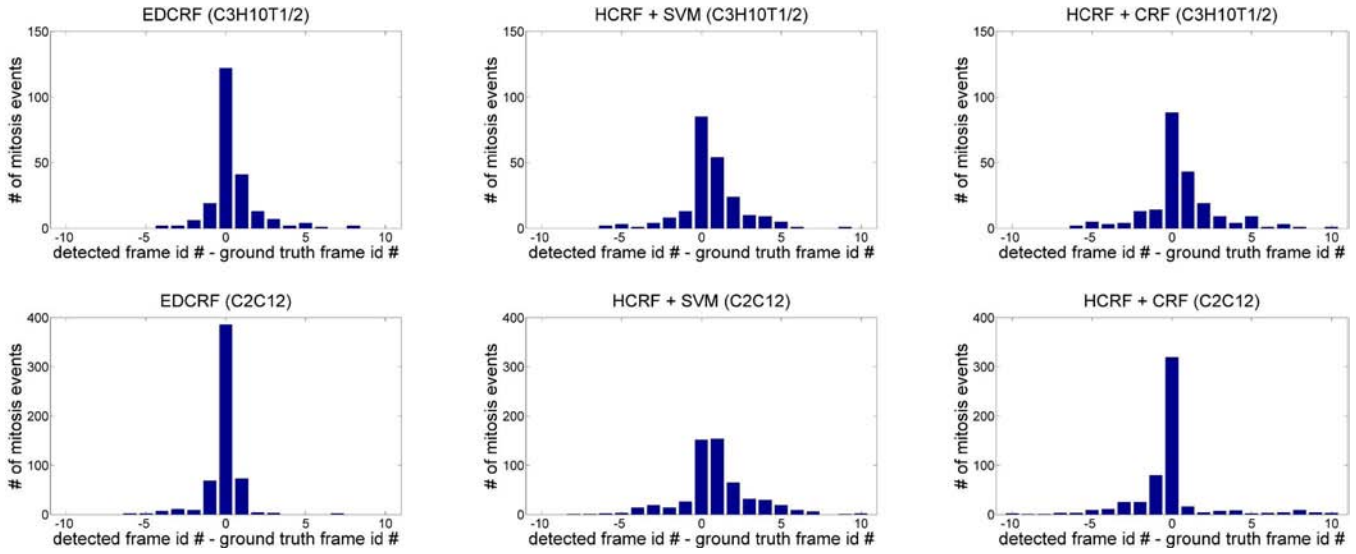

Fig. 7. Temporal localization precision of birth events of three approaches: EDCRF (left), $\mathrm{HCRF} + \mathrm{SVM}$ (middle), and $\mathrm{HCRF} + \mathrm{CRF}$ (right) on two cell populations: C3H10T1/2 (top) and C2C12 (bottom). The histograms show the frequency distribution of birth event timing errors when at most 10 frame error is allowed. Timing error is measured as the frame difference between the patches containing the ground truth and the detected result of the birth event among true positive samples. The temporal localization of EDCRF is more accurate than the alternatives.

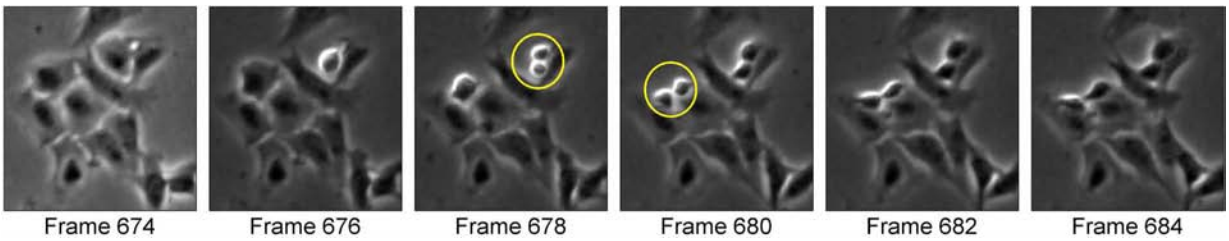

Fig. 8. Sample images illustrating examples of mitosis detection on the C2C12 microscopy image sequence. Each of the yellow circles in frames 678 and 680 surrounds a detected birth event. The EDCRF model temporally localizes birth events when there is a distinct boundary between daughter cells.

TABLE III
AVERAGE AND STANDARD DEVIATION OF THE TIMING ERROR OF BIRTH EVENTS IN TERMS OF (ABSOLUTE) FRAME DIFFERENCE. THE ERROR OF EDCRF IS SMALLER THAN THE ALTERNATIVE MODELS. THE IMPROVEMENT IN PERFORMANCE IS STATISTICALLY SIGNIFICANT

Cell type	EDCRF	HCRF+SVM	HCRF+CRF
C3H10T1/2	0.828 ± 1.334	1.273 ± 1.528	1.438 ± 1.826
C2C12	0.482 ± 0.957	1.685 ± 1.769	1.189 ± 2.120

mitosis occur due to either imperfect extraction of candidate patch sequences or inaccurate temporal localization of birth events.

Fig. 7 shows the distribution of the frame differences between the human and computer annotations of birth events among true positive samples on C3H10T1/2 and C2C12 sequences when at most 10 frame difference is allowed in temporal localization of birth events. The averages of the (absolute) frame differences using EDCRF are smaller than using the alternative models as shown in Table III. EDCRF achieves statistically significant improvements in the temporal localization of birth events; when applying Student's t-tests, we obtain p-values less than 0.001 for all of the four cases: comparison with $\mathrm{HCRF} + \mathrm{SVM}$ on C3H10T1/2 ($p = 0.0006$), $\mathrm{HCRF} + \mathrm{CRF}$ on C3H10T1/2 ($p < 0.0001$), $\mathrm{HCRF} + \mathrm{SVM}$ on C2C12 ($p < 0.0001$), and $\mathrm{HCRF} + \mathrm{CRF}$ on C2C12 ($p < 0.0001$). In addition to the lesser performance of HCRF in the identification of mitosis occurrence, SVM and CRF also fall short of the capability of EDCRF in the temporal localization of birth events. SVM is not capable of modeling temporal dynamic and CRF does not capture the hidden state structures in candidate patch sequences.

Using our design, the overall process of mitosis detection is more computationally efficient compared to the previous work [15]. By removing the time-consuming preconditioning [17], our approach can process a test image of 1392×1040 pixels in less than 5 s, while the previous method spends more than 5 min on the preconditioning step alone when using a computer with a dual core 2-GHz processor and 2-GB memory. This computational improvement enables real-time analysis of microscopy images periodically taken even with a short time interval. The previously used preconditioning scheme [17] is not required because cells show distinctive characteristics during mitosis. Mitotic cells can be recognized without applying the complex method devised for nonmitotic cells rather than mitotic cells.

Fig. 8 demonstrates two examples of birth events in the C2C12 myoblastic stem cell population automatically detected by our approach. Our approach shows good performance on the

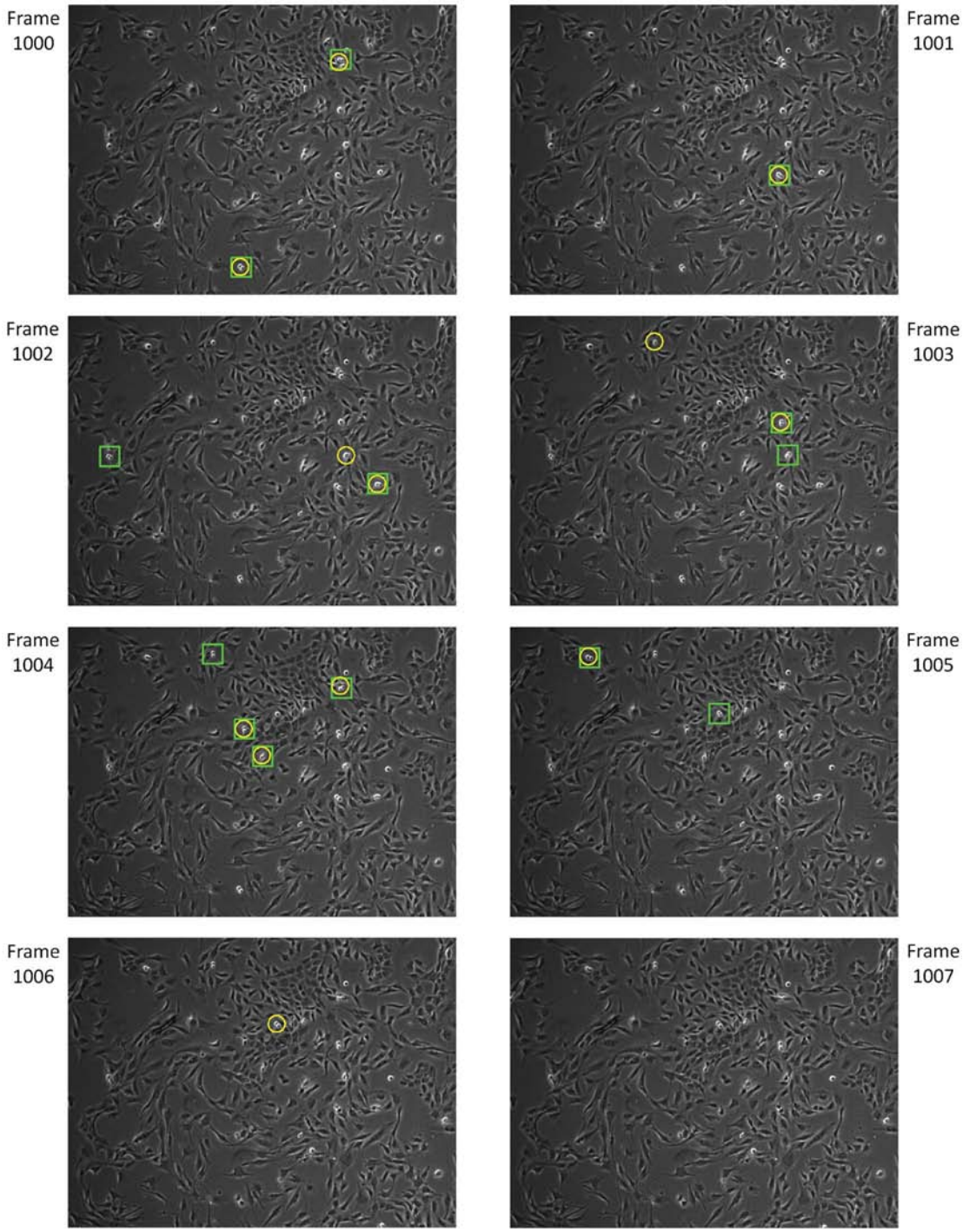

Fig. 9. Sample images illustrating examples of mitosis detection on the C2C12 microscopy image sequence from frames 1000 through 1007. Each of the yellow circles surrounds a detected birth event produced by our approach, whereas each of green squares encloses a ground truth birth event annotated by a human. During these eight frames, twelve birth events are correctly detected within one frame error and one birth event is missed in frame 1002.

C2C12 stem population with higher confluency (approximately 80%–90%) as shown in Fig. 9.

VI. Conclusion and Future Work

We have proposed an effective approach for mitosis detection, specifically birth event detection and temporal localization. Mitosis detection accuracy and speed are considerably improved compared to previous work by developing a probabilistic model for event detection and bypassing the use of time consuming modules. Experimental results on two types of stem cell populations validate the efficacy of our approach.

The mitosis detection algorithm described here will facilitate the quantification of biological metrics for cell proliferation. Such quantification will be useful in the study and characterization of biological processes and may have applications in high throughput screens that are reliant on cell proliferation measurements including identification of potent anti-mitotic drugs for chemotherapy as well as determination of drug sensitivity

in normal and diseased cells. In addition, we plan to develop a real-time cell tracking system that incorporates the functionality of our mitosis detection approach. The system would facilitate online monitoring and adaptive control of stem cell expansions by helping to make online decisions about when to subculture the stem cells as well as alerting the users of abnormalities of cell behaviors.

ACKNOWLEDGMENT

The authors would like to thank P. Campbell, L. Weiss, and Z. Yin for providing helpful comments on the manuscript.

REFERENCES

[1] H. Quastler and F. G. Sherman, "Cell population kinetics in the intestinal epithelium of the mouse," *Exp. Cell Res.*, vol. 17, no. 3, pp. 420–438, 1959.

[2] "Assays for cell proliferation studies," Genet. Eng. Biotechn. N. vol. 26, no. 6, 2006 [Online]. Available: http://www.genengnews.com/gen-articles/assays-for-cell-proliferation-studies/1442/

[3] C. Zimmer, E. Labruyère, V. Meas-Yedid, N. Guillén, and J.-C. Olivo-Marin, "Segmentation and tracking of migrating cells in videomicroscopy with parametric active contours: A tool for cell-based drug testing," *IEEE Trans. Med. Imag.*, vol. 21, no. 10, pp. 1212–1221, Oct. 2002.

[4] A. J. Hand, T. Sun, D. C. Barber, D. R. Hose, and S. Macneil, "Automated tracking of migrating cells in phase-contrast video microscopy sequences using image registration," *J. Microsc.*, vol. 234, no. 1, pp. 62–79, 2008.

[5] K. Li, E. D. Miller, M. Chen, T. Kanade, L. E. Weiss, and P. G. Campbell, "Computer vision tracking of stemness," in *Proc. IEEE Int. Symp. Biomed. Imag.*, 2008, pp. 847–850.

[6] D. House, M. L. Walker, Z. Wu, J. Y. Wong, and M. Betke, "Tracking of cell populations to understand thier spatio-temporal behavior in response to physical stimuli," in *Proc. IEEE Conf. Comput. Vis. Pattern Recognit. Workshop Math. Methods Biomed. Image Anal.*, 2009, pp. 186–193.

[7] F. Yang, M. A. Mackey, F. Ianzini, G. Gallardo, and M. Sonka, "Cell segmentation, tracking, and mitosis detection using temporal context," in *Proc. Int. Conf. Med. Image Computing Computer Assist. Intervent.*, 2005, pp. 302–309.

[8] J. Huth, M. Buchholz, J. M. Kraus, M. Schmucker, G. von Wichert, D. Krndija, T. Seufferlein, T. M. Gress, and H. A. Kestler, "Significantly improved precision of cell migration analysis in time-lapse video microscopy through use of a fully automated tracking system," *BMC Cell Biol.*, vol. 11, no. 1, pp. 24–35, 2005.

[9] O. Debeir, P. Van Ham, R. Kiss, and C. Decaestecker, "Tracking of migrating cells under phase-contrast video microscopy with combined mean-shift processes," *IEEE Trans. Med. Imag.*, vol. 24, no. 6, pp. 697–711, Jun. 2005.

[10] O. Al-Kofahi, R. J. Radke, S. K. Goderie, Q. Shen, S. Temple, and B. Roysam, "Automated cell lineage construction: A rapid method to analyze clonal development established with murine neural progenitor cells," *Cell Cycle*, vol. 5, no. 3, pp. 327–335, 2006.

[11] D. Padfield, J. Rittscher, N. Thomas, and B. Roysam, "Spatio-temporal cell cycle phase analysis using level sets and fast marching methods," *Med. Image Anal.*, vol. 13, no. 1, pp. 143–155, 2009.

[12] O. Debeir, V. Mégalizzi, N. Warzée, R. Kiss, and C. Decaestecker, "Videomicroscopic extraction of specific information on cell proliferation and migration *in virto*," *Exp. Cell Res.*, vol. 314, no. 16, pp. 2985–2998, 2008.

[13] P. Viola and M. Jones, "Rapid object detection using a boosted cascade of simple features," in *Proc. Comput. Vis. Pattern Recognit.*, 2001, pp. 511–518.

[14] Y. Freund and R. E. Schapire, "A decision-theoretic generalization of on-line learning and an application to boosting," *J. Comput. Syst. Sci.*, vol. 55, no. 1, pp. 119–139, 1997.

[15] A.-A. Liu, K. Li, and T. Kanade, "Mitosis sequence detection using hidden conditional random fields," in *Proc. IEEE Int. Symp. Biomed. Imag.*, 2010.

[16] A. Quattoni, S. Wang, L. Morency, M. Collins, and T. Darrell, "Hidden conditional random fields," *IEEE Trans. Pattern Anal. Mach. Intell.*, vol. 29, no. 10, pp. 1848–1853, Oct. 2007.

[17] K. Li and T. Kanade, "Nonnegative mixed-norm preconditioning for microscopy image segmentation," in *Proc. Int. Conf. Inf. Process. Med. Imag.*, 2009, pp. 362–373.

[18] L. P. Morency, A. Quattoni, and T. Darrell, "Latent-dynamic discriminative models for continuous gesture recognition," in *Proc. Comput. Vis. Pattern Recognit.*, 2007, pp. 1–8.

[19] D. G. Lowe, "Distinctive image features from scale-invariant keypoints," *Int. J. Comput. Vis.*, vol. 60, no. 2, pp. 91–110, 2004.

[20] S. Lazebnik, C. Schmid, and J. Ponce, "A sparse texture representation using local affine regions," *IEEE Trans. Pattern Anal. Mach. Intell.*, vol. 27, no. 8, pp. 1265–1278, Aug. 2005.

[21] A. Quattoni, M. Collins, and T. Darrell, "Conditional random fields for object recognition," in *Proc. Neural Inf. Process. Syst.*, 2004, pp. 1097–1104.

[22] A. Gunawardana, M. Mahajan, A. Acero, and J. C. Platt, "Hidden conditional random fields for phone classification," *Interspeech*, pp. 1117–1120, 2005.

[23] S. B. Wang, A. Quattoni, L.-P. Morency, D. Demirdjian, and T. Darrell, "Hidden conditional random fields for gesture recognition," in *Proc. Comput. Vis. Pattern Recognit.*, 2006, pp. 1521–1527.

[24] J. Lafferty, A. McCallum, and F. Pereira, "Conditional random fields: Probabilistic models for segmenting and labelling sequence data," in *Proc. Int. Conf. Mach. Learn.*, 2001, pp. 282–289.

[25] S. Kumar and M. Herbert, "Discriminative random fields: A framework for contextual interaction in classification," in *Proc. Int. Conf. Comput. Vis.*, 2003, pp. 1150–1157.

[26] J. Pearl, *Probabilistic Reasoning in Intelligent Systems: Networks of Plausible Inference*. San Fransisco, CA: Morgan Kaufmann, 1988.

APPENDIX A4: DATA-DRIVEN PREDICTION ON STEM CELL CULTURE PROCESS

Based on published work:

Data-driven Prediction on Stem Cell Culture Process

Zhaozheng Yin, Dai Fei Ker, Silvina Junkers, Takeo Kanade, Mei Chen, Lee Weiss, and Phil Campbell

Conference Proceedings of IEEE Engineering in Medicine and Biology Society. 2011 Aug-Sep; 3577-3580.

A4.1 RELEVANCE TO THESIS

In Chapter 6, a real-time computer-vision based system was devised to monitor and predict the growth of C2C12 cells as a paradigm muscle progenitor population for stem cell manufacture. A simple, 2^{nd} order polynomial curve fitting model was used to predict C2C12 cell growth up to 4 hours in advance. In this section, Zhaozheng Yin, a postdoctoral researcher at the Robotics Institute devised a data-driven approach for improving confluency predictions by using previously acquired data of C2C12 cells cultured under similar conditions. This methodology can predict C2C12 cell growth up to 8 hours in advance and outperformed both polynomial and exponential prediction models. This data-driven approach will be useful for building robust prediction models and facilitate growth monitoring of specific cell types for cell manufacture and production.

Data-driven Prediction on Stem Cell Culture Process

Zhaozheng Yin, Dai Fei Ker, Silvina Junkers, Takeo Kanade, Mei Chen, Lee Weiss, and Phil Campbell

***Abstract*— Stem cell expansion culture aims to generate sufficient number of clinical-grade cells for cell-based therapies. One challenge for *ex vivo* expansion is to decide the appropriate time to perform subculture. Traditionally, this decision has been reliant on human estimation of cell confluency and predicting when confluency will approach a desired threshold. However, the use of human operators results in highly subjective decision-making and is prone to inter- and intra-operator variability. Using a real-time cell image analysis system, we propose a data-driven approach to model the cell growth process and predict the cell confluency levels, signaling times to subculture. This approach has great potential as a tool for adaptive real-time control of subculturing, and it can be integrated with robotic cell culture systems to achieve complete automation.**

I. Introduction

Stem cell engineering promises to revolutionize regenerative medicine by helping to repair diseased or damaged tissues and organs. Starting with the relatively small number of primary stem cells available in isolates from the body, one of the critical bioprocessing steps required by successful cell-based therapies is to generate a sufficient number of clinical-grade stem cells through *ex vivo* cell culture expansions [4]. However, tight control of the expansion process remains a challenge. In particular, determining the appropriate time to perform cell subculturing is important. Delayed subculturing of cells can result in cell overgrowth, which leads to loss of stem cell differentiative potential (stemness); whereas premature subculturing can lead to longer production time to achieve targeted cell yields, with associated added costs. Traditionally, the decision to subculture is based on cell confluency which is related to the cell packing densities in the culture vessel. However, estimation of cell confluency by human operators is a highly subjective task and prone to inter- and intra-operator variability [5]. Furthermore, it is not practical or cost-effective for human operators to manually observe and monitor cell cultures 24/7. Automating the decision on when to subculture cells will result in more consistent outcomes and reduce variability, leading to more efficient and reliable stem cell culture systems.

Time-lapse microscopy imaging has been used to monitor the cell growth process [3] where the degree of cell confluency level in images is used as a metric to assess the cell culture process. To augment human monitoring, we propose a data-driven approach to model the cell growth process and predict the optimal confluency for a real-time adaptive subculture system. First, time-lapse images of cells under the same culture condition are acquired to monitor the cell growth process, and to compute the cell confluency over time. These experiments are terminated without further subculture when the computed confluency exceeds a pre-determined cell confluency level. These pre-recorded images with computed time series of confluency metrics serve as training data for subsequent real-time adaptive control experiments. We then build a linear subspace using principle component analysis (PCA) on the training data. When performing a new cell culture experiment with the same culture conditions as our training experiments, we project the observed confluency data onto the linear subspace to model the cell growth process and predict the future confluency. One application of our prediction approach is to notify a human operator in advance when to perform a subculture. For example, 4 hours prior to exceeding a pre-determined confluency level (e.g. 50%), the image analysis and prediction system alerts a human operator via text messaging and/or email to prepare for subculture. The goal is to help human operators expand a population of stem cells to reach a target number in an efficient manner without exceeding or being far away from the pre-determined optimal confluency level (i.e., avoiding delayed or premature subculture).

In this paper, we first introduce in Section II how we compute confluency metrics to monitor cell growth processes. Then, in Section III we present our data-driven model. The dynamic prediction on cell confluency levels is described in Section IV. In Section V we quantitatively compare our data-driven approach with other parametric models and introduce the application of our prediction system.

II. Monitoring Cell Growth Process

During the cell culture experiment, we capture real-time phase contrast microscopy images to monitor the degree of confluency inside the field of view. The confluency metric is defined as the number of pixels occupied by cells divided by the total number of pixels in the image. For a given phase contrast image (Fig. 1a), we restore its corresponding artifact-free image without the halo or shade-off effects [6], as shown in Fig. 1b. In the restored image, cell pixels

This work was supported by NIH grants RO1EB004343 & RO1EB007369, CMU Cell Image Analysis Consortium and Intel Labs budget.

Zhaozheng Yin, Silvina Junkers, Takeo Kanade and Lee Weiss are with the Robotics Institute, Carnegie Mellon University, Pittsburgh, PA15213 USA (Phone: 412-268-3016; e-mail: {yinz,sjunkers,tk,lew}@cs.cmu.edu).

Dai Fei Ker is with the Biological Sciences Department, Carnegie Mellon University, Pittsburgh, PA15213 USA (e-mail: eker@andrew.cmu.edu).

Mei Chen is with Intel Science and Technology Center, Pittsburgh, PA15213, USA (e-mail: mei.chen@intel.com).

Phil Campbell is with the Institute of Complex Engineering Systems, Carnegie Mellon University, Pittsburgh, PA15213 USA (e-mail: pcampbel@cs.cmu.edu).

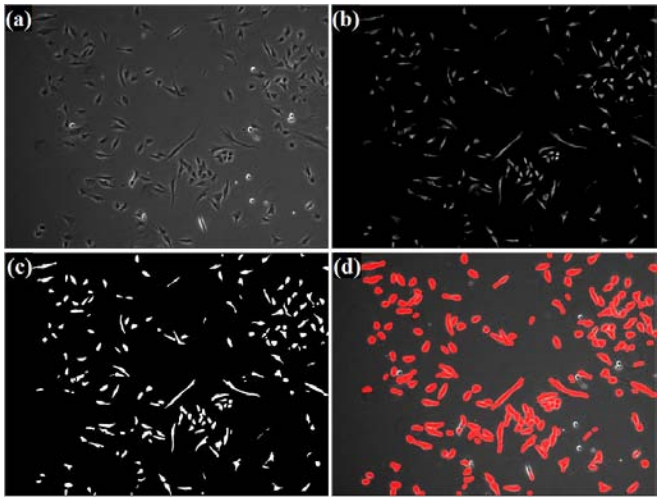

Fig. 1. Compute confluency. (a) A phase contrast microscopy image; (b) Restored image without halo or shade-off artifacts; (c) The segmented cell masks by globally thresholding the restored image; (d) Segmentation results (red) overlaid on the original image.

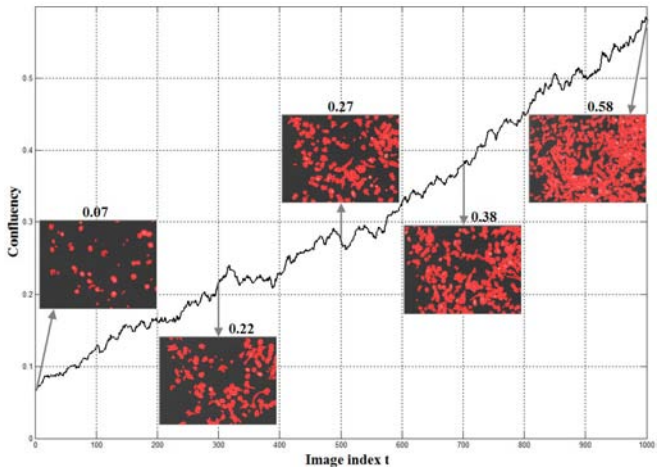

Fig. 2. The confluency increases during the culture process. Five sample images overlaid with segmented cell masks (red) show the confluency level at five time instants.

have positive values while background pixels have near-zero values, which is amenable to image segmentation by thresholding. The thresholded binary mask is shown in Fig. 1c. The resultant cell mask overlaid on top of the original image is shown in Fig. 1d, which proves to be a good estimation of the confluency metric.

Given a time-lapse microscopy image sequence, we compute the confluency metric for each individual image. This produces time series data on confluency. As shown in Fig. 2, while stem cells keep dividing (mitosis), the confluency of the culture process increases accordingly. The small "dips" observed in the confluency curve correspond to minor changes in cell shapes over a period time.

III. Modeling Cell Growth Process

Monitoring cell growth with time-lapse microscopy imaging generates time series confluency data (e.g Fig. 2). Parametric models on the cell growth process can be obtained by data-fitting. For example, we can fit the second-order polynomial model on the observed confluency data by

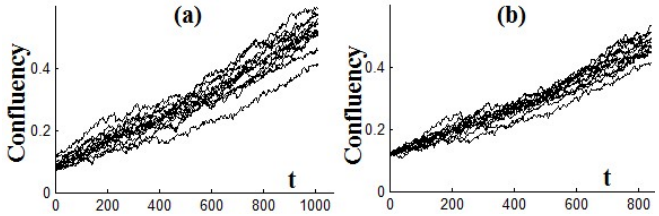

Fig. 3. Align time series confluency curves. (a) The original confluency metrics of N time-lapse image sequences; (b) Aligned curves such that their cell culture processes start from the same initial confluency.

$$\mathbf{x}(t) = \mathbf{p}_2 t^2 + \mathbf{p}_1 t + \mathbf{p}_0 \tag{1}$$

where $\mathbf{x} = [\mathbf{x}(0), \cdots, \mathbf{x}(t), \cdots, \mathbf{x}(T)]^T$ is a vector storing the observed confluency metrics from time $t = 0$ to time $t = T$, and $\mathbf{p} = [\mathbf{p}_1, \mathbf{p}_2, \mathbf{p}_3]^T$ is the parameter vector. Or, we can fit exponential model onto the data by

$$\mathbf{x}(t) = e^{kt} + c \tag{2}$$

where k and c are the scalar parameters. All the parameters $(\mathbf{p}, k, c)$ are computed using the least square technique [1].

However, these parametric models that depend on specific cell types and culture experiments might lack practical or biological meanings. Instead, we propose a data-driven approach that models the growth process based on observed training data without assuming any specific model. We ran N cell culture experiments on the same type of cells using the same culture condition to obtain the training data. Images of the cell culture experiments were captured every 5 minutes using a phase contrast microscopy imaging system, which generated N time-lapse image sequences for training purposes. We computed confluency metrics for all the N sequences (Fig. 3a). Since the first image of each sequence may have different degrees of confluency (i.e., the number of seed cells may be different for the N sequences), we search the largest initial confluency of the N curves in Fig. 3a, and then align all the N curves such that they start from the same initial condition (Fig. 3b).

Then, we apply PCA [2] onto the training data using Singular Value Decomposition (SVD)

$$\mathbf{X} = \mathbf{U}\mathbf{S}\mathbf{V}^T \tag{3}$$

where data matrix $\mathbf{X} = [\mathbf{x}_1, \cdots, \mathbf{x}_N]$ stores the vectors of the confluency metrics of the N image sequences, $\mathbf{U}$ and $\mathbf{V}$ are two orthogonal matrices, and $\mathbf{S}$ is a diagonal matrix with rank-ordered singular values (Fig. 4). We choose the column vectors of $\mathbf{V}$ that correspond to the first K (e.g. $K = 2$) largest singular values to span a linear subspace for our data-driven modeling.

For a new cell culture experiment having the same type of cells and the same culture condition as our training experiments, we monitor its culture process and compute the observed confluency, $\mathbf{z}$. The culture process can be modeled in our trained linear subspace by

$$\mathbf{y} = \sum_{k=1}^{K} a_k \mathbf{v}_k \tag{4}$$

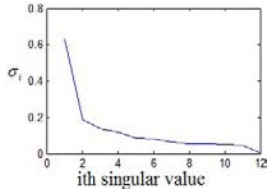

Fig. 4. The variance (singular value) of each principle component.

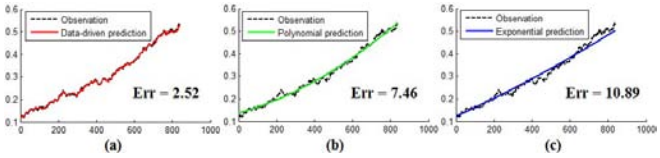

Fig. 5. Modeling cell growth by three methods: (a) Data-driven; (b) Polynomial, and (c) Exponential. The data-driven model fits the observed data with the least error on the culture process.

where $\mathbf{v}_k$ denotes the kth principle vector in $\mathbf{V}$, the coefficient a_k is computed by

$$a_k = \mathbf{v}_k^T \mathbf{z}. \tag{5}$$

The performance of the modeling is evaluated by the sum of absolute difference between the modeled culture process, $\mathbf{y}$, and the observed culture process, $\mathbf{z}$,

$$\text{Err} = \sum_{t=0}^{T} |\mathbf{y}(t) - \mathbf{z}(t)|. \tag{6}$$

Compared to the two parametric models (polynomial and exponential), the data-driven model fits the observed data with the least error on the culture process in Fig. 5.

IV. Predicting Cell Confluency

Our goal is to accurately predict the cell confluency at a future time $t+L$ based on the observed confluency data from time 0 till time t, where L is the prediction time lag. When $L = 1$, we predict the confluency at the next frame. When $L = 48$, we predict the confluency 4 hours later (images are captured every 5 minutes, and the time unit is represented by the image index.) In this section, the data-driven model (Eq. 4) is further extended to dynamic prediction. Denote time-dependent data matrix $\mathbf{X}^{(t)} = [\mathbf{x}_1^{(t)}, \cdots, \mathbf{x}_N^{(t)}]$ where $\mathbf{x}_i^{(t)} = [\mathbf{x}_i(0), \cdots, \mathbf{x}_i(t)]^T$ (i.e., $\mathbf{x}_i^{(t)}$ is the observed time series confluency of sequence i from time 0 till time t), we perform SVD

$$\mathbf{X}^{(t)} = \mathbf{U}^{(t)} \mathbf{S}^{(t)} {\mathbf{V}^{(t)}}^T \tag{7}$$

on all the t's ($t = 0, \cdots, T$). Thus, for any time index t, we get a set of K principle components , $\{\mathbf{v}_1^{(t)}, \cdots, \mathbf{v}_K^{(t)}\}$.

When predicting the confluency level for a new cell culture experiment, we first compute the coefficients based on the current observed time series data, $\mathbf{z}^{(t)} = [\mathbf{z}(0), \cdots, \mathbf{z}(t)]^T$,

$$a_k^{(t)} = {\mathbf{v}_k^{(t)}}^T \mathbf{z}^{(t)} \tag{8}$$

then the confluency at time $t + L$ is predicted by

$$\mathbf{z}^{(t+L)}(t+L) = \sum_{k=1}^{K} a_k^{(t)} \mathbf{v}_k^{(t+L)}(t+L) \tag{9}$$

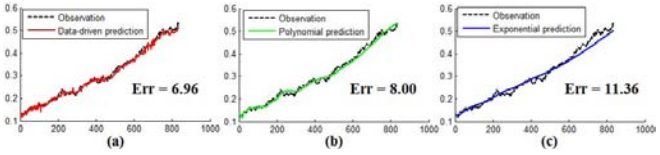

Fig. 6. Predicting the confluency in the next image using three prediction methods: (a) Data-driven; (b) Polynomial, and (c) Exponential. The data-driven model has the least prediction error on the culture process.

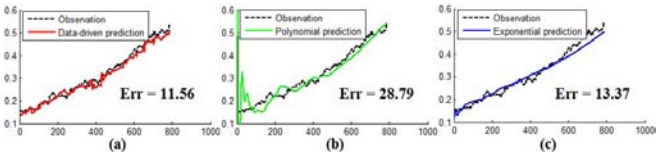

Fig. 7. Predicting the confluency 4 hours later using three prediction methods: (a) Data-driven; (b) Polynomial, and (c) Exponential. The data-driven model is more stable compared to the parametric models and it has the least prediction error on the culture process.

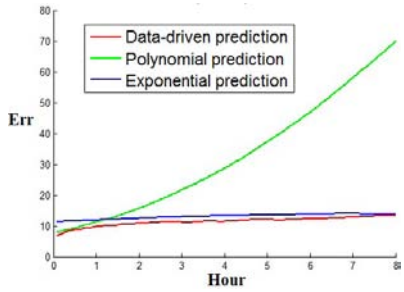

Fig. 8. The prediction error of three methods regarding to different prediction time lags. The data-driven prediction is stable and it outperforms the other two parametric methods consistently with the least prediction error.

Using the evaluation criterion in Eq. 6, we compare the data-driven prediction method to the other two predictions using parametric models. As shown in Fig. 6, when predicting the confluency in the temporal domain with a small time lag, all three prediction methods work reasonably well and the data-driven prediction achieves the least prediction error. When the prediction time lag (L) increases, the error of all the prediction methods increase (Fig. 7). In particular, the prediction by a polynomial model is quite unstable at the beginning when there is not enough data for model fitting (Fig. 7b). The data-driven prediction still achieves the least prediction error for the larger prediction lag.

We further quantitatively evaluate how well the three prediction methods can predict future confluency by changing the time lag from $L = 1$ (5 minutes) to $L = 96$ (8 hours). As shown in Fig. 8, the data-driven prediction outperforms the other two methods consistently with the least prediction error, and the prediction by data-driven or exponential model is much more stable than the prediction by polynomial model as the time lag increases.

V. Experiments

We recorded a total of 48 image sequences under four different cell culture conditions with sample images shown in Fig. 9. The images were captured every 5 minutes and each sequence consists of 1000 images at the resolution of 1392*1040 pixels. Under each culture condition, we have

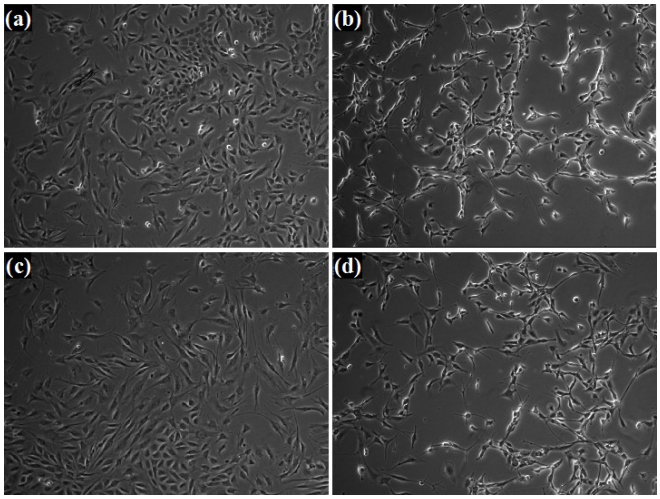

Fig. 9. Sample images from four cell culture conditions. (a) Control; (b) With FGF2; (c) With BMP2; (d) With FGF2+BMP2.

TABLE I

THE PREDICTION ERROR OF THREE METHODS WITH $L = 24$.

	Control	FGF2	BMP2	FGF2+BMP2
Data driven	122.2	68.7	154.0	137.6
Polynomial	146.2	105.3	179.6	168.2
Exponential	148.9	97.4	309.0	211.2

TABLE II

THE PREDICTION ERROR OF THREE METHODS WITH $L = 48$.

	Control	FGF2	BMP2	FGF2+BMP2
Data driven	136.0	74.4	169.6	157.8
Polynomial	259.5	222.7	304.8	315.6
Exponential	164.7	112.6	340.9	235.3

TABLE III

THE PREDICTION ERROR OF THREE METHODS WITH $L = 96$.

	Control	FGF2	BMP2	FGF2+BMP2
Data driven	153.4	78.4	192.6	178.9
Polynomial	631.7	628.9	714.8	809.7
Exponential	188.4	136.3	400.5	278.7

12 image sequences. We use the "leave-one-out" strategy to evaluate the prediction performance. After selecting one out of the 12 sequences, the remaining 11 sequences undergo PCA analysis to obtain the principle components (Eq. 7). Then, we run the prediction (Eq. 9) on the selected sequence and compare the prediction with the observation using Eq. 6. We repeat the "leave-one-out" evaluation for each of the 12 sequences and use the summation of all the prediction errors as the final evaluation criterion on the 12 sequences. As shown in Tables 1, 2 and 3, the data-driven prediction achieves the least error at confluency prediction over all the four culture conditions for different prediction time lags.

The data-driven prediction on cell culture process is useful for automating the decision process for determining when to perform subculture. A human operator first runs several experiments to culture the cells until they reach a pre-determined cell confluency level for subculture. The recorded image sequences corresponding to these experiments will be used to build the data-driven model in Eq. 4 and compute the time series principle components in Eq. 7. Using the same type of cells and under the same culture condition, the

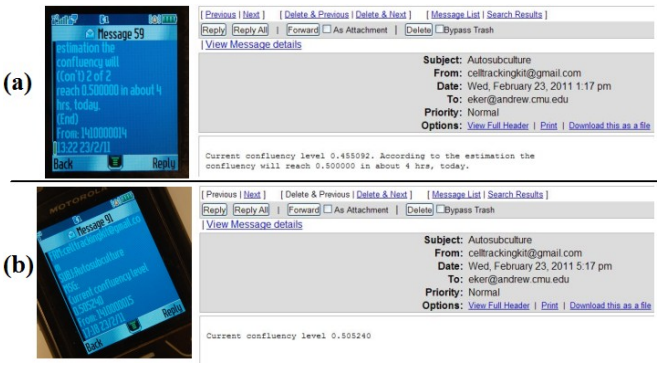

Fig. 10. Advance notification for cell culture. (a) A human operator was notified by text message and email 4 hours prior to exceeding a pre-determined cell confluency level; (b) Confirmation text message and email were sent when the cell confluency level approached the pre-determined threshold.

human operator starts the recursive cell culture/subculture process whose goal is to culture a sufficient number of cells. In the meantime, the human operator sets up the image analysis and prediction system such that it can notify him/her h (e.g. $h = 4$) hours prior to exceeding a pre-determined cell confluency level, to prepare for subculture. Fig. 10 shows a successful cell culture experiment by the advance notification.

VI. CONCLUSION

Determining the appropriate time to perform subculture is important to optimize the process of stem cell expansion. We monitor the process of cell growth by computing the degree of cell confluency in phase-contrast microscopy images. Based on the cell confluency measurements, we propose a data-driven approach to model the cell growth process and predict when a pre-determined cell confluency threshold will be exceeded, requiring cells to be subcultured. Compared to the typical parametric models for predicting cell growth, our data-driven approach learns the cell growth model from a training set of cell culture experiments and achieves higher prediction accuracy on cell culture experiments that have the same culture condition as training experiments. This data-driven prediction has great potential as a tool for adaptive realtime control of subculturing, and it can be integrated with robotic cell culture systems to achieve complete automation.

REFERENCES

[1] C. Bishop,"Pattern Recognition and Machine Learning," Springer, 2006.
[2] R. Duda, P. Hart, and D. Stork, "Pattern Classification," Wiley, 2001.
[3] M. Kino-oka, and J.E. Prenosil, "Development of an On-Line Monitoring System of Human Keratinocyte Growth by Image Analysis and Its Application to Bioreactor Culture," *Biotechnol. Bioeng.*, 67(2): 234-9, 2000.
[4] Y. Liu, P. Hourd, A. Chandra, and D. J. Williams, "Human Cell Culture Process Capability: a Comparison of Manual and Automated Production," *J. Tissue Eng. Regen. Med.*, 4:45-54, 2010
[5] F. S. Veraitch, R. Scott, J. Wong, Gary. J. Lye, and C. Mason, " The Impact of Manual Processing on the Expansion and Directed Differentiation of Embryonic Stem Cells" *Biotechnology and Bioengineering*, 99(5): 1216-1229, 2008.
[6] Z. Yin, K. Li, T. Kanade and M. Chen, "Understanding the Optics to Aid Microscopy Image Segmentation," *Proceedings of the 13th International Conference on Medical Image Computing and Computer Assisted Intervention (MICCAI)*, 2010.

APPENDIX A5: RESTORING DIC MICROSCOPY IMAGES FROM MULTIPLE SHEAR DIRECTIONS

Based on published work:

Restoring DIC Microscopy Images from Multiple Shear Directions

Zhaozheng Yin, Dai Fei Ker, Takeo Kanade

Information Processing in Medical Imaging: Proceedings of the 22nd International Conference. 2011 July; **22** 384-397.

A5.1 RELEVANCE TO THESIS

Cell detection is a critical step for automated cell tracking in time-lapse microscopy images. In this section, Zhaozheng Yin, a postdoctoral researcher at the Robotics Institute devised a method for detecting cells in Differential Interference Contrast (DIC) microscopy images. This algorithm estimates the shear angle from multiple DIC images and a reconstructed DIC image is produced. The reconstructed DIC image is artifact-free with respect to bias retardation (pseudo 3D effect commonly seen in DIC images) and is amenable to cell segmentation techniques. Future work will involve integrating this cell detection method with an automated phase-contrast time-lapse microscope for multi-modal (DIC and phase-contrast) time-lapse imaging and cell tracking.

Restoring DIC Microscopy Images from Multiple Shear Directions

Zhaozheng Yin[1] Dai Fei Elmer Ker[2] Takeo Kanade[1]

[1]Robotics Institute, [2]Department of Biological Sciences
Carnegie Mellon University, Pittsburgh, US

Abstract. Differential Interference Contrast (DIC) microscopy is a non-destructive imaging modality that has been widely used by biologists to capture microscopy images of live biological specimens. However, as a qualitative technique, DIC microscopy records specimen's physical properties in an indirect way by mapping the *gradient* of specimen's optical path length (OPL) into the image intensity. In this paper, we propose to restore DIC microscopy images by quantitatively estimating specimen's OPL from a collection of DIC images captured from multiple shear directions. We acquire the DIC images by rotating the specimen dish on the microscope stage and design an Iterative Closest Point algorithm to register the images. The shear directions of the image dataset are automatically estimated by our coarse-to-fine grid search algorithm. We develop a direct solver on a regularized quadratic cost function to restore DIC microscopy images. The restoration from multiple shear directions decreases the ambiguity among different individual restorations. The restored DIC images are directly proportional to specimen's physical measurements, which is very amenable for microscopy image analysis such as cell segmentation.

1 Introduction

Under a traditional brightfield microscope, living specimens such as cells are colorless and transparent because they are predominantly phase objects that absorb and scatter little illumination light. That is, cells do not significantly alter the amplitude of the light waves passing through them and as a result, produces little or no contrast when viewed under a brightfield microscope. For tissue culture cells, a cell's optical path length (OPL, product of its refractive index and geometric thickness) is normally different from that of the surrounding medium (about $0.125\mu m$ or a quarter wavelength of green light). This optical path difference induces a small phase difference between the light waves passing through cells and those traversing the surrounding medium. Since human eyes are sensitive to amplitude differences between light waves as opposed to phase differences, Differential Interference Contrast (DIC) microscopy technique was invented in 1950s to convert these minute phase variations to intensity changes that can be easily detected by human eyes (see textbook [12]).

The DIC microscope works by splitting a polarized illumination light wave into two component waves that are spatially displaced (sheared) along a specific direction, and then recombining the two waves after they travel through adjacent locations on the

specimen plate. The recombination (interference) is sensitive to phase variations between the two component waves. An adjustable bias (bias retardation) can be added into the phase variation. Because the phase variation between the two waves is caused by OPL difference at two adjacent locations, this microscopy imaging technique is then called "differential interference," and the observed intensity in DIC images is proportional to the OPL *gradient* along the shear direction. The relief-like images generated by DIC microscopy have the pseudo 3D shadow-cast effects as if the specimens are illuminated from an oblique lighting resource (e.g. Fig. 1(a,b)), but this artifact only indicates the orientation of a specimen's OPL gradient rather than the real topographical structure.

1.1 Related Work

Since the intensity of a DIC image is not a linear mapping of specimen's inherent properties such as refractive index, thickness or OPL, this has triggered strong research interest in reconstructing the original physical properties of specimens from DIC images. We summarize the related work in three aspects: hardware-related techniques, reconstruction from a single DIC image and reconstruction using multiple DIC images.

(1) Arnison et al. [1] proposed a hardware extension to the conventional differential interference by inserting an extra quarter wave plate in the optical layout of a DIC microscope, and restored the phase objects by varying bias setting and using geometric phase-shift techniques. Shribak et al. [15] developed an orientation-independent DIC microscopy by adding liquid crystal devices in the common DIC microscopes. The setup of these new optical configurations might be complicated and inaccessible to the common biology labs.

(2) Noticing the gradient interpretation of DIC images, line integration methods were developed to reconstruct DIC images [8]. The line-by-line integration along shear direction introduces new streaking artifacts in reconstructed images and it is sensitive to gradient noise, thus Hilbert transform [2] and other ad hoc techniques such as low-pass filtering [7] were explored to reduce the streaking artifacts to a certain degree. General image processing algorithms such as deconvolution by Wiener filter [7, 11] or by Landweber iterations [6] have been applied to reconstruct optical path length from DIC images. A preconditioning approach was recently proposed in [10] where the DIC image is reconstructed by minimizing a nonnegative mixed-norm constrained cost function. We reimplemented these three types of approaches and applied them on a pair of DIC images of the same specimens captured from two different shear directions. As shown in Fig. 1(c) and (d), we can observe the streak artifacts by line integration. Fig. 1(e) and (f) show the unsatisfactory restoration results by Wiener filtering with 1% noise-to-signal power ratio of the additive noise. The deconvolution performance depends on the prior knowledge of various hardware parameters (such as shear directions and bias setting) and image noise models. Fig. 1(g) and (h) show the reconstruction results by the preconditioning method. It is time-consuming to estimate the direct measurement on specimens by the iterative preconditioning method.

From Fig. 1, we have a common observation that the reconstructions of the image pair (Fig. 1(c,d), Fig. 1(e,f), and Fig. 1(g,h)) are not the same for the same specimens. That is, when biologists analyze specimens, they will obtain different measurements

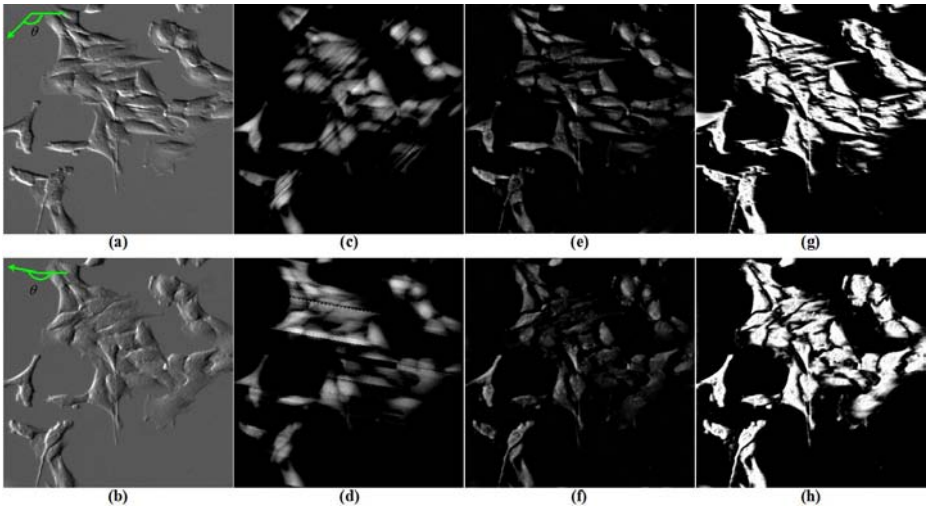

Fig. 1. Reconstructing optical path length from DIC images. (a,b) Two DIC image of the same specimens captured from two different shear directions (the arrow denotes the shear direction θ); (c,d) Reconstruction by line integration enhanced by low-pass filtering; (e,f) Reconstruction by deconvolution (Wiener filtering); (g,h) Reconstruction by preconditioning.

on the specimen's optical path length according to different shear directions. This is very undesirable because biologist don't know which direction-specific reconstruction unveils the real properties of specimens.

(3) A few approaches have been proposed to restore specimen's properties from multiple DIC images [1, 6, 9, 13, 15]. These approaches either rotate prisms, change bias settings or step the shear azimuth to capture multiple DIC images, and they require at least two images captured from a pair of orthogonal shear directions. Without specially-designed hardware, it is hard to rotate the specimen dish or prism manually by exact 90 degrees to satisfy the orthogonal requirement.

1.2 Our Proposal

We propose a novel approach to restore DIC microscopy images captured from multiple shear directions without the strict orthogonal requirement. In Section 2, we derived a closed-form solution for the restoration. Since the DIC images were captured by manually rotating the dish on the stage of a common DIC microscope, there are Euclidean transformation (rotation and translation) among captured DIC images. We designed an Iterative Closest Point (ICP) algorithm to register the image dataset (Section 3). Rather than measuring the shear directions of the DIC images manually, we propose a coarse-to-fine grid search algorithm to find the shear directions automatically (Section 4). We show our experiment results in Section 5 with the conclusion followed in Section 6.

2 Problem Formulation and Restoration Method

Based on the gradient interpretation of DIC images, we have the following simplified DIC imaging model

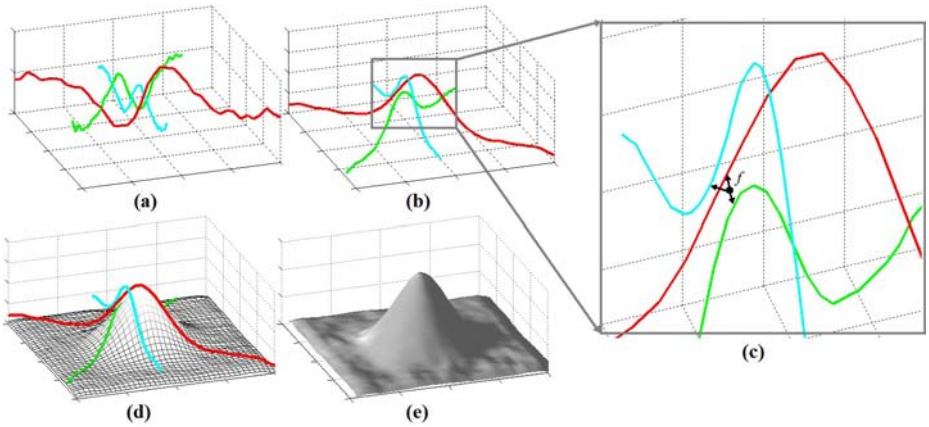

Fig. 2. Estimate the optical path length in DIC images. (a) The three observed gradient signals along different shear directions; (b) The three signals after integration do not intersect in the OPL space (i.e. there is no consensus among the restored signals); (c) We propose to restore DIC images (i.e. estimate the optical path length) by minimize the total distance to all integrated signals; (d) The spatial smooth constraint (gray mesh) is considered during the restoration; (e) The restoration result using three DIC images.

$$\mathbf{g} = \nabla_\theta \mathbf{f} \tag{1}$$

where $\mathbf{g}(u, v)$ is an observed DIC image[1], ∇_θ is the gradient operator along the shear direction θ and $\mathbf{f}(u, v)$ is the DIC image to be restored. This imaging model is also used by some other DIC reconstruction methods such as the iterative preconditioning method [10] and deconvolution by Landweber iteration [6]. More accurate and complicated DIC imaging models can be referred to [14].

Based on Eq.1, the DIC image can be restored by applying line-by-line integration on the observed gradient $\mathbf{g}$ along the shear direction θ

$$\mathbf{f} = \int \mathbf{g}\, d\mathbf{x}^\theta \tag{2}$$

where $\mathbf{x}^\theta$ denotes a location on the lines along the shear direction. For a line on the specimen plate with M locations, we can observe $M - 1$ gradient values by DIC microscopy. The line integration method reverses the differential problem by estimating the OPL values at M locations from observed $M - 1$ gradient values, thus there are more unknowns than available equations. The under-constrained equation system plus the image acquisition noise may make the restored signal inconsistent when we perform line integration along different shear directions. As shown in Fig. 2(a), at a specimen location, three gradient signals are extracted from three DIC images along their shear directions. When we integrate the three gradient signals independently (Fig. 2(b)), the three reconstructed signals do not intersect in the OPL space - they have different restoration values on $\mathbf{f}$ at the same specimen location! To avoid the ambiguity and achieve the consensus among different restorations, we propose to estimate the true $\mathbf{f}$

[1] We drop the 2D location indices (u, v) in all the equations for concise expressions.

in a least-square sense. In other words, the real $\mathbf{f}$ at that location should have the minimum total distance to all integrated signal curves (Fig. 2(c)). Thus, we are looking for an image $\mathbf{f}$ to minimize

$$\sum_{i=1}^{K} \int_{\mathcal{R}^2} (\mathbf{f} - \int \mathbf{g}_i \, d\mathbf{x}^{\theta_i})^2 d\mathbf{x} \tag{3}$$

where i indexes the K DIC images captured from different shear directions θ_i on the same specimens, $\mathbf{x} = (u, v)$ is a pixel location on the 2D Euclidean space $\mathcal{R}^2$. The minimization on Eq. 3 needs to carry out the line integration $\int \mathbf{g}_i \, d\mathbf{x}^{\theta_i}$ explicitly for each DIC image. However, the line integration itself is not a satisfactory restoration as we see in Fig. 1(c) and (d). Instead, we propose to restore $\mathbf{f}$ by minimizing a cost function in the gradient domain directly

$$\sum_{i=1}^{K} \int_{\mathcal{R}^2} (\nabla_{\theta_i} \mathbf{f} - \mathbf{g}_i)^2 d\mathbf{x}. \tag{4}$$

The goal is to compute an $\mathbf{f}$ whose gradients along different shear directions are as close as possible to the corresponding given gradients, $\mathbf{g}_i$'s. After mapping the pixel location from 2D Euclidean space to a new surface defined by the K shear directions

$$\{\mathbf{x} = (u, v), \mathbf{x} \in \mathcal{R}^2\} \rightarrow \{\boldsymbol{\theta} = (\theta_1, \theta_2, \cdots, \theta_K), \boldsymbol{\theta} \in \Theta\} \tag{5}$$

and using the commutativity of $\sum$ and $\int$ operations, the cost function (Eq. 4) is converted into

$$\int_{\Theta} \sum_{i=1}^{K} (\nabla_{\theta_i} \mathbf{f} - \mathbf{g}_i)^2 d\boldsymbol{\theta}. \tag{6}$$

Eq. 6 only measures the fidelity of the restoration to all the observed data. We enhances the data fidelity with smooth and sparse regularizations and propose the following objective function for restoration

$$O(\mathbf{f}) = \int_{\Theta} \left[\left(\sum_{i=1}^{K} (\mathbf{d}_{\theta_i} * \mathbf{f} - \mathbf{g}_i)^2 \right) + \omega_s (\mathbf{a} * \mathbf{f})^2 + \omega_r \mathbf{f}^2 \right] d\boldsymbol{\theta} \tag{7}$$

where $\mathbf{d}_\theta$ is a differential kernel along the shear direction θ, "*" is the convolution operation, $\mathbf{d}_{\theta_i} * \mathbf{f}$ is equivalent to $\nabla_{\theta_i} \mathbf{f}$, $\mathbf{a}$ is a kernel for local smooth, ω_s and ω_r are weighting coefficients for the smooth and sparse regularizations, respectively. $\mathbf{d}_{\theta_i}$ can be defined by a directional first-derivative-of-Gaussian kernel [10]. The smooth constraint encourages nearby pixels to have the same restoration values (Fig. 2(d)). For example, we can regularize a restored pixel value to be close to the average of its neighboring pixels (i.e. $\mathbf{a} = [1\ 1\ 1;\ 1\ -8\ 1;\ 1\ 1\ 1]/8$ for 8-connected neighborhood). The l_2 sparse regularization penalizes large $\mathbf{f}$ values and enforces the restored background pixels (with equal OPL at adjacent locations) to be close to zero. A stronger sparse regularization is using l_1 norm but there is no closed-form solution for that. More discussions on the regularizations can be referred to the rich research work on compressive sensing [3].

The solution that minimizes Eq. 7 must satisfy the Euler-Lagrange equation

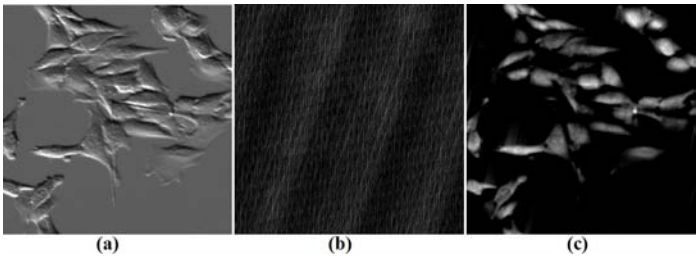

Fig. 3. Restoring a DIC image. (a) An input image; (b) Restoration by inverse filtering; (c) Our restoration by minimizing a regularized cost function.

$$\frac{\partial \mathbf{E}}{\partial \mathbf{f}} - \sum_{i=1}^{K} \frac{\partial}{\partial \theta_i} \frac{\partial \mathbf{E}}{\partial \mathbf{f}_{\theta_i}} = 0 \tag{8}$$

where $\mathbf{f}_{\theta_i}$ is a shorthand notation of $\mathbf{d}_{\theta_i} * \mathbf{f}$ and $\mathbf{E}$ is the integrand inside Eq. 7

$$\mathbf{E} = \left(\sum_{i=1}^{K} (\mathbf{d}_{\theta_i} * \mathbf{f} - \mathbf{g}_i)^2 \right) + \omega_s (\mathbf{a} * \mathbf{f})^2 + \omega_r \mathbf{f}^2. \tag{9}$$

Substituting $\mathbf{E}$ into Eq. 8 for the differentiating, we have

$$2\omega_s \mathbf{a} * \mathbf{a} * \mathbf{f} + 2\omega_r \mathbf{f} - 2 \sum_{i=1}^{K} \mathbf{d}_{\theta_i} * (\mathbf{d}_{\theta_i} * \mathbf{f} - \mathbf{g}_i) = 0. \tag{10}$$

Now, applying Fourier transform, $\mathcal{F}$, on both sides of this equation, we obtain

$$2\omega_s \mathbf{A}^2 \cdot \mathbf{F} + 2\omega_r \mathbf{F} - 2 \sum_{i=1}^{K} \mathbf{D}_{\theta_i}^2 \cdot \mathbf{F} + 2 \sum_{i=1}^{K} \mathbf{D}_{\theta_i} \cdot \mathbf{G}_i = 0 \tag{11}$$

where $\mathbf{A} = \mathcal{F}\{\mathbf{a}\}$, $\mathbf{F} = \mathcal{F}\{\mathbf{f}\}$, $\mathbf{D}_{\theta_i} = \mathcal{F}\{\mathbf{d}_{\theta_i}\}$, $\mathbf{G}_i = \mathcal{F}\{\mathbf{g}_i\}$, "$\cdot$" denotes the element-wise production and $\mathbf{D}_{\theta_i}^2 = \mathbf{D}_{\theta_i} \cdot \mathbf{D}_{\theta_i}$. Solving Eq. 11 for $\mathbf{F}$, we have

$$\mathbf{F} = -(\sum_{i=1}^{K} \mathbf{D}_{\theta_i} \cdot \mathbf{G}_i)./(\omega_s \mathbf{A}^2 + \omega_r - \sum_{i=1}^{K} \mathbf{D}_{\theta_i}^2). \tag{12}$$

where "$./$" denotes the element-wise division. $\mathbf{f}$ is then restored by $\mathbf{f} = \mathcal{F}^{-1}\{\mathbf{F}\}$. Fig. 2(e) shows a restored result using three images with different shear directions.

For a single DIC image with shear direction θ, the direct solution is

$$\mathbf{F} = -(\mathbf{D}_\theta \cdot \mathbf{G})./(\omega_s \mathbf{A}^2 + \omega_r - \mathbf{D}_\theta^2). \tag{13}$$

If without regularizations ($\omega_s = \omega_r = 0$), Eq. 13 is degraded into an inverse filtering

$$\mathbf{F} = \mathbf{G}./\mathbf{D}_\theta. \tag{14}$$

However, the simple inverse filtering can not restore a correct DIC image (Fig. 3(b)), which justifies the needs of regularization. As a comparison, our restoration by Eq. 13 with $\omega_s = 0.1$ and $\omega_r = 0.001$ is shown in Fig. 3(c) that is much better than the inverse filtering. Please note that the restoration from a single shear direction (Eq. 13) contains

ambiguity to measure the real specimen property thus we have derived solution (Eq. 12) to restore DIC images from multiple shear directions. Eq. 13 is only used in Algorithm 2 (Section 4) for estimating the shear direction of each individual DIC image.

3 Register a Collection of DIC Images

When capturing a collection of DIC images with different shear directions by rotating and translating dishes, we must register those images such that the same pixel location in the image dataset represents the same specimen sample in the world. Note: this registration step can be waived if there is a DIC microscope with rotatable prisms at hand. We revised the Iterative Closest Point (ICP) idea [4] to register two DIC images. Harris corner detector [5] and local non-max suppression are used to locate corners as feature points for matching in the ICP algorithm. The corners are tolerant to appearance changes in DIC images from different shear directions. However, the ICP algorithm can converge to the optimum only when the initialization (rotation $\mathbf{R}_0$ and translation $\mathbf{T}_0$) is close to the optimum. To find the correct $\mathbf{R}$ and $\mathbf{T}$ to register images, we uniformly sample the entire search space of all possible initializations (e.g. every 30 degrees of rotation and every 100 pixels of translation) and run the ICP algorithm from these initializations to find the global optimal $\mathbf{R}$ and $\mathbf{T}$. The new designed ICP algorithm is summarized below. Fig. 4 shows an registration example using this ICP algorithm.

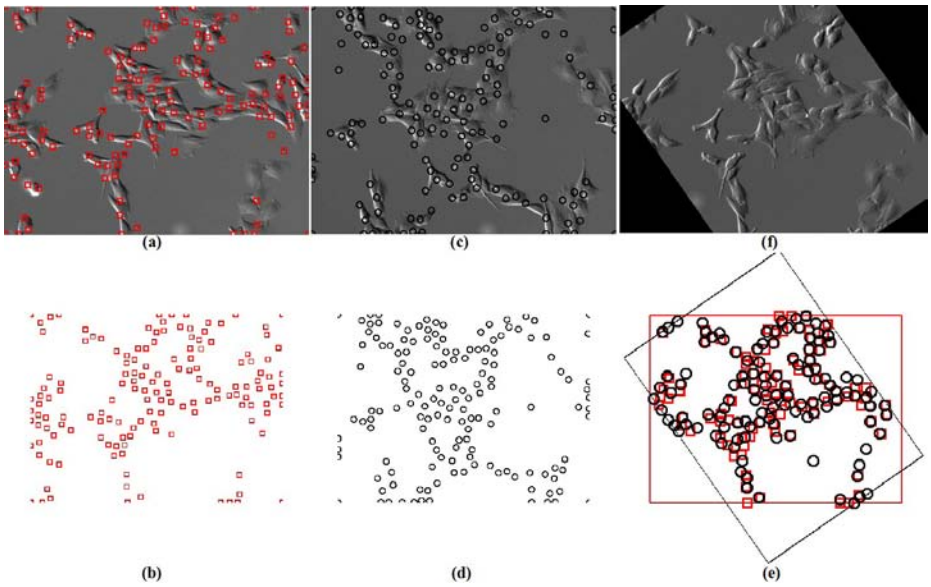

Fig. 4. Register two DIC images by Iterated Closest Point algorithm. (a,b) Image 1 and its corner points (red squares); (c,d) Image 2 and its corner points (black circles); (e) The two groups of corner points are matched with the least total distance cost; (f) The registered image 2 regarding to image 1 based on the Euclidean transformation computed from matched corner points.

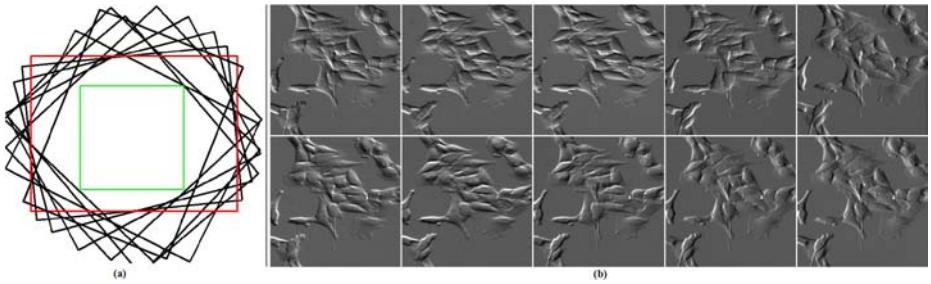

Fig. 5. Register a collection of images and extract the sub-images within the overlapped regions for our analysis. (a): Nine images are registered regarding to the first image. (b) The ten sub-images within the overlapped square regions.

For a collection of DIC images, we randomly pick a reference image and register all the others regarding to it. The registered images overlap in a polygon area and we crop the largest square sub-images from the overlapped region for our analysis (Fig. 5).

Algorithm I: ICP Algorithm to Register Two DIC Images

Extract two groups of corner points $\{\mathbf{Q}_j\}$ and $\{\mathbf{P}_i\}$ from image 1 and image 2, respectively. Compute the centroids: $\bar{\mathbf{P}} = \frac{1}{|\mathbf{P}|}\sum_i \mathbf{P}_i$, and $\bar{\mathbf{Q}} = \frac{1}{|\mathbf{Q}|}\sum_j \mathbf{Q}_j$. Update $\mathbf{P}_i \leftarrow \mathbf{P}_i - \bar{\mathbf{P}}$, $\mathbf{Q}_j \leftarrow \mathbf{Q}_j - \bar{\mathbf{Q}}$.
Initialize $\mathbf{R} = \mathbf{R}_0$, $\mathbf{T} = \mathbf{T}_0$, and $c = 0$.
Repeat the following steps until there is no change on c.

1. Bi-directional Matching: $\forall \mathbf{P}_i$, find the closest $\mathbf{Q}_j$ in the Euclidean space. For $\mathbf{Q}_j$, find the closest $\mathbf{P}_k$. If $i = k$, the two corner points are matched, and update $c+ = |\mathbf{P}_i - \mathbf{Q}_j|$.

2. Transformation: For all matched corner points, compute $\mathbf{W} = \sum_{<i,j>} \mathbf{P}_i \mathbf{Q}_j^T$. Take the singular value decomposition (SVD) of matrix $\mathbf{W}$, $\mathbf{W} = \mathbf{U}\mathbf{\Sigma}\mathbf{V}^T$. Compute the rotation matrix as $\mathbf{R} = \mathbf{V}\mathbf{U}^T$, and the translation vector as $\mathbf{T} = \bar{\mathbf{Q}} - \mathbf{R}\bar{\mathbf{P}}$. $\forall \mathbf{P}_i$, update $\mathbf{P}_i \leftarrow \mathbf{R}\mathbf{P}_i + \mathbf{T}$.

Use the final matched points to compute $\mathbf{R}^*$ and $\mathbf{T}^*$, rotate and translate image 2 regarding to image 1 accordingly.

4 Estimate the Shear Directions

After registration, the shear direction difference between the first image and the other $K-1$ registered images are actually the rotation angle θ_r^i ($i = 1...K$ and $\theta_r^1 = 0$). In other words, if the shear direction of the first image is θ_s, the shear directions of the rest images are $\theta_s - \theta_r^i$. Since θ_r^i's are already known from the registration step, we only need to estimate a single unknown variable θ_s. As shown in Fig. 6(g), when correct shear directions are estimated for a pair of DIC images, the difference between the two restorations reaches the minimum. We use this fact to estimate the shear direction over the collection of registered images by a fast coarse-to-fine grid search algorithm.

Algorithm II: Coarse-to-Fine Grid Search for Shear Direction θ_s

Initialize $lb = 0$, $ub = 360$ and $\delta_\theta = 30$.

while $\delta_\theta > 1$
  for $\theta_s = lb; \theta_s < ub; \theta_s = \theta_s + \delta_\theta$
    for $i = 1; i < K; i++$
      Solve $\mathbf{f}_i$ with $\theta = \theta_s - \theta_r^i$ through Eq. 13;
    $cost[\theta_s] = \sum_{\substack{i \neq j \\ i,j=1\ldots K}} |\mathbf{f}_i - \mathbf{f}_j|$
  $\theta_s^* \leftarrow \arg\min cost[\theta_s]$; $\delta_\theta \leftarrow \delta_\theta/4$; $lb \leftarrow \theta_s^* - 2\delta_\theta$; $ub \leftarrow \theta_s^* + 2\delta_\theta$;
Return θ_s^*;

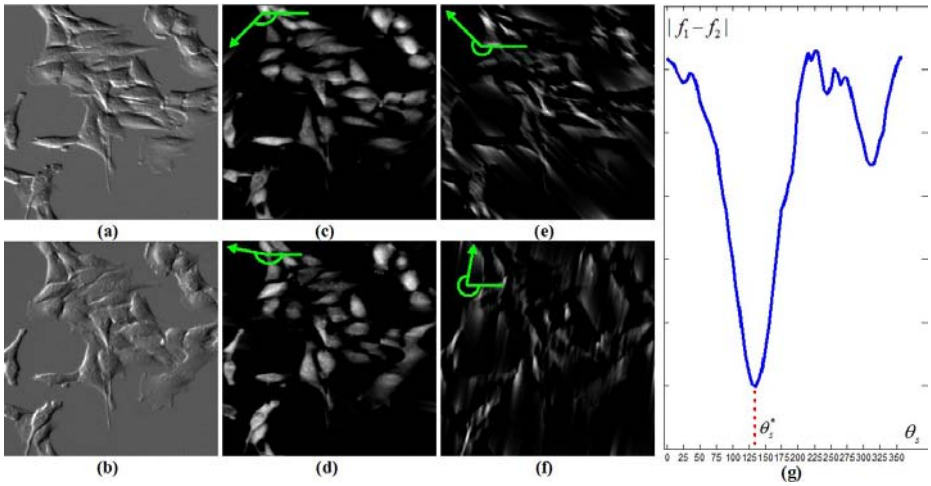

Fig. 6. Estimate the shear direction. (a,b) Image 1 and 2; (c,d) The restorations corresponding to the correct shear directions; (e,f): The restorations corresponding to wrong shear directions; (g) The difference between two restored images is a function of the shear direction.

5 Experiment Results

We captured DIC images from different shear directions by manually rotating the specimen dish on the stage. The collected images are registered automatically by our ICP algorithm and the shear directions of each image is estimated by our coarse-to-fine grid search algorithm.

First, we qualitatively evaluate our restoration results. Fig. 7(a) shows an image (700*700 pixels) on two cells with high magnification. When we apply the direct solver on the captured images individually, we observe different restoration results (Fig. 7(c-h)). The ensemble restoration on the entire collection of images reveals the cells' optical path length much better and has less noise left on the restoration (Fig. 7(b)). Fig. 8 show the other three collections of DIC images we acquired with low magnification and their image restorations. Compared to the independent restorations (e.g. the last two columns of Figure 8), the jointly restored image by an ensemble of DIC images are closer to the physical properties of cells. There is less ambiguity to compute the optical path length in joint restoration than the rotation-variant independent restoration.

To quantitatively evaluate the effect of our restoration results on microscopy image analysis, we apply it onto the cell segmentation task. As we see in the third column

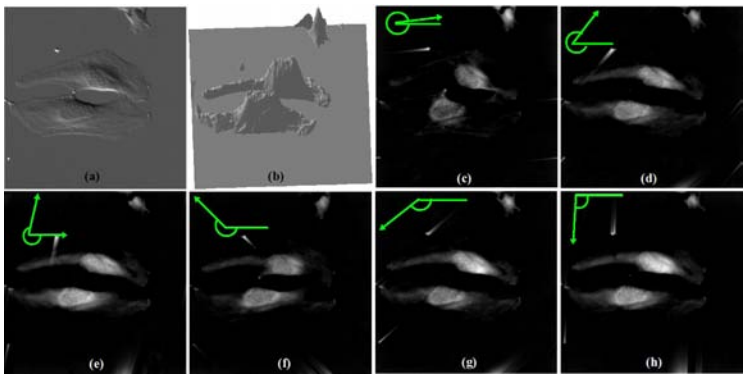

Fig. 7. Reconstructing DIC images. (a) One DIC image of the image collection; (b) The reconstructed OPL from a collection of DIC images (3D surface view); (c-i) The independent restoration from individual DIC images (green arrows denote the shear directions).

of Fig. 8, since the pixel values in the restored images represent the specimen's inherent properties, there is no pseudo 3D shadow-cast effect in the images. In the restored images, cell pixels are always positive against approximately zero background, thus images can be easily segmented by straightforward thresholding for further applications of cell counting, tracking etc., which is not easily possible with original DIC images. We manually label all cell boundaries in each image collection as ground truth masks. After thresholding the restored DIC image to obtain the cell mask, we compare it with the manually-labelled ground truth mask using the accuracy as the evaluation measure

$$\text{ACC} = (|\text{TP}| + |N| - |\text{FP}|)/(|P| + |N|) \tag{15}$$

where cell and background pixels are denoted as positive (P) and negative (N) respectively, true positive (TP) stands for those cell pixels correctly labelled by both human annotator and computer algorithms, and false positive (FP) are those cell pixels classified by computer algorithms mistakenly. We use the same technique in [16] to learn the best threshold for segmentation.

With K DIC images, we pick k ($k = 1...K$) of them as a collection and run our restoration algorithm on this collection. For example, when $k = 1$ we run the restoration algorithm on each single DIC image. When $k = 5$, we pick 5 images from the K DIC images and run the restoration. We exhaustively tested all the possible combinatorial choices, and computed the mean and standard deviation on the accuracy regarding to different image collection sizes. As we see in Fig. 9, there are more ambiguities (the vertical red bar in Fig. 9) among different restoration results when the image collection size k is small. As more images are added into the image collection, the restoration accuracy increases and the ambiguity decreases. The accuracy curve levels off when enough DIC images from different shear directions are included into the image collection. Overall, we achieve the segmentation accuracy of $81\% - 95\%$ on the three collections of DIC images. Difficulties were encountered during the restoration of predominantly flat cells that consequently had low gradient values in the observed DIC images. Less sparsity regularization on these regions may overcome the challenge. We leave the spatially-adaptive regularization in the future work to explore.

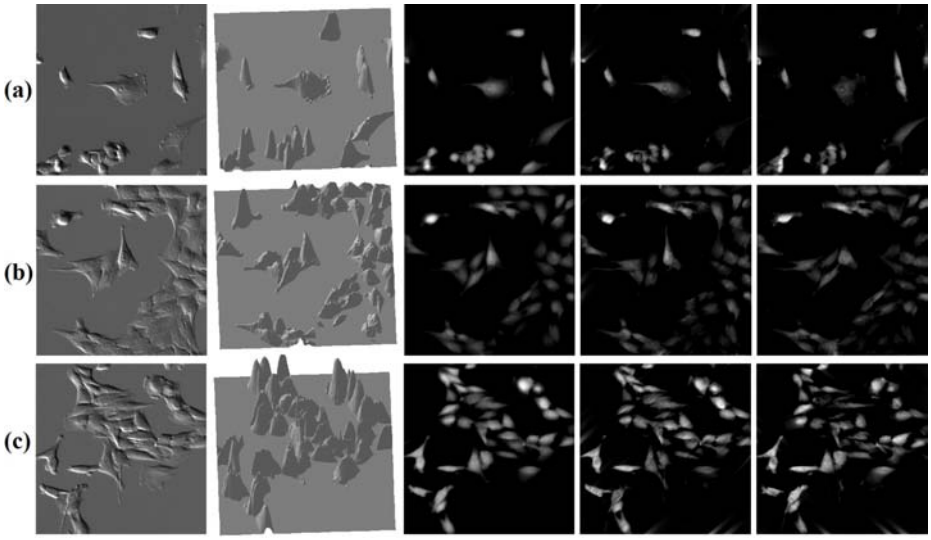

Fig. 8. Restoring DIC images. Column 1: one sample image in each collection; Column 2: the jointly reconstructed OPL (3D surface view); Column 3: The reconstructed DIC images whose intensity values correspond to the reconstructed OPL values; Column 4 and 5: Two independent restorations of DIC images with different shear directions, as comparisons to the ensemble restoration.

6 Conclusions

In DIC microscopy images, the intensity values are proportional to the gradient of specimen's optical path length (OPL). To quantitatively measure specimen's physical properties directly, we propose to restore DIC images from multiple shear directions. The specimen dish is manually rotated to acquire a collection of DIC images with different shear directions. An Iterative Closest Point algorithm is designed to register these images, and the shear directions of the image dataset are automatically estimated by our coarse-to-fine grid search algorithm. We formulate the restoration problem by minimizing a regularized a cost function with a closed-form solution.

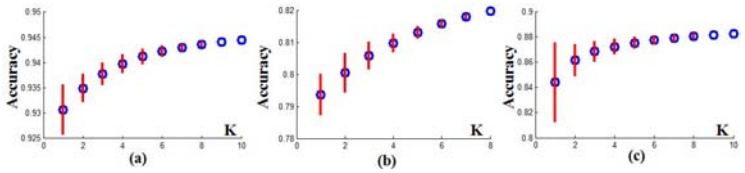

Fig. 9. The mean (blue circle) and stand deviation (red bar) of the segmentation accuracy when using different image collection size k. (a,b,c) are evaluation results from three image datasets corresponding to Figure 8(a,b,c), respectively.

Compared to the reconstruction methods based on a single DIC image which may reconstruct different optical path lengths according to different shear directions, our

method is orientation-invariant. Without the strict requirement of at least two orthogonal shear directions as needed by the previous multiple-image-based reconstruction techniques, our approach can restore DIC images from various shear directions. As qualitatively and quantitatively proved by our experiments, restoration from multiple shear directions can decrease the ambiguity among different individual restorations. The restored DIC images are directly proportional to specimen's physical measurements without the pseudo 3D effect, which is very amenable for microscopy image analysis such as cell segmentation.

Acknowledgements

We would like to thank Dr. Frederick Lanni for useful discussions and assistance with DIC microscopy. This work was supported by NIH grants RO1EB004343 & RO1EB007369.

References

1. Arnison, M., Larkin, K., Sheppard, C., Smith, N., Cogswell, C.: Linear phase imaging using differential interference contrast microscopy. J. Microsc. 214, 7–12 (2003)
2. Arnison, M., Cogswell, C., Smith, N., Fekete, P., Larkin, K.: Using the hilbert transform for 3d visualization of differential interference contrast microscope images. J. Microsc. 199(1), 79–84 (2000)
3. Baraniuk, R.: Compressive sensing. IEEE Sig. Proc. Mag. 24(4), 118–121 (2007)
4. Besel, P., Mckay, N.: A method for registration of 3-d shapes. IEEE Trans. on Pattern Recognition and Machine Intelligence 14(2), 239–256 (1992)
5. Harris, C., Stephens, M.: A combined corner and edge detector. In: the 4th Alvey Vision Conference (1988)
6. Heise, B., Arminger, B.: Some aspects about quantitative reconstruction for differential interference contrast (dic) microscopy. In: ICIAM07 (2007)
7. Heise, B., Snnleitner, A., Klement, E.: Dic image reconstruction on large cell scans. Microscopy Research and Techniques 66, 312–320 (2005)
8. Kam, Z.: Microscopic differential interference contrast image processing by line integration (lid) and deconvolution. Bioimaging 6, 166–176 (1998)
9. King, S., Libertun, A., Piestun, R., Cogswell, C.: Quantitative phase microscopy through differential interference imaging. J. BioMed. Opt. 13, 024020 (2008)
10. Li, K., Kanade, T.: Nonnegative mixed-norm preconditioning for microscopy image segmentation. In: Information Processing in Medical Imaging (2009)
11. Munster, E., Vliet, L., Aten, J.: Reconstruction of optical path length distributions from images obtained by a wide-field differential interference contrast microscope. J. Microsc. 188, 149–157 (1997)
12. Murphy, D.: Fundamentals of Light Microscopy and Electronic Imaging. Wiley (2001)
13. Preza, C.: Rotational-diversity phase estimation from differential-interference-contrast microscopy images. J. of the Opt. Soc. of America A 17(3), 415–424 (2000)
14. Preza, C., Snyder, D., Conchello, J.A.: Theoretical development and experimental evaluation of imaging models for differential interference contrast microscopy. J. Opt. Soc. Am. A 16(9), 2185–2199 (1999)
15. Shribak, M., LaFountain, J., Biggs, D., Inoue, S.: Orientation-independent differential interference contrast (dic) microscopy and its combination with orientation-independent polarization system. J. Biomed. Opt. 13(1), 014011 (2008)
16. Yin, Z., Li, K., Kanade, T., Chen, M.: Understanding the optics to aid microscopy image segmentation. In: Medical Image Computing and Computer Assisted Intervention (2010)

APPENDIX A6: ROLE OF RHOA SPECIFIC GUANINE EXCHANGE FACTORS IN REGULATION OF ENDOMITOSIS IN MEGAKARYOCYTES

Based on published work:

Role of RhoA Specific Guanine Exchange Factors in Regulation of Endomitosis in Megakaryocytes

Yuan Gao, Elenoe Smith, Dai Fei Elmer Ker, Phil Campbell, Ee-chun Cheng, Siying Zou, Sharon Lin, Lin Wang, Stephanie Halene, Diane S. Krause

Developmental Cell. 2012 March; **Accepted**.

A6.1 RELEVANCE TO THESIS

This section is the result of collaborative work with Diane Krause's research group at Yale University and illustrates the use of fluorescence time-lapse microscopy to understand the mechanism of endomitosis during megakaryocyte differentiation. The final version of the manuscript did not include fluorescence time-lapse microscopy data acquired at Carnegie Mellon University but it is included in this thesis for reference.

Role of RhoA Specific Guanine Exchange Factors in Regulation of Endomitosis in Megakaryocytes

[1]Yuan Gao, [2]Elenoe Smith, [3]Elmer Ker, [3]Phil Campbell, [2]Ee-chun Cheng, [2]Siying Zou, [1]Sharon Lin, [1]Lin Wang, [4]Stephanie Halene, [1]Diane S. Krause

[1] Department of Laboratory Medicine, Yale University, New Haven, CT 06520, USA.
[2] Department of Cell Biology, Yale University, New Haven, CT 06905, USA.
[3] Biomedical Engineering and Biological Sciences, Carnegie Mellon University, Pittsburgh, PA 15213, USA.
[4] Department of Internal Medicine, Yale University, New Haven, CT 06520, USA.

Summary

Polyploidization can precede the development of aneuploidy in cancer. Polyploidization in megakaryocytes, in contrast, is a highly controlled developmental process critical for efficient platelet production via unknown mechanisms. Using primary cells, we demonstrate that the guanine exchange factors GEF-H1 and ECT2, which are often overexpressed in cancer and are essential for RhoA activation during cytokinesis, must be downregulated for megakaryocyte polyploidization. The first (2N-to-4N) endomitotic cycle requires GEF-H1 downregulation while subsequent cycles (>4N) require ECT2 downregulation. Exogenous expression of both GEF-H1 and ECT2 prevents endomitosis, resulting in proliferation of 2N megakaryocytes. Furthermore, we have shown that the mechanism by which polyploidization is prevented in megakaryocytes lacking Mkl1, which is mutated in megakaryocytic leukemia, is via elevated GEF-H1 expression; shRNA-mediated GEF-H1 knockdown alone rescues this ploidy defect. These novel mechanistic insights enhance our understanding of normal versus malignant megakaryocytopoiesis, as well as aberrant mitosis in aneuploid cancers.

Highlights

- *Lack of RhoA activation at the* equatorial regions *region during endomitotic cytokinesis in megakaryocytes.*
- *RhoA GEFs, GEF-H1 and ECT2, must be downregulated for megakaryocyte polyploidization*
- *Exogenous expression of GEF-H1 and ECT2 results in proliferation of 2N megakaryocytes.*
- *GEF-H1 downregulation in megakaryocytes is MKL1 dependent*

Introduction

Polyploidy resulting from cellular stress precedes aneuploidy, which can lead to tumors associated with transformation to malignancy and a poor prognosis (Nguyen and Ravid, 2006; Nguyen and Ravid, 2010). In contrast, polyploidy of megakaryocytes (Mk), the hematopoietic cells that give rise to platelets, is a tightly controlled normal differentiation process. Diploid megakaryoblasts differentiated from hematopoietic stem cells undergo a progressive increase in ploidy (up to 128N) due to repeated DNA replication without cell division, a process termed endomitosis, resulting in large multilobulated, polyploid nuclei (Battinelli et al., 2007). Polyploidization is essential for efficient platelet production. In megakaryoblastic leukemia, low ploidy megakaryoblasts predominate (Raslova et al., 2007).

Studies using time-lapse microscopy to observe endomitotic Mk suggest that the initial endomitotic cleavage event in which cells progress from 2N to 4N occurs due to failure at late cytokinesis with normal cleavage furrow ingression followed by furrow regression (Geddis et al., 2007; Papadantonakis et al., 2008; Lordier et al., 2008; Leysi-Derilou et al., 2010). These endomitotic Mk form an apparently intact midzone with normal localization of essential

components including Survivin, Aurora B, INCENP, PRC1 (protein regulating cytokinesis 1), MKLP1 and 2 (mitotic kinesin-like protein), MgcRacGAP and microtubules (Geddis and Kaushansky, 2006; Lordier et al., 2008;). During cytokinesis, RhoA signaling is required to establish the actomyosin ring at the cleavage furrow, generating the contraction force for completion of cytokinesis (Bement et al., 2005; Narumiya and Yasuda, 2006; Melendez J et al., 2011). Activated RhoA and its effectors (ROCK, Citron, LIM and mDia) are localized to the cleavage furrow (Madaule et al., 1998; Yasui et al., 1998; Kosako et al., 2002; Tolliday et al., 2002). Dominant-negative Citron and ROCK inhibitors prevent normal cytokinesis (Madaule , 1998; Kosako et al., 2000). In contrast to normal cytokinesis, the contractile ring of Mk undergoing endomitosis lacks non-muscle myosin IIA and contains decreased levels of RhoA and actin at the 2N to 4N transition; in higher ploidy cells, RhoA is not detectable at the cleavage furrow during anaphase (Geddis and Kaushansky, 2006; Lordier et al., 2008).

Rho family small GTPases (e.g. RhoA, Rac1, and Cdc42) are molecular switches that regulate many cellular processes including actin cytoskeleton reorganization, microtubule dynamics, cell cycle progression and cytokinesis (Etienne-Manneville and Hall, 2002). Rho GTPase switching from the inactive GDP-bound state to the active GTP-bound state is facilitated by a group of proteins called Dbl family guanine nucleotide-exchange factors (GEFs), which have a tandem Dbl homology (DH) - Pleckstrin homology (PH) domain, in which the DH domain contains GDP/GTP exchange activity (Rossman et al., 2005). GEFs are involved in RhoA localization and activation during different stages of cytokinesis. Upon breakdown of the nuclear envelope during mitosis, the GEF ECT2 (Epithelial Cell Transforming Sequence 2) is dispersed from the nucleus to the cytoplasm, and recruited to the central spindle by the central spindlin complex (formed by

MKlp1 and MgcRacGAP) during late anaphase for establishment of the cleavage furrow (Petronczki et al., 2007; Yuce et al., 2005). ECT2, required for cell cycle progression, is an oncogene that resides on chromosome 3q26, a region frequently targeted for chromosomal alterations in human tumors and overexpressed in many primary human tumors (Fields and Justilien, 2010; Iyoda et al., 2010). RNAi knock-down of ECT2 results in mitotic failure and binucleate cells due to the lack of cleavage furrow ingression (Birkenfeld et al., 2007). There are multiple studies suggested that ECT2 is important for RhoA localization and activation during cleavage furrow formation and ingression (Yuce et al., 2005; Nishimura and Yonemura, 2005; Yoshizaki et al., 2004), whereas some evidence suggested ECT2 may not be directly responsible for RhoA activation during furrow ingression. Without ECT2, RhoA still gets activated, but is mislocalized from the cleavage furrow (Chalamalasetty et al., 2006; Birkenfeld et al., 2007). An N-terminal fragment of ECT2 lacking the catalytic DH/PH domain can rescue the furrow ingression defect in ECT2 RNAi treated cells (Chalamalasetty et al., 2006). Thus, ECT2 recruits RhoA to the cleavage furrow, but may not directly catalyze its activation.

The microtubule associated protein GEF-H1, plays a critical role in cytokinesis by activating RhoA at the cleavage furrow (Birkenfeld et al., 2007). Association with polymerized microtubules inactivates GEF-H1 (Krendel et al., 2002). A truncated form of GEF-H1 lacking its microtubule-binding ability was discovered in the monocytic leukemia cell line U937 and is able to induce tumor formation in nude mice (Brecht et al., 2005). Also *GEF-H1* is transcriptionally activated by mutant p53, and its expression is strongly induced in mutant *p53* cell lines, leading to accelerated tumor cell proliferation (Mizuarai et al., 2006). During mitosis, GEF-H1 is first associated with the microtubule spindle, and later with the midbody (Birkenfeld et al., 2007).

The same authors also show that GEF-H1 binding to microtubules is facilitated by phosphorylation at Ser^{885} and Ser^{959} by the mitotic kinases Aurora A/B and Cdk1, respectively. At the onset of cytokinesis, GEF-H1 is dephosphorylated and released from microtubules so that it can activate RhoA. In contrast to ECT2 RNAi, in which cytokinesis is blocked and there is no cleavage furrow formation, GEF-H1 knock down causes a defect at a later stage of cytokinesis - the cleavage furrow is induced normally, but the furrow fails to close completely resulting in binucleate cells (Birkenfeld et al., 2007).

Because of the importance of mitotic GEFs in RhoA localization and activation during cytokinesis, we hypothesized that decreased RhoA activation in Mk endomitosis may be caused by a decrease in mitotic GEFs. In the present work, we show that both GEF-H1 and ECT2 are downregulated at the mRNA and protein levels during Mk polyploidization. We show that MKL1-regulated GEF-H1 downregulation is required for endomitosis of 2N cells to become 4N, whereas ECT2 downregulation is required for polyploidization beyond the 4N stage. Together, these decreases in ECT2 and GEF-H1 are responsible for the decreased RhoA signaling that occurs in endomitosis, and downregulation of GEF-H1 represents one of the initiating events of endomitosis.

Results

Establishment of in vitro models to study megakaryocyte endomitosis

We used primary murine Mk to study the involvement of Dbl family GEFs in Mk endomitosis. The first endomitotic event from 2N to 4N Mk occurs due to failure of cytokinesis at a late stage of cytokinesis with cleavage furrow regression. In contrast, there are different reports for when

subsequent endomitotic events driving 4N to higher ploidy Mk interrupt the normal cytokinesis machinery. Some report significant cleavage furrow formation for higher ploidy Mks (Lordier et al., 2008; Leysi-Derilou et al., 2010), while others report little apparent cleavage furrow formation in high ploidy endomitosis (Geddis et al., 2007; Papadantonakis et al., 2008). Therefore, we first examined how primary mouse Mk undergo endomitosis at different stages using Mks from GFP-tagged Histone 2B (H2B-GFP) transgenic mice visualized by timelapse microscopy for changes in both chromatin and cell morphology during endomitosis. Mk progenitors (MkP, $Kit^{+}CD41^{+}$) sorted from BM were cultured in Tpo-only differentiation medium (DM) to promote Mk polyploidization. MkP endomitotic events were recorded by time-lapse microscopy, and 2N, 4N and higher ploidy MKs were distinguished based on division history as well as their cell size after mitosis or endomitosis, a method established previously (Levine et al., 1982; Leysi-Derilou et al., 2010; Tomer, 2004; Tomer et al., 1988). Of the 2N cells (24 events) whose DNA division events we observed, 80% of 2N DNA divisions resulted in endomitosis with clear cleavage furrow formation followed by regression and formation of 4N cells (Fig. 1a, Movie S1), 7% of 2N cells underwent endomitosis without significant cleavage furrow ingression, and 13% of 2N cells underwent normal mitosis with complete cytokinesis. In contrast, for division of cells that started out with ≥ 4N DNA (37 events), 86% of divisions were endomitotic without noticeable cleavage furrow ingression (Fig. 1b, Movie S2), and 14% were endomitotic with significant cleavage furrow ingression followed by regression. Our data confirm that there are two distinct phases of endomitosis in mouse primary Mks: for the 2N to 4N transition, the cleavage furrow forms but fails to complete cytokinesis; and for ≥4N endomitosis, there is usually, but not always, little to no cleavage furrow ingression.

RhoA is not activated at the cleavage furrow during endomitosis

RhoA activity is important for cleavage furrow ingression during cytokinesis. To understand the mechanisms underlying the failure to complete cytokinesis in 2N to 4N Mk endomitosis, we assayed localization of active RhoA during endomitosis using a FRET-based RhoA biosensor. As a control, total RhoA was also assessed. The biphenotypic megakaryocyte-erythroid progenitor population as defined by Akashi et al. and refined (Lin-Sca-Kit^{+}CD41^{-} CD150^{+}CD105^{-}) and renamed 'preMegE' by Pronk *et al.* (Akashi et al., 2000; Pronk et al., 2007), was sorted from BM and cultured in growth medium (GM) with SCF, TPO, IL-3 and Flt-3 to serve as normal mitotic controls. Under these conditions, 100% of 2N cells undergoing mitosis complete cytokinesis (data not showed). RhoA is highly concentrated at the equatorial cortex as previously reported (Yuce et al., 2005), and also weakly associated with the central spindle in preMegE cells (Fig. 2a i-iii), while at the end of cytokinesis, RhoA is localized to the midbody (Fig. 2a iv-vi). When MkP are cultured in DM, during endomitotic anaphase and cytokinesis, less RhoA is seen, but it is still localized to the equatorial region (Fig. 2a vii-ix) and midbody (Fig. 2a x-xii). To better quantify the change of RhoA protein level during Mk differentiation, the RhoA protein levels from different stage of Mk differentiation as well as in platelets were analyzed by Western-Blotting. As shown in Figure S1, total RhoA protein was only slightly decreased (20%) during Mk differentiation, which is in agreement with the almost constant level of RhoA during Mk differentiation of CD34^{+} human blood cells (Chang et al. 2007).

In contrast to previous reports, we observed central spindle abnormalities in endomitotic cells (Fig. 2a viii), where the central spindle was either missing or misshapen. To assess RhoA activation directly, a widely-used single molecule RhoA activation FRET probe (Birkenfeld et al.,

2007; Pertz et al., 2006), pBabe-Puro-RhoA Biosensor, was transduced into primary mouse megakaryocytes, and the FRET efficiencies (FRET/CFP ratio) in cells entering anaphase were monitored with a Leica SP5 scanning microscope equipped with temperature and CO_2 control. Similar to endogenous RhoA shown above, CFP fluorescence of the biosensor was concentrated at the equatorial region of endomitotic cells (Fig. 2b; CFP panel). However, there was no significant FRET signal in this region, indicating lack of RhoA activation during megakaryocyte endomitosis at the cleavage furrow. As a positive control, we also analyzed RhoA activation during normal mitosis of NIH3T3 cells transduced with same RhoA biosensor under identical conditions. As shown in Figure 2c, NIH3T3 cells undergo mitosis show accumulation of RhoA biosensor at the equatorial region and also have high FRET signal at the cleavage furrow indicating high RhoA activity at this region, in agreement with published data on RhoA activation during cytokinesis in NIH3T3 cells (Yoshizaki et al., 2003). Our data provide the first direct evidence that during 2N to 4N endomitosis, there is a failure of RhoA activation at the cleavage furrow, even though RhoA is localized correctly to this region.

GEF-H1 and ECT2 levels decrease during Mk polyploidization

To investigate the mechanisms underlying the failure of RhoA activation in Mks during endomitosis of 2N cells, and the absence of RhoA protein at the cleavage furrow region during endomitosis of higher ploidy cells, we assessed whether the mitosis-associated GEFs, ECT2 and GEF-H1, are differentially expressed during Mk differentiation. WT PreMegE and MkP were cultured in DM, and RNA expression assessed by quantitative RT-PCR over time. As shown in Figure 3, MkPs have lower levels of both GEF-H1 and ECT2 mRNA compared with preMegE, and Tpo treatment of preMegE decreases GEF-H1 and ECT2 mRNA levels by 67% and 78%,

respectively. GEF-H1 mRNA levels subsequently increased after prolonged Tpo exposure when high ploidy Mk were forming, whereas ECT2 mRNA levels remained low. GEF-H1 and ECT2 protein levels also decreased (Fig. 3c), but with slightly different kinetics than the mRNA: GEF-H1 protein reached a nadir after 1 day of culture of preMegE in Tpo medium, and then began to increase; in contrast, ECT2 protein levels were significantly decreased after two days, and then remained low.

GEF-H1 and ECT2 levels during endomitosis

ECT2 expression is induced by growth factors that promote cell cycle entry, and cells in G0 have little ECT2 (Saito et al., 2003). However, it is unlikely that decreased GEF-H1 and ECT2 levels during Tpo-induced Mk differentiation are caused by cell cycle exit. First, Tpo induces Mk progenitor cell cycling (Drayer, 2006). Second, the level of Anillin protein, an indicator of mitotic activity, which peaks in mitosis and decreases dramatically upon mitotic exit (Zhao and Fang, 2005), increased dramatically upon Mk Tpo treatment (Fig. S1), indicating increased cell cycling after Tpo treatment. To directly confirm that Mks undergoing the cell cycle have decreased GEF-H1 and ECT2 levels, we examined GEF-H1 and ECT2 protein in endomitotic Mks by immunofluorescence. In mitotic control cells (preMegEs in GM for one day), the microtubule spindle is normal, and GEF-H1 co-localizes with the microtubule spindle as reported previously (Birkenfeld et al., 2007) (Fig. 4a i-iii). In contrast, in endomitotic MkP cultured in DM for one day, the GEF-H1 protein level is low with little fluorescence signal detected above background (Fig. 4a iv-vi). After 2 days in DM, in polyploid (>4N) cells undergoing anaphase, the spindle appeared normal, and GEF-H1 protein was again easily detected with localization to the microtubule spindle (Fig. 4a vii-ix). The relative increase in

GEF-H1 was consistent with the changes in protein levels detected by Western blotting (Fig. 3c). In preMegE mitosis controls, ECT2 localized to the central spindle (Fig. 4b i-iii) as published previously (Tatsumoto et al., 1999; Yuce et al., 2005). During 2N to 4N endomitosis of MkP, ECT2 was easily detected and localized to the central spindle (Fig. 4b iv-vi). The immunofluorescence signal between these two samples did not show any apparent differences (Fig. 4bi, 4biv), although the ECT2 protein level in Mkp is about 30% lower than that of preMegE by Western-Blot (Fig. 3c). In high ploidy cells, ECT2 protein levels were very low (Fig. 4b, vii-ix), which is in agreement with the Western Blot data (Fig. 3c, S1). These data not only confirm that in endomitotic Mk cells, GEF-H1 and ECT2 levels decreases (albeit with different kinetics), but also suggest that during Mk differentiation, loss of GEF-H1 predominates in low ploidy Mk, whereas loss of ECT2 occurs later and predominates in higher ploidy endomitosis.

Ectopic expression of GEF-H1 or ECT2 causes low ploidy Mks in vitro

To test whether the decreases in GEF-H1 and/or ECT2 cause the sequential stages of endomitosis, we expressed exogenous GEF-H1 or ECT2 by retroviral transduction of preMegE cells, which were then induced to differentiate with DM in which 80% of mitotic events are endomitotic. After 3 days in DM, the ploidy of GFP positive (control vector vs. ECT2 overexpression vs. GEF-H1 overexpression) $CD41^+$ Mks was assessed by flow cytometry. Enforced expression of ECT2 or GEF-H1 did not affect the percentage of cells that were $CD41^+$ (Fig. S2), suggesting that exogenous GEF-H1 or ECT2 does not affect preMegE differentiation down the Mk lineage. Cells transduced with empty viral vector had a normal Mk ploidy distribution. Although enforced expression of either GEF-H1 or ECT2 resulted in significantly

decreased mean ploidy (Fig. 5a,b), the ploidy profiles were significantly different. GEF-H1 caused an increase in 2N cells, although Mks that became 4N were still able to become highly polyploid (Fig. 5a, middle). In contrast, ECT2 expression led to accumulation at the 2N, 4N and 8N stage with far fewer cells having >8N (Figure 5b, right). We believe that the 8N peak in cells overexpressing ECT2 represents the G2/M peak of cycling 4N cells. Expression of GEF-H1 and ECT2 was confirmed by Western blot (figure 5d). To evaluate whether enforced expression of GEF-H1 plus ECT2 completely prevents endomitosis, we transduced preMegE cells with both GEF-H1 (with IRES-RFP) and ECT2 (with IRES-GFP) retroviruses. After 3 days in Tpo, the ploidy of $CD41^+$ RFP+ and GFP+ (double positive) cells was determined. Compared with cells only expressing GEF-H1 or ECT2, double positive cells have more 2N cells, and far fewer >4N cells (Fig. 5c, far right, upper panel). These data indicate that exogenous expression of GEF-H1 prevents the progression of cells from 2N to 4N in the first endomitotic event, whereas exogenous expression of ECT2 prevents the subsequent >4N endomitotic events to form highly polyploid Mk. Since RhoA acts downstream of ECT2 and GEF-H1, we next tested whether the dominant-negative RhoA mutant RhoA N19 can block the effect on Mk ploidy caused by enforced expression of ECT2 or GEF-H1 in Mk. As shown in Fig. 5c (lower panel), the ability to make high ploidy Mk was restored in cells expressing both GEF-H1 and RhoA N19 or ECT2 and RhoA N19 compared with only expressing GEF-H1 or ECT2 (Fig. 2c, upper panel).

To assess whether downregulation of GEF-H1 plays a role in polyploidization of Mk *in vivo*, GEF-H1 transduced CD45.1 BM cells were transplanted into lethally irradiated WT CD45.2 mice. After 6 weeks, the ploidy of GFP positive (control vector vs. GEF-H1 transduced) Mks was assessed. In agreement with *in vitro* differentiation, ectopic expression of GEF-H1 resulted

in more 2N Mks (27.8%) compared with empty vector (13.1%), leading to a decrease in the average ploidy (Fig. 5e, f). However, as seen *in vitro*, those GEF-H1 transduced cells that did become 4N were able to undergo subsequent further polyploidization. These data demonstrate that enforced GEF-H1 decreases the likelihood of 2N to 4N endomitotic events in Mks *in vivo*.

Down-regulation of GEF-H1 during Mk differentiation is mediated by MKL1

Our lab previously demonstrated that knockout of the transcriptional cofactor Megakaryoblastic leukemia 1 (MKL1) leads to reduced Mk ploidy *in vivo* (Cheng et al., 2009). To study whether the down-regulation of GEF-H1 and/or ECT2 during Mk differentiation is MKL1 dependent, we analyzed GEF-H1 and ECT2 mRNA levels during Mk differentiation of preMegE and MkP from $Mkl1^{-/-}$ and WT mice. GEF-H1 levels in both preMegE and MkP are more than 15 times higher in $Mkl1^{-/-}$ mice than in WT mice (Fig. 6a). Unlike WT cells, there is little decrease of GEF-H1 mRNA in $Mkl1^{-/-}$ cells differentiated *in vitro*. In contrast, ECT2 mRNA levels are the same in $Mkl1^{-/-}$ vs. WT cells (Fig. 6b).

We next assessed GEF-H1 protein expression and localization in $Mkl1^{-/-}$ vs. WT preMegE cultured for 1 day in DM. GEF-H1expression is much higher in $Mkl1^{-/-}$ Mk than WT, although it is localized to both the cell periphery and the microtubule spindle compared with predominantly spindle localization in WT cells during normal mitosis (Fig. 6c). No obvious differences between WT and $Mkl1^{-/-}$ cells were found in ECT2 detection or localization (data not shown). As expected with higher GEF-H1 levels in Mkl1 knock out preMegE and Mk, GTP-bound active RhoA levels in preMegE with or without 24h exposure to Tpo are higher than wild type (Fig. S3). However the RhoA activity in $Mkl1^{-/-}$ cells is able to decrease after one day in Tpo similar

to wild type cells (Fig. S3). To further confirm that GEF-H1 down-regulation is MKL1-dependent, we assessed the GEF-H1 mRNA levels in nonhematopoietic 293FT cells transfected with control vector, wild type, constitutive active, or dominant negative MKL1 constructs. Wild type MKL1 slightly decreased GEF-H1, constitutively active MKL1 further decreased GEF-H1 levels, and dominant negative MKL1 actually increased GEF-H1 levels (Fig. 6d,e). MKL1 is part of the t(1;22)(p13;q13) chromosomal translocation, associated with acute megakaryoblastic leukemia (Mercher, 2001; Ma 2001). To test whether GEF-H1 is dysregulated in acute megakaryoblastic leukemia containing the MKL1 translocation, we analyzed the levels of GEF-H1 and ECT2 in 6133 cells, a megakaryoblastic leukemia cell line derived from a transgenic mouse in which MKL1 was knocked in downstream of exon 1 of RBM15 to allow expression of the OTT-MKL1 fusion product (Mercher et al., 2009), compared with wild type preMegE. As shown (Fig. 6f), 6133 cells express elevated GEF-H1 and ECT2 compared to normal Mk progenitor preMegE. In summary, GEF-H1 is down-regulated by MKL1 during Mk differentiation, whereas the ECT2 decrease is MKL1-independent, and acute megakaryoblastic leukemia cells have increased GEF-H1 expression.

Knock-down of GEF-H1 rescues the ploidy defect in Mkl1$^{-/-}$ Mks

In order to test whether downregulation of GEF-H1 alone can restore polyploidization in Mkl1$^{-/-}$ Mk, we decreased GEF-H1 by shRNA in WT and Mkl1$^{-/-}$ PreMegE, that were then differentiated in DM. As expected, GEF-H1 shRNA had no effect on WT Mk ploidy compared with a control shRNA targeting luciferase (Fig. 7a). Mks differentiated from Mkl1$^{-/-}$ cells transduced with control shRNA had lower ploidy than WT cells (Fig. 7a). However, transduction of Mkl1$^{-/-}$ Mks with GEF-H1 shRNA led to much higher ploidy (Fig. 7a, far right). The average ploidy for each

condition (Fig. 7b) demonstrates that shRNA against GEF-H1 restores the ploidy level of Mkl1$^{-/-}$ cells to that of WT cells. The GEF-H1 shRNA construct was validated in mouse NIH3T3 cells, in which there was approximately 70% knock-down (Fig. 7c).

Discussion

Our data confirm that there are two distinct stages of Mk endomitosis. For the 2N to 4N transition, cleavage furrow ingression occurs followed by furrow regression, whereas in endomitosis associated with ≥ 4N cells, there is little cleavage furrow ingression. Our data provide the first direct evidence that RhoA activation is absent from the cleavage furrow during the first of endomitotic cleavage, and that two mitotic GEFs, GEF-H1 and ECT2, are down-regulated during megakaryocyte differentiation. Overexpression of GEF-H1 in differentiating Mk leads to more 2N MKs, but for those cells that do fail to complete cytokinesis, high levels of polyploidization are still achievable. In contrast, exogenous ECT2 inhibits 4N polyploid cells undergoing endomitosis but does not affect proliferation of 2N and 4N cells. Enforced overexpression of both GEF-H1 and ECT2 completely prevents polyploidization of primary megakaryocytes. A schematic summarizing our findings that GEFH1 and ECT2 are essential for subsequent stages of Mk endomitosis is shown in Figure S4.

We conclude that decrease of GEF-H1 during megakaryocytopoiesis is mediated by the transcriptional cofactor MKL1, based on the markedly elevated GEF-H1 expression in Mkl1$^{-/-}$ Mk, and the downregulation of GEF-H1 in 293FT cells overexpressing constitutively active MKL1. The block of polyploidization in Mkl1$^{-/-}$ Mk can be restored by shRNA-mediated downregulation of GEF-H1, further confirming that GEF-H1 is downstream of MKL1.

Using primary murine preMegE and MkP differentiated *in vitro* down the Mk lineage with TPO, we observed late cytokinesis defects in the first round of endomitosis whereas for later rounds of endomitosis (>=4N), the majority of endomitosis occurred without apparent cleavage furrow ingression. These data differ from reports on endomitosis of human CD34+ derived Mk, especially cord blood CD34+, in which only about 30% of 2N cells undergo endomitosis, and the majority of high ploidy cells showed significant furrow ingression, and some high ploidy cells were able to complete cytokinesis and divide to two high ploidy cells (Lordier et al., 2008; Leysi-Derilou et al., 2010). The low endomitosis ratio at the 2N stage of the human CD34+ derived Mks may be due to contamination with other cell types, and the majority of immunofluorescence images of those cells may represent normal mitotic divisions. Alternatively, there may be intrinsic differences between murine and human megakaryopoiesis, especially that of cord blood. While the absence of cleavage furrow formation in high ploidy endomitosis has been reported previously as being associated with a lack of accumulation of RhoA (Lordier et al., 2008, Geddis et al., 2006), the mechanism of cytokinesis failure in the early rounds of endomitosis was previously unknown since RhoA was correctly localized to the cleavage furrow at the 2N stage. Here we show that this correctly localized RhoA is not activated in cells undergoing endomitosis with a FRET-based RhoA activity biosensor in live Mk.

We show that the mRNA and protein levels of two RhoA GEFs involved in cytokinesis are decreased with different kinetics during Mk differentiation: the reduction of GEF-H1 occurs at the 2N to 4N stage, while the significant reduction of ECT2 protein occurs at 4N and higher stages. Forced expressing GEF-H1 results in a higher percentage of Mk that are 2N, although

high ploidy Mk can still form, whereas forced expression of ECT2 results in accumulation of 2N to 8N Mks, and a lack of higher ploidy Mk. Taken together, these data suggest that loss of GEF-H1 and ECT2 play distinct roles in Mk polyploidization: in low ploidy cells, with correct ECT2 localization at the central spindle, RhoA is recruited to the equatorial region, but due to the lack of GEF-H1 protein, most of this RhoA is inactive. In high ploidy cells, despite restored levels of GEF-H1, significantly decreased levels of ECT2 lead to failure of RhoA recruitment to the equatorial region. GEF-H1 levels decrease again in platelets (Fig. S1). As we and others reported previously (Halene et al., 2010; Patel et al., 2005), the extensive microtubule network and actin cytoskeleton are essential for Mk maturation, platelet formation and function. It is thus possible that the reappearance of GEF-H1, a unique microtubule-associated RhoA GEF, in higher ploidy Mks may be essential for subsequent Mk maturation but not for platelet function.

Our data from $Mkl1^{-/-}$ mice and overexpression of constitutively active (nuclear) MKL1 in 293FT cells suggest that MKL1 down-regulates GEF-H1 mRNA, but not ECT2. MKL1 is a transcriptional cofactor for SRF. MKL1 is up-regulated and required for Mk maturation and the formation of highly polyploid Mk (Cheng et al., 2009). There is a confirmed SRF binding site close to the GEF-H1 promoter region (Cooper et al., 2007). The mechanism by which MKL1 causes reduction of GEF-H1 during Mk differentiation requires further study.

Acute megakaryoblastic leukemia is characterized by a high percentage of immature, low ploidy megakaryoblasts. We showed that GEF-H1 and ECT2 levels are dramatically increased in a megakaryoblastic leukemia cell line derived from a mouse AMKL model in which the t(1;22) fusion protein is encoded from the endogenous murine RBM15 locus. How and whether the

RBM15-MKL1 fusion protein regulates GEF-H1 and/or ECT2 expression remains to be shown. One possibility is that RBM15-MKL1 inhibits MKL1 activity, but this would not explain the increase in ECT2 levels. Future studies will need to explore the levels of GEF-H1 and ECT2 in AMKL patient samples, and whether targeting of either of these GEFs could be used to promote megakaryocyte polyploidy and maturation.

Furthermore, these novel mechanistic insights into the normal polyploidization process of Mk differentiation have important implications for aneuploid cells, and their malignant transformation. In normal Mk, although there are high levels of cyclin E (Eliades et al., 2010) and D (Muntean et al., 2007) activity, which are required to overcome the cell cycle checkpoints in high ploidy cells undergoing endomitosis, proliferation is controlled due to the lack of GEF-H1 and ECT2, which promotes polyploidy and stops expansion. In contrast, abnormal polyploid cells formed under stress conditions, with highly active GEF-H1 and ECT2, can divide, expand and transform to malignant aneuploid cells. Therefore GEF-H1 and ECT2 are potential therapeutic targets for cancer cell proliferation and expansion.

Experimental Procedures

Plasmids

pBabe-Puro-RhoA Biosensor retroviral plasmids from Klaus Hahn (Chapel Hill, NC) were purchased from Addgene. Full length human GEF-H1 and ECT2 cDNAs were obtained from Open Biosystems (Huntsville, AL). GEF-H1 was subcloned into the XhoI-EcoRI sites of the MigR1 IRES GFP retrovirus vector (kind gift of Warren Pear, Univ. of Pennsylvania) using a 5'-primer containing an HA-tag sequence CCGCTCGAGATGTACCCATACGATGTTCCAGAT

and a 3'- primer AGAATTCTTAGCTCTCGGAGGCTACAGC. The ECT2 cDNA digested with EcoRI was inserted into MigR1's EcoRI sites. A clone with the correct ECT2 orientation was confirmed by sequencing. To make the MigR1 IRES RFP, MigR1 GEF-H1 IRES RFP and MigR1 ECT2 IRES RFP retroviral vectors, the GFP fragments in the vectors were replaced with RFP from pCDNA3-TagRFP (kind gift of Roger Tsien, Univ. of California, San Diego) by PCR cloning with a 5'- primer GGG CC ATGGTGTCTAAGGGCGAAGAGCTG and a 3'- primer GGGGTCGACTTACTTGTACAGCTCGTCCATGCC at NcoI-SalI sites. Mieg3 RhoA N19 retroviral plasmids were a kind gift of Yi Zheng (Cincinnati, OH). The full-length Mkl1 expression plasmid was a kind gift of Stephan Morris (Memphis, TN). Constitutively active and dominant negative forms were produced by deletion of the N-terminal actin binding domain and transcriptional activation domains, respectively (Cen et al., 2003).

Cell sorting

All mouse procedures were performed according to Yale University Animal Care and Use Committee – approved protocols and complied with federal laws. Murine bone marrow (BM) cells were obtained by crushing hips, femurs and tibias in cold PBS with 1% FBS. After lineage depletion with the BD IMag™ Mouse Hematopoietic Progenitor (Stem) Cell Enrichment kit (BD Biosciences, San Jose, CA), the remaining BM cells were stained with FITC anti-CD41, PE anti-lineage markers, PE-Cy5 anti-CD150, PE-Cy7 anti-CD105, Alexa 647 anti-Sca1, and APC-Hy7 anti-Kit (CD117) antibodies (eBioscience, San Diego, CA, and Biolegend, San Diego, CA). The preMegE population, defined as the $Lin^-Sca^-Kit^+CD41^-CD105^-CD150^+$, and MkP population, defined as $Lin^-Sca^-Kit^+CD41^+$, were separated using a FACSAria sorter. For sorting MkP from

H2B-GFP transgenic mice (Jackson Laboratory, Bar Harbor, ME), we replace FITC anti-CD41 antibody with eFluoro-450 labeled anti-CD41 antibody (eBioscience).

Cell culture, megakaryocyte differentiation, and Western blotting

For expansion, sorted preMegE were cultured at 1 x10^6 cells/mL in Growth Medium containing StemSpan (StemCell Technologies, Vancouver, BC, Canada) supplemented with 30% BIT9500 (StemCell Technologies), 100 ng/mL murine SCF, 50 ng/mL murine Flt3-L, 10 ng/mL murine IL-3 (all purchased from PeproTech, Rocky Hill, NJ), 50 ng/mL murine Tpo, (from ConnStem, Cheshire, CT) and penicillin/streptomycin. For differentiation, sorted preMegE and MkP were cultured for three days in Differentiation Medium similar to the Growth Medium but with all cytokines replaced with 20 ng/mL murine Tpo. 6133 cells, a gift from Thomas Mercher (Villejuif, France), were grown as described (Mercher et al., 2009). For Western-blotting, about 1x10^5 cells per sample were washed with cold PBS buffer, lysed with RIPA buffer for 15 minutes, then centrifuged at 18,000g for 15 minutes. Platelet lysate was prepared as described (Halene et al., 2009), and 20 μg of lysate from each sample was analyzed by Western blot with the following antibodies: mouse anti-α-tubulin antibody (1:2000, Sigma-Aldrich), rabbit anti-GEF-H1 antibody (1:1000, Upstate), and rabbit anti-ECT2 antibody (1:500, Santa Cruz), and the corresponding secondary antibody. The density of protein bands was analyzed with ImageJ.

Time-lapse video microscopy

Primary murine MkP from H2B-GFP transgenic mice were sorted and cultured in 35mm glass bottom dishes (MatTeK, Ashland, MA) in differentiation medium. To maintain non-adherent cells within the field of view for time-lapse microscopy, 1% methylcellulose was added to

increase the viscosity to reduce cell movement caused by Brownian motion and convection currents. Live cell imaging was performed using a Vivaview system (Olympus, Japan) with a 20x objective. DIC and green fluorescence images were taken every 5 minutes for two days with an Orca-R2 camera (Hamamatsu, Japan). Imaging data were analyzed, compiled and exported into Quick Time video with Metamorph for Vivaview software.

Immunofluorescent staining and confocal analysis

PreMegE and MkP cells cultured as indicated, were cytospun onto glass slides, fixed with 3.7% formaldehyde for 15 minutes, and permeabilized with 0.1% Triton-X-100 (Sigma-Aldrich) for 15 minutes. After blocking (PBS plus 3% BSA), slides were incubated with mouse anti-α-tubulin antibody (1:200, Sigma-Aldrich) plus rabbit anti-GEF-H1 antibody (1:200, Upstate) or rabbit anti-ECT2 antibody (1:100, Santa Cruz), or incubated with rabbit anti-tubulin antibody (Abcam, Cambridge, MA) plus mouse anti-RhoA antibody (1:100 Santa Cruz). Bound antibody was detected using Alexa-488 labeled donkey anti-mouse secondary antibody and Alexa-555 labeled donkey anti-rabbit secondary antibody, or Alexa-488 labeled anti-rabbit secondary antibody and Alexa-555 labeled anti-mouse secondary antibody (Invitrogen). Fluorescent images were obtained on a Leica SP5 confocal microscope (Leica microsystem, Wetzlar, Germany).

Virus production and preMegE transduction

For retrovirus production, in a T-175 flask, 90% confluent 293 GP cells constitutively expressing Gag/Pol were transfected with 40 μg pBabe-Puro-RhoA Biosensor, MigR1 empty vector control, MigR1-GEF-H1, MigR1-ECT2 or Mieg3 RhoA N19 and 14 μg of VSVG packaging plasmid by Lipofectamine 2000 (Invitrogen) according to the manufacturer's instructions. Supernatant was

collected at 48 and 72 hours. Combined collections were spun at 3700g through Amicon filters (Millipore, Billerica, MA) to concentrate the virus to approximately 1×10^8 per ml, and aliquots stored at -80°C. Freshly sorted 5×10^4 preMegE cells in growth medium were infected with indicated viruses in the presence of polybrene (8 ug/mL) by spinfection at 900*g* for 1 hour at 30°C. After two days in growth medium, the cells were switched to differentiation medium for 8 hours before FRET analysis or another 3 days for ploidy analysis.

FRET analysis of RhoA activation in endomitotic cells

RhoA activity during endomitosis was visualized using a widely-used RhoA biosensor FRET probe (Pertz et al., 2006). After two days of viral transduction of preMegE cells, the live cell DNA was stained with Hoechst red 33342 for 15 minutes, then the cells were washed and placed in differentiation medium in a 35 mm glass bottom dish. After 8 hours, dividing cells in prometaphase expressing the RhoA biosensor were identified by YFP-fluorescence and chromosome morphology by UV excitation on a Leica SP5 confocal microscope equipped with temperature and CO2 control. Then CFP, FRET, YFP and DIC images were acquired using a 63× NA 1.4 objective. The fluorescence emission resulted from excitation with 458 (for CFP and FRET) and 514 (for YFP) nm laser lines from an argon laser through acousto-optical filter was detected with a prism spectrophotometer detection system, at a 490–500 nm spectral band width setting for CFP and a 520–590 nm spectral band width setting for FRET and YFP. Image analysis was performed using ImageJ essentially as described by Hodgson et al., 2010. Briefly, after shading correction and background subtraction, each CFP and the FRET image was multiplied with a binary threshold based mask to eliminate noise outside of the cell. Then, the FRET ratio image was generated by dividing the raw FRET image with the CFP image.

Quantitative RT-PCR

Total RNA from 5×10^4 cells was isolated using the RNAqueous-Micro Kit (Applied Biosystems, Foster City, CA), and treated with RNase-free DNase I to removed genomic DNA. First strand cDNA was produced using Superscript II Reverse Transcriptase (Invitrogen) and random primers (Invitrogen) with 20 ng RNA from each sample. Gene expression levels were quantified on an iCycler iQ RT machine (Bio-Rad, Hercules, CA) with 2 μl of cDNA product from each sample using TaqMan probes (Applied Biosystems) as follows: murine GEF-H1: Mm00434757_m1; murine ECT2: Mm01289559_g1; and Eukaryotic18S rRNA: Hs99999901_s1. Relative gene levels were calculated from standard curves and normalized to 18s levels.

Flow cytometric analysis of DNA content and surface markers

In vitro differentiated megakaryocytes were collected, washed, and stained with APC-conjugated anti-CD41 antibody. The cells were then fixed and permeabilized using BD cytofix/cytoperm on ice for 30 minutes. After incubation with RNAase at 37°C for 30 min, nuclear DNA was stained with propidium iodide at 1 g/mL and analyzed using a FACS Calibur cytometer (BD Biosciences) and FlowJo software (TreeStar, Ashland, OR). In experiments using MigR1 RFP vectors, the nuclear DNA was stained with DAPI, and analyzed on a BD LSRII cytometer. To assay the megakaryocyte ploidy of transplanted mice, BM cells were collected, red cell lysis performed with PharmLyse (BD Biosciences), and ploidy analyzed as described above.

Murine bone marrow transplant

WT CD45.1 (B6.SJL-PtprcaPep3b/BoyJ mice) and CD45.2 (C57Bl6) mice were purchased from the Jackson Laboratory. After pre-treatment with 150 mg/kg 5FU for 4 days, red cell deplete BM from CD45.1 donor mice (4-6 weeks old) was transduced with empty vector or MigR1 GEF-H1 retrovirus by spinfection in Stemspan medium with 30% BIT9500, supplemented with 100 ng/ml SCF, 50 ng/ml TPO, 50 ng/ml Flt3 ligand, and 10 ng/ml IL-3. Lethally irradiated recipient C57Bl6/J mice were transplanted with 1 million cells 24 hours after transduction. Transplant efficiencies were monitored by detecting the CD45.1 ratio in the peripheral blood 4 weeks post-transplantation. GFP positive megakaryocyte ploidy from recipient mice was analyzed 6 weeks post-transplantation.

RNA interference

The lentivirus pGIPZ vector containing shRNA targeting GEF-H1 (RHS4430-101128431) was obtained from Open Biosystems. The mir30 shRNA GEF-H1 sequence was cut with restriction enzymes Hpa1 and Bsut1, and ligated into the CMV-YFP-shRNA retroviral vector (gift from D. Wu, Yale University) digested with Hpa1, and retrovirus produced as described above. CMV-YFP vector containing shRNA targeting luciferase was used as a control. Sorted preMegE cells from WT or Mkl1$^{-/-}$ mice (kind gift from Stephan Morris, Memphis, TN) were transduced with the shRNA viruses, and incubated for 3 days in growth medium followed by 3 days in differentiation medium, and the ploidy of YFP positive cells then assessed. To confirm the GEF-H1 shRNA efficiency, NIH3T3 cells were also transduced. After three days, YFP cells were sorted, and GEF-H1 protein levels detected by Western Blot.

Statistical analysis

Data are represented as means ± s.e.m of at least three independent experiments. Statistical significance was calculated with Student's *t*-test. $^{*}P<0.05$, $^{**}P<0.01$, $^{***}P<0.005$.

Reference

Akashi, K., Traver, D., Miyamoto, T., and Weissman, I.L. (2000). A clonogenic common myeloid progenitor that gives rise to all myeloid lineages. Nature *404*, 193-197.

Battinelli, E.M., Hartwig, J.H., and Italiano, J.E., Jr. (2007). Delivering new insight into the biology of megakaryopoiesis and thrombopoiesis. Curr Opin Hematol *14*, 419-426.

Bement, W.M., Benink, H.A., and von Dassow, G. (2005). A microtubule-dependent zone of active RhoA during cleavage plane specification. J Cell Biol *170*, 91-101.

Birkenfeld, J., Nalbant, P., Bohl, B.P., Pertz, O., Hahn, K.M., and Bokoch, G.M. (2007). GEF-H1 modulates localized RhoA activation during cytokinesis under the control of mitotic kinases. Dev Cell *12*, 699-712.

Brecht, M., Steenvoorden, A.C., Collard, J.G., Luf, S., Erz, D., Bartram, C.R., and Janssen, J.W. (2005). Activation of gef-h1, a guanine nucleotide exchange factor for RhoA, by DNA transfection. Int J Cancer *113*, 533-540.

Chang, Y., Auradé, F., Larbret, F., Zhang, Y., Le Couedic, J.P., Momeux, L., Larghero, J., Bertoglio, J., Louache, F., Cramer, E., Vainchenker, W., and Debili, N. (2007). Proplatelet formation is regulated by the Rho/ROCK pathway. Blood. 109, 4229-4236.

Cen, B., Selvaraj, A., Burgess, R.C., Hitzler, J.K., Ma, Z., Morris, S.W., and Prywes, R. (2003). Megakaryoblastic leukemia 1, a potent transcriptional coactivator for serum response factor (SRF), is required for serum induction of SRF target genes. Mol Cell Biol *23*, 6597-6608.

Chalamalasetty, R.B., Hummer, S., Nigg, E.A., and Sillje, H.H. (2006). Influence of human Ect2 depletion and overexpression on cleavage furrow formation and abscission. J Cell Sci *119*, 3008-3019.

Cheng, E.C., Luo, Q., Bruscia, E.M., Renda, M.J., Troy, J.A., Massaro, S.A., Tuck, D., Schulz, V., Mane, S.M., Berliner, N.*, et al.* (2009). Role for MKL1 in megakaryocytic maturation. Blood *113*, 2826-2834.

Cooper, S.J., Trinklein, N.D., Nguyen, L., and Myers, R.M. (2007). Serum response factor binding sites differ in three human cell types. Genome Res *17*, 136-144.

Drayer, A.L., Olthof , S.G., and Vellenga, E. (2006) Mammalian target of rapamycin is required for thrombopoietin-induced proliferation of megakaryocyte progenitors. Stem Cells. *24*, 105-114.

Eliades, A., Papadantonakis, N., and Ravid, K. (2010). New roles for cyclin E in megakaryocytic polyploidization. J Biol Chem *285*, 18909-18917.

Etienne-Manneville, S., and Hall, A. (2002). Rho GTPases in cell biology. Nature *420*, 629-635.

Fields, A.P., and Justilien, V. (2010). The guanine nucleotide exchange factor (GEF) Ect2 is an oncogene in human cancer. Adv Enzyme Regul *50*, 190-200.

Geddis, A.E., Fox, N.E., Tkachenko, E., and Kaushansky, K. (2007). Endomitotic megakaryocytes that form a bipolar spindle exhibit cleavage furrow ingression followed by furrow regression. Cell Cycle *6*, 455-460.

Geddis, A.E., and Kaushansky, K. (2006). Endomitotic megakaryocytes form a midzone in anaphase but have a deficiency in cleavage furrow formation. Cell Cycle *5*, 538-545.

Halene, S., Gao, Y., Hahn, K., Massaro, S., Italiano, J.E., Jr., Schulz, V., Lin, S., Kupfer, G.M., and Krause, D.S. (2010). Serum response factor is an essential transcription factor in megakaryocytic maturation. Blood *116*, 1942-1950.

Hodgson, L., Shen, F., and Hahn, K. (2010). Biosensors for characterizing dynamics of Rho family GTPases in living cells. Curr Prot Cell Biol *46,* 14.11.1-14.11.26.

Iyoda, M., Kasamatsu, A., Ishigami, T., Nakashima, D., Endo-Sakamoto, Y., Ogawara, K., Shiiba, M., Tanzawa, H., and Uzawa, K. (2010). Epithelial cell transforming sequence 2 in human oral cancer. PLoS One *5*, e14082.

Kosako, H., Yoshida, T., Matsumura, F., Ishizaki, T., Narumiya, S., and Inagaki, M. (2000). Rho-kinase/ROCK is involved in cytokinesis through the phosphorylation of myosin light chain and not ezrin/radixin/moesin proteins at the cleavage furrow. Oncogene *19***,** 6059-6064.

Krendel, M., Zenke, F.T., and Bokoch, G.M. (2002). Nucleotide exchange factor GEF-H1 mediates cross-talk between microtubules and the actin cytoskeleton. Nat Cell Biol *4*, 294-301.

Levine, R.F., Hazzard, K.C., and Lamberg, J.D. (1982). The significance of megakaryocyte size. Blood *60*, 1122-1131.

Leysi-Derilou, Y., Robert, A., Duchesne, C., Garnier, A., Boyer, L., and Pineault, N. (2010). Polyploid megakaryocytes can complete cytokinesis. Cell Cycle *9*.

Lordier, L., Jalil, A., Aurade, F., Larbret, F., Larghero, J., Debili, N., Vainchenker, W., and Chang, Y. (2008). Megakaryocyte endomitosis is a failure of late cytokinesis related to defects in the contractile ring and Rho/Rock signaling. Blood *112*, 3164-3174.

Madaule, P., Eda, M., Watanabe, N., Fujisawa, K., Matsuoka, T., Bito, H., Ishizaki, T., and Narumiya, S. (1998). Role of citron kinase as a target of the small GTPase Rho in cytokinesis Nature *394*, 491-494

Ma Z**.**, Morris S**.**W**.**, Valentine V**.**, Li M**.**, Herbrick J**.**A**.**, Cui X**.**, Bouman D**.**, Li Y**.**, Mehta P**.**K**.**, Nizetic D**.**, Kaneko Y**.**, Chan G**.**C**.**, Chan L**.**C**.**, Squire J**.**, Scherer SW, and Hitzler J**.**K. (2001).

Fusion of two novel genes, RBM15 and MKL1, in the t(1;22)(p13;q13) of acute megakaryoblastic leukemia. Nat Genet *28*, 220-221.

Melendez J., Stengel K., Zhou X., Chauhan B.K., Debidda M., Andreassen P., Lang R.A., and Zheng Y. (2011). RhoA GTPase is dispensable for actomyosin regulation but is essential for mitosis in primary mouse embryonic fibroblasts. J Biol Chem *286*, 15132-15137

Mercher T., Coniat M.B., Monni R., Mauchauffé M., Khac F.N., Gressin L., Mugneret F., Leblanc T., Dastugue N., Berger R., and Bernard O.A. (2001). Involvement of a human gene related to the Drosophila spen gene in the recurrent t(1;22) translocation of acute megakaryocytic leukemia. Proc Natl Acad Sci U S A *98*. 5776-5779.

Mercher T, Raffel G.D., Moore S.A., Cornejo M.G., Baudry-Bluteau D., Cagnard N., Jesneck J.L., Pikman Y., Cullen D., Williams I.R., Akashi K., Shigematsu H., Bourquin J.P., Giovannini M., Vainchenker W., Levine R.L., Lee B.H., Bernard O.A., and Gilliland D.G. (2009). The OTT-MAL fusion oncogene activates RBPJ-mediated transcription and induces acute megakaryoblastic leukemia in a knockin mouse model. J Clin Invest. *119*, 852-864.

Mizuarai, S., Yamanaka, K., and Kotani, H. (2006). Mutant p53 induces the GEF-H1 oncogene, a guanine nucleotide exchange factor-H1 for RhoA, resulting in accelerated cell proliferation in tumor cells. Cancer Res *66*, 6319-6326.

Muntean, A.G., Pang, L., Poncz, M., Dowdy, S.F., Blobel, G.A., and Crispino, J.D. (2007). Cyclin D-Cdk4 is regulated by GATA-1 and required for megakaryocyte growth and polyploidization. Blood *109*, 5199-5207.

Narumiya, S., and Yasuda, S. (2006). Rho GTPases in animal cell mitosis. Curr Opin Cell Biol *18*, 199-205.

Nguyen, H.G., and Ravid, K. (2006). Tetraploidy/aneuploidy and stem cells in cancer promotion: The role of chromosome passenger proteins. Journal of Cellular Physiology *208*, 12-22.

Nguyen, H.G., and Ravid, K. (2010). Polyploidy: mechanisms and cancer promotion in hematopoietic and other cells. Adv Exp Med Biol *676*, 105-122.

Nishimura Y., and Yonemura S. (2006). Centralspindlin regulates ECT2 and RhoA accumulation at the equatorial cortex during cytokinesis. J Cell Sci 19, 104-114

Papadantonakis, N., Makitalo, M., McCrann, D.J., Liu, K., Nguyen, H.G., Martin, G., Patel-Hett, S., Italiano, J.E., and Ravid, K. (2008). Direct visualization of the endomitotic cell cycle in living megakaryocytes: differential patterns in low and high ploidy cells. Cell Cycle *7*, 2352-2356.

Patel, S.R., Richardson, J.L., Schulze, H., Kahle, E., Galjart, N., Drabek, K., Shivdasani, R.A., Hartwig, J.H., and Italiano, J.E., Jr. (2005). Differential roles of microtubule assembly and sliding in proplatelet formation by megakaryocytes. Blood *106*, 4076-4085.

Petronczki, M., Glotzer, M., Kraut, N., and Peters, J.M. (2007). Polo-like kinase 1 triggers the initiation of cytokinesis in human cells by promoting recruitment of the RhoGEF Ect2 to the central spindle. Dev Cell *12*, 713-725.

Pertz, O., Hodgson, L., Klemke, R.L., and Hahn, K.M. (2006). Spatiotemporal dynamics of RhoA activity in migrating cells. Nature *440*, 1069-1072.

Pronk, C.J., Rossi, D.J., Mansson, R., Attema, J.L., Norddahl, G.L., Chan, C.K., Sigvardsson, M., Weissman, I.L., and Bryder, D. (2007). Elucidation of the phenotypic, functional, and molecular topography of a myeloerythroid progenitor cell hierarchy. Cell Stem Cell *1*, 428-442.

Raslova, H., Kauffmann, A., Sekkai, D., Ripoche, H., Larbret, F., Robert, T., Le Roux, D.T., Kroemer, G., Debili, N., Dessen, P.*, et al.* (2007). Interrelation between polyploidization and megakaryocyte differentiation: a gene profiling approach. Blood *109*, 3225-3234.

Rossman, K.L., Der, C.J., and Sondek, J. (2005). GEF means go: turning on RHO GTPases with guanine nucleotide-exchange factors. Nat Rev Mol Cell Biol *6*, 167-180.

Saito, S., Tatsumoto, T., Lorenzi, M.V., Chedid, M., Kapoor, V., Sakata, H., Rubin, J., and Miki, T. (2003). Rho exchange factor ECT2 is induced by growth factors and regulates cytokinesis through the N-terminal cell cycle regulator-related domains. J Cell Biochem *90*, 819-836.

Tatsumoto, T., Xie, X., Blumenthal, R., Okamoto, I., and Miki, T. (1999). Human ECT2 is an exchange factor for Rho GTPases, phosphorylated in G2/M phases, and involved in cytokinesis. J Cell Biol *147*, 921-928.

Tomer, A. (2004). Human marrow megakaryocyte differentiation: multiparameter correlative analysis identifies von Willebrand factor as a sensitive and distinctive marker for early (2N and 4N) megakaryocytes. Blood *104*, 2722-2727.

Tomer, A., Harker, L.A., and Burstein, S.A. (1988). Flow cytometric analysis of normal human megakaryocytes. Blood *71*, 1244-1252.

Tolliday, N., VerPlank, L. and Li, R. *(*2002). Rho1 directs formin-mediated actin ring assembly during budding yeast cytokinesis. Curr. Biol. *12,* 1864-*1870.*

Yasui, Y., Amano, M., Nagata, K., Inagaki, N., Nakamura, H., Saya, H., Kaibuchi, K. and Inagaki, M. (1998). Roles of Rho-associated kinase in cytokinesis; mutations in Rho-associated kinase phosphorylation sites impair cytokinetic segregation of glial filaments. J. Cell Biol. *143,* 1249-1258.

Yoshizaki H., Ohba Y., Parrini MC., Dulyaninova NG., Bresnick AR., Mochizuki N., and Matsuda M., (2004). Cell type-specific regulation of RhoA activity during cytokinesis. J Biol Chem *279*, 44756-44762.

Yoshizaki, H., Ohba, Y., Kurokawa, K., Itoh, RE., Nakamura, T., Mochizuki, N., Nagashima, K., and Matsuda, M. (2003). Activity of Rho-family GTPases during cell division as visualized with FRET-based probes. J cell Biol *162*, 223-232.

Yuce, O., Piekny, A., and Glotzer, M. (2005). An ECT2-centralspindlin complex regulates the localization and function of RhoA. J Cell Biol *170*, 571-582.

Zhao, W.M., and Fang, G. (2005). Anillin is a substrate of anaphase-promoting complex/cyclosome (APC/C) that controls spatial contractility of myosin during late cytokinesis. J Biol Chem *280*, 33516-33524.

Acknowledgments:

We thank Susannah Kassmer and Stephanie Donaldson for assistance with mice, Ping-Xia Zhang for expert technical assistance, and Emanuela Bruscia and Shangqin Guo for helpful discussions. This work was supported by the R01DK086267, the Yale Center of Excellence in Molecular Hematology (P30DK072442), the State of Connecticut Stem Cell Research Fund, and the Yale Cancer Center (P30CA016359). The authors declare that they have no competing financial interests. Y.G. designed and performed the study and wrote the manuscript. E.S. designed and created plasmids, performed experiments, modified manuscript and provided intellectual input. E.K. and P.C. performed some time-lapse experiments. E.C. produced the stable HEL cell clones. S.Z. performed experiments, and provided a figure. S.L. helped with mouse transplantation and other mouse work. L.W. provided assistance with plasmid and retroviral vectors. S.H. provided reagents and intellectual input. D.S.K. oversaw the studies and wrote the manuscript.

Figure legends

Figure 1. Endomitosis of MkP induced by Tpo. (A) 2N to 4N Mk endomitosis shows cleavage furrow ingression with subsequent regression, resulting in one 4N cell. (B) 4N to 8N Mk

endomitosis showing no apparent cleavage furrow. The figures show overlays of DIC (gray) with green fluorescent H2B-GFP (green) images taken every 5 minutes. The time of each image relative to the first is indicated in each frame.

Figure 2. Active RhoA is absent from the cleavage furrow during the first endomitotic cleavage. (A) Shown are (top) preMegE in growth medium, which undergo normal mitosis, and (bottom) MkP undergoing their first endomitotic cleavage after one day of culture in Tpo. Total RhoA (red) is localized correctly to the cleavage furrow during preMegE mitosis and MkP endomitosis at both anaphase and telophase. The stages of cell division were visualized by nuclear DAPI staining (blue) and the mitotic spindle and central spindle with anti-α-tubulin (green) antibody. (B) RhoA activation patterns during endomitosis. Mouse primary preMegE cells were transduced with the RhoA biosensor virus for 48 h before switching to differentiation medium. After 8 hours, the RhoA activation pattern throughout endomitosis was assessed by the RhoA biosensor's FRET/CFP ratio, which represents RhoA activity (FRET), red color in FRET images indicates high RhoA activation. CFP channel indicated biosensor (and RhoA) localization. All images were processed identically. Elapsed time (minutes) with starting time set to 0 (8h post-Tpo administration) is indicated at the right corner of each picture. NIH3T3 cells, grown in normal 10% BS DMEM medium, transduced with same biosensor, were used as normal mitosis control. Images are representative of at least 4 similar images for each condition.

Figure 3. GEF-H1 and ECT2 are down-regulated during megakaryocyte differentiation. Data shown for freshly sorted (d0) preMegE and MkP cells from WT mice, as well as preMegE cultured in DM for the time indicated. (A) Relative levels of GEF-H1 mRNA are reduced during

Mk differentiation. ***, P<0.005, versus value of preMegE day 0. (B) Relative levels of ECT2 mRNA were also decreased. ***, P<0.005, versus value of preMegE day 0. (C) The protein levels of GEF-H1 and ECT2 are reduced with different kinetics as shown by Western-blotting. Anti-α-tubulin was used as the loading control. Relative protein level of each sample after normalization to tubulin and setting preMegE level as 1 are indicated above each band.

Figure 4. GEF-H1 and ECT2 are reduced in endomitotic Mk. PreMegE were grown in GM and MkP in DM. (A) Cells were stained with anti-GEF-H1 (red), anti-α-tubulin (green) and DAPI. Examples of normal mitosis (i-iii, preMegE cultured in growth medium), 2N to 4N endomitosis (iv-vi), and ≥ 4N endomitosis (vii-ix) are shown. GEF-H1 protein level is reduced at the 2N to 4N stage of endomitosis and increases at later stages (2 days) of endomitosis. (B) ECT2 protein, stained with anti-ECT2 antibody (red), is clearly detected in preMegE undergoing mitosis (i – iii), and at the 2N to 4N stage of endomitosis (iv-vi), but ECT2 levels are reduced at later stages (2 days) of endomitosis (vii-ix).

Figure 5. Differential effects of overexpressing GEF-H1 or ECT2 on polyploidization of Mk. (A-C) PreMegE cells in growth medium were transduced with retroviral vectors (control and expressing individual GEFs) and cultured for two days, then transferred to differentiation medium for 3 days before the ploidy of each sample was assessed. (A) Shown is the effect of overexpressing control (GFP) virus, GEF-H1 or ECT2 encoding virus. Ploidy of GFP+ cells in each condition is shown. The percentages of Mk in 2N, 4N, and ≥ 8N ploidy are indicated. (B) The average ploidy of Mks expressing GFP only (control), GEF-H1 or ECT2 is compared. ***, *P*<0.005, versus control. (C) In this experiment, cells were transduced with 2 retroviral vectors

(one encoding RFP and the other GFP). Controls received vectors encoding only RFP and GFP. GEF-H1 (upper second panel) received GFP control plus GEF-H1-ires-RFP vectors, ECT2 (upper third panel) received ECT2-ires-GFP plus control RFP vectors, the upper fourth panel shows cells transduced with ECT2-ires-GFP plus GEF-H1-ires-RFP. Samples in lower panel were transduced with RhoAN19-ires-GFP together with RFP control (left), GEF-H1-ires-RFP (middle), or ECT2-ires-RFP (right). Ploidy is shown for GFP+RFP+ (double positive) cells. (D) Western blot of HEL cells transduced with the indicated virus validate expression vectors. (E) Overexpression of GEF-H1 also decreases polyploidization of Mk *in vivo*. CD45.1 BM cells were transduced with control (GFP only) or GEF-H1–ires-GFP virus, and transplanted into lethally irradiated CD45.2 mice. After 6 weeks, the ploidy of GFP positive Mk was analyzed. Representative ploidy profiles from GFP+ Mks expressing empty virus or GEF-H1 are shown. (F) Average ploidy of GFP positive Mks recovered 6 weeks post-transplant. *, $P<0.05$, versus the value of control.

Figure 6. Down-regulation of GEF-H1 is MKL1- dependent. (A) The relative mRNA level of GEF-H1 is significantly increased in Mkl1$^{-/-}$ Mk, and shows very little decrease with Mk differentiation. WT or Mkl1$^{-/-}$ preMegE or MkP were cultured in DM as indicated. ***, $P<0.005$, versus the corresponding WT control. (B) Relative ECT2 mRNA levels are the same for WT and Mkl1$^{-/-}$ cells. In both, ECT2 mRNA decreases during Mk differentiation. $P>0.1$ for the values of Mkl1$^{-/-}$ versus the corresponding WT control, (C) PreMegE cultured in growth medium (mitotic controls, i-iii and vii-ix) and MkP cultured in Tpo-only medium, which induces endomitosis, were immunostained as indicated. Unlike WT MkP (iv-vi), Mkl1$^{-/-}$ MkP do not show a loss of GEF-H1 protein level in response to TPO induction (x-xii). (D and E) 293FT cells were

transduced with empty vector (-); WT Mkl1 (WT); constitutively active (CA) Mkl1, which lacks the actin binding domain; or dominant negative (DN) Mkl1, which lacks the transcriptional activation domain, but can still heterodimerize with endogenous Mkl1. Overexpression of CA MKL1 significantly reduces endogenous GEF-H1 mRNA (D) and protein (E) levels compared to cells transduced with empty vector (-), wild type Mkl1 (WT) and dominant negative (DN) Mkl1. GAPDH was used as a loading control in (E). ***, $P<0.005$, and **, $P<0.01$, versus the value of empty vector (-). (F) Quantitative RT-PCR reveals much higher levels of GEF-H1 and ECT2 mRNA in the 6133 cell line compared to WT PreMegE with PreMegE value set to 1. Values normalized to 18S RNA. ***, $P<0.005$.

Figure 7. Knockdown of GEF-H1 restores polyploidy in Mkl1$^{-/-}$ Mks in vitro. (A) WT or Mkl1$^{-/-}$ preMegE were transduced with retrovirus encoding either shRNA targeting luciferase or GEF-H1, as indicated. After Tpo induced differentiation, ploidy was assessed. A representative ploidy plot for each condition is shown. The percentages of Mk in 2N, 4N, 8N and ≥ 16N ploidy are indicated. (B) Average ploidy of these samples. *** $P<0.005$. (C) Validation of shRNA mediated knockdown of GEF-H1 protein in NIH3T3 cells transduced with the indicated constructs. GFP positive shRNA expressing cells were sorted, and analyzed by Western Blot. GAPDH was used as the loading control.

Fig. 1

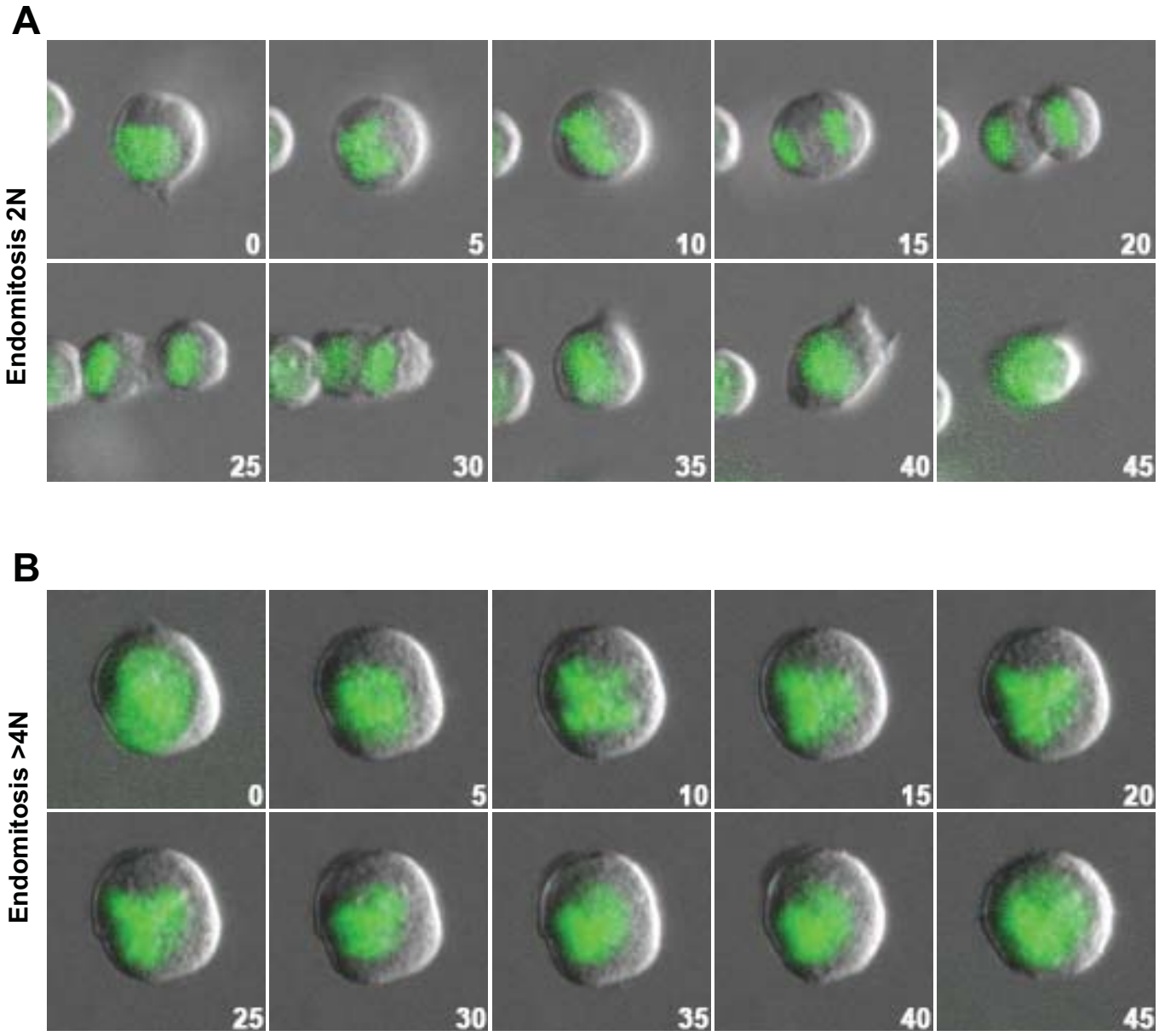
A
Endomitosis 2N
0
5
10
15
20
25
30
35
40
45
B
Endomitosis >4N
0
5
10
15
20
25
30
35
40
45

Fig.2

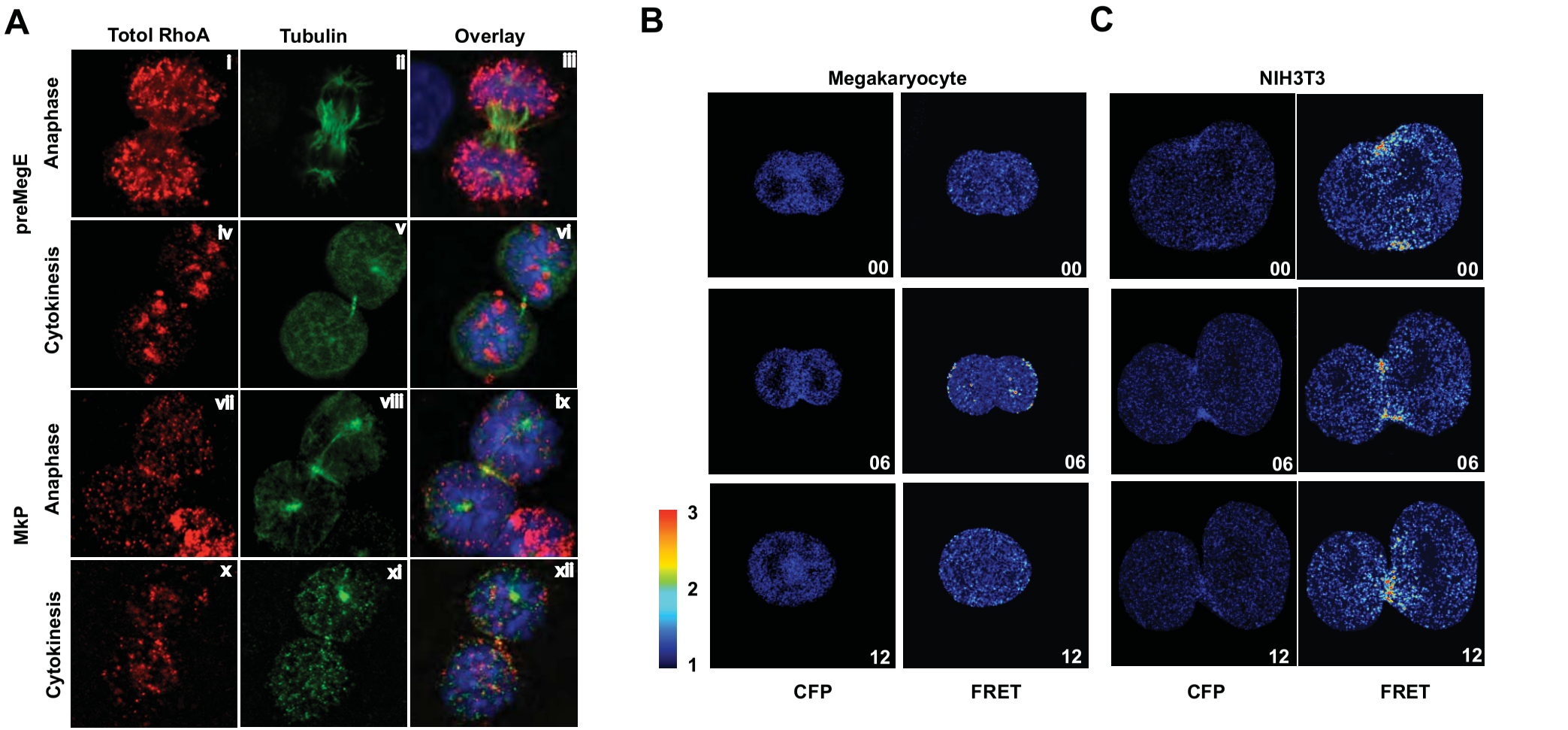
A
Totol RhoA
Tubulin
Overlay
preMegE
MkP
Anaphase
Cytokinesis
Anaphase
Cytokinesis
i
ii
iii
iv
v
vi
vii
viii
ix
x
xi
xii
B
C
Megakaryocyte
NIH3T3
00
06
12
3
2
1
CFP
FRET
CFP
FRET

Fig.3

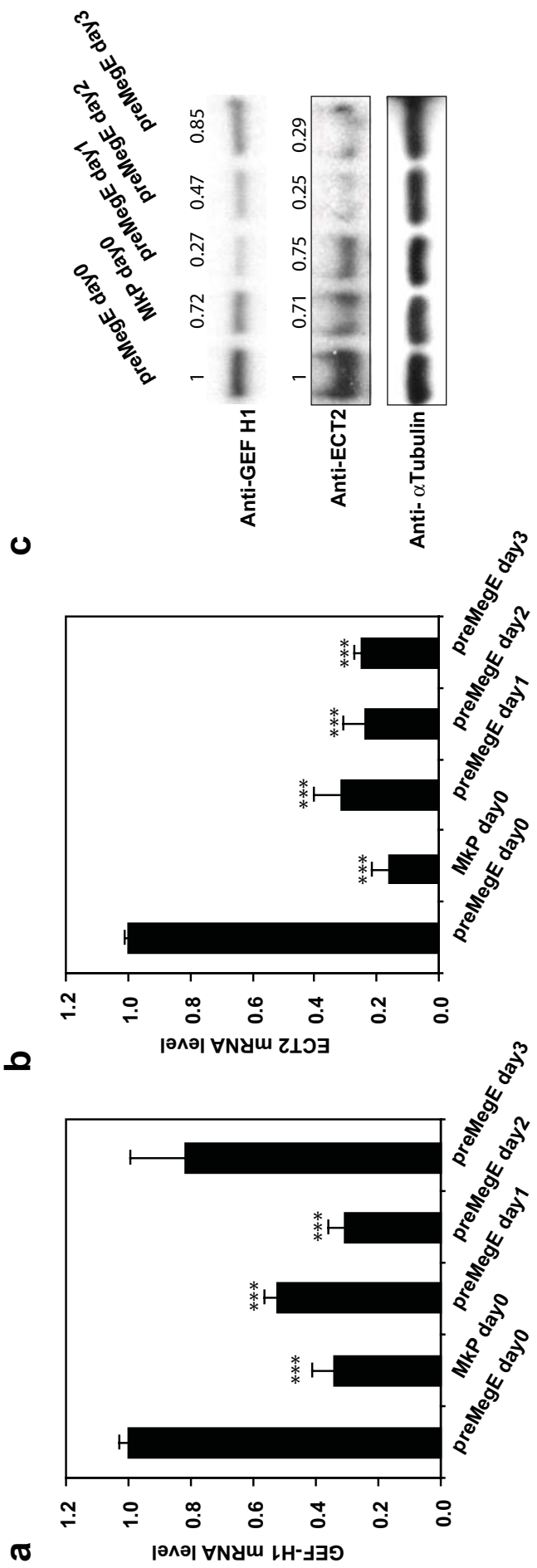
a
GEF-H1 mRNA level
1.2
1.0
0.8
0.6
0.4
0.2
0.0
***
***
***
preMegE day0
MkP day0
preMegE day1
preMegE day2
preMegE day3
b
ECT2 mRNA level
1.2
1.0
0.8
0.6
0.4
0.2
0.0
***
***
***
preMegE day0
MkP day0
preMegE day1
preMegE day2
preMegE day3
c
preMegE day0
MkP day0
preMegE day1
preMegE day2
preMegE day3
1
0.72
0.27
0.47
0.85
Anti-GEF H1
1
0.71
0.75
0.25
0.29
Anti-ECT2
Anti- αTubulin

Fig.4

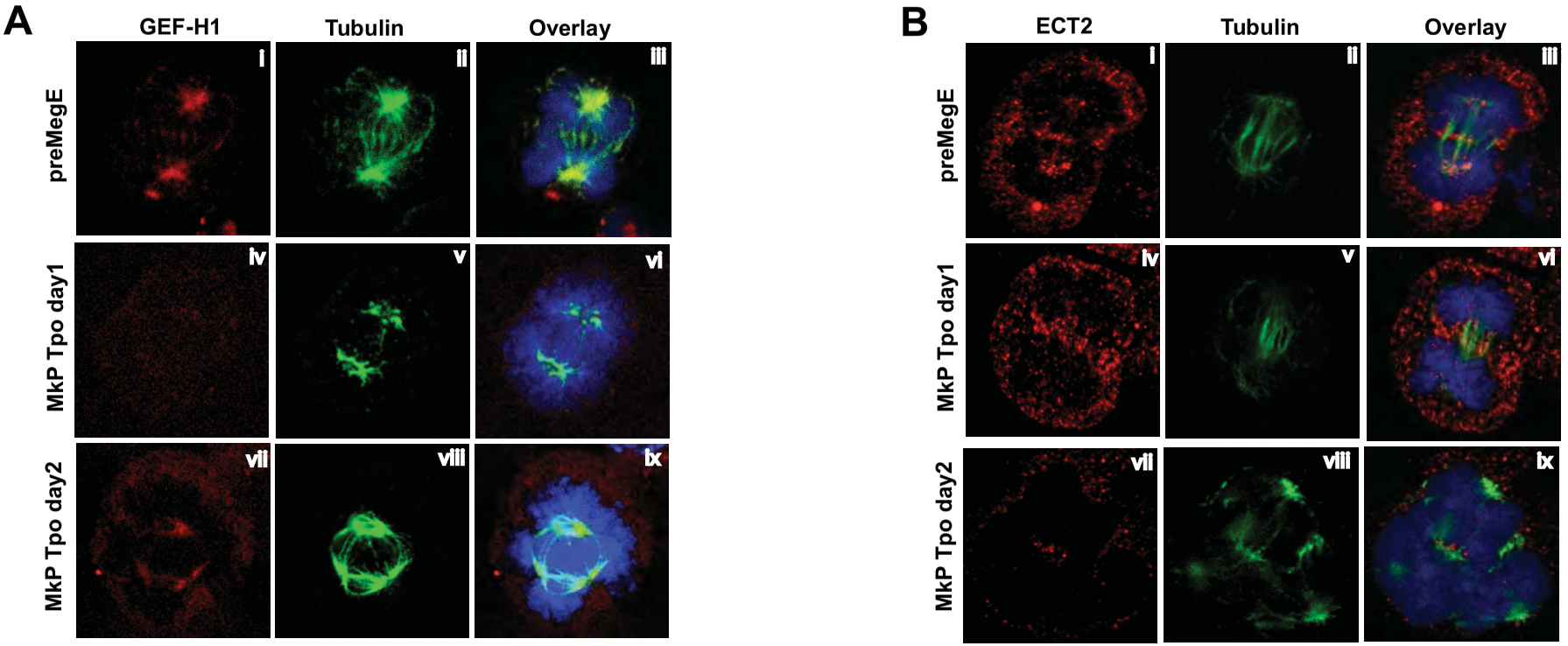
A
GEF-H1
Tubulin
Overlay
preMegE
MkP Tpo day1
MkP Tpo day2
i
ii
iii
iv
v
vi
vii
viii
ix
B
ECT2
Tubulin
Overlay
preMegE
MkP Tpo day1
MkP Tpo day2
i
ii
iii
iv
v
vi
vii
viii
ix

Fig.5

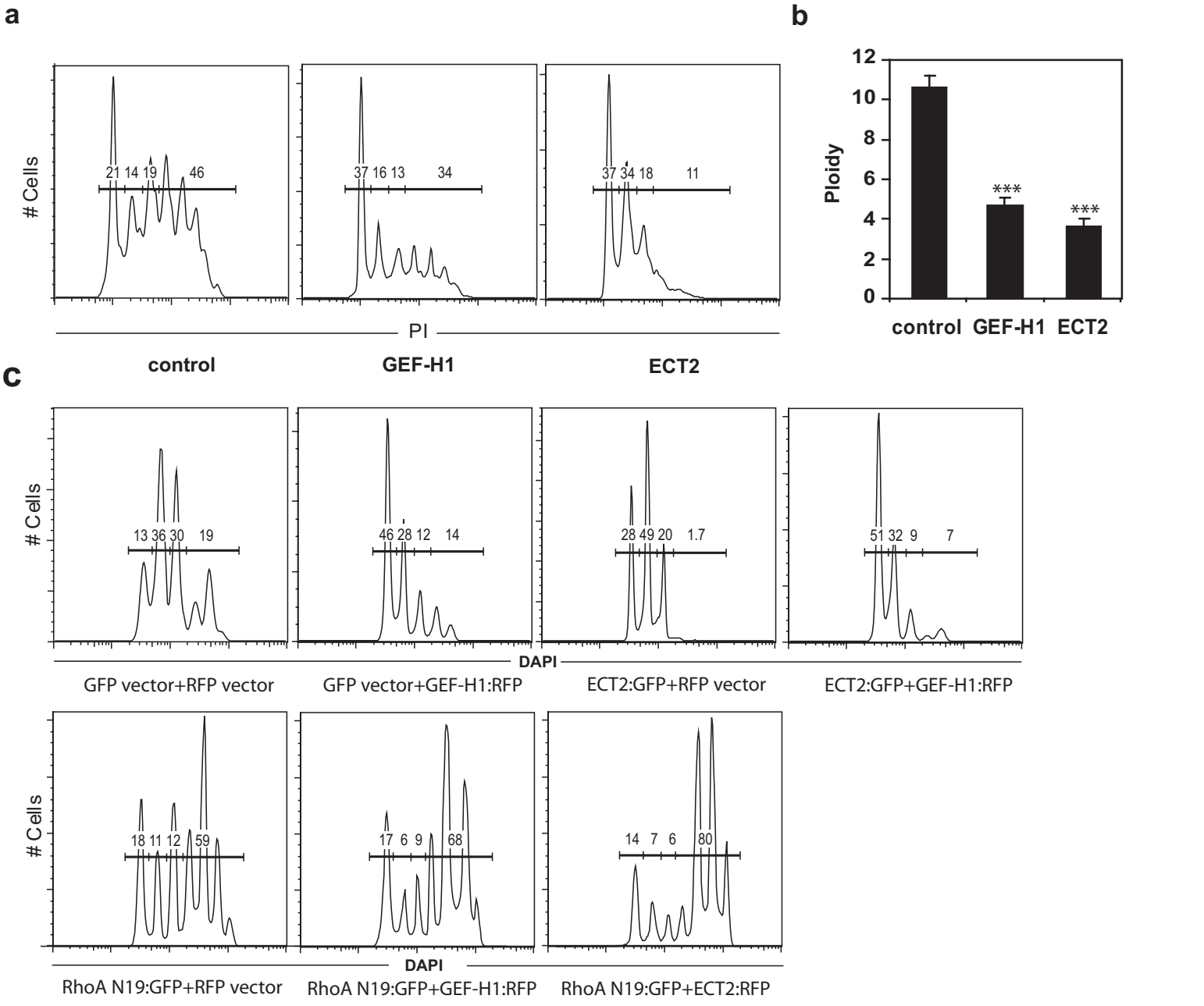
a
Cells
21 14 19 46
37 16 13 34
37 34 18 11
PI
control
GEF-H1
ECT2
b
Ploidy
12
10
8
6
4
2
0
***
***
control GEF-H1 ECT2
c
Cells
13 36 30 19
46 28 12 14
28 49 20 1.7
51 32 9 7
DAPI
GFP vector+RFP vector
GFP vector+GEF-H1:RFP
ECT2:GFP+RFP vector
ECT2:GFP+GEF-H1:RFP
Cells
18 11 12 59
17 6 9 68
14 7 6 80
DAPI
RhoA N19:GFP+RFP vector
RhoA N19:GFP+GEF-H1:RFP
RhoA N19:GFP+ECT2:RFP

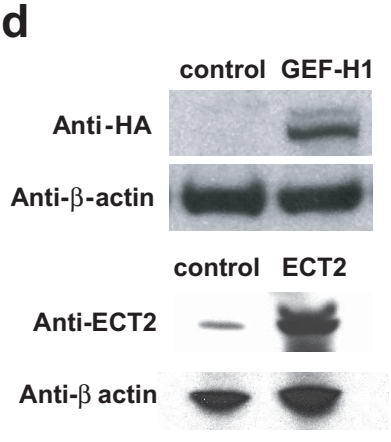
d
control GEF-H1
Anti-HA
Anti-β-actin
control ECT2
Anti-ECT2
Anti-β actin

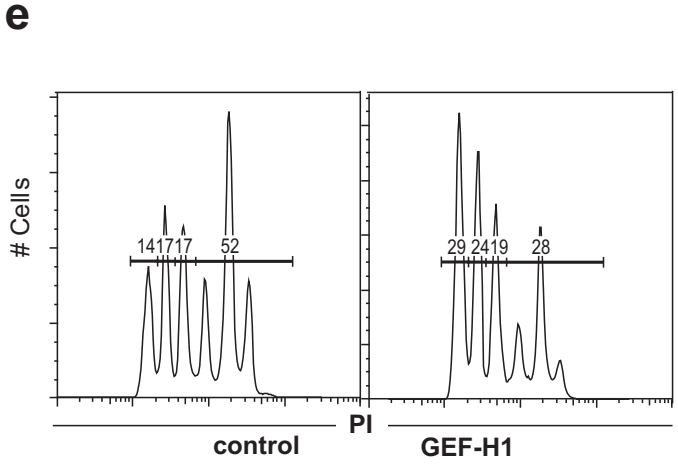
e
Cells
14 17 17 52
29 24 19 28
PI
control
GEF-H1

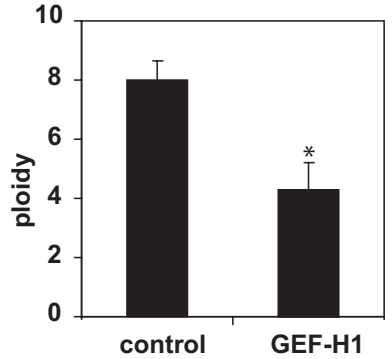
f
ploidy
10
8
6
4
2
0
*
control
GEF-H1

Figure 6

Fig.6

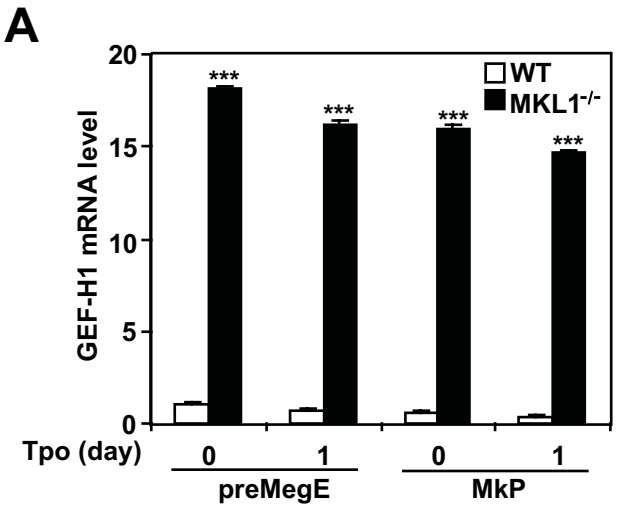

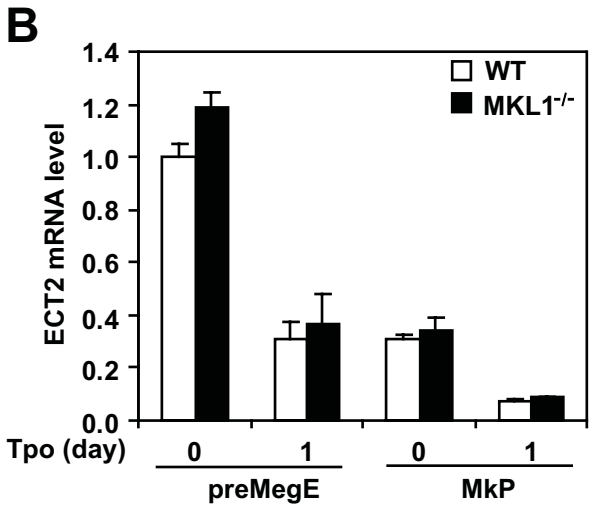

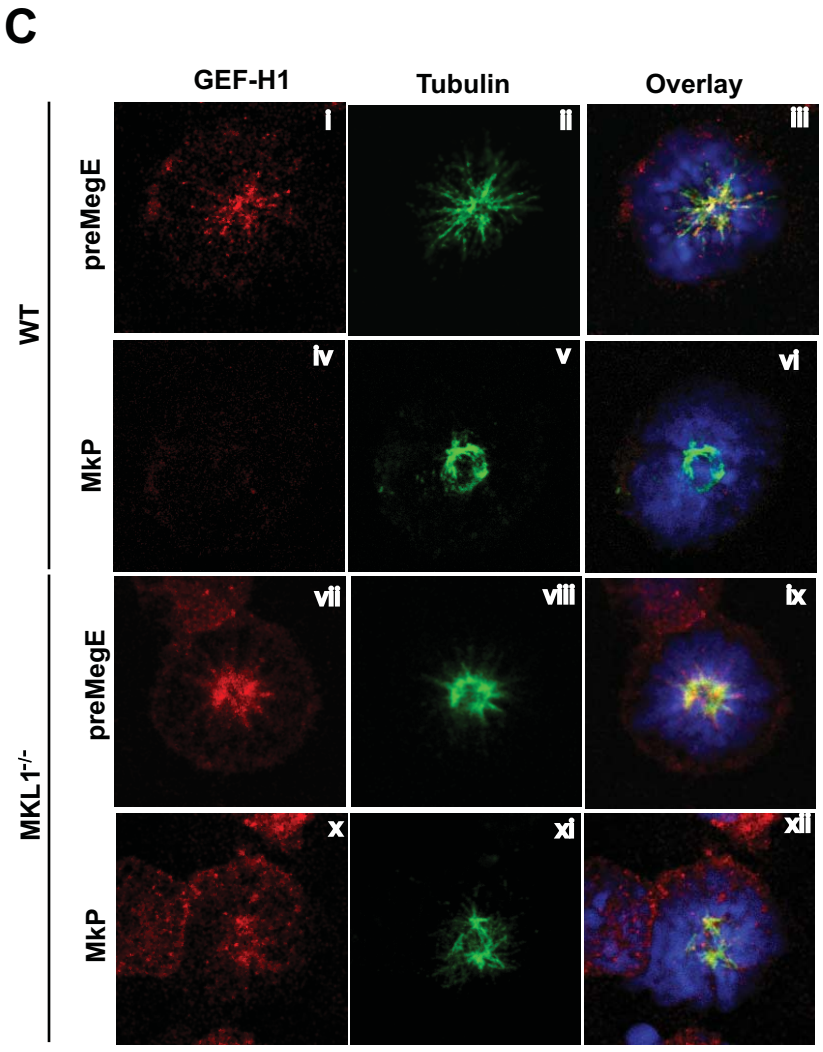

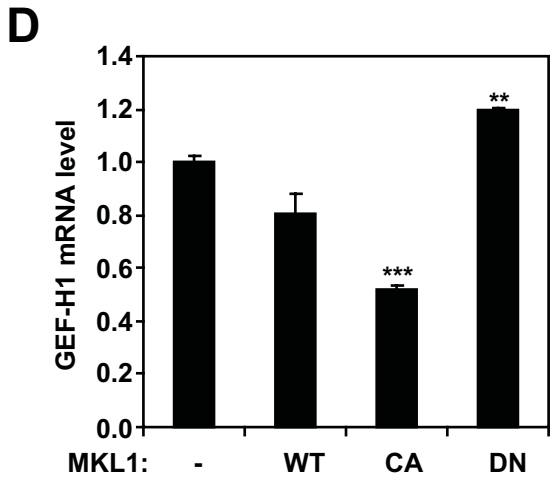

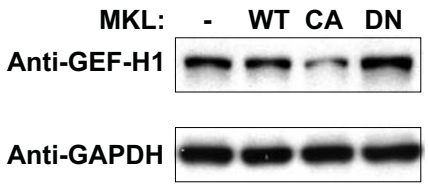

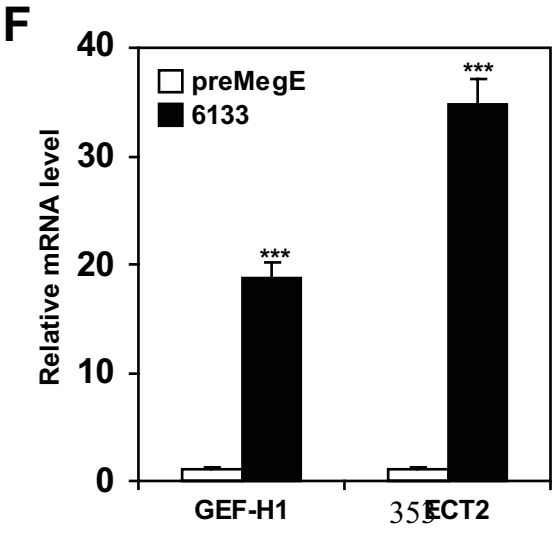

Figure 7

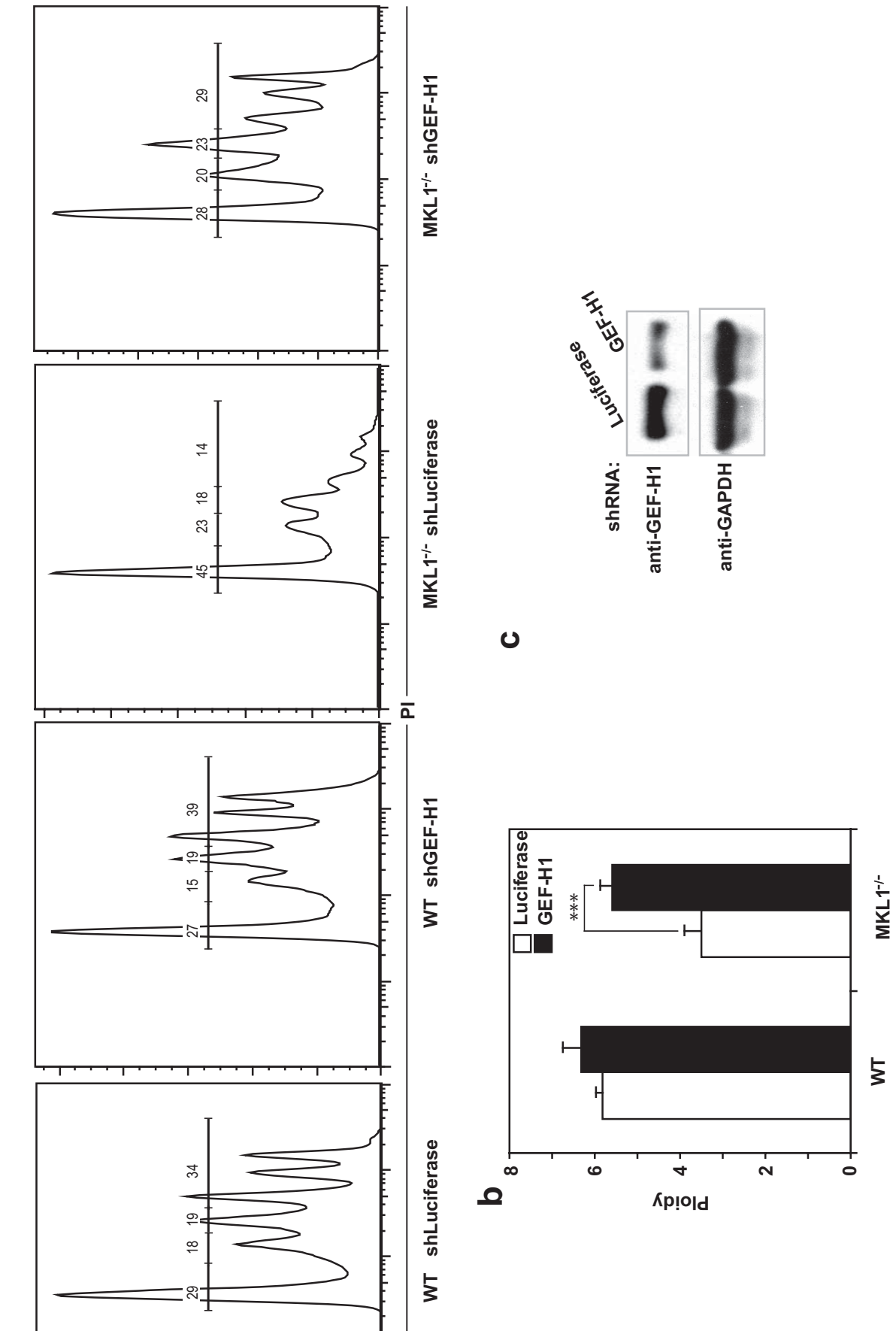
Fig.7
a
Cells
WT shLuciferase
WT shGEF-H1
MKL1-/- shLuciferase
MKL1-/- shGEF-H1
PI
b
Ploidy
Luciferase
GEF-H1
***
WT
MKL1-/-
c
shRNA:
Luciferase
GEF-H1
anti-GEF-H1
anti-GAPDH

Inventory of all supplemental items with explanation of their relationship to the main figures

Supplemental Movie S1 shows the movie of the cells from which still images are shown in Figure 1A.

Supplemental Movie S2 shows the movie of the cells from which still images are shown in Figure 1B.

Supplemental Figure S1 shows quantification of total and activated RhoA protein levels during Mk differentiation, as well as in platelets. Also shown is the relative level of anillin protein over time, which is relevant to the data shown in Figure 4. Thus, Figure S1 is a supplement to Figure 2 and also to Figure 4.

Supplemental Figure S2 shows the gating strategy used to obtain the data shown in Figure 5. It is a supplement to Figure 5.

Supplemental Figure S3 shows a blot of total and activated RhoA levels. It is a supplement to Figure 6.

Supplemental Figure S4 is a model summarizing all of the data obtained. We refer to this figure at the end of the manuscript, and it relates to all of the figures (Fig 1-7) by summarizing all of the data in the manuscript.

Supplemental figures and legends (Gao et al)

Figure S1

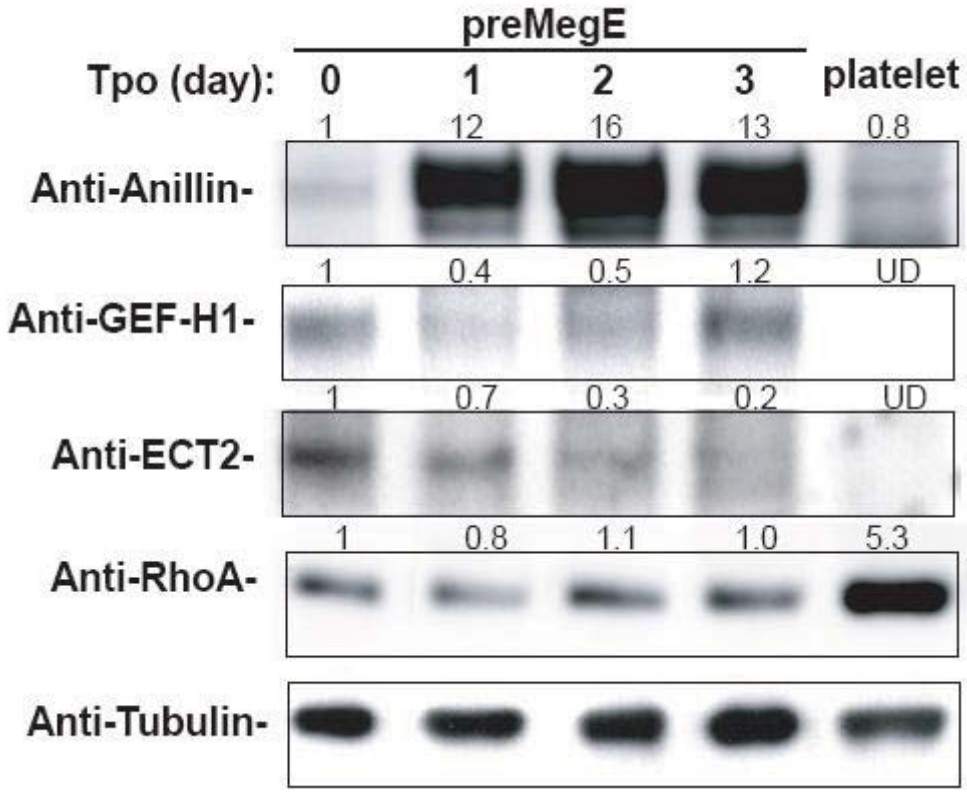

Figure S1. Western-Blot for Anillin, GEF-H1, ECT2, RhoA and α Tubulin from Tpo treated preMegE and platelets. Relative levels of each protein after normalized to tubulin and setting preMegE level to 1 are labeled above each band. Both GEF-H1 and ECT2 were undetectable (UD) in platelets.

Figure S2

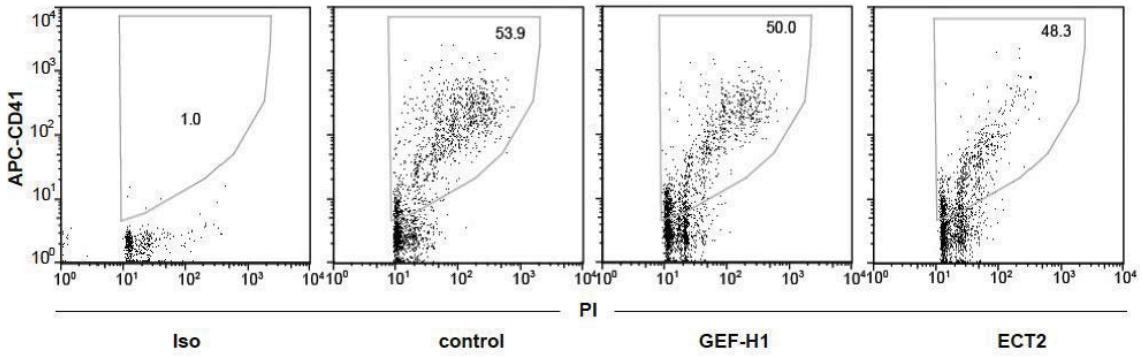

Figure S2. Enforced overexpression of GEF-H1 and ECT2, as labeled, does not significantly change the percentage of cells that are $CD41^+$ compared with control cells transduced with GFP vector. An isotype (Iso) control antibody was used to determine gating of the $CD41^+$ population.

Figure S3

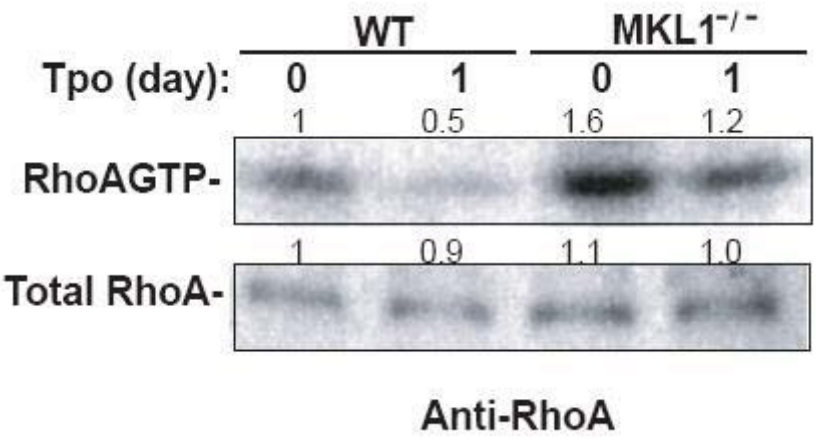

Figure S3. GTP-bound active RhoA level from WT and MKL1$^{-/-}$ preMegE with or without culture in Tpo for one day as analyzed by RhoA effector pull down using the RhoA Activation Assay Kit from Millipore. Briefly, 2x10^5 preMegE before and after culturing in Tpo were washed with PBS, and lysed in 300 µl lysis buffer, which contains Mg^{2+} to maintain RhoA in its GTP-bound state. For the pull down, 10 µl beads coated with GST-Rhotekin Rho binding domain were added to the lysate, incubated for 40 minutes, then washed twice with lysis buffer. Relative protein level of each sample after normalization to Total RhoA and setting preMegE Tpo day0 level as 1 are labeled above each band.

Figure S4

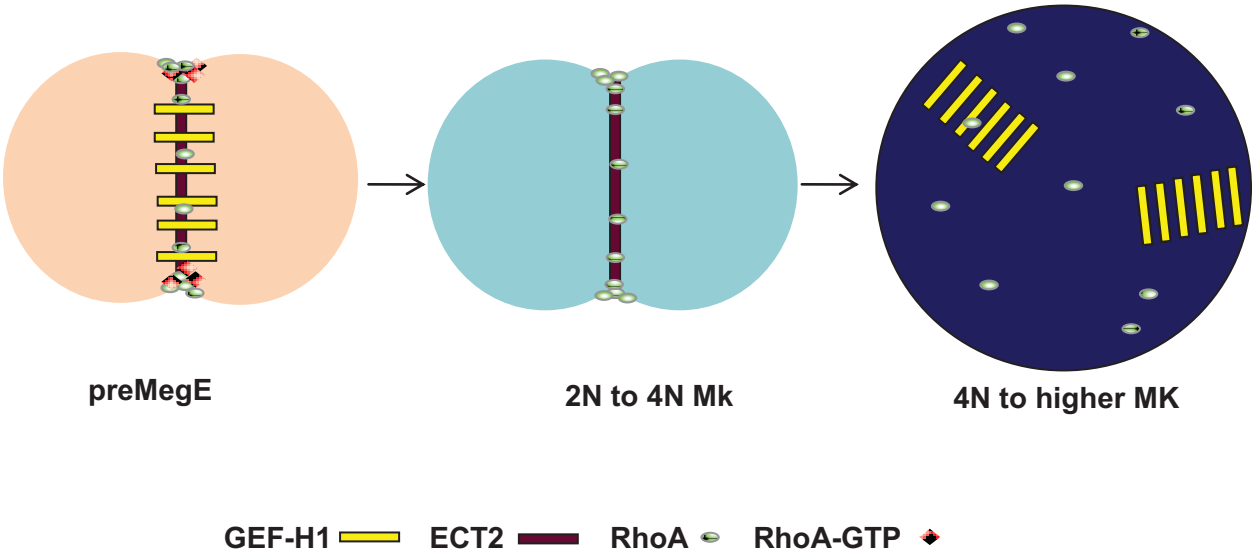

Figure S4. The schematic shows the how the lack of GEF-H1 and ECT2 acts to promote endomitosis during Mk polyploidization. In mitotic preMegE cells, ECT2 localizes to the central spindle midzone, and recruits RhoA protein to the central spindle and equatorial cortex; and GEF-H1 localizes to the central spindle and activates RhoA at the cleavage furrow. After Tpo induced differentiation, endomitotic 2N Mks have adequate ECT2 localization to the midzone, and RhoA is also localized normally. However, due to the lack of GEF-H1, most of this RhoA is inactive. In endomitosis of high ploidy Mks, although GEF-H1 is again present, since the ECT2 protein level is significantly decreased, RhoA is no longer recruited to the central spindle and equatorial cortex.

Legends for Supplemental Movies S1 and S2

Movie S1. An example of endomitosis of 2N to 4N Mk with significant cleavage furrow ingression, followed by regression with formation of a 4N cell.

Movie S2. An example of endomitosis of 4N to 8N Mk without apparent cleavage furrow formation.